REPORT DOCUMENTATION PAGE

Form Approved
OMB No. 0704-0188

1. AGENCY USE ONLY (Leave blank)	2. REPORT DATE	3. REPORT TYPE AND DATES COVERED
	February 28, 1994	Final report for 15 March 1990 to 30 September 1993

4. TITLE AND SUBTITLE
Displacive Transformation in Ceramics

5. FUNDING NUMBERS
AFOSR 90 0174
61103D
3484/CS

6. AUTHOR(S)
Professors W. M. Kriven, C. M. Wayman
Professors D. A. Payne, H. Chen, J. D. Bass

7. PERFORMING ORGANIZATION NAME(S) AND ADDRESS(ES)
University of Illinois at Urbana-Champaign
Dept. of Materials Science and Engineering
1304 West Green Street
Urbana, IL 61801

8. PERFORMING ORGANIZATION REPORT NUMBER
AFOSR-TR- 94 0151

9. SPONSORING/MONITORING AGENCY NAME(S) AND ADDRESS(ES)
AFOSR/NC, Division of Chemistry and Materials Sciences
Building 410
Bolling AFB, D.C. 20332-6448

10. SPONSORING/MONITORING AGENCY REPORT NUMBER
AFOSR 90 0174

11. SUPPLEMENTARY NOTES

12a. DISTRIBUTION/AVAILABILITY STATEMENT
Public Availability

Approved for public release;
distribution unlimited.

12b. DISTRIBUTION CODE

13. ABSTRACT *(Maximum 200 words)*

An interdisciplinary study of displacive phase transformations in ceramics has been undertaken. The unifying themes were to obtain an in-depth understanding of (i) nucleation and (ii) transformation mechanisms. The ceramic systems focused on, and studied from different perspective, included lead titanate ($PbTiO_3$), potassium niobate ($KNbO_3$), yttrium barium copper oxide ($YBa_2Cu_3O_{6+x}$) and dicalcium silicate (Ca_2SiO_4). The cubic to tetragonal transformation in $PbTiO_3$ was proven to be martensitic, and the experimental observations illustrated a predicted theoretical mechanism of common habit plane variants which had not yet been observed in any other system. Shape memory and superelasticity effects were discovered in doped $PbTiO_3$ ceramics which exhibited field-induced antiferroelectric to ferroelectric transformations. The effect of oxygen partial pressures on the transformation mechanism and microstructure in $YBa_2Cu_3O_{6+x}$ single crystals, leading to elastic deformation, has been ascertained. A comprehensive understanding of the complex sequence of ferroelastic transformations in Ca_2SiO_4 with volume changes up to 12 % has been achieved. For the first time, a case study of martensitic nucleation in a $KNbO_3$ ceramic has almost been assembled, with complementary aspects of theoretical lattice dynamics, phonon properties, (RT) elastic moduli and in situ hot stage TEM microstructural studies having been determined prior to and during transformation.

14. SUBJECT TERMS	15. NUMBER OF PAGES
Ceramics, displacive phase transformations, martensitic nucleation, precursor phenomena, elastic properties, mechanisms, crystallography, lattice dynamic theory	563
	16. PRICE CODE

17. SECURITY CLASSIFICATION OF REPORT	18. SECURITY CLASSIFICATION OF THIS PAGE	19. SECURITY CLASSIFICATION OF ABSTRACT	20. LIMITATION OF ABSTRACT
			UL

DISPLACIVE TRANSFORMATIONS IN CERAMICS

A

UNIVERSITY RESEARCH INITIATIVE PROGRAM

FINAL REPORT

Feb 28th 1994

University of Illinois at Urbana-Champaign,
Department of Materials Science and Engineering,
1304 West Green St., Urbana, IL 61801

Principle Investigators

Professors:

W. M. Kriven (Co-director)
C. M . Wayman (Co-director)
D. A. Payne
H. Chen
J. D. Bass

Table of Contents

Section 1. INTRODUCTION AND OVERALL OBJECTIVES

This URI effort has been a comprehensive interdisciplinary program of basic research on displacive, possibly martensitic phase transformations in ceramics. The objectives were:

(i) to raise the level of understanding of these mechanisms to that comparable with martensitic transformations in metal systems,

(ii) to shed more light on the phenomenon of martensitic nucleation in any solid state system, through the study of this phenomonon in ceramics.

Potential applications lie in several fields of materials science and engineering, such as in electronic ceramics or in structural damage control in ceramic-ceramic composites, both at ambient or at elevated temperatures. Some such applications are briefly described as follows.

The electrical changes accompanying transformations in perovskite-structures are well established in the electronic ceramic industries. More recently, however, ferroelastic transformations in non-perovskites which involve comparatively large volume and/or unit cell shape changes have been attracting interest as potential new types of large force actuator materials. For many of the most important needs, the inadequacy of the present solid state detectors (i.e., the small forces produced) is probably the "Archilles heel" or rate determining step in the evolution of "smart" or adaptive systems. Compared to conventional actuators, however, the forces produced by non-perovskite transformations could yield large forces which are orders of magnitude greater than those currently available. Furthermore, martensitic transformations proceed with the speed of sound and the low symmetry crystal structure changes involved offer the possibility of crystallographic reversibility, or "shape memory" behavior. While cyclic reversibility may not always be available under ambient conditions, there may still be a place for "one shot" systems, or for high temperature actuation up to 2000°C for example. Thus with a knowledge of a variety of ceramic martensitic transformations, the required forces could be tailored for a given application. Since the current state of knowledge in the identification and understanding of martensitic transformations in ceramics is still emerging and limited, this is the charge of this URI program.

In the area of structural damage control where the brittleness of ceramics is the major limitation, transformation toughening by the tetragonal to

monoclinic transformation in zirconia has been established as a viable brittleness-reducing mechanism. Toughnesses of 16 MPa $m^{1/2}$ can be achieved in yttria-stabilized zirconia (Y-ZTP) materials or of 12 M Pa $m^{1/2}$ in zirconia-toughened alumina (ZTA). In the Al_2O_3-CeO_2 doped-SrO_2-ZrO_2 microstructures developed by Ceramatec Inc., toughness values of 20 MPa $m^{1/2}$ have been obtained through a combination of transformation toughening and SrO_2 platelet bridging across Al_2O_3 grains.

However, not all ceramics are chemically unreactive with zirconia, so that other potential transformation tougheners exhibiting positive volume changes have been identified by Kriven. The lanthanide sesquioxides exhibit signs of inducing a three-fold increase in toughness in magnesia at 1150°C by transformation toughening. The temperature could possibly be higher, depending on the atomic number of the lanthanide.

By comparison, SiC fiber-reinforced SiC matrices developed in France can give toughness values up to 30 M Pa $m^{1/2}$ in vacuum. While these are impressive values for ceramics, the disadvantage of SiC ceramics is the lack of chemical stability at elevated temperatures in an oxidizing atmosphere. In the fiber pullout mechanism of toughening which is thought to be the most powerful to date in ceramics, in non-graphite coated fibers, the requisite interfacial weakening relies on thermal expansion mismatch between matrix and fiber. If such exists at room temperature it is unlikely to exist at high temperatures or vice versa.

Stress-induced martensitic phase transformations are much less dependent on thermal expansion mismatch. Furthermore, in a two phase composite the microstructure tends to remain stable and not to undergo pronounced grain growth for example.

Thus the goal of high temperature, chemically stable, tough ceramic composites has been elusive to achieve to date. An interesting concept which could lead to achieving this goal, however, is to use martensitic transformations at strategic places such as fiber-matrix interfaces to act as "transformation weakeners" of the interface. The transformation weakeners may need to have negative volume changes or large angular shape changes. The crack-tip, stress-induced transformation of the ceramic coating promotes not only fiber pullout mechanisms, but also dissipates crack energy as well as causing frictional work to be done in climbing up the fiber interface. Since toughening mechanisms are multiplicative rather than additive, a significant high temperature toughening effect may be achieved.

Section 2. OUTLINE OF RESEARCH PROGRESS

During this program, the pace of research has been steadily increasing as evidenced by the quality and number of reprints included in the appendix of this report. The strategy has been to focus on a few ceramic systems and to study them in depth from different complementary aspects. This has helped to bridge the gap across sub disciplines and hence to improve communication between the PI groups. Several subgroups have emerged consisting of various permutations and combinations of researchers.

A particularly successful joint venture was the two-day Workshop held on campus on April 2nd and 3rd in 1992. The lecture schedule and abstracts are presented in the following Section of this report. The two consultant theoreticians, Professors Armen Khachaturyan and Phil Clapp participated, as well as some faculty from the Physics and Materials Science and Department. Notably Professor Ansell Anderson, past Head of the Physics Department and his post doctoral research associate Dr. Zhu also participated in the Workshop, sharing some of their experimental and theoretical work on phonon interactions in $KNbO_3$. Professor Armen Khachaturyan introduced his new theory of martensitic nucleation by adaptive phase formation which shed a different and valuable perspective on this phenomenon. All of the URI members alike found the Workshop to be very beneficial and an opportunity to take stock of the directions and results of research progress as well as to see areas of overlap and gaps.

Since the Workshop, a $KNbO_3$ subgroup consisting of eight regularly meeting reseachers was formed with the specific aim of systematically studying or "combing through" the five phases and four consecutive transformations. The aim was to provide at least one well documentated example of the nucleation mechanism in this ceramic in the context of its crystallographic and microstructural mechanisms. Complementary expertises of neutron diffraction, elastic constant measurements, in situ transmission and hot stage optical microscopy studies, as well as theoretical martensitic analyses were successfully carried out in parallel by the different research groups. Indeed, a premonitory effect was detected before the cubic the tetragonal transformation in lead titanate both by neutron diffraction, (Chen group) elastic moduli measurements (Bass group) and in situ hot stage TEM observations (Kriven group). Theoretical calculations of the apparently martensitic

mechanism to correlate with experimental observations, are still outstanding, but are planned by the Kriven group, depending on the availability of funding.

Another unusual phase transformation has been examined, in which an additional experimental variable was introduced, viz., electric field, to induce a change in symmetry, by a field-forced transformation between antiferroelectric and ferroelectric states in $Pb(Zr,Sn,Ti)O_3$. The order parameters were now spontaneous strain ε and spontaneous polarization P. A martensitic-type formalism has been published to explain the critical field and temperature dependencies for reversible and irreversible transformations. The effects of grain size, boundary confinement and internal stresses have also been considered for fine grain polycrystalline microstructures where experimental variables now include temperature, electric field and hydrostatic pressure. Through this approach a more fundamental understanding of phase transformation behavior in ceramic systems has started to evolve, and the role of ceramic microstructure on mechanical properties was under investigation. For example, we have recently demonstrated a shape memory effect and superelastic behavior in PZST ceramics, and these new properties should find use in electromechanical actuators, adaptive structures and other smart applications.

While the exploratory search for new ceramic transformations was still underway by the Kriven group, the systems studied included the perovskites $KNbO_3$ and the non-perovskites Ca_2SiO_4, Sr_2SiO_4 and $2Ln_2O_3 \cdot Al_2O_3$ type of compounds. An in-depth understanding of the complex sequence of ferroelastic phase transformations in the Ca_2SiO_4 system has been obtained. The cubic to tetragonal transformation in $PbTiO_3$ has been quantitatively shown by the Wayman group to be martensitic. Detailed summaries of the research progress of each group are presented in each individual section.

As an indication of scientific activity and interactions it should be mentioned that Professors Wayman, Chen and Kriven are members of an eight-person committee to organize the next International Conference on Solid to Solid Phase Transformations to be held in 1994 through the Carnegie Mellon University. This series of conferences are held only every seven to ten years. The conferences have been sponsored by the NSF and various scientific societies such as the ASM. Professor Kriven is an invited overview speaker on the topic of "Displacive and Martensitic Transformations in Ceramics."

Section 3. TOTAL RESEARCH PERSONNEL

Personnel

The total personnel listed below include those who spent only part of the time working on this program.

Post doctoral research associates:

B. N. Sun	(crystal growth facility)
P. Han	(crystal growth facility)
C. C. Chou	(Wayman)
L. C. Yang	(Wayman)
I. Nettleship	(Kriven and crystal growth facility)
O. O. Popoola	(Kriven)
Y. J. Kim	(Kriven)
C. M. Huang	(Kriven)
C. S. Zha	(Bass)
A. G. Kalinichev	(Bass)
M. Kitamura	(Visiting Scientist, Chen)
J. Sariel	(Visiting Scientist, Chen)

Graduate Ph. D. students:

Ms M. Holma	(Chen)
N. Takesue	(Chen)
J. R. LaGraff	(Payne)
P. Yang	(Payne)
Y. Huang	(Payne)
Y. J. Kim	(Kriven)
B. Kim	(Wayman)

Graduate M S students:

B. Kim	(Wayman)
J. L. Shull	(NSF student Fellow, Kriven)
J. J. Cooper	(Kriven, part time)

Undergraduate senior thesis student:

R. Russell	(Kriven)

Theses completed:

- "Crystallography and Microstructural Studies of Phase Transformations in Two Ceramic Systems: Dysprosia (Dy_2O_3) and Dicalcium Silicate (Ca_2SiO_4)"
  by Youn Joong Kim., with Professor W. M. Kriven
  Ph.D. thesis submitted August 1991.

- "The Alpha to Beta and Reverse Transformation in NiS"
  by Ben Kim, with Professor C. M. Wayman
  M.S. thesis submitted May 1992.

- "Chemical Preparation and Phase Stability of Strontium Orthosilicate (Sr_2SiO_4),"
  by James Lee shull, Jr. (supported by an NSF Fellowship),
  with Professor W. M. Kriven.
  M.S. thesis submitted June 1993.

INTERDISCIPLINARY WORKSHOP

Department of Materials Science and Engineering
University Research Initiative Program
Workshop on Phase Transformations in Ceramics
2nd and 3rd April 1992
Tower Room, 4th Floor Beckman Institute

Thursday April 2nd

8.30 - 8.55am	Coffee and Donuts
8.55 - 9.00	Welcoming Comments (Profs. W. Kriven and D. Payne)
Theoretical Session	**Chairman: Prof. Marv Wayman**
9.00 - 9.50	"Adaptive Phase in Martensitic Transformations," Prof. A. G. Khachaturyan
9.50 - 10.20	Discussion
10.20 - 10.30	Break
10.30 - 11.20	"Computer Simulation of Martensitic Transformations," Prof. P. C. Clapp
11.20 - 11.45	Discussion
11.45 - 1.00	Lunch in the Beckman Cafeteria
$PbTiO_3$ Session	**Chairman: Prof. David Payne**
1.15 - 2.00 pm	"Thermal Stability of Field-Forced and Field-Assisted Antiferroelectric -Ferroelectric Phase Transformations in $Pb(Zr,Sn,Ti)O_3$," P. Yang and D. A. Payne (35 + 10)
2.00 - 2.40	"Cubic to Tetragonal Transformation and Ferroelectric Domain Structures in $PbTiO_3$," C. C. Chou and C. M. Wayman (30 + 10 mins)
	Chairman: Prof. Haydn Chen
2.40 - 3.00	"Growth and Phase Transformations of $PbTiO_3$ Crystals," B. N. Sun (15 + 5)
3.00 - 3.30	"Electronic Structure of $BaTiO_3$ and $PbTiO_3$," M. Holma and H. Chen (20 +10)
3.30 - 4.00	"Premonitory Phenomena and Transformation Kinetics from Cubic-Tetragonl Phase in $PbTiO_3$," N. Takesue and H. Chen (20 + 10)
4.00- 4.30	"The Elastic Properties of Ceramics by Brillouin Spectroscopy," J. D. Bass, C. Z. Zha and A. Kalinichev (20 + 10)
4.30 - 5.00	Discussion

Friday April 3rd 1992

8.30 - 9.00	Coffee and Donuts
$KNbO_3$ Session	**Chairman: Prof. David Payne**
9.00 - 9.20am	"Crystal growth of $KNbO_3$ by an Improved Kyropoulos Method," P. D. Han (15 + 5)
9.20 - 9.50am	"Defect Structure in $KNbO_3$," O. O. Popoola and W. M. Kriven (20 + 10)
9.50 - 10.20	"Thermal Conductivity of $KNbO_3$," Daming Zhu and A. C. Anderson (20+ 10)
10.20 - 10.50	"Temperature-Dependent Phonon Dispersion and Lattice Dynamics of $KNbO_3$," M. Holma and H. Chen (20 + 10 min)
10.50- 11.30	"Phase Transformations, Oxygen Mobility and Defect Clustering in $YBa_2Cu_3O_{6+x}$," J. R. LaGraff and D. A. Payne (30 + 10)
11.30 - 11.45	Discussion
11.45 - 1.15 pm	Lunch in the Beckman Cafeteria
Ca_2SiO_4 and NiS Session	**Chairperson: Prof. Trudy Kriven**
1.15 - 2.00	"Mechanisms of Ferroelastic Phase Transformations in Ca_2SiO_4," Y. J. Kim and W. M. Kriven (35 + 10)
2.00 - 2.20	"Phase Transformations in the Ni-S System," J. J. Cooper and W. M. Kriven (15 + 5)
2.20 - 2.40	"Deformation Behavior in NiS," B. Kim and C. M. Wayman (15 + 5)
2.40-3.30	Wrap up Discussion

Adaptive Phase in Martensitic Transformation

A. G. Khachaturyan
Department of Mechanics and Materials Science
Rutgers University
P.O. Box 909
Piscataway, NJ 08855

Abstract

An appearance of an intermediate martensite phase called adaptive martensite may be expected if the surface energy of a boundary between two orientational variants of the normal martensite phase is very low and the typical lattice mismatch-related elastic energy is high. The adaptive martensite is formed as an elastically constrained phase when the scale of structure heterogeneities induced by the crystal strain accommodation is reduced to the microscopic scale commensurate with the twin plane interplanar distance. An example of the cubic → tetragonal transformation is considered where the adaptive phase has a pseudo-orthorhombic lattice. It is shown that the $(5, \bar{2})$ 7R martensite in β' NiAl alloys and the intermediate phase recently found just above the temperature of the fcc → fct martensite transformation in Fe-Pd are examples of the adaptive martensite. A possible role of the adaptive phase in the thermal nucleation of the martensite is discussed. The nucleation of the normal martensite may be bypassed by nucleation of the adaptive phase which transforms to the normal martensite during the growth.

Computer Simulation of Martensitic Transformations* +

P. C. Clapp
Center for Materials Simulation
Institute of Materials Science
University of Connecticut
Storrs, CT 06269-3136

Abstract

Using Molecular Dynamics simulations and Embedded Atom Method potentials, coherent martensitic nucleation of the tetragonal L1o phase has been seen to occur at special heterogeneous sites of the ordered bcc B2 phase of NiAl via thermal activation in arrays of approximately 10,000 atoms. The fluctuation strain path and critical nucleation configuration have been identified, along with the contributions of coupled localized phonon modes near the nucleation site. The localized modes involved in the nucleation process are found to be much softer, and go "critical" much sooner than the bulk phonon modes. The dynamics of the atomistic processes will be illustrated through computer movies.

* Supported by the Division of Materials Science, DOE.
+ Work performed in collaboration with Y. Shao and J. A. Rifkin.

Thermal Stability of Field-Forced and Field-Assisted Antiferroelectric-Ferroelectric Phase Transformations in $Pb(Zr,Sn,Ti)O_3$

Pin Yang and David A. Payne
Department of Materials Science and Engineering
Materials Research Laboratory
and Beckman Institute
University of Illinois at Urbana-Champaign
Urbana, IL 61801

Abstract

Antiferroelectic (AFE)-ferroelectric (FE) phase transformations in tin modified lead zirconate titanate, i.e., $Pb(Zr,Sn,Ti)O_3$ or PZST. A martensite-type approach is developed to explain the observed thermal hysteresis and field-induced transformation behavior. A model is proposed with transformation fields were the forward (E_F) and reverse (E_A) field strengths are related to the transformation barrier to the ferroelectric state, and to the AFE sublattice coupling, respectively. The thermal stability of the AFE sate can therefore be determined with respect to the field-induced transformation behavior. A distinction is made between field-**forced** and field-**assisted** transformations, which depend on temperature and thermal hysteresis, and which are related to reversible and irreversible field-induced characteristics. Data are reported for polarizations and strains, and discussed with respect to the proposed thermodynamic model and device applications.

Cubic to Tetragonal Transformation and Ferroelectric Domain Structures in $PbTiO_3$

C. C. Chou and C. M. Wayman
Department of Materials Science and Engineering
University of Illinois at Urbana-Champaign
Urbana, IL 61801

Abstract

The cubic to tetragonal (C/T) phase transformation in $PbTiO_3$ single als has been studied in both the forward and reverse modes and found to show martensitic characteristics. Microstructural features were investigated by heating stage optical microscopy, and room temperature transmission electron microscopy. During transformation, a small hysteresis is involved. The phase front passes swiftly through the crystal and surface relief accompanying the transformation is seen. It is found that the habit planes vary within a certain range. Not only different specimens show this real variation, but also the same specimen under different transformations follows this, indicating the importance of local arrangements near the habit plane interfaces. Theoretical predictions, with only a minute change of lattice parameters, show that experimental data appear to fit calculated results fairly well, if one considers interfacial conditions. The results show a certain degree of consistency, which implies that the martensitic phenomenological crystallographic theory applies. Previous work on perovskite materials will be discussed.

The domain structures of poly-domain $PbTiO_3$ crystals grown by flux methods have also been studied using optical microscopy, scanning electron microscopy and transmission electron microscopy. Results of domain boundary arrangements in these crystals will be presented. 90° and 180° domain boundaries were systematically analyzed by various diffraction conditions. It is found that extreme fringes were observed to vary differently in 90° and 180° domain boundaries, indicating a basic difference between these two types of boundaries. Although it was reported that 90° domain boundaries are δ-type boundaries in $BaTiO_3$, our results show that a displacement plays an important role at boundaries in $PbTiO_3$ and the extreme fringe contrast behavior of 90° boundaries becomes mixed type. 180° domain boundaries in lead titanate crystals show intriguing extreme (outermost) fringe contrast behavior. In the present work, an analysis based upon the two beam dynamical theory was conducted and a rule similar to stacking-fault contrast analysis was established to predict the geometric configuration of a 180° domain boundary using the extreme fringe contrast (EFC) behav r. Using different diffraction vectors, the EFC of 180° domain boundaries varies. This has been exploited to determine the polarization vector arrangement at two sides of the boundary, and therefore the entire polarization configuration can be uniquely determined.

Crystal Growth and Phase Transformations of $PbTiO_3$ Crystals

B. N. Sun
Department of Materials Science and Engineering
University of Illinois at Urbana-Champaign
Urbana, IL 61801

Abstract

Pure lead titanate ($PbTiO_3$) crystals of centimeter size were grown from high-temperature solutions by RNT (reduced nucleation technique) using PbO as a self-flux. The theoretical principles leading to successful growth experiments will be discussed. Phase transformation of the grown crystals was studied by differential scanning calorimetry, X-ray diffraction, electrical measurements and optical microscopy.

Electronic Structure of $BaTiO_3$ and $PbTiO_3$

M. E. Holma and Haydn Chen
Department of Materials Science and Engineering
University of Illinois at Urbana-Champaign
Urbana, IL 61801

Abstract

Theoretical band structures are calculated for the perovskite compounds $BaTiO_3$ and $PbTiO_3$ based on the extended Hueckel tight-binding (XHTB) method. The electronic structure and total electronic energies are calculated for the cubic and tetragonal structures; the total density of states and partial density of states for individual atomic orbitals are presented. The total electronic energies, obtained by integrating over energy states of all electrons, show that the tetragonal structure is stable as compared to the cubic structure. The difference in electronic total energy between the two structures is 0.58 eV/unit cell for $BaTiO_3$. Excellent agreement exists between the calculated total density of states and experimental data of the width and structure of the valence band. The partial density of states also show good agreement with experimental data related to the valence and conduction bands. Results of the calculations for $PbTiO_3$ will be discussed.

Premonitory Phenomena and Transformation Kinetics from Cubic-Tetragonal Phase in $PbTiO_3$

Naohisa Takesue and Haydn Chen
Department of Materials Science and Engineering
University of Illinois at Urbana-Champaign
Urbana, IL 61801

Abstract

In-situ diffuse x-ray scattering techniques have been employed to study the pretransition phenomenon in $PbTiO_3$. Continuous monitoring of the (002) reflection was made as a function of temperature during heating and cooling cycles. A hysteresis is noted for the apparent cubic-to-tetragonal transition temperature (T_c = 462°C upon cooling, and T_c = 470°C during heating), typical of a first-order transformation. It was observed that diffuse intensity adjacent to the (002) peak appears above T_c because of the heterophase fluctuation of the low-temperature tetragonal phase. The kinetics of the displacive transition just below T_c during cooling was investigated. Domain redistribution was observed. Other information such as the thermal expansion coefficient and the volume change during the transformation will also be studied.

The Elastic Properties of Ceramics by Brillouin Spectroscopy

J. D. Bass, C. S. Zha, and A. Kalinichev
Department of Geology
University of Illinois at Urbana-Champaign
Urbana, IL 61801

Abstract

We have undertaken a program to measure the single-crystal elastic properties of ceramics with low crystallographic symmetry, under both ambient conditions and at high pressures and temperatures. Our goals are to determine P and T derivatives of the single crystal moduli, c_{ij}, and also to examine the behavior of acoustic phonons in the neighborhood of displacive transformations. The experimental technique utilized is Brillouin spectroscopy. This light scattering technique allows the velocities of high-frequency phonons, and thus c_{ij}'s, to be measured on very small samples of arbitrarily low crystallographic symmetry. It is amenable to high-pressure measurements using diamond anvil high-pressure cells, and high temperature work using a conventional furnace.

Thus far our efforts have concentrated on the monoclinic form of ZrO_2, and orthorhombic $KNbO_3$. Results on the elastic properties of these will be presented. We have also obtained sound velocities of M-ZrO_2 inside a diamond anvil cell. The major challenge in these measurements is to maintain close control of the crystallographic orientation of the sample, because these ceramics display, in general, strong acoustic anisotropy. A partial set of elastic moduli for zirconia in the diamond cell shows that these experimental difficulties are surmountable. Our efforts are now being directed at the high pressure moduli of zirconia, and the high temperature moduli of $KNbO_3$.

Crystal Growth of $KNbO_3$ By an Improved Kyropoulos Method

P. D. Han
Department of Materials Science and Engineering
University of Illinois at Urbana-Champaign
Urbana, IL 61801

Abstract

Large single crystals of $KNbO_3$ were grown by an improved Kyropoulos technique from a self-fluxed system. Imperfections of as-grown crystals of $KNbO_3$, such as cracks, twinning and colors will be discussed in the context of phase transformations and synthesis conditions. Two distinct types of cracks were observed in as-grown crystals resulting from phase transformations during cooling from growth temperature to room temperature (i.e., cubic to tetragonal at 435°C and tetragonal to orthorhombic at 225°C). Cracking in as-grown crystals was reduced by making the temperature gradient in the furnace as small as possible. Twins were able to be removed by a polarization process at 198°C under an applied electrical field between 400 ~ 600 V/cm.

Defect Structures in $KNbO_3$

Oludele Popoola and W. M. Kriven
Department of Materials Science and Engineering
University of Illinois at Urbana-Champaign
Urbana, IL 61801

Abstract

The atomic defects generated during growth of (001) $KNbO_3$ are characterized by transmissions electron microscopy. Apart from the single domain structure exhibited by this crystal, the microstructure consisted of various defects such as δ boundaries, stacking faults and twins. The stacking faults were readily distinguished from the inversion boundaries by the presence of threading dislocations. Theoretical predictions and experimental observations will be correlated.

Thermal Transport Properties of Some Ferroelectric Materials

Da-Ming Zhu*
Department of Physics
University of Missouri at Kansas City
Kansas City, MO 64110

Abstract

We have conducted studies of thermal transport properties of several ferroelectric materials over a wide temperature range, aimed at understanding the behavior of thermal conductivity of the materials near the ferroelectric to paraelectric phase transitions and phonon interactions with ferroelectric domain boundaries. One system which we have studied is RB_2ZnCl_4 which undergoes successive phase transitions from normal to incommensurate phase and finally to commensurate ferroelectric phases with decreasing temperature. The thermal conductivities of single crystal Rb_2ZnCl_4 were found to resemble the behavior of typical glassy materials at temperature above about 30K. At temperature below 0.5K, the thermal conductivity show characteristic of boundary diffusive scattering of phonon in crystals. The other system which we have studied is $KNbO_3$. The thermal conductivity of a single crystal $KNbO_3$ sample which contains a large number of ferroelectric domains was found to be extraordinarily small at low temperature (nearly an order of magnitude smaller than that of a typical insulating glass), a result which is consistent with phonon scattering at ferroelectric domain boundaries. The experimental data will be compared with those obtained from KDP and other ferroelectric materials, and possible connections between these results will be discussed.

* In collaboration with A. C. Anderson, Department of Physics ,University of Illinois at Urbana-Champaign.

Temperature-Dependent Phonon Dispersion and Lattice Dynamics of $KNbO_3$

M. Holma and Haydn Chen
Department of Materials Science and Engineering
University of Illinois at Urbana-Champaign
Urbana, IL 61801

Abstract

Inelastic neutron scattering measurements of the transverse and longitudinal phonon branches in the directions [100] and [110] are reported for the cubic perovskite $KNbO_3$. The results were obtained at temperatures of 878K, 798K, and 643K. The dispersion curves presented show evidence of extreme overdamped scattering in the transverse acoustic (TA) mode attributed to coupling to a diffuse excitation. The broadening of the TA mode is both temperature-dependent and highly anisotropic. The temperature dependence of the lowest frequency transverse optic has been investigated. The experimental results were used to obtain the parameters for models in the data analysis. Rigid ion, rigid shell and deformable shell models were applied to study the lattice dynamics. The results of these models, including theoretical dispersion curves, inelastic structure factors and force constants, are presented and compared with available experimental measurements.

Phase Transformations, Oxygen Mobility, and Defect Clustering in $YBa_2Cu_3O_{6+x}$

J. R. LaGraff and D. A. Payne
Department of Materials Science and Engineering
Materials Research Laboratory
Science and Technology Center for Superconductivity
University of Illinois at Urbana-Champaign
105 South Goodwin Avenue
Urbana, IL 61801

Abstract

This study reports oxygen diffusion characteristics and electrical transport properties for the high-temperature superconductor YBCO in the vicinity of the orthorhombic to tetragonal phase transformation. Combined *in-situ* electrical resistance measurements and hot-stage optical microscopy as a function of temperature (350-780°C) and oxygen partial pressure (0.001-1 atm) allowed for both oxygen diffusion behavior and phase transformation characteristics to be simultaneously monitored. The comparison of single crystal and polycrystalline data has enabled the distinction to be made between bulk diffusion characteristics and those affected by surfaces and interfaces (i.e., grain boundaries). Properties reported for intrinsic oxygen diffusion behavior, include, subtle changes in the oxygen mobility between orthorhombic and tetragonal structures; concentration-dependent chemical diffusivity, and possible interactions of oxygen ordering with mobility.

Mechanisms of Ferroelastic Phase Transformations in Ca_2SiO_4

Y. J. Kim and W. M. Kriven
Department of Materials Science and Engineering
University of Illinois at Urbana-Champaign
Urbana, IL 61801

Five polymorphs have been reported for the pure dicalcium silicate (Ca_2SiO_4)-----α, α'_H, α'_L, β and γ. From structural and microstructural characterizations of polycrystalline samples of pure Ca_2SiO_4, Ba-stabilized Ca_2SiO_4 and Ca_2SiO_4-dispersed in ceramic matrices, phase transformation mechanisms of these polymorphs were studied. The Sr_2SiO_4 and Ba_2SiO_4 systems were compared with the Ca_2SiO_4 system.

Throughout the whole transformation sequence, a symmetry element of 2/m was conserved. The $\alpha \rightarrow \alpha'_H$ (Pmcn?) transformation generated three rotation-related domains, which suggested the existence of a 6/m symmetry element for α, with a space group of $P6_3/mmc$. In this case, the $\alpha \rightarrow \alpha'_H$ transformation was ferroelastic. The $\alpha'_L \rightarrow \beta(P2_1/n)$ transformation also generated two twinned domains, (on {100} and {001}), and could also be ferroelastic.

The $\beta \rightarrow \gamma$ (Pcmn) transformation, accompanied by a large volume increase (~12%), was stress-induced. This transformation can be displacive in the sense of its instantaneous reaction. However, it is required to overcome comparatively high energy barriers due to the breaking of some oxygen bonds in the structures. The strains built into β by the previous ferroelastic transformations, as well as the strong repulsive forces between Si^{4+} and Ca^{2+} ions are suggested to be the major driving forces for the $\beta \rightarrow \gamma$ transformation.

TEM studies revealed various modulated structures in the α'_L and β phases of Ca_2SiO_4 as well as in the α' and β phases of Sr_2SiO_4. Previous studies also reported more than five different modulated structures in the Ca_2SiO_4-Ba_2SiO_4 system. The stability of crystal structures in the A_2SiO_4 type system (where A = Ca, Sr, Ba) was related to these modulated structures in conjunction with the mechanisms of phase transformations.

Phase Transformations in the Nickel Sulfide System

Jemima Cooper and W. M. Kriven
Department of Materials Science and Engineering
University of Illinois at Urbana-Champaign
Urbana, IL 61801

Abstract

A review of the literature indicates that monosulfide NiS forms three distinct phases; hexagonal α - $Ni_{1-x}S$ ($0 < x < 0.034$), rhombohedral β - $Ni_{1-x}S$ ($0 < x < 0.009$) and hexagonal γ - $Ni_{1-x}S$ ($0 < x < 0.06$). The temperature of the α → β transformation (282° C - 379° C) is dependant upon composition. The transformation is accompanied by a volume increase of ~3 vol. % (dependent upon composition). The α phase may be metastably retained at room temperature by quenching. Upon cooling, retained α phase undergoes a transition to γ NiS at ~-8° C (dependant upon composition). There is no change in symmetry upon transformation but a sudden volume increase is observed, leading to cracking of the crystals. It is possible to repeatedly cycle through the α → γ transition, and a hysteresis is observed. The α – γ NiS transition is a transition from a paramagnetic metal to an antiferromagnetic semiconductor. Substitution of Fe, As, Se alters the transition temperature.

Diffusionless Transformation in NiS

Ben Kim
Department of Materials Science and Engineering
University of Illinois at Urbana-Champaign
Urbana, IL 61801

Abstract

At room temperature, NiS (Millerite) has a rhombohedral crystal structure. Upon heating to approximately 385°C, it transforms into a new phase, which has a hexagonal crystal structure. In this project, the transformation characteristics of NiS were studied with the following experiments: hot-stage optical microscopy, hot-stage x-ray diffraction, dilatometry measurements, and electrical resistivity measurements. The hot-stage x-ray diffraction patterns confirmed the structural change at approximately 385°C. This change of crystal structure was observed as surface relief with the aid of hot-stage optical microscope. Moreover, the surface relief observed with the hot-stage optical microscope resembled that of typical martensites found in *metals and ceramics*. Both the dilatometry and resistivity measurements revealed a large hysterisis, spanning a temperature range of approximately 225°C. Also, from the dilatometry measurements, the volume change associated with the transformation was calculated to be approximately 4.6%. Through the resistivity measurements and hot-stage optical microscopy, it was seen that the transformation was a function of temperature rather than time. Furthermore, the hot-stage x-ray diffraction results illustrated indirectly that there was no compositional change during the transformation. All experiments performed to date on NiS strongly indicate a diffusionless transformation in NiS.

Department of Materials Science and Engineering
University Research Initiative Program
Workshop on Phase Transformations in Ceramics
2nd and 3rd April 1992
Tower Room, 4th Floor Beckman Institute

Thursday April 2nd

8.30 - 8.55am	Coffee and Donuts
8.55 - 9.00	Welcoming Comments (Profs. W. Kriven and D. Payne)
Theoretical Session	**Chairman: Prof. Marv Wayman**
9.00 - 9.50	"Adaptive Phase in Martensitic Transformations," Prof. A. G. Khachaturyan
9.50 - 10.20	Discussion
10.20 - 10.30	Break
10.30 - 11.20	"Computer Simulation of Martensitic Transformations," Prof. P. C. Clapp
11.20 - 11.45	Discussion
11.45 - 1.00	Lunch in the Beckman Cafeteria
$PbTiO_3$ Session	**Chairman: Prof. David Payne**
1.15 - 2.00 pm	"Thermal Stability of Field-Forced and Field-Assisted Antiferroelectric -Ferroelectric Phase Transformations in $Pb(Zr,Sn,Ti)O_3$," P. Yang and D. A. Payne (35 + 10)
2.00 - 2.40	"Cubic to Tetragonal Transformation and Ferroelectric Domain Structures in $PbTiO_3$,"C. C. Chou and C. M. Wayman (30 + 10 mins)
	Chairman: Prof. Haydn Chen
2.40 - 3.00	"Growth and Phase Transformations of $PbTiO_3$ Crystals," B. N. Sun (15 + 5)
3.00 - 3.30	"Electronic Structure of $BaTiO_3$ and $PbTiO_3$," M. Holma and H. Chen (20 +10)
3.30 - 4.00	"Premonitory Phenomena and Transformation Kinetics from Cubic-Tetragonl Phase in $PbTiO_3$,"N. Takesue and H. Chen (20 + 10)
4.00- 4.30	"The Elastic Properties of Ceramics by Brillouin Spectroscopy," J. D. Bass, C. Z. Zha and A. Kalinichev (20 + 10)
4.30 - 5.00	Discussion

Friday April 3rd 1992

8.30 - 9.00	Coffee and Donuts
$KNbO_3$ Session	**Chairman: Prof. David Payne**
9.00 - 9.20am	"Crystal growth of $KNbO_3$ by an Improved Kyropoulos Method," P. D. Han (15 + 5)
9.20 - 9.50am	"Defect Structure in $KNbO_3$," O. O. Popoola and W. M. Kriven (20 + 10)
9.50 - 10.20	"Thermal Conductivity of $KNbO_3$," Daming Zhu and A. C. Anderson (20+ 10)
10.20 - 10.50	"Temperature-Dependent Phonon Dispersion and Lattice Dynamics of $KNbO_3$," M. Holma and H. Chen (20 + 10 min)
10.50- 11.30	"Phase Transformations, Oxygen Mobility and Defect Clustering in $YBa_2Cu_3O_{6+x}$," J. R. LaGraff and D. A. Payne (30 + 10)
11.30 - 11.45	Discussion
11.45 - 1.15 pm	Lunch in the Beckman Cafeteria
Ca_2SiO_4 and NiS Session	**Chairperson: Prof. Trudy Kriven**
1.15 - 2.00	"Mechanisms of Ferroelastic Phase Transformations in Ca_2SiO_4," Y. J. Kim and W. M. Kriven (35 + 10)
2.00 - 2.20	"Phase Transformations in the Ni-S System," J. J. Cooper and W. M. Kriven (15 + 5)
2.20 - 2.40	"Deformation Behavior in NiS," B. Kim and C. M. Wayman (15 + 5)
2.40-3.30	Wrap up Discussion

Mechanisms of Ferroelastic Phase Transformations in Ca_2SiO_4

Y. J. Kim and W. M. Kriven
Department of Materials Science and Engineering
University of Illinois at Urbana-Champaign
Urbana, IL 61801

Five polymorphs have been reported for the pure dicalcium silicate (Ca_2SiO_4)-----α, α'_H, α'_L, β and γ. From structural and microstructural characterizations of polycrystalline samples of pure Ca_2SiO_4, Ba-stabilized Ca_2SiO_4 and Ca_2SiO_4-dispersed in ceramic matrices, phase transformation mechanisms of these polymorphs were studied. The Sr_2SiO_4 and Ba_2SiO_4 systems were compared with the Ca_2SiO_4 system.

Throughout the whole transformation sequence, a symmetry element of 2/m was conserved. The $\alpha \rightarrow \alpha'_H$ (Pmcn?) transformation generated three rotation-related domains, which suggested the existence of a 6/m symmetry element for α, with a space group of $P6_3/mmc$. In this case, the $\alpha \rightarrow \alpha'_H$ transformation was ferroelastic. The $\alpha'_L \rightarrow \beta(P2_1/n)$ transformation also generated two twinned domains, (on {100} and {001}), and could also be ferroelastic.

The $\beta \rightarrow \gamma$ (Pcmn) transformation, accompanied by a large volume increase (~12%), was stress-induced. This transformation can be displacive in the sense of its instantaneous reaction. However, it is required to overcome comparatively high energy barriers due to the breaking of some oxygen bonds in the structures. The strains built into β by the previous ferroelastic transformations, as well as the strong repulsive forces between Si^{4+} and Ca^{2+} ions are suggested to be the major driving forces for the $\beta \rightarrow \gamma$ transformation.

TEM studies revealed various modulated structures in the α'_L and β phases of Ca_2SiO_4 as well as in the α' and β phases of Sr_2SiO_4. Previous studies also reported more than five different modulated structures in the Ca_2SiO_4-Ba_2SiO_4 system. The stability of crystal structures in the A_2SiO_4 type system (where A = Ca, Sr, Ba) was related to these modulated structures in conjunction with the mechanisms of phase transformations.

Mechanisms of Ferroelastic Phase Transformations in Ca_2SiO_4

Y. J. Kim and W. M. Kriven
Department of Materials Science and Engineering
University of Illinois at Urbana-Champaign
Urbana, IL 61801

Five polymorphs have been reported for the pure dicalcium silicate (Ca_2SiO_4)-----α, α'_H, α'_L, β and γ. From structural and microstructural characterizations of polycrystalline samples of pure Ca_2SiO_4, Ba-stabilized Ca_2SiO_4 and Ca_2SiO_4-dispersed in ceramic matrices, phase transformation mechanisms of these polymorphs were studied. The Sr_2SiO_4 and Ba_2SiO_4 systems were compared with the Ca_2SiO_4 system.

Throughout the whole transformation sequence, a symmetry element of 2/m was conserved. The $\alpha \rightarrow \alpha'_H$ (Pmcn?) transformation generated three rotation-related domains, which suggested the existence of a 6/m symmetry element for α, with a space group of $P6_3/mmc$. In this case, the $\alpha \rightarrow \alpha'_H$ transformation was ferroelastic. The $\alpha'_L \rightarrow \beta(P2_1/n)$ transformation also generated two twinned domains, (on {100} and {001}), and could also be ferroelastic.

The $\beta \rightarrow \gamma$ (Pcmn) transformation, accompanied by a large volume increase (~12%), was stress-induced. This transformation can be displacive in the sense of its instantaneous reaction. However, it is required to overcome comparatively high energy barriers due to the breaking of some oxygen bonds in the structures. The strains built into β by the previous ferroelastic transformations, as well as the strong repulsive forces between Si^{4+} and Ca^{2+} ions are suggested to be the major driving forces for the $\beta \rightarrow \gamma$ transformation.

TEM studies revealed various modulated structures in the α'_L and β phases of Ca_2SiO_4 as well as in the α' and β phases of Sr_2SiO_4. Previous studies also reported more than five different modulated structures in the Ca_2SiO_4-Ba_2SiO_4 system. The stability of crystal structures in the A_2SiO_4 type system (where A = Ca, Sr, Ba) was related to these modulated structures in conjunction with the mechanisms of phase transformations.

Mechanisms of Ferroelastic Phase Transformations in Ca_2SiO_4

Y. J. Kim and W. M. Kriven
Department of Materials Science and Engineering
University of Illinois at Urbana-Champaign
Urbana, IL 61801

Five polymorphs have been reported for the pure dicalcium silicate (Ca_2SiO_4)-----α, α'_H, α'_L, β and γ. From structural and microstructural characterizations of polycrystalline samples of pure Ca_2SiO_4, Ba-stabilized Ca_2SiO_4 and Ca_2SiO_4-dispersed in ceramic matrices, phase transformation mechanisms of these polymorphs were studied. The Sr_2SiO_4 and Ba_2SiO_4 systems were compared with the Ca_2SiO_4 system.

Throughout the whole transformation sequence, a symmetry element of 2/m was conserved. The $\alpha \rightarrow \alpha'_H$ (Pmcn?) transformation generated three rotation-related domains, which suggested the existence of a 6/m symmetry element for α, with a space group of $P6_3/mmc$. In this case, the $\alpha \rightarrow \alpha'_H$ transformation was ferroelastic. The $\alpha'_L \rightarrow \beta(P2_1/n)$ transformation also generated two twinned domains, (on {100} and {001}), and could also be ferroelastic.

The $\beta \rightarrow \gamma$ (Pcmn) transformation, accompanied by a large volume increase (~12%), was stress-induced. This transformation can be displacive in the sense of its instantaneous reaction. However, it is required to overcome comparatively high energy barriers due to the breaking of some oxygen bonds in the structures. The strains built into β by the previous ferroelastic transformations, as well as the strong repulsive forces between Si^{4+} and Ca^{2+} ions are suggested to be the major driving forces for the $\beta \rightarrow \gamma$ transformation.

TEM studies revealed various modulated structures in the α'_L and β phases of Ca_2SiO_4 as well as in the α' and β phases of Sr_2SiO_4. Previous studies also reported more than five different modulated structures in the Ca_2SiO_4-Ba_2SiO_4 system. The stability of crystal structures in the A_2SiO_4 type system (where A = Ca, Sr, Ba) was related to these modulated structures in conjunction with the mechanisms of phase transformations.

Mechanisms of Ferroelastic Phase Transformations in Ca_2SiO_4

Y. J. Kim and W. M. Kriven
Department of Materials Science and Engineering
University of Illinois at Urbana-Champaign
Urbana, IL 61801

Five polymorphs have been reported for the pure dicalcium silicate (Ca_2SiO_4)-----α, α'_H, α'_L, β and γ. From structural and microstructural characterizations of polycrystalline samples of pure Ca_2SiO_4, Ba-stabilized Ca_2SiO_4 and Ca_2SiO_4-dispersed in ceramic matrices, phase transformation mechanisms of these polymorphs were studied. The Sr_2SiO_4 and Ba_2SiO_4 systems were compared with the Ca_2SiO_4 system.

Throughout the whole transformation sequence, a symmetry element of 2/m was conserved. The $\alpha \rightarrow \alpha'_H$ (Pmcn?) transformation generated three rotation-related domains, which suggested the existence of a 6/m symmetry element for α, with a space group of $P6_3/mmc$. In this case, the $\alpha \rightarrow \alpha'_H$ transformation was ferroelastic. The $\alpha'_L \rightarrow \beta(P2_1/n)$ transformation also generated two twinned domains, (on {100} and {001}), and could also be ferroelastic.

The $\beta \rightarrow \gamma$ (Pcmn) transformation, accompanied by a large volume increase (~12%), was stress-induced. This transformation can be displacive in the sense of its instantaneous reaction. However, it is required to overcome comparatively high energy barriers due to the breaking of some oxygen bonds in the structures. The strains built into β by the previous ferroelastic transformations, as well as the strong repulsive forces between Si^{4+} and Ca^{2+} ions are suggested to be the major driving forces for the $\beta \rightarrow \gamma$ transformation.

TEM studies revealed various modulated structures in the α'_L and β phases of Ca_2SiO_4 as well as in the α' and β phases of Sr_2SiO_4. Previous studies also reported more than five different modulated structures in the Ca_2SiO_4-Ba_2SiO_4 system. The stability of crystal structures in the A_2SiO_4 type system (where A = Ca, Sr, Ba) was related to these modulated structures in conjunction with the mechanisms of phase transformations.

Mechanisms of Ferroelastic Phase Transformations in Ca_2SiO_4

Y. J. Kim and W. M. Kriven
Department of Materials Science and Engineering
University of Illinois at Urbana-Champaign
Urbana, IL 61801

Five polymorphs have been reported for the pure dicalcium silicate (Ca_2SiO_4)-----α, α'_H, α'_L, β and γ. From structural and microstructural characterizations of polycrystalline samples of pure Ca_2SiO_4, Ba-stabilized Ca_2SiO_4 and Ca_2SiO_4-dispersed in ceramic matrices, phase transformation mechanisms of these polymorphs were studied. The Sr_2SiO_4 and Ba_2SiO_4 systems were compared with the Ca_2SiO_4 system.

Throughout the whole transformation sequence, a symmetry element of 2/m was conserved. The $\alpha \rightarrow \alpha'_H$ (Pmcn?) transformation generated three rotation-related domains, which suggested the existence of a 6/m symmetry element for α, with a space group of $P6_3/mmc$. In this case, the $\alpha \rightarrow \alpha'_H$ transformation was ferroelastic. The $\alpha'_L \rightarrow \beta(P2_1/n)$ transformation also generated two twinned domains, (on {100} and {001}), and could also be ferroelastic.

The $\beta \rightarrow \gamma$ (Pcmn) transformation, accompanied by a large volume increase (~12%), was stress-induced. This transformation can be displacive in the sense of its instantaneous reaction. However, it is required to overcome comparatively high energy barriers due to the breaking of some oxygen bonds in the structures. The strains built into β by the previous ferroelastic transformations, as well as the strong repulsive forces between Si^{4+} and Ca^{2+} ions are suggested to be the major driving forces for the $\beta \rightarrow \gamma$ transformation.

TEM studies revealed various modulated structures in the α'_L and β phases of Ca_2SiO_4 as well as in the α' and β phases of Sr_2SiO_4. Previous studies also reported more than five different modulated structures in the Ca_2SiO_4-Ba_2SiO_4 system. The stability of crystal structures in the A_2SiO_4 type system (where A = Ca, Sr, Ba) was related to these modulated structures in conjunction with the mechanisms of phase transformations.

PROFESSOR J. D. BASS

Final Report to the AFOSR
Elastic Properties of Ceramics Under Extreme Conditions

Jay D. Bass

A. Work Statement and Objectives

The basic objectives of this research effort were threefold: First, to obtain high-quality measurements of the single-crystal stiffness constants (elastic moduli, c_{ij}) of ceramic materials which undergo displacive transformations; Second, to develop the methods and equipment needed to carry out elasticity measurements at high pressures and at high temperatures, and to characterize the elasticity of ceramics at high P and T , especially in the vicinity of phase transitions. Such measurements of material properties are needed for theories of the nucleation of phase transitions in ceramics to be evaluated and tested. In particular, a common hypothesis for the mechanism of displacive phase transformations is the 'soft mode' concept, in which a phonon mode softens, or tends to zero frequency, as a precursor to nucleation of the product phase. For phase transitions which are triggered by stress, such as the tetragonal to monoclinic transition in ZrO_2, a soft mode would likely be apparent in the elastic moduli. In order to test the soft mode theory of nucleation, and to understand the role of stress in triggering phase transformations, we have initiated a research program to measure the elastic moduli of microscopic-sized ceramic single crystals at high pressure and temperature using the light scattering technique of Brillouin spectroscopy. An accurate and complete characterization of the single crystal moduli has never been reported on low symmetry samples such as many ceramics of technological importance. Our objectives included development of hardware and calculational procedures necessary to carry out such experiments, and measurements of the elastic properties of ZrO_2, $KNbO_3$, and $PbTiO_3$, all of which undergo displacive transformations and are being studied in detail by various members of the URI team.

B. Status of Research Effort.

Crystalline Ceramics

The thrust of this research has been to investigate the elastic properties of ceramics that undergo displacive phase transitions as a means toward understanding nucleation mechanisms, as well as changes in physical, electronic, and optical properties. Our efforts have concentrated on the monoclinic form of zirconia M-ZrO_2, tetragonal $PbTiO_3$, and orthorhombic $KNbO_3$. For M-ZrO_2 we have thus far measured the single-crystal elastic moduli under ambient conditions, and obtained a partial set of elastic moduli in a diamond anvil cell as a first test of our high pressure capability (Figures 1 and 2). To date, only one experimental study of the c_{ij} of M-ZrO_2 has been reported, and for many moduli the results of that study were in poor agreement with those of theoretical calculations. A conspicuous discrepancy was found not only in the magnitude, but in the sign of some shear moduli (Table 1). The results of our measurements are in very good agreement with the theoretical study, and there are no discrepancies in sign for any of the

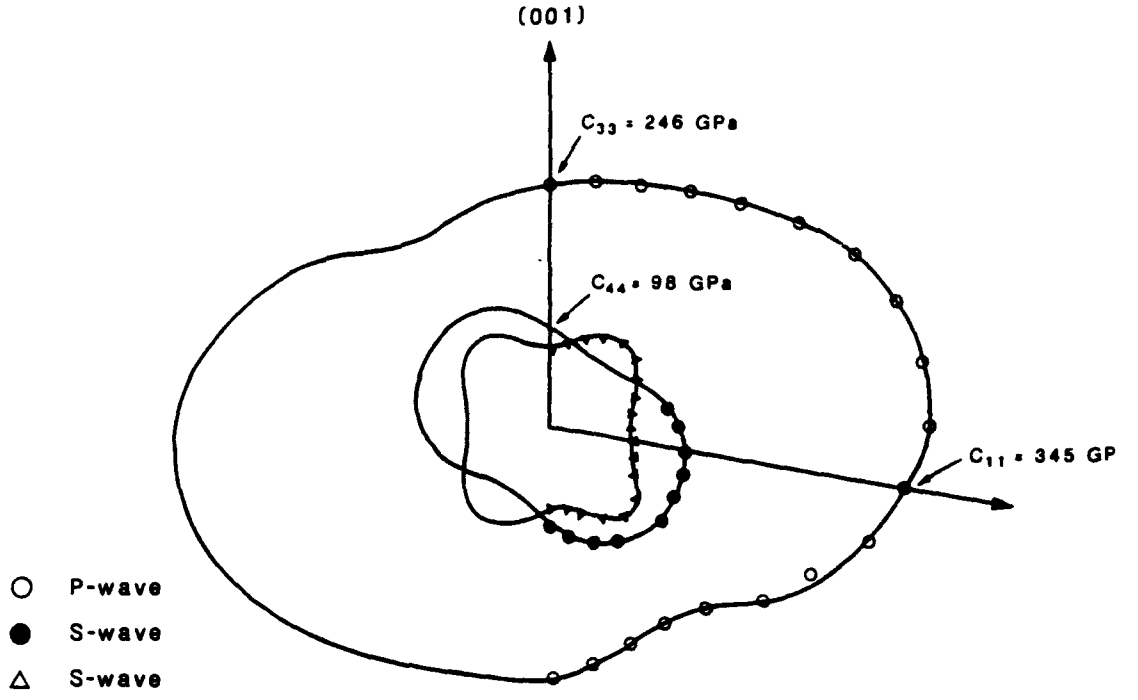

Figure 1: Elastic moduli of M-ZrO_2 as a function of crystallographic direction in the a-c crystallographic plane, as measured in this study by Brillouin scattering measurements. Moduli increase radially outward with distance from the center. The elastic anisotropy of the crystal is apparent in this projection. Both the longitudinal and two shear modes are shown.

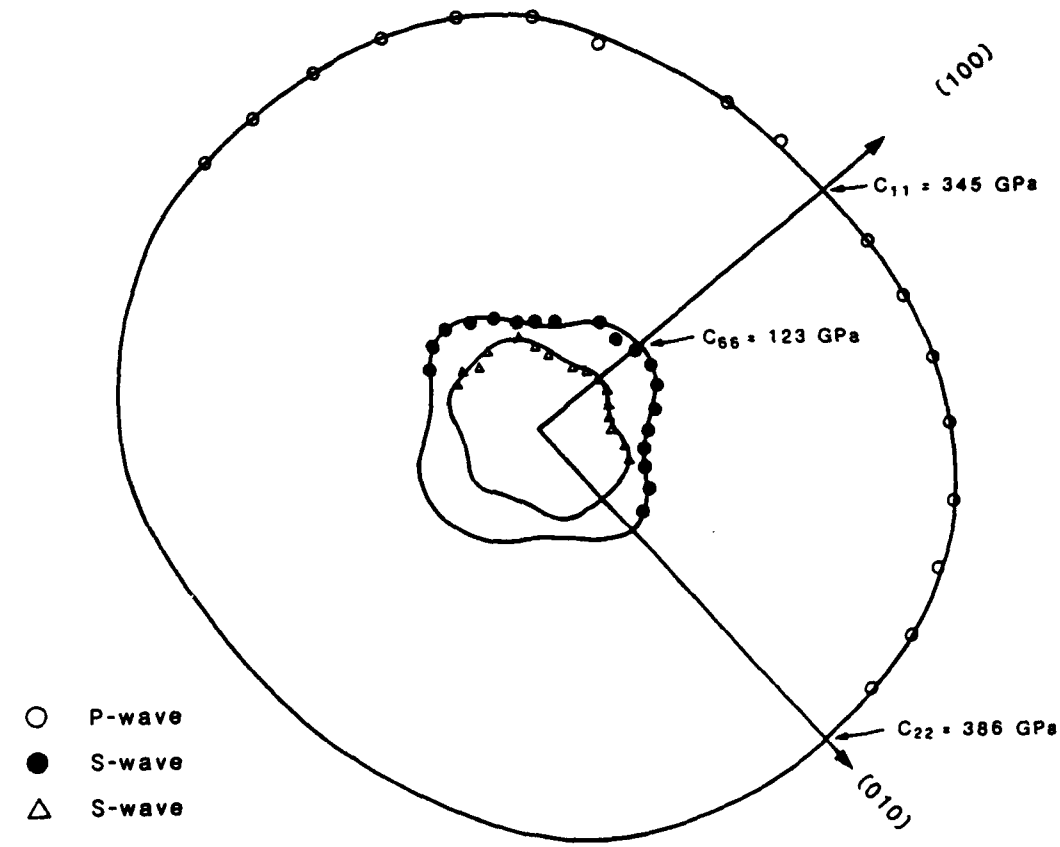

Figure 2: Elastic moduli of M-ZrO_2 as a function of crystallographic direction in the a-b crystallographic plane, measured in a diamond-anvil pressure cell (DAC). There is no pressure on the sample. This figure shows that an internally consistent set of measurements is obtained, in agreement with measurements outside of the DAC.

Table 1.

Single Crystal Elastic Moduli of Monoclinic ZrO_2

Modulus (GPa)	Measured: This Study[a]	Measured: Nevitt et al. (1988)	Calculated: Cohen et al. (1988)
C_{11}	350.5±2.3	358 ±45	349
C_{22}	385.6±4.2	426 ±11	398
C_{33}	245.3±2.5	240 ±28	268
C_{44}	101.0±4.8	99 ± 2	147
C_{55}	80.0±1.1	79 ±10	131
C_{66}	123.1±1.8	130 ± 2	180
C_{12}	176.7±3.9	144 ±29	207
C_{13}	74.9±3.1	67 ±64	125
C_{23}	163.1±5.0	127 ±25	153
C_{15}	30.5±1.7	-26 ± 5	64
C_{25}	-5.7±3.9	38 ± 8	-27
C_{35}	9.7±1.5	-23 ± 4	57
C_{46}	-20.0±2.8	-39 ±10	-26

[a] Based upon 102 velocity measurements in 37 directions. RMS error = 83 m/s.

[b] Based upon 50 velocity measurements in 13 directions.

moduli. This indicates that the interatomic potentials used in the calculations are fairly realistic.

We have examined the optical absorption spectum of $PbTiO_3$ as a function of pressure up to 30 GPa. Because the absorption spectrum is sensitive to the energy of electronic transitions in a material, these measurements help place constraints on, and are a natural compliment to, the theoretical band structure calculations of Hayden Chen's group. The transition from a ferroelectric to paraelectric phase, identified previously at 12.1 GPa on the basis of the Raman spectra, is evident in the absorption spectrum as well. Our experiments indicate that the tetragonal-cubic transition is second order. Because the transition seems to be first order at one atmosphere and high temperatures, we expect the existence of a tricritical point at an intermediate P and T. This range of conditions is accessible with an externally heated diamond anvil cell, and experiments to determine the location of this tricritical point will be pursued.

$KNbO_3$ undergoes a series of displacive phase transformations to successively higher symmetry. As a compliment to the investigation of precursory phenomena near the transition temperatures by neutron diffraction (Hayden Chen), we are characterizing the elastic moduli of $KNbO_3$. A paper describing the results of our ambient condition experiments has been published in *Journal of Applied Physics* . These results represent the first report of the complete set of elastic moduli on $KNbO_3$. Because Brillouin scattering is a higher frequency experiment than is neutron diffraction, a combination of our data with that of Hayden Chen will give a very complete description of the dispersion curves for acoustic phonons in $KNbO_3$, thus providing a wealth of information on the nature of the phase transitions. The high-temperature measurements needed to understand the phase transitions are in progress.

We have also completed a study of the STP elastic properties of $PbTiO_3$, one of the most thoroughly studied polar ceramics. Due to the difficulty of obtaining suitable samples for single-crystal studies, the elastic, piezoelectric, and dielectric properties have been poorly characterized thus far, and the results reported in the literature to date are quite contradictory.

Our data on the acoustic velocities in $PbTiO_3$ are shown in Fig. 3 along with a theoretical fit to the measurements. The elastic, piezoelectric, and dielectric constants obtained from this theoretical fit are given in Table 2, along with literature data for 'single crystal' and ceramic samples for comparison. Our data differ from previous results by as much as 50% to 300% for some moduli. Older results are plagued by problems due to sample porosity, twinning, and impurities. The present Brillouin data yield a very high degree of internal consistency and are, we believe, the most accurate results to date.

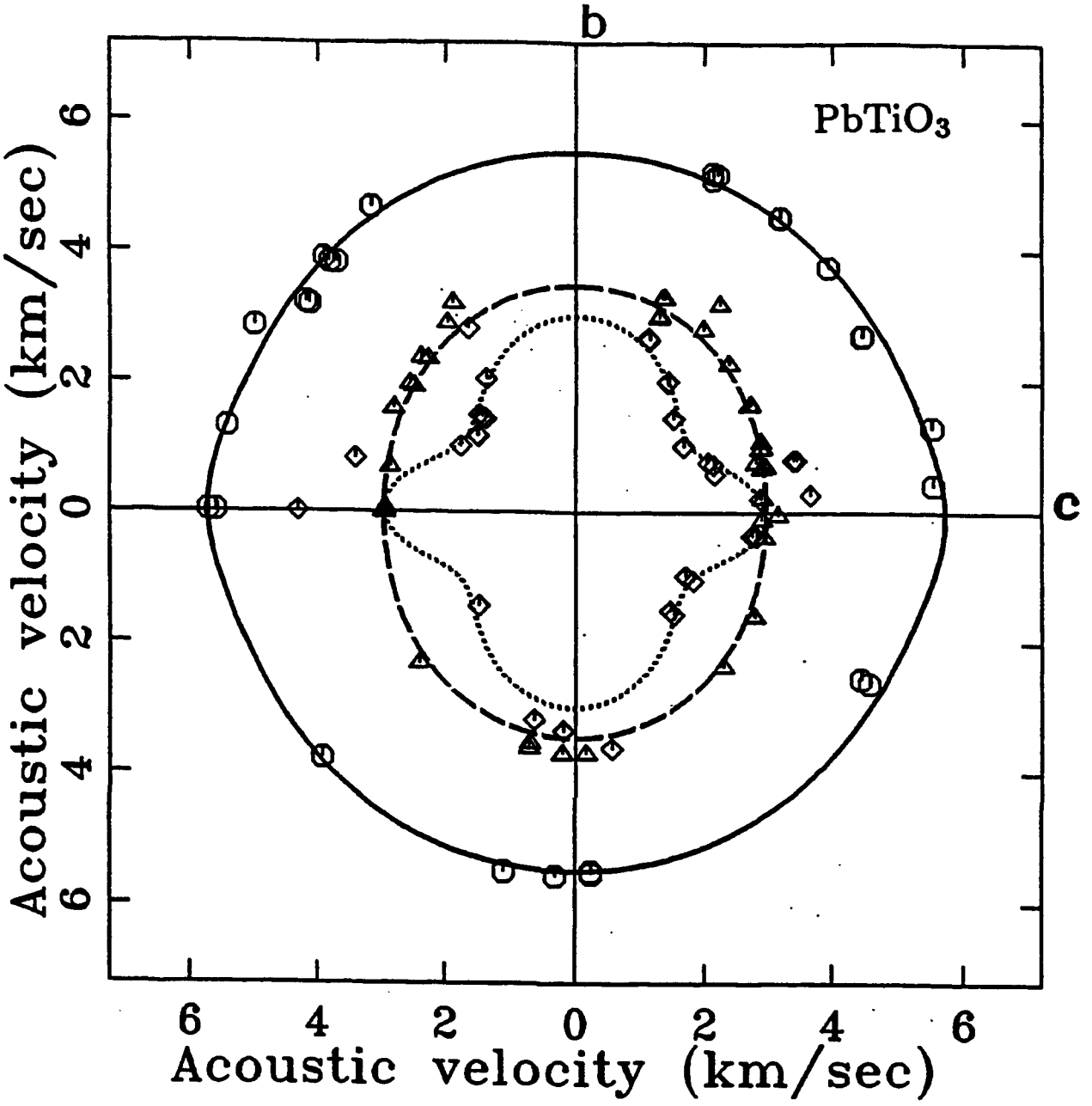

Fig. 3. Sound velocities in the b-c crystallographic plane. Best fit using the reported set of the elastic and piezoelectric constants. Symbols — experimental data, full line — compressional wave; dashed and dotted lines — shear waves polarized nearly prependicular and parallel to the plane, respectively.

Table 2. **Elastic, piezoelectric, and dielectric constants of $PbTiO_3$ at room temperature.**

	This study	Literature
	Elastic stiffness constants (GPa)	
C_{11}^E	241	160[a]
C_{33}^E	68	152[a]
C_{44}^E	70	63[a]
C_{66}^E	96	
C_{12}^E	112	42[a]
C_{13}^E	52	46[a]
	Elastic compliance constants (10^{-3}/GPa)	
S_{11}^E	0.585	0.72[b] 0.75[c]
S_{33}^E	1.889	3.25[b] 0.80[c]
S_{44}^E	1.425	1.22[b] 1.79[c]
S_{66}^E	1.043	0.79[b] 1.80[c]
S_{12}^E	-0.228	-0.21[b] -0.15[c]
S_{13}^E	-0.272	-0.11[c]
	Piezoelectric strain constants (10^{-11} C/N)	
d_{15}	1.74	0.65[b] 5.3[c]
d_{31}	-2.6	-0.25[b] -0.44[c]
d_{33}	-3.0	1.2[b] 5.1[c]
	Piezoelectric stress constants (C/m^2)	
e_{15}	1.22	3.55[a] 0.50[c]
e_{31}	-10.9	1.32[a] 6.50[c]
e_{33}	-4.74	6.80[a] 3.00[c]
	Dielectric constants	
ϵ_{11}^T	102[e]	130[d] 210[b] 230[a]
ϵ_{33}^T	93[e]	120[d] 126[b] 170[a]
ϵ_{11}^S	100	100[d] 115[b] 210[a]
ϵ_{33}^S	13[e]	35[d] 51[b] 140[a]

[a] Ceramics, 2.5mol%La_2O_3, 1.0mol%MnO_2, Ref.1.
[b] Single crystal, Ref.2.
[c] Ceramics, 1.25mol%La_2O_3, 1.0mol%MnO_2, Ref.3.
[d] Single crystal high frequency measurements, Ref.4.
[e] Calculated using our Brillouin data.

Facilities Development: High Pressure-Temperature Facilities

We have constructed several types of equipment needed to carry out our research objectives. A diamond anvil high pressure cell for Brillouin spectroscopic measurements was specially designed and built at the University of Illinois to measure the pressure derivatives of elastic moduli. In order to characterize the pressure exerted on a sample we use the pressure dependence of the fluorescence spectrum of ruby (Cr doped Al_2O_3), and a spectrometer integrated with an optical microscope was built to measure fluorescence spectra. This same spectrometer can be used to measure the visible absorption spectrum of samples under pressure, and this has proved a convenient method for identifying the onset of high pressure phase transitions. Ancillary equipment that has been developed and built in-house includes a diamond faceting instrument for grinding faces that are exactly parallel on the diamond anvils, as well as for repair of anvils, and a microdrilling machine for making microscopic holes (as small as 50 μm) in the steel gaskets used between the diamond anvils.

Preliminary Investigations on Simple Systems

Our program into high pressure and temperature brillouin spectroscopy represents a novel research direction with equipment designed and built in-house, and many experimental techniques needed to be developed by our group. As mentioned above we have completed a study of the high pressure optical properties of $PbTiO_3$ and initiated a study of the moduli of zirconia at high pressure. However, it is necessary to perform a series of initial experiments on simple systems so that we can compare our results with independent studies of other properties.

We have undertaken a study of a high pressure phase transition in potassium bromide, KBr. This material is an ideal candidate for initial high pressure work because it is known to undergo a major structural phase transition at about 1.8 GPa, and it is also a simple ionic solid which is amenable to theoretical modeling of physical properties. We have been successful in measuring the sound velocities in KBr up to about 10 GPa, well above the phase transition. These experiments were performed on a polycrystalline sample compressed in the diamond anvil cell. We have found, as expected, a pronounced increase in the elastic properties at the transition to the high pressure B2 phase at 1.8 GPa (Figure 3). This study is important for demonstrating the accuracy of our pressure measuring apparatus, the suitability of Brillouin scattering for measuring elastic moduli at high pressures in a diamond cell, and the feasibility of working with polycrystalline samples at high-pressure conditions.

As a first material to be investigated at high temperatures, we chose a series of silicate glasses. The reason for choosing glasses as the first high temperature samples is that they are elastically isotropic. Therefore, it is not necessary to carry out the involved crystallographic orientation work required of crystalline samples. In addition to being of great interest to ceramists, these experiments allow us to

assess our ability to make high temperature measurements. We have obtained data on sodium and potassium silicate glasses and melts to temperatures of 1200°C. Melting of the samples was apparent from disappearance of the shear mode, and an analysis of the Brillouin lineshape has yielded information on the viscosity and atomic structure of the melt. On the basis of our experience with glasses and melts we have redesigned our high temperature furnace for operation to 1600°C under a controlled atmosphere and with crystalline samples. In addition, the computer programs developed to analyse the melt data will be used to investigate ultrasonic attenuation in the neighborhood of phase transitions in crystalline ceramics. The experiments on an elastically simple system such as melts was a necessary and natural part of developing the capability to do high temperature experimentation and fulfill the major objectives of this program.

Summary of Research Effort

In conclusion, we have thus far carried out research in the following areas:
Design and construction of equipment for high pressure elasticity using diamond anvil cells, and for high temperature work.
Elastic properties of single crystal ZrO_2, $KNbO_3$, and $PbTiO_3$ under ambient conditions and at high pressures.
Optical absorption and phase transitions of $PbTiO_3$ at high pressures.
Elasticity and structure of silicate glasses and melts.

D. Publications

Published and In Press

Masnik, J. E., J. Kieffer, and J. D. Bass, Structural relaxations in the GHz frequency range in glass forming silicate melts, *Materials Research Soc. Symp. Proc.*, vol. 248, 505-510, (1992).

Zha, C. S., A. Kalinichev, J. D. Bass, C. T. A. Suchital, and D. A. Payne, Pressure dependence of optical absorption in $PbTiO_3$ to 35 GPa: Observation of the tetragonal to cubic phase transition, *J. Appl. Phys.*, 72, 3705-3707, 1992.

A. G. Kalinichev, J. D. Bass, C. S. Zha, P. O. Han, and D. A. Payne, Elastic properties of orthorhombic $KNbO_3$ single crystals by Brillouin scattering, *J. Appl. Phys.*, 74, 6603-6608, 1993.

In Preparation

The Elastic Properties of Monoclinic Zirconia, for submission to the Journal of the American Ceramic Society, J. D. Bass, C. S. Zha, and P. D. Han.

Elasticity of the B1-B2 High Pressure Phase Transition in KBr, for submission to Physical Review B, J. D. Bass and C. S. Zha.

E. Interactions

Papers Presented at Meetings

High-Frequency Relaxational Spectroscopy in Liquid Alkalai-Silicate Systems, J. E. Maznik, J. Kieffer, and J. D. Bass, 93rd Annual Meeting of the American Ceramic Society, Cincinnati, Ohio, April 28 - May 2, 1991.

Structural Relaxations in the GHz Frequency Range in Glass Forming Silicate Melts, Fall Meeting of the Materials Research Society, Boston, Mass. Dec. 2-6, 1991.

Brillouin Scattering Measurements of Structural Relaxations in High-Temperature Silicate Systems, J. E. Maznik, J. Kieffer, and J. D. Bass, Spring Meeting of the American Geophysical Union, Montreal, Canada, May 12-16, 1992.

Personnel Associated with the Project

Dr. C. S. Zha, Postdoctoral Research Associate, 1/91-6/92.

Dr. A. Kalinichev, Postdoctoral Research Associate, 2/92 - 9/93.

PROFESSOR H. CHEN

AFOSR URI FINAL REPORT
(Haydn Chen)

(a) Objectives:

The overall objective of this work is to achieve a fundamental understanding of the transformation mechanism(s) governing and the crystallography associated with the displacive transformations in ceramic systems with special emphasis placed upon the perovskite group (e.g. $PbTiO_3$ and $KNbO_3$). Some specific themes are:
(1) Pre-transitional phenomena associate with the paraelectric-to-ferroelectric transitions,
(2) Phonon properties associated with the transformations, and
(3) Nucleation mechanism and defect-induced transformation.

(b) Significant Accomplishments:

Our research strategy has been divided into three parts: (1) theoretical investigation of electronic structure and phonon dispersion relationship, (2) inelastic neutron scattering measurements, and (3) diffuse x-ray scattering measurements. A substantive description of significant achievements and progress towards achieving the research objective is given below.

Electronic Structure Calculations

The total density of states (DOS) and the electronic total energy were calculated for $PbTiO_3$ and $BaTiO_3$ in both the cubic and tetragonal phases of these materials using the extended Hückel tight-binding method [1]. The change in electronic total energy was used as an estimate of the phase stability of the tetragonal structure as compared with the cubic structure. The DOS were compared with experimental results. $BaTiO_3$ is a well studied system whereas considerably less information is known for $PbTiO_3$. The former system was therefore used as a standard to verify the method employed for the electronic energy calculation.

The calculated band structure for $BaTiO_3$ (Fig. 1) shows the characteristic features of titanate perovskites. The total valence band consists of widely spaced sub-bands that are due to (in order of increasing energy) Ti 3p, O 2s, Ba 5p, and O 2p states. The contributions to the first conduction sub-band are primarily due to the Ti 4s, Ti 3d and Ba 6s states. As expected, the Ba 6s states are unoccupied, indicating a complete charge transfer consistent with the tight-binding model. The DOS show a band gap of 3 eV. Calculated results are consistent with the experimental x-ray photoemmision spectroscopy (XPS) data (Fig. 2). There is no significant difference in density of states between the cubic and tetragonal phases, although the change in electronic total energy, 0.3 eV/unit cell, indicates more stability in the tetragonal structure.

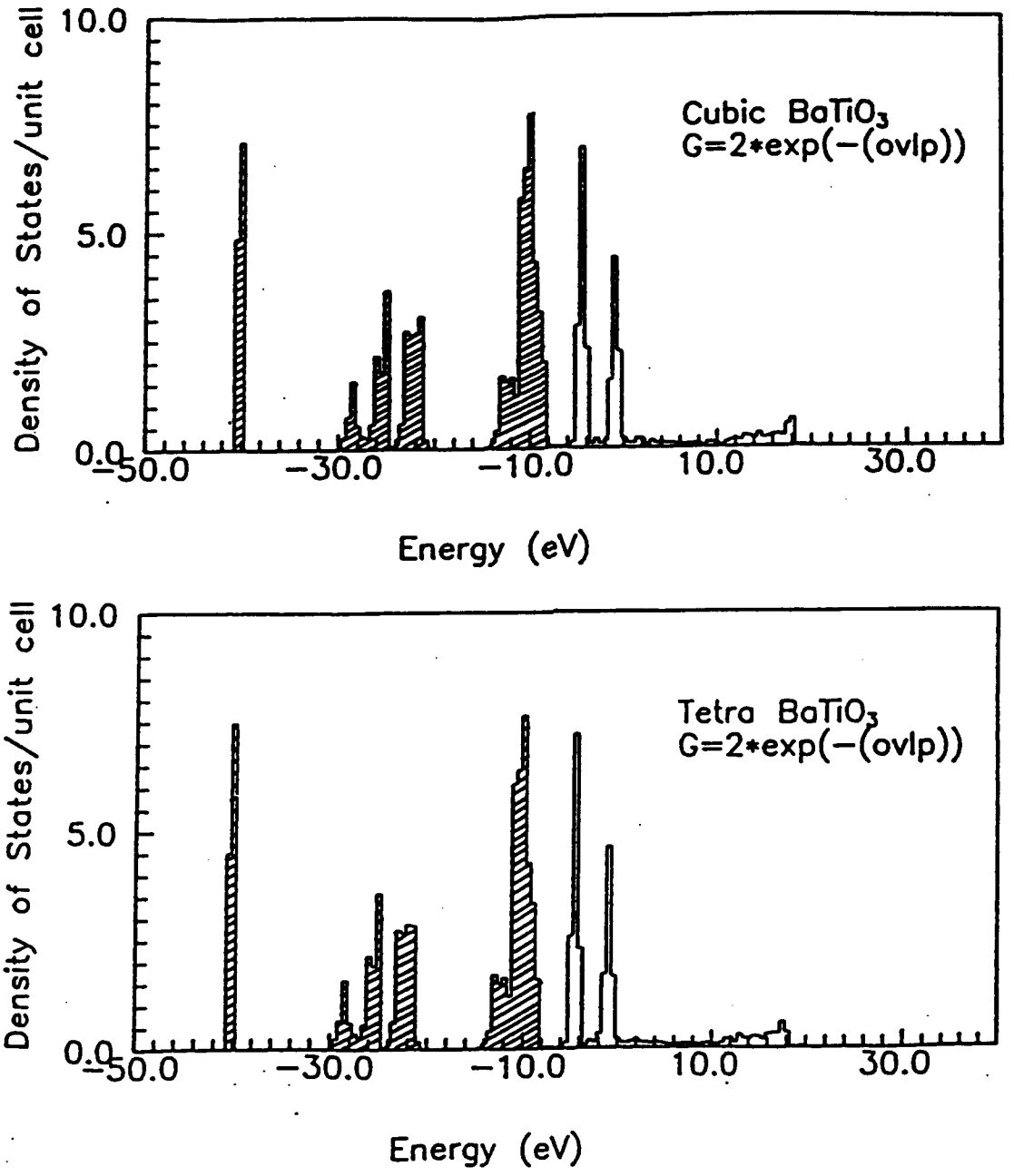

Figure 1 Total Density of States per unit cell versus energy (eV) measured relative to vacuum level for cubic and tetragonal $BaTiO_3$. Shaded regions indicate occupied states.

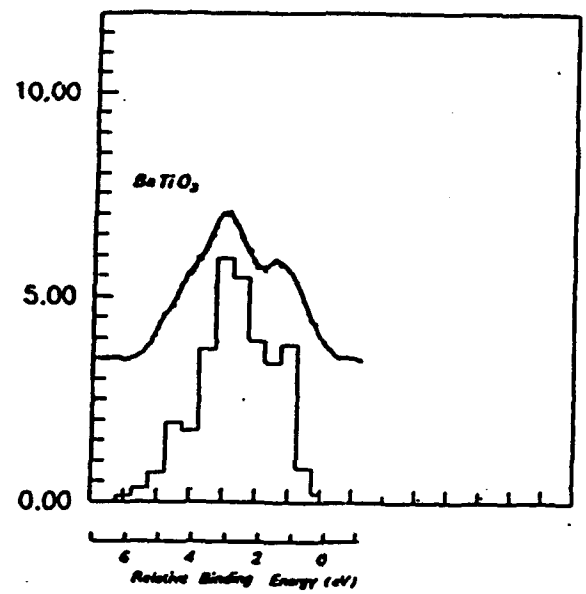

Figure 2 Enlarged view of the valence band of cubic $BaTiO_3$. Superimposed is XPS valence band data.

The results obtained for $PbTiO_3$ show similar features to that of the $BaTiO_3$. The primary effect of the substitution of Pb is to contribute states to the valence band, which interact strongly with the O 2p state. Pb also contributes to the conduction band from the Pb 6p states. This results in overlapping valence and conduction bands, a result perhaps related to the extraordinarily large conductivity in this system as compared to other perovskites. The Pb 6p is partially occupied which contradicts with the original assumption of the complete charge transfer. The structural transition appears to change the structure of the density of states, primarily in the conduction band and little change is observed in the valence band. The change in electronic total energy was 0.75 eV/unit cell, indicating some stability in the tetragonal structure.

The contradicting results obtained for the $PbTiO_3$ case suggest that the ionicity of Pb and O appears to be a major factor in the calculation. The validity of the atomic orbital assumption in the tight-binding method is then in question. It is suspected that a total charge transfer does not occur in this system. A self-consistent-field calculation is currently underway to obtain the wave function and ionicity in $PbTiO_3$ which will then be used for DOS calculation.

There exist very little experimental data on $PbTiO_3$ to compare with our band structure calculation, but a study of XPS data does provide some information. The results for Ti $L_{II,III}$ XPS indicate little change in the Ti states when Pb substitutes for Ba -- this agrees with our current calculations. The O K-level XPS data indicated there is a substantial change in the O p-like states when Pb substitutes for Ba. This, again, agrees with the calculated electronic structures. In conclusion, the current results imply that the ionicity in $PbTiO_3$ must be considered -- the atomic orbital must be reconsidered and a self-consistent-field calculation needs to be performed to obtain the electronic wave functions.

Inelastic Neutron Scattering

This technique has been employed to determine the phonon dispersion relationships and to investigate their roles in the displacive transformations of ceramics with initial emphasis focused on the cubic-to-tetragonal transition in $KNbO_3$. A model of the structural phase transition proposed an instability in a normal vibrational mode of the lattice; refinements associated the existence of the soft mode with the appearance of critical fluctuations. The dynamical nature of these pre-transitional effects is best studied using neutrons for several reasons. Investigation of phonon modes may be studied exclusively by inelastic neutron scattering. Similarly, sufficient energy resolution in inelastic scattering permits measurement of the dynamic susceptibility.

Previous work on these materials has revealed interesting phenomena. For example, investigation of the pre-transitional behavior of the orthorhombic-to-rhombohedral phase transition in $KNbO_3$ has established that chains of Nb atoms vibrate independently with large amplitudes in the $[010]_{ort}$ direction. Another pre-transitional phenomenon observed is the transverse soft optic mode, in which a mode determination showed that all but the Nb atoms in the lattice were moving. Other researchers confirmed the dynamical nature of these pre-

transitional effects. Studies on $PbTiO_3$ demonstrate some similar aspects to $KNbO_3$; it also has an underdamped zone center soft mode. However, the soft mode behavior is nearly isotropic in $PbTiO_3$, but highly anisotropic in $KNbO_3$. Precursor effects have not been observed in $PbTiO_3$.

We have conducted a series of inelastic neutron scattering measurements on $KNbO_3$ single crystals above the cubic-to-tetragonal transition temperature (~435°C) using the HFIR neutron facility at the Oak Ridge National Laboratory. A summary of the phonon dispersion relationship along the $[001]_{cubic}$ direction is shown in Fig.3 at 605°C and 525°C. Both temperatures show a broad, flat transverse acoustic (TA) mode and the low energy "soft" transverse optical (TO) mode. Also shown are the temperature independent longitudinal acoustic (LA) and the lowest energy longitudinal optic (LO) modes. Contrary to a previous report by Nunes et al. [2] the current results show an enhanced coupling between the TA and the TO modes. Both of these phonon modes are soft and their eigenvectors represent the transverse vibrations of the Nb atom (located in the body-centered position) and the oxygen octahedron (connection among 6 face-centered oxygen atoms) in the perovskite structure for the TA and TO mode, respectively. This strong coupling in the cubic phase is believed to be the main driving force for the ensuing phase transition for which the tetragonal structure requires a relative displacement of the Nb atom from the oxygen octahedron.

The lattice dynamics of $KNbO_3$ were treated theoretically using a rigid-shell model [3]. Physically, this corresponds to assuming short harmonic forces act between nearest neighbors only. The long range Coulomb forces are modeled by monopole and dipole type interactions. The ion is described as consisting of the nucleus and inner shell electrons and an electron shell. Coupling between the isotropically polarizable electron shells constitutes the monopole contribution. Displacement between the core and inner shell electrons and the outer electron shell give rise to dipole interactions. In addition, the charges on the ions are allowed to vary. There are a total of fourteen parameters used in the model. The results of a preliminary fit to the experimental data are shown in Figure 4. Reasonably good agreement is obtained for the TA and LA modes. Although agreement on other modes is not yet satisfactory, which should improve upon further refinement with the consideration of anharmonicity, the low energy TO mode is apparent in our model calculation.

The inelastic neutron scattering results demonstrate interesting pre-transitional phenomena in the phonon properties. As the transition temperature is approached from above, there is an enhanced coupling, at q~0.2, between the TA and TO modes (see Fig. 5). This coupling is anharmonic in nature. In addition, there is evidence of coupling between the transverse optic and diffuse excitation, the nature of which is not understood. This anharmonicity effect manifests itself in the increased line width of the phonon mode and associated damping corresponding to a decreased phonon lifetime. The theoretical modeling provides some insight to the observed anomalous behavior. An analysis of the atomic displacements [4] using a rigid-shell model suggests that at reduced wave vector, q= 0.2 - 0.5, the Nb atoms move with respect to an

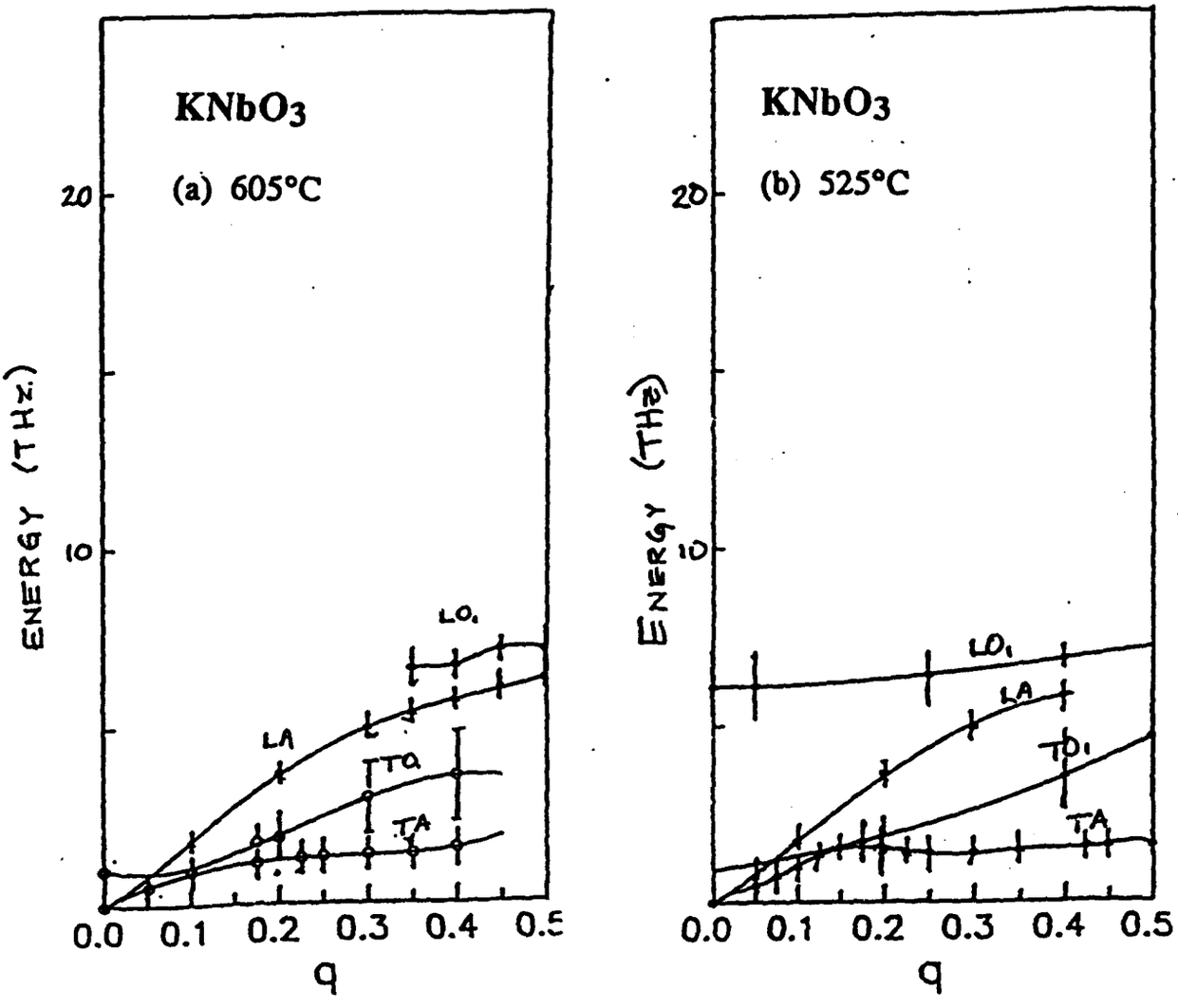

Figure 3 Phonon dispersion curves of the cubic phase of $KNbO_3$ at (a) 605°C and (b) 525°C. The transition temperature is 430°C. The figures show the phonon energy (THz) versus reduced wave vector along the $[001]_{cubic}$ direction. (Lines are a guide to the eye.)

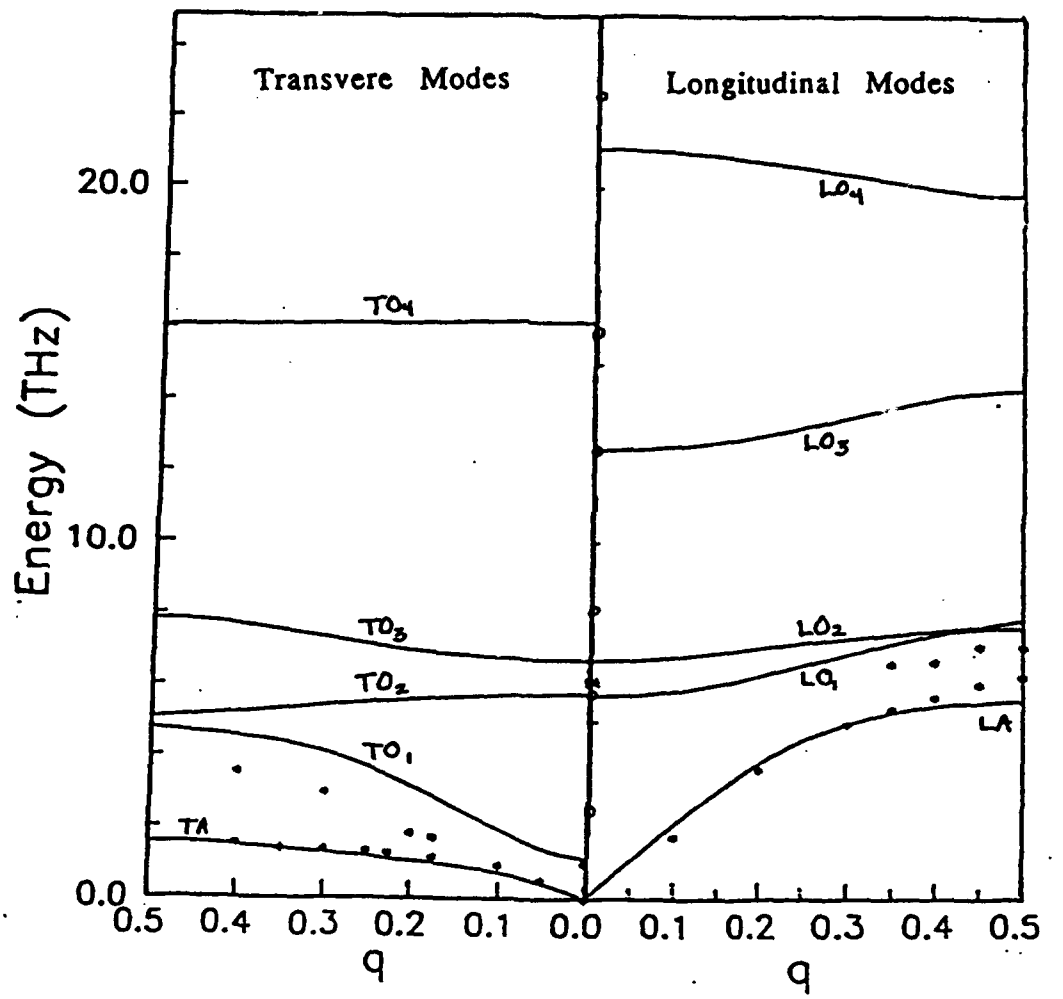

Figure 4 Theoretical rigid-shell model calculation fitted to the experimental phonon dispersion curves of $KNbO_3$ along the $[001]_{cubic}$ direction at 605°C.

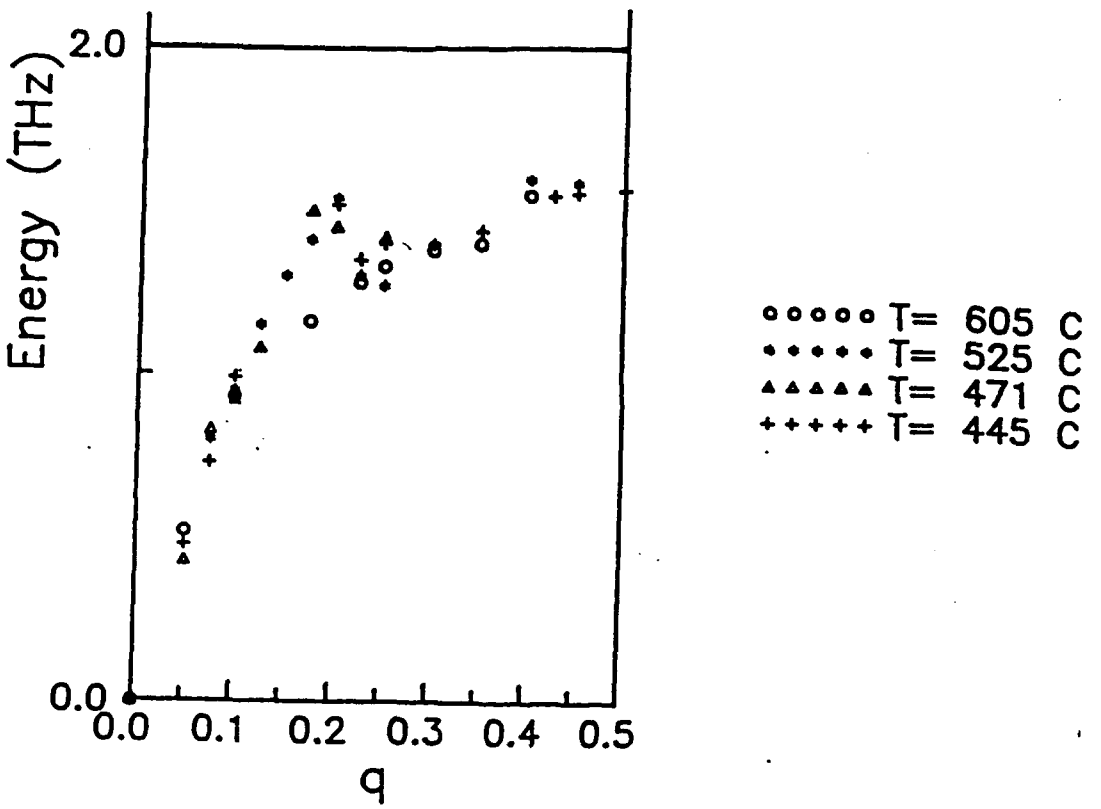

Figure 5 Temperature dependence coupling of the $[001]_{cubic}$ transverse acoustic (TA) mode with the transverse optical (TO) mode in $KNbO_3$.

essentially rigid oxygen octahedral in the transverse acoustic mode. For smaller wave vectors, displacement occur in all ions.

Based upon our investigation the softening is incomplete and the transition is of the first order kind. A phenomenological model suggests that competing displacive interactions can lead to the anomalous phonon dispersion curves and structural instabilities, where the positions of phonon anomalies and mode softening are affected by cancellation of relatively large and opposite forces. This model suggests that phonon dispersion anomalies and high anisotropy lead naturally to the concept of embryo-like regions with a specific correlation length. The predicted behavior should occur for a wide range of temperatures above the transition temperature. Quasi elastic neutron scattering and/or diffuse x-ray scattering are experimental methods suitable to examining the possible existence of these precursor embryo-like domains in the cubic phase.

Diffuse X-ray Scattering

Diffuse x-ray scattering intensities from a $PbTiO_3$ single crystal near the $[002]_{tet}$ superlattice reflection position have been monitored at temperatures covering the cubic-to-tetragonal transition point. The magnitude of thermal expansion as determined from the Bragg peak position is shown in Figure 6 for both the cubic and the tetragonal phases in cooling and heating cycles. A discontinuous change in the lattice parameter is noticed, indicative of a first-order transition. This is also shown by a hysteresis of 8 degrees for the transition temperatures (T_c) of 462°C and 470°C for the cooling and the heating cycles, respectively. A volume change of about 2% is noticed at the transformation temperature.

Cooling from above T_c to one degree below it showed a kinetic behavior which could be attributed to the domain distribution that gave rise to a preferred orientation of the tetragonal phase with its c axis perpendicular to the specimen surface. This behavior can be seen in Figure 7 where a continuous growth of the $[002]_{tet}$ peak occurs at the expense of the $[200]_{tet}$ peak until the latter is nearly completely consumed. Most of the 90° domains are eliminated after 100 minute anneal at 461°C. The cause for the domain redistribution is believed to be due to the confining stress exerting on the sample as the single crystal sample was embedded in an adhesive cement mold on an hot stage. Therefore, lateral confinement of the sample provides a larger degree of freedom for the specimen to expand in a direction normal to the sample surface. With the lattice parameter "c" being larger than "a" in the tetragonal phase, a preferred orientation thus forms. Back transformation during heating is spontaneous, no kinetics is observed. This is to be expected when a low-symmetry phase (tetragonal) reverts back to a high-symmetry one (cubic).

Presence of tetragonal fluctuations is observed in the cubic phase of $PbTiO_3$ at temperatures as high as 80° above T_c as evidenced by the asymmetric diffuse tails near the $[002]_{cubic}$ peak (Fig. 8). This diffuse intensity becomes more pronounced near T_c. Current explanation of this behavior is associated with the local tetragonality pinned by impurities or other defects such as vacancies. This local tetragonal fluctuations will result in coherent scattering of x-rays as if it is

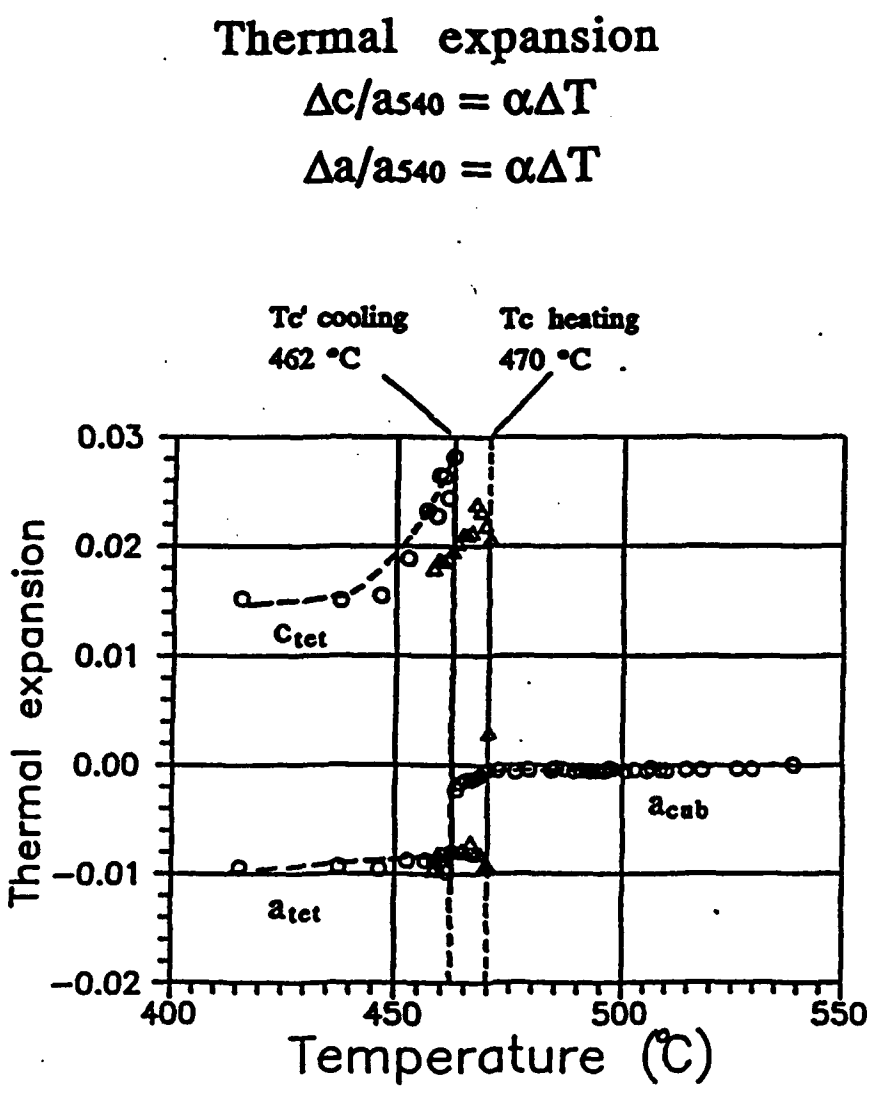

Figure 6 The magnitude of thermal expansion normalized by the lattice constant at 540°C for $PbTiO_3$. Triangles are data points on heating cycle whereas circles on cooling cycle.

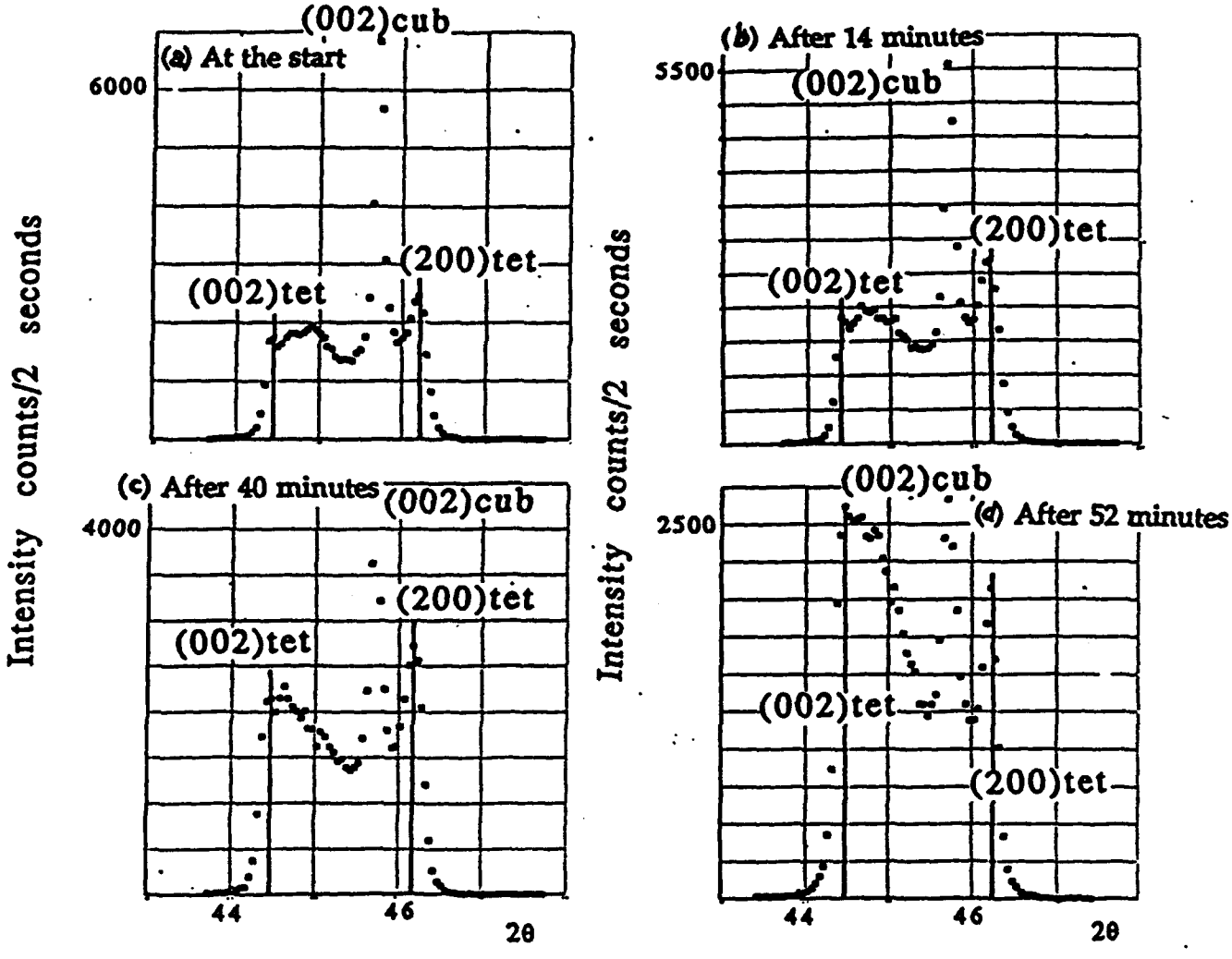

Figure 7 Temporal evolution of the 90° tetragonal domain nucleation and growth in $PbTiO_3$. The cubic peak and the splitting of the two tetragonal (002) and (200) peaks were monitored at 461°C.

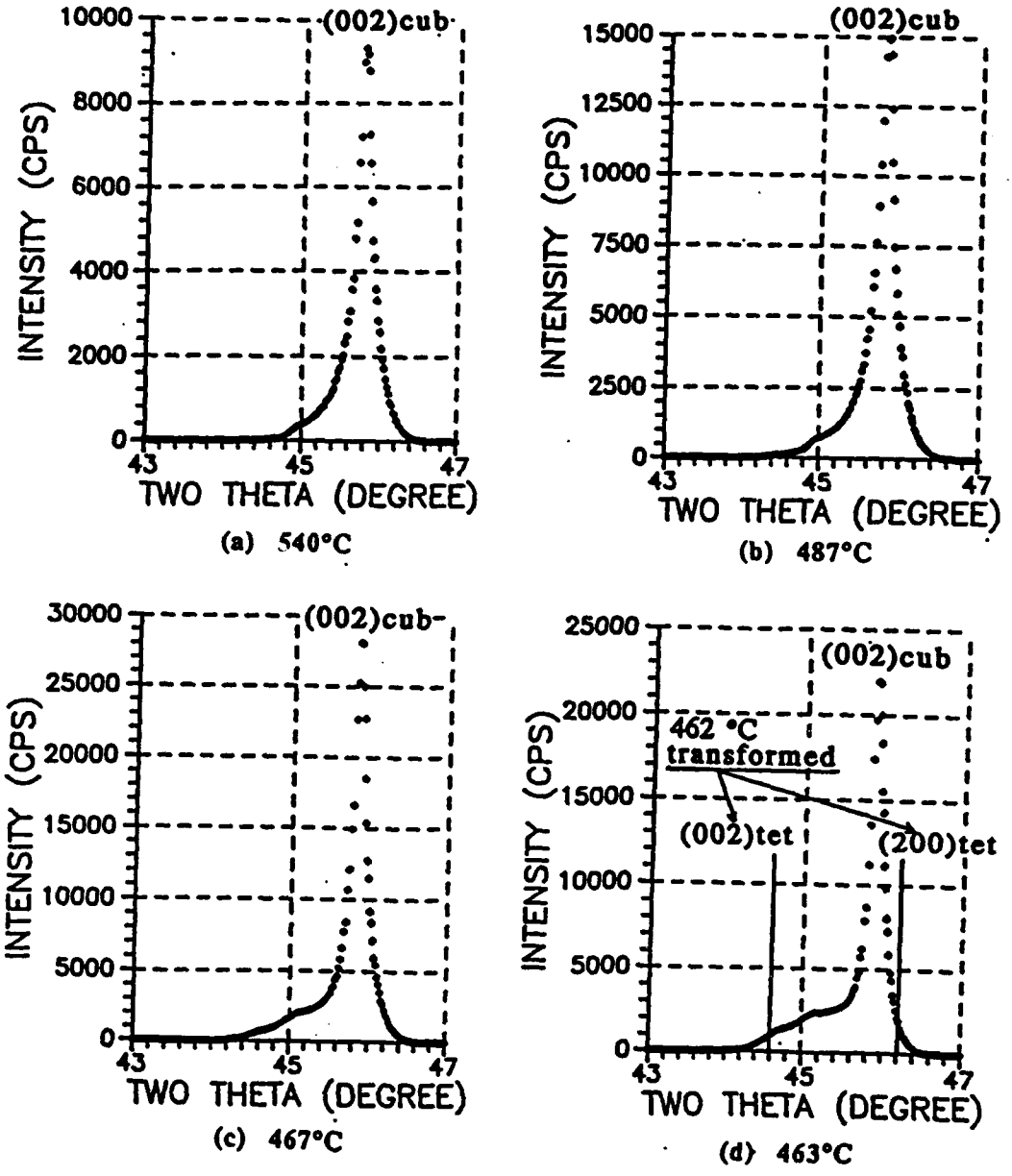

Figure 8 The $[002]_{cubic}$ peak observed in $PbTiO_3$ at several temperatures above T_c (=462°C) during cooling: (a) at 540°C, (b) at 487°C, (c) at 467°C, and (d) at 463°C.

from a cubic phase with slightly larger lattice parameter, thereby producing a broad, diffuse maximum at the lower angle side of the $[002]_{cubic}$ peak. These local tetragonal fluctuations may be considered as "embryonic" fluctuations which eventually become frozen in to initiate the transformation below T_c. Other possible explanation of the observed pre-transitional phenomenon is due to the concept of Frankel that "heterophase" fluctuation, which is a thermally activated process having no connection with impurities or defects, may occur at temperatures above T_c. Further investigation is needed in order to differentiate these two possible scenarios.

The soft phonon modes in $KNbO_3$ as observed by our inelastic neutron scattering measurements also manifest themselves in the x-ray thermal diffuse scattering (TDS) pattern in a surprising but extremely informative way as evidenced by our synchrotron radiation measurements carried out at NSLS, Brookhaven National Laboratory. Preliminary results show that the TDS distribution, arising from low-energy transverse phonon modes propagating along the $<100>_{cubic}$ directions, consists of disk shaped sheets of intensities perpendicular to the cubic axes, extending out to the Brillouin zone boundaries and intersecting all fundamental peaks. This observation is contrary to the usual TDS streaks seen in many other systems exhibiting soft phonon modes. The 2-dimensional nature of the TDS in $KNbO_3$ necessarily implies a one-dimensional character of the soft phonons in real space. The one dimensional nature of the propagating soft phonons may have their origin in anti-ferroelectric dipole interactions in the cubic phase to minimize the total free energy -- a subject of great importance but needing further investigation.

References:

[1] L. A. Gunnes, R. D. Leapman, C. N. Wilker, R. Hoffman and A. B. Kunz, Phys. Rev., B25, (1982) 7157.

H.R.P. Inouye, M. Kitamura, C. M. Wayman and H. Chen, Phil. Mag., 63(6), (1991) 345-353.

M. Holma, M. Kitamura and H. Chen, J. Appl. Phys., (1994) in press.

[2] J. D. Nunes, J. D. Axe and G. Shirane, Ferroelectrics, 2 (1971) 291.

[3] C. H. Perry, R. Currat, H. Buhay, R. M. Migoni, W. G. Stirling and J. D. Axe, Phys. Rev., B39 (1989) 8666.

R. A. Cowley, Phys. Rev., 134 (1964) A981.

W. G. Stirling, J. Phys. C: Solid State Phys., 5 (1972) 2711.

[4] M. Holma and H. Chen, presented in ACA Annual Meeting, Pittsburgh, PA (1992).

(c) List of Publications:

1. Calculation of K-Absorption Edge Energy and Its Chemical Shift of Common Metals
   M. Kitamura and Haydn Chen, J. Phys. Chem. Solids, **52(5)**, 731-734 (1991).

2. Phase Stability of Al_3Nb as a Function of Nickel Additions
   H.R.P. Inouye, M. Kitamura, C.M. Wayman and Haydn Chen, Phil. Mag. **63(6)**, 345-353 (1991).

3. Phase Stability of Ni-Based Intermetallic Compounds Ni_3X Studied by Recursion Method
   J. Park, S. Muramatsu, M. Kitamura, H.R.P. Inoue, and Haydn Chen, Materials Chemistry and Physics, **33**, 214-220 (1993).

4. Pre-Transitional Behavior in Cubic Potassium Niobate
   M. Holma, H. Hong, M. Nelson and Haydn Chen, in Applications of Synchrotron Radiation Techniques to Materials Science, MRS Publication, Pittsburgh, PA, Vol. **307**, 293-298 (1993)

5. Electronic Structure Calculations of Barium Titanate and Lead Titanate Using the Extended Hückel Tight-Binding Method (XHTB)
   M. Holma, M. Kitamura and Haydn Chen, J. Appl. Phys. (1994) in press.

6. X-Ray Thermal Diffuse Scattering Study of Soft Modes in Paraelectric $BaTiO_3$
   N. Takesue, M. Maglione and Haydn Chen, Phys. Rev. Lett. (1994) submitted.

7. Linear Chain Structure in Cubic $KNbO_3$
   M. Holma and Haydn Chen, Proc. Int. Conf. on Solid->Solid Phase Transformations in Inorganic Materials '94, Pittsburgh, PA, July 17-22 (1994) abstract accepted.

8. Pre-Transitional Phenomena and Defect-Induced Cubic-to-Tetragonal Transformation in $PbTiO_3$ and $KNbO_3$
   N. Takesue, M. Holma and Haydn Chen, Proc. Int. Conf. on Solid->Solid Phase Transformations in Inorganic Materials '94, Pittsburgh, PA, July 17-22 (1994) abstract accepted.

9. Pretransition Phenomena and Transformation Kinetics Across the Cubic-to-Tetragonal Transition in $PbTiO_3$
   N. Takesue and Haydn Chen, Ferroelectrics (1994) in preparation.

10. Inelastic Neutron Scattering Study and Lattice Dynamics in $KNbO_3$
    M. Holma and Haydn Chen, Phys. Rev. (1994) in preparation.

(d) Personnel

Prof. Haydn Chen — Principal Investigator
Department of Materials Science & Engineering
University of Illinois
Urbana, IL 61801

Dr. M. Kitamura — Visiting Scholar (Jan.- June, 1991)
Department of Applied Electronics
Utsunomiya University
Utsunomiya, Japan

Ms. M. Holma — Ph.D. Candidate (Degree Expected in Jan. 1994)
Department of Physics
University of Illinois
Urbana, IL 61801

Mr. N. Takesue — Graduate Student
Department of Materials Science & Engineering
University of Illinois
Urbana, IL 61801

PROFESSOR W. M. KRIVEN

AFOSR URI FINAL REPORT
(Professor Waltraud M. Kriven)

(a) OBJECTIVES OF THE RESEARCH EFFORT

The aim of this part of the interdisciplinary research effort were to obtain a basic scientific understanding of martensitic nucleation and transformations mechanisms in some specific ceramics. It is worthwhile to mention that simultaneously with this URI, there was in place a large AFOSR grant on "Transformation Toughening of Composite Ceramics" [AFOSR 89 0300] for which Professor Kriven was the principal investigator. The URI work pursued here was to provide some basic scientific knowledge of transformation mechanisms in candidate tougheners, such as dicalcium silicate, and nickel sulfide (NiS).

In dicalcium silicate (Ca_2SiO_4), the detailed transformations mechanisms between the five polymorphs occurring on cooling from the melt were to elucidated. The reasons why this system was chosen was because it represented a material whcih was a non-perovskite and underwnet large positive volume and unit cel shape changes which may have had a significant effect on the mechanical properties of a ceramic composite. In the accompanying transformation toughening project, attempts were being made to apply dicalcium silicate as a transformation toughener of ceramics.

Related to the monoclinic (β) to orthorhombic (γ) transformation in Ca_2SiO_4, thought to be most likely to yield transformation toughening, the decomposition and subsequent transformation mechanisms in hillebrandite ($Ca_2SiO_4 \bullet H_2O$), a hydrated form of Ca_2SiO_4, would be studied. Phase transformation mechanisms were also studied in the iso-structural strontium orthosilicate (Sr_2SiO_4) where the transformation temperatures of some of the transformations were closer to room temperature and permitted in situ studies. Nickel sulfide (NiS) particles embedded in glass which had catastrophically fractured were also studied to ascertain any relationship to the transformation therein.

In the spirit of interdisciplinary collaboration, our TEM expertise was also focussed on studying the nucleation and transformation mechanisms in the perovskite, potassium niobate ($KNbO_3$). Large single crystal specimens were grown by Professor Payne's group (by Dr. Pengdi Han and Dr. Bing Nan Sun). Professor Haydn Chen's group then studied pre-transitional phenomena and phonon properties by theoretical and neutron diffraction techniques. Professor Kriven's group were to make corresponding in situ TEM observations of possible pre-transformational phenomena, as well as to document the complete transformation sequence in $KNbO_3$. A complete set of elastic moduli for $KNbO_3$ at ambient and higher temperature conditions were to be measured using Brillouin spectroscopy, by Professor Jay Bass's group.

(b) STATUS OF THE RESEARCH EFFORT

The work on dicalcium silicate (Ca_2SiO_4), hillebrandite, ($Ca_2SiO_4 \bullet H_2O$), strontium orthosilicate (Sr_2SiO_4) and nickel sulfide (NiS) has been published or submitted for publication (see section (c) below and enclosed reprints and preprints).

The work on potassium niobate is still in the process of being written up and published collaboratively with Dr. O. Popoola who is now a senior research scientist at the Ford Research Laboratories in Dearborn Michigan. The in situ TEM study of the transformation mechanisms will be presented at the up coming International Conference of Phase Transformations '94 . A brief overview of the $KNbO_4$ work is presented here as follows.

Status of Research Effort in Potassium Niobate ($KNbO_3$)

Introduction

$KNbO_3$ is isostructural with $BaTiO_3$ and undergoes a series of phase transformations during cooling as depicted in Table 1. The cubic → tetragonal phase transformation is responsible for the paraelectric to ferroelectric transition in the crystal. The ferroelectric state is maintained during subsequent phase transitions. However, each phase is characterized by different polarization vectors. The exact transformation temperature may vary depending on the impurity content in the crystal. All of the phase transformations are accompanied by negligible volume changes. The nucleation of new phases generally occurs at defects such as surfaces, stacking faults, dislocations and grain boundaries [1-3]. The domain structures in the tetragonal and orthorhombic ferroelectric phases are intimately linked on account of the nature of the impurity sites in both phases. While the impurity site density may determine the onset and kinetics of the phase transformations, the structural mechanisms (lattice correspondence, orientation relations, order of transformation) remain the same. A variety of techniques (X-ray photoelectron spectroscopy, optical microscopy, interferrometry) have been used to study the various aspects of phase transformations in $KNbO_3$ [4-7]. Most of these studies dealt with physical properties such as dielectric constraints, refractive index, and transition heat and entropy changes). The few electron microscopy studies conducted so far have essentially focused on identifying the nature of domains and domain well behavior.

The aim of this study was to perform detailed transmission electron microscopy studies of phase transformation mechanisms in $KNbO_3$.

Table 1.

Phase	**IV**	**III**	**II**	**I**	**Melt**
State	F	F	F	P	
Crystal System	Rhomb	Orthorhombic	Tetragonal	Cubic	
Space Group	R3m	Bmm2	P4mm	Pm3m	
Polarization Vector (P)	//[111]	//[001]	//[001]		
Transformation temperature (°C)		-10	225	418	
Unit Cell Volume ($Å^3$)	64.77	64.73	64.92	65.18	

F = Ferroelectric, P = Paraelectric.

Experimental Procedures

Thin slices were cut from flux grown single crystals and mechanically polished to a thickness of 150 μm using a mixture of diamond paste and isopropyl alcohol. 3 mm diameter discs were then ultrasonically drilled, dimpled on one side to a thickness of about 50 μm and mounted on to Cu grids for support. Final perforations were achieved by argon ion beam milling under an accelerating voltage of 6 KV and a gun current not exceeding 1 μA at room temperature. Under these conditions, no irradiation-induced domain boundary motion, domain nucleation or dislocation creation was expected. The thinned samples were observed on a Philips CN 12 TEM operated at 120 KV for microstructural characterization prior to phase transformation experiments. In other studies the details of the phase transformations, previously observed and selected TEM samples were mounted on a specially designed double tilt high temperature specimen holder. In situ experiments were performed at Argonne National Laboratory using the HVEM Tandem Facility. The samples were heated at approximately 2°C/min up to 578°C, dwelled overnight (in excess of 10 hrs) to allow for maximum lattice relaxation in the cubic phase. The dwelled samples are cooled at a rate of 2°C/min. Structural changes were observed both in bright field and dark field modes. The microscope was fitted with a video system, permitting a recording of the transformation sequences. Once a transformation was observed, the transformed sample was reheated to induce the reverse transformation.

Experimental Results

1. RT Microstructure of $KNbO_3$

Figure 1 shows a low magnification bright field obtained for a symmetrical excitation of the [100] zone axis. Dark lines of contrast intersecting the crystal edge [011] at 60° and 90° are clearly visible. Other lines parallel to [011] are also clearly visible. This indicates the presence of a complex domain structure in the $KNbO_3$ crystals studied. On a pseudo cubic {001} face, the 60° domain line can appear either parallel to an edge or at an angle of 45° with it. The 90° and 180° domain lines lie parallel to an edge but only the former are visible.

A higher magnification bright field image, showing the complexity of the domain structure is shown in Figure 2. Two distinct types of boundaries can be clearly seen. The first type marked A is characterized by lamellar bands with straight edges. The second, B, is wedge shaped. Area C shows the region of intersection between A and B. Figure 3a, is a higher magnification micrograph of region A. The associated diffraction pattern (Figure 3b) clearly show the $[001]_P$ zone axis of the orthorhombic phase.

From these two micrographs, some distinctive features can be observed:

- The ferroelectric domains formed bands with boundaries parallel to the $<001>_P$ direction.
- These was a sharp contrast between two adjacent domains in the bright field image.
- High order diffraction spots are split in the first order (001) Laue zone.

These characteristics are those of 90° ferroelectric domains. They lie on {100} and have their ferroelectric axis perpendicular to one another. This domain configuration is the most commonly observed on the samples studied.

Figure 4 shows the higher magnification micrograph of the wedge-shaped domains (labelled B in Figure 2) and the associated $\{100\}_P$ diffraction pattern. Detailed analyses of these micrographs revealed the following:

- There was no background intensity variation across the boundary whatever the diffraction vector **g** used.
- The boundaries are wedge-shaped and no spot splitting was observed in the first order Laue {001} diffraction pattern.
- The wedge shaped domains had a core contrast consisting of alternating bright and dark lines when the diffraction deviation parameters S = 5° in the multi-beam condition.
- No superlattice spots were visible in the diffraction pattern.
- The extreme fringe contrast, using **g** = 001 (see Figure 5) showed an asymmetric bright field image and a symmetric dark field image.

These observations permitted the identification of these boundaries as 180° domain boundaries. These boundaries have their polarization vectors parallel to each other with opposite axial orientations.

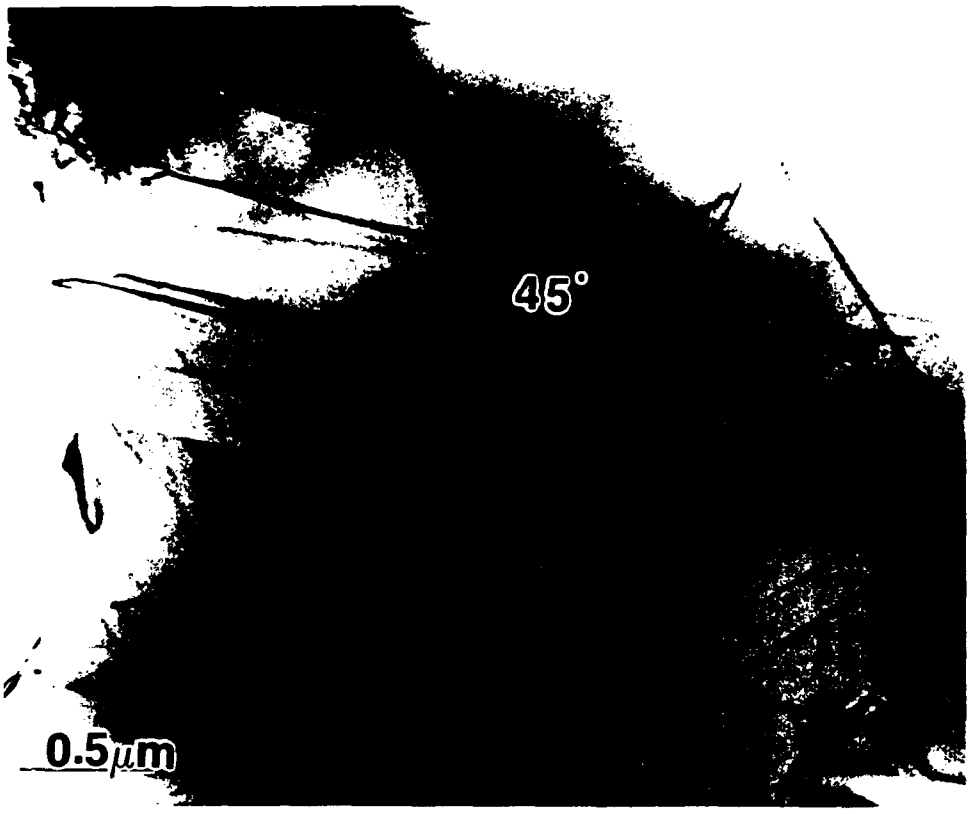

Figure 1. Bright field TEM image of $KNbO_3$ showing lines of contrast parallel to the crystal edge $[011]_P$ direction. Other lines at 60° and 45° are also shown.

Figure 2. Higher magnification TEM bright field micrograph showing the complex domain configuration in $KNbO_3$.

Figure 3. BF image and the associated <001>P diffraction pattern of 90° domains in $KNbO_3$. Note the splitting of the spots perpendicular to the lamellae boundaries.

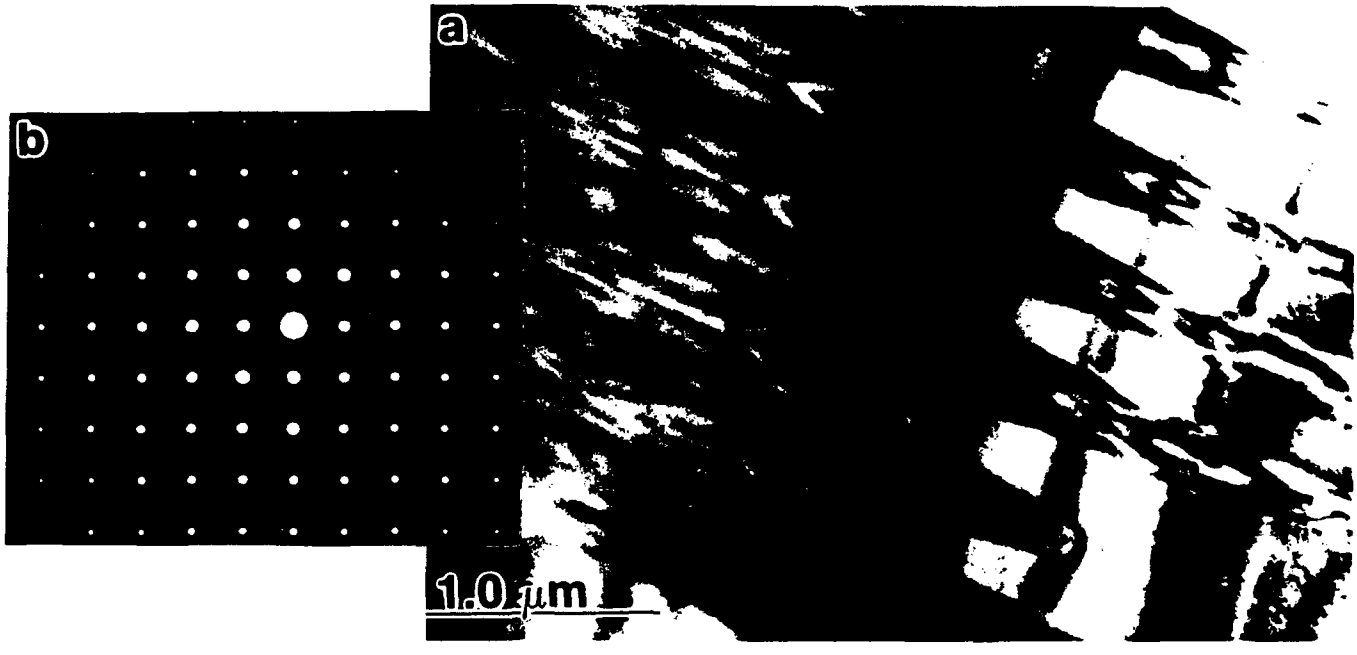

Figure 4. Wedge shaped 180° domains in $KNbO_3$ and the associated [001 diffraction pattern.

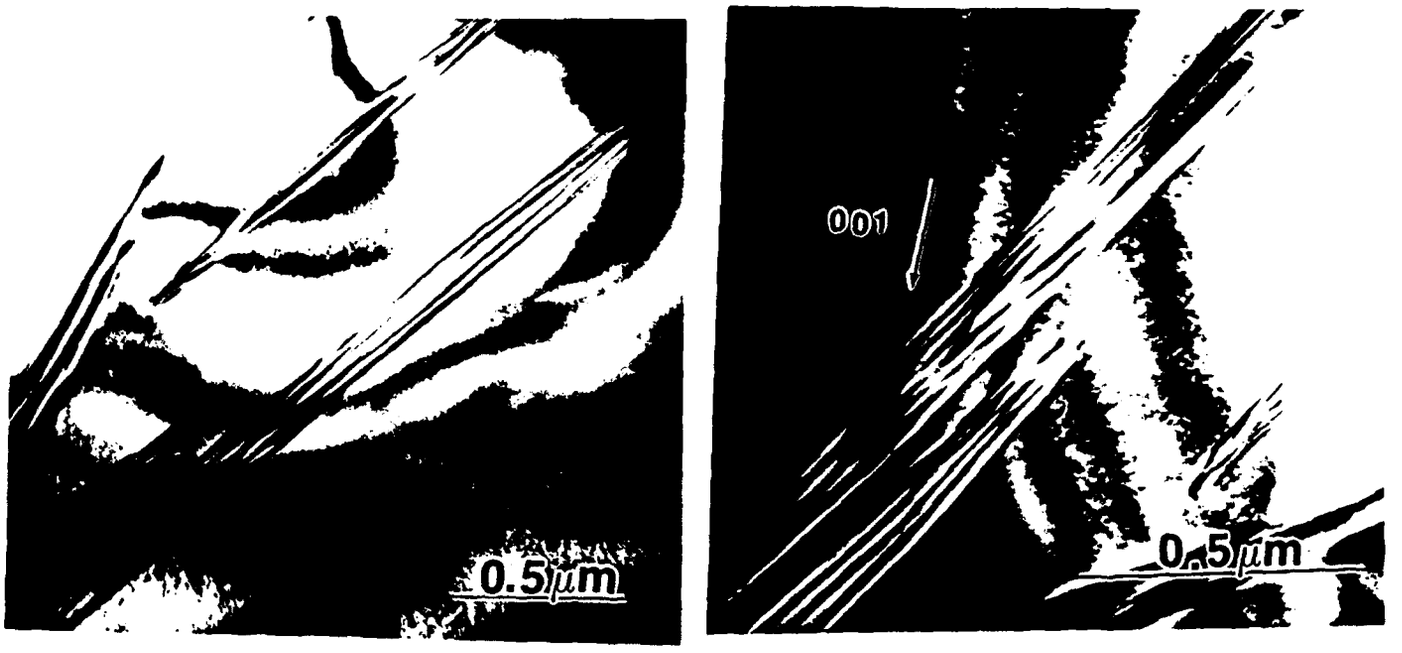

Figure 5. Extreme fringe contrast behavior of the 180° wedge shaped domains.

2. *Phase Transformations in $KNbO_3$*

Cubic → Tetragonal Phase Transformation

After an overnight dwell at 510°C, the cubic phase microstructure was featureless. A few grain boundaries could be revealed. Figure 6a shows a typical microstructure of the cubic phase. Upon cooling, the microstructure remained unchanged until 440°C. The lattice parameter changes associated with a temperature variation could not be detected by electron diffraction. At 440°C, there appeared a quasi-periodic microdomain structure (Figure 6b). These microdomains were stable and did not disappear or coalesce with time at 440°C. A further decrease in temperature resulted in the nucleation of ferroelectric domain structures. These ferroelectric domains, nucleated independently, one after the other and were parallel to each other. There was no collective transformation front as the domains appeared to grow independently. Spontaneous nucleation of ferroelectric domains was followed by a certain amount of growth along the lamellar axis (Figure 6c). The growth was arrested after a few seconds, and a temperature decrease was needed to ensure further growth of the ferroelectric lamellae. The longitudinal growth rate was faster than the thickening rate. (A video tape was made of the entire transformation experiment). The transformation was complete at 410°C. Further cooling resulted in the re-arrangement of the ferroelectric domains. Typical tetragonal domain configurations are shown in Figure 7. The reverse transformation upon heating (tetragonal to cubic) started at 418°C with a transformation front that swept through the crystal instantaneously. The cubic → tetragonal transformation (and the reverse) had no microstructural memory effect, i.e., repeated transformation cycles did not necessarily produce the same microstructures. The tetragonal ferroelectric plates were divided into multiple thin plates (white ··nes arrowed in Figure 7b).

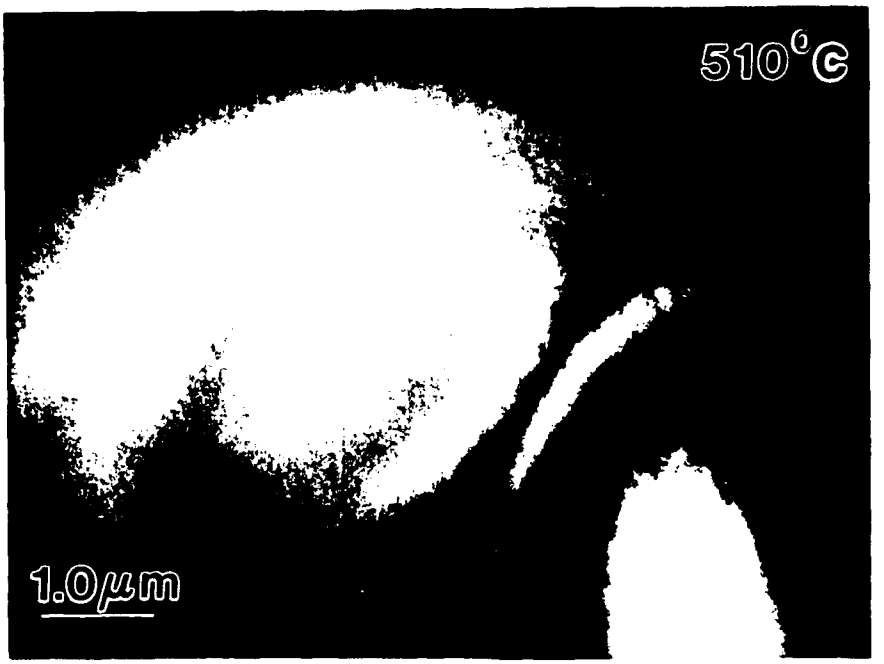

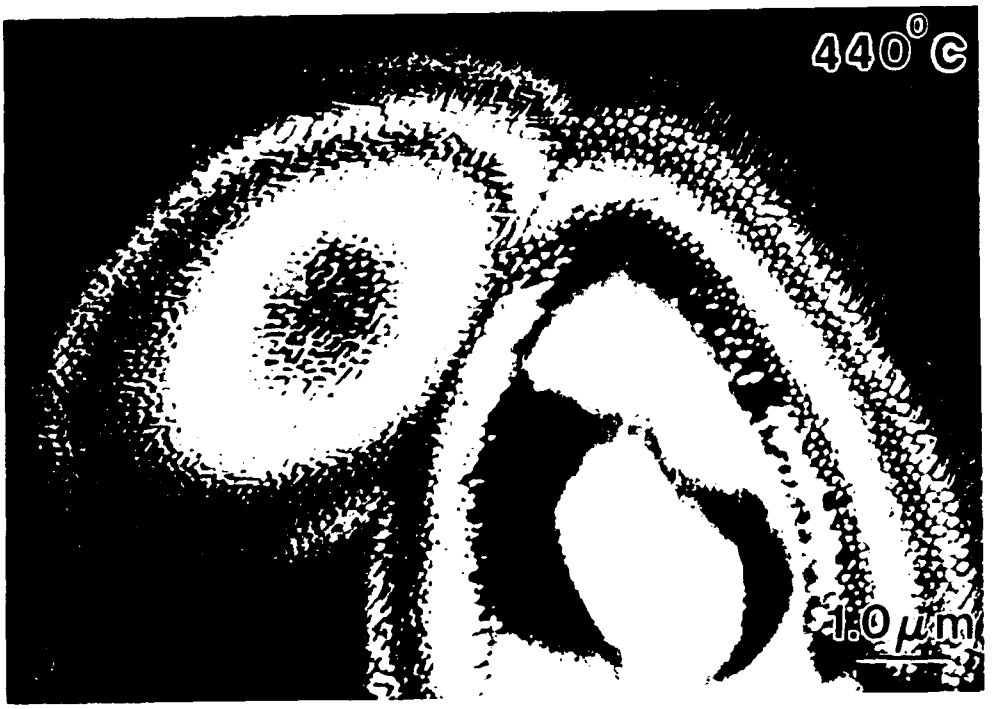

Figure 6. TEM bright field image showing the microstructure of $KNbO_3$ at various temperatures: (a) 510°C, (b) 440°C and (c) 425°C.

Figure 6. TEM bright field image showing the microstructure of $KNbO_3$ at various temperatures: (a) 510°C, (b) 440°C and (c) 425°C.

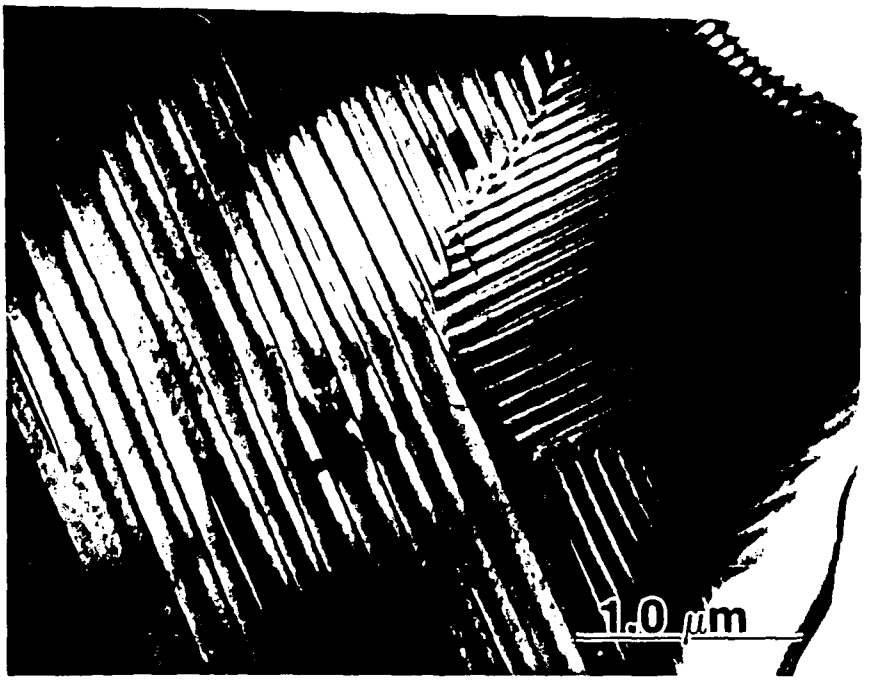

Figure 7a. Typical microstructures in the tetragonal phase of $KNbO_3$.

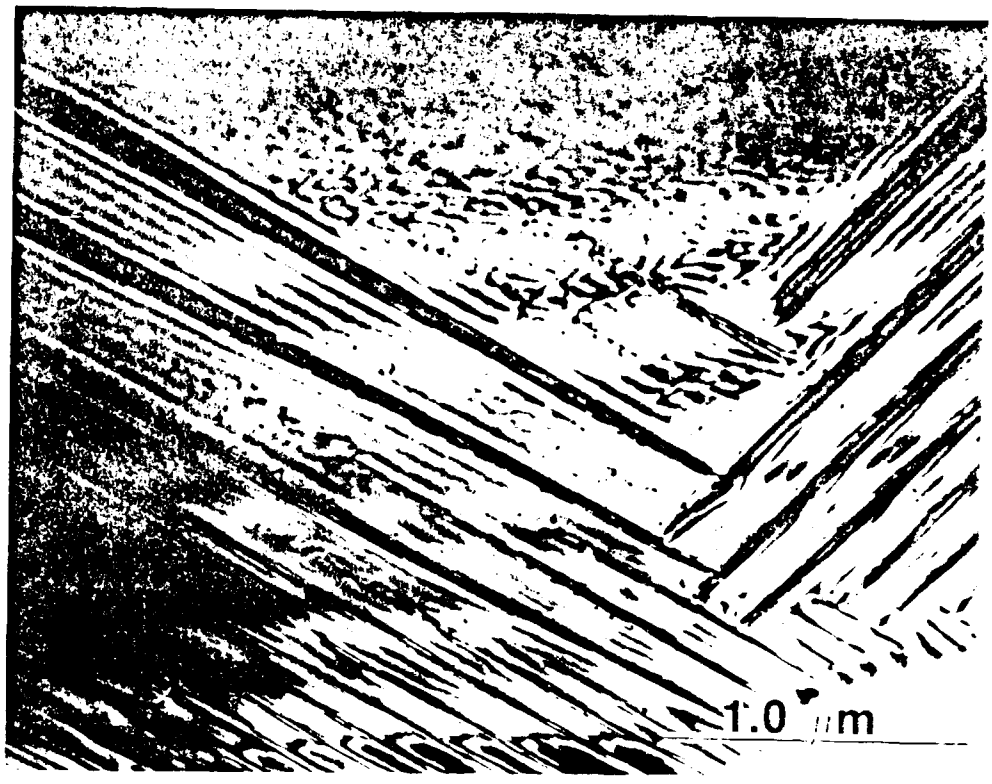

Figure 7b. Typical microstructures in the tetragonal phase of $KNbO_3$.

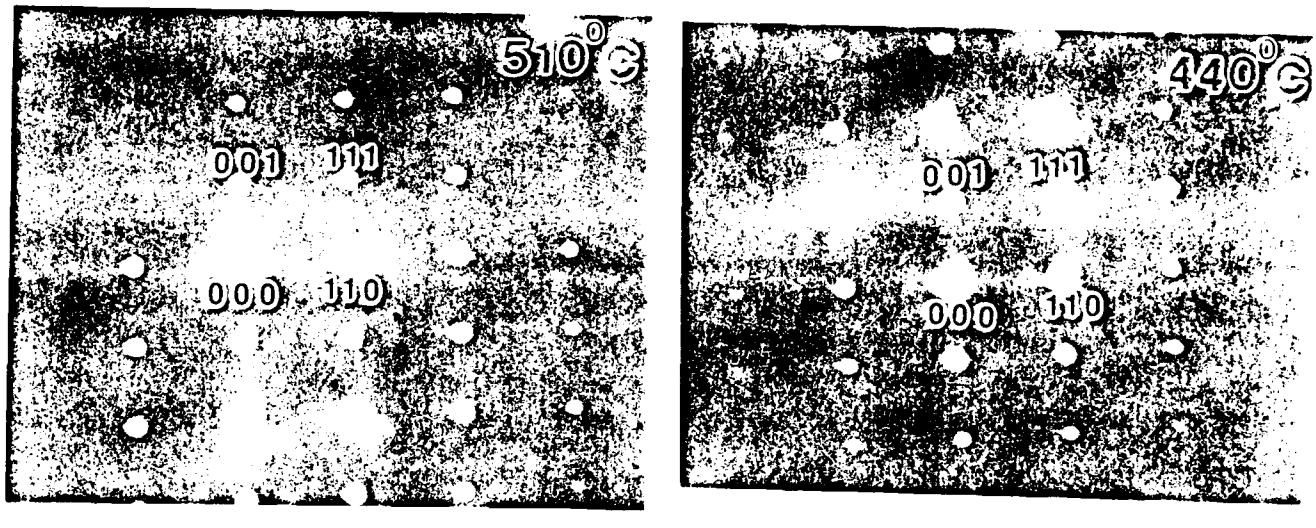

Figure 8. Diffraction patterns at various temperatures (a) 510°C, (b) 440°C and (c) 396°C.

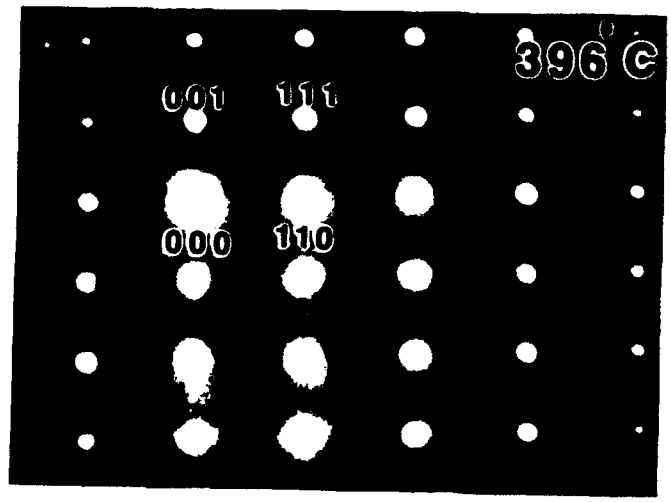

Figure 8. Diffraction patterns at various temperatures (a) 510°C, (b) 440°C and (c) 396°C.

Figure 8 shows the selected area diffraction patterns taken at 510°C (cubic phase), 440°C (pretransition microdomains) and 396°C (tetragonal phase) respectively. Figures 8a and b show that the microdomains were formed in the cubic phase. While there was microstructural memory during this phase of the transformation, complete crystallographic memory was observed on repeated experiments. The reversible orientation relationship was "the cube on cube" relation in which:

$$[110]_c // [110]_t \text{ and } (001)_c // (001)_t.$$

Discussion and Conclusion

The theory of domain wall orientations [8,9] predicts that an uncharged 90° domain wall should coincide with a $\{001\}_P$ type plane while the 180° walls should be parallel to a $[001]_P$ direction. The pre-transformation microdomains observed in this study had extinction effects. There was a shift between two parts of parallel stripes along the direction perpendicular to the stripes and they lost their contrast when **g** was parallel to their elongating directions. These observations implied two things:

- The stripes were not the normal ferroelectric microdomains as their contrast could not represent either domain or domain walls.
- There was a certain displacement field **R(n)** of certain ions as the extinction condition **g•R(n)** was fulfilled in certain cases. The nature of the ion that was displaced remains uncertain. However, by analogy to the mechanism in $BaTiO_3$, we think that the Nb ions were displaced. Displacement of K ions would have resulted in much higher contrast of the microdomains. This was in agreement with the models of Comes et al.[10] and Aitoh et al.[11] According to these models, Nb

ions are displaced from the center of the oxygen octahedra along the equivalent eight <111>p directions. This implied that the Nb atoms had eight local disorder positions. The observed zebra-like microdomains observed in this study may have been the local ordered domains with modulated structures, i.e., in each stripe, the Nb ion was displaced along one <111>p direction. This disorder → order transition occurred in the cubic phase and was premonitory to the cubic → tetragonal phase transformation. Our experimental evidence showed that the transformation had an hysteresis and that the fraction coverted was temperature dependent. It also showed a reversible crystallographic orientation relationship. The overall transformation mechanism could be assumed to be composed of order-disorder and displacive mechanisms, associated with the Γ_{25} soft phonon of the transition. Cowley [12] showed that Γ_{25}, in the soft phonon of the cubic → tetragonal transition had an intrinsic vector corresponding to the displacement of Nb ions along <001>p. Therefore, below the transition point, the condensed displacement would give rise to a displacive polarization P_d which was parallel to <001>p. The order-disorder phase transition could be described in terms of pseudo-spin waves [11]. The optical transverse soft phonon may be strongly coupled to the pseudo-spin waves. The displacive polarization would always be parallel to the order-disorder one. Couplings between the pseudo-spin waves and other degrees of freedom (acoustic phonon for example) would make it possible to form long range commensurate or incommensurately modulated structures.

The main conclusions of this investigation are as follows:

- $KNbO_3$ consists of 60°, 90° and 180° domains at room temperature.
- The cubic → tetragonal phase transformation started at 438°C, and was completed at 410°C. It had all the characteristics of a first-order displacive transformation.
- There was a pre-transformation formation of ordered microdomains.
- A mechanism of order-disorder and displacive transformation modes are used to explain the phase change.

References

1. Landholt-Börnstein, "Numerical Data and Functional Relationships in Science and Technology," Ed. K. H. Hellwege Group III: Crystal and Solid State Physics, Vol. 16.
2. S. Triebwasser, Physical Review, Vol. 101, 3, (1956) 993.
3. R. H. Kulkarni, R. M. Chaudhari and S. A. Ingle, J. Phys. D: Appl. Phys., Vol. 6 (1973) 1816.
4. S. A. Ingle and A. P. David, Ferroelectric, Vol. 97 (1989) 201.
5. K. A. Deshmukh and S. A. Ingle, J. Phys. D: Appl. Phys., Vol. 4 (1971) 124.
6. F. Jona and A. Shirane, "Ferroelectric Crystals" Pergamon Press, Oxford, 1962.
7. C. Jun, F. Chan-gao, Li Qi and Feng Duan, J. Phys. C: Solid State, 21 (1988) 2255.
8. J. Fousek and V. Janovec, J. Appl. Phys., 40 (1969) 135.
9. J. Sapriel, Phys. Rev. B, 12 (1975) 5128.
10. R. Comes, M. Lambert and A. Guinier, Solid State Comm., 6 (1968) 715.
11. K. Aitoh, L. E. Zang, Nakamure. Y and N. Nishima, Ferroelectrics, 63 (1985) 29.
12. R. A. Cowley, Phys. Rev., 134 (1964) 981.
13. R. Blinic and B. Zeks, "Soft Modes in Ferroelectric and Antiferroelectric", North Holland, Amsterdam 1974.

(c) WRITTEN PUBLICATIONS

REFERREED JOURNALS OR BOOKS

- "Phase Transformations in Dicalcium Silicate. II: TEM Studies of Crystallography, Microstructures and Mechanisms," Y. J. Kim, I. Nettleship and W. M. Kriven, J. Am. Ceram. Soc., 75 [9] 2407-2419 (1992).

- "Chemical Preparation and Phase Stability of Ca_2SiO_4 and Sr_2SiO_4 Powders," I. Nettleship, J. L. Shull Jr. and W. M. Kriven, J. European Ceramic Society, 11 291-298 (1993).

- "Chemical Synthesis and Characterization of Calcium Aluminate Powders," M. A. Gulgun, O. O. Popoola and W. M. Kriven, J. Am. Ceram. Soc., (1994) in press.

- "Phase Stability of Chemically Derived Enstatite ($MgSiO_3$) Powders," C. M. Huang, D. H. Kuo, Y. J. Kim and W. M. Kriven, J. Am. Ceram. Soc., (1994) submitted.

- "A TEM Study on the Decomposition of Synthetic Hillebrandite ($Ca_2SiO_4 \bullet H_2O$)," Y. J. Kim and W. M. Kriven, J. Materials Research, (1994) accepted.

- "XPS Study of Bonding Between Polyvinyl Alcohol and a Titanate Cross Coupling Agent," M. A. Gulgun, W. M. Kriven and O. O. Popoola, J. Materials Research, (1994) submitted.

- "Twinning in Structural Ceramics, " W. M. Kriven. (invited review paper) in Twinning in Advanced Materials, Edited by M. H. Yoo and M. Wuttig. Published by The Minerals, Metals and Materials Society (TMS), Warrendale, PA.(1994), in preparation.

- "Crystallography of the Cubic → Tetragonal Phase Transformation in $KNbO_3$," O. O. Popoola and W. M. Kriven. Phil. Mag., in preparation.

CONFERENCE PROCEEDINGS

- "Transformation Mechanisms in Dicalcium and Distrontium Orthosilicates," Y. J. Kim, J. L. Shull, B. N. Sun and W. M. Kriven. Proc. Int'l. Conf. on Martensitic Transformations, (ICOMAT '92). Publ. by Monterey Institute for Advanced Studies, Monterey CA, USA. 683-688 (1993).

- "Microstructure and Phase Transformation in $KNbO_3$," O. O. Popoola and W. M. Kriven. Proc. 51st Annual Meeting of Microscopy Society of America. Publ. San Fransisco Press, pp 956-957 (1993).

- "Phase Transformations in Ceramics," W. M. Kriven (invited paper). Proc. 51st Annual Meeting of Microscopy Society of America. Publ. by San Fransisco Press, pp 952-953 (1993).

- "TEM Characterization of the α'and β Phases in Polycrystalline Distrontium Silicate (Sr_2SiO_4)," Y. J. Kim, J. L. Shull and W. M. Kriven. Proc. 50th Annual Meeting of the Electron Microscopy Society of America (EMSA). Edited by G. W. Bailey, J. Bentley and J. A. Small, pp 354-355 (1992).

- "In Situ TEM Study of Hillebrandite ($Ca_2SiO_4 \bullet H_2O$) Decomposition," Y. J. Kim and W. M. Kriven, Proc. 13th Int. Congr. on Electron Microscopy, to be held in Paris, France in July 17-21; pp 1-2 (1994), submitted.

- "Phase Transformations in $KNbO_3$ Perovskite Ceramic," O. O. Popoola and W. M. Kriven. Proc. International Conference on Solid → Solid Phase Transformations, Pittsburgh, PA, July 17-22 1994, in preparation.

- "The Mechanism of the Tetragonal to Monoclinic Transformation in YNbO4," J. L. Shull, B. N. Sun and W. M. Kriven. Proc. International Conference on Solid → Solid Phase Transformations, Pittsburgh, PA, July 17-22 1994, in preparation.

- "High Temperature Phase Transformation in $Y_4Al_2O_9$, $Gd_4Al_2O_9$, and $Dy_4Al_2O_9$," J. L. Shull and W. M. Kriven, Proc. International Conference on Solid → Solid Phase Transformations, Pittsburgh, PA, July 17-22 1994, in preparation.

- "Displacive and Martensitic Transformations in Ceramics," W. M. Kriven. (Invited overview paper). Proc. International Conference on Solid to Solid Phase Transformations, Pittsburgh, PA July,1994, in preparation.

(d) PERSONNEL AND DEGREES AWARDED

PERSONNEL

- Professor Waltraud M. Kriven
  Principal Investigator

- Youn Joong Kim (Ph. D. student)

- James Lee Shull (M. S student with stipend from an NSF fellowship and operating costs covered by this AFOSR URI grant).

- Dr. Ian Nettleship (post doctoral research associate), now Assistant Professor in the Dept. of Materials Science and Engineering, at the University of Pittsburgh.

- Dr. O. O. Popoola (post doctoral research associate) now Senior Research Scientist in the Materials Systems Reliability Department at Ford Research Laboratory.

- Dr. Youg Joon Kim (post doctoral research associate), now director of the Electron Microscopy Facility at the Korea Basic Science Center, in Taejeon, South Korea.

- Dr. Chao Ming Huang (post doctoral research associate) currently still working in our group under another AFOSR contract.

THESES

"Crystallography and Microstructural Studies of Phase Transformations in Two Ceramic Systems: Dysprosia (Dy_2O_3) and Dicalcium Silicate (Ca_2SiO_4)."
Ph.D. thesis, submitted in June 1991.

- "Chemical Preparation and Phase Stability of Strontium Orthosilicate (Sr_2SiO_4),"
by James Lee shull, Jr.
M.S. thesis submited June 1993.

(e) INTRACTIONS

(i) PAPERS PRESENTED AT MEETINGS

- "Preparation and Metastability of β Dicalium Silicate Polycrystals," I. Nettleship*, Y.J. Kim and W.M. Kriven. Presented at 93rd Annual Meeting of the American Ceramic Society, held in Cincinnati, OH, April 28th-May 2nd 1991.

- "Crystallography and Microstructure of Polycrystalline α'_L in β-Ca_2SiO_4," Y.J. Kim,* I. Nettleship and W.M. Kriven. Presented at 93rd Annual Meeting of the American Ceramic Society, held in Cincinnati, OH, April 28th-May 2nd 1991.

- "Crystallography and Microstructural Studies of the $\beta \rightarrow \gamma$ Transformation in Ca_2SiO_4," Y.J. Kim, I. Nettleship and W.M. Kriven*. Presented at 93rd Annual Meeting of the American Ceramic Society, held in Cincinnati, OH, April 28th-May 2nd 1991.

- "Microstructural Studies of Ce_2OS Precipitates in a CeS Matrix," Y.J. Kim, O.O. Popoola* and W.M. Kriven. Presented at 93rd Annual Meeting of the American Ceramic Society, held in Cincinnati, OH, April 28th-May 2nd 1991.

- "Microstructure and Microchemistry of Nickel Sulfide Inclusions in Plate Glass," J.J. Coooper*, O.O. Popoola and W.M. Kriven. Presented at 93rd Annual Meeting of the American Ceramic Society, held in Cincinnati, OH, April 28th-May 2nd 1991.

- "Preparation of Calcium Aluminate Powders Using a Sol-Gel Method," M.A. Gulgun*, O.O. Popoola, I. Nettleship and W.M. Kriven. Presented at 93rd Annual Meeting of the American Ceramic Society, held in Cincinnati, OH, April 28th-May 2nd 1991.

- "TEM Characterization of a Modulated β Phase in Polycrystalline Dicalcium Silicate," Y.J. Kim*, I. Nettleship and W.M. Kriven. Presented at 49th Annual Meeting of the Electron Microscopy Society of America (EMSA), San Jose, California (1991).

- "Microstructural and Microchemical Characterization of Nickel Sulfide Inclusions in Plate Glass," J.J. Cooper*, O.O. Popoola and W.M. Kriven.Presented at 49th Annual Meeting of the Electron Microscopy Society of America (EMSA), San Jose, California (1991).

- "On Possible Origins of the Displacive β to γ Transformations in Ca_2SiO_4: Role of Lattice Strains and Non-bonded Forces," Y. J. Kim* and W. M. Kriven. Presented at Am. Ceram. Soc. Fall Meeting on *Atomic Structure, Bonding and Properties of Ceramics* as Abstract{#10-BF-91F). Held on Marco Island in Florida on October 13-18th 1991.

- "Preparation and Hydration Kinetics of Fine $CaAl_2O_4$ Powders," M. A. Gulgun*, O. O. Popoola, I. Nettleship, W. M. Kriven and J.F. Young. Presented at Materials Research Society Fall Meeting, Dec 1991, Boston, MA.

- "On Phase Transformation Mechanisms in Dicalcium Silicate (Ca_2SiO_4)," Y.J. Kim and W. M. Kriven*. Invited talk presented at the Fall meeting of the American Geolophysical Union held in San Fransisco, California, Dec 9-13th 1991.

- "Preparation and Phase Stability of Strontium Orthosilicate (Sr_2SiO_4)," J. L. Shull* Jr., I. Nettleship and W. M. Kriven. Presented at the Annual Meeting of the American Ceramic Society, abstract # [197-B-92], April 12-16th, 1992 in Minneapolis, MN.

- "Crystallography and Phase Transformations of Modulated α'-Sr_2SiO_4, ," Y. J. Kim*, J. L. Shull Jr. and W. M. Kriven. Presented at the Annual Meeting of the American Ceramic Society, abstract # [198-B-92], April 12-16th, 1992 in Minneapolis, MN.

- "Microstructure and Phase Transformations of Nickel Sulfide Inclusions in Plate Glass," J. J. Cooper, O. O. Popoola and W. M. Kriven. Abstract # [27-BP-92].Presented at the Annual Meeting of the American Ceramic Society, April 12-16th, 1992 in Minneapolis, MN.

- "Transformation Mechanisms in Dicalcium Silicate and Distrontium Orthosilicates," Y. J. Kim, J.L. Shull, B. N. Sun and W. M. Kriven*. Presented at the International Conference on Martensitic Transformations (ICOMAT '92). Held in Monterey, CA, July 20-24th 1992.

- "TEM Characterization of the α' and β Phases in Polycrystalline Distrontium Silicate (Sr_2SiO_4)," Y. J. Kim, J. S. Shull and W. M. Kriven. Presented at the 50th Annual Meeting of the Electron Microscopy Society of America (EMSA), held in Boston, Aug 16-21, 1992.

- "Characterisation of Nickel Sulphide Stones in Glass," J. J. Cooper, O. O. Popoola and W. M. Kriven. Presented at Austceram '92, International Ceramics Conference and Exhibition held in Australia, August 16-21st, 1992.

- "Phase Transformations and Fracture Associated with Nickel Sulfide Stones in Glass," W. M. Kriven*, J. J. Cooper and O. O. Popoola. Presented at 53rd Annual Conference on glass Problems, Nov 17-18th 1992, Ohio State University.

- "Transformation Mechanisms and Induced Fracture in Ceramics," W. M. Kriven*. Presented at the Materials Research Society, Spring Meeting, held in San Fransisco, California in April 16-18th 1993.

- "Phase Transformations in Chemically Derived Enstatite Powders," D. H. Kuo*, C. M. Huang, Y. J. Kim and W. M. Kriven. Presented at the Annual Meeting of the American Ceramic Society, held in Cincinnati in April 18-22nd, 1993.

- "Transformation Mechanisms in Distrontium Silicate (Sr_2SiO_4)," Y. J. Kim*, J. L. Shull Jr., and W. M. Kriven. Presented at the Annual Meeting of the American Ceramic Society, held in Cincinnati in April 18-22nd, 1993.

- "The Orthorhombic (o) to Tetragonal (t) Transformation in $KNbO_3$," O. O. Popoola* and W. M. Kriven. Presented at the Annual Meeting of the American Ceramic Society, held in Cincinnati in April 18-22nd, 1993.

- "Calcination Behavior of Chemically Prepared Calcium Aluminate," M. A. Gulgun*, O. O. Popoola and W. M. Kriven. Presented at the Annual Meeting of the American Ceramic Society, held in Cincinnati in April 18-22nd, 1993.

- "Crystal Growth and Characterization of Distrontium Silicate," B. N. Sun*, J. L. Shull and W. M. Kriven. Presented at the Annual Meeting of the American Ceramic Society, held in Cincinnati in April 18-22nd, 1993.

- "Synthesis of Silicate and Aluminate Powders by a Modified Pechini Process," M. A. Gulgun*, C. M. Huang, D. H. Kuo, J. L. Shull*, K. G. Slavick, T. K Swanson, W. M. Kriven, I. Nettleship and R. Russel. Presented at the Annual Meeting of the American Ceramic Society, held in Cincinnati in April 18-22nd, 1993.

- " TEM Investigation of Crystallization Kinetics in Calcium Aluminate Powders," M. A. Gulgun*, O. O. Popoola and W. M. Kriven. Presented at the Joint Meeeting of the Central States Electron Microscopy Society, Sangamon State University, Springfield, Illinois, May 20th 1993.

- "Phase Transformation Induced Intragranular Microcracks in Enstatite," D. H. Kuo*, C. M. Huang, Y. J. Kim and W. M. Kriven. Presented at the Joint Meeeting of the Central States Electron Microscopy Society, Sangamon State University, Springfield, Illinois, May 20th 1993.

- "Pretransitional Phenomena, Transformation Mechanisms and Crystallography of $PbTiO_3$ and $KNbO_3$," H. Chen*, C. M. Wayman, W. M. Kriven and J. D. Bass. Presented at 8th International Meeting on Ferroelectricity (IMF8) held at NIST in August, 1993

- "TEM Study of the Decomposition of Synthetic Hillebrandite," Y. J. Kim and W. M. Kriven*. To be presented at the Annual Meeting of the American Ceramic Society, Indianapolis, IN, April 24-28 1994.

- "Phase Transformations in Potassium Niobate Perovskite Ceramic," O. O. Popoola and W. M. Kriven. To be presented at the International Conference on Solid to Solid Phase Transformations, Pittsburgh, PA July,1994.

- "The Mechanism of the Tetragonal to Monoclinic Transformation in $YNbO_4$," J. L. Shull, B. N. Sun and W. M. Kriven. To be presented at the International Conference on Solid to Solid Phase Transformations, Pittsburgh, PA July,1994.

- "High Temperature Phase Transformation in $Y_4Al_2O_9$, $Gd_4Al_2O_9$, and $Dy_4Al_2O_9$," J. L. Shull and W. M. Kriven. To be presented at the International Conference on Solid to Solid Phase Transformations, Pittsburgh, PA July,1994.

INVITED LECTURES

- "SEM and TEM in Materials Science," W.M. Kriven. Invited lecture, American Chemical Society Annual Meeting, Tutorial Sessions in Materials Science, New York, NY, Aug 25th 1991.

- "On Phase Transformation Mechanisms in Dicalcium Silicate (Ca_2SiO_4)," Y.J. Kim and W. M. Kriven*. Invited lecture presented at the Fall meeting of the American Geolophysical Union held in San Fransisco, California, Dec 9-13th 1991.

- "Phase Transformations and Toughening Mechanisms in Composite Ceramics," W. M. Kriven. Invited lecture presented at the Materials Science and Engineering Departmental Colloquium, University of Illinois at Urbana-Champaign, on February 10th 1992.

- "Phase Transformations and Toughening Mechanisms in Composite Ceramics," W. M. Kriven. Invited lecture presented at the Materials Science and Engineering Departmental Seminar, Massachussetts Institute of Technology (MIT), on February 18th 1992.

- "Toughening Mechanisms in Non-Zirconia Composites," W. M. Kriven*. Invited lecture, abstract # [42-C-92]. Presented at the Annual Meeting of the American Ceramic Society, April 12-16th, 1992 in Minneapolis, MN.

- "Phase Transformations and Toughening Mechanisms in Composite Ceramics," W. M. Kriven. Invited lecture presented at the Materials Science and Engineering Departmental Seminar, Illinois Institute of Technology (IIT), on April 30th 1992.

- "Electron Microscopy Observations of Micromechanical Behavior in Ceramic Composites," W. M. Kriven. Invited seminar presented in the Materials Science and Engineering Laboratory, National Institute of Science and Technology (NIST), Gaithesburg, MD. per Dr. S. M. Wiederhorn. Held on Oct 29th 1992.

- "Transformation-Induced Fracture in Ceramic Composites," W. M. Kriven*. Invited lecture, presented at the Annual Meeting of the American Ceramic Society, held in Cincinnati in April 18-22, 1993.

- "Phase Transformations in Ceramics," W. M. Kriven*. Invited lecture, Presented at the Microscopy Society of America (MSA) Annual Meeting, held in Cincinnati in Aug 1-6, 1993.

- "Volume Changes During Transformation in Ceramics," W. M. Kriven*. Invited lecture presented at the ASM Fall Meeting in the Symposium on Effect of Plastic Deformation on the Thermodynamics, Kinetics and Mechanisms of Phase Transformations," held in Pittsburgh, PA, Oct 17-21, 1993.

- "Twinning in Structural Ceramics," W. M. Kriven.* Invited lecture presented at TMS Fall Meeting in Symposium on Twinning in Advanced Materials. Held in Pittsburgh, PA, Oct 17-21, 1993.

- "Ceramics Via Organic and Inorganic Synthesis," W. M. Kriven*. Invited lecture to be presented to the Illinois Association of Chemistry Teachers, Annual Meeting at the University of Illinois at Urbana-Champaign, March 4th 1994.

- "Displacive and Martensitic Transformations in Ceramics," W. M. Kriven.* Invited overview paper, to be presented at International Conference on Solid to Solid Phase Transformations in Inorganic Materials '94. To be held in Pittsburgh in July 17-22, 1994.

(e) (ii) CONSULTATIVE AND ADVISORY FUNCTIONS TO OTHER LABORATORIES AND AGENCIES

None

(f) NEW DISCOVERIES, INVENTIONS OR PATENTS

None

(g) ANY OTHER STATEMENTS TO PROVIDE ADDITIONAL INSIGHTS

None

PROFESSOR D. A. PAYNE

PHASE TRANSFORMATIONS IN FERROIC CERAMICS, D. A. PAYNE

a. Objectives and Statement of Work

1. Establish a materials synthesis and processing facility for the preparation and characterization of single crystals and polycrystalline specimens of suitable size and perfection for intrinsic property measurements.
2. Investigate phase transformations in ferroic ceramics, and contribute to the understanding of nucleation and growth mechanisms for displacive transformations.
3. Determine the role of domain and twin configurations on switching characteristics and phase transformation behavior in terms of crystallography, thermodynamics and kinetic factors.
4. Examine hysteresis behavior and thermal stability of phase transformations, and evaluate in terms of martensitic models for ceramic materials.
5. Develop theoretical models to explain the phenomenology of displacive transformations and predict the possibility of unusual properties.
6. Make self-consistent thermodynamic calculations to determine the appropriateness of the proposed model.
7. Design material systems and structures and demonstrate the feasibility of novel applications associated with phase transformation behavior.
8. Investigate the role of coordination and molecular building blocks on transformation behavior and structure-property relations.

b. Significant Accomplishments

Major collaborations occurred during the URI project on the materials synthesis, processing, crystal growth, characterization and property measurements on ceramic materials which exhibit unusual phase transformation behavior. For example, we established and equipped laboratories for (i) materials chemistry, synthesis, chemical preparation and analysis, (ii) powder processing, sintering and hot-pressing, (iii) a state-of-the-art crystal growth facility for melt, flux and hydrothermal methods, (iv) a thermal analysis facility for the determination of intrinsic properties associated with phase transformations, including enthalpy and dimensional changes, and (v) specialized equipment for electrical and mechanical measurements. Notable achievements, include, the growth of large crystals of sufficient size for property measurements (e.g., electrical, mechanical, optical, structural, etc.) by members of the URI group. For

example, we made significant achievements and received international recognition for the growth of large $PbTiO_3$ and $YBa_2Cu_3O_{6+x}$ single crystals. In addition we made contributions to the growth of ZrO_2, $2CaO.SiO_2$, $2Y_2O_3.Al_2O_3$, $ReNbO_4$, $KNbO_3$, $BaTiO_3$, LiB_3O_5 and $KTiOPO_4$.

An example of a notable achievement was the development of an accelerating crucible rotation method for the growth of single crystals of the highest perfection by a self-flux technique. For example, we supplied large single domain crystals of $PbTiO_3$ and $KNbO_3$ to Professor Bass and collaborated on the determination of intrinsic elastic constants by Brillouin scattering methods, and the effects of pressure on phase transformation behavior. Similar crystals were studied by Professor Chen on pre-transformation behavior, and by Professor Wayman on the crystallography of domain configurations. In addition, LiB_3O_5 and $KTiOPO_4$ crystals were grown by a self-flux method, and the effects of trigonal (B), tetrahedral (P) and octahedral (Ti) coordinations were investigated on phase transformation behavior. Electrical and optical properties were determined in the vicinity of the transformation, and the materials could find applications for second harmonic generation and blue light emission.

With respect to polycrystalline ceramics, and electromechanical properties, we made a significant contribution to the understanding of competing phases at antiferroelectric (AFE) -to- ferroelectric (FE) phase transformations. We prepared materials in the Pb(Zr, Sn, Ti)O_3 system (PZST) by chemical processing and hot-pressing methods, and investigated the phase transformation between FE rhombohedral and AFE tetragonal structures. Thermal analysis determined the transformation to be first order, with considerable thermal hysteresis. Through collaboration with Professor C. M. Wayman, we developed a martensitic approach to explain the observed thermal behavior for the displacive material. A thermodynamic formalism was developed to explain how the normally low temperature (LT) FE state could be induced from the higher temperature (HT) AFE state on application of an electric field. The electric work done could overcome the thermodynamic barrier (ΔG^*) into the FE state, and depending upon the temperature of operation, the thermodynamic approach could explain reversible-irreversible phenomena associated with shape and volume changes. In addition, the thermodynamic approach predicted shape-memory and superelastic properties, which were subsequently discovered in the predicted temperature ranges. These important discoveries could have significant applications for electrically deformable ceramics in adaptive structures and smart systems where electrically driven distortions could be maximized in the vicinity of a phase transformation.

Another unusual type of phase transformation behavior was investigated where a change in oxygen partial pressure (pO_2) at constant temperature could induce a structural change between orthorhombic (LT) and tetragonal (HT) states in $YBa_2Cu_3O_{6+x}$. Single crystals were grown and observed in the hot-stage of an optical microscope. Changes in shape, twin structure and electrical properties were monitored, and used to explain the kinetics of transformation between the respective states in terms of oxygen diffusivity, rate controlling activation energies and kinetic factors. Elastic deformations were shown to be dependent on oxygen concentration. A viscoelastic model was developed to explain the observed twin wall motion and switching behavior in terms of a yield stress, twin wall viscosity and oxygen mobility. Novel features of the phase transformation behavior relate oxygen content with elastic deformations, and these could give rise to novel developments for oxygen sensing devices with mechanical actuation in fuel and combustion systems.

c. Publications - D. A. Payne

J. R. LaGraff, P. D. Han and D. A. Payne, "Electrical Measurements Near the Orthorhomic-Tetragonal Phase Transformation in Single Crystal $YBa_2Cu_3O_{7-\delta}$" Physica C 169:355-360 (1990).

J. R. LaGraff, P. D. Han and D. A. Payne, "Normal State Electrical Measurements Near the Ferroelastic Phase Transition in Single Crystal $YBa_2Cu_3O_{7-\delta}$," Proc. VII ISAF IEEE Symp 54-57 (1991).

J. R. LaGraff, P. D. Han and D. A. Payne, "Resistance Measurements and Oxygen Out-Diffusion Near the Orthorhomic-Tetragonal Phase Transformation," Physical Review B, 43: 441-447 (1991).

J. R. LaGraff, P. Han and D. A. Payne, "Oxygen In-Diffusion and Out-Diffusion in Single Crystal $YBa_2Cu_3O_{7-\delta}$" Mat. Res. Soc. Symp. Proc. 209:801-806 (1991).

J. R. LaGraff and D. A. Payne, "Oxygen Stoichiometry and Mobility Effects on Domain Wall Motion in Ferroelastic $YBa_2Cu_3O_{7-\delta}$" Ferroelectrics 130:87-105 (1992).

P. Yang and D. A. Payne, "Thermal Stability of Field-Forced and Field-Assisted Antiferroelectric-Ferroelectric Phase Transformations in PZST," J. Appl. Phys., 71:1361-1367 (1992).

J. R. LaGraff and D. A. Payne, "Chemical Diffusion of Oxygen in Single Crystal and Polycrystalline $YBa_2Cu_3O_{6+x}$ via Electrical Resistance Measurements," Physical Review B, 47:3380-3390 (1993).

C. S. Zha, A. G. Kalinichev, J. D. Bass, C. T. A. Suchicital, and D. A. Payne, "Pressure Dependence of the Optical Absorption Edge of $PbTiO_3$ up to 35 GPa: Observation of the Tetragonal-to-Cubic Phase Transition ," J. Appl. Phys., 72:3705-3707 (1992).

B. N. Sun, Y. Huang and D. A. Payne, "Growth of Large $PbTiO_3$ Crystals by a Self-Flux Technique," J. Crystal Growth, Proc 10th Int'l Conf. on Crystal Growth, San Diego, CA 128:867-870 (1993).

P. Yang and D. A. Payne, "Shape Memory and Superelasticity for Ceramics with Field-Induced Antiferroelectric-Ferroelectric Phase Transformations," J. Am. Ceram. Soc. (submitted September 1993).

J. R. LaGraff and D. A. Payne, "Concentration-Dependent Oxygen Diffusivity in $YBa_2Cu_3O_{6+x}$: Part I, Argon Annealing Studies," Physica C 212:470-477 (1993).

J. R. LaGraff and D. A. Payne, "Concentration-Dependent Oxygen Diffusivity in $YBa_2Cu_3O_{6+x}$: Part II, Oxygen Partial Pressure Studies," Physica C 212:478-486 (1993).

J. R. LaGraff and D. A. Payne, "Concentration-Dependent Oxygen Diffusivity in $YBa_2Cu_3O_{6+x}$: Part III, Diffusion Mechanisms," Physica C 212:487-496 (1993).

P. Yang and D. A. Payne, "Grain-Size Dependence of Ferroelectric-Antiferroelectric Phase Transformations in $Pb(Zr,Sn,Ti)O_3$ Dielectrics," Cer. Trans. 32 347-354 (1993).

W. L. Warren, B. A. Tuttle, B. N. Sun, Y. Huang and D. A. Payne, "Paramagnetic Resonance of Platinum Ions in $PbTiO_3$ Single Crystals," Appl. Phys. Letts. 62:146-148 (1993).

W. L. Warren, B. A. Tuttle, B. N. Sun, Y. Huang and D. A. Payne, "Optically Induced Paramagnetic Defects in $PbTiO_3$ Single Crystals," Proc. Mat. Res. Soc. Symp. (1993).

P. Yang and D. A. Payne, "The Effect of Hydrostatic Pressure on Antiferroelectric-to-Ferroelectric Phase Transformations in $Pb(Zr,Sn,Ti)O_3$ Ceramics," J. Am. Ceram. Soc. (submitted October 1993).

A. G. Kalinichev, J. D. Bass, C. S. Zha, D. A. Payne and P. Han, "Elastic Properties of Orthorhombic $KNbO_3$ Single Crystals by Brillouin Scattering," J. Appl. Phys. 74:6603-6608 (1993).

P. Yang and D. A. Payne, "Shape Memory and Superelasticity for Ceramics with Field Induced Antiferroelectric-Ferroelectric Phase Transformations," Proc. Int. Conf. Martensitic Transformations, ICOMAT (1992) Eds., C. M. Wayman and J. Perkins, 719-724 (1993)

B. N. Sun, Y. Huang and D. A. Payne, "Growth of Isometric Lead Titanate ($PbTiO_3$) Crystals from High-Temperature Solutions," J. Crystal Growth (submitted, February 1994).

P. Yang and D. A. Payne, "Hydrostatic Pressure and Electric Field Effects on Antiferroelectric-to-Ferroelectric Phase Transformations in Tin-Modified Lead Zirconate Titanate Ceramics," J. Appl. Phys. (submitted, February 1994).

D. A. Payne and P. Yang, "Microstructure Dependent Dielectric Properties for Ferroelectric to Antiferroelectric Phase Transformations in Tin-Modified Lead Zirconate," Brit. Ceram. Proc. (submitted, February 1994).

Y. Huang, P. D. Han, D. A. Payne and D. Shen, "Dielectric Properties of Lithium Triborate Crystals," J. Am. Ceram. Soc. (to be submitted, 1994).

Y. Huang, P. D. Han, D. A. Payne and D. Shen, "A Study of Proton Exchange in Single Crystal $KTiOPO_4$ by FTIR Spectroscopy," J. Appl. Phys. (to be submitted, 1994).

Y. Huang and D. A. Payne, "Crystal Growth of Potassium Titanyl Phosphate by a Floating Seed Method," J. Crystal Growth (to be submitted, 1994).

Y. Huang and D. A. Payne, "Optical Spectra of Cr^{3+} Ions in Potassium Titanyl Phosphate $KTiOPO_4$," Appl. Phys. Letts. (to be submitted, 1994).

Y. Huang and D. A. Payne, "Dielectric Relaxation and Defects in Lead Titanate Single Crystals," J. Am. Ceram. Soc. (to be submitted, 1994).

Y. Huang and D. A. Payne, "Absorption Characteristics in Band-Edge Region of the Infrared Spectra for Lead Titanate Crystals," J. Appl. Phys. (to be submitted, 1994).

d. Professional Personnel (1990-1993)

Dr. D. A. Payne, Professor, Materials Science and Engineering

Dr. P. D. Han, Senior Research Associate, Materials Science and Engineering
Dr. B. N. Sun, Senior Research Associate, Materials Science and Engineering

LaGraff, J. Research Assistant
Chemical diffusion of oxygen in $YBa_2Cu_3O_{6+x}$. Ph.D. thesis, D.A. Payne, advisor (1992).

Yang, P. Research Assistant
Electrically induced antiferroelectric-ferroelectric phase transformations in lead-zirconate titanate stannate ceramics. Ph.D. thesis, D. A. Payne, advisor (1992).

Huang, Y. Research Assistant
Flux growth, characterization and structure property relations for inorganic oxide materials: LiB_3O_5, $KTiOPO_4$ and $PbTiO_3$. Ph.D. thesis, D. A. Payne, advisor (1993).

e. Papers presented at Meetings, Conferences, Seminars, etc. (AFOSR Research Group)

P. Yang and D. A. Payne, "Field-Enforced Phase Transformation in Modified $PbZrO_3$-$PbTiO_3$ Systems, *92nd Annual Meeting of the American Ceramic Society*, Dallas, TX, April 1990.

P. Yang and D. A. Payne, "Microstructure Dependence of a Field-Forced Phase Transformation in Modified$PbZrO_3$-$PbTiO_3$ Systems, *VII ISAF IEEE Symposium*, Urbana, IL, June 1990.

J. R. LaGraff, P. D. Han and D. A. Payne, "Electrical Measurements near the Ferroelastic Phase Transformation in Single Crystal $Ba_2Cu_3O_{7-\delta}$," *VII ISAF IEEE Symposium*, Urbana, IL, June 1990.

J. R. LaGraff, "Resistance Measurements Near the Orthorhombic-Tetragonal Transition in Single Crystal $Ba_2Cu_3O_{7-\delta}$" *Science and Technology Center for Superconductivity, Distinguished Visitor Workshop in Single Crystals and Oxygen Deficiency*, Chicago, IL, September 1990.

J. R. LaGraff, P. D. Han and D. A. Payne, "Oxygen In-Diffusion and Out-Diffusion in Single Crystal $Ba_2Cu_3O_{7-\delta}$, *1990 Fall Meeting of the Materials Research Society*, Boston, MA, November 1990.

J. R. LaGraff, P. D. Han and D. A. Payne, "Electrical Resistance Measurements Single Crystal, Bi-crystal and Polycrystal $YBa_2Cu_3O_{7-\delta}$," *1991 March Meeting of the American Physical Society*, Cincinnati, OH, March 1991.

J. R. LaGraff, "Resistance Measurements and Oxygen Out-Diffusion near the Orthorhombic-Tetragonal Phase Transformation in Single Crystal $YBa_2Cu_3O_{6+x}$," *1991 Sigma Xi Graduate Student Paper Contest*, Urbana, IL, April 1991.

J. R. LaGraff, P. D. Han and D. A. Payne, "Defect-Controlled Processes in Oxide Superconductors," *Symposium on Solid State Science and Technology*, Electrochemical Society and the American Vacuum Society, Urbana, IL, April 1991.

J. R. LaGraff, P. D. Han and D. A. Payne, "Electrical Resistance Measurements and the Role of Twin and Grain Boundaries on Oxygen Diffusion in Single Crystal, Bi-crystal and Polycrystal $YBa_2Cu_3O_{7-\delta}$," *93rd Annual Meeting of the American Ceramic Society*, Cincinnati, OH, April 1991.

P. Yang and D. A. Payne, "The Effect of Elastic Boundary Conditions on the Field-Forced Transformation in Antiferroelectrics," *93rd Annual Meeting of the American Ceramic Society*, Cincinnati, OH, April 1991.

J. R. LaGraff and D. A. Payne, "Oxygen Stoichiometry and Mobility Effects on Domain Wall Motion in Ferroelastic $YBa_2Cu_3O_{6+x}$," *NATO Advanced Study Institute on the Physics and Materials Science of High Temperature Superconductors*, Porto Carras, Greece, August 1991.

J. R. LaGraff and D. A. Payne, "Chemical Diffusion of Oxygen in $YBa_2Cu_3O_{6+x}$," *NATO Advanced Study Institute on the Physics and Materials Science of High* Temperature *Superconductors*, Porto Carras, Greece, August 1991.

J. R. LaGraff and D. A. Payne, "Oxygen Stoichiometry and Mobility Effects on Domain Wall Motion in Ferroelastic $YBa_2Cu_3O_{6+x}$," *International Summer School on Ferroelectric Ceramics*, Ascona, Switzerland, September 1991.

P. Yang and D. A. Payne, "Thermal Stability of Field-Forced Phase Transformations," Invited paper, *The American Ceramic Society: Electronics and Optical Materials Meeting*, Arlington, VA, October 1991.

J. R. LaGraff and D. A. Payne, "Phase Transformations, Oxygen Mobility and Defect Clustering in $YBa_2Cu_3O_{6+x}$," *URI Workshop on Phase Transformations in Ceramics*, Urbana, IL, April 1992.

J. R. LaGraff and D. A. Payne, "Chemical Diffusion of Oxygen in $YBa_2Cu_3O_{6+x}$ via Electrical Resistance Measurements II: Extrinsic Mechanisms," *94h Annual Meeting of the American Ceramic Society*, Minneapolis, MN, April 1992.

J. R. LaGraff and D. A. Payne, "Chemical Diffusion of Oxygen in $YBa_2Cu_3O_{6+x}$ via Electrical Resistance Measurements I: Intrinsic Mechanisms," *94h Annual Meeting of the American Ceramic Society*, Minneapolis, MN, April 1992.

Y. Huang, P. D. Han, D. A. Payne and D. Shen, "Proton Exchanged KTP and AL-Doped KTP Single Crystals," *94h Annual Meeting of the American Ceramic Society*, Minneapolis, MN, April 1992.

J. R. LaGraff and D. A. Payne, "The Chemical Diffusion of Oxygen in $YBa_2Cu_3O_{6+x}$ via Electrical Resistance Measurements: Intrinsic and Extrinsic Mechanisms," *1992 Spring Meeting of the Materials Research Society*, San Francisco, CA, April 1992.

P. Yang and D. A. Payne, "The Effect of Elastic Boundary Conditions on Field-Forced Antiferroelectric-to-Ferroelectric Phase Transformations in PZST Ceramics," *94h Annual Meeting of the American Ceramic Society*, Minneapolis, MN, April 1992.

P. Yang and D. A . Payne, "Antiferroelectric-Ferroelectric Phase Transformations in Ceramics: Opportunities for Shape-Memory and Superelastic Behavior," *American Ceramic Society International Congress*, San Francisco, CA 1992.

B. N. Sun, Y. Huang and D. A. Payne, "Growth of Large $PbTiO_3$ Crystals by a Self-Flux Technique," *International Conference on Crystal Growth*, San Diego, CA 1992.

Y. Huang, B. N. Sun, P. D. Han and D. A. Payne, "Growth and Morphology of Undoped and Al, Nb-doped KTP Single Crystals, *International Conference on Crystal Growth*, San Diego, CA 1992.

P. Yang and D. A. Payne, "Shape Memory and Superelasticity for Ceramics with Field Induced Antiferroelectric-Ferroelectric Phase Transformations," *Proc. ICOMAT-92*, Monterey, CA, July 1992.

J. R. LaGraff and D. A. Payne, "Concentration-Dependent Oxygen Diffusion in $YBa_2Cu_3O_{6+x}$" *95th Annual Meeting of the American Ceramic Society*, Cincinnati, OH, April 1993.

B. N. Sun, Y. Huang and D. A. Payne, "Growth, Defect Centers and Phase Transformation of Lead Titanate Crystals," *95th Annual Meeting of the American Ceramic Society*, Cincinnati, OH, April 1993.

Y. Huang, B. N. Sun and D. A. Payne, "Crystal Growth of Potassium Titanyl Phosphate by a New Seeding Technique," *95th Annual Meeting of the American Ceramic Society*, Cincinnati, OH, April 1993.

Y. Huang, B. N. Sun and D. A. Payne, "Dielectric Relaxation and Defects in Lead Titanate Single Crystals," *95th Annual Meeting of the American Ceramic Society*, Cincinnati, OH, April 1993.

D. A. Payne, Invited Talks (AFOSR), 1990-1993

VII ISAF Symposium, Urbana, IL, June 7, 1990
Dow Corning Corporation, Midland, MI, September 27, 1990
Pacific Coast Regional Meeting, American Ceramic Society, Seattle, WA,October 25, 1990

Special Ceramics 9 Meeting, British Ceramic Society, London, England, December 18, 1990
Annual Meeting of the American Ceramic Society, Cincinnati, OH, April 28, 1991
University of Pittsburgh, Pittsburgh, Pennsylvania, September 19, 1991
University of Missouri-Rolla, Rolla, Missouri, September 26, 1991
Cornell University, Ithaca, New York, October 3, 1991
Frontiers in Material Science: Chemistry and Technology, Rochester, New York, October 14, 1991
University of New Mexico, Albuquerque, New Mexico, November 1, 1991
Materials Research Society Fall Meeting, Boston, Massachusetts, December 2, 1991
Ohio State University, Columbus, Ohio, February 14, 1992
Case Western University, Cleveland, Ohio, March 31, 1992
International Form on Fine Ceramics, Nagoya, Japan, March 12, 1992
Annual Meeting of the American Ceramic Society, Minneapolis, Minnesota, April 12, 1992
International Academy of Ceramics Forum '92, Assisi, Italy, June 26, 1992
University of Minnesota, Minneapolis, Minnesota, October 5, 1992
3M Center, St. Paul, Minnesota, October 6, 1992
Northwestern University, Evanston, Illinois, October 15, 1992
American Ceramic Society, San Francisco, California, November 2, 1992
Queens University, Kingston, Ontario, Canada, December 15, 1992
Annual Meeting of the American Ceramic Society, Cincinnati, Ohio, April 18, 1993
University of Chicago, Chicago, Illinois, May 12, 1993
Fulrath Memorial International Symposium on Advanced Ceramics, Tokyo , Japan, August 30, 1993
3rd IUMRS-ICAM '93, International Conference on Advanced Materials, Tokyo, Japan, September 3, 1993
American Ceramic Society, PAC RIM Meeting, Honolulu, Hawaii, November 7, 1993
6th U.S.-Japan Seminar on Dielectric and Piezoelectric Ceramics, Maui, Hawaii, November 11, 1993
EPSCor-DOE, University of San Juan, Puerto Rico, December 10, 1993
Electroceramics Symposium, CMMP '93, Institute of Physics, Leeds, England, December 21, 1993

PROFESSOR C. M. WAYMAN

URI FINAL REPORT OF PROFESSOR C. M. WAYMAN

Professor Wayman has been recovering from a stroke since September 1993, so his complete final report is not available. However, some of his publications are listed below. It is anticipated that Professor Wayman will submit a supplement to the cumulative final report when he returns to the Department.

- "Cubic to Tetragonal Transformation in Lead Titanate ($PbTiO_3$) Single Crystals," C. C. Chou and C. M. Wayman, Materials Trans. JIM 33[3] 306-317 (1992).

- "Crystallography of the Cubic to Tetragonal Transformation in Lead Titanate Single Crystals," C. C. Chou, K. Wakasa and C. M. Wayman, Proc. Int. Conf. on Martensitic Transformations (ICOMAT '92) 695-700 (1992).

- "Habit Plane Variants in Ferroelectric Lead Titanate Crystals: I. Theoretical Considerations," L. C. Yang and C. M. Wayman, Acta Metal. et Mater., submitted.

- "Habit Plane Variants in Ferroelectric Lead Titanate Crystals: II. Experimental Observations," L. C. Yang and C. M. Wayman, Acta Metal. et Mater., submitted.

- "The Alpha to Beta Transformation in Stoichiometric Nickel Sulfide," B. Kim, C. C. Chou and C. M. Wayman, Proc. Int. on Martensitic Transformations (ICOMAT '92) 701-706 (1992).

APPENDIX: REPRINTS
(by topic)

LEAD TITANATE ($PbTiO_3$)

APPENDIX: Reprints or Pre-prints (by topic)

Lead Titanate ($PbTiO_3$)

- "Growth of Large $PbTiO_3$ Crystals by a Self-Flux Technique," B. N. Sun, Y. Huang and D. A. Payne, J. Cryst. Growth, 128 867-870 (1993).

- "Cubic to Tetragonal Transformation in Lead Titanate ($PbTiO_3$) Single Crystals," C. C. Chou and C. M. Wayman, Materials Trans. JIM 33[3] 306-317 (1992).

- "Pressure Dependence of Optical Absorption in $PbTiO_3$ to 35 GPA: Observation of the Tetragonal-To-Cubic Phase Transition," C. S. Zha, A. G. Kalinichev, J. D. Bass, C.T.A. Suchicital and D. A. Payne, J. Appl. Phys. 72(8) 3705-3707 (1992).

- "Paramagnetic Resonance of Platinum Ions in $PbTiO_3$ Single Crystals," W. L. Warren, B. A. Tuttle, B. N. Sun, Y. Huang and D. A. Payne, Appl. Phys. Lett., 62(2) 146-148 (1993).

- "Shape Memory and Superelasticity for Ceramics with Field-Induced Antiferroelectric-Ferroelectric Phase Transformation," P. Yang and D. A. Payne, Proc. Int. Conf. on Martensitic Transformations (ICOMAT '92) 719-724 (1993).

- "Crystallography of the Cubic to Tetragonal Transformation in Lead Titanate Single Crystals," C. C. Chou, K. Wakasa and C. M. Wayman, Proc. Int. Conf. on Martensitic Transformations (ICOMAT '92) 695-700 (1992).

- "Habit Plane Variants in Ferroelectric Lead Titanate Crystals: I. Theoretical Considerations," L. C. Yang and C. M. Wayman, Acta Metal. et Mater., submitted.

- "Habit Plane Variants in Ferroelectric Lead Titanate Crystals: II. Experimental Observations," L. C. Yang and C. M. Wayman, Acta Metal. et Mater., submitted.

- "Thermal Stability of Field-Forced and Field-Assisted Antiferroelectric-Ferroelectric Phase Transformations in $Pb(Zr,Sn,Ti)O_3$," P. Yang and D. A. Payne, J. Appl. Phys. 71(3) 1361-1367 (1992).

- "Grain-Size Dependence of Ferroelectric-Antiferroelectric Phase Transformations in $Pb(Zr,Sn,Ti)O_3$ Dielectrics," P. Yang and D. A. Payne, Cer. Trans., 32 347-354 (1993).

- "Electronic Structure of Barium Titanate Studies by the Extended Hückel Tight Binding Method," M. Holma, M. Kitamura and H. Chen, J. Appl. Phys. (1994) in press.

- "X-ray Diffuse Scattering Study of Soft Modes in Paraelectric $BaTiO_3$," N. Takesue and H. Chen, Physical Review Letters, submitted.

Potassium Niobate ($KNbO_3$)

- "Elastic Properties of Orthorhombic $KNbO_3$ Single Crystals by Brillouin Scattering," A. G. Kalinichev, J. D. Bass, C. S. Zha, P. D. Han and D. A. Payne, J. Appl. Phys., 74(11) 6603-6608 (1993).

- "Pre-Transitional Behavior in Cubic Potassium Niobate," M. Holma, H. Hong, M. Nelson and H. Chen, Mat. Res. Soc. Symp. Proc. Vol. 307, 1993.

- "Microstructure and Phase Transformation in $KNbO_3$," O. O. Popoola and W. M. Kriven, Proc. 51st Annual Meeting of Microscopy Society of America, Publ. San Francisco Press, pp. 956-957 (1993).

- "Linear Chain Structure in Cubic $KNbO_3$," M. Holma and H. Chen. Abstract accepted for Int. Conf. on Solid-Solid Phase Transformations in Inorganic Materials, Pittsburgh, PA 1994.

- "Phase Transformation in Potassium Niobate Perovskite Ceramics," O. O. Popoola and W. M. Kriven. Abstract accepted for Int. Conf. on Solid to Solid Phase Transformations, Pittsburgh, PA 1994.

Dicalcium Silicate (Ca_2SiO_4)

- "Phase Transformations in Dicalcium Silicate: II. TEM Studies of Crystallography, Microstructure and Mechanisms," Y. J. Kim, I. Nettleship and W. M. Kriven, J. Amer. Ceram. Soc., 75(9) 2407-2419 (1992).

- "Chemical Preparation and Phase Stability of Ca_2SiO_4 and Sr_2SiO_4 Powders," I. Nettleship, J. L. Shull and W. M. Kriven, J. European Cer. Soc., 11 291-298 (1993).

- "Transformation Mechanisms in Dicalcium and Distrontium Orthosilicates," Y. J. Kim, J. L. Shull, B. N. Sun and W. M. Kriven, Proc. Int. Conf. on Martensitic Transformations (ICOMAT '92) 683-688 (1992).

- "TEM Characterization of the α' and β Phases in Polycrystalline Distrontium Silicate (Sr_2SiO_4)," Y. J. Kim, J. L. Shull and W. M. Kriven, Proc. 50th Annual Meeting of the Electron Microscopy Society of America (EMSA), pp. 354-355 (1992).

- "A TEM Study on the Decomposition of Synthetic Hillebrandite ($Ca_2SiO_4 \bullet H_2O$)," Y. J. Kim and W. M. Kriven, J. Mat. Res., accepted.

Nickel Sulfide (NiS)

- "The Alpha to Beta Transformation in Stoichiometric Nickel Sulfide," B. Kim, C. C. Chou and C. M. Wayman, Proc. Int. on Martensitic Transformations (ICOMAT '92) 701-706 (1992).

- "Microstructural Investigation of Fracture-Initiating Nickel Sulfide Inclusions in Glass," O. O. Popoola, J. J. Cooper and W. M. Kriven, Cer. Sci. and Eng. Proceedings, 14[3-4] 284-294 (1993).

Yttrium Barium Copper Oxide ($YBa_2Cu_3O_{6+x}$)

- "Concentration-Dependent Oxygen Diffusivity in $YBa_2Cu_3O_{6+x}$: I. Argon Annealing Studies," J. R. LaGraff and D. A. Payne, Physica C, 212 470-477 (1993).

- "Concentration-Dependent Oxygen Diffusivity in $YBa_2Cu_3O_{6+x}$: II. Oxygen Partial Pressure Studies," J. R. LaGraff and D. A. Payne, Physica C, 212 478-486 (1993).

- "Concentration-Dependent Oxygen Diffusivity in $YBa_2Cu_3O_{6+x}$: III. Diffusion Mechanisms," J. R. LaGraff and D. A. Payne, Physica C, 212 487-496 (1993).

- "Chemical Diffusion of Oxygen in Single-Crystal and Polycrystalline $YBa_2Cu_3O_{6+x}$ Determined by Electrical-Resistance Measurements," J. R. LaGraff and D. A. Payne, Phys. Rev. B, 47(6) 3380-3390 (1993).

- "Chemical Diffusion of Oxygen in $YBa_2Cu_3O_{6+x}$," J. R. LaGraff and D. A. Payne, Phys. and Mat. Sci. of High Temp. Superconductors, II, 225-246 (1992).

- "Oxygen Stoichiometry and Mobility Effects on Domain Wall Motion in Ferroelastic $YBa_2Cu_3O_{7-\delta}$" J. R. LaGraff and D. A. Payne, Ferroelectrics, 130 87-105 (1992).

- "Oxygen In-Diffusion and Out-Diffusion in Single Crystal $YBa_2Cu_3O_{7-\delta}$" J. R. LaGraff, P. Han and D. A. Payne, Mat. Res. Soc. Symp. Proc., Vol 209 (1991).

- "Resistance Measurements and Oxygen Out-Diffusion Near the Orthorhombic-Tetragonal Phase Transformation in Single Crystal $YBa_2Cu_3O_{7-\delta}$" J. R. LaGraff, P. D. Han and D. A. Payne, Phys. Rev. B, 43(1) 441-447 (1991).

Phase Transformations and Twinning

- "Phase Transformations in Ceramics," W. M. Kriven, Proceedings 51st Annual Meeting of the Microscopy Society of America, Publ. San Francisco Press, pp. 952-953 (1993).

- "Displacive and Martensitic Transformation in Ceramics," W. M. Kriven. Abstract accepted for Int. Conf. on Solid to Solid Phase Transformation, Pittsburgh, PA (1994).

- "Twinning in Structural Ceramics," W. M. Kriven (invited review paper) in Twinning Advanced Materials, Edited by M. H. Yoo and M. Wuttig. Published by The Minerals, Metals and Materials Society (TMS), Warrendale, PA, in preparation.

Other Related Topics or Joint Co-Authors

- "Calculation of the *K*-Absorption Edge and Its Chemical Shift of Common Metals," M. Kitamura and H. Chen, J. Phys. Chem. Solids, 52(5) 731-734 (1991).

- "Phase Stability of Chemically Derived Enstatite ($MgSiO_3$) Powders," C. M. Huang, D. H. Kuo, Y. J. Kim and W. M. Kriven, submitted to J. Am. Ceram. Soc.

- "Chemical Synthesis and Characterization of Calcium Aluminate Powders," M. A. Gülgün, O. O. Popoola and W. M. Kriven, J. Am. Ceram. Soc., 77[2] 531-539 (1994).

- "XPS Studies of Bond Structure Between Polyvinyl Alcohol and a Titanate Cross Coupling Agent," M. A. Gülgün, O. O. Popoola and W. M. Kriven, J. Mat. Res., submitted.

- "Phase Stability of Ni-based Intermetallic Compounds Ni_3X Studied by the Recursion Method," J. Park, S. Muramatsu, M. Kitamura, H. R. P. Inoue and I. Chen, Mat. Chem. and Phys. 33 214-220 (1993).

- "The Mechanism of the Tetragonal to Monoclinic Transformation in $YNbO_4$," J. L. Shull, B. N. Sun and W. M. Kriven. Abstract accepted for Int. Conf. on Solid to Solid Phase Transformation, Pittsburgh, PA (1994).

- "High Temperature Phase Transformation in $Y_4Al_2O_9$, $Gd_4Al_2O_9$, and $Dy_4Al_2O_9$," J. L. Shull and W. M. Kriven. Abstract Int. Conf. on Solid to Solid Phase Transformations, Pittsburgh, PA (1994).

- "Structural Relaxations in the GHz Frequency Range in Glass Forming Silicate Melts," J. E. Masnik, J. Kieffer and J. D. Bass. Mat. Res. Soc. Symp. Proc. 248, 505-510, (1992).

Journal of Crystal Growth 128 (1993) 867–870
North-Holland

JOURNAL OF CRYSTAL GROWTH

Growth of large $PbTiO_3$ crystals by a self-flux technique

B.N. Sun, Y. Huang and D.A. Payne

Department of Materials Science and Engineering, Materials Research Laboratory, and Beckman Institute, University of Illinois at Urbana–Champaign, Urbana, Illinois 61801, USA

Pure lead titanate ($PbTiO_3$) crystals ($5\times5\times5$ mm^3) were grown from high-temperature solutions by a slow cooling technique using PbO as a self-flux. The optimum growth conditions were determined to be: (1) $(1-x)\,TiO_2 + x$ PbO with x (in mol%) varying from 0.78 to 0.82 for the starting compositions, (2) 930–1050°C as the growth temperature range and (3) 0.4–1.5°C/h as the cooling rates. Evaporation of PbO was significantly reduced by use of a double-crucible technique. The grown crystals were characterized by X-ray diffraction, chemical analysis and optical microscopy. The transformation temperatures (onset) of 492.5°C (on heating) and 491.3°C (on cooling) were determined by differential scanning calorimetry. The transformation process had a thermal hysteresis of 1.2°C from onset data.

1. Introduction

Lead titanate ($PbTiO_3$) is a potential ferroelectric material with a high Curie temperature of approximately 490°C [1–5] and a highly polar structure (P4mm, P_s(calculated) = 81 μC/cm^2) [3], and is of considerable interest for potential energy sensing and transducing applications. However, little is known about the basic properties of pure lead titanate due to difficulties encounted in the growth of crystals of sufficient size for experimental measurements, although the phase transformation behavior was reported as early as 1950 [1,6]. The aim of the present work is to investigate the best conditions for the growth of large single crystals of sufficient size for inelastic neutron scattering measurements.

Crystal growth of $PbTiO_3$ has been attempted by many workers. In most cases, small crystallites or thin platelets were obtained [7–10]. Thicker plates of uranium-doped crystals were obtained by Remeika and Glass [11]. Recently, Suchicital and Payne succeeded in growing nearly equidimensional crystals with an edge size of 3–4 mm from a KF-based complex flux system [12,13]. However, the grown crystals contained a significant amount of impurities (from the flux) which shifted the transformation temperature to 460°C. In the present contribution, we describe a method by which large equidimensional $PbTiO_3$ crystals were grown reproducibly without the addition of foreign impurities.

2. Experimental procedure

2.1. Crystal growth equipment

The crystal growth experiments were carried out in a vertical tube furnace (SiC heating elements) equipped with a programmable temperature controller. For each growth run, a pure platinum crucible of 50 ml capacity was placed on a refractory support. Two Pt/Pt–10%Rh thermocouples, in close contact with the Pt crucible, were connected to the temperature controller and the temperature monitor, respectively.

The starting oxides were PbO (> 99.9%) and TiO_2 (> 99.9%), both obtained from Aldrich. Due to the high volatility of PbO, a so-called double crucible technique was used to reduce the evaporation of PbO. The platinum crucible was covered with a closely fitting lid and buried in TiO_2 powders which was in turn contained in a second

covered alumina crucible. The weight loss inside the Pt crucible after a growth run was less than 1%.

2.2. Choice of growth parameters

For growth of highly pure $PbTiO_3$ crystals, PbO was chosen as the flux. This is due to the fact that PbO has been demonstrated to be a suitable high-temperature solvent for many oxides including perovskites (see, e.g., refs. [14–19]). In addition, PbO itself is a component of $PbTiO_3$, thus avoiding the incorporation of foreign ions into the crystal lattice. The system $PbO–TiO_2$ was investigated by Eisa et al. [20] who determined two eutectic temperatures, a higher at 1240°C with 10% excess TiO_2 and a lower at 838°C. The lower eutectic, situated at the composition of 15 mol% TiO_2 + 85 mol% PbO is of particular importance for flux growth experiments. The value of 838°C was taken as the lowest limit for the growth temperature.

For a typical growth run, 150 g of the mixture $(1-x)$ $TiO_2 + x$ PbO with x (in mol%) varying from 0.78 to 0.82 were pressed into the platinum crucible. The temperature program of the furnace was as follows: (i) heating from room temperature to 1100°C over 6 h; (ii) soaking at 1100°C for a period of 12–20 h; (iii) step-cooling to 1050°C; (iv) slow-cooling to 930°C at a constant rate of 0.3–1.5°C/h and (v) slow-cooling to room temperature in about 72 h.

3. Results and discussion

$PbTiO_3$ crystals grew mainly in the form of cubes and thick plates. Shown in fig. 1 are some crystals grown from the starting composition 80 mol% PbO + 20 mol% TiO_2 with a soaking time of 12 h and a cooling rate of 0.8°C/h. A soaking time of more than 10 h was necessary for complete dissolution of TiO_2. Undissolved TiO_2 particles could act as nucleation centers, which might dramatically reduce the size of grown crystals. Most crystals which were grown at a slow cooling rate had flat surfaces. High cooling rates induced growth instability, which caused either hopper or

Fig. 1. As-grown crystals of $PbTiO_3$. The starting composition was 80 mol%PbO + 20 mol% TiO_2 and the cooling rate was 0.8°C/h. 1 div = 1 mm.

dendritic morphology, with internal cavities and inclusions within the crystals [19].

Crystals were separated from the resolidified flux by a leaching process through use of hot acetic acid and were identified by X-ray analysis. Elemental analysis by atomic absorption spectroscopy yielded the composition: 63.70 wt% Pb, 14.95 wt% Ti (Pb/Ti = 0.99), indicating that the crystals were stoichiometric within the accuracy of the analytical method.

Optical examination under a polarizing microscope revealed typical ferroelectric domains in the grown crystals. An example is shown in fig. 2, indicating a- and c-type ferroelectric domains (bright and dark bands respectively) in the head-to-tail arrangement, resulting in 90° domain walls [21].

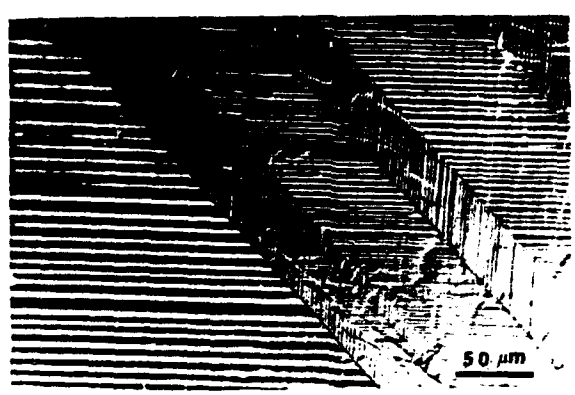

Fig. 2. Ferroelectric domain patterns observed on a $PbTiO_3$ platelet in polarized light, showing typical $a-c$ domains which intersect at 90° domain walls.

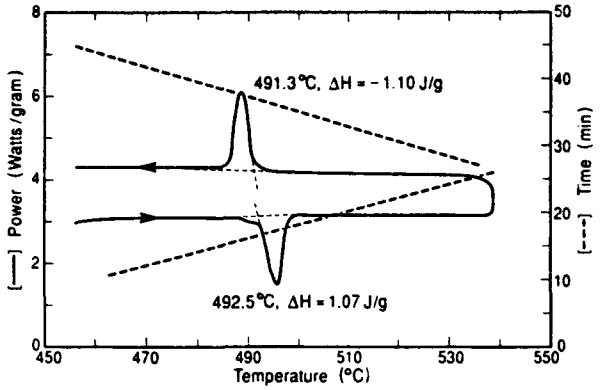

Fig. 3. Differential scanning calorimetry (DSC) analysis of $PbTiO_3$ crystals, showing endothermic and exothermic behavior on heating and cooling, respectively.

X-ray analysis on powder samples confirmed the room temperature structure to be tetragonal (P4mm) with $a = 3.896$ Å, $c = 4.158$ Å, in good agreement with values in the literature ($a = 3.905$ Å, $c = 4.164$ Å) [3–5,9].

The high temperature phase transformation was followed by differential scanning calorimetry (DSC). A typical result is given in fig. 3. The temperature range of interest, in the vicinity of the phase transformation point, was a reversible temperature cycle between 450 and 550°C at a rate of 5°C/min. An endotherm was observed at 495.8°C on heating, with an equivalent exothermic peak at 488.5°C on cooling. This behavior was attributed to the tetragonal → cubic and cubic → tetragonal reversible phase transformations, respectively [22–24]. The respective transformation temperatures (onset) were found to be 492.5 and 491.3°C. The temperatures were in good agreement with reported data (490°C) [1–5]. The transformation to the high temperature form (492.5°C) required an energy of 1.07 J/g on heating and released 1.10 J/g on cooling to the low temperature form.

4. Conclusion

Single crystals of $PbTiO_3$ were grown by a new method using a double crucible technique and PbO as a self flux. Large crystals ($5 \times 5 \times 5$ mm^3), suitable for inelastic neutron scattering experiments, were reproducibly grown. The grown crystals had a high purity and were equidimensional in form. Lattice parameters ($a = 3.896$ Å, $c = 4.158$ Å) were in good agreement with the literature. The crystals transformed to the polar tetragonal structure at 491.3°C on cooling.

Acknowledgment

The research was supported by the United States Air Force Office of Scientific Research as a grant (URI-41318) on Displacive Phase Transformations in Ceramics.

References

[1] G. Shirane, S. Hoshino and K. Suzuki, Phys. Rev. 80 (1950) 1105.
[2] G. Shirane and R. Pepinsky, Acta Cryst. 9 (1956) 131.
[3] A.M. Glazer and S.A. Mabud, Acta Cryst. B 34 (1978) 1065.
[4] M.F. Kuprianov, S.M. Zaitsev, E.F. Gagarina and E.G. Fesenko, Phase Transitions 4 (1983) 55.
[5] G. Shirane and S. Hoshino, J. Phys. Soc. Japan, 6 (1951) 265.
[6] G.A. Smolenski, Dokl. Akad. Nauk SSSR 70 (1950) 405.
[7] A.A. Shternberg and V.A. Kuznetsov, Soviet Phys.-Cryst. 13 (1969) 647.
[8] J. Kobayashi, J. Appl. Phys. 29 (1958) 866.
[9] E.G. Fesenko, A.F. Semenchev and V.G. Gavrilyatchenko, Ferroelectrics 13 (1976) 471.
[10] E.G. Fesenko, V.G. Gavrilyatchenko, R.I. Spinko, M.A. Martynenko, E.A. Grigor'eva and A.D. Feronov, Soviet Phys.-Cryst. 17 (1972) 122.
[11] J.P. Remeika and A.M. Glass, Mater, Res. Bull. 5 (1970) 37.
[12] C.T.A. Suchicital and D.A. Payne, in: Ceramic Transactions, Vol. 8, Ed. H. Ling (Am. Ceramic Soc., Columbus, OH, 1990) pp. 169–174.
[13] C.T.A. Suchicital and D.A. Payne, J. Crystal Growth 104 (1990) 211.
[14] J.P. Remeika, J. Am. Chem. Soc. 78 (1956) 4259.
[15] G. Garton and B.M. Wanklyn, J. Crystal Growth 1 (1967) 164.
[16] S. Nomura, H. Takabayashi and T. Nakagawa, Japan. J. Appl. Phys. 7 (1968) 600.
[17] M. Drofenik, L. Golic and D. Kolar, J. Crystal Growth 21 (1974) 305.
[18] I.H. Brunskill, R. Boutellier, W. Depmeier, H. Schmid and H.J. Scheel, J. Crystal Growth 56 (1982) 541.

[19] B.N. Sun, R. Boutellier, Ph. Sciau, E. Burkhardt, V. Rodriquez and H. Schmid, J. Crystal Growth 112 (1991) 71.
[20] M.A. Eisa, M.E. Abadir and A.M. Gadalla, Trans. J. Brit. Ceram. Soc. 79 (1980) 100.
[21] P.W. Forsbergh, Jr., Phys. Rev. 76 (1949) 1187.
[22] W. Smykatz-Koss, Differential Thermal Analysis: Application and Results in Mineralogy (Springer, Berlin, 1974).
[23] W. Gutt and A.J. Majumdar, in: Differential Thermal Analysis, Vol. 2, Ed. R.C. Mackenzie (Academic Press, New York, 1975) pp. 79–117.
[24] R.S. Roth, J. Res. Natl. Bur. Std. (US) 58 (1957) 75.

Materials Transactions, JIM, Vol. 33, No. 3 (1992), pp. 306 to 317

Cubic to Tetragonal Martensitic Transformation in Lead Titanate ($PbTiO_3$) Single Crystals

C. C. Chou* and C. M. Wayman*

The cubic to tetragonal (C/T) phase transformation in $PbTiO_3$ single crystals has been studied in both the forward and reverse modes and found to show martensitic characteristics. Microstructural features were investigated by heating stage optical microscopy, and room temperature transmission electron microscopy. During transformation, a small hysteresis is involved. The phase front passes swiftly through the crystal and surface relief accompanying the transformation is seen. The twinning system involved was identified as a compound twin in the tetragonal phase with $K_1=\{110\}$, $\eta_1=\langle\bar{1}10\rangle$, $K_2=\{\bar{1}10\}$, and $\eta_2=\langle 110\rangle$. The phase boundaries (habit planes) were frozen by controlling the temperature profile. It is found that the habit planes vary within a certain range. Not only different specimens show this real variation, but also the same specimen under different transformations follows this, indicating the importance of local arrangements near the habit plane interfaces. Theoretical predictions, with only a minute change of lattice parameters, show that experimental data appear to fit calculated results fairly well, if one considers interfacial conditions. The results show a certain degree of consistency, which implies that the martensitic phenomenological crystallographic theory applies. Discussions on the microstructural features as well as previous work on perovskite materials are presented.

(Received October 28, 1991)

Keywords: martensitic transformation, lead titanate, perovskite materials, phase boundary, habit plane, phenomenological crystallographic theory

I. Introduction

Martensite was originally used to designate the hard microconstituent found in quenched steels. Since then, other materials have been found to exhibit the same type of solid state phase transformation, known as a martensitic transformation. The most distinct feature of a martensitic transformation is its crystallographic characteristics, which imply a "military" (as opposed to "civilian") mode of atomic transfer from the parent to the product phase[1]. These transformations feature a coordinated structural change involving a lattice correspondence and a planar semicoherent parent-product interface which, during transformation movement, produces an invariant plane strain shape deformation. Microstructural inhomogeneities on a fine scale during a martensitic reaction—slip, twinning, or faulting—are usually observed at the electron microscope scale. This secondary deformation provides the invariant plane condition at the macroscopic scale and maintains a semicoherent glissile interface between the martensite and the parent phase.

The phenomenological crystallographic theory of martensitic transformations[2]-[4] is well established, and has been applied successfully to many metallic alloy systems[5]-[7], and more recently to ceramics and other systems[8]. It has been reported that the Wechsler-Lieberman-Read (WLR) theory can be applied to the cubic-tetragonal phase transition of semiconducting perovskite-type crystals[9], which have sufficient free charge available to provide a termination for the spontaneous polarization at the interface. On the other hand, crystals with high resistivity, though showing sharp first order phase boundaries, apparently do not follow theoretical predictions[10][11]. In their interpretation, the reason for this is that the free charges present in (semi-)conducting crystals neutralize the bound polarization charges inside the crystal. Whereas in highly insulating crystals, the absence of free charges imposes the restriction that phase boundaries be free of any exess polarization charge. The accumulated polarization charge at a phase boundary results in stored electrical energy which dominates the crystallographic characteristics once it prevails. However, the evidence here is thin because no other crystallographic data were used other than very limited habit plane data.

Lead titanate has a ferroelectric phase transition temperature, T_c, near 500°C[12][13]. $PbTiO_3$ is cubic above T_c and exhibits a strong tetragonal distortion at 20°C: $c/a=1.06$ which persists up to T_c ($c/a=1.01$)[14][15]. The lattice constant a increases smoothly upon heating, while the constants c and c/a decrease. At T_c, the lattice constants c and a change abruptly and the structure becomes cubic. Since the volume of the unit cell decreases sharply as a result of this transition, the linear expansion coefficient of a polycrystalline sample is negative below T_c[12]-[15]. The transformation is first order[10]. $PbTiO_3$ single crystals present a highly polar structure with very high spontaneous polarization in the perovskite family[12][13][16]. Because of its large tetragonality and detectable negative volume change near T_c, $PbTiO_3$ provides a more sensitve indication of the role of lattice variation during transformation. In the present experiments, we study microstructural features to understand basic

* Department of Materials Science and Engineering, University of Illinois at Urbana-Champaign, Urbana, Illinois 61801, USA.

crystallographic characteristics in this material, present a real scatter of the habit plane, and verify the appplicability of the phenomenological crystallographic theory to this perovskite system.

II. Experimental Procedure

$PbTiO_3$ crystals were grown[17] by slow cooling from a flux, containing KF, Pb_3O_4, PbF_2, KBF_4, and TiO_2, at a temperature below the transformation temperature in a 50 cm^3 platinum crucible. A vertical tube furnace with sealed-end quartz tube was programmed to give a controlled cooling rate to below 300°C. Crystal growth proceeds in an oxygen atmosphere and at a very slow cooling rate. The as-grown crystals were mostly cubic in shape or elongated cubic or orthogonal forms. After washing in hot concentrated acetic acid, in order to dissolve any attached solidified flux, and polishing with Al_2O_3 powders of various sizes, the crystals show a transparent amber tint.

Transformation characteristics were studied using heating stage optical microscopy and conventional transmission electron microscopy at room temperature. Specimens for optical microscopy were ground by hand to a thickness about 80 μm or less and polished using Al_2O_3 powder. Some coarser scratches were intentionally retained as fiducial lines. *In situ* transformation experiments were performed using heating stage optical microscopy. The specimens used were high quality crystals with sharp flat {100} surfaces and the microscope used was a Nikon UM-2. The specimens were investigated using polarized light and put in a heating stage which was designed to be able to control the temperature profile quickly and to "freeze" phase boundaries. TEM specimens were hand ground and then treated by a commercial dimpling machine down to 10 μm. An ion miller was employed at 6 kV, 0.5 mA, each gun with tilting angle at 18° for further thinning. After perforation, the specimens were further ion bombarded at reduced voltage and tilting angle for several minutes. TEM investigations were conducted using a Hitachi H800 microscope at 200 kV with a double-tilt specimen holder.

III. Results

The results obtained can be divided into two major parts: experimental determination of crystallographic characteristics, and theoretical calculations.

1. Crystallographic characteristics

The single crystals used show lower transformation temperatures than those previously reported[12,15]. The crystals used have transformation temperatures shown in Table 1. The reduction of T_c may be caused by solid solution of multi-elements during crystal growth. The resistance of the crystals measured is as high as $1.0\times10^{-8}\,\Omega/cm^2$ or more[17]. Surface relief of the tetragonal phase is often seen in as grown crystals and/or crystals after C/T transformation. A typical example is shown in Fig. 1. Surface relief forms along two directions which are closely related to two variants shown in this orientation. Surface tilting is clearly observed as black and bright patches by appropriately adjusting the specimen position and orientation. Note that interfaces between variants are not exactly parallel, indicating a possible variation of habit plane trace during phase transformation.

Table 1 Transformation temperatures of $PbTiO_3$ specimens studied.

Specimen No.	M_s (°C)	A_s (°C)
1	451	460
2	450	455
3	451	455
4	455	462
5	453	457
6	450	454
7	455	460

Figure 2(a) shows $PbTiO_3$ lattice parameters as a function of temperature[17]. At room temperature, the crystal is tetragonal showing lattice parameters $a=0.39029$ nm and $c=0.41344$ nm and the values of $a=0.3961$ nm, $c=0.4012$ nm and $a_0=0.3972$ nm apply at T_c[17]. Again, the tetragonality is a little smaller than that reported in previous work[12,14]. Figure 2(b) shows the $PbTiO_3$ volume change as a function of temperature[17]. Note the negative slope and rapid increase (and then decrease)† of volume change below T_c as the temperature decreases, indicating an intriguing lattice structure variation, as discussed later.

The inhomogeneous shear was introduced as internal twins in the tetragonal phase. A ferroelectric material has regions where the magnitude and direction of the polarization are the same in each region, though the polarization may differ in orientation in neighboring regions. These regions are known as ferroelectric domains which are separated by domain boundaries. From symmetry, there are two types of domain boundaries in $PbTiO_3$, that is, 90° and 180° boundaries. The angles refer to the angle between the domain polarization vectors on either side of the boundary. From a [100] orientation two different morphologies of 90° domain boundaries are usually seen. One is straight with sharp images, and the other shows wavy morphology and fringe contrast, as shown in Fig. 3(a) and (b) respectively. The sharp boundaries are termed a-a type domain boundaries, because the polarization vectors in two adjacent domains are all perpendicular to the viewing direction and the *a*-axis in each domain points to the viewing direction. On the other hand, the fringed boundaries are inclined to the viewing direction and the polarization

† The present X-ray data show slightly different characteristics from those in previous work (Ref. (12)), which may be due to impurities in the crystals. Since we use the crystals from Ref. (17), the corresponding X-ray data were adopted. The impurity effect may influence the characteristic values of a phase transformation, such as T_c, tetragonality, etc., but is believed not to affect its nature.

Fig. 1 Optical micrograph showing surface relief of tetragonal phase in an as-grown $PbTiO_3$ single crystal. Similar features can be observed after other C/T transformations. Note that interfaces are not exactly parallel.

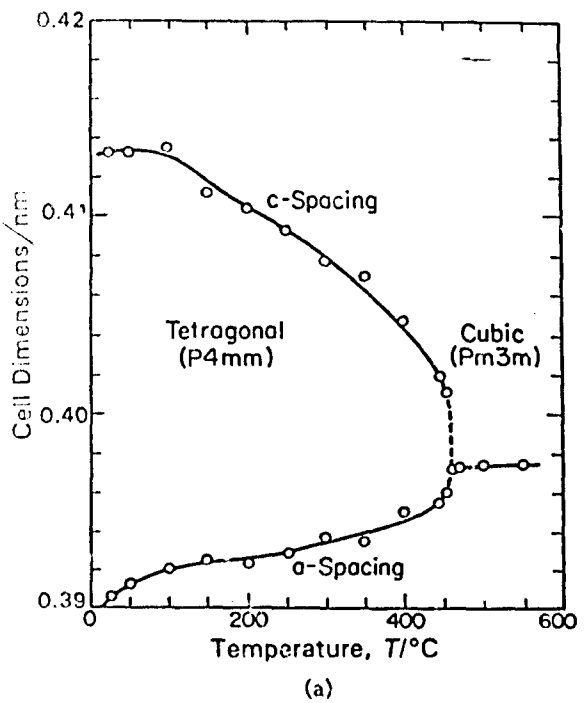

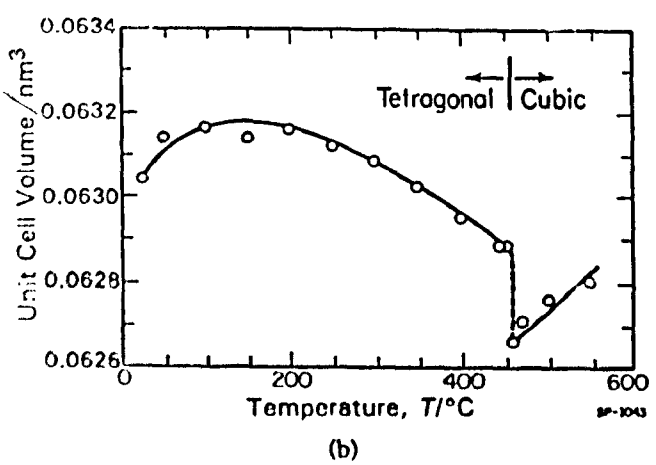

Fig. 2 X-ray data showing (a) lattice parameters; (b) unit cell volume of $PbTiO_3$ as a function of temperature.

Fig. 3 Electron micrographs showing 90° domain boundaries. (a) a-c domain boundaries; (b) a-a domain boundaries.

vectors in two adjacent domains are alternatively parallel to or perpendicular to the viewing direction. The *a*-axis and *c*-axis point to the viewing direction and hence the domain boundaries are called a-c type. Actually, from a crystallographic viewpoint, a 90° domain boundary is a twinning plane between two adjacent domains. For a-a domains, this is readily seen, as shown in Fig. 4(a). The symmetrically distributed diffraction reflections imply that the two adjacent domains are twin-related. Diffraction patterns as shown in Fig. 4(b) were derived by tilting a-c type domain boundaries from a [100] zone to a [111] zone. Again, a twinning relation was derived from the symmetrical distribution of diffraction reflections. In both cases, the twinning planes, K_1, are {110} type planes. The corresponding schematic models showing atomic arrangements are in Fig. 4(c) and (d). Figure 4(c) clearly shows that the twinning direction, η_1, is along a $\langle\bar{1}10\rangle$ type direction due to the tetragonal distortion during transformation. The invariant plane, K_2, is the $\{\bar{1}10\}$ plane which is the other diagonal plane of the tetragonal cell. Figure 4(d) is more complex, but can be immediately

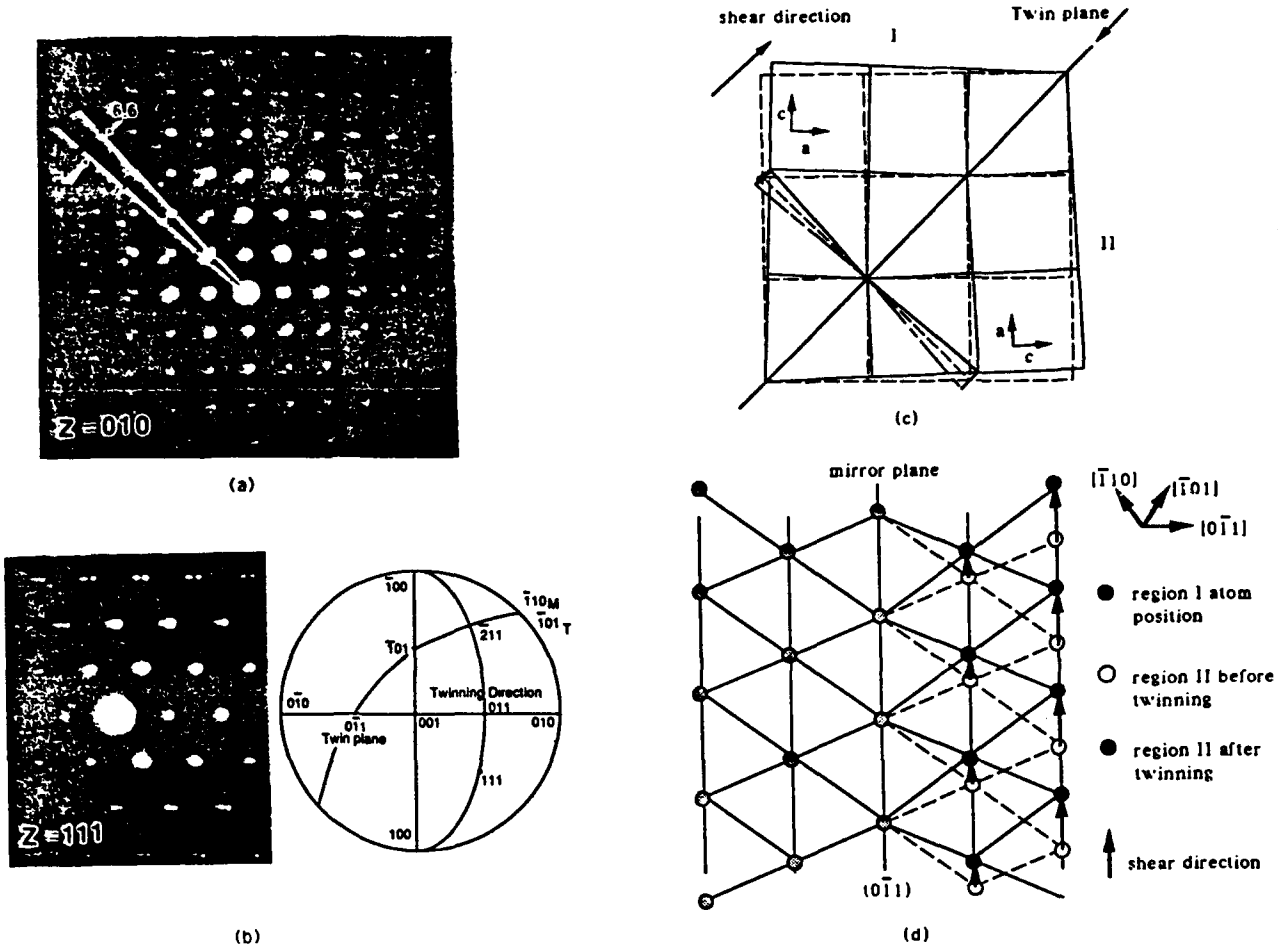

Fig. 4 (a) Diffraction pattern taken from a $[100]_c$ orientation showing a-a type domain arrangements; two adjacent domains are twin related; (b) diffraction pattern derived by tilting an a-c domain to a [111] orientation and corresponding stereographic projection showing the twinning relation; (c) corresponding atomic model describing the twinnig relation for (a); (d) schematic model showing atomic arrangements corresponding to (b).

realized by studying the stereographic projection in (b). The result of the twinning system is the same as that derived from Fig. 4(c). Therefore the elements for the twinning system in $PbTiO_3$ crystals are determined. The twinning magnitude can also be determined from splitting in the diffraction pattern, Fig. 4(a), or from X-ray data. The results are shown in Table 2. It is found that this is a compound twinning system†. The result can be seen in a stereographic projection, Fig. 5.

Phase transformation characteristics were partly derived by heating stage optical microscopy. Figure 6(a) shows a single interface type phase transformation. This is a typical habit plane (or phase boundary) in a $PbTiO_3$ crystal during transformation as seen using polarized light. The phase boundary is sharp and straight with an angle about 30° to a [010] direction. This sharp boundary implies that the boundary is almost in an edge-on position. One can easily distinguish the cubic phase by

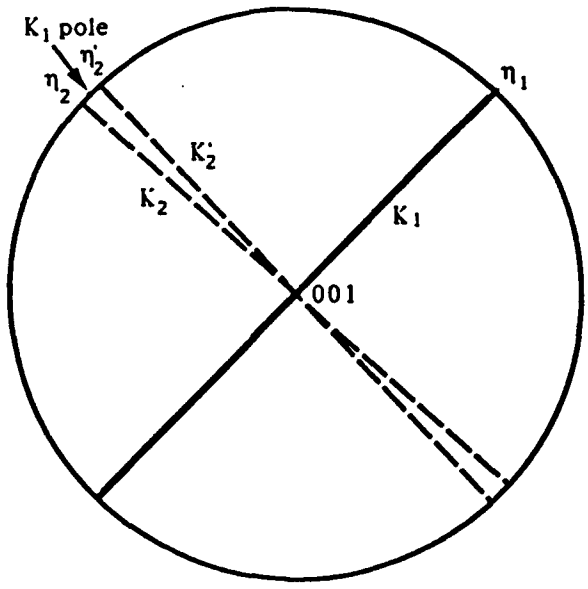

Fig. 5 [001] stereographic projection showing the relation between twinning elements for $PbTiO_3$ tetragonal phase.

† When K_1 is a rational plane and η_2 a rational direction, this is twinning of the first kind; when K_2 is a rational plane and η_1 a rational direction, this is a twin of the second kind; when all four elements K_1, K_2, η_1 and η_2 are rational, the twin is compound.

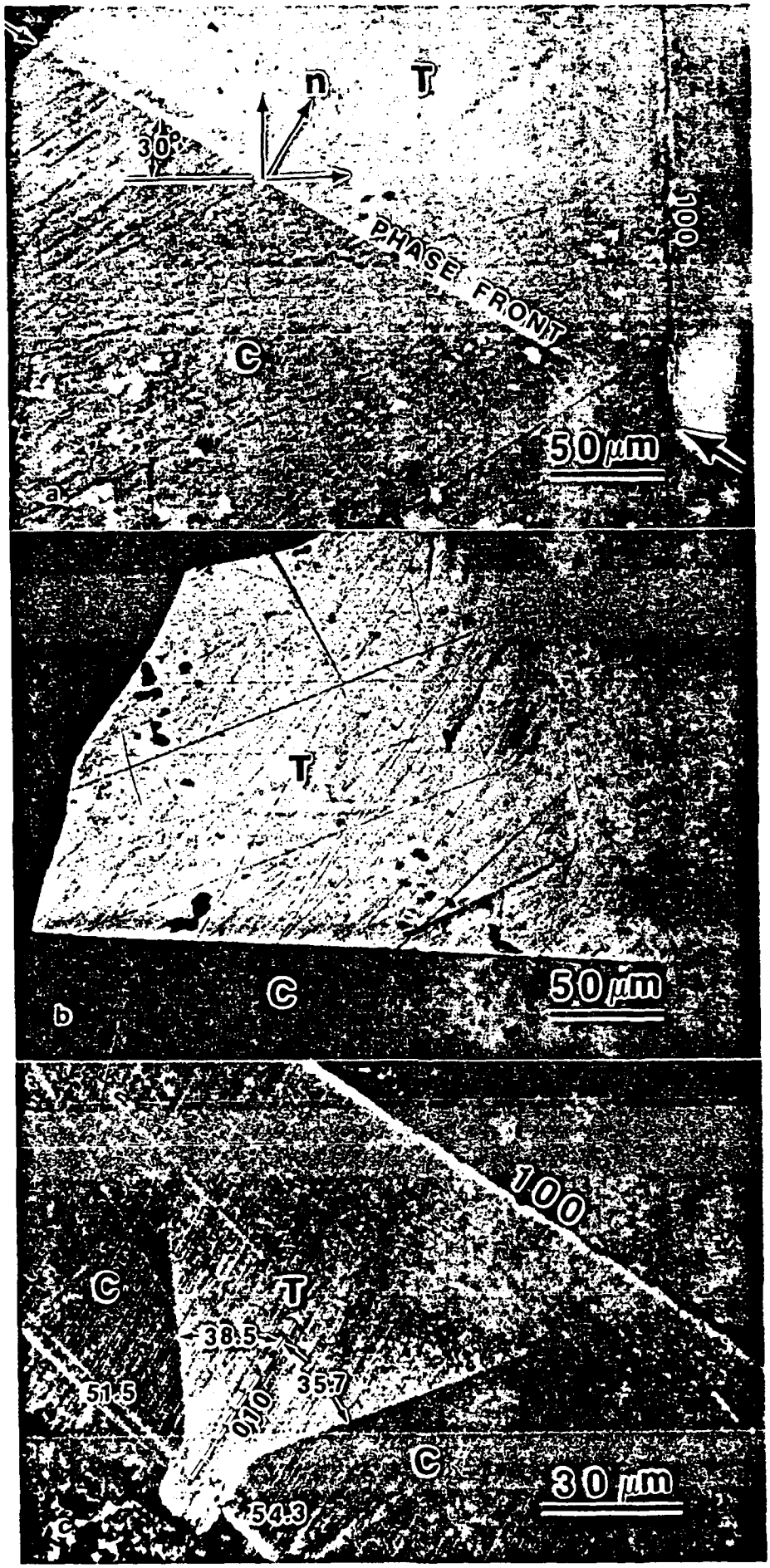
n
T
30°
PHASE FRONT
100
C
50 μm
a
T
C
50 μm
b
100
C
T
38.5
35.7
51.5
010
C
30 μm
54.3
c

Fig. 6 Optical micrographs using polarized light showing (a) a sharp single C/T phase boundary during transformation, making an angle about 30° from a {100} plane; (b) the same specimen rotated to a position where the cubic phase becomes extinct; (c) double C/T phase boundaries during transformation, showing distorted region at phase front intersection and non-uniform contrast distribution in the tetragonal phase; (d) a habit plane affected by microstructural inhomogeneity which is in the form of a-a type domains; (e) another single C/T phase boundary in a different specimen, making an angle of about 35° from a (100) plane.

Table 2 Twinning elements in $PbTiO_3$ tetragonal phase.

	K_1	η_1	K_2	η_2	s
Room temp	{110}	⟨$\bar{1}$10⟩	{$\bar{1}$10}	⟨110⟩	0.115
T_c	{110}	⟨$\bar{1}$10⟩	{$\bar{1}$10}	⟨110⟩	0.0256

rotating the crystal. The cubic phase becomes extinct because of isotropy, Fig. 6(b). One notices that the contrast near the boundary is different from regions farther away, indicating that a local distortion exists. This distorted region appears to vary case by case. For instance, the intersection of two interfaces shows a broader contrast region; the contrast near the specimen center may be different from that of the edge. Figure 6(c) shows a two-interface type phase transformation where the two interfaces are not symmetrically distributed along a (010) plane. The angles between the two interfaces and the (010) plane are 38.5° and 35.7° respectively. It is clear that at the intersection of the two phase fronts a distorted region with different contrast is generated, and this changes the original habit plane configuration. In the tetragonal region, one sees a non-uniform contrast distribution, indicating birefringence variation which is closely related to the lattice parameter variation. We point out that brighter patches sometime show up in the

cubic region before the habit plane approaches it, suggesting some local perturbation in the crystal. Figure 6(d) shows a typical situation where the habit plane may be affected by microstructural inhomogeneity, as indicated. a-a type domains form at this region which show 45° stripes from a {100} plane. The habit plane is bent when it reaches this region. Similarly, a habit plane may be influenced by other factors, such as temperature inhomogeneity, impurity effects etc., which may substantially change the habit plane orientation during transformation. Other single crystals were also used to measure the habit planes. We found that the habit plane appears to vary from crystal to crystal, Fig. 6(e); more interestingly, the same crystal may show a habit plane a little deviated from a previous one or even a little change in orientation during phase front movement. All the angles from a {100} plane to the habit planes were measured and the results are collected in Table 3.

Because of the difficulty of performing two surface analysis of the habit plane in this case, we used another method to derive three dimensional information. In some transformations, the traces of phase boundaries are parallel to {100} planes or with several degrees deviation, shown in Fig. 7. These boundaries often show inclined features, i.e., the boundaries show a bright color at their edges under polarized light as indicated. From such boundaries, we derive the distribution of the third direction cosine, and accordingly the largest angle from a {100} plane is not more than 5°, and most are within 2°. Therefore, we are able to construct the distribution of the habit planes. The results are shown in Fig. 8. It is clear that the habit plane during transformation scatters around a range.

To determine the shape strain, the scratch displacement technique is ordinarily used[18][19]. However the displacements in the present case are extremely small, Fig. 9. Straight fiducial lines were not seen bent across the boundary, indicating a very small shape strain during transformation.

2. Theoretical calculations

The crystallography of the cubic to tetragonal phase transformation was analyzed using phenomenological crystallographic theory formulated by Bowles and Mackenzie[3], but treatments of Wechsler-Lieberman-Read[2] and Bullough-Bilby[20] are equivalent. A computer program based upon the Bowles-Mackenzie formulation[21] was used in this work.

The fundamental basis of the phenomenological theories is the experimental observation that the transformation is macroscopically a homogeneous distortion in which the habit plane between the parent and martensite crystals is both undistorted and unrotated. Upon the requirement that the martensitic transformation is observed as an invariant plane strain, the theory also incorporates a lattice invariant shear, and a rotation with the Bain (structural) distortion to derive a final invariant plane strain. The basic equation of the phenomenological theories can be expressed as

Table 3 Angles of habit planes (during transformation) from {11} planes.

Specimen No.	Angle 1	Angle 2
1-1	59.3	30.7
1-2	60.3	29.7
2-1	55.0	35.0
	56.0	34.0
2-2*	51.0 (53.0)	39.0 (37.0)
3-1	57.0	33.0
3-2**	51.5	38.5
	54.3	35.7
3-3	50.5	39.5
4-1	55.0	35.0
4-2	55.0	35.0
4-3	57.0	33.0
5-1	56.0	34.0
	57.0	33.0
5-2	58.8	31.2
6-1	65.0	25.0
	63.0	27.0
6-2*	50.0 (57.0)	40.0 (33.0)
	55.0	35.0
6-3	61.0	29.0
	63.0	27.0
	58.5	31.5
7-1***	58.0	32.0

* Curved interface
** Two phase fronts
*** Some phase front traces nearly parallel to {100} type planes, as discussed in the text.

$$\mathbf{P}_1=\mathbf{RBP}_2 \tag{1}$$

where $\mathbf{P}_1$, is the shape deformation, and $\mathbf{P}_2$, $\mathbf{B}$ and $\mathbf{R}$ represent the lattice invariant shear, the Bain distortion and the rigid body rotation, respectively. Since both $\mathbf{P}_1$ and $\mathbf{P}_2$ are invariant plane strains, they can be represented as:

$$\mathbf{P}_i=\mathbf{I}+m_i\mathbf{d}_i\mathbf{p}_i' \tag{2}$$

where $\mathbf{I}$ is the unit matrix, m_i is the magnitude of the displacement, $\mathbf{d}_i$ is a unit column vector in the direction of the displacement, and $\mathbf{p}_i'$ is a unit row vector representing the normal to the invariant plane.

Bowles and Mackenzie utilized an equivalent expression to eq. (1)

$$\mathbf{P}_1\mathbf{P}_2^{-1}=\mathbf{RB}=\mathbf{S} \tag{3}$$

where the matrix $\mathbf{S}$, the resultant of two invariant plane strains, is an invariant line strain.

From the experimental lattice parameters of the parent and martensite phases and the assumed Bain (lattice) correspondence, the principal distortions and thus the matrix $\mathbf{B}$ are determined. Invariant lines and invariant normals are calculated from $\mathbf{B}$, and their combinations applied with the appropriate rigid body rotations $\mathbf{R}$ give four invariant planes. The rigid body rotation matrix to put undistorted lines and normals into their original positions is given by Euler's theorem. Once $\mathbf{S}=\mathbf{RB}$ is determined, $\mathbf{P}_1$ and $\mathbf{P}_2$ can be determined from eq. (3) and the assumed (or known) $\mathbf{p}_2'$ and $\mathbf{d}_2$.

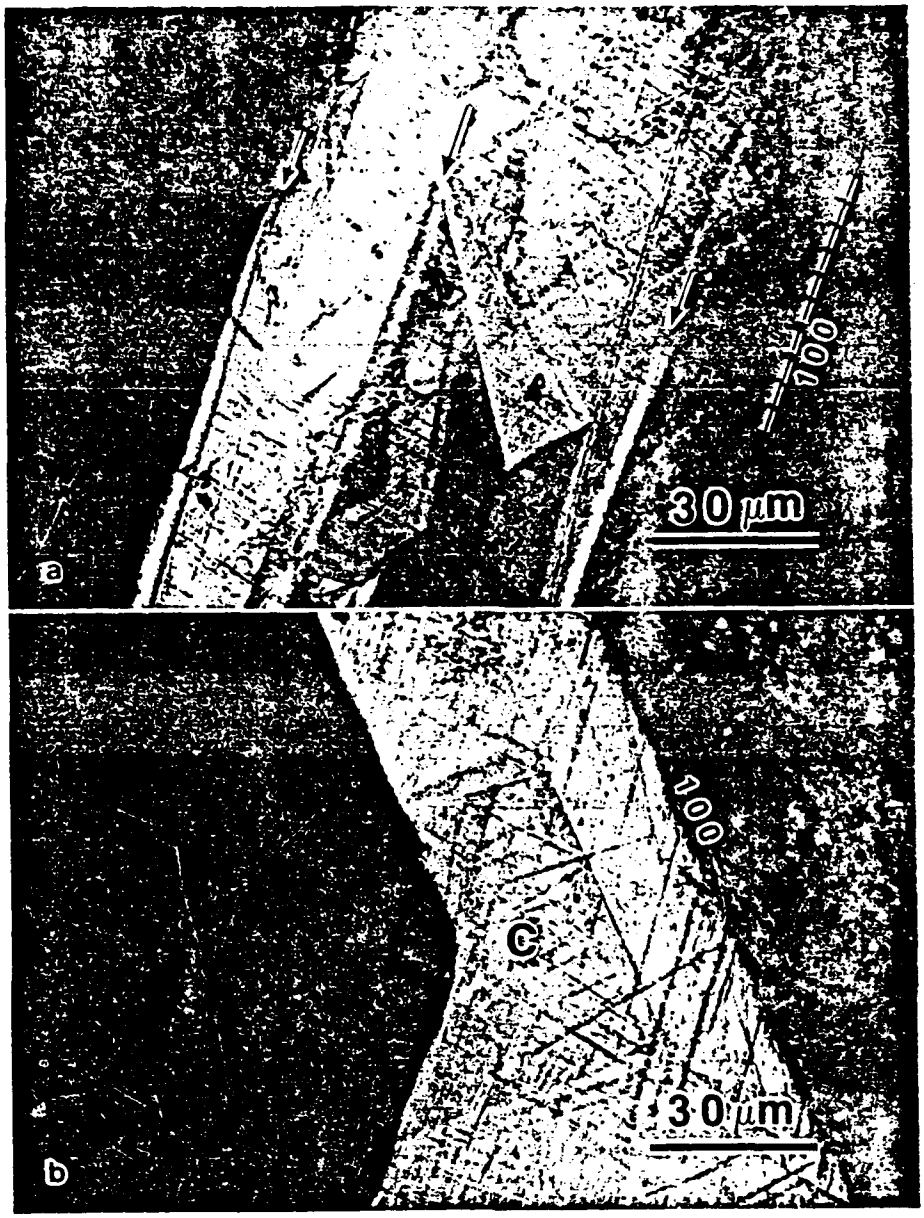

Fig. 7 Optical micrographs using polarized light showing (a) phase boundary spikes nearly parallel to a (100) plane; during transformation, these spikes nucleate from the lower part and extend to the whole specimen; (b) rectangular shaped phase boundary formed during C/T transformation. Note that these boundaries are nearly parallel to {100} planes or with only several degrees deviation.

In the present case, we assume transformation occurs from cubic to tetragonal structures. The lattice correspondences and lattice invariant shear systems in $PbTiO_3$ are listed in Tables 4 and 5. Since we know that $PbTiO_3$ has a negative linear expansion coefficient (therefore negative volume change) below T_c, and the lattice parameter c decreases and a increases as the temperature increases, we can derive

$$(a/a_0)^2(c/a_0) > 1, \quad \text{when} \quad C \rightarrow T \tag{4}$$

That is, the increasing rate of c/a_0 is greater than that of $(a/a_0)^2$. Considering the lattice parameters of $PbTiO_3$ carefully, one realizes that the "lattice parameters at T_c" derived by X-ray may be different from those when transformation actually occurs, since the transformation occurs swiftly and the nature of X-ray measurements is not really "on-time". We need to consider the local lattice conditions, such as: real lattice parameters when transformation occurs, lattice perturbations, temperature inhomogeneity, etc. However, we do not know the "real" conditions around the habit plane at transformation, but can estimate the principal strains as follows. Based upon the lattice constants mentioned before and the relation shown in eq. (4), we calculate possible habit planes by holding η_{11} constant ($\eta_{11}=\eta_{22}$) and varying η_{33}. The ranges of η_{11} and η_{33} are: $1>\eta_{11}>0.994949$ and $1<\eta_{33}<1.012626$. We find that the habit plane shows the same tendency for each set of η_{11} and η_{33}. That is, the

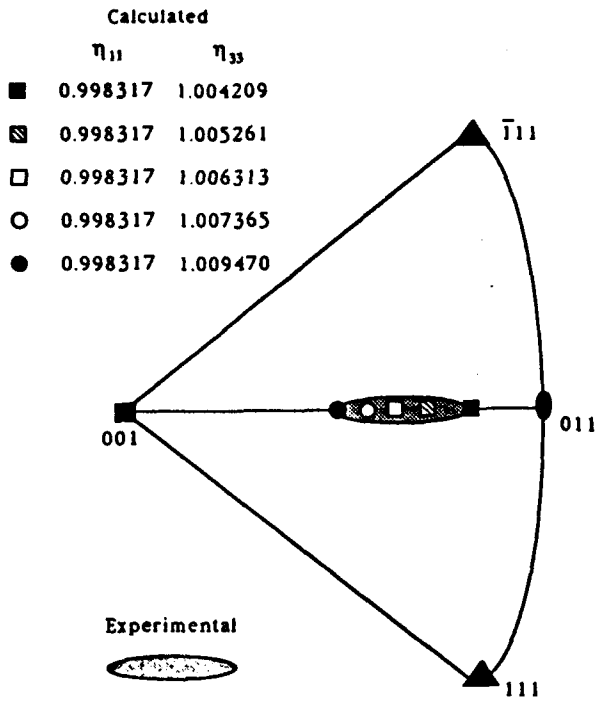

Fig. 8 Experimental and calculated habit plane distribution shown in stereographic projection.

Table 4 Lattice correspondence (LC) and transformation matrix for cubic and tetragonal phases of $PbTiO_3$.*

Lattice correspondence	[UVW]	[uvw]	T
I	1 0 0	1 0 0	1 0 0
	0 1 0	0 1 0	0 1 0
	0 0 1	0 0 1	0 0 1
II	1 0 0	0 1 0	0 0 1
	0 1 0	0 0 1	1 0 0
	0 0 1	1 0 0	0 1 0
III	1 0 0	0 0 1	0 1 0
	0 1 0	1 0 0	0 0 1
	0 0 1	0 1 0	1 0 0
IV	1 0 0	0 1 0	0 1 0
	0 1 0	1 0 0	1 0 0
	0 0 1	0 0 $\bar{1}$	0 0 $\bar{1}$
V	1 0 0	1 0 0	1 0 0
	0 1 0	0 0 $\bar{1}$	0 0 1
	0 0 1	0 1 0	0 $\bar{1}$ 0
VI	1 0 0	0 0 $\bar{1}$	0 0 1
	0 1 0	0 1 0	0 1 0
	0 0 1	1 0 0	1 0 0

* where

$$\begin{bmatrix} u \\ v \\ w \end{bmatrix}_{Tetra} = T \begin{bmatrix} U \\ V \\ W \end{bmatrix}_{Cubic}$$

habit plane scatters linearly over a range, and is very sensitive to the relative values of $(\eta_{33}-1)/(\eta_{11}-1)$, i.e., the principal strains. Moreover, if η_{11} is different from η_{22} when transformation occurs, the habit plane normal may deviate sideways from the {001}-{011} zone which explains the lateral scatter of experimental data seen in Fig. 8. We sumarize a set of calculations using lattice correspondence I and lattice invariant shear system (101) [$\bar{1}$01] to show the general characteristics of the calculated crystallography, as listed in Table 6. The calculated habit plane varies within a range similar to that observed in the experiments if we input reasonable values of principal distortions based upon available lattice parameters and take into account a possible local lattice perturbation. Similar scatter characteristics can also be derived by varying a dilatational parameter, δ[3], which describes a uniform lattice distortion at the boundary as discussed

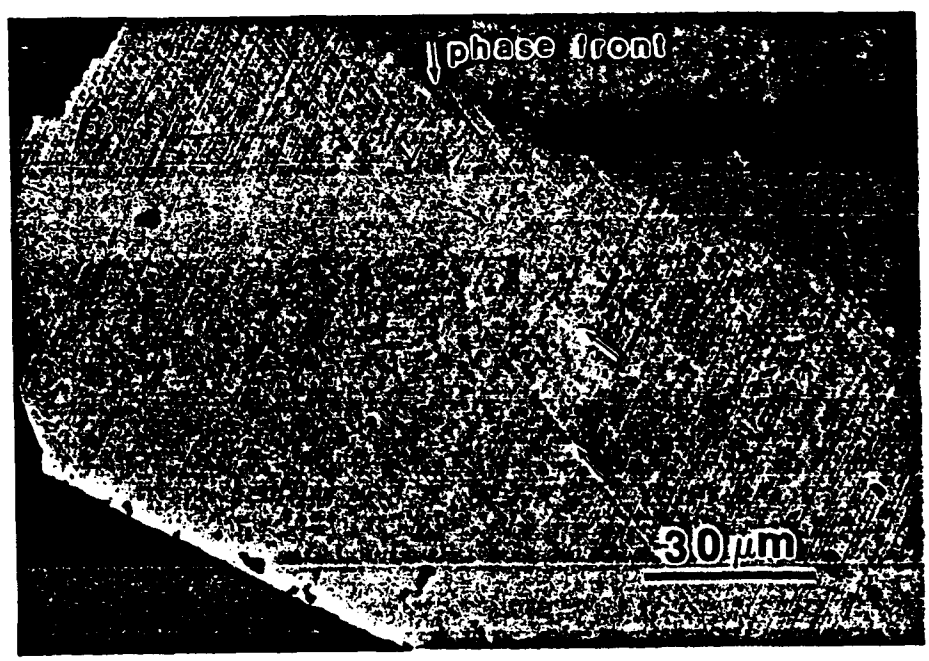

Fig. 9 Optical micrograph showing fiducial lines across a phase boundary. The fiducial lines appear not to be bent due to the very small transformation shape strain.

Table 5 Lattice invariant shear systems employed for $PbTiO_3$.

LC I	$(101)[\bar{1}01]$	LC II $(011)[01\bar{1}]$	LC III $(110)[1\bar{1}0]$
	$(\bar{1}01)[\bar{1}01]$	$(110)[\bar{1}10]$	$(101)[10\bar{1}]$
	$(011)[0\bar{1}1]$	$(01\bar{1})[011]$	$(1\bar{1}0)[110]$
	$(0\bar{1}1)[011]$	$(\bar{1}10)[110]$	$(10\bar{1})[101]$
LC IV	$(10\bar{1})[\bar{1}0\bar{1}]$	LC V $(1\bar{1}0)[\bar{1}\bar{1}0]$	LC VI $(\bar{1}10)[\bar{1}\bar{1}0]$
	$(\bar{1}0\bar{1})[10\bar{1}]$	$(0\bar{1}1)[0\bar{1}\bar{1}]$	$(\bar{1}01)[\bar{1}0\bar{1}]$
	$(01\bar{1})[0\bar{1}\bar{1}]$	$(\bar{1}\bar{1}0)[1\bar{1}0]$	$(\bar{1}\bar{1}0)[\bar{1}10]$
	$(0\bar{1}\bar{1})[01\bar{1}]$	$(0\bar{1}\bar{1})[0\bar{1}1]$	$(\bar{1}0\bar{1})[\bar{1}01]$

Table 6 Effect of principal distortion values on the results of crystallographic analysis (LCI-1).

η_{11}	0.998317	0.998317	0.998317	0.998317	0.998317
η_{33}	1.004209	1.005261	1.006313	1.007365	1.009470
Solution 1					
$V-V_0$	0.000652	0.001880	0.002929	0.003977	0.006075
m_1	0.004022	0.005252	0.006302	0.007353	0.009454
p_1	-.762924	-.824731	-.856502	-.878487	-.907004
	-.646485	-.565521	-.516140	-.477761	-.421117
	0.002263	0.002090	0.002053	0.001956	0.001945
d_1	-.761653	-.823282	-.855040	-.877020	-.905487
	0.647981	0.567630	0.518559	0.480451	0.424370
	0.002176	0.002026	0.001906	0.001900	0.001773
Angle from [010]	40.3°	34.4°	31.1°	28.5°	24.9°

later. The calculated shape strain magnitude m_1 is about one tenth to one twentieth that in ferrous martensitic transformations. This is the reason why we can hardly see any obvious bending of fiducial lines. It is seen that the theoretical calculations appear to fit experimental results quite well if we consider the interfacial properties of the habit plane. A more complete set of calculations will be published elsewhere.

IV. Discussion

It has been suggested that the WLR theory should be applicable to perovskite-type ferroelectric crystals[4]. DiDomenico and Wemple[9] did present evidence on semiconducting perovskite-type crystals showing habit planes quantitatively explainable in terms of the WLR crystallographic theory. However, crystals with high resistivity were reported not always with predicted habit plane normals[10][11]. Since then, it has been considered that the cubic to tetragonal transformation in perovskite crystals with high resistivity can not be classified in the family of martensitic transformations[22]. However, the microstructural characteristics of $PbTiO_3$ in the present experiment have shown: (i) reversible surface upheavals; (ii) irrational habit planes; (iii) a fine inhomogeneous structure which is twinning in this case; (iv) that all atoms move less than an interatomic distance; and (v) the transformation process is clearly first order. Although the precise orientation relationship between the two phases is not determined quantitatively in the present experiments, the relationship between the principal axes in both phases is easily derived. That is, the three orthogonal axes in the cubic phase are essentially parallel to certain orthogonal axes in the tetragonal phase. All the above crystallographic features fall within the classification scheme for martensitic transformations[1][23].

During the cubic to tetragonal transformation in $PbTiO_3$, several features were observed. Most significantly, some of the cubic-tetragonal interfaces (or habit plane) show sharp, straight first order phase boundaries which scatter within a certain range, and some show bright and broader edges. If we consider this using a three dimensional construction, as shown in Fig. 10, the morphology of the habit plane depends on the viewing direction. For instance, viewing from direction **c**, a sharp interface can be seen; from direction **a**, a broad interface appears; on the other hand, one may not see any phase boundary or only some faint feature from direction **b**. Boundaries shown in Fig. 6 are those viewing from a direction similar to **c**, and Fig. 7 shows boundaries viewing from an **a** direction. Interpretation in this way explains fairly well the morphology of habit planes observed in $PbTiO_3$, and the habit plane distribution can be fit with theoretical calculations by considering local lattice parameter perturbations. However, previous works on $BaTiO_3$ claimed that in some high resistivity $BaTiO_3$ crystals the cubic-tetragonal phase boundary is of the W-L-R type, but contrary to theoretical predictions[10][11]. The cubic-tetragonal phase transition in about 20 $BaTiO_3$ single crystals was investigated[10][11] and about 30% of the crystals exhibited phase boundaries at angles very close to that predicted by theory; 60% of them showed a broad phase boundary approximately perpendicular to the 90° domain walls of the a-c domain structure and the remaining 10% changed from cubic to tetragonal via a broad and complicated square net pattern[11][24]. In all cases the a-c domain structure was clearly visible right up

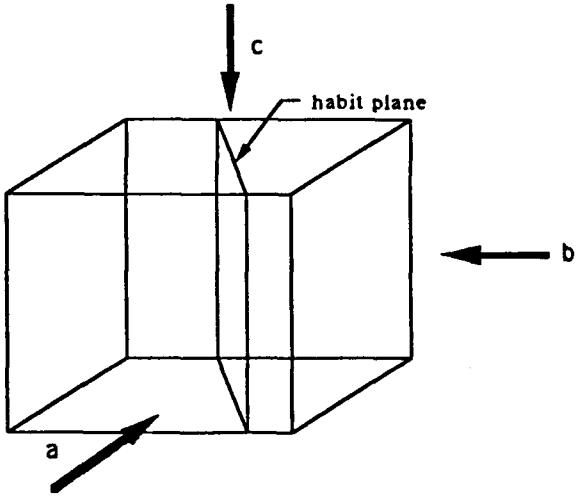

Fig. 10 Three dimensional arrangement of a habit plane. Viewing from three different cube directions reveals different morphological characteristics. See text for discussion.

to the phase boundary and in all cases a strain pattern with the same period as the a-c domain structure was clearly visible in the cubic phase on the high temperature side of the phase boundary. Reviewing these previous results carefully, we can see that the situation in $BaTiO_3$ is quite similar to that in $PbTiO_3$. Besides the 30% habit planes which show sharp interfaces and are consistent with the theoretical calculations, the 60% habit planes approximately perpendicular to the 90° domain walls of the a-c domain structure are actually parallel to a {100} plane since the traces of a-c domain boundaries should be parallel to a {100} plane, which may be just the case shown in Figure 7 and can be derived viewing from an appropriate direction, like c in Fig. 10. We do not see complicated square net patterns in $PbTiO_3$ and therefore it is difficult to compare the remaining 10% of the habit planes. It seems that the apparent inconsistency in previous works is because three dimensional considerations were not taken into account.

If the specimen is thin enough, one sees a pronounced contrast variation around the phase boundary under polarlized light, as shown in Fig. 6. This is clearly related to a strain field and one further notes that this pattern appears at the tetragonal side, with a width of tens of microns. An interpretation of this is that a coherent unrotated interface forms with severe elastic strain over an appreciable distance owing to lattice-matching. However, the contrast variation regions appear to vary case by case, indicating a possibility that local lattice distortions may vary depending on the ambient conditions. To reduce the misfit strain energy to a minimum, the lower symmetry crystal phase should be twined so that the sign of the strain reverses in going from one twin to the next along the habit plane. This then defines a plane of "zero average distortion"[4]. The theory of WLR is based on an interface plane between the martensite and its parent which remains macroscopically unrotated and undistorted as a result of the shape deformation. It is implicit in this account that the "fit" of the martensite to its parent is isotropic. Bowles and Mackenzie have shown that if the habit plane contains a small scale isotropic distortion, the condition of an invariant plane strain for the habit plane is slightly relaxed[3]. Therefore, the Bowles-Mackenzie theory, on the other hand, holds that the habit plane is unrotated but may be isotropically distorted by some 1 or 2 percent[3]. They introduced a dilatation parameter, δ, which in effect slightly relaxes the requirement that the habit plane is undistorted, but this modification is not without criticism[23]. We do not know in fact if the habit plane is isotropically distorted (or not) during transformation from the present experiments. However, we can think in another way that the parameter δ is more than a "correction factor", and may contain substantial physical meaning. The significance of this is that the parameter δ may function as an indicator of local lattice arrangements causing a habit plane change. This offers a certain degree of freedom: to take into account a perturbation or local lattice distortion during transformation due to composition, defects, temperature inhomogeneity, etc., which may substantially influence the crystallographic characteristics. In the present experiments, the same crystal sometimes showed habit planes with different angles from a {100} plane, providing evidence for this consideration.

Although the transformation strains in $PbTiO_3$ are quite small (Table 6) compared to those of ferrous alloys, a small change in the relative values of the principal strains introduces a dramatic shift of the habit plane. That is, the tetragonality of the C/T transformation is a major factor determining the crystallographic characteristics. The tetragonality can be affected by impurities, structural inhomogeneities, a temperature perturbation, strain conditions, etc. The crystals used in the present case[17] offer a good example. It is thus obvious that even a very small perturbation of lattice distortion during transformation will shift the habit plane. This is evidenced by the shift of the same phase front at different positions during transformation, Fig. 6(c)-(e). This consideration may explain the scattering of habit plane normals observed in experiments. The reason why the scattering phenomenon is not seen in $BaTiO_3$ and KTN is probably due to the very small tetragonalities and distortions involved.

$PbTiO_3$ has a much higher polarization value than $BaTiO_3$ and KTN[16] and the resistivity of the crystals used is much higher than a semiconductor. Therefore the stored electrical energy should be much higher at the phase boundary in this case according to an argument made by previous workers[9]-[11]. If this is true, the electrostatic and/or electrostriction energy may overwhelm the strain energy, and dominate the transformation characteristics. We do not know the exact relation between the strain and electrical energies in the present experiment, and more detailed work is needed. However, if the electrical energy prevails and the transformation characteristics are solely dominated by this rather than by a perturbation of lattice arrangements, it appears that the same crystal could show identical habit plane characteristics because the stored electrical energy is the same. This is not the case we observe. Therefore we suggest a re-investigation of the role of electrical energy.

V. Conclusions

(i) The cubic to tetragonal (C/T) phase transformation in $PbTiO_3$ single crystals shows martensitic characteristics. Microstructural features investigated using heating stage optical microscopy and transmission electron microscopy show a small hysteresis involved, the difference between the A_s and M_s temperatures being about 5°C. The phase front passes swiftly through the crystal; surface relief accompanying the transformation is also seen. The twinning system involved has been identified as a compound twin in the tetragonal phase with $K_1=\{110\}$, $\eta_1=\langle\bar{1}10\rangle$, $K_2=\{\bar{1}10\}$, $\eta_2=\langle110\rangle$.

(ii) The phase boundaries (habit planes) were "frozen" by controlling the temperature profile. It was

found that the habit planes vary within a certain range. Not only did different specimens show this phenomenon, but also the same specimen under different transformations also follows this, indicating the importance of local distortion near the interfaces during transformation. The present experimental results suggest a re-investigation of the role of stored electrical energy.

(iii) Theoretical predictions with varying principal distortions show that experimental data appear to fit calculated results quite well, if one considers the effect of local lattice distortions during transformation. The results show a certain degree of consistency, which imply that the phenomenological martensitic crystallographic theory does indeed apply to $PbTiO_3$.

Acknowledgments

The authors are grateful to Professor D. A. Payne and Dr. C. T. Suchicital for providing crystals and valuable discussions. This project is supported by Air Force Office of Scientific Research under contract AFOSR-90-0174.

REFERENCES

(1) J. W. Christian: *The Theory of Transformations in Metals and Alloys*, Pergamon Press, Oxford, (1965) and (1975).
(2) M. S. Wechsler, D. S. Lieberman and T. A. Read: Trans. AIME, 197 (1953), 1503.
(3) J. S. Bowles and J. K. Mackenzie: Acta Metall., 2 (1954), 129, 138, 224.
(4) D. S. Lieberman, M. S. Wechsler and T. A. Read: J. Appl. Phys., 26 (1955), 473.
(5) C. M. Wayman: *Introduction to the Crystallography of Martensitic Transformations*, Macmillan, New York, (1964).
(6) H. Warlimont and Delaey: *Progress in Materials Science*, ed. by B. Chalmers, J. W. Christian and T. B. Massalski, 18 (1974).
(7) Z. Nishiyama: *Martensitic Transformations*, Academic Press, New York (1978).
(8) G. K. Bansal and A. H. Heuer: Acta Metall., 20 (1972), 1281; 22 (1974), 409.
(9) M. DiDomenico, Jr. and S. H. Wemple: Phys. Rev., 155 (1967), 539.
(10) T. J. Parker and J. C. Burfoot: Brit. J. Appl. Phys., 17 (1966), 207.
(11) T. J. Parker and J. C. Burfoot: Brit. J. Appl. Phys., 2 (1969), 1168.
(12) G. Shirane, S. Hoshino and K. Suzuki: Phys. Rev., 80 (1950), 1105.
(13) G. A. Smolenskii: Sov. J. Technical Physics, 21 (1951), 1045.
(14) H. D. Megaw: Proc. Roy. Soc., A189 (1947), 261.
(15) G. Shirane and S. Hoshino: J. Phys. Soc. Japan, 6 (1951), 265.
(16) G. Shirane, R. Pepinsky and B. C. Frazer: Acta Cryst., 9 (1956), 131.
(17) C. T. Suchicital: Ph. D Dissertation, University of Illinois, (1988).
(18) J. S. Bowles and A. J. Morton: Acta Metall., 12 (1964), 629.
(19) E. J. Efsic and C. M. Wayman: Trans. TMS-AIME, 239 (1967), 873.
(20) R. Bullough and B. A. Bilby: Proc. Phys. Soc., B69 (1956), 1276.
(21) H. M. Ledbetter and C. M. Wayman: Mater. Sci. Engr., 7 (1971), 151.
(22) M. Cohen, G. B. Olson and P. C. Clapp: Proc. ICOMAT (1979), 1.
(23) D. S. Lieberman: *Phase Transformations*, ASM, Metals Park, Ohio (1970), Chap. 1.
(24) P. W. Forsbergh: Phys. Rev., 76 (1949), 1187.

Pressure dependence of optical absorption in $PbTiO_3$ to 35 GPa: Observation of the tetragonal-to-cubic phase transition

C. S. Zha[a] and A. G. Kalinichev[b]
Department of Materials Science and Engineering and Department of Geology, University of Illinois at Urbana-Champaign, Urbana, Illinois 61801

J. D. Bass
Department of Geology, University of Illinois at Urbana-Champaign, Urbana, Illinois 61801

C. T. A. Suchicital[c]
Department of Materials Science and Engineering, University of Illinois at Urbana-Champaign, Urbana, Illinois 61801

D. A. Payne
Department of Materials Science and Engineering, University of Illinois at Urbana-Champaign, Urbana, Illinois 61801

(Received 11 May 1992; accepted for publication 12 July 1992)

Optical absorption of the polar material $PbTiO_3$ has been studied up to 35 GPa (350 kbar) in the visible range of wavelengths using a single crystal samples compressed in a diamond anvil high pressure cell. The absorption edge shifts toward lower energies with increasing pressure. Pressure dependence of the absorption edge undergoes significant changes at about 11.5 ± 0.3 GPa, close to the previously identified tetragonal-cubic phase transition. The change in pressure dependence of the spectra is consistent with second-order character of the transition.

I. INTRODUCTION

Lead titanate, $PbTiO_3$, an important member of the perovskite family of ferroic materials, has a first-order cubic-to-tetragonal phase transition on cooling through $T_c = 763$ K (Curie point) at atmospheric pressure.[1] The effect of pressure on the properties of $PbTiO_3$, and their relationship to the phase transition, has been studied by several authors.[2-8] However, unlike its Ba analog, $BaTiO_3$, accurate values of the single-crystal ferroelectric properties of pure $PbTiO_3$ are unavailable because of experimental difficulties in polarization reversal measurements. In addition, reduced values of electrical resistivity[4] often dictates the use of samples doped with U[4,7,8] or Nb[5] as charge compensators.[1] As a consequence, some discrepancies in reported data[2,4,5,7] may be partly attributed to the differences in crystal quality and composition.

The temperature of the polar-paraelectric phase transition is known to decrease with increasing hydrostatic pressure. From an x-ray study of pure $PbTiO_3$ ceramics up to 1.8 GPa Kabalkina and Vereshchagin[2] obtained a linear pressure dependence of T_c with a slope as steep as -180 K/GPa, which extrapolates to a transition pressure $P_c \approx 2.7$ GPa at room temperature assuming the transition remains first-order. Later, from studies of the dielectric properties of U-doped single crystals, Samara[4] observed a significant nonlinearity in the pressure dependence of T_c with the slope decreasing from -84 K/GPa at low pressure to -50 K/GPa at 2.2 GPa. These results imply that $P_c > 8$ GPa at room temperature. Samara also noted that the first-order character of the phase transition becomes less pronounced with increasing pressure and suggested a change from first- to second-order character with the tricritical point at ~ 4.5 GPa.

A second-order phase transition at $P_c = 12.1$ GPa and room temperature has indeed been identified from the high-pressure Raman study of undoped $PbTiO_3$ crystals.[6] On the other hand, dielectric and x-ray measurements for Nb-doped polycrystalline specimens[5] suggest a first-order phase transition at 5.8 GPa and room temperature. These latter data are in contradiction with more recent x-ray diffraction measurements for U-doped crystals[7,8] up to 6 GPa from which a second-order transition at ~ 13 GPa may be expected by extrapolation.

The pressure-temperature phase diagram of $PbTiO_3$ and the position of the tricritical point have been recently analyzed within the framework of a phenomenological theory of ferroelectricity.[9] From this analysis the high-pressure second-order phase transition is to be expected at room temperature. However, the Raman data of Sanjurjo *et al.*[6] remain the only direct experimental evidence for it.

Optical absorption has already proven useful for understanding the properties and phase transitions of ferroelectrics in response to changes in external parameters.[10-12] In the present study we have attempted to identify the high-pressure phase transition in $PbTiO_3$ from optical absorption data obtained over a wide range of pressure up to 35 GPa. Our intent is to resolve difference among previous studies, and to extend the pressure range of investigation using nominally undoped crystals.

[a]Present address: Geophysical Laboratory, Carnegie Institution of Washington, 5251 Broad Branch Rd., N.W., Washington, DC 20015-1305.

[b]On leave from: Institute of Experimental Mineralogy, Russian Academy of Sciences, 142432 Chernogolovka, Moscow District, Russia.

[c]Present address: Department of Chemical, Bio, and Materials Engineering, Arizona State University, Tempe, AZ 85287.

 0021-8979/92/203705-03$04.00

II. EXPERIMENT

The $PbTiO_3$ crystals used in our study were grown by slow cooling from a temperature of 900 °C in a KF-PbO-PbF_2 flux. Details of the crystal growth procedure are presented elsewhere.[13] A qualitative chemical analysis of the resulting crystals by dc arc emission spectroscopy showed the presence of impurities at the 0.5 wt % level or lower, with most impurities having substantially lower concentrations. These results were confirmed by quantitative electron probe microanalysis, which yielded 0.33 wt % K_2O and all other impurities below the detection limit. All samples were multidomain on a length scale ranging from a few micrometers or less up to several tenths of a mm.

The optical system used in our experiments is similar to the one described by Welber.[14] A Mao–Bell[15] type of diamond anvil high-pressure cell was used to compress the samples. The gaskets with a central hole about 200 μm in diameter were made of 0.5-mm-thick stainless steel 301, and preindented to between 50–70 μm. $PbTiO_3$ crystals approximately 80 μm in linear dimensions and ~ 10 μm thick were loaded into the cylindrical gasket hole together with several ruby chips used for pressure measurements by the ruby fluorescence technique.[16] The pressure transmitting medium was a 4:1 methanol:ethanol mixture, which provided a hydrostatic medium up to 10.5 GPa, and quasihydrostatic pressure to about 20 GPa.[17] In our experiments, the R_1 and R_2 peaks of ruby fluorescence were well resolved up to the highest pressure (35 GPa) indicating nearly hydrostatic conditions.

A tungsten halogen lamp (100 W OLYMPUS HAL-L) has been used as a light source that gave an incident beam in the 4000 to 8000 Å range of wavelengths. Light passing through a source aperture of 20 μm was focused to a smaller spot in the gasket hole by an objective lens. The image formed was sharp and very well defined. At each pressure the optical transmission spectrum (I/I_0 vs λ) was obtained by comparing the intensities of transmitted light from two measurements: (1) with the light transmitted through the pressurized sample (intensity I); and (2) with the light transmitted adjacent to the sample, through the alcohol mixture and diamond alone (intensity I_0).

Radiation transmitted through the cell was analyzed using a 0.32 m scanning monochrometer and was detected by a Hamamatsu photomultiplier tube R943-02 together with photon counting electronics. A pinhole was put in the imaging plane of the sample immediately before the monochrometer as a spatial filter to cut out extraneous radiation and decrease the background light.

Thirty-six measurements have been made in the pressure region from 0.03 to 32.7 GPa in four separate experiments. Most of the measurements were carried out between 7 and 17 GPa where the phase transition was expected. All measurements were made at room temperature (~ 20 °C).

III. RESULTS AND DISCUSSION

Typical transmission spectra collected at different pressures are shown in Fig. 1. The crystal absorbs visible light

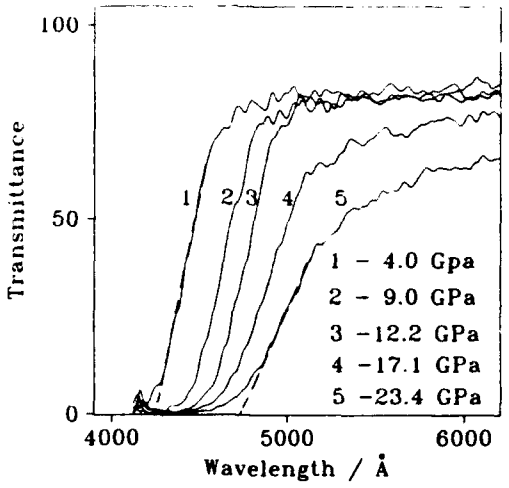

FIG. 1. Transmittance spectra of $PbTiO_3$ single crystals at various pressures. Dashed lines illustrate the definition of the absorption edge.

in the violet range of wavelengths, as could be expected from its yellowish color. This intense absorption is clearly caused by Ti ions, as judged by analogy with the known fundamental absorption edge of crystalline $BaTiO_3$ at a wavelength $\lambda \approx 4000$ Å at room pressure.[12] Similar absorption spectra have also been reported very recently for $PbTiO_3$ powder at ambient conditions.[18] With increasing pressure, absorption shifts significantly to longer wavelengths (Fig. 1).

The observed pressure dependence of optical absorption is most conveniently discussed in terms of an absorption edge. In our study, we define the absorption edge as the maximum slope of the transmittance decline at lower wavelengths, extrapolated by a straight line to zero transmittance. This intuitively clear definition of the absorption edge is illustrated by dashed lines in Fig. 1 for two pressures.

It should be noted that the definition of an absorption edge is, to some degree, arbitrary. The definition used by us, as well as several other definitions, can be found in the literature of previous studies by other investigators.[19–21] We have analyzed our data using several of these definitions, and each yields slightly different wavelengths for the absolute value of the edge. However, all definitions result in the same pressure dependence of the absorption edge and do not affect the following discussion.

The pressure dependence of the optical absorption edge of $PbTiO_3$ is shown in Fig. 2 for the whole pressure range studied. The qualitative picture obtained is very similar to the temperature and pressure dependence of the absorption edge of SbSI near its polar phase transition.[10,11] The absorption edge shifts with pressure to longer wavelengths with an initial slope of 15 Å/GPa, increasing to 47 Å/GPa at ≈ 11.5 GPa. At this pressure, a sudden drop of the slope to 12 Å/GPa takes place, and the slope continues to increase further to 32 Å/GPa at the highest pressure of the present study.

The sharp change in slope at 11.5 ± 0.3 GPa (Fig. 2) clearly indicates the presence of a phase transition at this

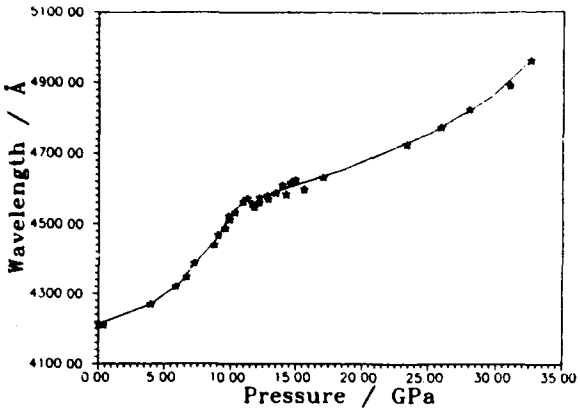

FIG. 2. Pressure dependence of the optical absorption edge of $PbTiO_3$. The size of the symbols approximately corresponds to experimental errors involved.

pressure. The change is consistent with a second-order transition, inasmuch as a first-order phase transition should result in a sudden change $\Delta\lambda$ of the absorption edge wavelength as the crystal passes through the Curie point (see, e.g., Ref. 12).

Moreover, the observed transition pressure corresponds to the pressure of a second-order phase transition found earlier in $PbTiO_3$ at room temperature by Raman spectroscopy (12.1 ± 0.2 GPa).[6] The transition pressure from our measurements is also in reasonable agreement with an extrapolation of more recent high-pressure x-ray data on spontaneous strain ($P_c \approx 13$ GPa).[7]

It is worth noting that we find no evidence for a phase transition in $PbTiO_3$ at much lower pressures. In contrast, the dielectric measurements of Ikeda[5] indicate a first order transition in Nb-doped samples at 5.8 GPa. The transition noticed in the latter study may be due to a depression of P_c by the dopant. Alternatively, the discrepancy may result from the different apparatus used. Ikeda carried out measurements on polycrystalline samples in a solid medium apparatus, using epoxy resin as the pressure transmitting medium. Under nonhydrostatic conditions the presence of high shear stresses on the sample might lower the transition pressure drastically. If the transition pressure is systematically affected by shear stresses, this might also explain the small difference in P_c between our study and Sanjurjo *et al.*[6] The pressure medium used in our experiment (4:1 methanol:ethanol) freezes at approximately 10.5 GPa, whereas the methanol-ethanol-water mixture used by Sanjurjo *et al.* remains liquid to somewhat higher pressures. However, as noted previously, the ruby fluorescence spectra in our experiments indicated that the pressure distribution in the diamond cell was nearly hydrostatic.[17] Moreover, the difference between our work and that of Sanjurjo *et al.*[6] is within the mutual uncertainties of the two sets of experiments, and may not reflect any real difference in the experimental conditions.

In conclusion, we have measured optical absorption spectra of polar $PbTiO_3$ single crystals at room temperature and in the pressure range 35 GPa (350 kbar). Pressure dependence of the absorption edge derived from the measurements has been examined and exhibits a change in slope by a factor of ~ 3 at about 11.5 ± 0.3 GPa, indicating a phase transition in the material. This behavior of the absorption edge is consistent with second-order character for the transition.

ACKNOWLEDGMENTS

The study has been supported by the Air Force Office of Scientific Research through the University Research Initiative Program (AFOSR-90-0174) to JDB and DAP, and the National Science Foundation through grant EAR90-18676 to JDB.

[1] M. L. Lines and A. M. Glass, *Principles and Applications of Ferroelectrics and Related Materials* (Oxford University Press, Oxford, U.K., 1977).
[2] S. A. Kabalkina and L. F. Vereshchagin, Sov. Phys. Dokl. **7**, 310 (1962).
[3] G. A. Samara, in *Advances in High Pressure Research*, edited by R. S. Brady (Academic, New York, 1969), p. 155.
[4] G. A. Samara, Ferroelectrics **2**, 277 (1971).
[5] T. Ikeda, Solid State Commun. **16**, 103 (1975).
[6] J. A. Sanjurjo, E. López-Cruz, and G. Burns, Phys. Rev. B **28**, 7260 (1983).
[7] R. J. Nelmes and A. Kartusiak, J. Phys. C **19**, L725 (1986).
[8] R. Ramirez, H. Vincent, R. J. Nelmes, and A. Kartusiak, Solid State Commun. **77**, 927 (1991).
[9] R. Ramirez, M. F. Lapeña, and J. A. Gonzalo, Phys. Rev. B **42**, 2604 (1990).
[10] G. Harbeke, J. Phys. Chem. Solids **24**, 957 (1963).
[11] V. M. Fridkin, K. Gulyamov, V. A. Lyakhovitskaya, V. N. Nosov, and N. A. Tikhomirova, Sov. Phys. Solid State **8**, 1510 (1966).
[12] E. Fatuzzo and W. J. Merz, *Ferroelectricity* (North-Holland, Amsterdam, 1967), pp. 262–265.
[13] C. T. A. Suchicital and D.A. Payne, J. Cryst. Growth **104**, 211 (1990).
[14] B. Welber, Rev. Sci. Instrum. **47**, 183 (1976).
[15] H. K. Mao, P. M. Bell, K. J. Dunn, R. M. Chrenko, and R. C. DeVries, Rev. Sci. Instrum. **50**, 1002 (1979).
[16] J. D. Barnett, S. Block, and G. J. Piermarini, Rev. Sci. Instrum. **44**, 1 (1973).
[17] J. M. Besson and J. P. Pinceaux, Rev. Sci. Instrum. **50**, 541 (1979).
[18] Z. Qifa, Z. Qing, L. Yiongxiang, Z. Liangying, and Y. Xi, Ferroelectrics Lett. **13**, 115 (1991).
[19] R. Kern, J. Phys. Chem. Solids **23**, 249 (1962).
[20] B. Welber, C. K. Kim, M. Cardona, and S. Rodrigues, Solid State Commun. **17**, 1021 (1975).
[21] Q. Williams, E. Knittle, R. Reichlin, S. Martin, and R. Jeanloz, J. Geophys. Res. **95B**, 21549 (1990).

Paramagnetic resonance of platinum ions in $PbTiO_3$ single crystals

W. L. Warren and B. A. Tuttle
Glass and Electronic Ceramics Department, Sandia National Laboratories, Albuquerque, New Mexico 87185

B. N. Sun, Y. Huang, and D. A. Payne
Department of Materials Science and Engineering, Materials Research Laboratory, and Beckman Institute, University of Illinois at Urbana-Champaign, Urbana, Illinois 61801

(Received 4 August 1992; accepted for publication 26 October 1992)

Optical excitation of trivalent platinum ($5d^7$, t^6e) ions in lead titanate single crystals have been observed for the first time by electron paramagnetic resonance (EPR). The g and hyperfine coupling A tensors were found to be axial: $g_\parallel = 1.938$, $g_\perp = 2.478$, $A_\parallel = 0.0164\ cm^{-1}$, and $A_\perp = 0.0324\ cm^{-1}$. Analysis of the EPR spectra using crystal field theory indicates that the Pt^{+3} ions are in tetragonally distorted (elongated) octahedral sites, strongly suggesting that they substitute for the central Ti^{+4} ions in the perovskite lattice.

Transition metal ions in type ABO_3 perovskite compounds have been widely studied by electron paramagnetic resonance (EPR) and optical spectroscopy methods.[1-4] In most cases it is believed that they behave as deep centers and can significantly affect the electronic and optical properties of the ceramic involved. In recent years, $PbTiO_3$, and lead zirconate titanate (PZT), ceramics have attracted much attention for use in nonvolatile semiconductor memories, displays, optical shutters, and infrared imaging devices. However, unlike $BaTiO_3$ and $SrTiO_3$, very little is known about the nature or identity of paramagnetic centers in $PbTiO_3$.[5,6] In this study, we have used EPR to obtain such information in $PbTiO_3$ crystals; we find evidence for Pt^{+3} ions in the optically illuminated ceramics. The observation of Pt in the $PbTiO_3$ crystals may be of considerable importance since it is widely used as the primary electrode in many of the aforementioned device applications.

The $PbTiO_3$ crystals were grown by a self-flux method. The starting method was comprised of 78–82 mol % PbO (>99.9%) and 18–22 mol % TiO_2 (>99.9%). The mixture was placed in a pure platinum crucible (most likely the source of Pt observed in this work) of 50 ml capacity and heated to 1100 °C for over 15 h, slowly cooled to 930 °C at a constant rate of approximately 0.3–1.5 °C/h, and then cooled to room temperature in approximately 72 h. Greater experimental details are provided in Ref. 7.

The EPR measurements were made at 77 K using an X-band ($\nu = 9.425\,464$ GHz) Bruker ESP-300E spectrometer. An optical access EPR cavity was used to UV illuminate the sample *in situ* with 2.8 eV monochromatic light. An Oriel 100 W Hg arc lamp in conjunction with a 2.8 eV narrow-band interference filter was used as the monochromatic light source. The light power density was 1 mW/cm^2.

The as-received $PbTiO_3$ crystals were fairly free of paramagnetic transition metals (unlike $BaTiO_3$); however, they did exhibit a fairly large axially symmetric Fe^{+3} EPR signal; this center will be discussed elsewhere.[8] Following 2.8 eV illuminate at 77 K, a new EPR signal was activated, with clearly resolved hyperfine structure, as illustrated in Fig. 1. In EPR, the chemical signature of the paramagnetic defect is uniquely characterized by its hyperfine structure, where the number of spectral lines is given by $2I+1$, where I is the nuclear spin. For an element with several isotopes having different nuclear moments and spin, the EPR spectrum will be a superposition of the electronic Zeeman and nuclear hyperfine spectrum of each isotope weighted by its natural abundance.

We attribute the observed spectra in Fig. 1 to an impurity with several possible isotopes having $I=0$ or $I=1/2$. The central lines (marked by the arrows) are due to the $I=0$ isotopes whereas the two satellite lines about each central line are due to the $I=1/2$ isotopes. We find that the experimental ratio of the double integrated intensity of the central line to the satellite lines is 1.96, in excellent agreement with that expected for platinum ions (1.9586). Platinum has four stable isotopes of which ^{194}Pt, ^{196}Pt, and ^{198}Pt are 66.2% abundant and have $I=0$, while ^{195}Pt is 33.8% abundant and has $I=1/2$. Platinum is the only element in the periodic table that can explain the EPR spectrum of Fig. 1.

Having determined that the EPR signal is due to a Pt impurity, we rotated the $PbTiO_3$ crystal within the (100) plane to determine the magnetic anisotropy. The observed anisotropy of the effective g-value is illustrated in Fig. 2. The observed $S=1/2$, $I=1/2$ spectra can be fit by the following spin Hamiltonian,

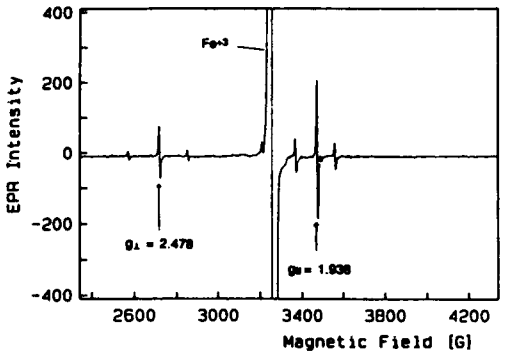

FIG. 1. EPR spectrum showing the Pt^{+3} resonance following 2.8 eV illumination at 77 K. The external magnetic field is parallel to the [001] direction.

 0003-6951/93/020146-03$06.00

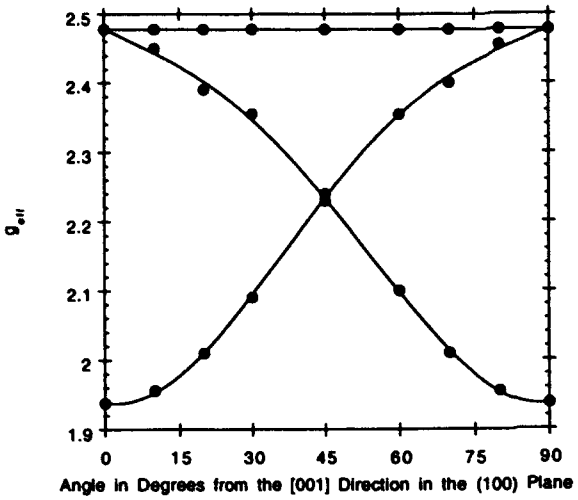

FIG. 2. Angular variation of the effective g-value of the Pt^{+3} resonance; the resonance exhibits axial symmetry. The external magnetic field was rotated about the [001] direction within the (100) plane.

$$H_s = g_{\parallel}\beta H_z S_z + g_{\perp}\beta(H_x S_x + H_y S_y) + A_{\parallel} S_z I_z + A_{\perp}(S_x I_x + S_y I_y) \quad (1)$$

where $g_{\parallel}$ ($g_{\perp}$) is the g-value parallel (perpendicular) to the symmetry axis, β is the Bohr magneton, H is the magnetic field, $A_{\parallel}$ ($A_{\perp}$) is the nuclear hyperfine coupling constant parallel (perpendicular) to the symmetry axis, and S (I) is the electron (nuclear) spin. The axial spin Hamiltonian parameters are $g_{\parallel} = 1.938 \pm 0.001$, $g_{\perp} = 2.478 \pm 0.001$, $A_{\parallel} = 0.0164 \pm 0.0002$ cm^{-1}, and $A_{\perp} = 0.0324 \pm 0.0002$ cm^{-1}. The identification of $g_{\perp}$ was determined by the rotation of the magnetic field around one of the crystal axes, i.e., rotation within the (100) plane yielded an orientation independent resonance line (Fig. 2) which results from paramagnets whose z axes always remain perpendicular to the external magnetic field. Since the g-tensors exhibit axial symmetry, and it is well known that $PbTiO_3$ has a tetragonal crystal structure, we expect that the Pt ion substitutes for the Ti^{+4} ion in the $PbTiO_3$ crystal. It is further reasonable that the Pt substitutes for the Ti since the ionic radii of the Pt^{+4} (0.77 Å) and Ti^{+4} (0.75 Å) ions are very similar.

From crystal field theory it is possible to determine the structure, and oxidation state, of the optically generated Pt ion in this perovskite lattice. Since the ground state of the Pt resonance can be fit using an $S=1/2$, $I=1/2$ system, two oxidation states are possible for the Pt ion, Pt^{+3} (d^7, t^6e) and Pt^{+} (d^9, t^6e^3) as long as the Pt ion is in a tetragonally distorted, strong octahedral field as schematically illustrated in Fig. 3.[9] Under the strong field limit, the octahedral crystal field must be greater than the spin pairing energy; $5d$ ions are almost always under the strong field approximation.[10,11] Since the Pt substitutes for the Ti^{+4} ion in the lattice, it is more reasonable from charge considerations to assume that the oxidation state of the Pt is $+3$ rather than $+1$, as was assumed for $BaTiO_3$ crystals doped with Pt.[12]

For d^7 (t^6,e) ions, i.e., Pt^{+3}, in tetragonally elongated, strong octahedral fields, the g-tensors are predicted to be[13]

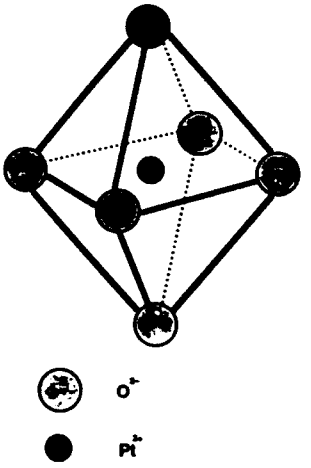

FIG. 3. Schematic illustration of the chemical environment around the Pt^{+3} ion in the $PbTiO_3$ perovskite lattice.

$$g_{\parallel} \approx g_e - 3\lambda^2/\Delta^2, \quad (2)$$

$$g_{\perp} \approx g_e(1 - 3\lambda/\Delta) - 6\lambda^2/\Delta^2, \quad (3)$$

where λ is the spin-orbit coupling constant ($\lambda < 0$), and Δ is the crystal field splitting. From Eqs. (2) and (3) it is easy to see that $g_{\perp} > g_{\parallel}$, $g_{\parallel} < g_e$ and $g_{\perp} > g_e$ which are all experimentally observed, and consistent with our assignment of Pt^{+3}.[14]

At this juncture, it should be mentioned that these results also indicate that the oxidation state of the *diamagnetic* Pt ions in the virgin, unilluminated, $PbTiO_3$ crystals is $+4$. Since the greatest density of optically generated Pt^{+3} ions was observed with photon energies around 2.8 eV (a photon energy of 2.8 eV roughly corresponds to the optical band gap of these crystals), it is reasonable to assume that it is the capture of the photogenerated electrons at diamagnetic Pt^{+4} ions that makes them negatively charged and paramagnetic.

It is also interesting to note that the optically generated Pt^{+3} ions are metastable at room temperature, i.e., if the UV-illuminated ceramic is warmed to 300 K, and then recooled to 77 K, the Pt^{+3} EPR resonance is no longer observed. Last, the Pt^{+3} EPR signal could only be observed at temperatures < 120 K in accord with that observed for Pt^{+3} ions in Al_2O_3,[15] $BaTiO_3$,[12] and yttrium aluminum garnets;[16] this observation is believed to be due to the very short spin-lattice relaxation time of Pt^{+3} ions at $T > 200$ K.[17]

In conclusion, we have been able to observe the optical generation of Pt^{+3} ions in $PbTiO_3$ crystals. Since the EPR spectrum is axially symmetric, and can be described by an $S=1/2$, $I=1/2$ system, it has been argued that the Pt^{+3} ions are in a tetragonally distorted strong octahedral field, and have substituted for the central Ti^{+4} ions in this perovskite lattice.

[1] R. N. Schwartz and B. A. Wechsler, J. Am. Ceram. Soc. 73, 3200 (1990).
[2] P. Moretti and F. M. Michel-Claendini, Phys. Rev. B 36, 3522 (1987).

[3] E. Possenriede, O. F. Schirmer, J. Albers, and G. Godefroy, Ferroelectrics **107**, 313 (1990).
[4] K. A. Muller, W. Berlinger, and J. Albers, Phys. Rev. B **32**, 5837 (1985).
[5] A. Molak and K. Wojcki, Ferroelectrics **125**, 349 (1992).
[6] D. Hennings and H. Pomplun, J. Am. Ceram. Soc. **57**, 527 (1974).
[7] B. N. Sun, Y. Huang, and D. A. Payne (unpublished).
[8] B. N. Sun, Y. Huang, D. A. Payne, W. L. Warren, and B. A. Tuttle (unpublished). The Fe impurity may come from the starting materials.
[9] The tetragonal distortion may arise from the Jahn–Teller effect.
[10] A. Abragram and B. Bleaney, *Electron Paramagnetic Resonance of Transition Ions* (Dover, New York, 1970).
[11] J. E. Wertz and J. R. Bolton, *Electron Spin Resonance* (Chapman and Hall, New York, 1986).
[12] Z. Sroubek, K. Zdansky, and E. Simanek, Phys. Status Solidi **3**, K1 (1963).
[13] H. H. Tippins, Phys. Rev. **160**, 343 (1967). Equations (2) and (3) ignore the effects of covalency.
[14] These g-tensor relationships do not uniquely support the d^7 assignment; they are consistent with it.
[15] S. Geschwind and J. P. Remeika, J. Appl. Phys. **33**, 370 (1962).
[16] J. A. Hodges and R. A. Serway, Phys. Rev. **151**, 196 (1966).
[17] U. Hochli and K. A. Muller, Phys. Rev. Lett. **12**, 730 (1964).

Proceedings of

The International Conference on

Martensitic Transformations

(ICOMAT-92)

20-24 July 1992
Monterey, California

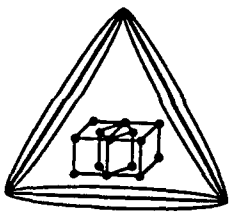

ICOMAT-92

Edited by C.M. Wayman and J. Perkins

Proceedings of the International Conference on Martensitic Transformations (1992)
Monterey Institute for Advanced Studies © 1993
Monterey, California, USA

SHAPE MEMORY AND SUPERELASTICITY FOR CERAMICS WITH FIELD-INDUCED ANTIFERROELECTRIC-FERROELECTRIC PHASE TRANSFORMATIONS

Pin Yang and David A. Payne

University of Illinois
Department of Materials Science and Engineering
105 South Goodwin Avenue
Urbana, Illinois 61801 USA

ABSTRACT

Electrically induced deformations associated with antiferroelectric (AFE)-to-ferroelectric (FE) phase transformations in tin modified lead zirconate titanate (PZST) ceramics are reported. The total strain is comprised of a (i) spontaneous strain which occurs at the phase transformation and a (ii) strain associated with domain alignment on poling. Therefore, the total induced strain is greater than the converse piezoelectric effect normally associated with ferroelectric materials, and as such, is attractive for potential device applications. Depending on reversible and irreversible characteristics, associated with the temperature of operation and thermal hysteresis, the deformation process can be classified as superelastic or shape memory behavior. Superelasticity is observed at temperatures above the FE-AFE transformation temperature (T_A) with immediate strain recovery upon release of the electric field. Electrically induced irreversible strains, within the thermal hysteresis region ($T_F < T < T_A$), are recoverable upon heating above T_A; and give rise to a shape memory effect, the extent of which is dependent on the magnitude of the AFE sublattice coupling. Shape memory and superelastic behavior are explained in terms of competing thermodynamic stabilities for the AFE and FE phases. Implications to other ceramic systems are indicated.

1. INTRODUCTION

In this paper we report on phase transformation studies in the $Pb(Zr,Sn,Ti)O_3$ system (i.e., PZST). [1] Attention is paid to strain e and polarization P changes as a FE phase is induced from an AFE phase as a function of electric field strength E at temperature T. Previously we proposed a model by which issues relating to phase stability and reversability could be predicted [2]. The model included thermodynamic barriers ΔG^* to transformation and a region of associated thermal hysteresis ΔT. Now we report (i) a shape memory effect and (ii) superelasticity for PZST electrical ceramics. These phenomena depend upon whether the electrically induced strain deformations occur (i) within the thermal hysteresis region or (ii) at higher temperatures. Similar to metallic alloy systems [3,4], (i) the shape memory effect occurs when the induced deformations at one temperature are recoverable at a higher temperature, and (ii) superelasticity behavior is when the induced deformations at constant temperature are recoverable upon unloading [5]. Both deformation and strain recovery processes

usually involve martensitic-type phase transformations. By analogy with metallic alloy systems, shape memory effects have been reported previously for mechanically deformed ZrO_2 [6] and $(Pb,La)(Zr,Ti)O_3$ [7] ceramics. We now report electrically deformed shape memory effects and superelastic properties for PZST ceramics. These effects were anticipated from our previous work on field-induced AFE-FE phase transformations [2]. Special attention is paid now to induced deformations and strain recovery processes, with emphasis on thermal stability of the AFE phase.

2. EXPERIMENTAL METHOD

PZST compositions close to a morphotropic phase boundary [1] were prepared by a method previously reported [2] according to the formula $Pb_{(1-0.5z)}Nb_z[(Zr_{1-x},Sn_x)_{1-y}Ti_y]_{0.98}O_3$. Throughout the text an abbreviated notation is used: PZST X/Y/Z (which is equivalent to 100x/100y/100z). A small amount of Nb_2O_5 was added for dielectric strength purposes.

Field-induced deformations were measured normal to the field direction (i.e., e_{31}, transverse strain) by a strain gauge bonded to the specimen. Induced polarizations were also determined at 0.3Hz on a modified Sawyer-Tower circuit. Care was taken for temperature compensation in the strain measurements through use of a dummy gauge in the test cell. Transformation temperatures were characterized by differential scanning calorimetry (DSC), and dimensional changes by thermal mechanical analysis (TMA). The heating and cooling rates were 10°C/min. Standard X-ray diffraction (XRD) techniques were used for phase analysis, and the determination of any structural orientation effects.

3. RESULTS

(1) Phase Transformations and Strain Recovery

Phase transformations are illustrated in figure 1 for PZST 43/8/2 as a function of increasing and decreasing temperature. The TMA results indicate the low temperature FE phase (rhombohedral) transformed into the higher temperature AFE phase (tetragonal) with an abrupt decrease in volume

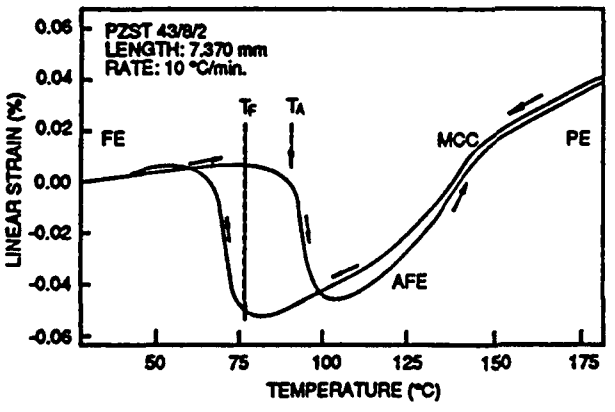

Figure 1. Thermal strains and hysteresis for the FE-AFE transformation in PZST 43/8/2.

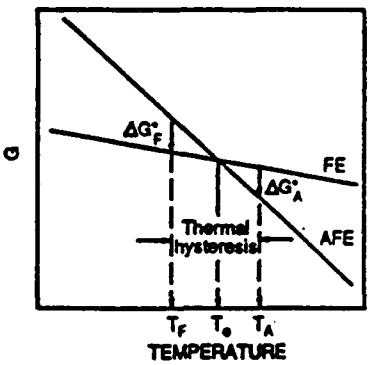

Figure 2. Thermodynamic stability for the FE-AFE transformation, which occurs spontaneously when the free energy difference (ΔG) exceeds the transformation barrier (ΔG^*).

(ΔV), followed by expansion through a multicell cubic (MCC) region before transformation into the paraelectric (PE) cubic phase. The onset temperatures for the AFE and FE transformations are T_A and T_F, on heating and cooling, respectively. Note, the region of thermal hysteresis. Figure 2 is a schematic of the thermodynamic stabilities for the FE and AFE phases. The observation of thermal hysteresis (figure 1) suggests the transformation does not proceed initially when the free energies are equivalent ($G^{FE} = G^{AFE}$ at $T = T_o$), but that there are thermodynamic barriers to be overcome (ΔG^*_A, ΔG^*_F) before the transformation can proceed. This leads to overheating ($T_A - T_o$) and undercooling ($T_o - T_F$) before the transformations can be initiated. Because of the region of thermal hysteresis ($\Delta T = T_A - T_F$) the pathway passes through a region of metastability (higher free energy) before the transformation occurs; therefore, the existing phase within this region (FE or AFE) depends upon the previous thermal history of the specimen (heating or cooling). Consequently, thermally induced transformational strains can only be recovered when the free energy difference between the two phases is greater than the transformation barrier (i.e., for $T < T_F$, $\Delta G^{AFE-FE} > \Delta G^*_F$, and for $T > T_A$, $\Delta G^{FE-AFE} > \Delta G^*_A$).

Similar to the aforementioned case of mechanical stress σ induced transformations in shape memory alloys, the present case of electric-field-induced AFE-FE transformations (at $T > T_A$) is accompanied by shape and volume changes with plastic deformations (i.e., a critical field E_F is necessary to yield a non-linear strain). The minimum amount of electric work done (-PdE) to induce the transformation must be greater than the free energy difference between the two phases (ΔG_o^{FE-AFE}) and the thermodynamic barrier (ΔG^*_F) [2] i.e.,

$$-P_F dE \geq \Delta G_o^{FE-AFE} + \Delta G^*_F. \qquad (1)$$

When E is subsequently reduced for $T > T_A$, the free energy difference between the two phases ΔG_o^{FE-AFE} provides a driving force for strain recovery.

(2) Superelasticity and Shape Memory Effect.

An example of superelasticity is given in figure 3 for PZST 42/4/2 at room temperature ($T > T_A$). The field-induced strain ε_{31} develops as the FE phase evolves at field strengths greater than E_F. However, the strain is recoverable when E decreases to E_A, and the material reverts back to the AFE form. The field-induced superelastic properties are of interest for electromechanical actuator applications [8,9]. As the operating T approaches T_A, the field-induced strain deformations become less recoverable, i.e., as ΔG_o^{FE-AFE} approaches zero. Figure 4 illustrates the lack of ε_{31} recovery

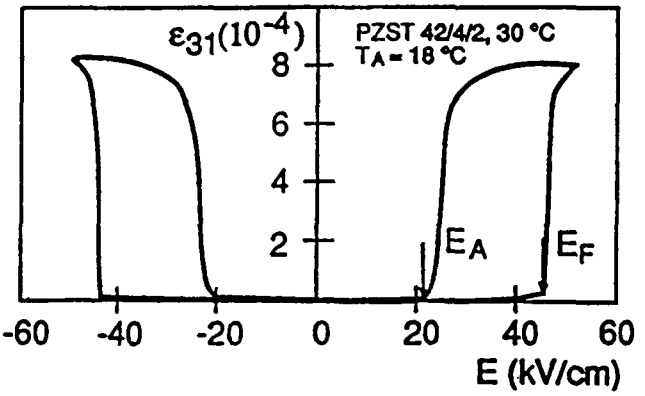

Figure 3. Superelasticity associated with the field-induced FE-AFE transformation for PZST 42/4/2. The field-induced strain above T_A is recoverable when the holding field is released below E_A.

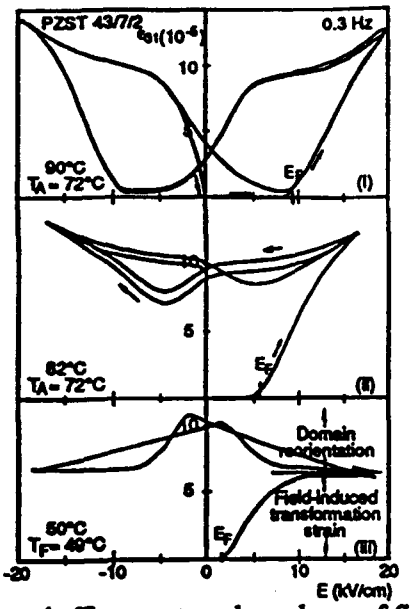

Figure 4. Temperature dependence of field-induced strains for PZST 43/7/2 under dynamic (0.3 Hz) loading conditions. On cooling into the AFE-FE transformation (i and ii), the extent of recoverable strain decreases as the AFE sublattice coupling softens, and approaches zero at the FE transformation temperature (T_A). The electrically induced deformations now become characteristic of FE domain reorientations (iii).

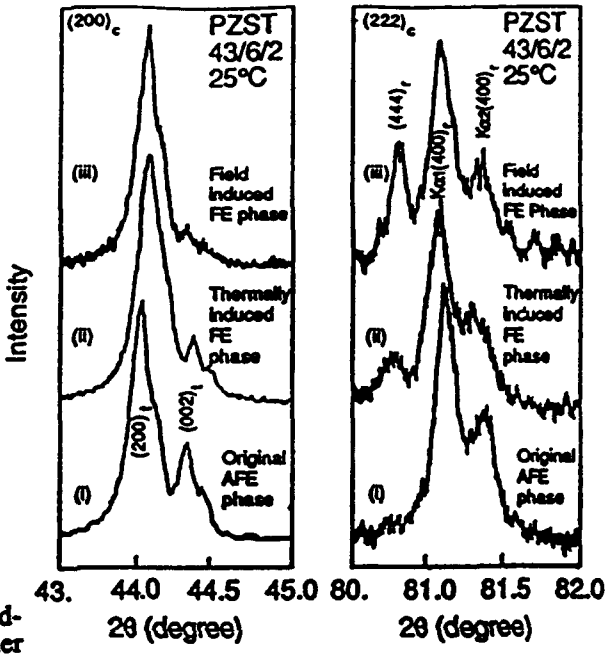

Figure 5. X-ray diffraction data (at 25°C) for PZST 43/6/2 within the thermal hysteresis region (T_F = 16°C, T_A = 52°C), (i) before and (ii) after cooling into or (iii) field-inducing the FE phase. High angle data indicate a significant domain alignment and texturing for the field-induced case (iii), compared with the thermal case (ii), as judged by the relative intensities of the $(444)_t$ reflection.

for PZST 43/7/2 (with T_A = 72°C) as T decreases from (i) 90°C to (ii) 82°C. Operation of electromechanical actuators in this temperature region would be a serious problem! Eventually, (iii) when T ≈ T_F, the FE phase is irreversibly stabilized and the induced strain is irrecoverable. Figure 4 (iii) illustrates subsequent domain orientation strains for the FE phase. The irreversible deformation process can be attributed to the lack of free energy difference between the two phases in the thermal hysteresis region, and the inability to overcome the reverse barrier ΔG_A^* for strain recovery. The induced deformation strains can be recovered by heating above T_A (i.e., thermal depoling), thus demonstrating a shape memory effect.

(3) Phase Identification and Texture

In shape memory alloys a preferred orientation and texture develops on application of an applied stress. A variant which favors strain elongation grows preferentially with the deformation process. This texture and macroscopic deformation is released on heating, and is associated with strain recovery. Similar behavior has been observed for field-induced AFE-FE transformations. Figure 5 illustrates XRD data for PZST 43/6/2 (T_A= 52 °C, T_F=16 °C) which were determined at room temperature (25 °C). The tetragonal AFE phase is metastable on cooling into the thermal hysteresis region. Figure 5(i) indicates tetragonal splitting for low and high diffraction angles, which can be approximated by pseudocubic $(200)_c$ and $(222)_c$ peaks, respectively. The low angle data clearly illustrate tetragonal $(200)_t$ and $(002)_t$ splitting. On further cooling in an ice bath, and after

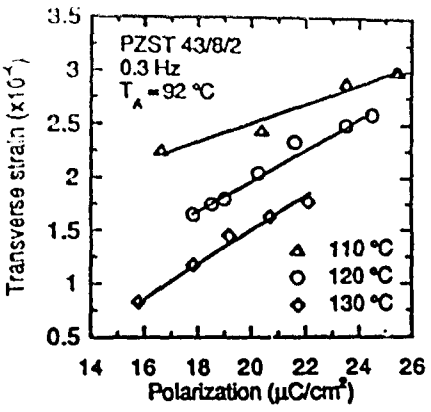

Figure 6. Field-induced polarization and strains for the AFE-FE switching at temperatures above T_A (92 °C). The strains and polarizations are for increasing field strengths. The linear dependence indicates a negligible contribution from electrostrictive processes to the polarizable deformable behavior for AFE ceramics.

redetermination of the structure at room temperature, the rhombohedral FE phase was now found to be metastable. The XRD data (figure 5 (ii)) can now be interpreted in term of a pseudocubic $(200)_c$ peak which splits into $(444)_r$ and $(400)_r$ rhombodehedral peaks at high angle. On application of an electric field, the $(444)_r$ peak grows preferentially (figure 5 (iii)) with respect to the thermally induced case (figure 5 (ii)), indicating field-induced reorientation and texturing effects. After thermal depoling at $T > T_A$, the subsequent room temperature XRD data were found to be similar to figure 5 (i), indicating the material had transformed back to the AFE phase. The results are consistent with a shape memory effect, which has significant field-induced macroscopic strain and orientational texturing.

4. DISCUSSION

(1) Electric Deformations and Strain Recovery Processes

Interpretation of field-induced strains and deformation processes are somewhat confused in the literature [8,9] for AFE-FE transformations, especially for measurements taken close to the transformation temperature and within the field-induced metastable thermal hysteresis region. Previous work [9,10] has attributed the induced strain to an electrostrictive effect, but this approach cannot explain the positive strains observed in both the longitudinal and transverse directions [11], where the transverse strain ε_{31} should be negative for electrostriction [12]. We have consistently shown in our work that the field-induced transverse strain ε_{31} is positive for AFE-FE transformations. Our results are consistent with (i) a positive strain associated with an increase in volume at the transformation and (ii) an additional strain associated with field-induced reorientation and texturing effects. Within the region of metastability (T_A-T_F), the field-induced transformation strain is irreversible (Figure 4 (iii)) and independent of field strength [2]. Further analysis of field-induced polarizations and strains are not consistent with an electrostrictive effect. Figure 6 illustrates P and ε at various T and E for PZST 43/8/2. The linear dependence negates an electrostrictive effect which should have a quadratic dependence on P.

Figure 3 indicates the FE phase was found to be transiently metastable under dynamic loading conditions (0.3 Hz) above E_F, but would revert back to the AFE phase below E_A. Since the spontaneous polarizations in the sublattice of the AFE structure are coupled in an antiparallel manner[2], the reverse transformation field strength (E_A) can be related to the extent of sublattice coupling at a particular temperature. The sublattice coupling weakens as T approaches the spontaneous transformation temperature (T_F). This softening of the sublattice is indicated in figure 4, especially for (ii), where the coupling is so weak that a strain minima occurs in the negative field direction, i.e., strain reversal has to be assisted by use of a back-switching field. Although stored

elastic strain energy and the thermoelastic transformation may be important for strain recovery [13,14], the present results indicate the importance of the AFE sublattice coupling for the strain memory effect in PZST ceramics which have field-induced AFE-FE transformations.

(2) Shape Memory Effects and Ferroic Materials

Certain ferroelectric ceramics are also ferroelastic [15] in that the orientation state of a domain wall can be moved to another orientation state through application of an electric field or a mechanical stress. Such materials are potential candidates for shape memory effects. However, ceramic materials usually have small transformational strains and thermal hysteresis, and superelasticity and shape memory behavior are rarely reported. Although the magnitude of the macroscopic deformation and strain recovery is small compared with shape memory alloys, this does not preclude the behavior at the microscopic level in ferroic materials. We have indeed observed shape memory behavior for domain configurations in ferroic materials on thermal cycling. Future work is directed at understanding these phenomena, and maximizing shape memory and superelastic properties for potential device applications.

ACKNOWLEDGEMENT

The research was supported by a grant from the Air Force Office of Scientific Research (URI-41318) on Displacive Phase Transformations in Ceramics.

REFERENCES

1. Jaffe, B. , Cook, W. R. and Jaffe, H.: Piezoelectric Ceramics, (J. P. Roberts and P. Popper, eds.),Vol. 3, (Academic, London), 1971, p.135.
2. Yang, P. and Payne, D. A.: J. Appl. Phys.,1992, 71, 1361.
3. Delaey, L., Krishnan, R.V., Tas, H. and Warlimont, H.: J. Mat. Sci., 1974, 9, 1521.
4. Otsuka, K. and Shimizu, K.:Int. Met. Rev., 1986, 31, 93.
5. Otsuka, K. and Wayman C. M.: Reviews on the Deformation Behavior of Materials, (P. Feltham ed.), Vol 2 (2), (Freund Publishing House LTD. Israel), 1977, p. 81.
6. Reyes-Morel, P. E., Cherng, J. A. and Chen, I. W.: J. Am. Ceram. Soc.,1988, 71, 648.
7. Wadhawan, V. K., Kernion, M. C., Kimura, T. and Newnham, R. E.: Ferroelectrics, 1981, 37, 575.
8. Uchino, K. and Nomura, S.: Ferroelectrics, 1983, 50, 191.
9. Pan, W. Y., Dam, C. Q., Zhang, Q. M. and Cross, L. E.: J. Appl. Phys., 1989, 66, 6014.
10. Uchino, K.: M. R. S. Int'l. Mtg. on Adv. Mats., Vol. 9, 1989, 489.
11. Newnham, R. E., Xu, Q. C.,Kumar, S. and Cross, L. E.: U.S. Army Research Office Workshop on Smart Materials, Structures, and Mathematical Issues, (C. A. Rogers, ed.), (VPISU), Blacksburg, VA, 1988, p. 147.
12. Cross. L. E., Jang, S. J., Newnham, R. E., Nomura, S. and Uchino, K.: Ferroelectrics, 1980, 23, 187.
13. Kurdjumov G. V.: J. Metals, 1959, 11, 449.
14. Cohen, M.and Wayman, C. M.: Metallurgical Treatises, (J. K.Tien and J. F. Elliott, eds.), (AIME), 1982, p.445.
15. Aizu, K.: J. Phys. Soc., Jpn., 1973, 32, 1278.

Proceedings of

The International Conference on

Martensitic Transformations

(ICOMAT-92)

20-24 July 1992
Monterey, California

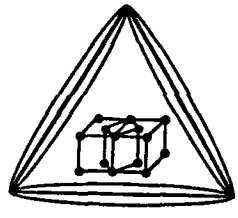

ICOMAT-92

Edited by C.M. Wayman and J. Perkins

gs of the International Conference on Martensitic Transformations (1992)
Monterey, Institute for Advanced Studies © 1993
Monterey, California, USA

CRYSTALLOGRAPHY OF THE CUBIC TO TETRAGONAL TRANSFORMATION IN LEAD TITANATE SINGLE CRYSTALS

Chen-Chia Chou*, Kunio Wakasa and C. Marvin Wayman***

*University of Illinois
Department of Materials Science and Engineering
1304 West Green Street
Urbana, Illinois 61801 USA

**Hiroshima University
School of Dentistry
Department of Dental Materials
1-2-3, Kasumi, Minami-Ku
Hiroshima 734 JAPAN

ABSTRACT

The cubic to tetragonal (C/T) transformation of flux-grown lead titanate single crystals has been investigated using optical microscopy (OM), transmission electron microscopy (TEM) and electron and X-ray diffraction. Theoretical calculations on transformation characteristics based upon the martensite crystallographic theory of Bowles and Mackenzie were also carried out. Habit plane between the parent and the product phases were studied by "freezing" the two phases during transformation using in-situ hot-stage OM. The habit planes vary within a certain range. Not only different specimens show this real variation, but also the same specimen under different transformations follows this, indicating the importance of local arrangements near the habit plane interfaces. With only a minute change of lattice parameters in calculations, it is shown that experimental data appear to be consistent with calculated results, if one considers lattice parameter variation. The results imply that the martensitic crystallographic theory applies. Discussions on the microstructural features as well as previous work on perovskite materials are presented.

1. INTRODUCTION

The phenomenological crystallographic theory of martensitic transformations [1-3] has been applied successfully to many metallic alloy systems [4-6], and more recently to ceramics and other systems [7]. The Wechsler-Lieberman-Read (WLR) theory can be applied to the cubic-tetragonal(C/T) phase transition of semiconducting perovrkite-type crystals [8], which have sufficient free charge available to provide a termination for the spontaneous polarization at the interface. On the other hand, crystals with high resistivity, though showing sharp first order phase boundaries, were reported not to follow theoretical predictions [9,10]. Supposely, the reason for this is that the free charges present in (semi-)conducting crystals neutralize the bound polarization charges inside the crystal. Whereas in highly insulating crystals, the absence of free charges imposes the restriction that phase boundaries be free of any exess polarization charge. The accumulated polarization charge at a phase boundary results in stored electrical energy which dominates the crystallographic characteristics once it prevails. However, the evidence here is thin because no other crystallographic data were used other than very limited habit plane data.

Lead titanate has a ferroelectric phase transition temperature, T_C, near 500° C [11,12], is cubic above T_C and exhibits a strong tetragonal distortion at 20°C: c/a=1.06 which persists up to T_C (c/a=1.01) [13,14]. The lattice constant a increases smoothly upon heating, while the constants c and c/a decrease. At T_C, c and a change abruptly and the structure becomes cubic. Since the volume of the unit cell decreases sharply as a result of this transition, the linear expansion coefficient of a polycrystalline sample is negative below T_C [11-14]. The transformation is first order [9]. $PbTiO_3$ single crystals present a highly polar structure with very high spontaneous polarization in the perovskite family [11,12,15]. Because of its large tetragonality and detectable negative volume change near T_C, $PbTiO_3$ provides a more sensitve indication of the role of lattice variation during transformation. In this paper, we present calculations based upon the theory of Bowles and Mackenzie, and the comparison with experimental data to verify the appplicability of the phenomenological crystallographic theory to this perovskite system.

2. EXPERIMENTAL PROCEDURE

$PbTiO_3$ crystals were grown [17] by slow cooling from a flux, containing KF, Pb_3O_4, PbF_2, KBF_4, and TiO_2 in a 50 cc platinum crucible, as described in our previous work [18]. The as-grown crystals were mostly cubic in shape or elongated cubic or orthogonal forms and show a transparent amber tint. Transformation characteristics were studied using hot-stage optical microscopy and conventional transmission electron microscopy. Specimen preparation was described elsewhere [18]. The specimens used were high quality crystals with sharp, flat {100} surfaces and the microscope used was a Nikon UM-2. The specimens were investigated using polarized light and put in a heating stage designed to control the temperature profile quickly and to "freeze" phase boundaries. TEM investigations were conducted using a Hitachi H800 microscope at 200KV with a double-tilt specimen holder.

A computer program [16] based upon the Bowles-Mackenzie formulation [2] was used for the phenomenological calculations. The latticee correspondence was assumed with the *c*-axis of the tetragonal structure deriving from either the *a*-, *b*-, or *c*-axis of the cubic parent. Experimental lattice parameters of the parent and martensite phases at T_C are based on those of Suchicital et. al.[17]; a=3.961Å, c=4.012Å and a_O=3.972Å were used in the present work.

3. RESULTS

3.1 Experimental

The inhomogeneous shear was introduced as internal twins in the tetragonal phase of $PbTiO_3$ crystals. A ferroelectric material has regions where the magnitude and direction of the polarization are the same in each region, though the polarization may differ in orientation in neighboring regions. These regions are ferroelectric domains separated by domain boundaries. From symmetry, there are two types of domain boundaries in $PbTiO_3$: 90° and 180° boundaries. The angles refer to the angle between the domain polarization vectors on either side of the boundary. From a [100] orientation two different morphologies of 90° domain boundaries are usually seen. One is straight with sharp images, and the other shows wavy morphology and fringe contrast. From a crystallographic viewpoint, a 90° domain boundary is a twinning plane between two adjacent domains. Figure 1(a) and (b) shows TEM images of a-c and a-a domains. The symmetrical diffraction reflections [18] imply that the two adjacent domains are twin-related. The ratio between the parent (wider domains) and the twin (thinner domains), x, was measured from a number of edge-on configurations. Ordinarily, volume fractions of the matrix and twin give an average x value. Here we consider local lattice purturbation, and measure x values at different regions. The x values vary from case to case with a range from 1.2 to 3.5. For instance, the x ratio in figure 1(a) is 3.06 and in figure 1(b) is 1.45. The twinning plane, K_1, in both a-a and a-c type domains is {110}. The corresponding schematic model showing atomic arrangements are in figures 1 (c) and (d). Figure 1(c) clearly shows that the twinning direction, η_1, is along a <110> type direction due to the tetragonal distortion. The invariant plane, K_2, is the $(\bar{1}10)$ plane which is the other diagonal plane of the tetragonal cell. Figure 1(d) shows how the twinning magnitude was calculated; it can also be determined from splitting in an a-a domain diffraction pattern or from x-ray data. The twinning magnitude of the present crystals is 0.115 at room temperature and 0.0256 at T_C.

Transformation characteristics were partly derived by in-situ hot stage optical microscopy. Figure 2(a) shows a single interface type transformation. This is a typical habit plane (or phase boundary) in a $PbTiO_3$ crystal during transformation seen using polarized light. The boundary is sharp and straight with an angle about 30° from [010]. This sharp boundary implies that it is almost in an edge-on position. One can easily distinguish the cubic phase by rotating the crystal; it becomes extinct because of isotropy. One notes that the contrast near the boundary is different from regions farther away, indicating that a local distortion exists. This distorted region appears to vary case by case. For instance, the intersection of two interfaces shows a broader contrast region; the contrast near the specimen center may be different from that of the edge. Figure 2(b) shows another single-interface transformation in which the phase front is not straight. One notes that patches of bright bands form in the cubic region before the phase front passes through and the slope of the phase front varies at each bright and dark region, indicating the influence of lattice parameter variation. Brighter patches often show up in the cubic region before the habit plane approaches it if a slow heating or cooling rate is used, suggesting some local perturbation in the crystal. In the tetragonal region, one also sees a non-uniform contrast distribution, indicating birefringence variation which is closely related to the lattice parameter variation as well. Other factors changing the original habit plane configuration have been reported elsewhere [18]. Other single crystals were also used to measure the habit planes. We found that the habit plane appears to vary from crystal to crystal; and more interestingly, the same crystal may show a habit plane deviated from a previous one or even change orientation during phase front movement. The results indicate that the habit planes vary from about 25° to about 40° from a {100} plane.

3.2 Calculations

The crystallography of the C/T phase transformation was analyzed using a computer program based upon the Bowles-Mackenzie formulation [2]. In the present case, we assume transformation is from cubic to tetragonal. There are three ways to assume the lattice correspondence, i. e. the *c*-axis of the tetragonal phase is derived from either the *a*-, *b*-, or *c*-

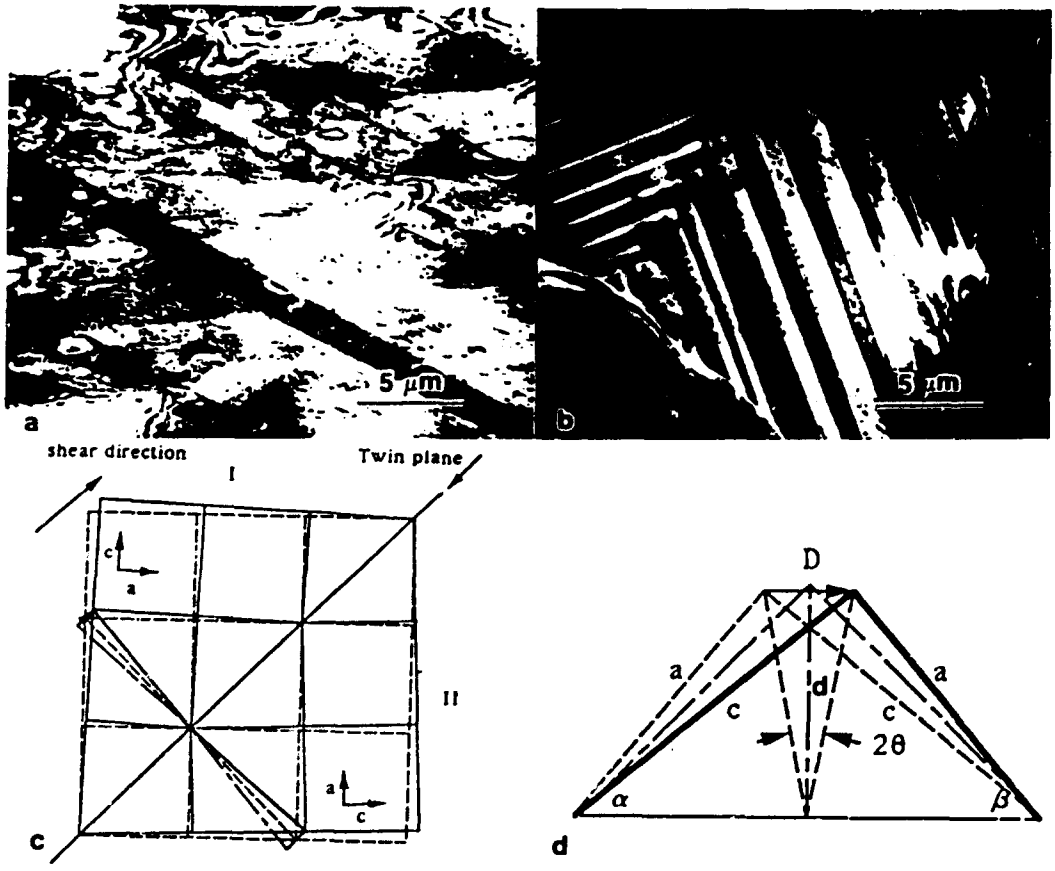

Figure 1 (a) a-c type domains tilted to a [111]c zone show edge-on configuration used to measure matrix/twin ratio; (b a-a domains at a $<100>_c$ zone showing {110}<110> twinning systerm and a different matrix/twin ratio; (c atomic model describing twinning relation in (b); (d) scheme used for twinning shear magnitude calculation.

Figure 2 Micrographs showing phase fronts during C/T transformation. (a) a typical C/T boundary showin birefringence difference at tetragonal side due to strain field; (b) distorted phase front in a lattice perturbatio region (black and bright patches) due to local lattice parameter variation.

axis of the cubic phase. However for a ferroelectric material polarization is involved in the c direction, which is also a direction of the anion displacement. Therefore, the c-axis of the tetragonal phase along positive or negative a-axis directions represent different meaning. So there are six lattice correspondences in total. The lattice invariant shear plane was assumed to be a $(110)_C$ plane since this is the observed twinning plane using TEM. There is only one shear direction in a twin plane which produces the twin structure, and there are four possible twin planes per lattice correspondence. Therefore the total number of lattice invariant shear systems is twenty four. The lattice correspondences (LC) and lattice invariant shear(LIS) systems in $PbTiO_3$ were reported in ref.18. Since $PbTiO_3$ has a negative linear expansion coefficient (therefore negative volume change) below T_c, and the lattice parameter c increases and a decreases as the temperature decreases, we can derive

$$(a/a_o)^2 (c/a_o) > 1, \quad \text{when C-->T} \qquad (1)$$

That is, the increasing value of c/a_o is greater than that of $(a/a_o)^2$. Considering the lattice parameters of $PbTiO_3$ carefully, the "lattice parameters at T_c" derived by X-ray may be different from those when transformation actually occurs, since the transformation occurs swiftly and the x-ray measurements are not real-time and are average in nature. We need to consider the local lattice conditions, such as real lattice parameters when transformation occurs, lattice perturbations, inhomogeneity, etc. However, we do not know the "real" condi-tions at the habit plane at transformation, but can estimate the principal strains as follows. Based upon the lattice constants mentioned before and equation (1), the ranges of η_{11} and η_{33} are: $1 > \eta_{11} > 0.994949$ and $1 < \eta_{33} < 1.012626$. The values of η_{11} and η_{33} can be assumed with a small increment within the limit (Table 1). We calculate a possible set of crystallographic data by holding η_{11} constant ($\eta_{11}=\eta_{22}$) and varying η_{33}. Other calculations proceeded using different combinations of η_{11} and η_{33}. We sumarize two sets of calculations using LC I and LIS system (101) $[\bar{1}01]$ to show the general characteristics of the calculated crystallography, as listed in Table 2. Here we list principal distortion combination code (PDC)(the two numbers represent the principal distortions η_{11} and η_{33} used for calculation, as in Table 1), magnitude of strains m_1 and m_2, habit plane normal p_1, direction of shape strain d_1 and the angle of the habit plane from a {100} plane. Since we know that there is a volume increase from cubic to tetragonal, data with V/Vo smaller than 1 are ignored. On the other hand, we can estimate the other limit from the volume change during transformation. Using available x-ray data [17], the V/Vo is calculated as 1.0045, indicating that the suitable principal distortion combination in one set of data ranging from 22a to 24a and the corresponding calculated habit planes show about 27° to 40° from a {100} plane; the other set shows a similar trend except for the smaller range of data points due to limited input data. We find that the habit plane shows the same tendency for each set of η_{11} and η_{33}. That is, the habit plane scatters linearly over a range, and is very sensitive to the relative values of $(\eta_{33}-1)/(\eta_{11}-1)$, i.e., the principal strains. A comparison of experimental and calculated data shows that the calculated data can explain the habit plane variation in experiments. Moreover, if η_{11} is different from η_{22}, the habit plane normal may deviate sideways from the {001}-{011} zone which explains the lateral scatter of experimental data [18].

	η_{11}	η_{33}
1	0.999159	1.001052
1a		1.002104
2	0.9988317	1.003157
2a		1.004209
3	0.997475	1.005261
3a		1.006313
4	0.996633	1.007365
4a		1.008417
5	0.995791	1.009470
5a		1.010522
6	0.994949	1.011574
6a		1.012626

Table 1 Principal distortions employed for calculations

The calculated shape strain magnitude m_1 is about one tenth to one twentieth that in ferrous martensitic transformations. This may be one of the reasons why we can see no obvious bending of fiducial lines. The experimental m_2 value was calculated based upon equation [19]

$$m_2 = s\,(x-1)/(x+1) \qquad (2)$$

and the parent/twin ratio x and twinning magnitude derived from experiments are $1.2<x<3.5$ and 0.0256 respectively. The m_2 value is therefore calculated as $0.00284<m_2<0.01421$, which fits theoretical values. Therefore, it appears that the theoretical calculations are consistent with experimental results quite well if we consider a lattice parameter purturbation.

4. DISCUSSION

It has been suggested that the WLR theory should apply to perovskite-type ferroelectric crystals [3]. DiDomenico and Wemple [8] presented evidence on semiconducting perovskite-type crystals showing habit planes quantitatively explainable in terms of the theory. However, crystals with high resistivity did not always show predicted habit plane normals [9,10]. Thus, it has been thought that the C/T transformation in perovskite crystals with high resistivity can not be classified in the family of martensitic transformations [20]. However, the microstructural characteristics of $PbTiO_3$ during C/T transformation have shown: (i) reversible surface upheavals; (ii) irrational habit planes; (iii) a fine inhomogeneous structure (twinning); (iv) all atoms move less than an interatomic distance; (v) the transformation

process is clearly first order. Although the precise orientation relationship between the two phases is not quantitatively determined in the present experiment, the relationship between the principal axes in both phases is easily derived; that is, the three orthogonal axes in the cubic phase are almost parallel to the orthogonal axes in the tetragonal phase. All these crystallographic features fall within the classification scheme for martensitic transformations [21, 22].

During the C/T transformation in $PbTiO_3$, several features were observed. Most significantly, some of the interfaces (habit plane) show sharp, straight first order phase boundaries which scatter within a certain range, and some show bright and broader edges. If we consider this from a three dimensional construction, the morphology of the habit plane depends on the viewing direction. As discussed [18], interpretation in this way explains the morphology of habit planes observed in $PbTiO_3$ fairly well, and the habit plane distribution can be fit with theoretical calculations upon considering local lattice parameter perturbations. However, previous works on $BaTiO_3$ claimed that in some high resistivity $BaTiO_3$ crystals the C/T phase boundary is of the WLR type, but contrary to theoretical predictions [9,10]. The phase transition in about 20 $BaTiO_3$ single crystals was investigated; about 30% of the crystals exhibited phase boundaries at angles very close to that predicted by theory; 60% of them showed a broad phase boundary approximately perpendicular to the 90° domain walls of the a-c domain structure and the remaining 10% changed from cubic to tetragonal via a broad and complicated square net pattern [10]. In all cases the a-c domain structure was clearly visible right up to the phase boundary and a strain pattern with the same period as the a-c domain structure was clearly visible in the cubic phase on the high temperature side of the boundary. Reviewing previous results carefully, we see that the situation in $BaTiO_3$ is quite similar to that in $PbTiO_3$. Besides the 30% habit planes which show sharp interfaces and are consistent with the theoretical calculations, the 60% habit planes approximately perpendicular to the 90° domain walls of the a-c domain

PDC	η_{33}	V/Vo	m_1	m_2	p_1		d_1		Angle from $00\bar{1}$
solution 1									
21	no solution								
21a	1.002104	.998735	.002101	.003369	.003662	.895004 -.446042	.003896	-.895370 -.445307	63.5
22	1.003157	.999783	.003152	.003369	.002431	.730453 -.682959	.002478	-.731559 -.681774	46.9
22a	1.004209	1.000832	.004202	.003369	.002242	.632483 -.774571	.002185	-.634048 -.773291	39.2
23	1.005261	1.001880	.005252	.003369	.002041	.565556 -.824707	.002019	-.567579 -.823316	34.4
23a	1.006313	1.002929	.006302	.003369	.001969	.516164 -.856487	.001967	-.518553 -.855044	31.1
24	1.007365	1.003977	.007353	.003369	.001924	.477759 -.878489	.001914	-.480466 -.877011	28.5
24a	1.008417	1.005026	.008403	.003369	.001887	.446789 -.894638	.001882	-.449790 -.893132	26.5
25	1.009470	1.006075	.009454	.003369	.001865	.421110 -.907008	.001853	-.424381 -.905482	24.9
25a	1.010522	1.007123	.010504	.003369	.001841	.399397 -.916776	.001837	-.402915 -.915236	23.5
26	1.011574	1.008172	.011555	.003369	.001827	.380715 -.924691	.001819	-.384475 -.923133	22.4
26a	1.012626	1.009220	.012605	.003369	.001811	.364419 -.931233	.001810	-.368392 -.929669	21.4
solution 2									
21	no solution								
21a	1.002104	.998735	.002101	.003369	.003662	-.895004 -.446042	.003896	.895370 -.445307	63.5
22	1.003157	.999783	.003152	.003369	.002431	-.730453 -.682959	.002478	.731559 -.681774	46.9
22a	1.004209	1.000832	.004202	.003369	.002242	-.632483 -.774571	.002185	.634048 -.773291	39.2
23	1.005261	1.001880	.005252	.003369	.002041	-.565556 -.824707	.002019	.567579 -.823316	34.4
23a	1.006313	1.002929	.006302	.003369	.001969	-.516164 -.856487	.001967	.518553 -.855044	31.1
24	1.007365	1.003977	.007353	.003369	.001924	-.477759 -.878489	.001914	.480466 -.877011	28.5
24a	1.008417	1.005026	.008403	.003369	.001887	-.446789 -.894638	.001882	.449790 -.893132	26.5
25	1.009470	1.006075	.009454	.003369	.001865	-.421110 -.907008	.001853	.424381 -.905482	24.9
25a	1.010522	1.007123	.010504	.003369	.001841	-.399397 -.916776	.001837	.402915 -.915236	23.5
26	1.011574	1.008172	.011555	.003369	.001827	-.380715 -.924691	.001819	.384475 -.923133	22.4
26a	1.012626	1.009220	.012605	.003369	.001811	-.364419 -.931233	.001810	.368392 -.929669	21.4
solution 1									
65	1.009470	0.999298	.009422	.010128	.007471	.731373 -.681973	.007428	-.734569 -.678493	47.3
65a	1.010522	1.000340	.010469	.010128	.007068	.693670 -.720258	.007029	-.697428 -.716620	44.2
66	1.011574	1.001381	.011516	.010128	.006786	.661224 -.750158	.006750	-.665490 -.746376	41.7
66a	1.012626	1.002422	.012562	.010128	.006571	.632915 -.774194	.006544	-.637668 -.770283	39.6
solution 2									
65	1.009470	0.999298	.009422	.010128	.007471	-.731373 -.681973	.007428	.734569 -.678493	47.3
65a	1.010522	1.000340	.010469	.010128	.007068	-.693670 -.720258	.007029	.697428 -.716620	44.2
66	1.011574	1.001381	.011516	.010128	.006786	-.661224 -.750158	.006750	.665490 -.746376	41.7
66a	1.012626	1.002422	.012562	.010128	.006571	-.632915 -.774194	.006544	.637668 -.770283	39.6

Table 2 Calculated crystallographic results of two sets of principal distortions (η_{11} =0.9988317) using LC1-LIS1.

structure are actually parallel to a {100} plane since the trace of a-c domain boundaries should be parallel to a {100} plane, which can be derived viewing from the other two directions which count 2/3 of the definable habit planes, just like 60% out of 90% in earlier experiments. We see no complicated square net patterns in $PbTiO_3$ and therefore it is difficult to compare the remaining 10% habit planes. It seems that the inconsistency in previous works comes from ignoring three dimensional considerations.

Although the transformation strain of $PbTiO_3$ is quite small, from Table 2, compared to ferrous alloys, a small change in the relative values of the principal strains introduces a dramatic shift of the habit plane. That is, the tetragonality of the C/T transformation is the major factor determining the crystallographic characteristics. The tetragonality can be affected by impurity, structural inhomogeneity, temperature perturbation, strain conditions, etc. Crystals used in the present case offer a good example. It is thus clear that even a very small perturbation on lattice distortion during transformation will shift the habit plane. This is evidenced by the shift of the same phase front at different positions during transformation (figures 6 (c)-(e) in ref.8). This consideration may explain the scattering nature of the habit plane normals observed in experiments.

5. CONCLUSIONS

The cubic to tetragonal phase transformation in $PbTiO_3$ crystals shows martensitic characteristics. The phase front passes swiftly through the crystal; surface relief accompanying the transformation is also seen. The twinning system involved has been identified as a compound twin in the tetragonal phase of {110}<110>type. The phase boundaries (habit planes) were "frozen" by controlling the temperature profile. It was found that the habit planes vary within a certain range. Not only did different specimens show this phenomenon, but also the same specimen under different transformations also follows this, indicating the importance of local lattice parameter near the interfaces during transformation. Theoretical predictions with varying principal distortions show that experimental data appear to be consistent with calculated results, if one considers the effect of local lattice purturbations during transformation. The results show a certain degree of consistency, which imply that the phenomenological martensitic crystallographic theory may apply to perovskite materials.

ACKNOWLEDGEMENT

The authors are grateful to Professor D. A. Payne and Dr. C. T. Suchicital for providing crystals. The project is supported by Air Force Office of Scientific Research under contract: AFOSR-90-0174.

REFERENCES

1. Wechsler,M. S., Lieberman,D. S. and Read, T. A.: Trans. AIME, 1953, 197 , 1503.
2. Bowles, J. S. and Mackenzie, J. K.: Acta Metall., 1954, 2 , 129, 138, 224.
3. Lieberman, D. S., Wechsler, M. S. and Read, T. A.: J. Appl. Phys., 1955, 26 , 473.
4. Wayman, C. M.: Introduction to the Crystallography of Martensitic Transformations, (Macmillan, New York), 1964.
5. Warlimont, H. and Delaey, :Progress in Materials Science (B. Chalmers, J. W. Christian and T. B. Massalski ed.), 1974, 18 .
6. Nishiyama, Z.: Martensitic Transformations, (Academic press, New York), 1978.
7. Bansal, G. K. and Heuer, A. H.: Acta Metall., 1972, 20, 1281; 1974, 22, 409.
8. DiDomenico, M., Jr., and Wemple, S. H.: Phys. Rev., 11967, 155, 539.
9. Parker, T. J. and Burfoot, J. C.: BritJ. Appl. Phys., 1966, 17, 207.
10. Parker, T. J. and Burfoot, J. C.: BritJ. Appl. Phys., 1969, 2, 1168.
11. Shirane, G., Hoshino, S. and Suzuki, K.: Phys. Rev., 1950, 80, 1105.
12. Smolenskii, G. A.: Sov. J. Technical Physics, 1951, 21, 1045.
13. Megaw, H. D.: Proc. Roy. Soc., 1974, A189, 261.
14. Shirane, G. and Hoshino, S.: J. Phys. Soc. Japan, 1951, 6, 265.
15. Shirane, G., Pepinsky, R. and Frazer, B. C.: Acta Cryst., 1956, 9, 131.
16. Ledbetter, H. M. and Wayman, C. M.: Mater. Sci. Engr., 1971, 7, 151.
17. Suchicital, C. T.: Ph.D Dissertation, University of Illinois, 1988.
18. Chou, C.C. and Wayman, C.M.: Mat. Trans. JIM, 1992, 33 (3), 304.
19. Adachi, K. and Wayman, C.M.: Met. Trans., 1985, 16A ,1581.
20. Cohen, M., Olson, G. B. and Clapp, P. C.: Proc. ICOMAT,1979, 1.
21. D. S. Lieberman: Phase Transformations, (ASM, Metals Park, Ohio), 1970, Chap.1.
22. Christian, J.W.: The Theory of Transformations in Metals and Alloys, (Pergamon Press, Oxford), 1965 and 1975.

Habit Plane Variants in Ferroelectric Lead Titanate Crystals I. Theoretical Considerations

Li-chang Yang and C.M. Wayman

Department of Materials Science and Engineering,
University of Illinois at Urbana-Champaign, Urbana, IL 61801

Abstract

Instead of viewing the domain structures as a simple combination of 90 and 180 degree domains, a different concept of habit plane variants is proposed to redefine the domains in ferroelectric lead titanate crystals. Habit plane variants from martensitic theory refer to the invariant (undistorted and unrotated) interface plane which separates the two phases during transformation. The cubic to tetragonal transformation in lead titanate exhibits the characteristics of a martensitic-type transformation, and thus domain structures may be connected to the habit plane variants. In order to define habit plane variants, lattice parameters for lead titanate obtained from high temperature x-ray diffraction were used in calculations. According to the calculations, there are total of twenty-four habit plane variants. The domain structures based upon these variants are considered. The concept of habit plane variants thus gives the twinning and domain structures in lead titanate a direct relationship to the phase transformation.

1. Introduction

The cubic-to-tetragonal transformation in lead titanate resembles a martensitic type transformation in many respects. Lead titanate has a cubic symmetry at high temperature (> 500 C) while it goes through a transformation to the tetragonal phase at 490 C. This transformation, as studied by Fesenko et al. [1] [2], shows several characteristics of a martensitic transformation. A schematic diagram representing two of his results is redrawn in Fig. 1. In general, the nature of the tetragonal/cubic interface in a given crystal depends on the direction of the temperature gradient. A single interface transformation results (Fig. 1(a)) when grad T is parallel to the interface normal. The indices of such an interface are {320}, and stacks of parallel "90° twins" with {110} twin plane are created in the tetragonal phase behind the interface. On the other hand if grad T is parallel to the mean phase front normal, this results in a succession of wedges, each facet of which corresponds to a {320} plane, e.g., (023) and (320), and the wedge segments are separated by {110} planes as shown in Fig. 1(b). In metallurgical terminology Figs. 1(a) and (b) would correspond to single-interface and spear-type martensite, respectively. Given that the tetragonal/cubic interface is normally macroscopically planar, Fesenko et al. [1] argue that such a front shape suggests that the elastic energy of the front is predominant over an electric contribution. They further noted that the twin boundaries in the tetragonal phase could be removed by the application of an appropriate mechanical stress (~30 kg/cm^2). Although it is still not clear if the tetragonal substructure (twinning) is due to transformation twins, the observed interface plane(s)

was found to be in good agreement with calculations using martensite crystallographic theory [2].

Domain structures in lead titanate, which were suggested [1] [2] to be due to the transformation, can be categorized into several types. Hu et al. [3] found that there are only four different domain boundaries in a tetragonal ferroelectric material: 90 degree a-c and a-a, and 180 degree a-a and c-c domain boundaries. Some basic definitions of these domains and domain boundaries are given in the Appendix. It was observed that different image contrasts from these domains [4] may be developed when the samples are etched. Using optical microscopy, different domain boundaries can be distinguished. 90 degree a-c domains show more contrast than 90 degree a-a domains. Similarly, 180 degree c-c type domains exhibit more contrast than 180 degree a-a domains. These domain boundaries are not formed separately. 180 degree domain boundaries may sometimes be found within the 90 degree domains.

Viewing domains in a large scale, one finds some interesting domain patterns in lead titanate: parallel bands [5], herringbones [6], and more complicated "square net" types [7]. Domain patterns like parallel bands are usually observed on the as-grown crystal surface, especially when a fast cooling rate is used after the termination of effective crystal growth. Figure 2 shows a typical pattern of parallel bands after a crystal growth run using a cooling rate of 100 ^{o}C/hr through the transformation region. As will be shown [8] the structures of these bands consist of alternating 90 degree a-c and a-a type domains. It is noted from Fig. 2 that 90 degree

a-c domains show more contrast than 90 degree a-a domains. The sizes of these bands, as seen from Fig. 2, are between 20 to 100 μm. The fine lamellae within each band are the traces of twin planes, as marked by "t", whereas the planes which separate these bands are the junction planes*, as indicated by "j". It is also found that there are some 180 degree domain boundaries formed within these (90 degree domain) bands. Herringbone domains, on the other hand, also show parallel bands and fine lamellae, as shown in Fig. 3. But these bands run 45 degrees with respect to the usual parallel bands, while the fine lamellae within the bands intersect the junction planes at 45 degrees. As we reported [9] the fundamental structures of a herringbone consist of 90 degree a-c type domains and the fine lamellae are {101} twin planes. Square net type domains, which will not be considered here, are formed by the intersections of parallel bands.

It is the purpose of this paper to use the concept of habit plane variants, taken from martensitic theory, to redefine the domain structures in ferroelectric lead titanate materials. Instead of viewing the domains in lead titanate as a simple combination of 90 and 180 degree domains, the domains observed should be martensites if the transformation follows the martensitic theory. A theoretical martensitic calculation was conducted to define the habit plane variants, which were then compared with the experimental observations [8]. To use the martensitic theory, lattice parameters of lead titanate [10] around the

*Junction planes may be regarded as impingement planes between different habit plane variants.

transformation region measured by high-temperature x-ray diffraction were employed in the calculations. The detailed structures of various domain patterns were revealed by using electron back scattering patterns (EBSP) in an SEM. The results and the fundamental mechanisms of EBSP are reported in another paper [8].

2. Cubic-to-Tetragonal Transformation

The cubic-to-tetragonal transformation of lead titanate is characterized by high temperature x-ray diffraction from which the temperature variation of lattice parameters for both phases can be extracted. Shirane et al. [10] studied the transformation by using the Debye-Scherrer technique. In their studies, powder samples were sealed in a thin capillary tube, then inserted into a hot stage in the Debye-Scherrer camera. The temperatures of the hot stage were controlled to ramping up to 535 C. A much finer temperature interval near 490 C was used to monitor the behavior of the transformation. Lattice parameters extrapolated from (143), (134) and (422) peaks in the back reflection region are shown in Fig 4. It is noted that the crystals went through a cubic-to-tetragonal transformation at 490 C. Lattice parameters near the transformation for both phases, a_c=3.958 Å, a_t=3.942 Å and c_t=4.011 Å, are taken for the martensitic calculations in the following section.

3. Martensitic Transformation and Habit Plane Variants

Martensitic crystallographic theory, either by Bowles-Mackenize

(BM) [11] or Wechsler-Lieberman-Read (WLR) [12], describes the crystallographic relations, the habit plane, and the macroscopic shape deformation from only the lattice parameters of the two phases in a transformation. The transformations of some metal alloys, such as Au-Cd, Fe-Ni, In-Tl, ...etc., have been successfully examined by using the theory. It is generally agreed from the experimental observations that during a transformation there is an invariant habit plane, which is undistorted and unrotated, between the two phases. A pure Bain deformation alone does not result an invariant plane. The condition that the habit plane be invariant can only be satisfied when a lattice-invariant deformation (an inhomogeneous shear), in addition to a small rotation, is included in the transformation deformation. This lattice-invariant deformation may be accomplished by forming either a twin or a slip substructure in the martensite phase.

It is not uncommon to observe a martensitic transformation with no apparent habit plane. In three of the most classical metallurgical cases studied, Au-Cd [13], In-Tl [14], and Mn-Cu [15] the structure is completely martensitic at room temperature and usually one sees the martensite internal twins and certain planar traces, the latter corresponding to junction planes between habit plane variants, the habit planes passing out of the crystal as it were. The simplest example here is the well-known single interface transformation in Au-47.5%Cd crystals transformed in a temperature gradient where a single variant of martensite is nucleated and grows by the passage of a single interface from the cool end to the warm end [13]. After transformation is complete all that there is left to

see are the martensite transformation twins.

Phase transformation in lead titanate follows the same picture. Single-interface transformation brings the cubic phase into the tetragonal phase and leaves twin substructures in the tetragonal phase. This interface plane (habit plane) was characterized as a plane of the {023} type [1] [16]. And the twin plane belongs to {101} type planes. Therefore, all the domain structures found in the tetragonal (martensite) phase are connected with the cubic (parent) phase through this cubic-to-tetragonal martensitic transformation. Domains, instead of viewing as a lump of 90 and 180 degree domains, should be considered as resulting from these habit plane variants. Therefore, habit plane variants must be defined first such that the domain structures in lead titanate can be fully understood.

The basic equation [11] of the phenomenological martensitic theory is described by the matrix product of a lattice-invariant deformation, S, Bain deformation, B, and rigid body rotation, R, which gives the transformation shape deformation, P_1, such that the habit plane is invariant,

$$P_1 = \delta R B S \qquad (1)$$

where δ is an adjustable dilatation factor. The lattice-invariant deformation S can be moved to the left hand side of the equation, which gives the final equation as

$$P_1P_2 = \delta\, R\, B \qquad (2)$$

where S^{-1} is replaced by P_2. The product P_1P_2 gives an invariant line strain such that lines lying in both the habit plane and twin plane, i.e., their intersection, are invariant.

Following Bowles and Mackenzie [11] and ignoring for a moment the dilatation parameter δ, a scalar, we can write

$$P_1 = R\, \bar{S}\, B = R\, B\, S \qquad (1a)$$

where $\bar{S}$ designates that the inhomogeneous shear occurs after the Bain distortion and S means vice versa. Even though $\bar{S}$ in the present case means twinning in the tetragonal martensite, it is preferable for purposes of mathematical simplicity to allow S to precede the Bain distortion because then an orthonomal (cubic) axis system can be used for the strain matrix representation and no metric tensor is required. Since, for example, the (101) twinning plane in the martensite is derived (from the correspondence) from the (101) plane in the parent, the S matrix represents a slip shear. The complete equivalence, mathematically, of twinning and slip as the inhomogeneous shear has been demonstrated by Wechsler, Lieberman, and Read [12]. Of course it is to be noted that certain {101} planes in the parent, notably those parallel to the tetragonal c-axis, remain mirror planes after the Bain distortion and thus cannot correspond to twinning planes in the martensite. This restricts the number of habit plane solutions as is discussed in the paper and requires

care in distinction doing the reverse calculation: given the habit plane, calculate the twin plane. According to Bowles-Mackenzie, the twinning plane in the martensite is derived from a mirror plane in the parent. It is not to be inferred, however, that any mirror plane {hkl} in the parent always becomes a possible twin plane in the martensite.

The Bowles-Mackenzie dilatation parameter δ has been used in Eq. (1) but not employed in the present calculations. δ represents a uniform expansion or contraction in the habit plane and in order to explain certain transformations, notably in ferrous alloys, values of δ =1.01-1.02 (i.e., 1-2% strain) have been suggested. Such values are amenable to experimental verification but have not been so detected. This is not to deny the possible importance of such a parameter in ferroelectrics such as the present case because the principal strains of the Bain deformation ($\epsilon_i = \eta_i - 1$) are from one to two orders of magnitude smaller than those in ferrous alloys where in the f.c.c.-b.c.c. case the c-axis changes by some 20%, in contrast to 1.3% in the present case.

According to equation (2), two different modes of calculations can be performed. One can calculate the habit planes by assuming the twin planes, or calculate the twin planes by assuming the habit planes. First, the case of "forward" calculation, getting the possible habit planes from assumed twin planes, is considered. For a cubic-to-tetragonal transformation, there are six choices of lattice correspondences, as shown in Table 1. Lattice correspondence LC-1, $[100]_c=[100]_t$, $[010]_c=[010]_t$, and $[001]_c=[001]_t$ being the simplest one, was chosen first. Lattice parameters

from high temperature x-ray diffraction measurements were used for calculating the Bain deformation, B. The principal distortions of the Bain deformation were computed by $\eta_1 = a_t/a_c$, $\eta_2 = a_t/a_c$, and $\eta_3 = c_t/a_c$. The twinning elements {101}<101> for lead titanate, as listed in Table 2, were used as input data. For lead titanate, there are only twelve possible twinning elements. Since there are six different {101} twin planes and for each twin plane there are two opposite shear directions. With these twinning elements, habit planes can be easily obtained from the BM theory. As shown in Table 3, for example, for each twinning element there are four habit plane solutions[#]. Two of them are with high shear strains while other two are with low. It is noted that the values of four habit planes and directions of shape deformation are the same, except for the minus sign and the permutations. They are crystallographically equivalent. The four habit plane solutions are thus considered to be degenerate. More detailed discussion on the degeneracy of the habit plane solutions [17] [18] and the conditions under which the degeneracy occurs will be given later. It should be pointed out that for LC-1 the planes (110) and $(\bar{1}10)$ can not be a possible twin plane for a tetragonal phase [12], since they contain the axis of expansion, the c-axis. Four twinning elements are therefore ruled out for the case of LC-1. Complete calculations of the habit planes for LC-1 from the eight remaining twinning elements are summarized in Table 4. It is seen that those twinning elements having the same twin planes but with opposite shear directions, for instance No. 1 and 2, give the same habit planes solutions.

[#]For internal consistency all calculations have been carried out using six significant figures so that, for example, the scalar product of two orthogonal unit vectors u•v=0.000000, etc.

It is also found that not all habit planes of the {0.835, 0.549, 0.005} type are obtained from the calculations; planes like (0.005, 0.835, 0.549) and (0.835, 0.005, 0.549) are excluded. These result partly because the case discussed here is valid for the cubic-to-tetragonal transformation and the lattice parameter "c" was greater than "a", and partly by the way the lattice correspondence is chosen. If a different Bain deformation or lattice correspondence is used, then other {0.835, 0.549, 0.005} planes will be excluded. A more detailed discussion on the exclusion of certain planes as being habit planes will be given later.

The habit plane solutions may be viewed more clearly graphically. A stereographic projection showing all the possible habit plane solutions for LC-1 is plotted in Fig. 5, where the {101} twin planes and the habit planes are marked. It is noted that the habit planes locate at positions very close to {023}, which has been observed experimentally [1] [16], except that there are two solutions for each {023} pole. Note that planes like (032) and (302) are excluded. Totally, there are 16 possible habit planes for LC-1. Eight habit planes lying on the edge of the projection belong to the group of high shear strains while other eight near (001) poles are with low shear strains. Remember that these conclusions are drawn based on the results for LC-1. Different habit plane solutions may be obtained if another lattice correspondence is considered. When all six lattice correspondences are used, two sets of 24 crystallographically equivalent habit plane solutions with low shear strains may be obtained.

In a reverse mode of calculation, twinning elements may be

obtained by using the habit planes as input data. As will be seen later this reverse approach actually is more important than the forward one for we are more interested in the structures of the martensite phase. The values of the habit planes obtained from previous calculations were used as input data. One case is shown in Table 5. There are four twinning element solutions for each set of the habit plane and direction of shape deformation. Two solutions have low shape deformation strains, 0.013, while other two have high. Therefore, the later two twinning elements are considered less feasible. Two twinning elements, (-0.707, 0.000, -0.707)[0.707, 0.000, -0.707] and (0.698, 0.000, -0.716)[-0.716, -0.000, -0.698] being considered to be crystallographically and energetically equivalent, are possible for a given habit plane. As compared to the previous calculations where only one degenerate solution is produced, the degeneracy in the present case leads to two equivalent solutions. The importance of these results must be pointed out: that each habit plane results in two types of (twinning) substructure in the martensite phase, which should be observed with the same probability.

Table 6 summarizes the calculation results for all 24 habit planes. Each habit plane produces two equivalent {101}<101> twinning elements. Habit plane variants in lead titanate can now be defined simply by these. For each lattice correspondence, there are eight habit plane variants with low shear strains and shape deformation. Totally 24 habit plane variants can be defined in lead titanate when all the six lattice correspondences are considered.

4. Discussion

4.1 Habit Planes and Twin Planes in Lead Titanate

The relation between habit planes and twin planes in lead titanate, in a sense, is analogous to the second undistorted plane, K_2, and the composition plane, K_1, of a mechanical twin. First, the loci of the habit plane normals are not too far from the second undistorted plane, K_2. The separation between the {0.835, 0.549, 0.005} habit planes and {110} poles is about 11.68°. Secondly, both habit planes and twin planes are invariant in the martensitic theory, which are similar to the K_1 and K_2 planes in a mechanical twin. A stereographic projection of the cubic structure showing the relation between twin planes and habit planes of lead titanate is drawn in Fig. 6. There are four habit planes lying in positions about 11.68° from each of the {101} poles. Six {101} planes, therefore, produce six four-habit-plane groups which give a total of 24 habit planes. For each habit plane there are four twin plane solutions of which two equivalent {101} twin planes locate about 53.78° from the habit plane. For instance, the habit plane (023) has two equivalent twin plane solutions, (101) and $(\bar{1}01)$, with low shear strains. Conversely, for each twin plane there are four equivalent habit plane solutions, locating in the positions close to the K_2 planes. The twin plane (101), for example, has four habit plane solutions of which planes $(0\bar{2}3)$ and $(0\overline{23})$ are quite close to the $(0\bar{1}1)$ and $(0\overline{11})$ planes.

It was found from forward calculations that not all the 24 {023} planes are the possible habit planes for a given lattice correspondence,

certain planes being excluded as habit planes. For example, (032) and (302) are not possible habit plane solutions for LC-1. Considering the four habit planes around the (011) pole in Fig. 6, for LC-1 the two on the left are the possible ones whereas the other two on the right are not. For a cubic-to-tetragonal transformation, if c/a>1 is the case then habit planes always locate at positions to the left of the (011) pole. On the other hand, if c/a is smaller than one then the habit planes are the ones on the right of the (011) pole. The exact positions of the habit planes are determined by the c/a ratio and the volume change or more specifically by the principal distortions of the Bain deformation.

4.2 Degeneracy of the Habit Plane Solutions (Forward Calculation)

It is known from martensitic theory that either habit planes or twin planes can be obtained by assuming the other counterpart is known. In the forward calculation, in general, one twin plane results in four different habit plane solutions. However, in some cases degeneracy may occur which produces two or even one solution. Christian [17] and Wechsler [18] discussed the general conditions under which the degeneracy of the habit plane solutions for the cubic-to-tetragonal transformation may occur. According to Wechsler's analysis [18] degeneracy in the habit plane occurs when:

(1) K-degeneracy results when $t(=d_2 \times p_2)$ is a twofold (or fourfold) axis and is either parallel or perpendicular to the expansion axis of the lattice deformation;

(2) g-degeneracy may result if d_2 or p_2 is a twofold (or fourfold)

axis of symmetry, depending upon the numerical values of the components of d_2 and p_2.

Thus twinning elements like {101}<101> will result in a double degeneracy, K- and g-degeneracy, which reduces the number of the habit plane solutions into one. K- degeneracy occurs when the great circle containing both the normal of the twin plane, p_2, and shear direction, d_2, is of the {100} or {110} type which results a reflection symmetry in the invariant lines. Whereas the g-degeneracy occurs when either the twin plane or shear direction is of {100} or {110} type which gives the same principal values for two different inhomogeneous shear strains, g_1 and g_2. The K- and g-degeneracy in fact are determined by the symmetry of the twinning elements, which can be well explained by using a graphic representation [19] [20]. Figure 7 shows a plot of a stereographic projection for the cubic-to-tetragonal transformation in lead titanate in which the invariant lines, X_1 and X_2, and invariant normals, N_1 and N_2, are located*. As known from the BM theory, the habit plane solutions are uniquely determined by the four sets of the invariant lines and invariant normals, which are produced due to the combined effect of the Bain deformation B and lattice-invariant deformation S. Mathematically, the relation between the invariant lines X_i, habit plane p_1, and twin plane p_2 can be described as follows.

*The discussion of K- and g-degeneracy in Wechsler's paper [18] was based on the WLR theory. Here a new graphic representation from the BM theory is used. The concept of K- and g-degeneracy is thus extended to the BM theory in which the symmetry of invariant lines and normals is considered.

$$X_i \parallel p_1 \times p_2 \qquad (3)$$

Similarly, the invariant normals are parallel to the direction given by the cross product of the direction of shape deformation, d_1, and twinning shear direction, d_2.

$$N_i \parallel d_1 \times d_2 \qquad (4)$$

Using Eq. (3) and (4) and referring back to Eq. (2), the invariant lines therefore locate in a stereographic projection at the intersections of the twin plane and the initial loci of all the directions unchanged in magnitude due to the Bain deformation, whereas the invariant normals lie at the intersections of the initial loci of the plane normals and the great circle of the twinning shear direction, d_2, such that the condition $d_2 \cdot N_i = 0$ is satisfied. It will be shown later that the positions of these directions and plane normals in a stereographic projection in fact are related to the degeneracy of the habit plane solutions. Consider one case in which the twinning element $(101)[\bar{1}01]$ is involved. Traces of the K_1 and K_0 planes are labeled in Fig. 7. Two cones, C_d and C_n, representing the initial loci of all the directions and plane normals, are drawn in Fig. 7. The semivertex angles [18] [20] of these cones are given by

$$\theta = \tan^{-1}\left(\frac{1-\eta_3^2}{\eta_1^2-1}\right)^{\frac{1}{2}} \qquad \text{and} \qquad \psi = \tan^{-1}\left(\frac{1-\eta_3^2}{\eta_1^2-1}\right)^{\frac{1}{2}}\left(\frac{\eta_1}{\eta_3}\right),$$

where θ and Ψ are for C_d and C_n respectively. The shear plane K_1

intersects with C_d at X_1 and X_2 which give the invariant lines. Whereas the trace K_0, which is the great circle of the shear direction d_2, intersects the cone C_n at the invariant normals, N_1 and N_2. It is seen from Fig. 7 that these invariant lines, X_1 and X_2, and invariant normals, N_1 and N_2, possess a reflection symmetry about the (010) plane which results a case of "K-degeneracy" discussed both by Christian and Wechsler wherein the number of the habit plane solutions due to the K-degeneracy is reduced to two.

The habit plane solutions are further reduced because the twin plane and shear direction locate exactly at the {101} poles, which gives so called "g-degeneracy". This g-degeneracy results in another reflection symmetry in the indices** of invariant lines and normals about the {101} plane. Therefore, K- and g-degeneracy account for the double degeneracy in our forward calculations.

4.3 Degeneracy of the Twin Plane Solutions (Reverse Calculation)

In the foregoing discussion, the degeneracy of the habit plane solutions for a forward calculation is well explained by the K- and g-degeneracy. However, there is a "quasi K-degeneracy" in our reverse calculations which reduces the number of the twinning element solutions to three, in contrast to one in the forward case. This kind of degeneracy, in a sense, is not a true degeneracy, since each degeneracy should reduce the number of the solutions into half. However, the indices of the first two

**A complete derivation for the generalized conditions of K- and g-degeneracy from BM representation will be published in another paper.

twinning element solutions with low shape deformation, as seen from Table 5, are close enough to term it a degeneracy. This type of twin plane degeneracy is quite interesting since degenerate microstructures may have been observed in some metal alloys [21]. However, detailed discussion on the degeneracy for the reverse calculations is not found.

In a reverse calculation, in general, four twinning elements are obtained from each habit plane. In the discussion of K- and g-degeneracy in the habit plane solutions, Christian and Wechsler considered the symmetry of the twinning elements. Similarly, the symmetry element of the habit planes should be considered in order to account for the degeneracy of the twinning elements in a reverse calculation. For lead titanate, the habit planes {0.835, 0.549, 0.005} and direction of shape deformation <0.832, 0.554, 0.005>, rigorously speaking, do not possess any particular symmetry element. Therefore, one should see no degeneracy in the twinning element solutions. However, it is noted that the habit planes {0.835, 0.549, 0.005} and direction of shape deformation <0.832, 0.554, 0.005> are not too far from planes {0.835, 0.549, 0.000} and <0.832, 0.554, 0.000>, and the twinning element solutions from this hypothetical habit plane and direction of shape deformation degenerate into two groups, as seen from Table 7. For each group, there are two crystallographic equivalent twinning element solutions. This type of degeneracy can be identified as due to the K-degeneracy in Christian and Wechsler's cases. Since both the habit plane and direction of shape deformation lie on the (100) trace, this results in a reflection symmetry in the invariant lines and normals about the plane (100). Neither habit plane (0.000, 0.549, -

0.835) normal nor direction of the shape deformation [0.000, -0.554, -0.832] is in {110}, therefore, there is no g-degeneracy. When the habit plane is not exactly on the {100} or {101} traces but in a position slightly deviated from this exact K-degeneracy, a condition of "quasi K-degeneracy" may occur, as shown in Fig 8. On the other hand, there may also be a case for "quasi g-degeneracy" if the habit plane or direction of the shape deformation is a little away from the poles {100} or {101}. Now the question arises as how close the habit plane is to the traces of {100} or {101} to result in a quasi K-degeneracy. A computer simulation was thus carried out by assuming slight increases in the habit plane indices such that the habit plane is away more from the exact K-degeneracy condition. It is found that when the indices of the habit plane are increased to (0.05, 0.549, -0.835), which is about 2.86° from exact K-degeneracy condition, then the difference in the twin plane solutions starts to become apparent. The exact condition for the quasi K-degeneracy to be valid is not determined at this moment. However, from In-Tl alloys the habit planes are {0.016, 0.688, 0.725}[¶] and a pair of twin-related substructures [21] was found in the martensites, which gives a strong indication that the quasi K-degeneracy does exist especially when the habit planes indices are not too far from the exact K-degeneracy condition, i.e., the traces of {100} or {110}.

The degeneracy of the habit planes and twin planes in lead titanate

[¶]Habit planes have been recalculated for In-Tl alloys from which a different result was obtained. As compared to the normalized value obtained by Burkart and Read [14], {0.009, 0.700, 0.710}, current results are believed to be more accurate since six digits were used during calculations.

is summarized in Table 8. Twinning elements {101}<101> result a double degeneracy which reduces the number of habit plane solutions in a forward calculation into one. One the other hand, the habit plane system {0.835, 0.549, 0.005}<0.832, 0.554, 0.005> produces a condition of "quasi K-degeneracy" which gives three different twinning element solutions. Among these three, however, only the one with low strain has two crystallographic equivalent twinning elements.

It should be noted that in the forward calculation both X_i's are variants and N_i's are variants and the four predicted habit planes are also variants. This results because the twin plane is crystallographically degenerate, i.e., {h0h}. On the other hand in the reverse calculation the habit plane (input) is non-degenerate {hkl} leading to only one "proper" twin plane of the form {h0h}; further, the invariant lines and normals are not variants. Additional symmetries in the reverse calculation would result were the habit plane of the form {0kl}.

4.4 Habit Plane Variants and Domain Structures

It is concluded from the above calculations that there are 24 habit plane variants in lead titanate and for each variant there are two twin-related substructures in the martensite phase. Martensites, in general, are the end products of a martensitic transformation due to these habit plane variants, and therefore one should consider domain structures in lead titanate according to these variants. Considering the domain structures due to habit plane variant 1, for instance, two types of twin planes, $(\bar{1}0\bar{1})$ and $(10\bar{1})$, may be observed in the tetragonal phase as a result of the

movement of the habit plane $(02\bar{3})$. A simple schematic diagram representing the surface morphology of this variant is drawn in Fig. 9(a). Here, lattice correspondence LC-1 is assumed. While viewing from the top, there are only parallel traces of twin planes appearing on the surface. It is almost impossible to tell whether or not there are two different twin planes within this band. But if viewing from the side, two different twin planes may be observed, as shown in Fig. 9(a). Similar argument may also be applied to the case where the domain band is running horizontally. Considering variant 5, habit plane $(\bar{2}0\bar{3})$ will result in a domain structure with two twin planes, $(0\bar{1}\,\bar{1})$ and $(01\bar{1})$, which intersect the crystal surface and produce traces as parallel lines. The detailed domain arrangements can only be distinguished by viewing the sample from the side, as drawn in Fig. 9(b). According to the usual definition of domains, the structures due to these two variants are 90 degree "a-c" type domains. Because one twin which has the polarization pointing along the viewing direction is a "c" domain, and the other which has a polarization vector lying on the crystal surface is an "a" domain. A clear optical image contrast of these two variants may be obtained if the sample is acid etched.

On the other hand, a different surface morphology may be observed if a habit plane variant has twin planes of the (110) and $(\bar{1}10)$ types. Habit plane variants 13 to 16 and 21 to 24 belong to this case. Since the domains due to these variants are 90 degree a-a type, much lower image contrast will be developed even if the sample is etched. However, for these type of domains it is possible to observe a substructure with two different twin planes from the surface, as seen from Fig. 9(c).

5. Conclusion

It is now clear that the domains in the ferroelectric lead titanate should be considered as martensites while the phase transformation follows the crystallographic martensitic theory. The important results from theoretical calculations indicate that there is a double degeneracy, K and g, in the forward direction such that there are four crystallographic equivalent habit plane solutions for each twinning element. The habit planes are grouped around {101} poles and form six four-habit-plane groups which gives total 24 habit plane variants. In the reverse calculation, for each habit plane variant the quasi K-degeneracy produces only two crystallographically equivalent twinning elements within one domain band. The probability of observing these two twinning elements will be the same, since they are strain energetically equivalent. The theory thus predicts that there are total of 24 habit plane variants in the ferroelectric lead titanate materials. All the domain structures observed should comply with the habit plane variants even though the prominently banded structure is comprised of junction planes as a result of a merging of variants during transformation.

Acknowledgements

This work was supported by the Air Force Office of Scientific Research under an URI program and by the Army Research Office. Their support is gratefully acknowledged.

Appendix

Some basic definitions of the domains and domain boundaries

Basic definitions [4] for the domains observed in a tetragonal ferroelectric material are simply based upon the orientation of the polarization vector within a tetragonal unit cell relative to the viewing direction. A polarization is produced within a tetragonal unit cell since the positive charge center does not coincide with the negative one. The polarization vector, in this case, is along the "c" axis of the unit cell whereas other two unit cell edges, perpendicular to the c axis, are the "a" axes. A tetragonal unit cell is thus uniquely defined by the unit cell parameters: c and a. A "c" domain is defined when the polarization vector, the c axis, is along the viewing direction. On the other hand, a region called an "a" domain is defined when one unit cell edge, the a axis, is parallel to the viewing direction. In other words, the polarization vector for an "a" domain is always perpendicular to the viewing direction, whereas for a "c" domain the polarization vector is parallel to the viewing direction. Therefore, two different types of domains, "a" and "c", may be observed in a tetragonal ferroelectric material.

Two different domain boundaries are formed when "a" and "c" domains meet. A 180 degree domain boundary is formed when "c"-"c" or "a"-"a" domains appear side by side but with polarization vectors which are 180 degrees relative to each other. It should be pointed out that the boundary for 180 degree domains is not a twin plane. Another kind of domain boundary, the 90 degree type, is formed when the polarization

vectors of the two domains, roughly speaking, are 90 degrees relative to each other. The domains form a twin structure and the domain boundary is a twin plane. It is seen from Fig. 10(b) that 90 degree domains can be either a-c or a-a type, depending upon the relative position of their polarization vectors with respect to the viewing direction.

References

[1]E.G. Fesenko, M.A. Martynenko, V.G. Gavrilyachenko, and A.F. Semenchev, *Izvestiya Akademii Nauk SSSR, Seriya Fizicheskaya*, Vol. 39, No. 4 (1975), pp 762-765

[2]E.G. Fesenko, M.A. Martynenko, V.G. Gavrilyatchenko, and A.F. Semenchev, *Ferroelectrics*, Vol. 7 (1974), pp 309-310

[3]Y.H. Hu, H.M. Chan, Z.X. Wen and M.P. Harmer, *J. Am. Ceram. Soc.*, Vol. 69, No. 8 (1986), pp 594-602

[4]J.A. Hooton and W.J. Merz, *Phys. Rev.*, Vol. 98, No. 2 (1955), pp 409-413

[5]R.C. DeVries and J.E. Burke, *J. Am. Ceram. Soc.*, Vol. 40, No. 6 (1957), pp 200-206

[6]G. Arlt and P. Sasko, *J. Appl. Phys.*, Vol. 51, No. 9 (1980), pp 4956-4960

[7]P.W. Forsbergh, Jr., *Phys. Rev.*, Vol. 76, No. 8 (1949), pp 1187-1201

[8]L.C. Yang and C.M. Wayman, to be published

[9]L.C. Yang, I. Dumler, and C.M. Wayman, submitted to *J. Mat. Chem. Phys.*

[10]G. Shirane and S. Hoshino, *J. Phys. Soc. Japan*, Vol. 6, No. 4 (1951), pp 265-270

[11]J.S. Bowles and J.K. Mackenize, *Acta Metall.* 2, 129 (1954); 2, 138 (1954); 2, 224 (1954)

[12]M.S. Wechsler, D.S. Lieberman, and T.A. Read, *Trans. AIME*, Vol. 197 (1953), pp 1503-1515

[13]D.S. Lieberman, M.S. Wechsler and T.A. Read, *J. Appl. Phys.*, Vol. 26, No. 4 (1955), pp 473-484

[14]M.W. Burkart and T.A. Read, *Trans. AIME*, Vol. 197(1953), pp 1516-1524

[15]Z.S. Basiniski and J.W. Christian, *J. Inst. Met.*, Vol. 80 (1952), pp 659-666

[16]C.C. Chou and C.M. Wayman, *Materials Transactions, JIM*, Vol. 33, No. 3 (1992), pp 306-317

[17]J.W. Christian, *J. Inst. Met.*, Vol. 84 (1956), pp 386-394

[18]M.S. Wechsler, *Acta Metall.*, Vol. 7 (1959), pp 793-802

[19]D.S. Lieberman, *Acta Metall.*, Vol. 6 (1958), pp 680-693

[20]C.M. Wayman, *Introduction to the Crystallography of Martensitic Transformations*, Macmillan, 1964

[21]Z.S. Basinski and J.W. Christian, *Acta Metall.*, Vol. 4 (1956), pp 371-378

Figure Captions

Fig. 1: Schematic diagram representing two of Fesenko's results [2]. A temperature gradient is maintained across the lead titanate crystal which results an interface separating the cubic and tetragonal phases.

Fig. 2: Surface morphology of an as-grown sample after chemical etch, showing parallel banded-type domain structures in lead titanate. Note the difference in the image contrast between "a-c" and "a-a" type domains. The twin planes and junction planes are marked by "t" and "j" respectively.

Fig. 3: Typical herringbone type domain structures in lead titanate. Note the twin planes and junction planes as marked by "t" and "j" respectively.

Fig. 4: The variation of $PbTiO_3$ lattice parameters as a function of temperature [11]. Lattice parameters near the transformation region, as marked by an arrow, were used in the martensitic calculations.

Fig. 5: A stereographic projection of a cubic structure, showing the relation between the habit planes and the twinning elements in lead titanate for LC-1.

Fig. 6: A stereographic projection showing six four-habit-plane groups around each {101} pole, which gives total of 24 habit plane variants.

Fig. 7: A stereographic projection showing the invariant lines, X_1 and X_2 and normals, N_1 and N_2, which possess reflection symmetry about the plane (010). Negative poles, h3 and h4, are situated on the back side of the stereographic projection.

Fig. 8: Possible locations for quasi K- and g-degeneracy in twinning element solutions observed, as marked by the dotted lines.

Fig. 9: Schematics of domain bands due to habit plane variants, showing the possibility of two twinning elements within one variant. (a), (b), and (c) are domains which contain twin planes (101), (011), and (110) respectively.

Fig. 10: (a)An example of "a" and "c" domains where viewing direction is from the top. (b)An example of 90 degree a-a domains.

TABLE 1. Six parent-martensite lattice correspondences

parent	[100]	[010]	[001]
LC-1	[100]	[010]	[001]
LC-2	[010]	[001]	[100]
LC-3	[001]	[100]	[010]
LC-4	[010]	[100]	$[00\bar{1}]$
LC-5	[001]	[010]	$[\bar{1}00]$
LC-6	[100]	[001]	$[0\bar{1}0]$

TABLE 2. Possible twinning elements for lead titanate

1.	$(101)[\bar{1}01]$	5.	$(011)[0\bar{1}1]$	9.	$(110)[\bar{1}10]$
2.	$(101)[10\bar{1}]$	6.	$(011)[01\bar{1}]$	10.	$(110)[1\bar{1}0]$
3.	$(\bar{1}01)[101]$	7.	$(0\bar{1}1)[011]$	11.	$(\bar{1}10)[110]$
4.	$(\bar{1}01)[\bar{1}0\bar{1}]$	8.	$(0\bar{1}1)[0\bar{1}\bar{1}]$	12.	$(\bar{1}10)[\bar{1}\bar{1}0]$

TABLE 3. Example for a forward calculation*

•Input Data

Twinning Element : (101) $[\bar{1}01]$

Bain Strain : 0.996, 0.996, 1.013

•Calculation Results

Invariant Lines and Normals

X1	X2	N1	N2
-0.480	-0.480	0.486	0.486
0.734	-0.734	0.726	-0.726
0.480	0.480	0.486	0.486

Habit Planes and Directions of Shape Deformation

	P1	D1	M1	M2
1.	-0.835	-0.832	0.013	0.026
	-0.549	0.554		
	0.005	0.005		
2.	-0.835	-0.832	0.013	0.026
	0.549	-0.554		
	0.005	0.005		
3.	0.005	0.005	0.013	0.008
	0.549	-0.554		
	-0.835	-0.832		
4.	0.005	0.005	0.013	0.008
	-0.549	0.554		
	-0.835	-0.832		

Note :

P1 : habit planes

D1 : directions of shape deformation

M1 & M2 : magnitudes of shape deformation and inhomogeneous shear

*Although results are reported to three decimal places, all calculations have been carried out to six places for complete internal consistency.

TABLE 4. Habit plane results for LC-1

No.	Twin plane	Shear direction	Habit plane	Direction of shape deformation	M1 (Shape Deform.)	M2 (Inhomog. Shear)
1.	(101)	$[\bar{1}01]$	$(\bar{3}\bar{2}0)$	$[\bar{3}20]$	0.013	0.026
			$(\bar{3}20)$	$[\bar{3}\bar{2}0]$	0.013	0.026
			$(02\bar{3})$	$[0\bar{2}3]$	0.013	0.008
			$(0\bar{2}\bar{3})$	$[02\bar{3}]$	0.013	0.008
2.	(101)	$[10\bar{1}]$	$(\bar{3}\bar{2}0)$	$[\bar{3}20]$	0.013	0.026
			$(\bar{3}20)$	$[\bar{3}\bar{2}0]$	0.013	0.026
			$(02\bar{3})$	$[0\bar{2}3]$	0.013	0.008
			$(0\bar{2}\bar{3})$	$[02\bar{3}]$	0.013	0.008
3.	$(\bar{1}01)$	[101]	$(3\bar{2}0)$	[320]	0.013	0.026
			$(32\bar{0})$	$[3\bar{2}0]$	0.013	0.026
			$(\bar{0}2\bar{3})$	$[\bar{0}\bar{2}3]$	0.013	0.008
			$(\bar{0}\bar{2}3)$	$[\bar{0}2\bar{3}]$	0.013	0.008
4.	$(\bar{1}01)$	$[\bar{1}0\bar{1}]$	$(3\bar{2}0)$	[320]	0.013	0.026
			$(32\bar{0})$	$[3\bar{2}0]$	0.013	0.026
			$(\bar{0}2\bar{3})$	$[\bar{0}\bar{2}3]$	0.013	0.008
			$(\bar{0}\bar{2}3)$	$[\bar{0}2\bar{3}]$	0.013	0.008

5.	(011)	[0$\bar{1}$1]	($\bar{2}$30)	[$\bar{2}$30]	0.013	0.026
			($\bar{2}$30)	[$\bar{2}$30]	0.013	0.026
			($\bar{2}$0$\bar{3}$)	[$\bar{2}$0$\bar{3}$]	0.013	0.008
			($\bar{2}$0$\bar{3}$)	[$\bar{2}$0$\bar{3}$]	0.013	0.008
6.	(011)	[0$\bar{1}\bar{1}$]	($\bar{2}$30)	[$\bar{2}$30]	0.013	0.026
			($\bar{2}$30)	[$\bar{2}$30]	0.013	0.026
			($\bar{2}$0$\bar{3}$)	[$\bar{2}$0$\bar{3}$]	0.013	0.008
			($\bar{2}$0$\bar{3}$)	[$\bar{2}$0$\bar{3}$]	0.013	0.008
7.	($\bar{0}$11)	[011]	(230)	[$\bar{2}$30]	0.013	0.026
			($\bar{2}$30)	[230]	0.013	0.026
			($\bar{2}$03)	[203]	0.013	0.008
			($\bar{2}$03)	[203]	0.013	0.008
8.	($\bar{0}$11)	[$\bar{0}\bar{1}\bar{1}$]	(230)	[$\bar{2}$30]	0.013	0.026
			($\bar{2}$30)	[230]	0.013	0.026
			($\bar{2}$03)	[203]	0.013	0.008
			($\bar{2}$03)	[203]	0.013	0.008

Note : To simplify this table, rational indices {320} were used to substitute the habit planes {0.835, 0.549, 0.005} and the directions of shape deformation <0.832, 0.554, 0.005>.

TABLE 5. Example for a reverse calculation

•Input Data

Habit Plane : (0.005, 0.549, -0.835)[0.005, -0.554, -0.832]

Bain Strain : 0.996, 0.996, 1.013

•Calculated Results

Invariant Lines and Normals

X1	X2	N1	N2
-0.480	0.493	0.486	-0.474
0.734	0.726	-0.726	-0.734
0.480	0.480	0.486	0.486

Twin Planes and Shear Directions

	P2	D2	M1	M2
1.	-0.707	0.707	0.013	0.008
	0.000	0.000		
	-0.707	-0.707		
2.	0.698	-0.716	0.013	0.008
	0.000	-0.000		
	-0.716	-0.698		
3.	0.430	0.440	0.019	0.025
	0.674	-0.676		
	-0.601	-0.592		
4.	-0.460	-0.469	0.019	0.039
	0.685	-0.686		
	-0.564	-0.555		

Note :

P2 & D2 : twin plane normals and shear directions.

M1 & M2 : magnitudes of shape deformation and inhomogeneous shear

TABLE 6. Habit Plane Variants in Lead Titanate for LC-1, LC-2, & LC-3

	Habit Planes	Twin Planes	Variants
LC-1	$(02\bar{3})[0\bar{2}\bar{3}]$	$(\bar{1}0\bar{1})[10\bar{1}]$ $(10\bar{1})[\bar{1}0\bar{1}]$	1
	$(0\bar{2}\bar{3})[02\bar{3}]$	$(\bar{1}0\bar{1})[10\bar{1}]$ $(10\bar{1})[\bar{1}0\bar{1}]$	2
	$(\bar{0}2\bar{3})[0\bar{2}\bar{3}]$	$(10\bar{1})[\bar{1}0\bar{1}]$ $(\bar{1}0\bar{1})[10\bar{1}]$	3
	$(\bar{0}\bar{2}\bar{3})[02\bar{3}]$	$(10\bar{1})[\bar{1}0\bar{1}]$ $(\bar{1}0\bar{1})[10\bar{1}]$	4
	$(\bar{2}0\bar{3})[20\bar{3}]$	$(0\bar{1}\bar{1})[01\bar{1}]$ $(01\bar{1})[0\bar{1}\bar{1}]$	5
	$(20\bar{3})[\bar{2}0\bar{3}]$	$(0\bar{1}\bar{1})[01\bar{1}]$ $(01\bar{1})[0\bar{1}\bar{1}]$	6
	$(\bar{2}\bar{0}\bar{3})[20\bar{3}]$	$(01\bar{1})[0\bar{1}\bar{1}]$ $(0\bar{1}\bar{1})[01\bar{1}]$	7
	$(\bar{2}0\bar{3})[\bar{2}0\bar{3}]$	$(01\bar{1})[0\bar{1}\bar{1}]$ $(0\bar{1}\bar{1})[01\bar{1}]$	8
LC-2	$(\bar{3}\bar{2}0)[\bar{3}20]$	$(\bar{1}0\bar{1})[\bar{1}01]$ $(\bar{1}01)[\bar{1}0\bar{1}]$	9
	$(\bar{3}20)[\bar{3}\bar{2}0]$	$(\bar{1}0\bar{1})[\bar{1}01]$ $(\bar{1}01)[\bar{1}0\bar{1}]$	10

	$(320)[3\bar{2}0]$	$(10\bar{1})[101]$ $(101)[10\bar{1}]$	11
	$(3\bar{2}0)[320]$	$(10\bar{1})[101]$ $(101)[10\bar{1}]$	12
	$(\bar{3}02)[\bar{3}0\bar{2}]$	$(\bar{1}\bar{1}0)[\bar{1}10]$ $(\bar{1}10)[\bar{1}\bar{1}0]$	13
	$(\bar{3}0\bar{2})[\bar{3}02]$	$(\bar{1}\bar{1}0)[\bar{1}10]$ $(\bar{1}10)[\bar{1}\bar{1}0]$	14
	$(30\bar{2})[302]$	$(1\bar{1}0)[110]$ $(110)[1\bar{1}0]$	15
	$(302)[30\bar{2}]$	$(1\bar{1}0)[110]$ $(110)[1\bar{1}0]$	16
LC-3	$(2\bar{3}0)[\bar{2}30]$	$(0\bar{1}\bar{1})[0\bar{1}1]$ $(0\bar{1}1)[0\bar{1}\bar{1}]$	17
	$(\bar{2}\bar{3}0)[2\bar{3}0]$	$(0\bar{1}\bar{1})[0\bar{1}1]$ $(0\bar{1}1)[0\bar{1}\bar{1}]$	18
	$(\bar{2}30)[230]$	$(01\bar{1})[011]$ $(011)[01\bar{1}]$	19
	$(230)[\bar{2}30]$	$(01\bar{1})[011]$ $(011)[01\bar{1}]$	20
	$(0\bar{3}\bar{2})[0\bar{3}2]$	$(\bar{1}\bar{1}0)[1\bar{1}0]$ $(1\bar{1}0)[\bar{1}\bar{1}0]$	21
	$(0\bar{3}2)[0\bar{3}\bar{2}]$	$(\bar{1}\bar{1}0)[1\bar{1}0]$ $(1\bar{1}0)[\bar{1}\bar{1}0]$	22

$(\overline{032})[\overline{032}]$	$(1\bar{1}0)[\overline{11}0]$ $(\overline{11}0)[1\bar{1}0]$	23
$(\overline{032})[\overline{032}]$	$(1\bar{1}0)[\overline{11}0]$ $(\overline{11}0)[1\bar{1}0]$	24

TABLE 7. Example of a reverse calculation with assumed habit plane indices

•Input Data

Habit Plane : (0.000, 0.549, -0.835)[0.000, -0.554, -0.832]

Bain Strain : 0.996, 0.996, 1.013

•Calculated Results

Invariant Lines and Normals

X1	X2	N1	N2
-0.486	0.486	0.480	-0.480
0.730	0.730	-0.730	-0.730
0.480	0.480	0.486	0.486

Twin Planes and Shear Directions

	P2	D2	M1	M2
1.	-0.702	0.712	0.013	0.008
	-0.000	0.000		
	-0.712	-0.702		
2.	0.702	-0.712	0.013	0.008
	-0.000	0.000		
	-0.712	-0.702		
3.	0.445	0.455	0.019	0.031
	0.680	-0.681		
	-0.583	-0.574		
4.	-0.445	-0.455	0.019	0.031
	0.680	-0.681		
	-0.583	-0.574		

Note :

P2 & D2 : twin plane normals and shear directions.

M1 & M2 : magnitudes of shape deformation and inhomogeneous shear

TABLE 8. Summary of degeneracy for habit planes and twin planes

	Input	Output	No. of Solutions	Degeneracy
1. Forward	twin planes (6)	habit planes (24)	1	K- & g-
2. Reverse	habit planes (24)	twin planes (6)	3	quasi K-

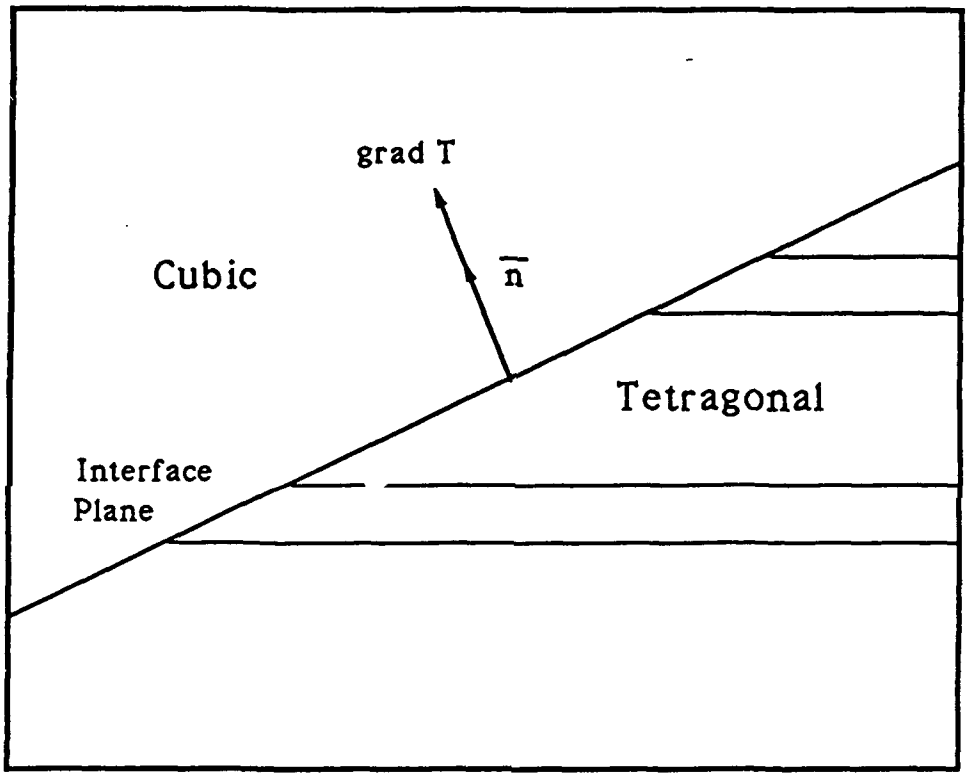

Fig. 1(a)

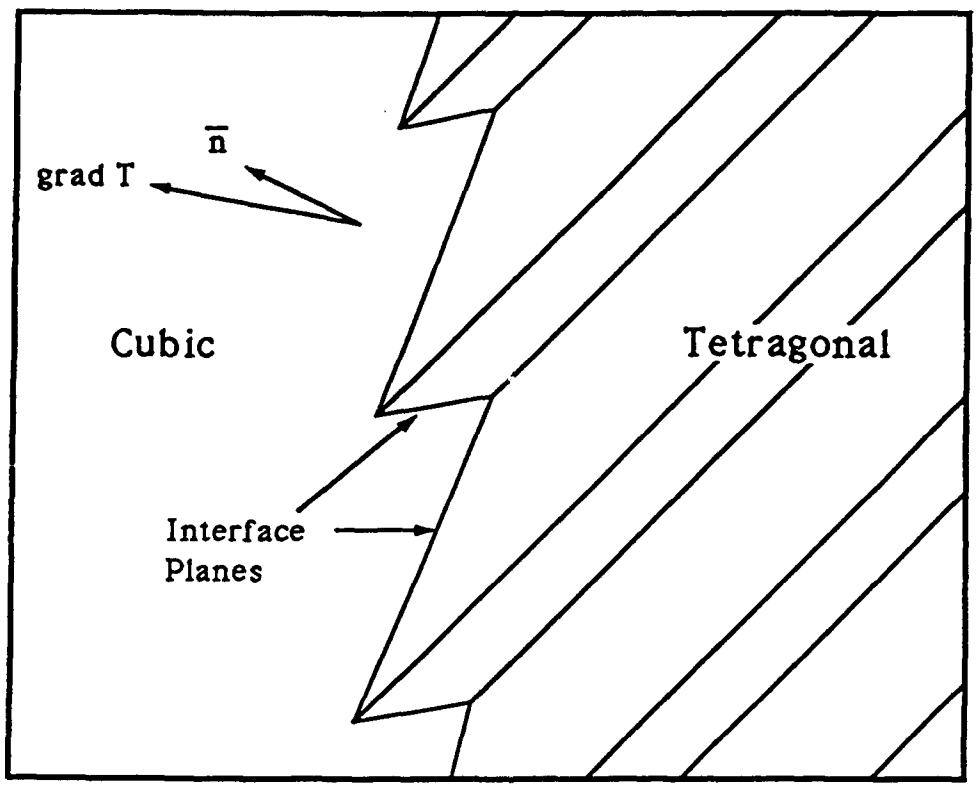

Fig. 1(b)

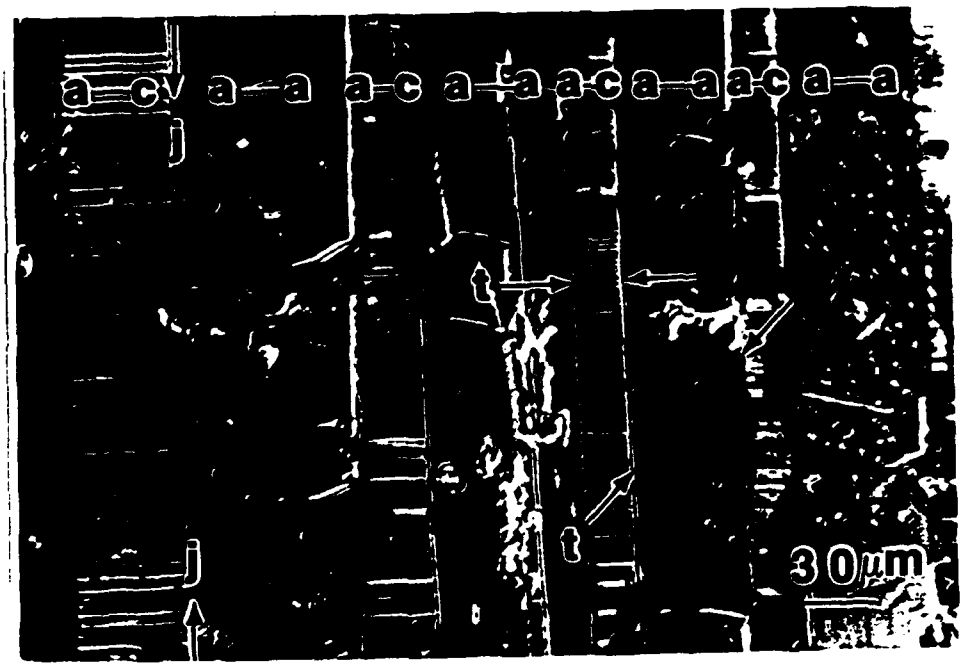

Fig. 2

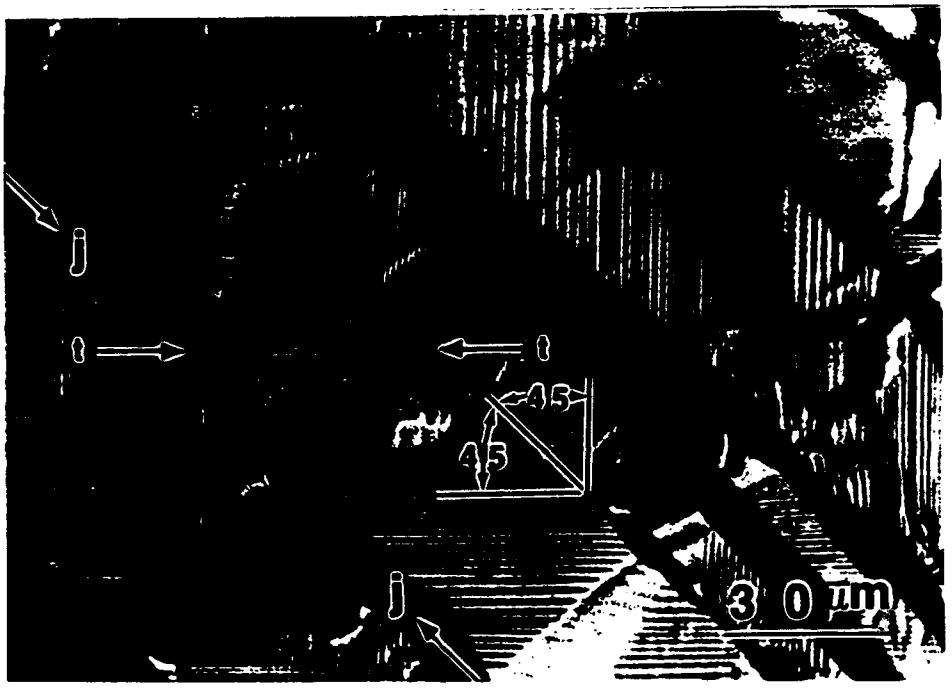

Fig. 3

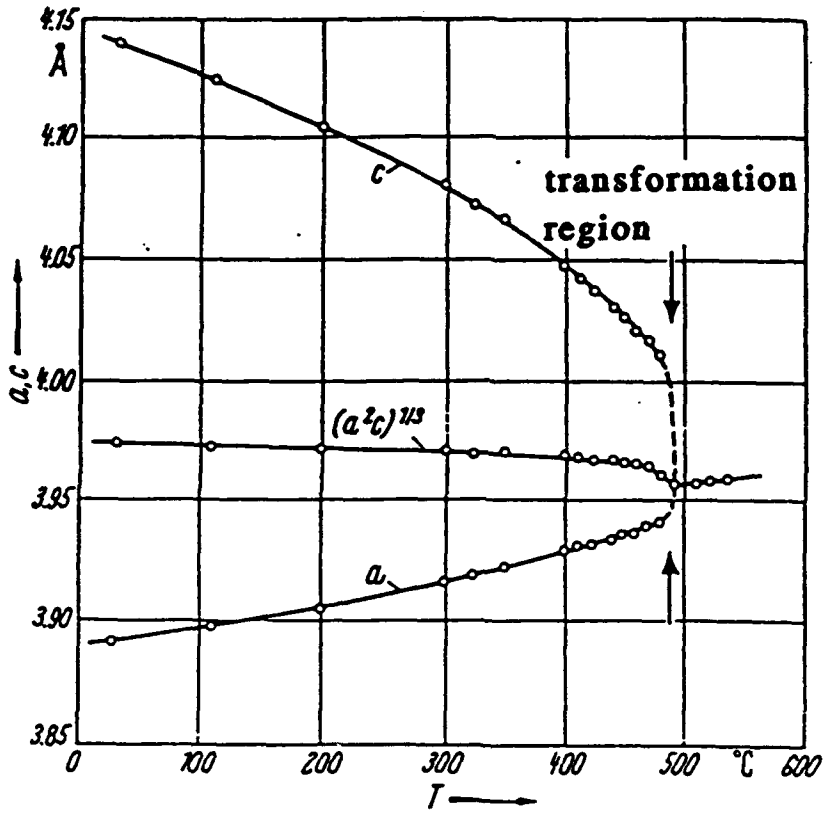
4.15
Å
4.10
4.05
4.00
3.95
3.90
3.85
a,c
c
transformation
region
$(a^2c)^{1/3}$
a
0
100
200
300
400
500
°C
600
T

Fig. 4

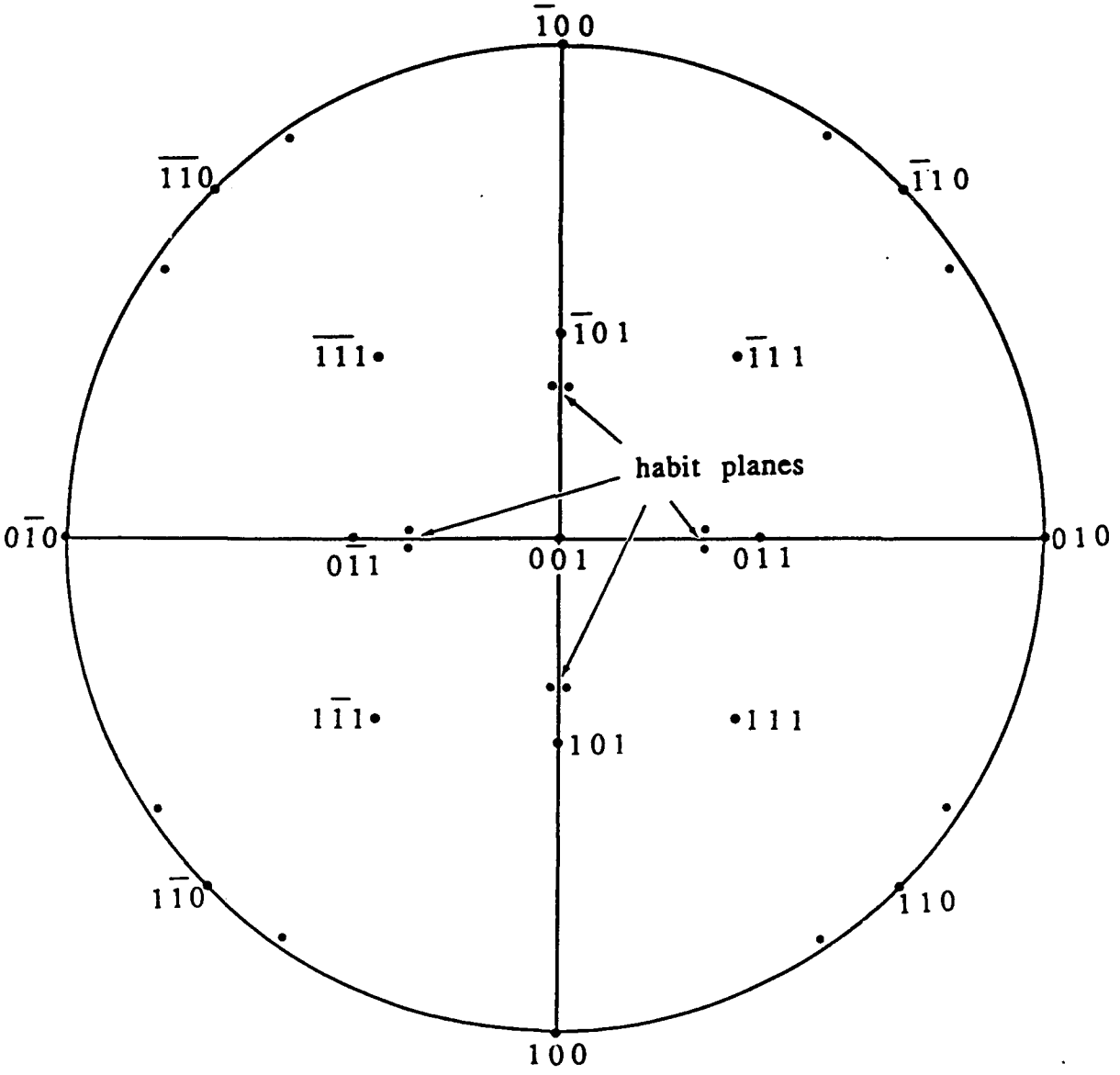
$\bar{1}00$
$\bar{1}\bar{1}0$
$\bar{1}10$
$\bar{1}01$
$\bar{1}\bar{1}\bar{1}$
$\bar{1}11$
habit planes
$0\bar{1}0$
$0\bar{1}\bar{1}$
001
011
010
$1\bar{1}\bar{1}$
111
101
$1\bar{1}0$
110
100

Fig. 5

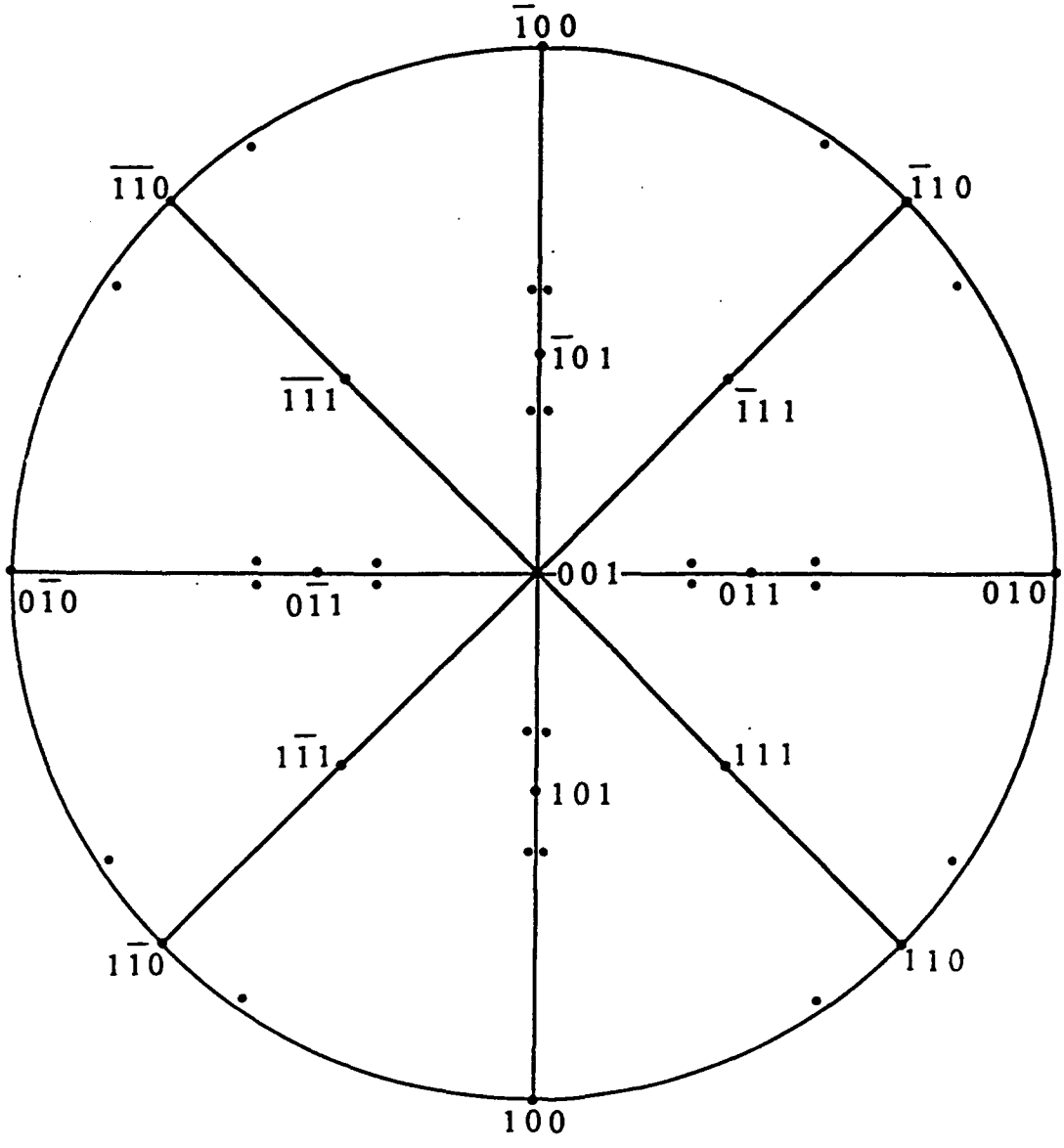
$\bar{1}00$
$\bar{1}\bar{1}0$
$\bar{1}10$
$\bar{1}01$
$\bar{1}\bar{1}\bar{1}$
$\bar{1}11$
$0\bar{1}0$
$0\bar{1}\bar{1}$
001
011
010
$1\bar{1}\bar{1}$
111
101
$1\bar{1}0$
110
100

Fig. 6

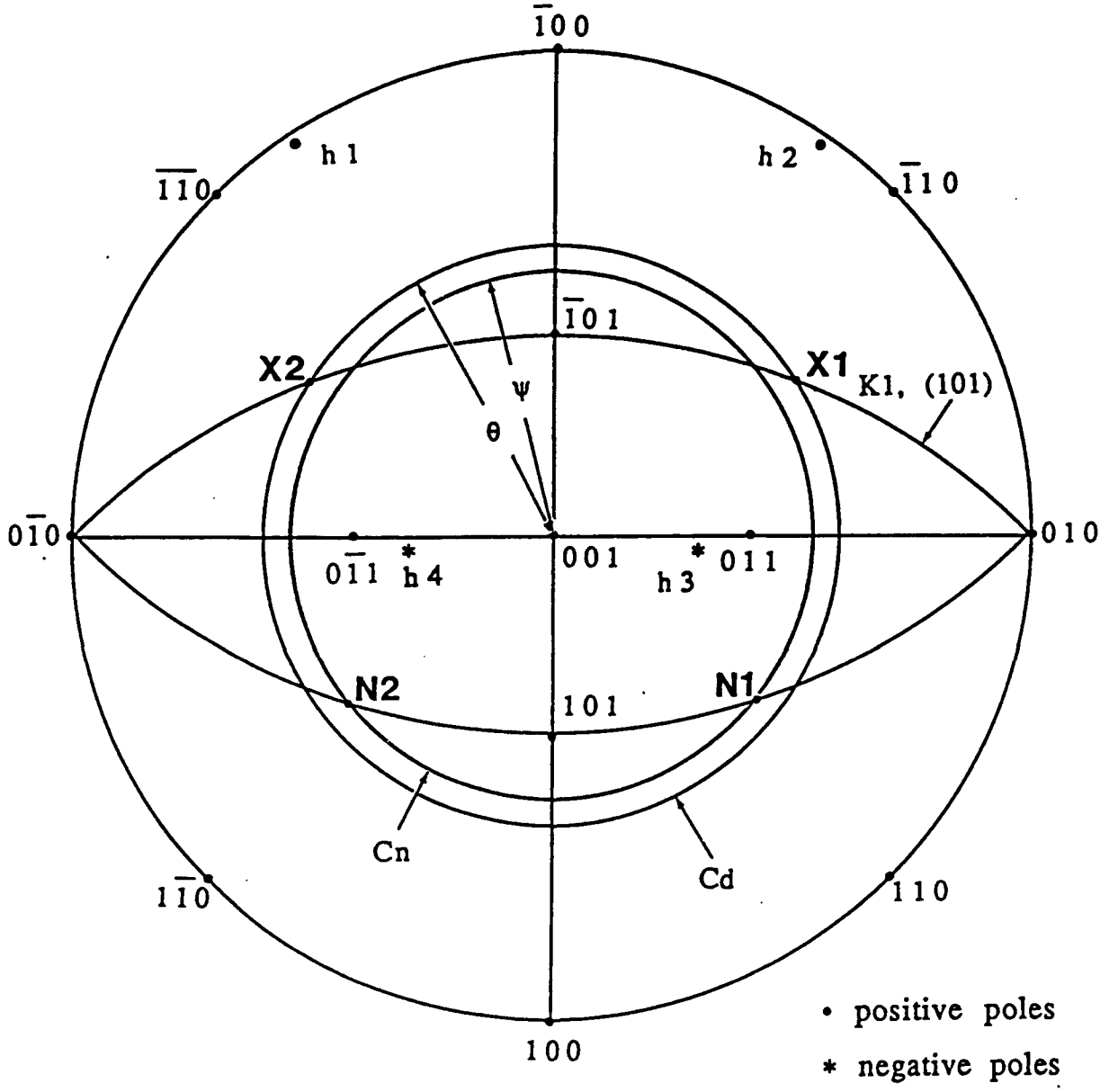
$\bar{1}00$
h1
h2
$\bar{1}\bar{1}0$
$\bar{1}10$
$\bar{1}01$
X2
X1
K1, (101)
ψ
θ
$0\bar{1}0$
010
$0\bar{1}1$
h4
001
h3
011
N2
N1
101
Cn
Cd
$1\bar{1}0$
110
100
• positive poles
* negative poles

Fig. 7

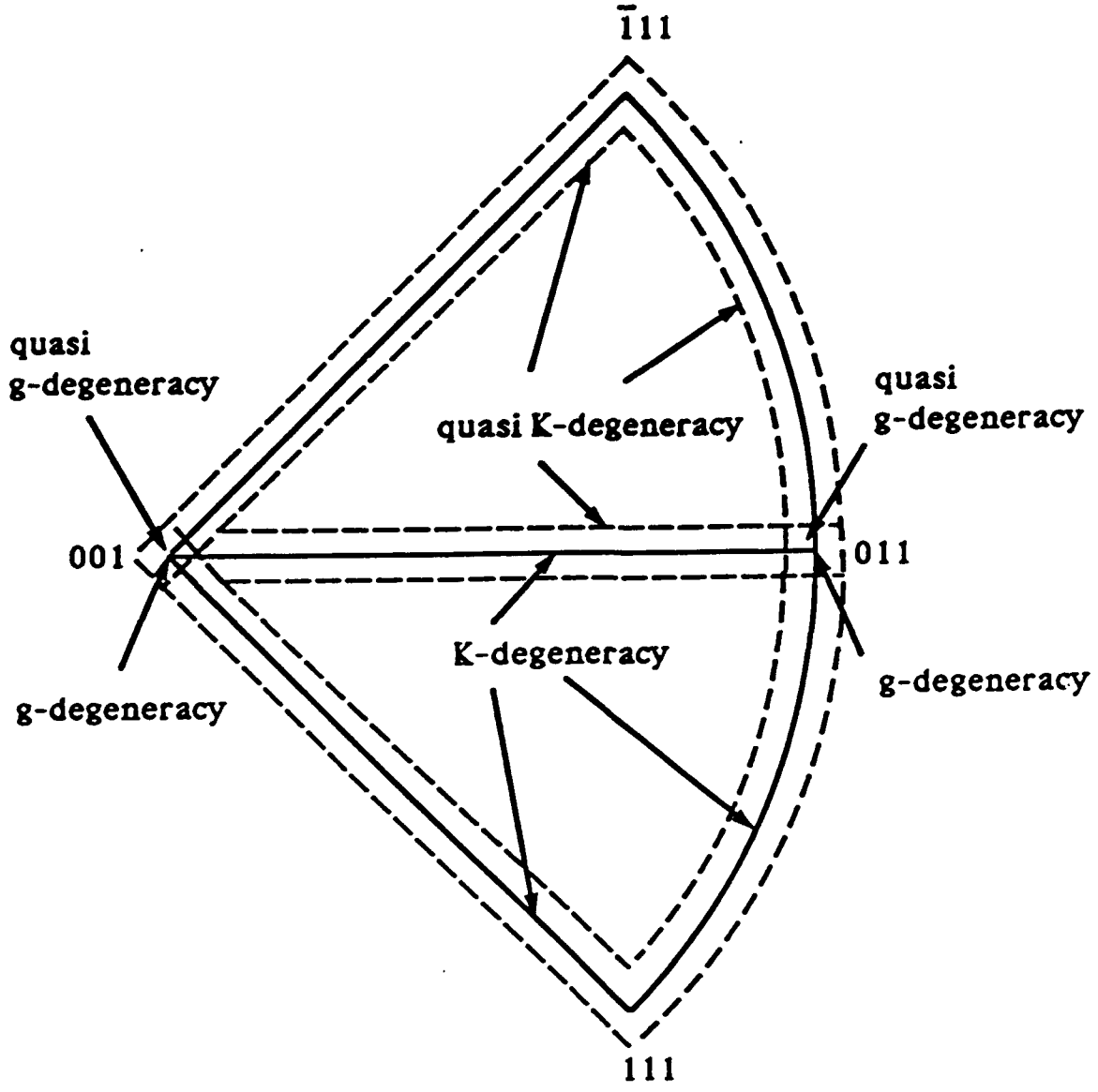
$\bar{1}11$
quasi
g-degeneracy
quasi K-degeneracy
quasi
g-degeneracy
001
011
K-degeneracy
g-degeneracy
g-degeneracy
111

Fig. 8

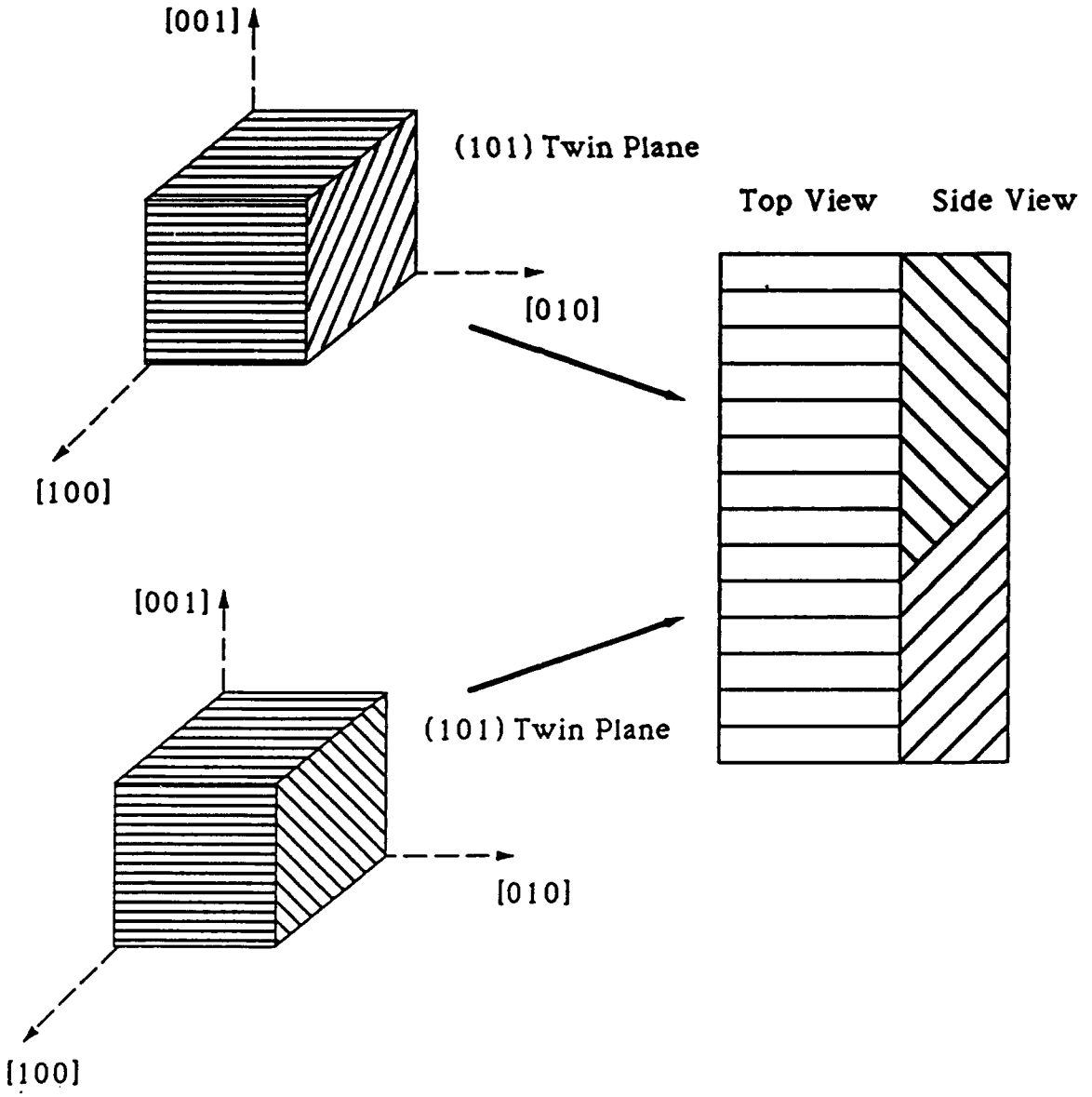
[001]
(101) Twin Plane
Top View
Side View
[010]
[100]
[001]
(101) Twin Plane
[010]
[100]

Fig. 9 (a)

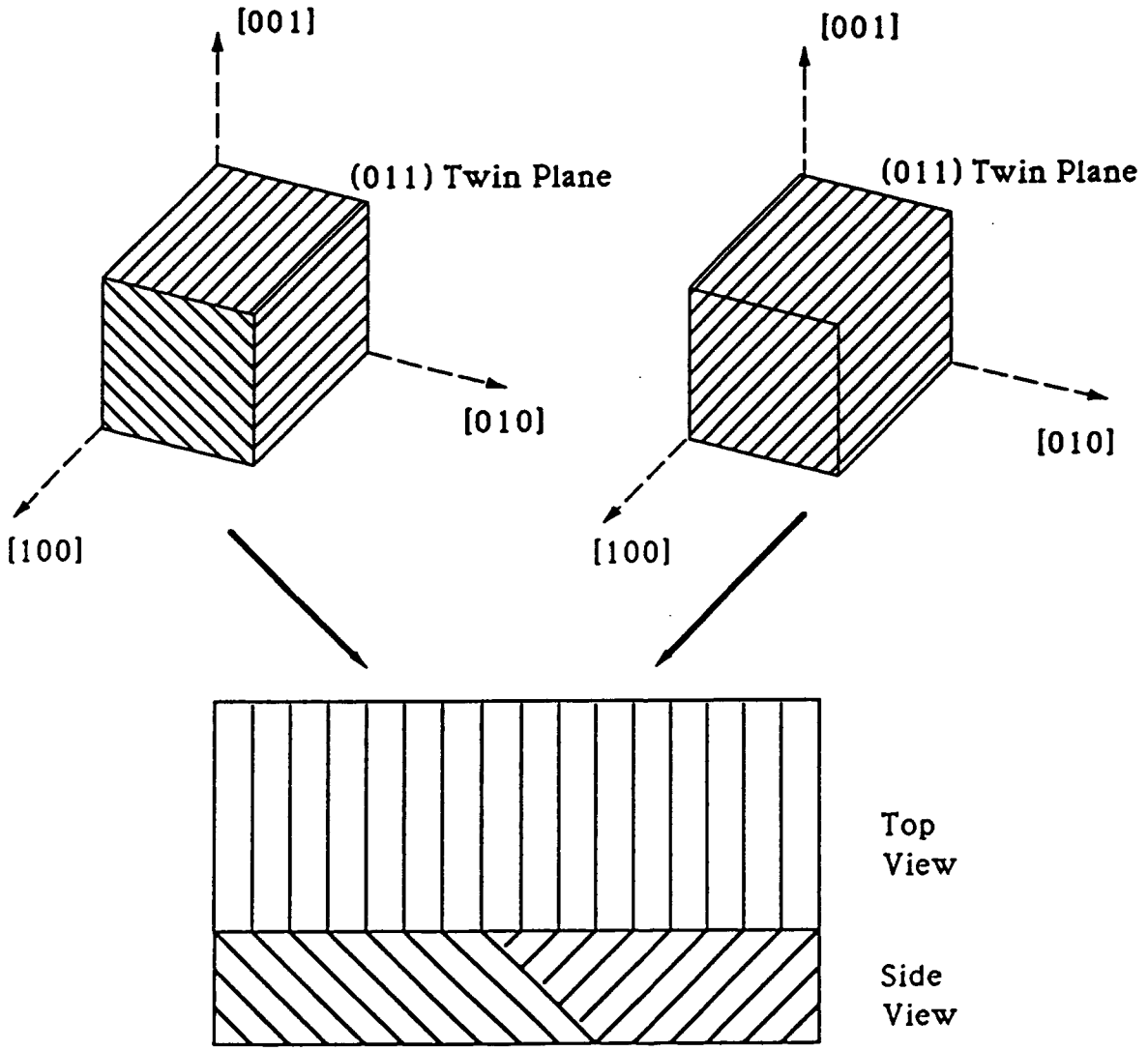
[001]
(011) Twin Plane
[010]
[100]
[001]
(011) Twin Plane
[010]
[100]
Top
View
Side
View

Fig. 9 (b)

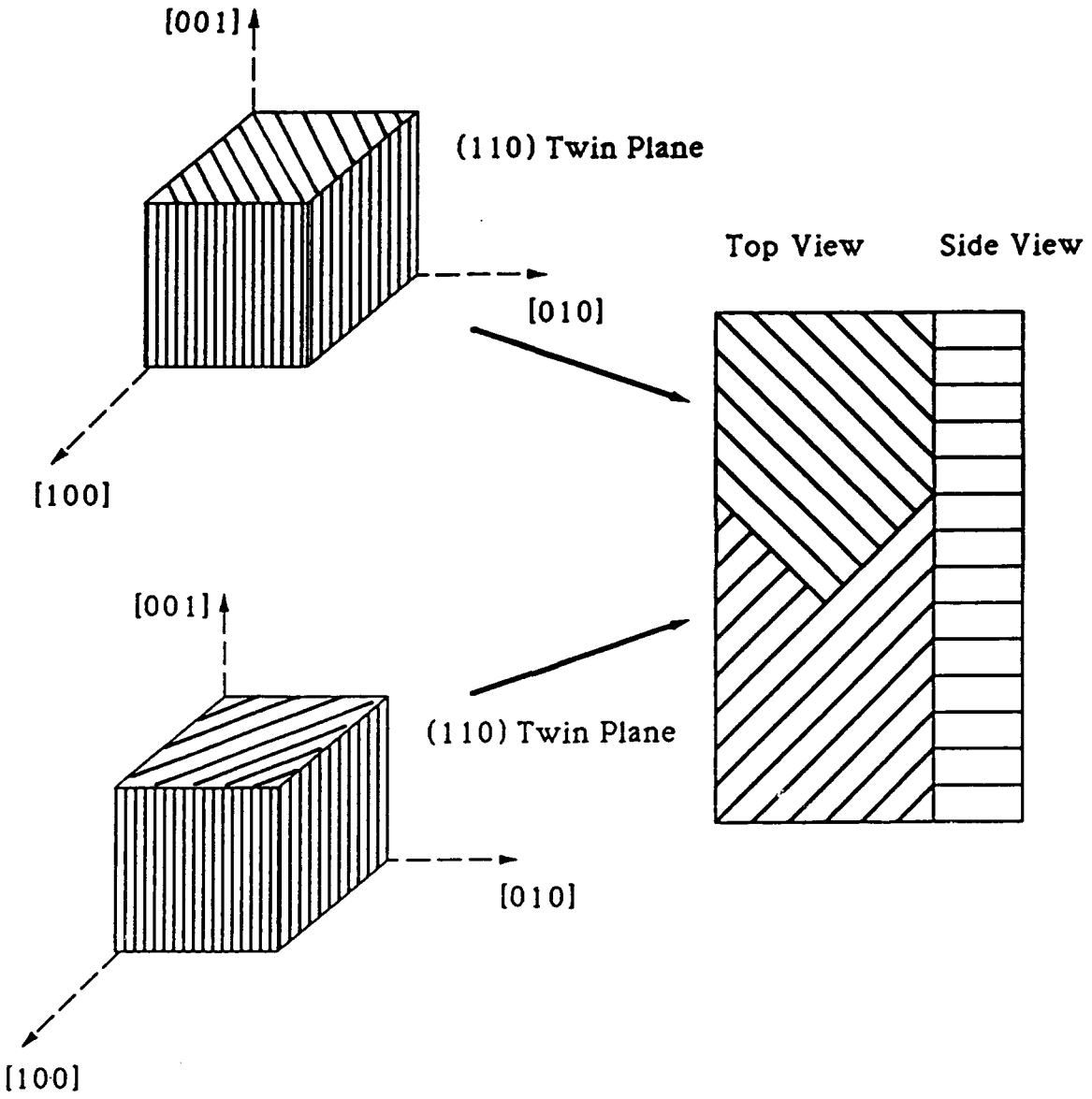
[001]
(110) Twin Plane
Top View
Side View
[010]
[100]
[001]
(110) Twin Plane
[010]
[100]

Fig. 9 (c)

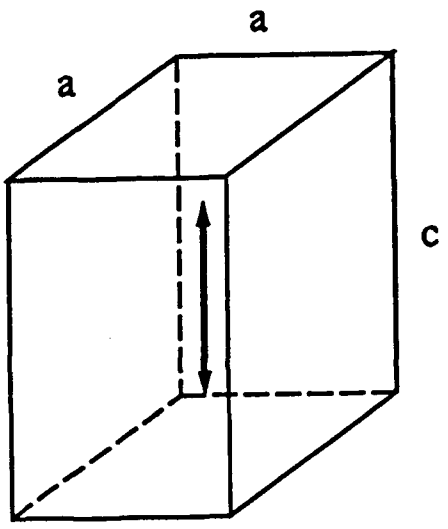

"c" domain

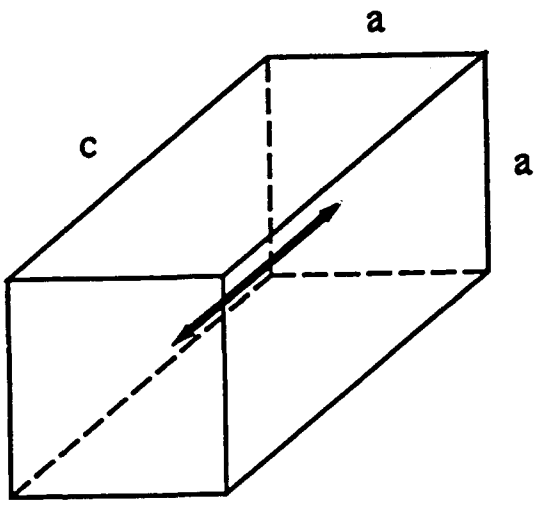

"a" domain

Fig. 10(a)

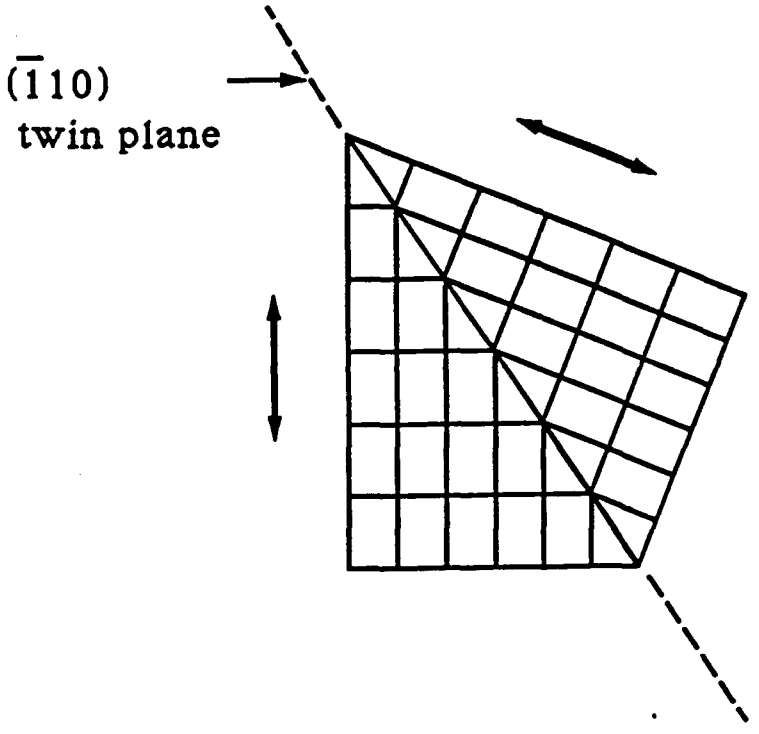

Fig. 10 (b)

Habit Plane Variants in Ferroelectric Lead Titanate Crystals II. Experimental Observations

Li-chang Yang and C.M. Wayman

Department of Materials Science and Engineering,
University of Illinois at Urbana-Champaign, Urbana, IL 61801

Abstract

A detailed study of the domain structures and habit plane variants in lead titanate is reported. From crystallographic martensitic calculations, it is found that there are twenty-four habit plane variants. For each variant, it is possible to observe a microstructure with two crystallographically equivalent twinning elements. A complete investigation regarding the three dimensional domain arrangements, domain orientations, and possible twin planes, has been conducted using optical microscopy, scanning electron microscopy (SEM) and electron back scattering patterns (EBSP). The results indicate that the most common domains, such as parallel bands and herringbone structures, consist of simply habit plane variants as predicted from the crystallographic martensite theory.

1. Introduction

In part I [1], theoretical martensite calculations were carried out to redefine the domain structures in lead titanate. It was found that twenty-four habit plane variants exist and that the 90 degree domains are substructures of the variants. Previous work also suggests two possible twinning elements for each domain band (or variant). They are energetically and crystallographically equivalent.

To verify the concept of habit plane variants, it is necessary to observe the twinning elements and variants experimentally. Several techniques were reported to be effective in observing domains and domain boundaries in the ferroelectric materials. For instance, optical microscopy [2], scanning electron microscopy (SEM) [3], or more advanced transmission electron microscopy (TEM) [4] [5] are standard methods employed for studying ferroelectric domains. Using these techniques, some fundamental understanding of domains has been achieved. As discussed in part I [1], in a tetragonal ferroelectric material there are only four different domain boundaries: 90 degree a-c and a-a, and 180 degree a-a and c-c types [3]. 180 degree domains do not form a twin structure whereas the 90 degree type forms a twin-related domain structure and the boundary is {101}. This information provides a basic understanding of the domain structures as well as the terminology "domains" and "domain boundaries" which have been used for years. Our interests in studying lead titanate crystals have been mainly on the characteristics of the transformation and its relation to the observed domain microstructures.

Therefore, the focus is on the domain structures which are closely related to the transformation, or martensitically speaking, the habit plane variants.

In this work, both optical microscopy and SEM were used to investigate the habit plane variants. From surface image contrast, one may be able to distinguish "a-a" and "a-c" type domains under the optical microscope. The high magnification of SEM helps in improving the resolution and, as will be shown later, may possibly provide some information on the three dimensional domain arrangements. On the other hand, crystallographic information on domains is obtained, not by TEM, but by electron back scattering patterns (EBSP) in an SEM. EBSP gives as much comparable structural information as from a TEM, i.e., the orientations of each domains and the possible twin planes. The fundamentals of EBSP are thus reviewed in the following section.

2. Electron Back Scattering Patterns

To enhance the capability of SEM, electron back scattering patterns (EBSP) were developed to provide structural phase information as well as the usual surface images. Venables et al. [6] were the first to install an EBSP in the SEM. In their system, a high energy electron beam (25 KeV) was focused onto the sample surface, and the diffracted electrons were collected by a fluorescent screen. The resulting Kikuchi-like diffraction patterns consist of several conic pairs, representing the intersections of diffracted cones (which satisfy Bragg's law), with the screen. Figure 1

shows a typical EBSP pattern from lead titanate. It is noted that there are several conic pairs and some intersections between the pairs. The corresponding diffraction plane of each conic pair locates exactly between the two conics. The intersections of the conic pairs give the positions of zone axes. A schematic diagram, Fig. 2, explains the fundamentals of conic pairs and zone axes in an EBSP. Structural phase information regarding the crystal orientation, phase identification, and lattice parameters can be extracted from the EBSP patterns by analyzing the interzonal angles and interplanar angles between the zone axes and conic pairs [7].

The fundamental mechanisms of EBSP differ from conventional SEM or TEM techniques in several aspects. First, instead of using secondary electrons, EBSP uses high energy back scattered electrons. And secondly, the substrate ot an EBSP specimen is usually tilted with respect to the beam, since the generation of back scattered electrons is more efficient when the substrate is tilted. The tilting angle was presently chosen to be 70.5°. One significant effect of tilting the substrate is that the diffraction patterns obtained exhibit the characteristics of a gnomonic projection. The distance between any two zone axes in a gnomonic projection is not in proportion to the interzonal angles. The interzonal angles must be measured with respect to the pattern center, or the beam center, which requires the use of a standard sample to locate the pattern center. Another effect of the tilting substrate is foreshortening of the image along one side, which limits the uses of EBSP. It has been found that the effect of foreshortening becomes more critical when the sizes of the microstructures are within the spatial resolution of EBSP, i.e., 200 nm. For

lead titanate the domain sizes are around 0.5 - 1.0 μm, which is about the spatial resolution of EBSP. Sometimes, it is difficult to obtain an EBSP for a particular domain.

Although there are limitations, EBSP is very effective in identifying domain structures in lead titanate [8]. The tetragonal phase of lead titanate at room temperature has a c/a value of 1.06, which is just above the limitation of EBSP, i.e., 4% measurement error in the lattice parameters. Three different EBSP patterns representing three possible polarization directions of a tetragonal unit cell have been obtained. A simple rule regarding the identification of domain orientations from these EBSP patterns has been developed [8], based upon the measurement of interzonal angles between two major zone axes. Detailed analysis of EBSP patterns is not repeated here, however, the results from previous work [8] are summarized in Table 1. In an EBSP pattern of lead titanate, as illustrated in Fig. 1, there are two major zone axes, <100> and <110>. The interzonal angles between the two major zone axes gives sufficient information to determine the domain orientation. For instance, a small interzonal angle, 43.2°, represents a "c" domain. Whereas if the interzonal angle is 45.0° or larger, then the domain is an "a" domain. The possible polarization direction of an "a" domain depends on the exact value of the interzonal angle. For the 45.0° case, the polarization vector of this "a" domain locates perpendicularly to the line joined by the two major zone axes and the domain is denoted as an "a↔" domain. On the other hand, if the interzonal angle is 46.8°, then the polarization direction is in the joined line and is an "a↕" domain. With this simple rule, the crystal

orientations of each domain in the habit plane variants can be easily identified. The meanings of a↔ and a↕ are also shown in Table 1.

Other important crystallographic information which may also be obtained from EBSP are the possible twin planes and twinning shear. As discussed above, an EBSP pattern of each domain is obtained by focussing the electron beam onto an individual domain area. However, when the electron beam straddles a domain boundary, a superposed EBSP pattern is obtained. This superposed pattern consists of a pattern from each domain, and shows symmetry about the twin plane normal. Thus the possible twin plane and twinning shear may be determined by analyzing the symmetry of EBSP patterns and their relative rotation. Determining the twinning shear from an EBSP pattern is a little different than in TEM. Due to the distortion introduced by the gnomonic projection, it is inappropriate to measure the interplanar angles directly from an EBSP. One must instead measure them with respect to the pattern center. Detailed analyses of the interplanar angles and twin planes will be discussed later.

3. Experimental Observations on Habit Plane Variants

3.1 Image Contrast Revealed from Optical Microscopy

According to theoretical calculations [1], two crystallographically equivalent twin planes may occur in each habit plane variant. Therefore, it is of interest to observe these twin planes experimentally. Some evidence on habit plane variants from optical microscopy is presented in Figure 3 in which the microstructure of three variants is shown. Sharp

image contrast was observed in variants "A", indicating that the domains are of the "a-c" type, and according to Fig. 9(a) from part I [1] these variants must have either (101) or $(\bar{1}01)$ twin planes. The twin planes in variants A, however, are not perpendicular to the plane of the surface, but are tilted at 45 degrees to the surface. Variant "B" shows very little contrast, but with some faint lines running at 45 degrees across the variant. According to Fig. 9(c) [1], this is a variant with a (110) twin plane. The twin planes in this case are perpendicular to the plane of the micrograph. The junction planes separating variants A and B, as marked by "j", are noted to be not very straight, in contrast to the straight traces of twin planes.

3.2 Three Dimensional Domain Arrangements Observed by SEM

There is a limitation of using optical microscopy to observe domain structures in lead titanate. The sizes of variants, as seen from Fig. 3, are between 20 to 100 μm, which can be easily recognized under an optical microscope. However the fine structures in each variant, especially those in the "a-a" domains, are hardly distinguished, because they are about 1 μm or smaller, which is beyond the resolution of optical microscopy. Also the depth of focus of the optical microscope is low, and it is almost impossible to see three dimensional domain arrangements. Scanning electron microscopy, however, provides the advantages of high magnification and high depth of focus. Three dimensional domain structures may be easily observed with SEM. A micrograph of an etched sample is shown in Fig. 4(a). The interesting finding here is that the twin planes of two variants, as seen from the side, are different, although they

all show parallel trace lines on the surface. Comparing to Fig. 9(b) [1], one variant is thus identified with an (011) type twin plane and the other with $(0\bar{1}1)$. Not only can one find two types of twin planes in two variants, but also it is possible to observe two different twin planes within one variant. As illustrated in Fig. 4(b), there are two different twin planes in this variant. These SEM results clearly support the ideas of habit plane variants as predicted from theoretical calculations: that for each variant there are two crystallographically equivalent substructures. As mentioned in part I [1], it is easy to see two different twin planes for variants with (110) and $(\bar{1}10)$ type twin planes only from the surface. One case is Fig. 4(c), where two variants are shown. Variant A on the left is an "a↕c" type domain, whereas variant B on the right is an "a-a" type. It is clearly seen that two types of twin planes are within variant B: (110) and $(\bar{1}10)$. Both are in the edge-on orientation.

Three dimensional domain arrangements in lead titanate are not as simple as implied from the surface. Due to the possibility of forming two types of twin planes in one variant, the twinning elements may change from one type to another just within a few μm below the surface. Figure 4(d) illustrates the changes of twin planes within one variant. As a result, for an as-grown lead titanate crystal it is almost impossible to claim that a variant with only one type of twin plane is obtained, even if only one type of twin plane is observed on the surface.

3.3 Domain Orientation and Possible Twin Planes Identified by EBSP

Crystallographic aspects of domain structures in parallel bands and

herringbone type domains are considered in this section. EBSP, as discussed in the above, is very effective in revealing the domain structures. The domain orientation as well as the twinning shear can be obtained by analyzing the interzonal angles and interplanar angles. However, both of these analyses require the position of the pattern center. It is thus necessary to have an EBSP measurement made on a standard silicon crystal first to locate the pattern center. The conditions for all measurements were chosen as 30 Kev and 31 mm working distance. Figure 5 shows an EBSP pattern from [100] silicon. Since the substrate holder was tilted at 70.5^{o}, the electron beam from the prominent [114] zone of the cubic crystal will hit the phosphor screen perpendicularly. Therefore, the pattern center locates exactly at the position of the [114] zone from a silicon EBSP pattern. A lead titanate single crystal with both parallel bands and herringbone type domains, as shown in Fig. 6, was then inserted into the SEM. All EBSP measurements were conducted on that sample without taking out the sample or recalibrating the system.

3.3a Parallel Bands

As seen from optical micrographs, parallel bands contain alternate domain bands. The examination of domain structures in parallel bands was conducted by focussing the electron beam at the individual domains and the twin boundaries of each of the bands. Three EBSP patterns from each band, as shown in Fig. 7, were taken. Patterns 7(a), 7(b), and 7(c) are from band 1 with less image contrast, whereas patterns 7(d), 7(e), and 7(f) are from adjacent band 2 with parallel trace lines. Detailed analyses

on these EBSP patterns for domain orientation identification were carried out by measuring the interzonal angles [8]. The angles between two <100> and <110> zone axes were obtained by determining the coordinates of two zone axes with respect to the pattern center, and then calculating the inverse cosine of the scalar product of the two zone axes vectors. Using this method, three different interzonal angles were obtained, representing three possible domain orientations. A simple rule [8] based on the interzonal angles between <100> and <110> zone axes was established from which the polarization vectors of each domain are uniquely determined. According to this rule, pattern 7(a) represents an "a↔" domain whereas pattern 7(b) indicates an "a↕" domain; this gives band 1 a structure of "a-a" type domains. On the other hand, patterns 7(d) and 7(e) are found to be "c" and "a↕" domains. Therefore band 2 consists of "a↕c" type domains. These results confirm the observations from optical microscopy that parallel bands contain alternate 90 degree "a-a" and "a-c" type domains.

More interesting EBSP patterns are the ones from the twin boundaries. Patterns 7(c) and 7(f) are for bands 1 and 2, respectively. It is noted that these patterns, in fact, consist of superposed EBSP patterns from each of the twins. The possible twin planes may be identified by comparing these superposed patterns to simulated ones with particular attention to {101} planes. Schematics showing the simulated superposed EBSP patterns from "a↔", "a↕" , and "c" domains are drawn in Fig. 8. These patterns are obtained by aligning two EBSP patterns with the assumed {101} twin planes, whereas other planes are drawn accordingly. Due to

the twinning shear, they may be offset, diverged or converged. For example, Fig. 8(a) shows a superposed pattern with (110) twin plane in which the (110) planes from two domains are aligned together whereas the $(\bar{1}10)$ and (010) planes diverge due to the twinning shear. Figure 8(b) shows another example with $(\bar{1}10)$ twin plane. The (110) and (010) planes from two domains are now diverged. Comparing pattern 7(c) to 8(b), the twin plane of band 1 is thus identified as a $(\bar{1}10)$ type. A similar consideration is applied to pattern 7(f) of band 2. Superposed EBSP patterns showing (101) or $(\bar{1}01)$ type twin planes are illustrated in Fig. 8(c) and 8(d). Two patterns from "c" and "a↕" domains are aligned with the assumed twin plane which results in the separation of (100), (110) and $(\bar{1}10)$ planes. It is noted that pattern 8(c) is different from 8(d). Pattern 8(c) with $(\bar{1}01)$ twin plane shows converged (110) and $(\bar{1}10)$ plane traces, whereas these planes diverge in the case of a (101) twin plane. According to this difference, the twin plane in band 2 is identified as a (101) type. The domain structures examined here therefore consist of "a-a" and "a↕c" type domains, and the associated twin planes of each variant are $(\bar{1}10)$ and (101).

The magnitude of the twinning shear may be determined by measuring the angle extended by the two (110) planes in the superposed pattern in Fig. 7(c). It is known that due to the distortion in the gnomonic projection the angle between the two conic pairs in an EBSP pattern does not represent the true interplanar angle. The true angle must be measured with respect to the pattern center. From simple geometry, the interplanar angle is obtained by calculating the inverse cosine of two

plane normals, while the plane normal of each plane is determined by a cross product of any two vectors in the plane. Therefore, one may choose two zone axes from each plane in an EBSP, and then determine the coordinates of these with respect to the pattern center. After a cross product calculation, two plane normals are thus determined: [0.560, 0.747, -0.358] and [0.677, 0.650, -0.346]. Taking the inverse cosine of the scalar product of the two plane normals, one gets the twinning shear angle, 8.68°. The corresponding twinning shear magnitude is about 0.153, in contrast to the value calculated from S(=c/a-a/c), 0.126. The difference is about 0.027 (or 1.55°). This is quite reasonable, since there is some measurement error in determining the coordinates of the zone axes.

3.3b Herringbone Structures

Similar EBSP measurements were also carried out for the herringbone domains. Two adjacent bands, bands 3 and 4, were considered, and three EBSP patterns from each band were obtained. The results are presented in Fig. 9. Patterns 9(a), 9(b), and 9(c) are from band 3, whereas the remaining three patterns are from band 4. Using the simple rule, patterns 9(a) and 9(d) are easily identified as "c" domains and patterns 9(b) and 9(f) are "a↔" and "a↕" domains, respectively. Band 3 thus consists of "a↔c" type domains and band 4 is of "a↕c" type domains. This gives the result that herringbone structures contain only 90 degree a-c type domains, which is quite consistent with the observations from optical microscopy.

The twin plane of herringbone domains may be determined in a

similar way as that for parallel bands. One can identify the twin plane by comparing the superposed EBSP patterns to the simulated ones. Two different superposed EBSP patterns, 9(c) and 9(f), were obtained for bands 3 and 4 in herringbone domains. It is noted that pattern 9(c) shows converged (110) planes on the left and diverged $(\bar{1}10)$ planes on the right. The (010) planes in the center are offset, whereas the (100) planes are merged together. On the other hand, pattern 9(f) has converged (110) and $(\bar{1}10)$ planes. Only one merged (010) plane is seen in pattern 9(f). As evidenced from Fig. 8 pattern 9(c) has a (011) twin plane and pattern 9(f) a $(\bar{1}01)$ twin plane. The herringbone domains examined here thus consist of "a↔c" and "a↕c" domain bands, with (011) and $(\bar{1}01)$ twin planes.

4. Discussion

To treat a ferroelectric phase transformation as a martensitic type transformation is still not conventional. One needs to investigate not only the microstructures of the domains (the martensites), but also the transformation characteristics as well. In part I, we have used the crystallographic martensitic theory to define the habit plane variants, and in part II, these variants were examined thoroughly by EBSP. However, it is still desirable to discuss the characteristics of ferroelectric transformations in detail to fully explore the differences or similarities between the transformations in ferroelectrics and in metals. Several aspects regarding the transformation characteristics in ferroelectrics, such as transformation volume change, principal strains, hysteresis, and conductivity, will be addressed particularly in the following.

Most ferroelectrics exhibit a small transformation volume change and small principal strains during transformation. Lead titanate has a 0.52% volume change and 0.9959 (a/a_o) principal strains [9], which in fact resembles the cases in In-Tl [10] and the R-phase in Ni-Ti [11]. Both In-Tl and the R-phase have a martensitic transformation close to room temperature, and the volume change during transformation is very small, only -0.13% and -0.012% for In-Tl and the R-phase, respectively (Table 2). Moreover, the magnitude of principal strains in these materials are on the same order. Therefore, there is no reason to disqualify ferroelectrics as martensite, even if small volume changes and principal strains are involved.

Secondly, the hysteresis in ferroelectric transformations is found to be very small. Within 2-5 degrees lead titanate is completely transformed into the ferroelectric state. However, one can not rule out the ferroelectric transformation as being a martensitic type transformation because of this small hysteresis, since the hysteresis in In-Tl and the R-phase is also very small: only 1-4 and 2 degrees for the In-Tl and R-phase cases (Table 2). Although the hysteresis in lead titanate is small, one can still see both martensite and parent phase at the same time by a properly designed heating stage in which a temperature gradient is maintained across the sample. Then a single-interface transformation [12] [13] may proceed as has been described before. At room temperature, lead titanate usually contains only habit plane variants, separated by junction planes.

One may argue that because of the electric charge effect there could be some differences between a transformation in ferroelectrics and one in metals. As observed by Fesenko et al. [12], the conductivity of an undoped lead titanate crystal is very high at the transformation region, e.g., $10^{-3}(\text{ohm-cm})^{-1}$, while it drops off dramatically at room temperature. Although one sees the ferroelectric effect at room temperature, the transformation strain is evidently still predominant over the electric charge effect during the high temperature transformation. At 490 °C, the habit planes {0 2 3} predicted by the martensitic theory carry the parent phase into a martensite structure, and the transformation twins, as required in a martensitic transformation to accommodate the transformation strain, are formed as a substructure within the habit plane variants.

From these various experimental considerations, the treatment of a ferroelectric transformation as a martensitic transformation is considered to be appropriate. The domains in lead titanate, as discussed in part I, may be correlated with habit plane variants through the considerations of a martensitic transformation. Banded type domains have been observed frequently in single crystal samples and ceramics [14] [15], however, it is still untraditional to use a concept from martensitic crystallographic theory to account for these microstructures. Only few papers have reported the success of using martensitic theory to characterize a transformation in ceramics, e.g., ZrO_2 [16] and $BaTiO_3$ [17]. A direct connection between the domains and transformation in ceramics is still very limited. The examination of domain bands by using optical

microscopy, SEM, and EBSP clearly demonstrates the validity of habit plane variants in ferroelectric materials. It is found from experiments that alternate bands in parallel band domains consist of "a-c" and "a-a" type domains. For herringbone domains, the domains are identified as due to "a↕c" and "a↔c" type domains. These 90 degree domains are the substructures of habit plane variants, as required by the martensitic theory.

The twin plane of variants is determined from EBSP by comparing superposed EBSP patterns to simulated ones. Four kinds of twin planes were found in the examples discussed in this paper. It is also possible to see all six twin planes in lead titanate. It must be pointed out that due to a lack of rotation freedom during EBSP measurements, one can not rotate the samples to the edge-on condition to get a more symmetrical EBSP pattern as in TEM. However, the difference between the superposed patterns is still large enough to distinguish between them. With all six simulated patterns, as illustrated in Fig. 8, {101} type twin planes for each variant may be easily identified.

Up to now, the microstructure of variants, i.e., the domain orientations and twin planes, have been thoroughly investigated. The problem not discussed in detail is the determination of the "junction planes" between the variants. Junction planes in lead titanate are deduced here to be {101} type planes. Several papers have reported that the junction planes for In-Tl [18] and Ni-Al [19] alloys, exhibiting a similar cubic-to-tetragonal transformation, belong to {101} type planes.

Schroeder and Wayman [20] discussed the relationship between the junction plane and twin planes in Cu-Zn alloys. They found that the junction plane is a bisecting plane between two variants, which would intersect the twin planes of each variant and provide a mirror reflection between them. From EBSP measurements, we found that the twin planes in parallel bands are (101) and $(\bar{1}10)$ planes. The junction plane* in this case must be the (011) plane. In a stereographic projection, Fig. 10(a), the great circles of two twin planes from adjacent variants intersect at the zone axis, Z_1. The only {101} type plane which would pass through this zone axis and provide a reflection symmetry for the two twin planes is the (011) plane. Similarly, the junction plane for herringbone type domains may also be determined from a stereographic projection. Since the twin planes of herringbone domains are $(\bar{1}01)$ and (011) type planes, the junction plane for this herringbone structure, as determined from the stereographic projection, is (110), Fig. 10(b).

5. Conclusions

In this paper, the microstructures of habit plane variants have been investigated by using optical microscopy, SEM, and EBSP. Optical micrographs clearly indicate that the images of "a↕c" and "a↔c" type domains show more contrast than "a-a" type domains. SEM micrographs provide further evidence on the three dimensional domain arrangements and confirm that for each habit plane variant there are two possible

*The junction plane considered here is only limited to the examples which were discussed in this paper. Other cases may be possible if different combinations of twin planes are involved.

twinning elements. By analyzing the interzonal and interplanar angles from EBSP, crystallographic information regarding the domain orientations and the twinning shear were obtained. The twin plane is determined by comparing superposed EBSP patterns to simulated ones. It is found that parallel bands consist of alternate "a-c" and "a-a" type domains, and the twin planes belong to {101} type. On the other hand, herringbones are formed with alternate "a↕c" and "a↔c" type domains. The junction planes separating the habit plane variants in the parallel bands and in herringbone domains are both identified as {101} type planes.

Therefore, given the above crystallographic characteristics, in addition to the transformation hysteresis, principal strains, and volume change, we consider the cubic-to-tetragonal transformation in $PbTiO_3$ to be fundamentally martensitic in nature.

Acknowledgements

This work was supported by the Air Force Office of Scientific Research under an URI program and by the Army Research Office. Their support is gratefully acknowledged.

References

[1] L.C. Yang and C.M. Wayman, Part I.

[2] J.A. Hooton and W.J. Merz, Phys. Rev., Vol. 98, No. 2 (1955), pp 409-413

[3] Y.H. Hu., H.M. Chan, Z.X. Wen, and M.P. Hamer, J. Amer. Cer. Soc., Vol. 69, No. 8 (1986), pp 594-602

[4] M. Tanaka and G. Honjo, J. Phys. Soc. Japan, Vol. 19, No. 6 (1964), pp 954-970

[5] V.V. Shakmanov and G.V. Spivak, Sov. Phys. Solid State, Vol. 10, No. 4 (1968), pp 802-806

[6] J.A. Venables and C.J. Harland, Phil. Mag., Vol. 27 (1973), pp 1193-1200

[7] D.J. Dingley and K. Baba-Kishi, Scanning Electron Microscopy, Vol. 1986, part II (1986) pp 383-391

[8] L.C. Yang, I. Dumler and C.M. Wayman, Mat. Chem. and Phys., in press.

[9] G. Shirane and S. Hoshino, J. Phys. Soc. Japan, Vol. 6, No. 4 (1951), pp 265-270

[10] L. Guttman, Trans. AIME, Vol. 188 (1950), pp 1472-1477

[11] C.M. Wayman, Japan Institute of Metals, Proc. of International Conference on Martensitic Transformations, (1986), pp 645-652

[12] E.G. Fesenko, M.A. Martynenko, V.G. Gavrilyatchenko and A.F. Semenchev, Ferroelectrics, Vol. 7 (1974), pp 309-310

[13] C.C. Chou and C.M. Wayman, Mat. Trans. JIM, Vol. 33, No. 3 (1992), pp 306-317

[14] F. Kulcsar, J. Amer. Cer. Soc., Vol. 39, No. 1 (1956), pp 13-17

[15] G. Arlt and P. Sasko, J. Appl. Phys., Vol. 51, No. 9 (1980), pp 4956-

4960

[16] G.K. Bansal and A.H. Heuer, Acta Metall., Vol. 22 (1974), pp 409-417

[17] M. DiDomenico, Jr. and S. H. Wemple, Phys. Rev., Vol. 155 (1967) pp 539-545

[18] A.H. Geisler, Acta Metall., Vol. 2 (1954), pp 639-642

[19] S. Chakravorty and C.M. Wayman, Metall. Trans. A, Vol. 7A (1976), pp 555-568 and 569-582

[20] T.A. Schroeder and C.M. Wayman, Acta Metall., Vol. 25 (1977), pp 1375-1391

Figure Captions

Fig. 1 A "c" domain EBSP pattern for lead titanate. Note the two major zone axes, (001) and (101). The interzonal angle between these two determines the polarization vector of the domain.

Fig. 2 A schematic diagram showing the fundamentals of EBSP. Diffracted electrons from a plane form a conic pair in an EBSP pattern. The intersection of two conic pairs gives the position of the zone axis.

Fig. 3 An optical micrograph showing three habit plane variants of parallel band domains. Variants "A" show more contrast, indicating domains are of "a-c" type. Variant "B" shows very little contrast, and is an "a-a" type domain.

Fig. 4 SEM micrographs showing three dimensional microstructures of habit plane variants. As seen from side view and indicated by arrow, (a)two different twinning elements occur in two variants. (b)two different twin planes are within one variant. (c)two variants with "a↕c" domains on the left and "a-a" domains on the right. Two twinning elements are noted in "a-a" domains. (d)Three dimensional domain arrangements showing the change of twinning elements within one variant.

Fig. 5 An EBSP pattern from a [100] silicon crystal. The pattern center locates at the [114] zone axis.

Fig. 6 A lead titanate crystal with (a)parallel bands and (b)herringbone domains. Note the optical micrograph image is reversed.

Fig. 7 EBSP patterns for a parallel bands. (a), (b), and (c) are from band 1 with less surface contrast whereas (d), (e), and (f) are from band 2 with more contrast. Domain structures of these patterns are: (a)"a↔" (b)"a↕" (d)"c" (e)"a↕", and (c)"a↔a↕" domain boundary with $(\bar{1}10)$ twin plane, (f)"a↕c" domain boundary with (101) twin plane.

Fig. 8 Schematics showing the simulated superposed EBSP patterns. Note the divergence or convergence of (110) and $(\bar{1}10)$ planes. "Bold" line indicates the twin plane position.

Fig. 9 EBSP patterns for herringbone domains. Patterns (a), (b), and (c) are for band 3, and patterns (d), (e), and (f) are for band 4. Domain structures of these patterns are: (a)"c" (b)"a↔" (d)"c" (e)"a↕", and (c)"a↔c" domain boundary with (011) twin plane, (f)"a↕c" domain boundary with $(\bar{1}01)$ twin plane.

Fig. 10 A stereographic projection illustrating the determination of junction planes for (a)parallel bands and (b)herringbone domains.

TABLE 1 Interzonal Angles Between 100 and 110 Type Zone Axes in Lead Titanate

	001 - 101 001 - 011	100 - 101 010 - 011	100 - 110 010 - 110
X-ray	43.2°	46.8°	45.0°
EBSP Patterns	Shorter	Longer	Intermediate
Domains	c-domain	a↕ domain	a↔ domain

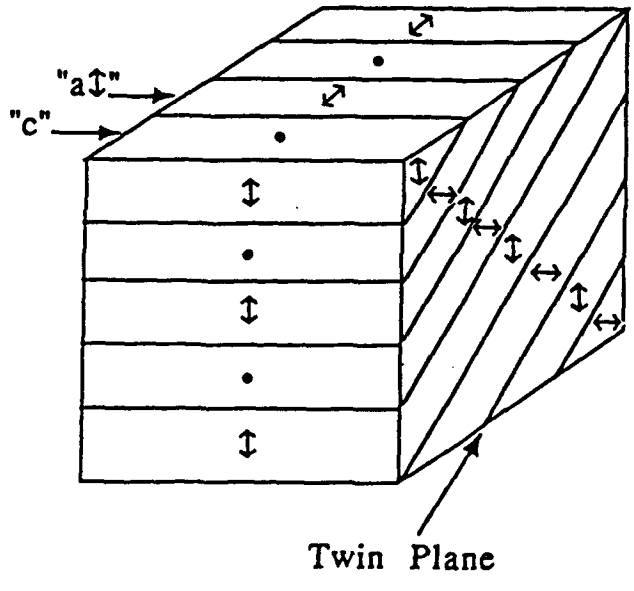

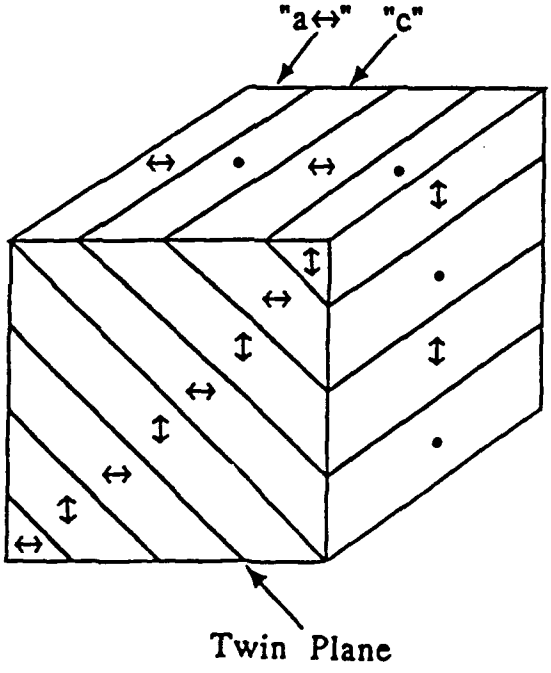

TABLE 2 Comparsions of Transformation Characteristics Between $PbTiO_3$ [9], In-Tl [10], and R-Phase in Ni-Ti [11]

	Phase Transformation	Volume Change	Principal Strains	Hysteresis
$PbTiO_3$	Cubic-->Tetragonal	0.52%	0.995958 0.995958 1.013391	2-5 °C
In-Tl	Cubic-->Tetragonal	-0.13%	0.98892 0.98892 1.021195	1-4 °C
Ni-Ti R-Phase	Cubic-->Rhombohedral	-0.012%	0.99528 0.99528 1.00938	2 °C

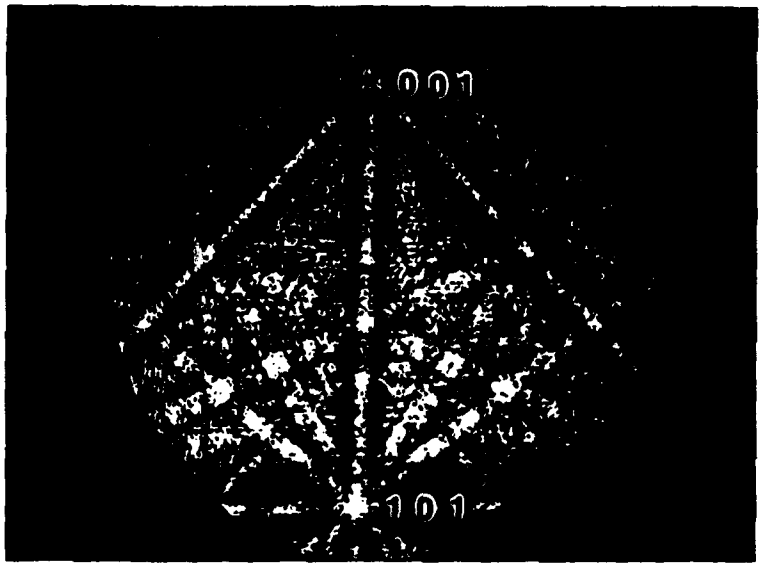

Fig. 1

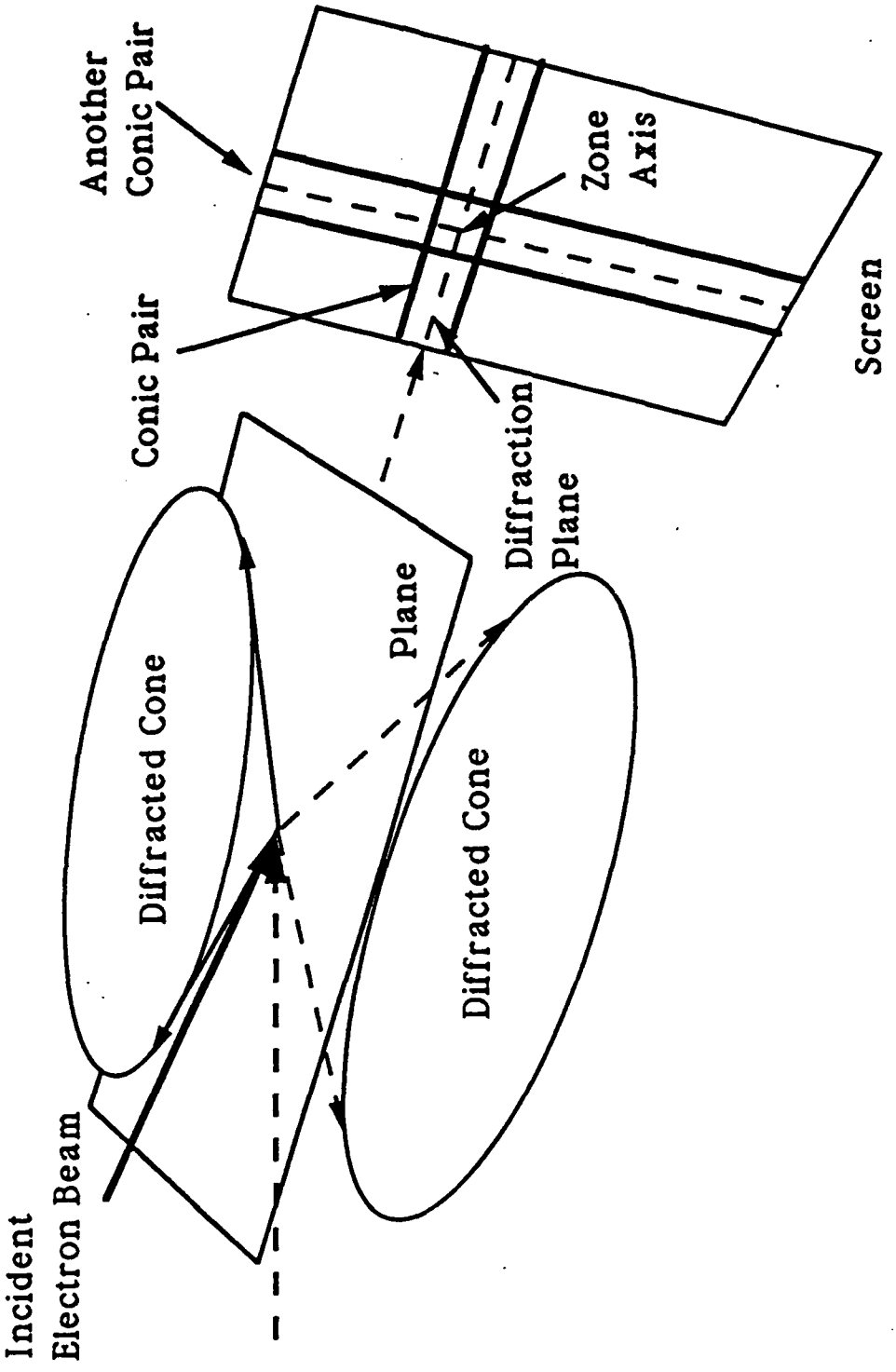
Another
Conic Pair
Zone
Axis
Conic Pair
Screen
Diffraction
Plane
Plane
Diffracted Cone
Diffracted Cone
Incident
Electron Beam

Fig. 2

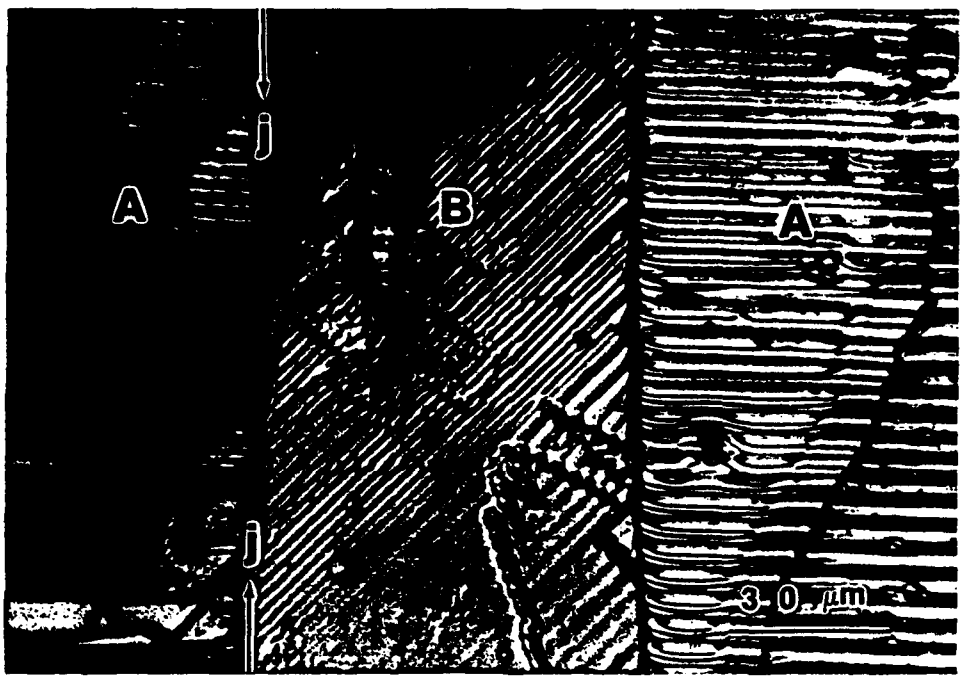

Fig. 3

Fig. 4(a)

Fig. 4(b)

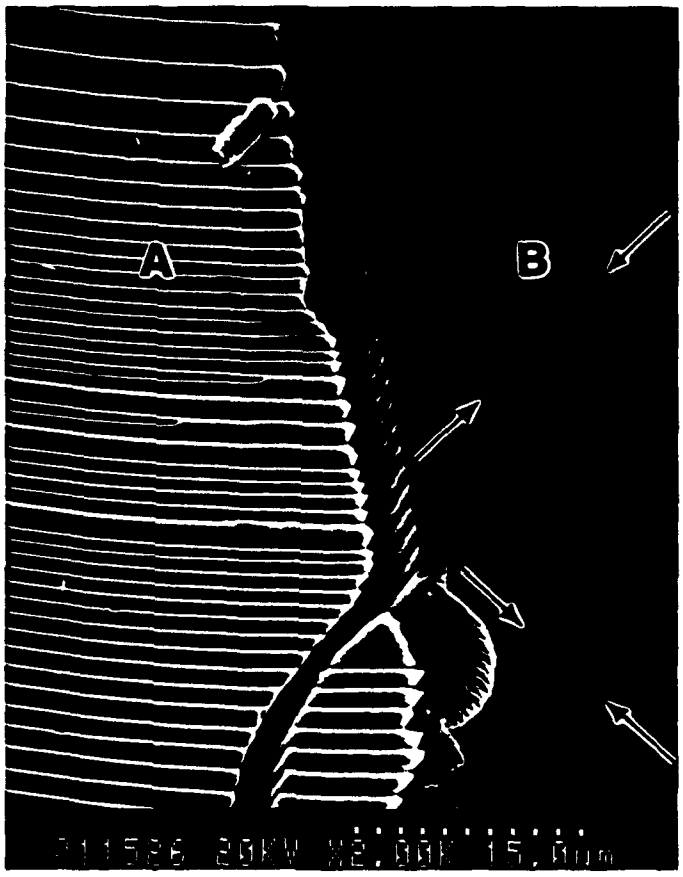

Fig. 4(c)

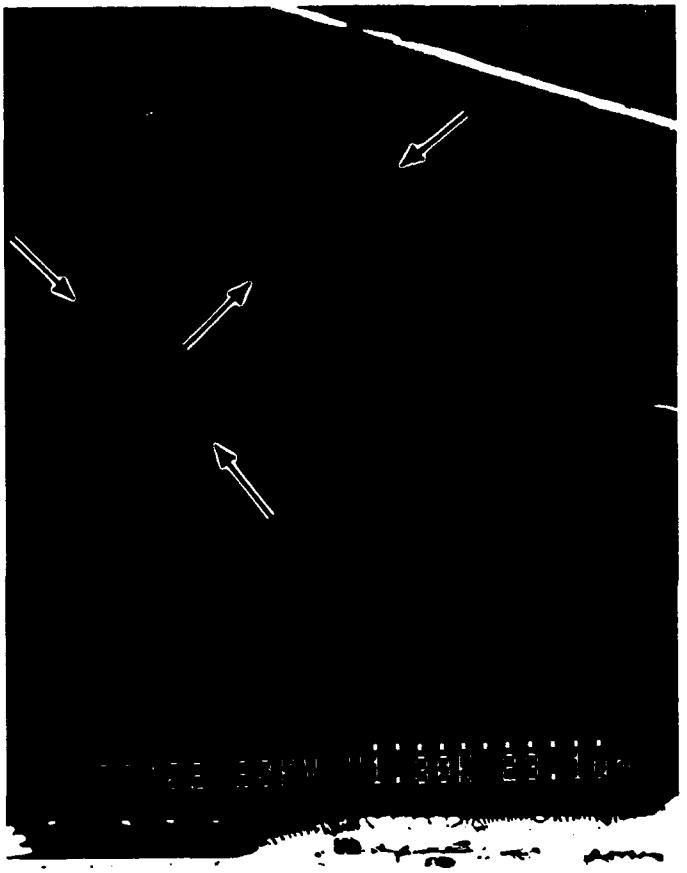

Fig. 4(d)

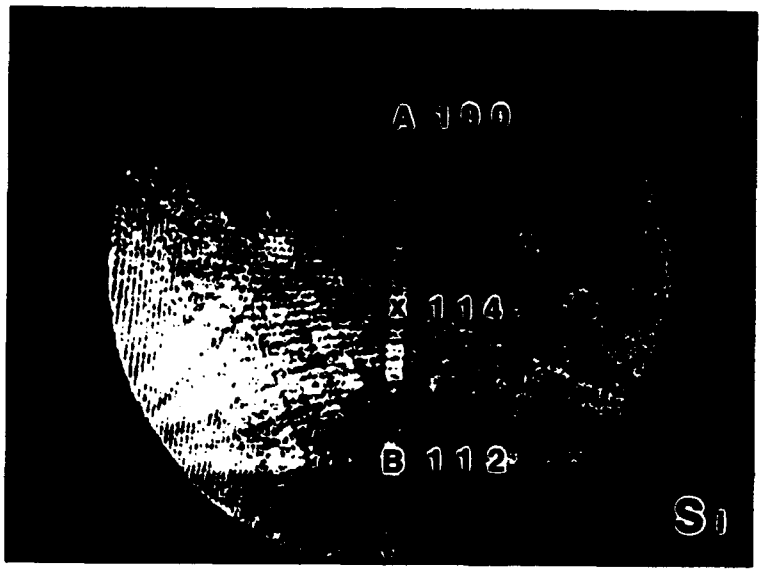

Fig. 5

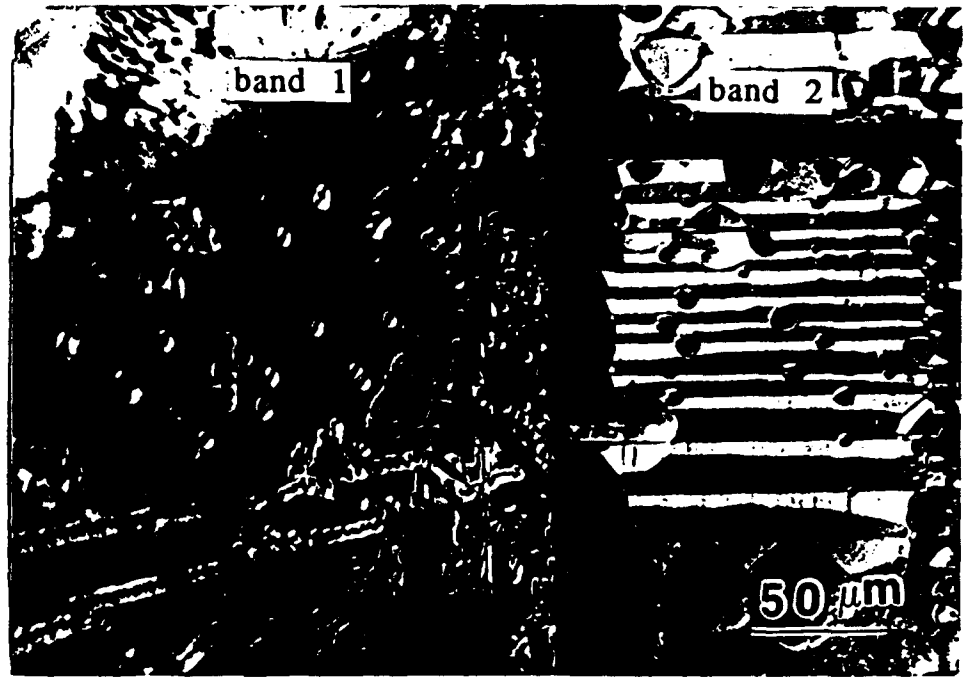

6(a)

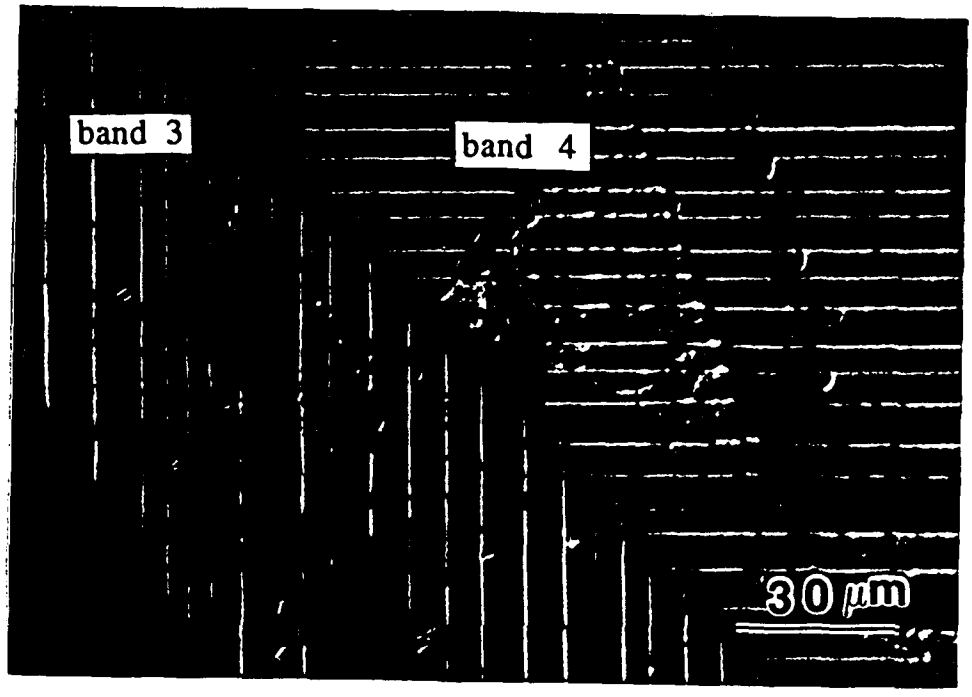

6(b)

Fig. 6

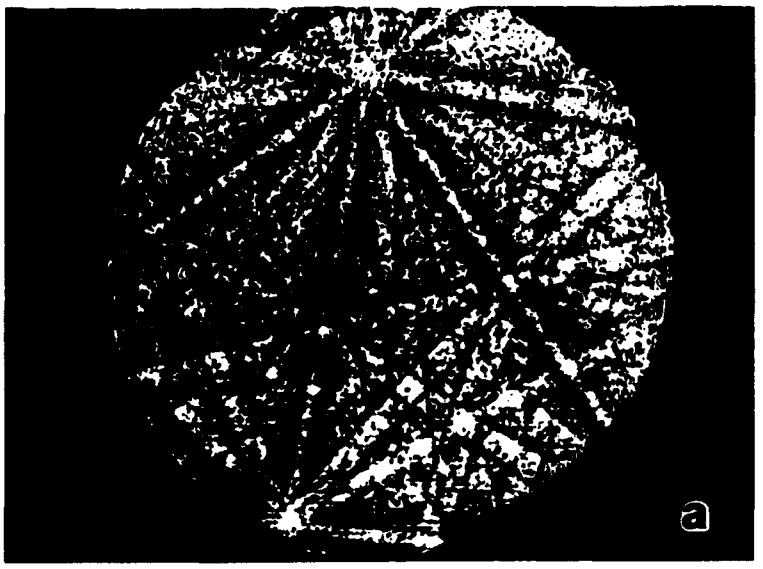

7(a)

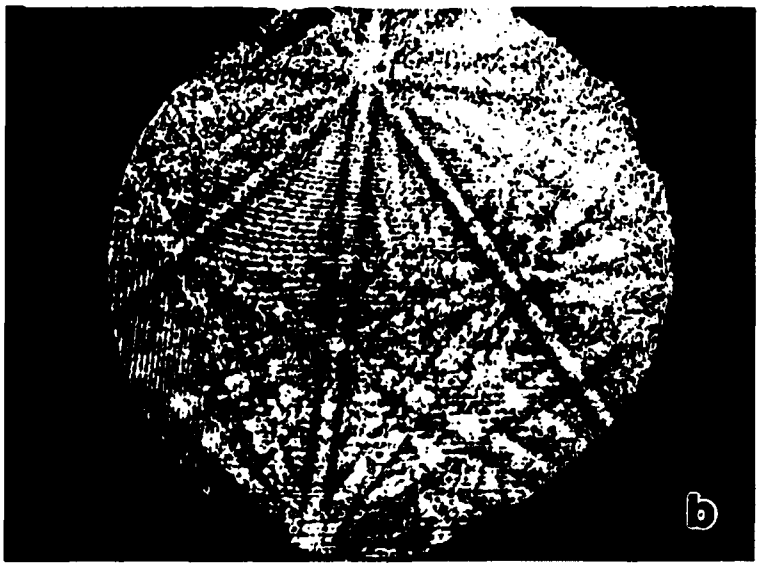

7(b)

Fig. 7

7(c)

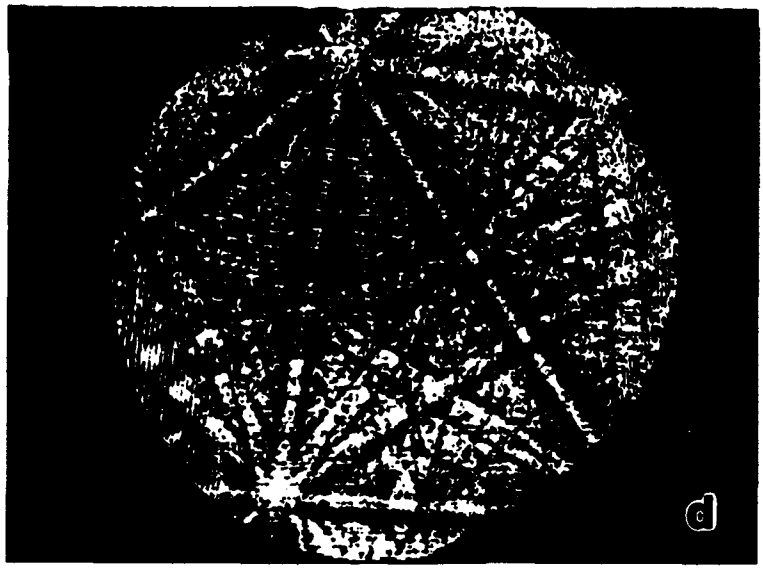

7(d)

Fig. 7

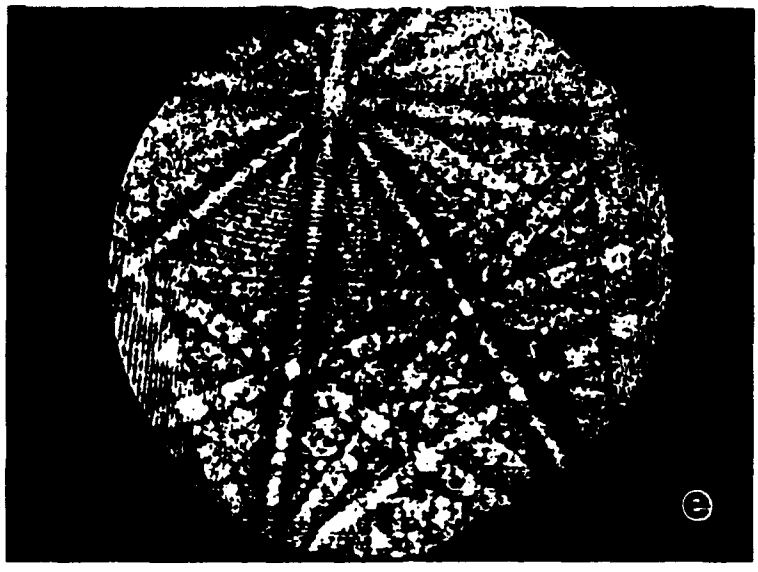

7(e)

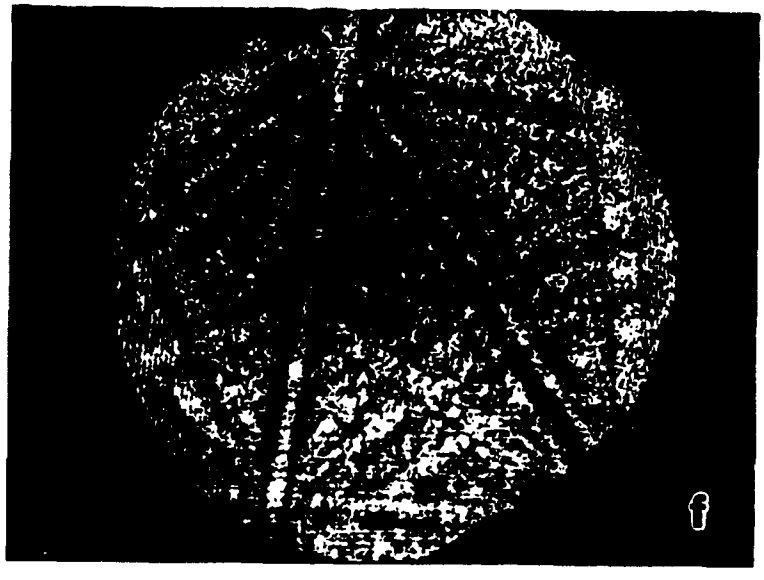

7(f)

Fig. 7

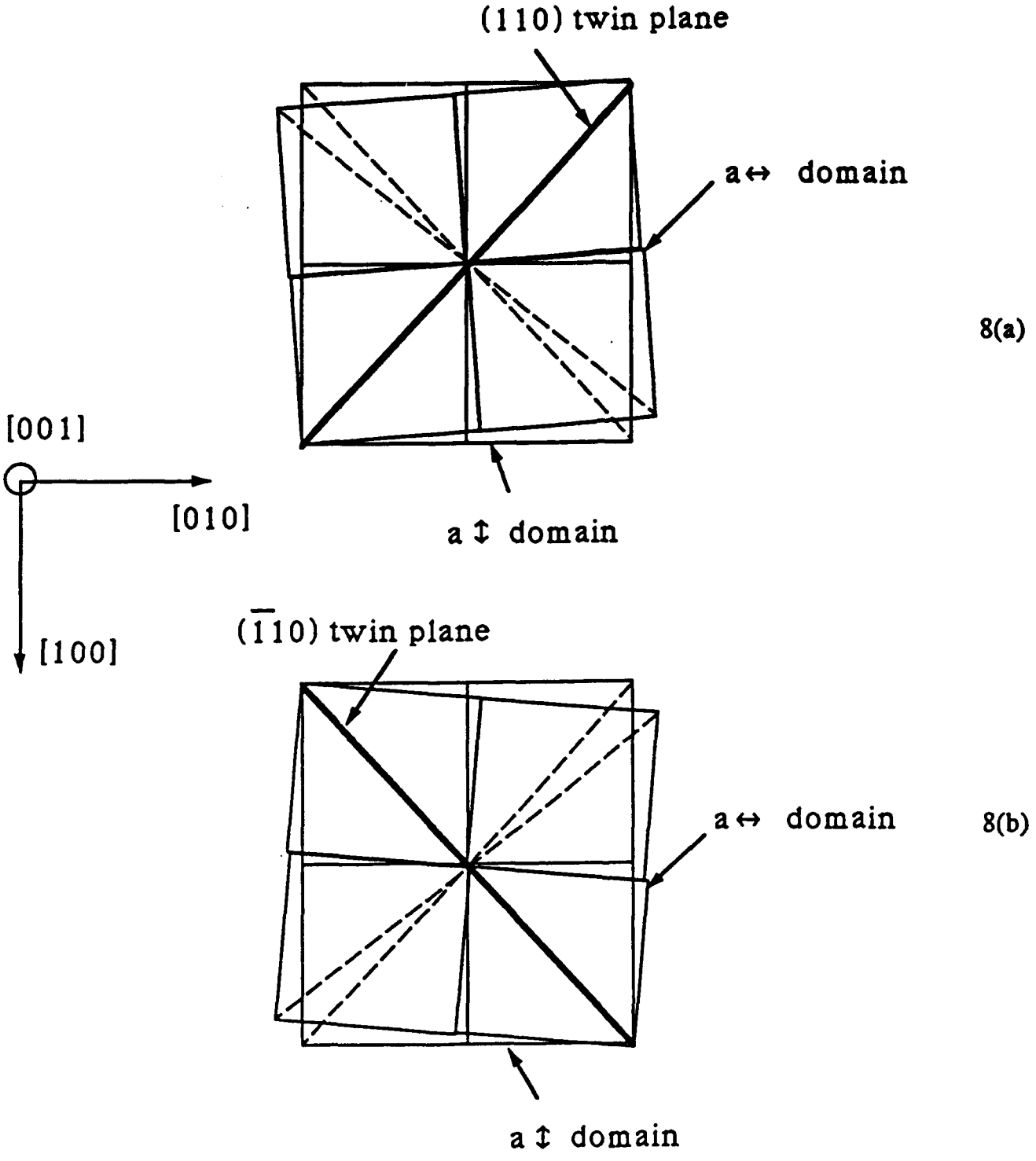
(110) twin plane
a↔ domain
8(a)
[001]
[010]
a↕ domain
[100]
(1̄10) twin plane
a↔ domain
8(b)
a↕ domain

Fig. 8

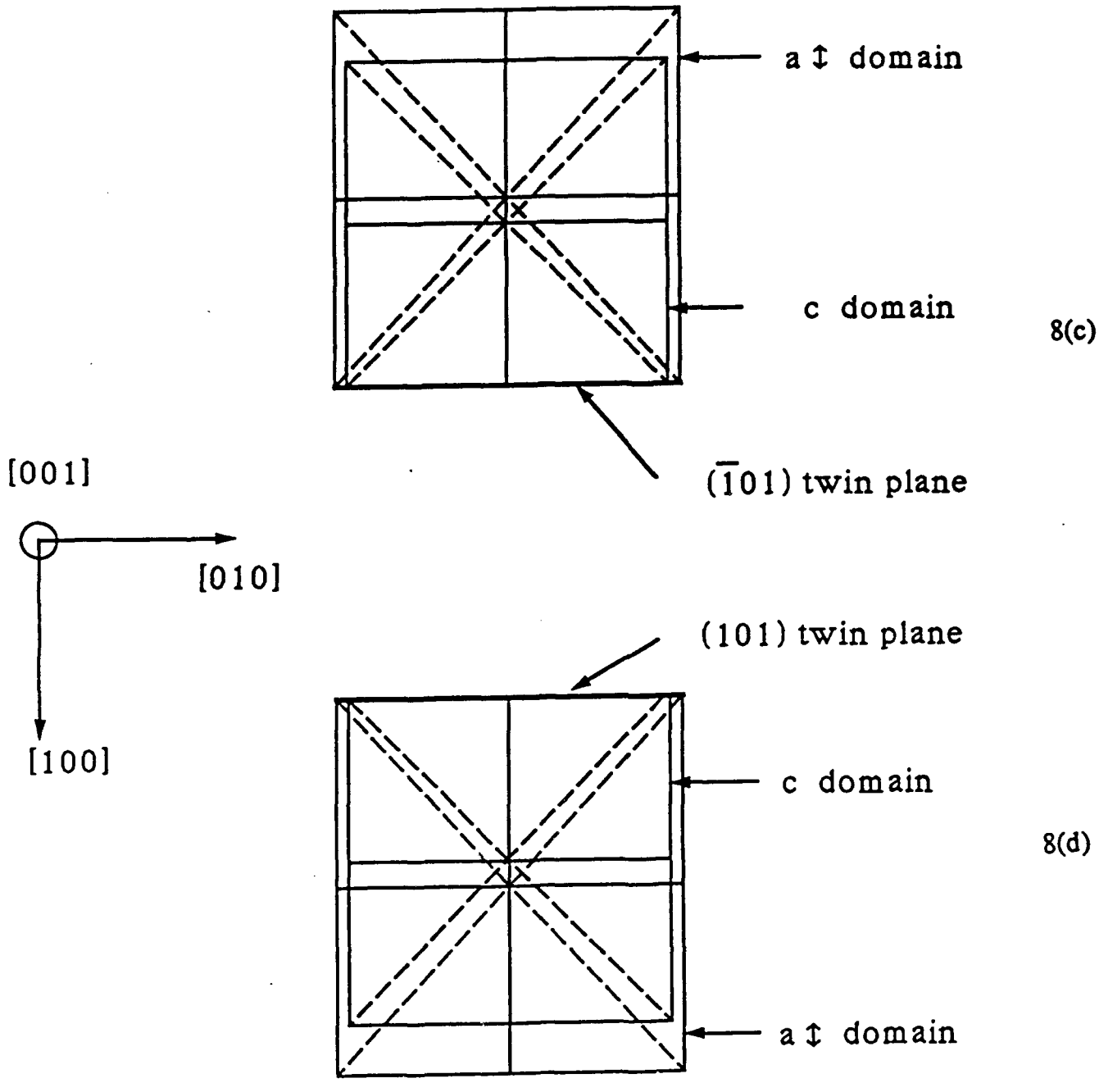
a ↕ domain
c domain
8(c)
(1̄01) twin plane
[001]
[010]
[100]
(101) twin plane
c domain
8(d)
a ↕ domain

Fig. 8

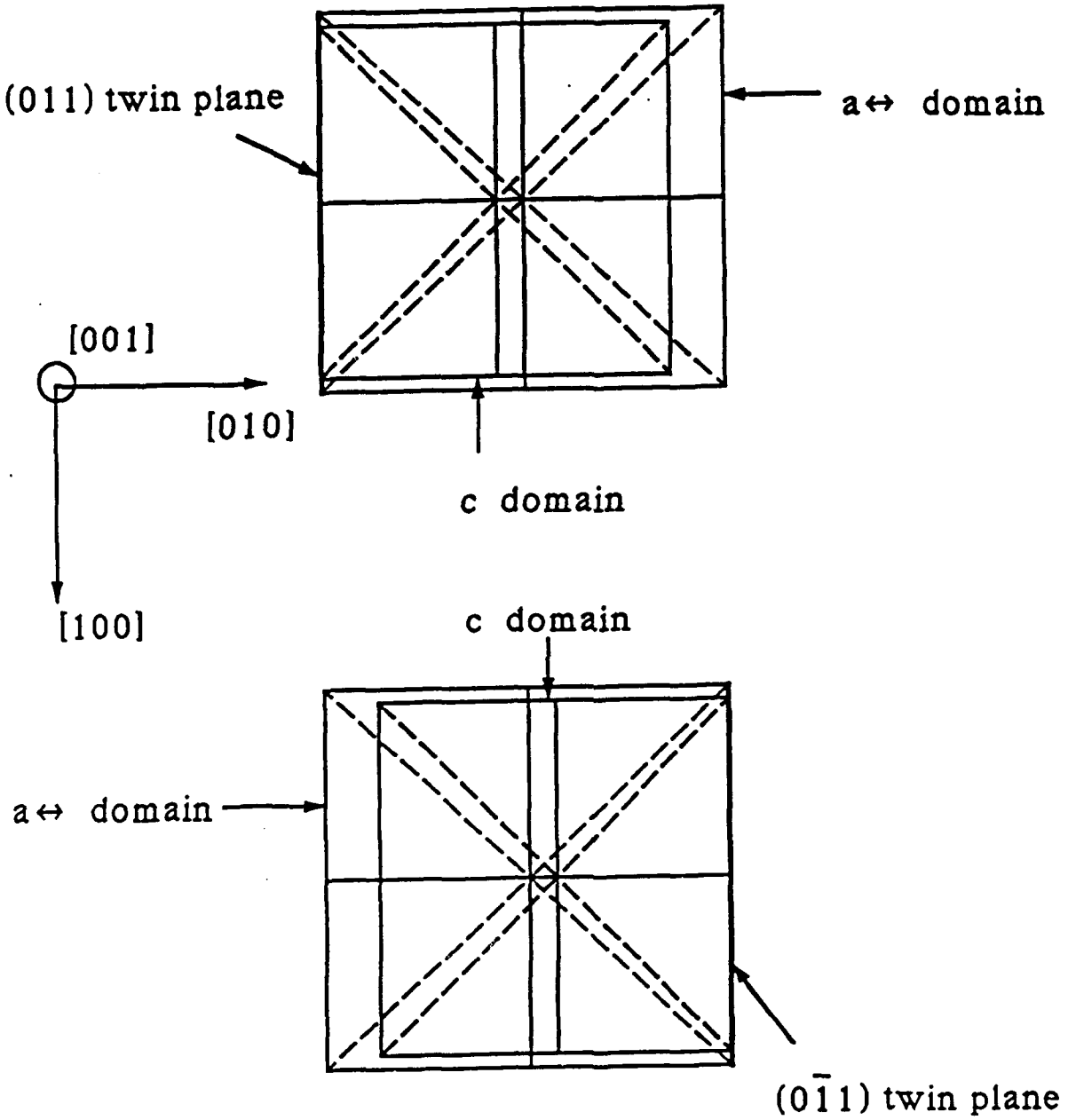
(011) twin plane
a↔ domain
8(e)
[001]
[010]
c domain
[100]
c domain
a↔ domain
8(f)
(0$\bar{1}$1) twin plane

Fig. 8

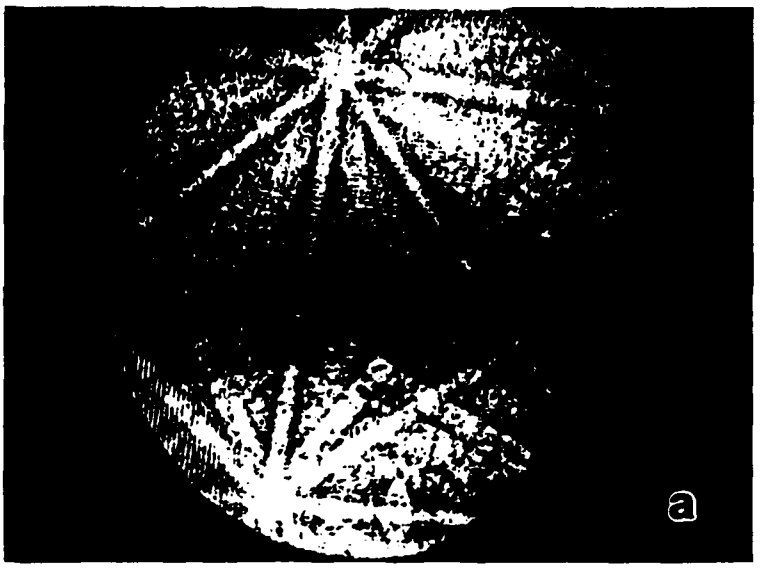

9(a)

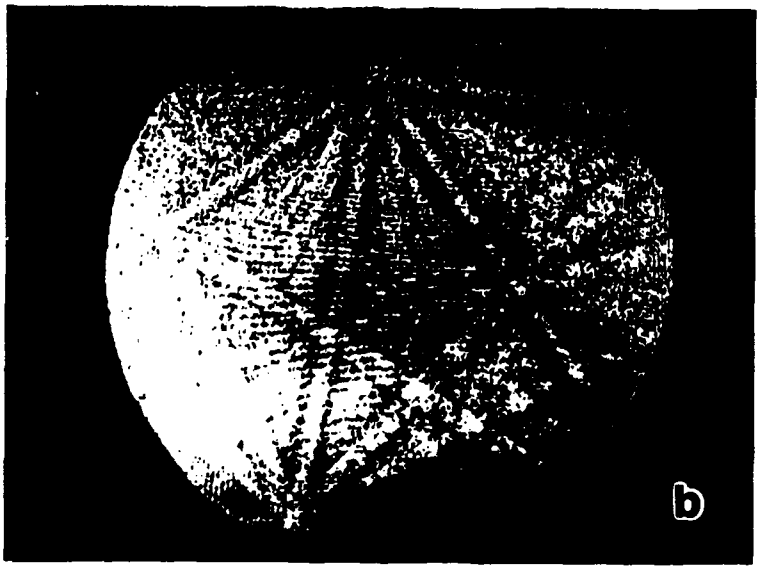

9(b)

Fig. 9

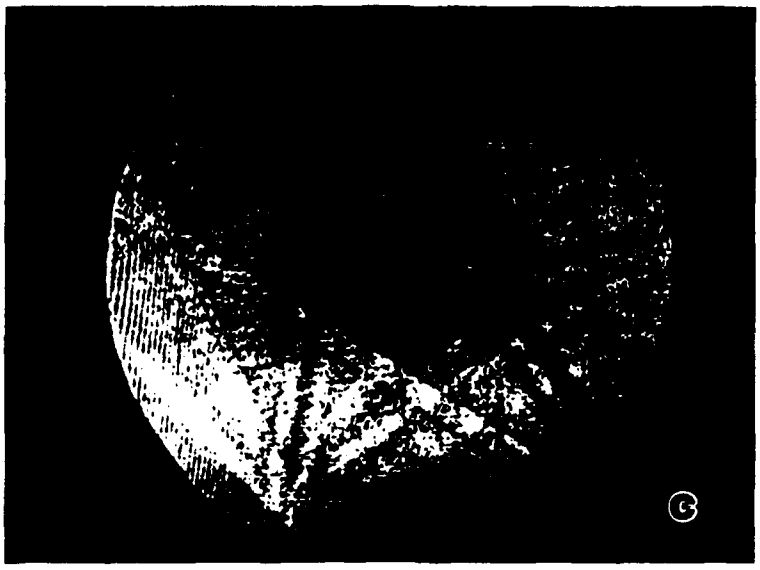

9(c)

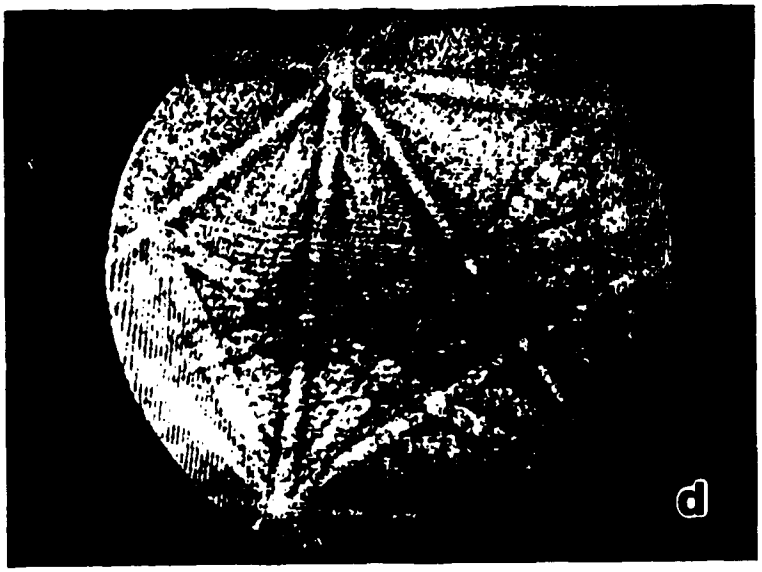

9(d)

Fig. 9

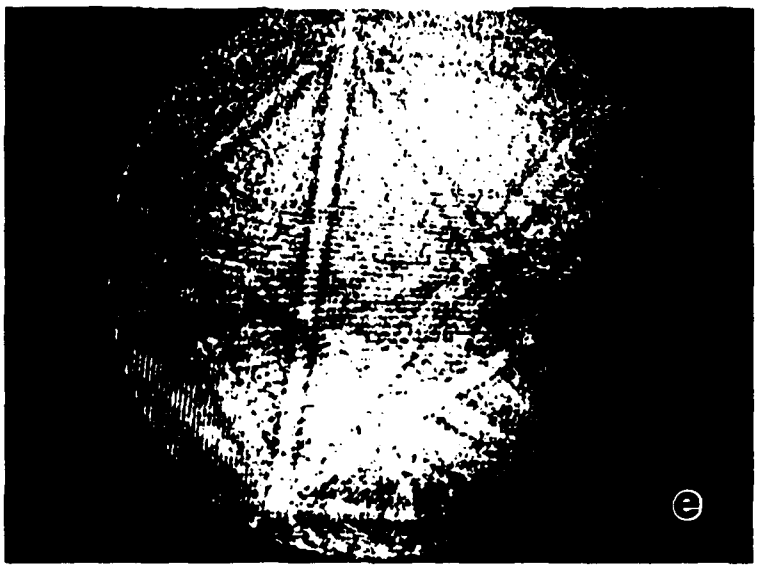

9(e)

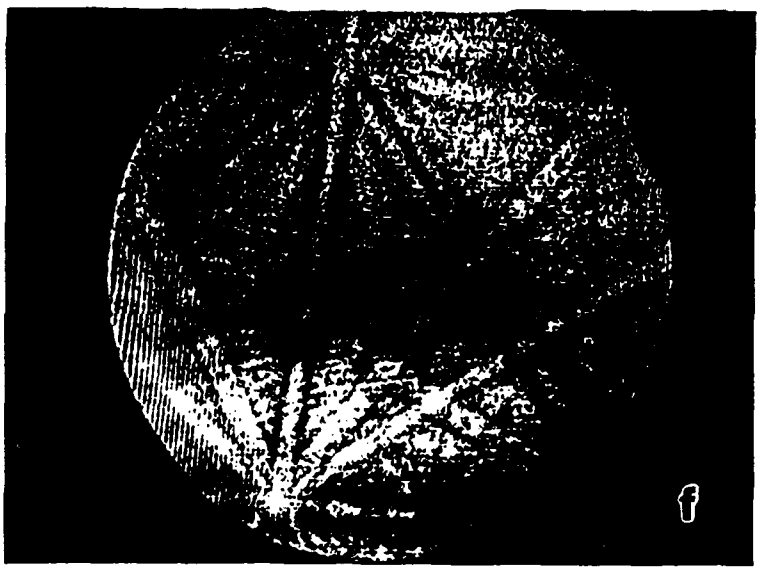

9(f)

Fig. 9

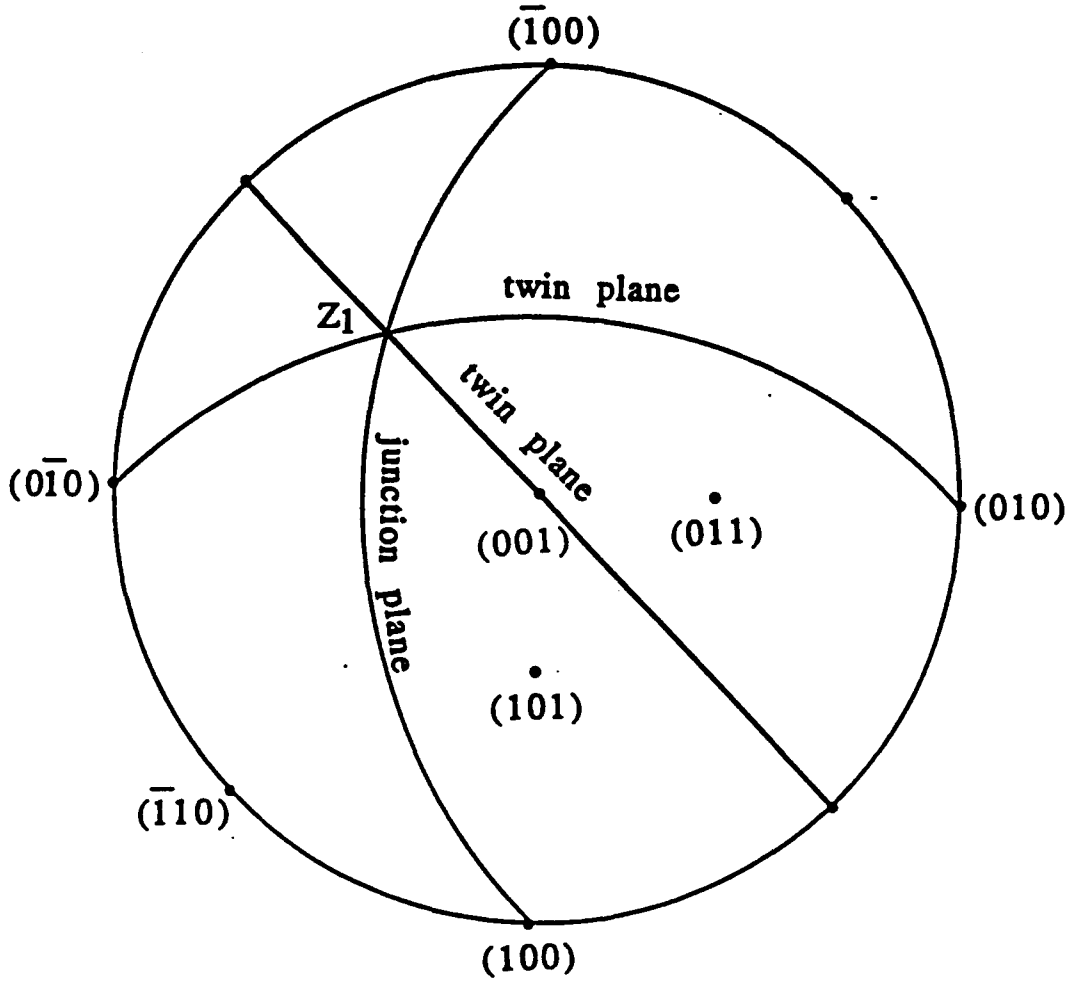
(1̄00)
twin plane
Z1
twin plane
junction plane
(01̄0)
(010)
(001)
(011)
(101)
(1̄10)
(100)

Fig. 10(a)

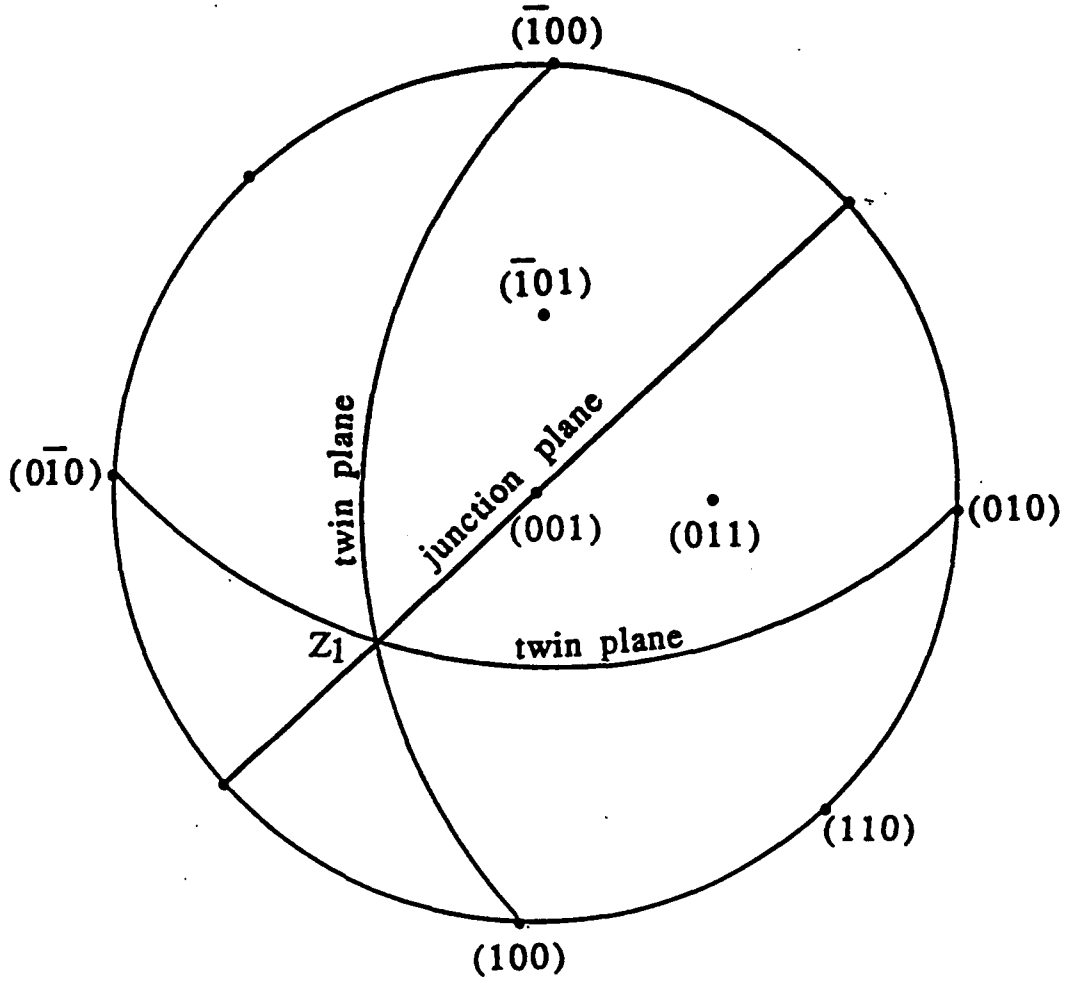
(1̄00)
(1̄01)
twin plane
junction plane
(0̄10)
(001)
(011)
(010)
Z1
twin plane
(110)
(100)

Fig. 10(b)

Thermal stability of field-forced and field-assisted antiferroelectric-ferroelectric phase transformations in $Pb(Zr,Sn,Ti)O_3$

Pin Yang and David A. Payne
Department of Materials Science and Engineering, Materials Research Laboratory and Beckman Institute, University of Illinois at Urbana-Champaign, Urbana, Illinois 61801

(Received 22 August 1991; accepted for publication 21 October 1991)

Antiferroelectric (AFE)-ferroelectric phase transformations in tin-modified lead zirconate titanate, i.e., $Pb(Zr,Sn,Ti)O_3$ are reported. A martensitic-type approach is developed to explain the observed thermal hysteresis and field-induced transformation behavior. A model is proposed with transformation fields where the forward E_F and reverse E_A field strengths are related to the transformation barrier to the ferroelectric state, and to the AFE sublattice coupling, respectively. The thermal stability of the AFE state can therefore be determined with respect to the field-induced transformation behavior. A distinction is made between field-forced and field-assisted transformations, which depend on temperature and thermal hysteresis, and which are related to reversible and irreversible field-induced characteristics. Data are reported for polarizations and strains, and discussed with respect to the proposed thermodynamic model and device applications.

I. INTRODUCTION

In this paper we report on phase transformation studies in the $Pb(Zr,Sn,Ti)O_3$ system (i.e., PZST).[1-3] Attention is paid to the effect of electric field E on phase stability, with emphasis on the induction of the ferroelectric (FE) state from the antiferroelectric (AFE) state as a function of temperature T. Previous studies have reported on induced polarizations P and strains ϵ,[1,4,5] and a general thermodynamic phenomenology[6-8] has evolved to explain the transformation behavior. However, several experimental observations of phase irreversibility[1,2,9] (to be discussed later) have yet to be explained, and are the subject of this study. The intent is to develop a model and formalism by which the thermal stability of field-induced FE-AFE transformations can be explained. This could become important and significant for device applications, where shape and volume changes accompany the induced transformation. For example, the thermal stability and recyclability of electromechanical actuators and positioners,[4,5,10,11] and electro-optical storage devices,[9] can be explained by this approach.

The thermodynamic formalism that has developed is particularly useful for describing the thermal stability of FE and AFE materials which transform into a paraelectric (PE) state on heating.[12] For example, the induction of FE properties from a PE state, with increasing field strength, can be described and predicted.[13] However, difficulty is experienced in mimicking the induced FE behavior from an AFE state, especially if the transformation is of the first order.[7,14] In this paper we propose a martensitic-type approach[15] to explain the field-induced first-order phase transformation behavior from AFE to FE states, with emphasis on thermal stability.

II. MODEL

The proposed model follows standard thermodynamic treatments with inclusion of a thermodynamic barrier ΔG^* for the phase transformation to proceed. Phase stability is dictated by the phase with the lowest free energy G. Figure 1 illustrates the change in free energy and free-energy difference ΔG as a function of temperature for FE and AFE states. For example, at temperatures above T_0 the AFE state is more stable. At temperatures below T_0, the free-energy difference between FE and AFE states, $\Delta G^{\text{FE-AFE}}$, becomes progressively more negative, and the driving force for the transformation to proceed increases accordingly. However, because of the transformation barrier ΔG^*, a region of thermal hysteresis exists and, the pathway passes through a region of metastability (higher free energy) before the transformation occurs. The transformation temperature T_F to the ferroelectric state occurs on cooling when $\Delta G^{\text{FE-AFE}} \geqslant \Delta G_F^*$. Similarly, a transformation to the AFE state occurs on heating T_A with a transformation barrier ΔG_A^*, and a region of metastability $T_A - T_0$, where $\Delta G^{\text{FE-AFE}} > 0$. The total thermal hysteresis ΔT is $T_A - T_F$, where $T_0 - T_F$ and $T_A - T_0$ represent the undercooling and overheating necessary to trigger the transformations over the respective barriers (ΔG_F^*, ΔG_A^*) into the FE or AFE states. A barrier gives rise to a discontinuity in certain properties at the phase transformation temperature, and is characteristic of a first-order transformation.

Below T_F, in the FE state, there is spontaneous polarization P_F, at zero field, that can be reoriented on application of an electric field of sufficient strength E_c to give rise to dielectric hysteresis. Above T_A, in the AFE state, there are equal but opposite spontaneous polarizations P_a, P_b on interpenetrating sublattices (a and b) which are coupled to give a net AFE polarization P_A of zero at zero field. Close to the phase transformation temperature (to be discussed below) the FE state can be induced from the AFE state on application of a suitable field strength.

Kittel[12] described the properties of AFE materials in terms of a free-energy expression

 0021-8979/92/031361-07$04.00

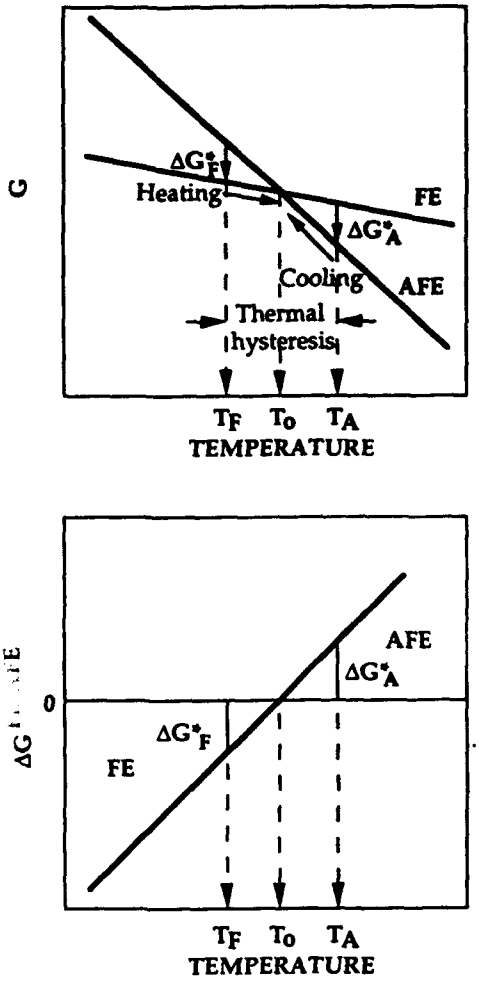

FIG. 1. Temperature dependence of free energy G and free-energy difference $\Delta G^{\text{FE-AFE}}$ between ferroelectric (FE) and antiferroelectric (AFE) states. The phase change occurs spontaneously on cooling when the free-energy difference $\Delta G^{\text{FE-AFE}}$ is greater than the transformation barrier ΔG_F^*.

$$G^{\text{AFE}}=f(P_a^2+P_b^2)+gP_aP_b+h(P_a^4+P_b^4)+j(P_a^6+P_b^6), \tag{1}$$

where f, g, h, and j are thermodynamic coefficients. Cross[16] later considered the induction of the FE state from the AFE state, and the total free energy for the FE state at high field and polarization can be expressed by

$$G^{\text{FE}}=\frac{1}{2}\left(f+\frac{g}{2}\right)P_F^2+\frac{1}{2}\left(f-\frac{g}{2}\right)P_A^2+\frac{h}{8}(P_F^4+6P_A^2P_F^2+P_A^4)+\frac{j}{32}[P_F^6+P_A^6+15P_F^2P_A^2(P_A^2+P_F^2)]-P_FE, \tag{2}$$

where $P_F=P_a+P_b$ and $P_A=P_a-P_b$ at E, and

$$\Delta G^{\text{FE-AFE}}=G^{\text{FE}}-G^{\text{AFE}}=-P_FE. \tag{3}$$

Figure 2 illustrates the lowering of the free-energy difference between the two states, $\Delta G^{\text{FE-AFE}}$, on application of an electric field. Compared with Fig. 1, $\Delta G^{\text{FE-AFE}}$ goes to zero now at a higher temperature T_0', i.e., the phase transformation temperature is shifted, and the low-temperature FE state becomes more stable. Under isothermal conditions T, the FE state can be induced from the AFE state when

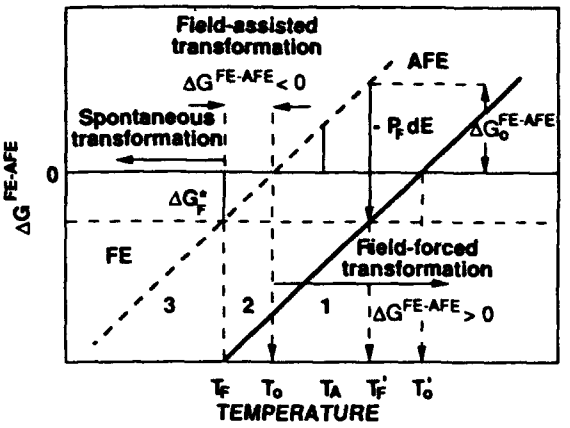

FIG. 2. The FE phase can be induced on cooling from the AFE state on application of an electric field. Above T_0, a field-forced transformation occurs when the electric work done is greater than the magnitude of the free-energy difference between the two states and the transformation barrier, $-P_FdE > \Delta G_0^{\text{FE-AFE}} + \Delta G_F^*$. Below T_0, where $\Delta G^{\text{FE-AFE}} < 0$, and between T_0 and T_F, the FE state can be field assisted from the metastable AFE phase. Below T_F, where the transformation barrier is exceeded, the phase transformation occurs spontaneously.

$$-P_FdE > \Delta G_0^{\text{FE-AFE}} + \Delta G_F^*, \tag{4}$$

where $\Delta G_0^{\text{FE-AFE}}$ is the free-energy difference at temperature T (Fig. 2).

We now consider three temperature regions for clarification and definition purposes: (i) When $T > T_0$, and $\Delta G^{\text{FE-AFE}}$ is positive, the electric field forces the transformation, which we refer to as a field-forced transformation; (ii) between T_0 and T_F, where $\Delta G^{\text{AF-AFE}}$ becomes negative, the electric field assists the transformation (from the metastable AFE state), and we distinguish this by a field-assisted transformation; and (iii) below T_F, where $\Delta G^{\text{FE-AFE}}$ is more negative than ΔG_F^*, the transformation occurs spontaneously, as discussed before.

We also define the field required to induce the FE state as E_F, which should be constant at constant temperature, and should increase with increasing temperature. For field-forced transformations and cyclic fields, the field at which the material reverts back to the AFE state E_A should also be constant at constant temperature, and also increase with increasing temperature ($> T_0'$). Both E_F and E_A are thermodynamic parameters that should be independent of maximum voltage oscillation level at constant temperature and composition (see below). For example, E_A can be related to the extent of sublattice coupling, when the poling field is released at a particular temperature. For field-assisted transformations this is not the case (i.e., constancy of E_A and E_F) since this is a region of metastability and irreversibility. The important issues of reversibility and temperature stability are discussed in a later section with experimental results.

The stability of FE and AFE states can be considered from the full Gibbs function

$$dG = -SdT - \epsilon d\sigma - PdE, \tag{5}$$

where S is entropy and σ stress. At equilibrium $dG^{FE} = dG^{AFE}$, and under experimental conditions of constant or zero stress change ($d\sigma = 0$), a modified Clausius–Clapeyron approach gives

$$\frac{dE}{dT} = -\frac{\Delta S}{\Delta P} = -\frac{\Delta H}{T\Delta P}, \tag{6}$$

where ΔH and ΔP are the enthalpy and polarization changes at the AFE-FE transformation. From initial considerations of free-energy changes near the equilibrium condition T_0 (Fig. 2), and assuming ΔH independent of temperature and $\Delta P = (P_F - P_A) \simeq P_F$,

$$\int_0^{E_0} dE = -\frac{\Delta H}{P_F}\int_{T_0}^{T}\frac{dT}{T}, \tag{7}$$

which gives

$$E_0 = -(\Delta H/P_F)\ln(T/T_0) + C \tag{8}$$

for the applied field E_0 necessary to induce the free-energy change ($\Delta G_0^{FE\text{-}AFE}$) and C is a constant. Now consider the additional case of a transformation barrier ΔG^* which requires a critical field E^* to overcome the free-energy difference between T_F and T_0,

$$E^* = -[-(\Delta H/P_F)\ln(T_F/T_0) + C] \tag{9}$$

and, therefore,

$$E_F = E_0 + E^*, \tag{10}$$

by comparison with Eq. (4). This gives the field E_F required to induce the FE state from the AFE state at a temperature close to T_0 by reducing the free-energy difference between the two states ($\Delta G^{FE\text{-}AFE}$) and overcoming the thermodynamic barrier ΔG^* by

$$E_F = -(\Delta H/P_F)\ln(T/T_F)$$

$$\simeq -(\Delta H/P_F T_F)(T - T_F). \tag{11}$$

This field E_F should increase linearly with increasing temperature difference $T - T_F$, and this dependence will be evaluated in Sec. IV A.

III. EXPERIMENTAL METHOD

Compositions close to a morphotropic phase boundary (MPB)[2] were chosen, and prepared by a hybrid coprecipitation mixed oxide method,[3,17] according to the formula $Pb_{(1-0.5z)}Nb_z[(Zr_{1-x},Sn_x)_{1-y}Ti_y]_{0.98}O_3$. An abbreviated notation is used in the rest of the paper: PZST X/Y/Z (equivalent to $100x/100y/100z$). For example, 43/8/2 represents a typical composition to be discussed below. This particular composition was FE at room temperature and transformed to the AFE state on heating. A small amount of Nb_2O_5 was added (1 mol %, $z = 0.02$) for dielectric strength purposes.[1,18]

Source materials (Alpha, Inc.) were mixed in a high shear blender. For 100-g batches of PZST product, the requisite amounts of metallo-organic precursors, titanium *n*-butoxide [$Ti(C_4H_9O)_4$] and a complex of zirconium *n*-butoxide butanol [$(C_4H_9O)_4Zr(C_4H_9OH)$] were mixed in isopropyl alcohol (100 ml) before introduction of the fine ceramic powders (Pb_3O_4, SnO_2, Nb_2O_5). After sufficient time for surface adsorption to occur, the mixed alkoxides were hydrolyzed by addition of a mixture of de-ionized water in isopropyl alcohol (1:4 by volume). The shear rate was increased to maintain fluid consistency. The final homogeneous mixture of coprecipitated powder with mixed oxides formed a slurry that was later dried in vacuum at 150 °C for 4 h. After drying and size reduction in a mortar and pestle, the composition was reacted at 860 °C for 4 h in air. X-ray diffraction (XRD) confirmed the formation of single-phase PZST. The calcined powder was then size reduced to a submicrometer consistency in a plastic ball mill using zirconia media in isopropyl alcohol. After drying and granulation, pressed cylinders, 1 cm in diameter by 2 cm thick, were formed in a cold-isostatic press at 25 000 psi. The preformed shapes were later hot pressed in an alumina-lined die at 1100 °C and 4000 psi for 2 h in air. Under those conditions, dense fine grain (0.4 μm) ceramics were formed. Larger grain sizes could be obtained (up to 6 μm) by heat treating at higher temperatures (1200–1360 °C) in an atmosphere containing excess PbO. A double-inverted crucible technique was used. Specimens were sliced from the hot-pressed form by a diamond wafering saw. For electric-field studies the thickness was approximately 200 μm, and the major surfaces were polished parallel with a submicrometer finish by diamond and alumina pastes. Specimens for study were annealed at 500 °C for 0.3 h in air before application of gold electrodes by sputtering.

Field-induced polarizations and transverse strains were determined on a Sawyer–Tower bridge with a strain gauge bonded to the specimen. Cyclic fields down to 0.3 Hz were used to minimize internal heating. Care was taken for temperature compensation in the strain measurements by use of a dummy gauge in the test cell. Electrical noise was minimized by using a dc heating system, with a programmable controller. All measurements were made on specimens that had been thermally depoled for 0.3 h at 30 °C above the FE-AFE transformation temperature T_A before cooling. Transformation temperatures (T_A, T_F) were determined by differential scanning calorimetry (DSC) and dimensional changes by thermal mechanical analysis (TMA). The heating and cooling rates were 10 °C/min.

IV. RESULTS AND DISCUSSION

Figure 3 gives DSC characteristics for 43/8/2, illustrating a sequence of phase transformations as a function of temperature, from FE to AFE states and eventually PE on heating [with a multicell cubic (MCC) region]. The onset temperatures for the AF and FE transformations are indicated ($T_A = 92$ °C, $T_F = 80$ °C) for heating and cooling cycles, respectively. The results are in accordance with the thermodynamic barriers ΔG^* and dependent thermal hysteresis ($\Delta T = 12$ °C) described in Fig. 1. Enthalpies of

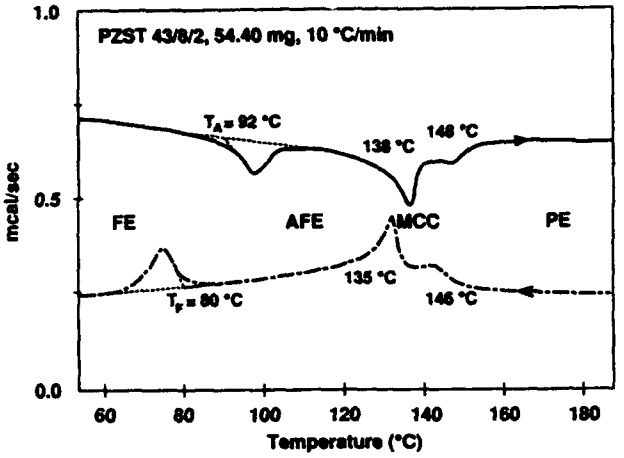

FIG. 3. Phase transformations and thermal hysteresis for PZST 43/8/2.

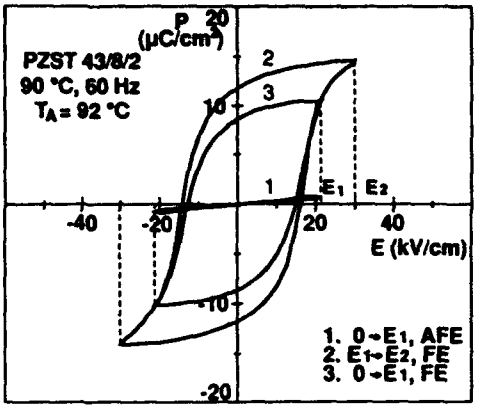

FIG. 5. Example of a field-assisted transformation, illustrating irreversibility between AFE and FE states. Initially (1) the AFE state is stable up to E_1, and reversible on switching. However, at greater field strengths (2), the FE phase is induced ($E_2 > E_1$) with hysteresis on switching, but does not revert back to the AFE state when the field strength is reduced below E_1. Metastability and irreversibility of the field-assisted FE state are illustrated for (3), where the field strength is reincreased, and the hysteresis loop is reopened, for a field strength E_1, comparable to the value at which the AFE state was initially stable.

transformation can be obtained from integration of endotherms and exotherms, and TMA results (not shown) determined a volume shrinkage ($\Delta V = 0.16\%$) on transforming from the FE to AFE states. That is, the AFE structure had a smaller unit cell, and changes in ΔH and ΔV indicated the transformation to be of the first order. The results are typical for the composition studied, and the AFE-FE thermal hysteresis ΔT was greater ($\sim 10\times$) than those commonly associated with PE-FE transformations.

Figure 4 illustrates the field-forced switching characteristics for a composition (42/4/2) which was AFE at room temperature. The opening up of the ferroelectric loop indicates the transformation field E_F was independent of maximum cyclic strength, in accordance with the proposed ΔG^* model and Eq. (4). Similarly, E_A was independent of E and can be related to the AFE sublattice coupling, as previously outlined. The reversible and stable field-forced measurements were made at approximately 25 °C above T_F.

Figure 5 illustrates polarization-field measurements for 43/8/2 (Fig. 3) at a temperature (90 °C) just below T_A

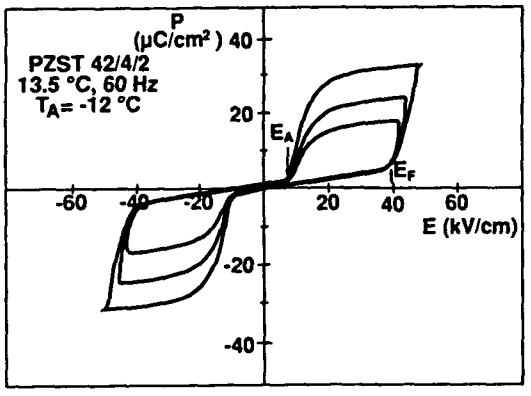

FIG. 4. Example of a field-forced transformation above T_A, illustrating forward and reverse field strengths, E_F and E_A, necessary for reversibility, which are independent of E, consistent with the thermodynamic model. E_F can be related to the barrier, $\Delta G^{FE\text{-}AFE} + \Delta G^*$, and E_A to the sublattice AFE coupling.

(92 °C) and above T_F (80 °C). The field-assisted transformation is irreversible between AFE and FE states. Initially, (1) the AFE state is stable up to E_1, and reversible on switching; however, (2) the FE state is induced when $E_2 > E_1$, and does not revert back to the AFE state when E is decreased ($< E_1$). Remnant polarization exists at zero field, and (3) the FE state persists at a field strength E_1 at which the AFE state was initially stable. Irreversibility is consistent with the proposed thermodynamic barrier model ΔG^* in the region of undercooling ($\Delta G^{FE\text{-}AFE} < 0$, $T > T_F$). In this region, the sublattice AFE coupling is weak and the applied electric work done ($-PdE$) forces the transformation over the barrier into the FE state. Since the sublattice coupling is weak, thermal energy alone cannot overcome the reverse transformation (back to the AFE state) and the FE state persists at weak fields. Irreversibility could be a problem for electromechanical actuator applications (for certain compositions and temperatures), but could be of use in bistable optical information storage system (based upon differential light scattering).

Induced polarizations and strains are illustrated in Fig. 6 for 43/7/2 at lower temperatures. For the field-forced transformation [Fig. 6(a)] close to T_A (72 °C) the temperature is shifted T_0' into the thermal hysteresis region (82 °C) on application of the electric field and metastability and irreversibility are now clearly indicated for the first two poling cycles (at 0.3 Hz). The transformation field E_F and permanent shape change (indicated by induced transformation ϵ) are in accordance with the thermodynamic model for a first-order transformation. Compared with Fig. 6(b), for purely FE switching, at a temperature (26 °C) well below the spontaneous transformation temperature T_F, there is now no transformation strain (since there was no spontaneous volume change), and the magnitude of the field-induced ϵ was less than the field-assisted case [Fig. 6(a)].

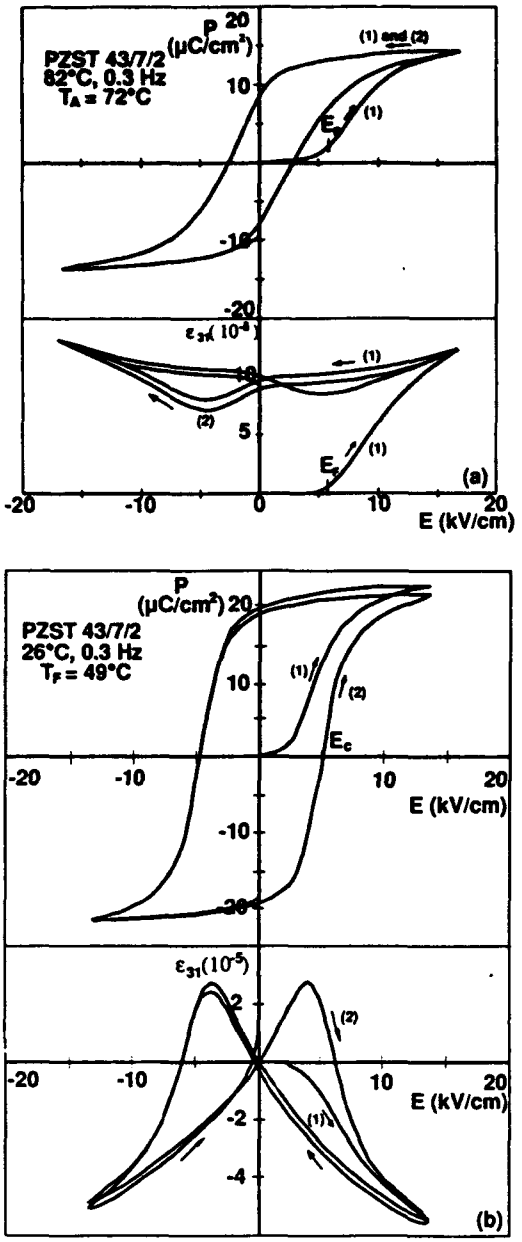

FIG. 6. The first two poling cycles for (a) field-assisted polarization and strain from AFE to FE states ($T \simeq T_A$), and (b) ferroelectric polarization and strain ($T < T_F$). Note: (a) the sudden transformation strain was greater than (b) the strain associated with domain switching.

The temperature dependence of transformation fields (E_F, E_A) is illustrated in Fig. 7, for 43/7/2, which was determined on cooling from the AFE to Fe states, and through the region of thermal hysteresis. The results are again in accordance with the proposed thermodynamic model [Eq. (4)], in that E_F and E_A increase linearly with temperature, with a shift in E_F as E_A goes to zero on cooling into the region of metastability. The shift may be associated with ΔH heating on cycling through the induced phase region. Note, for increasing undercooling, the field E_F required to trigger the instantaneous transformation (with remnant strain) is less than the field required to coerce ferroelectric switching E_c.

An estimate can be made of the temperature dependence of E_F from Eq. (11),

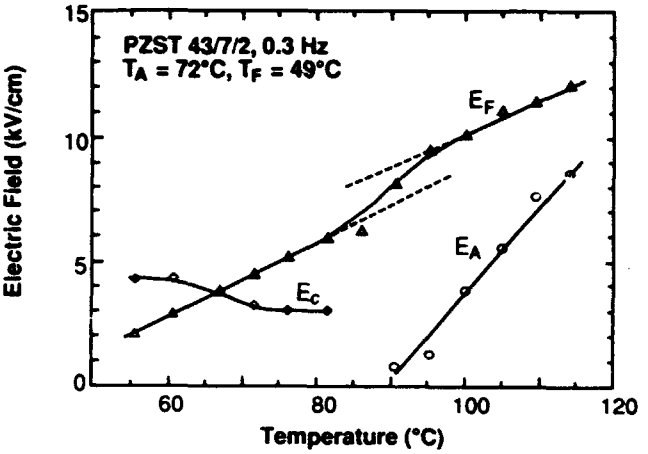

FIG. 7. Temperature dependence of transformation fields on cooling. Note at temperatures approaching T_F, $E_F < E_c$, i.e., the field-assisted transformation strength was less than the field required for domain switching.

$$E_F/(T - T_F) = -\Delta H/P_F T_F, \tag{12}$$

and compared with experimental data in Fig. 7. From DSC ($\Delta H = -2.3$ J/cm^3) and Sawyer–Tower data ($P_F = 23.94$ μC/cm^2) for 43/7/2 at $T_F = 49$ °C, the estimated value $(\Delta H/P_F T_F) = 0.30$ kV/cm K is in good agreement with experimental data [$E_F/(T - T_F) = 0.15$ kV/cm K]. This supports the proposed thermodynamic model for field-induced transformations.

For field-forced transformations to occur, the change in free energy must be greater than the combined thermodynamic barrier ΔG_F^* and the free-energy difference $\Delta G^{\text{FE-AFE}}$ between the two states [Eq. (4)], for the FE phase to nucleate and grow. The extent of FE phase development will depend on the magnitude of the excess field over E_F. Figure 8 illustrates the magnitude of the induced polarizations and strain, for 43/7/2, at a temperature (100 °C) greater than T_A (72 °C) for a field-forced transformation. The polarizations and strains increase linearly with field, in accordance with the thermodynamic model, and are recoverable. The reversible behavior would be important for reproducible electromechanical actuator applications where continuous displacements are necessary and attainable with recoverable transformation strains.

A. Thermal stability and field-induced properties

The proposed thermodynamic model has classified the field-induced FE behavior in terms of two distinct thermal regions: (i) above T_0, where $\Delta G^{\text{FE-AFE}} > 0$, for field-forced transformations; and (ii) below T_0, and between T_0 and T_F, where $\Delta G^{\text{FE-AFE}} < \Delta G^*$, for field-assisted transformations. The former are reversible for temperatures above T_A, and irreversible for temperatures between T_0 and T_A (unless T_F' is shifted above T_A). The latter are irreversible with temperature for field-assisted transformations. Consider the former case (i) where the electric work done ($-PdE$), must be greater than the nucleation barrier

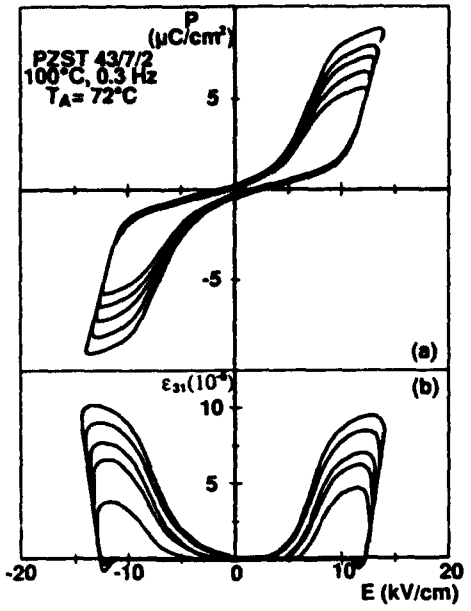

FIG. 8. Field-forced (a) polarizations and (b) strains as a function of field strength above T_A. An increasing dependence of induced polarization and strain with field above E_F relates to the extent of the induced ferroelectric phase.

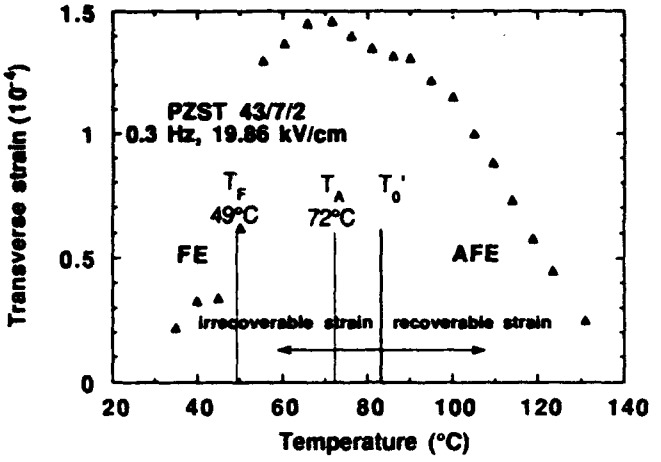

FIG. 10. Temperature dependence of field-induced transverse strain at constant field strength, illustrating reversible ($> T_F$) and irreversible regions for strain recovery. The maximum strain induced was in the thermal hysteresis region ($T_A > T > T_F$) close to T_A.

$(\Delta G_F^* + \Delta G^{\text{FE-AFE}})$ for the induction of the FE state. Excess field $(E - E_F)$ will aid in the growth of the FE phase and the development of field-forced properties. Eventually, at high field strengths, domain switching will occur, but this contribution to the overall properties will be less than the field-forced transformation behavior.

Consider now case (ii) for a field-assisted transformation. Figure 9 is for 43/7/2 in the thermal hysteresis region (50 °C) close to T_F (49 °C) where the AFE sublattice coupling is weak. As described previously, this is a region of

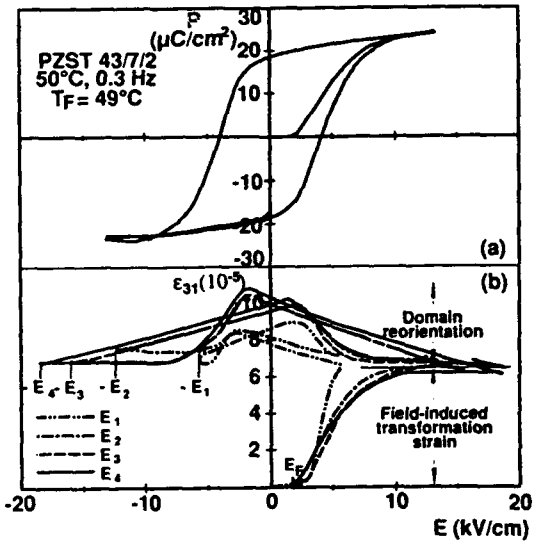

FIG. 9. Field-assisted (a) polarizations and (b) strains as a function of increasing field strength above T_F. By comparison with Fig. 8 (i.e., above T_A) the polarization and strain saturate for ferroelectric switching.

metastability and irreversibility, and once the transformation barrier ΔG_F^* is exceeded, energy is released and compensates for the strain energy associated with the spontaneous displacive transformation. Consequently, there should be a weak dependence of polarization and strain on electric field in the FE state for the field-assisted case. This is clearly indicated in Fig. 9 where the 9(a) polarization and 9(b) strain saturate with increasing field. For the forward bias case, the field-induced transformation strain reaches a constant value of approximately 6.4×10^{-5} and is independent of field strength above E_F (where $E_1 = 5.72$ kV/cm, $E_2 = 12.61$ kV/cm, $E_3 = 16.01$ kV/cm, $E_4 = 18.16$ kV/cm). In the ferroelectric state an additional strain is induced on field reversal. The strain associated with domain reorientation reaches a maximum value which is dependent upon the previous poling strength. For example, the total remanent strain at $E = 0$ is 10.3×10^{-5} for the E_4 condition, compared with 8.0×10^{-5} for E_1 [as indicated in Fig. 9(b)]. On complete reversal ($-E_4$) the strain decreases and saturates at the constant value of 6.4×10^{-5}. Therefore, the total strain at any field strength is comprised of a constant field-induced transformation strain (6.4×10^{-5}) and a field-dependent domain reorientation strain (up to 3.9×10^{-5}). Similar behavior has been reported for magnetic-field-induced martensitic transformations in ferrous alloys.[19,20] In the present case, and thermal regions, the properties (P, ϵ) associated with field-assisted transformations are nearly independent of E above E_F, unlike the former case of field-forced transformations, where P and ϵ were clearly dependent on E above E_F. Figure 9 also indicates that E_F, the field required to assist the transformation and displacements, is less than E_c, the field required to switch the ferroelectric domains in the thermal hysteresis region. This was mentioned previously with respect to the data in Fig. 7 and the discussion on irreversibility.

The question of reversible and irreversible field-induced transformations is summarized in Fig. 10 for 43/7/2

as a function of temperature. The field-induced strain is reported for a constant field level of 19.86 kV/cm. At high temperatures ($T > T_A$), outside the region of thermal hysteresis, the field-forced strain is reversible, in that it is recoverable and cyclable between E and E_F. The strain would be greater at higher field strengths (Fig. 8). Inside the region of thermal hysteresis ($T_A - T_F$) the field-assisted strain is irreversible, in that it is not recoverable or recyclable on reduction of E, unless T_0' becomes $> T_A$. The magnitude of the field-induced strain is greatest in the region of thermal hysteresis, close to T_A, but irrecoverable. For certain electromechanical actuator applications, where recyclable positioning is important, compositions and operating conditions within the AFE region are necessary for recoverable strain, even though the magnitude of the field-forced strain, at a comparable field level, would be less than the field-assisted strain. That is, the thermal stability of the AFE region becomes important when considering reproducible actuator applications.

V. CONCLUSIONS

A thermodynamic model was proposed to explain AFE-FE phase transformations in PZST. A martensitic-type approach was used, in that thermodynamic barriers were invoked for forward ΔG_A^* and reverse ΔG_F^* transformations. The model was shown to be in good agreement with thermal hysteresis and first-order transformation behavior. The model also explained field-induced properties, which were reversible or irreversible, depending upon thermal stability. The fields required to induce the FE state E_F and revert back to the AFE state E_A were shown to be related to the thermodynamic barrier ΔG_F^*, and to the AFE sublattice coupling, respectively. Both variables (E_A, E_F) were thermodynamic quantities, in that they were constant at constant temperature and independent of maximum voltage oscillation level. An indicator of phase stability was the field-induced FE hysteresis loop with values of E_F and E_A which increased with increasing temperature. The temperature dependence of transformation field strength was in accordance with the proposed model, and in good agreement with experimental results and calculations made by a modified Clausius–Clapeyron approach. The model was both qualitatively and quantitatively in agreement with the experimental results. A distinction was made between field-forced transformations (above T_0) and field-assisted transformations (between T_0 and T_F). The former were shown to be stable above T_A, with reversible polarizations and strains, and the latter were metastable, with irreversible polarizations and strains. The magnitude of the field-forced strain increased with increasing field level, in accordance with the proposed model, but was less than the field-assisted strain at an equivalent field strength. However, at temperatures above T_A, the field-forced strain was recoverable (unlike the field-induced strain in the region of thermal hysteresis) and suitable for electromechanical positioning. The thermal stability of the AFE region is an important criterion when considering reproducible actuator applications, and the proposed thermodynamic model should aid in the design of future compositions and working conditions (T, E). Issues relating to kinetic factors and microstructural effects are treatable by this model and will be reported in due course.

ACKNOWLEDGMENTS

The research was supported by a grant from the Air Force Office of Scientific Research (URI-41318).

[1] D. A. Berlincourt, H. H. A. Krueger, and B. Jaffe, J. Phys. Solids **25**, 659 (1964).
[2] B. Jaffe, W. R. Cook, Jr., and H. Jaffe, in *Piezoelectric Ceramics*, edited by J. P. Roberts and P. Popper (Academic, London, 1971).
[3] B. A. Tuttle, Ph.D. thesis, University of Illinois at Urbana-Champaign, 1981.
[4] K. Uchino and S. Nomura, Ferroelectrics **50**, 191 (1983).
[5] W. Y. Pan, Q. M. Zhang, A. Bhalla, and L. E. Cross, J. Am. Ceram. Soc. **72**, 571 (1989).
[6] A. Devonshire, Philos. Mag. **40**, 1040 (1949).
[7] I. S. Zheludev, *Physics of Crystalline Dielectrics: Volume 1, Crystallography and Spontaneous Polarization* (Plenum, New York, 1971).
[8] K. Okada, J. Phys. Soc. Jpn. **27**, 420 (1969).
[9] C. E. Land, J. Am. Ceram. Soc. **71**, 905 (1988).
[10] K. Uchino, Ceram. Bull. **65**, 647 (1986).
[11] W. Y. Pan, C. Q. Dam, Q. M. Zhang, and L. E. Cross, J. Appl. Phys. **66**, 6014 (1989).
[12] C. Kittel, Phys. Rev. **82**, 729 (1951).
[13] M. E. Lines and A. M. Glass, *Principles and Applications of Ferroelectrics and Related Materials* (Oxford University Press, Oxford, 1977).
[14] K. Okada, J. Phys. Soc. Jpn. **37**, 1126 (1974).
[15] L. Kaufman and M. Cohen, in *Progress in Metal Physics*, edited by B. Chalmers and R. King (Pergamon, New York, 1958), Vol. 7, p. 165.
[16] L. E. Cross, J. Phys. Soc. Jpn. **23**, 77 (1967).
[17] G. Haertling and C. E. Land, J. Am. Ceram. Soc. **54**, 1 (1971).
[18] G. W. Taylor, J. Appl. Phys. **38**, 4697 (1967).
[19] K. R. Satyanarayan, W. Eliasz, and A. P. Miodownik, Acta Metall. **16**, 877 (1968).
[20] T. Kakeshita, K. Shimizu, S. Funada, and M. Date, Acta Metall. **33**, 1281 (1985).

Cer. Trans. 32 (1993).

GRAIN-SIZE DEPENDENCE OF FERROELECTRIC-ANTIFERROELECTRIC PHASE TRANSFORMATIONS IN $Pb(Zr,Sn,Ti)O_3$ DIELECTRICS

P. Yang and D. A. Payne
Department of Materials Science and Engineering and
Materials Research Laboratory
University of Illinois at Urbana-Champaign, Urbana, Illinois 61801, U.S.A.

ABSTRACT

Phase transformations and microstructures in tin-modified lead zirconate titanate (PZST) ceramics were studied. Emphasis was placed on the effect of grain size on ferroelectric(FE) -antiferroelectric(AFE) phase transformations which could be induced by changes in temperature or electric-field strength. Differential scanning calorimetry (DSC) and thermal mechanical analyses (TMA) were used to determine the transformation temperatures, and Sawyer-Tower measurements were used to determine the field strengths necessary to induce the FE phase from the AFE phase. The transformation temperatures were found to decrease with decreasing grain size, and the field strengths increase somewhat with decreasing grain size. The results are discussed in terms of a strain energy model for a first-order transformation in a confined fine-grain ceramic microstructure.

INTRODUCTION

It is well known that structural changes at FE-AFE phase transformations (e.g., rhombohedral-tetragonal) lead to sudden changes in charge[1], heat[2] and high nonlinearities in field-induced polarizations[3,4]. These property changes can be used for voltage generation[5], energy storage[6], and conversion[7,8]. Future applications may include optical information storage[9,10] and ceramic actuators[11,12]. In this paper we report on the effect of microstructure on phase transformation behavior, especially transformation temperatures (T) and field-strengths (E). The results indicate the importance of ceramic processing conditions on the development of ceramic microstructures for reproducible and reliable properties in PZST dielectrics.

EXPERIMENTAL METHOD

PZST compositions close to a morphotropic phase boundary (MPB)[13] were prepared by a hybrid coprecipitation mixed oxide method[14] according to the formula $Pb_{(1-0.5z)}Nb_z[(Zr_{1-x},Sn_x)_{1-y}Ti_y]_{0.98}O_3$, abbreviated by PZST X/Y/Z

(equivalent to 100x/100y/100z) in the rest of the paper. A small amount of Nb_2O_3 was added for dielectric strength purposes[15,16].

The source materials were mixed in a high-shear blender. The requisite amounts of metallo-organic liquid precursors, titanium n-butoxide [$Ti(C_4H_9O)_4$] and a complex of zirconium n-butoxide butanol [$(C_4H_9O)_4Zr(C_4H_9OH)$] were mixed in isopropyl alcohol (100 ml) before introduction of fine ceramic powders (Pb_3O_4, SnO_2, Nb_2O_3). After sufficient time for surface adsorption to occur, the mixed alkoxides were hydrolyzed by addition of a mixture of deionized water in isopropyl alcohol (1:4 by volume). The shear rate was increased to maintain fluid consistency. The final suspension of coprecipitated powder with mixed oxides was concentrated on a hot plate at 80°C before drying in vacuum at 150°C for 4 hours. The powder was size reduced in a mortar and pestle, sieved through a nylon mesh and calcined at 860 °C for 4 hours in air. X-ray diffraction confirmed the formation of single phase PZST. The calcined powder was then reduced to a submicron consistency in a plastic ball mill with zirconia media in isopropyl alcohol. After drying and granulation, cylinders, 1 cm in diameter by 2 cm thick, were cold-isostatically pressed at 25,000 psi. A flow diagram is given in Figure 1. The preformed shapes were later hot pressed in an alumina-lined die at 1100 °C and 4000 psi for 2 hours in air. Under those conditions, dense ceramics were formed with fine-grain microstructures (0.4 μm). Larger grain sizes (up to 6 μm) were obtained by heat treatment at higher temperatures (1200-1360 °C) in an atmosphere containing excess PbO. A double-inverted crucible method[17] was used.

Specimens for DSC were sliced and ground to 200 μm and prepared 0.45 mm in diameter for maximum contact area with the test cell. The thin geometry minimized thermal resistance problems and enhanced the response of enthalpy changes. Transformation temperatures are defined at the onset of the endotherm or exotherm, on heating or cooling, respectively (Figure 2). Dimensional changes were characterized by thermal mechanical analysis (TMA). The heating and cooling rate for DSC and TMA was 10 °C/min. A Sawyer-Tower method was used to determine the transformation field strength (E_F) required to induce the FE phase from the AFE at constant temperature. Cyclic fields down to 0.3 Hz were

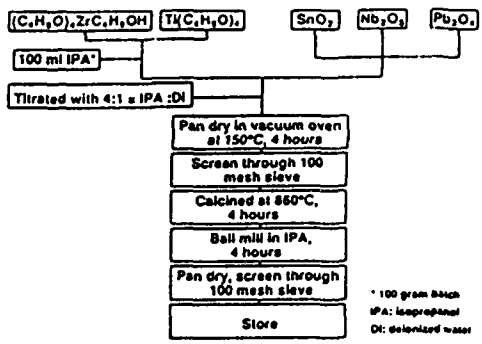

Figure 1 Preparation of PZST powder.

used to minimize internal heating. E_A was the field below which the FE would revert back to the AFE at temperatures above T_A.

RESULTS AND DISCUSSION

(1) Transformation Characteristics

Figure 2 gives DSC characteristics for PZST 43/8/2. The sequence of phase transformations is FE, AFE, multicell cubic (MCC) and finally, simple cubic paraelectric (PE) on heating. The onset temperatures for the AFE and FE transformations, on heating and cooling, are T_A and T_F respectively. Note, the region of thermal hysteresis (T_A-T_F). Enthalpies for transformation were obtained by integration of the endotherms and exotherms. Figure 3 gives TMA characteristics which indicate similar hysteretic behavior. The slope of these curves is the thermal expansion coefficient, and the results are similar to those reported by Berlincourt et al.[4] who showed that both the MCC and AFE phases had higher thermal expansion coefficients than the FE phase. An abrupt linear shrinkage of 0.053% was observed at the FE-AFE transformation. This indicates the AFE phase had a smaller unit cell than the FE phase. Therefore, the AFE-FE

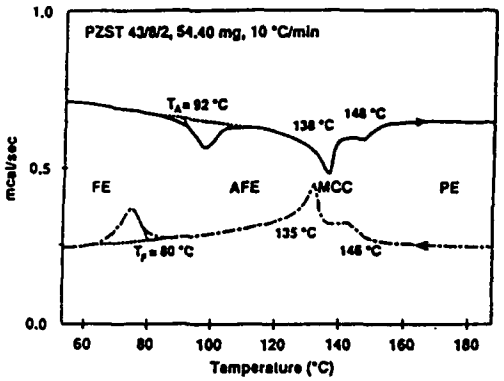

Figure 2 Phase transformation and thermal hysteresis for PZST 43/8/2.

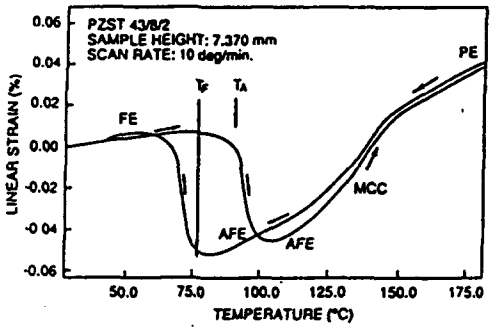

Figure 3 Thermal strain and hysteresis for PZST 43/8/2.

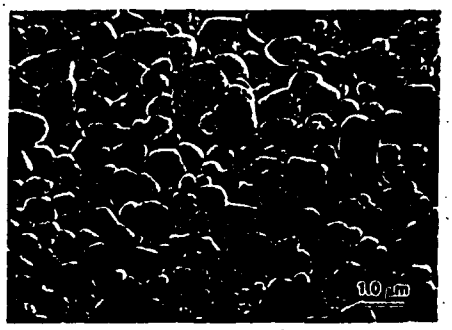

Figure 4 SEM photomicrograph of hot-pressed PZST 43/8/2 after heat treatment at 1150°C for 10 hours.

transformation shows discontinuities in enthalpy and volume and is of the first-order. These observations are typical of other compositions evaluated. However, the thermal hysteresis (~10°C) associated with the FE-AFE transformation is much greater than the hysteresis normally associated with FE-PE transformations (~1°C). The large thermal hysteresis associated with PZST provides a unique opportunity to study the effect of shape memory and superelasticity in ferroic ceramics. Details are reported elsewhere[18].

(2) Phase Transformation and Microstructure

The hot-pressed ceramics were dense and translucent. A typical microstructure is given in Figure 4 for PZST 43/8/2. DSC and dielectric measurements determined a decrease in transformation temperature (T_F and T_A) with decreasing grain size (Figure 5). This behavior was typical of all compositions studied in the PZST system. Somewhat similar behavior has been reported for $BaTiO_3$[19] and ZrO_2[20] ceramics. Although a surface area and energy contribution has been proposed for the transformation barrier in fine grain $BaTiO_3$[19], it is believed that in the present case, a confined elastic strain energy is responsible for the observed features[20, 21]. This would be especially so for a large discontinuity in ferroelastic strain at the transformation temperature. Thermal hysteresis and a constrained transformation - from a smaller unit cell AFE phase to a larger volume FE phase - would reduce the transformation temperature.

The effect of microstructure on internal stress can be considered from a thermodynamic point of view similar to arguments for electric field-forced AFE-FE transformations. Previous analysis[22] has shown that the transformation field E_F represents the minimum electric work done (-PdE) necessary to induced the transformation, i.e.,

$$-P_F dE \geq \Delta G_0^{FE\text{-}AFE} + \Delta G_F^* \qquad (1)$$

where P_F is the field induced polarization, $\Delta G_0^{FE\text{-}AFE}$ is the free energy difference between the two phases, and ΔG_F^* is the thermodynamic barrier for

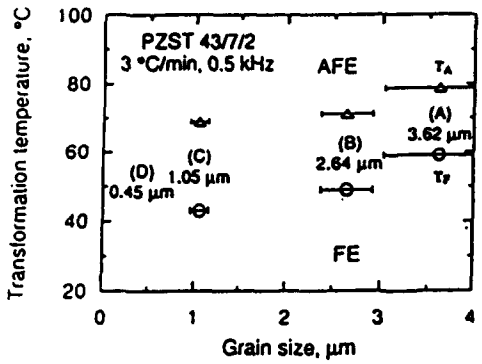

Figure 5 Grain-size dependence of transformation temperatures for PZST 43/7/2. Temperatures (T_A, T_F) decrease with decreasing grain size. For grain sizes less than 1 μm the transformation became more diffuse.

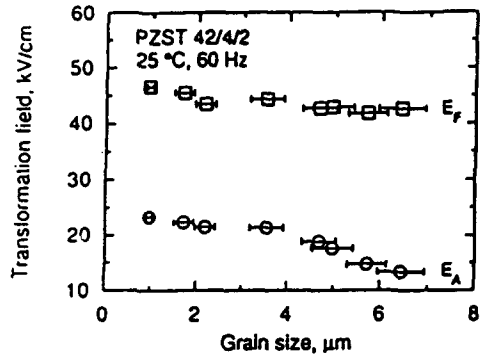

Figure 6 Grain-size dependence of transformation fields for PZST 42/4/2 at room temperature. Field strength (E_F, E_A) increase with decreasing grain size.

the first-order transformation. An increase in stored elastic strain energy in fine-grain ceramics would increase the total transformation barrier (ΔG_F^*), therefore, an increase in transformation field (E_F) would be expected. Figure 6 gives the effect of grain size on transformation fields (E_F and E_A) for PZST 42/4/2. The forward (E_F) and reverse field strength (E_A) are related to ΔG_F^*, and to the AFE sublattice coupling, respectively[22]. An increase in internal stress favors the smaller volume AFE phase, therefore, ΔG_F^* and the sublattice coupling, increase accordingly. As a result, transformation fields (E_F and E_A) increase with decreasing grain size. Details of the thermodynamic treatment for confined microstructures will be published elsewhere[23].

Figure 7 gives X-ray diffraction data for PZST 43/7/2 heat-treated to different grain sizes. The samples were carefully polished (to 0.3 μm) to avoid any surface damage. Different stress levels in different microstructures are indicated by the progressive merging of the split $(444)_r$ and $(400)_r$ peaks for FE rhombohedral PZST at room temperature. Specimen A (3.62μm) had a well defined pattern but as grain size decreased (and internal stress increased from B to D), the peaks eventually merged into a pseudocubic structure. The intensity of the $(444)_r$ peak decreased with decreasing grain size, which suggests the increase in internal stress in fine-grain ceramic microstructures tended to retard the FE-AFE transformation. Therefore, microstructure control is necessary for reliable and

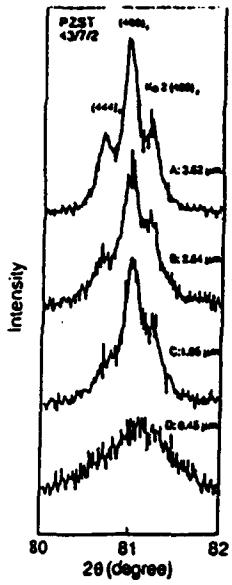

Figure 7 X-ray diffraction data for PZST 43/7/2 as a function of grain size. The structure becomes less rhombohedral and more pseudocubic as the grain size decreases.

reproducible properties in PZST dielectrics, and could be important in future electromechanical actuator systems.

CONCLUSIONS

Phase transformations in the PZST system were studied. The FE-AFE transformation was shown to be first order with significant ferroelastic strain. The AFE state had a smaller unit cell than the FE state, and on cooling into the FE state, the transformation strain could be clamped by the fine-grain ceramic microstructure. Experimental data indicate the transformation temperature decreased with decreasing grain size (6-0.5 μm) and the transformation field strength increased with decreasing grain size. The results are in accordance with a proposed thermodynamic model in which the stored elastic strain energy (resulting from the confined transformation) would favor the stability of the AFE state (i.e., a decrease in T_A and an increase in E_F with decreasing grain size). Therefore, microstructure control is important for FE-AFE transformations which exhibit significant thermal hysteresis.

ACKNOWLEDGMENT

The research was supported by a grant from the Air Force Office of Scientific Research (URI-41495) on Phase Transformations in Ceramics.

REFERENCES

1 D. Berlincourt, H. Jaffe, H. H. Krueger, and B. Jaffe, "Release of Electric Energy in PbNb(Zr,Ti,Sn)O_3 by Temperature- and by Pressure-Enforced Phase Transitions," *Appl. Phys. Lett.*, 3, 501-505, (1971).

2 P. D. Thacher, "Electrocaloric Effects in Some Ferroelectric and Antiferroelectric Pb(Zr,Ti)O_3 Compounds," *J. Appl. Phys.*, 39 [4], 1996-2002, (1968).

3 E. Sawaguchi, G. Shirane, and Y. Takagi, "Phase Transition in Lead Zirconate," *J. Phys. Soc. Jpn.*, 6 [5], 333-339, (1951).

4 D. Berlincourt, H. H. Krueger, and B. Jaffe, "Stability of Phases in Modified Lead Zirconate with Variations in Pressure, Electric Field, Temperature and Composition," *J. Phys. Chem. Solids*, 25, 659-674, (1964).

5 F. Bauer, K. Vollrath, Y. Fetiveau, and L. Eyraud, "Ferroelectric Ceramics: Application to Mechanical Electrical Energy Conversion Under Shock Compression," *Ferroelectrics*, 10, 61-64, (1976).

6 I. Burn, "Field-Enforced Ferroelectricity in Glass-Bonded Lead Zirconate," *Bull. Am. Ceram. Soc.*, 50, 90-98, (1963).

7 R. B. Olsen, W. F. Butler, D. A. Payne, B. A. Tuttle, and P. C. Held, "Observation of a Polarocaloric (Electrocaloric) Effect of 2 °C in the Lead Zirconate Modified with Sn^{+4} and Ti^{+4}," *Phys. Rev. Lett.*, 45 [17], 1436-1438, (1980).

8 B. A. Tuttle, D. A. Payne, and J. L. Mukherjee, "Ferroelectric Materials for Dielectric Power Conversion," *Ferroelectrics*, 27, 219-222, (1980).

9 S. Mancha, J. Bullington, R. Carter, and C. Dehainaut, "Antiferroelectric-Phase PLZT for Use in High Density Optical Data Storage," *Ferroelectrics*, 82, 99-104, (1988).

10 C. E. Land, "Bistable Optical Information Storage Using Antiferroelectric Phase-Lead Lanthanum Zirconate Titanate Ceramics," *J. Am. Ceram. Soc.*, 71 [11], 905-908, (1988).

11 K. Uchino and S. Momura, "Electrostriction in PZT Family Antiferroelectrics," *Ferroelectrics*, 50, 191-196, (1983).

12 W. Y. Pan, C. Q. Dam, Q. M. Zhang, and L. E. Cross, "Large Displacement Transducers Based On Electric Field Forced Phase Transition in Tetragonal ($Pb_{0.97}La_{0.02}$)(Ti,Zr,Sn)O_3 Family of Ceramics," *J. Appl. Phys.*, 66 [12], 6014-6023, (1989).

13 B. Jaffe, W. R. Cook, Jr., and H. Jaffe, Piezoelectric Ceramics, edited by J. P. Roberts and P. Popper, Academic Press, London, 1971.

14 G. Haertling and C. E. Land, "Hot-Pressed (Pb,La)(Zr,Ti)O_3 Ferroelectric Ceramics for Electrooptic Applications," *J. Am. Ceram. Soc.*, 54 [1], 1-11, (1971).

15 G. W. Taylor, "Electrical Properties of Niobium-Doped Ferroelectric Pb(Zr,Sn,Ti)O_3 Ceramics," *J. Appl. Phys.*, 38 [12], 4696-4706, (1967).

16 R. Gerson, "Variation in Ferroelectric Characteristics in Lead Zirconate Ceramics Due to Minor Chemical Modifications," *J. Appl. Phys.*, 31 [1], 188-194, (1960).

17 G. S. Snow, "Improvements in Atmosphere Sintering of Transparent PLZT Ceramics," *J. Am. Ceram. Soc.*, 56 [9], 479-480, (1974).
18 P. Yang and D. A. Payne, "Shape Memory and Superelasticity for Ceramics with Field-Induced Antiferroelectric-Ferroelectric Phase Transformations," to be published in the International Conference on Martensitic Transformations, ICOMA'92, Monterey, CA (May, 1992).
19 K. Uchino, E. Sadanaga, and T. Hirose, "Dependence of Crystal Structure on Particle Size in Barium Titanate," *J. Am. Ceram. Soc.*, 72 [8], 555-558, (1989).
20 F. F. Lange, "Transformation Toughening: Part 1. Size Effects Associated with the Thermodynamics of Constrained Transformations," *J. Mat. Sci.*, 17, 225-234, (1982).
21 W. R. Buessem, L. E. Cross, and A. K. Goswami, "Phenomenological Theory of High Permittivity in Fine-Grained Barium Titanate," *J. Am. Ceram. Soc.*, 49 [1], 33-36, (1977).
22 P. Yang and D. A. Payne, "Thermal Stability of Field-Forced and Field-Assisted Antiferroelectric-Ferroelectric Phase Transformations in $Pb(Zr,Sn,Ti)O_3$," *J. Appl. Phys.*, 71 [3], 1361-1367, (1992).
23 P. Yang and D. A. Payne, (in preparation, 1992).

J. Appl. Phys. (1994) in press.

Electronic Structure of Barium Titanate Studies by the Extended Hückel Tight Binding Method

M. Holma*, M. Kitamura** and Haydn Chen

Department of Materials Science and Engineering
University of Illinois at Urbana-Champaign
Urbana,IL 61801 USA

*Department of Physics, University of Illinois at Urbana-Champaign
**Department of Electrical and Electronic Engineering, Utsunomiya University, Utsunomiya 321, Japan

1 Abstract

The electronic structure of Barium Titanate is determined according to the extended Hückel tight binding method (XHTB) using atomic data based on a self-consistent field calculation. The effects of the phase transition on the partial density of states are studied. The electronic contribution to the phase stability of the compound is calculated from the total density of states. The tetragonal phase is found to be stable as compared to the cubic phase. The density of states is compared with available x-ray photoemission spectra and is found to be in good agreement with the experiments.

2 Introduction

The electronic structure of perovskites containing titanium has been the subject of a number of theoretical [1] - [5] and experimental [6] - [9] studies focussing primarily on $BaTiO_3$ and $SrTiO_3$. Matthiess [2] calculated the electronic structure of perovskite-type crystals using a linear combination of atomic orbitals-augmented plane wave method but did not include the contribution of the barium states. Michel-Calendini and Mesnard [3] have calculated the structure of both cubic and tetragonal barium titanate using a modified linear combination of atomic orbitals with non-orthogonal orbitals. However, the contribution of the barium states has not been included. The focus of this report is to evaluate the contribution of the electronic structure to the phase stability of $BaTiO_3$.

In an attempt to examine the phase stability of Barium Titanate, we have performed a series of calculations using the extended Hückel tight-binding method [10] to calculate the total density of states, the partial density of states and the electronic total energy for the cubic and tetragonal phases of $BaTiO_3$. The XHTB method has been applied previously to ionic perovskite-type compounds such as KMF_3 (with M = Mn, Fe, Co, Ni, Cu, and Zn)[11] and a K_2PdCl_6 crystal[11]. The band structure calculations show good agreement with experimental data relating to both the valence band as well as the conduction band. The XHTB method has also been applied to determining the phase stability of the intermetallic compound Al_3Nb as a function of nickel additions[12]. The electronic structure and total energies were calculated for both DO_{22} and $L1_2$ structures of Ni-doped Al_3 and were found to be in good agreement with x-ray diffraction experiments. This paper presents calculations

for $BaTiO_3$ based on the XHTB method. The results of the calculations are compared with relevant experimental data.

3 Theory

In this section we briefly describe the extended Hückel tight-binding method and the calculation procedure. Details of the theory and calculation for perovskite-type compunds are found in the paper by Kitamura and Muramatsu[13]. We solve the following Schroedinger equation:

$$\hat{H}\Psi_{\mathbf{k}}(\mathbf{r}) = E_{\mathbf{k}}\Psi_{\mathbf{k}} \tag{1}$$

where $\hat{H}$ is a one-electron Hamiltonian consisting of the kinetic energy term and a crystal potential, with the periodicity of the lattice. The one-electron wave function $\Psi_{\mathbf{k}}$ is specified by the wave vector, $\mathbf{k}$, restricted to the first Brillouin zone (BZ). According to the Bloch theorem in the tight-binding method the wave function is written:

$$\Psi_{\mathbf{k}}(\mathbf{r}) = \sum_{\mu,L} u_L^{(\mu)}(\mathbf{k})\chi_L^{(\mu)}(\mathbf{k},\mathbf{r}) \tag{2}$$

$$\chi_L^{(\mu)}(\mathbf{k},\mathbf{r}) = \sum_{\mathbf{r}_\mu} \exp(i\mathbf{k}\cdot\mathbf{r}_\mu)\phi_L^{(\mu)}(\mathbf{r}-\mathbf{r}_\mu)/N_\mu^{1/2} \tag{3}$$

where the summation over μ is taken for the five independent Ba, Ti, O(1), O(2) and O(3) ions; $\mathbf{r}_\mu$ denotes their positions throughout the crystal. The atomic orbital $\phi_L^{(\mu)}(\mathbf{r}-\mathbf{r}_\mu)$ is denoted by the collective index L = (l,m) for the μ ion located at $\mathbf{r}_\mu$. The quantum number l denotes both the principle quantum number in addition to the usual orbital-angular momentum quantum number and m denotes the degenerate components in a real base. N_μ is the number of the μ ion, being equal to N/5, where N is the total number ions forming the compound. The expansion coefficient $u_L^{(\mu)}(\mathbf{k})$ and the energy $E_\mathbf{k}$ as a function of wavevector, k, are obtained by solving the secular equation given in equations (3a), (3b) and (3c) of reference[13]. In evaluation of the matrix elements of $\hat{H}$ given in equation (3b) in reference [11] the Wolfsberg-Helmholtz approximation [14] is used,

$$\langle\phi_L^{(\mu)}(\mathbf{r})|\hat{H}|\phi_{L'}^{(\nu)}(\mathbf{r}-\mathbf{r}_\nu)\rangle = (G/2)(\varepsilon_l^{(\mu)}+\varepsilon_{L'}^{(\nu)})\langle\phi_L^{(\mu)}(\mathbf{r})|\phi_{L'}^{(\nu)}(\mathbf{r}-\mathbf{r}_\nu)\rangle \tag{4}$$

where G is an adjustable parameter taken to be 1.75 and $\varepsilon_L^{(\mu)}$ is the atomic energy of the L state of the μ ion. The overlap integral

$$\langle\phi_L^{(\mu)}(\mathbf{r})|\phi_{L'}^{(\nu)}(\mathbf{r}-\mathbf{r}_\nu)\rangle \tag{5}$$

can be transformed into basic overlap integrals by the use of direction cosines (α,β,γ) of $\mathbf{r}_\nu$, as shown in the table of Slater and Koster[15]. The primary objective of this paper is to calculate the total density of states and compare electronic total energies for the cubic and tetragonal phases. The electronic total energy E_{total} is given by $\int^{E_f} g(E)EdE$ using the

total density of states D(E) where E_f is the Fermi energy of the compound.

In the calculation procedure input data are atomic data of Herman and Skillman[16], lattice constants, and the value of the adjustable parameter G. The atomic positions of the ions in the tetragonal phase were taken from neutron powder diffraction refinement data. Using a self-consistent-field calculation based on the prescription of Herman and Skillman and with the use of Schwarz's exchange-correlation parameters[17], we obtain atomic orbitals. In the band structure calculation the atomic orbitals used are 5p and 6s for Ba^{+2},3p, 3d and 4s for Ti^{+4} and 2s and 2p for oxygen (-2).

4 Results and Discussion

The band structure Total Density of States for barium titanate shown in Figures 1 and 2 for the cubic and tetragonal phases respectively, shows the characteristic features of titanate perovskites. The total calculated occupied band consists of widly spaced subbands that result from (in order of increasing energy) Ti 3p, O 2s, Ba 5p and O 2p states. The contribution to the unoccupied band consists primarily of Ti 3d, Ti 4s and Ba 6s states. The density of states show a band gap of 3.0 eV in good agreement with measured values of 3.2 to 3.4 eV. From the electronic total energies calculated for the cubic and tetragonal phases it is shown that the tetragonal phase is stable as compared with the cubic phase and the energy difference is 0.58 eV/unit cell. The primary change between the cubic and tetragonal phases can be seen at the highest energy of the occupied states. This change results from a change in the 2p partial density of states of the axial oxygen atom as shown in Figure 2: this corresponds

to a change in the oxygen 2p state along the tetragonal c-axis.

The density of states have been compared to the relevant experimental data. Figure 3 is an enlarged view of the valence band region of cubic $BaTiO_3$. Four distinct features can be observed in the XPS spectra [5] that agree with the calculated result: two high energy peaks and two shoulders on the low energy side of the valence band. The calculated results agree in the relative peak heights as well as the widths. Figure 4 shows the wide range of XPS spectra[5] for cubic $BaTiO_3$ superimposed on the total density of states. The XPS spectrum mainly consists of five structures, and from the comparison of this spectrum with the calculated one, we can assign that in order of increasing energy. These structures correspond to Ti 3p, Ba 5s, O 2s, B 5p and O2p states. There is agreement with the valence band (composed primarily of the oxygen 2p states), the oxygen 2s states and the Ti 3p states. The Ba 5s states are not shown since they were not used in the calculation procedure. The inclusion of these states would, due to coulomb repulsion, raise the energy of the Ba 5p states. X-ray emission spectra can be related to the partial density of states of the corresponding emitting ion. Oxygen K x-ray emission is proportional to the oxygen 2p partial density of states: experimental data [9] is superimposed in Figure 5. There is good agreement with the calculated structure. In Figure 6, the emission spectra for Ba N_V x-ray emission [9] with the Ba 5p partial density of states is shown. The three features are apparent; however the observed shift of the central peak is again due to the omission in the calculation of the Ba 5s states as already mentioned. In Figure 11, x-ray absorption spectra of Ti [8] is superimposed on the Ti 3d partial density of states. The titanium $L_{2,3}$

absorption spectra results from transitions from the Ti 2p states to unoccupied levels derived primarity from the Ti 3d states. In the low energy region there is good agreement between the experimental and calculated results: for the high energy region there is some discrepancy. In the calculation, atomic states are not expected to be good approximations to conduction band states due to their large interaction and spatial extent. In the x-ray absorption process, multiple scattering theory leads to a result much better that the result obtained from the band structure calculations based on the XHTB method.

5 Conclusions

Band structure calculations for both the cubic and tetragonal structures of barium titanate have been performed based on an extended Huckel tight-binding method and the total density of states, partial density of states, and electronic total energies have been calculated. The tetragonal structure is shown to be stable as compared with the cubic phase based on electronic total energy. The agreement between theory and experimental results is excellent. The inclusion of further atomic states (Ba 5s orbital) would improve the small discrepancies observed with respect to the barium sites.

6 Acknowledgements

This research was supported by a URI program of the Air Force Office of Scientific Research, Contract No. 90-0174. One of us (M.K.) would like to acknowledge the support of the Japanese Ministry of Education for making his stay in the United States of America possible.

References

[1] A.H.Kahn and A. Leyendeckeer, Phys. Rev. **A135**, 1321 (1964).

[2] L.F.Mattheiss, Phys. Rev. **B6**, 4718 (1972).

[3] F.M.Michel-Calendini and G.Mesnard, J.Phys. C. **6**, 1709 (1973).

[4] S.P.Kowalczyk, F.R.mcFeely, L. Ley, V.T.Gritsyna, and D.A.Shirley, Solid State Comm. **23**, 161 (1977).

[5] P.Pertosa and F. Michel-Calendini, Phys. Rev. **B17**, 2011 (1978).

[6] F.L.Battye, H. Hoechst, and A. Goldman, Solid State Comm. **19**, 69 (1976).

[7] M. Rozova, D.E.Onopko, S. A. Titov, and Y. P. Kostikov, Sov. Phys. Solid State **23**, 992 (1981).

[8] I.G.Shveitser, M. Mazuritskii, and O.I.Prokopalo, Sov. Phys. Solid State **25**, 1305 (1983).

[9] V.V.Nemeshkalenko and A. Timoshevskii, phys. stat. sol. (b) **127**, 163 (2985).

[10] L.A.Grunes, R.D.Leapman, C.N.Wilker, R.Hoffman, and A. Kunz, Phys. Rev. **B25**, 7157 (1982).

[11] M. Kitamura and S.Muramatsu, Phys. Rev. **B42**, 1417 (1990).

[12] C. M. W. H.R.P.Inoue, M. Kitamura and H. Chen, Philo. Mag. Lett. **63**, 345 (1991).

[13] M. Kitamura and S.Muramatsu, Phys. Rev. **B41**, 1158 (1990).

[14] M.Wolfsberg and L. Helmholtz, J. Chem. Phys. **20**, 837 (1962).

[15] J.C.Slater and G.F.Koster, Phys. Rev. **94**, 1498 (1954).

[16] F.Herman and S. Skillman, *Atomic Structure Calculations*, Prentice-Hall, Englewood Cliffs, N.J., 1963.

[17] K.Schwartz, Phys. Rev. **B5**, 2466 (1972).

List of Figure Captions

Figure 1. Total density of states per unit cell versus energy (eV) measured relative to vacuum level for cubic and tetragonal $BaTiO_3$. Shaded regions indicate occupied states. Energy difference, E_{total}(tetra) - E_{total}(cubic), of the electronic total energies E_{total} between tetragonal and cubic phases is 0.58 eV/unit cell.

Figure 2. Partial density of states per unit cell versus energy (eV) of the axial oxygen 2p states measured relative to vacuum level for the cubic (a) and tetragonal (b) phases. Shaded regions indicate occupied states.

Figure 3. Enlarged view of the valence band of the cubic phase for G = 1.75. Superimposed is the XPS valence band spectrum. (Pertosa et. al., 1978).

Figure 4. Total density of states per unit cell versus energy (eV) measured relative to vacuum level for the cubic phase. Superimposed is XPS spectrum. (Pertosa et. al., 1978).

Figure 5. Partial density of states of oxygen 2p states for the cubic phase. Superimposed is oxygen K x-ray emission spectrum. (Nemoshkalenko et. al., 1985).

Figure 6. Partial density of states of barium 5p states for the cubic phase. Superimposed is Ba N_V x-ray emission spectrum. (Nemoshkalenko et. al., 1985).

Figure 7. Partial density of states of titanium 3d states for the cubic phase. Superimposed is Ti $L_{II,III}$ x-ray absorption spectrum. (Shveitser et. al., 1983).

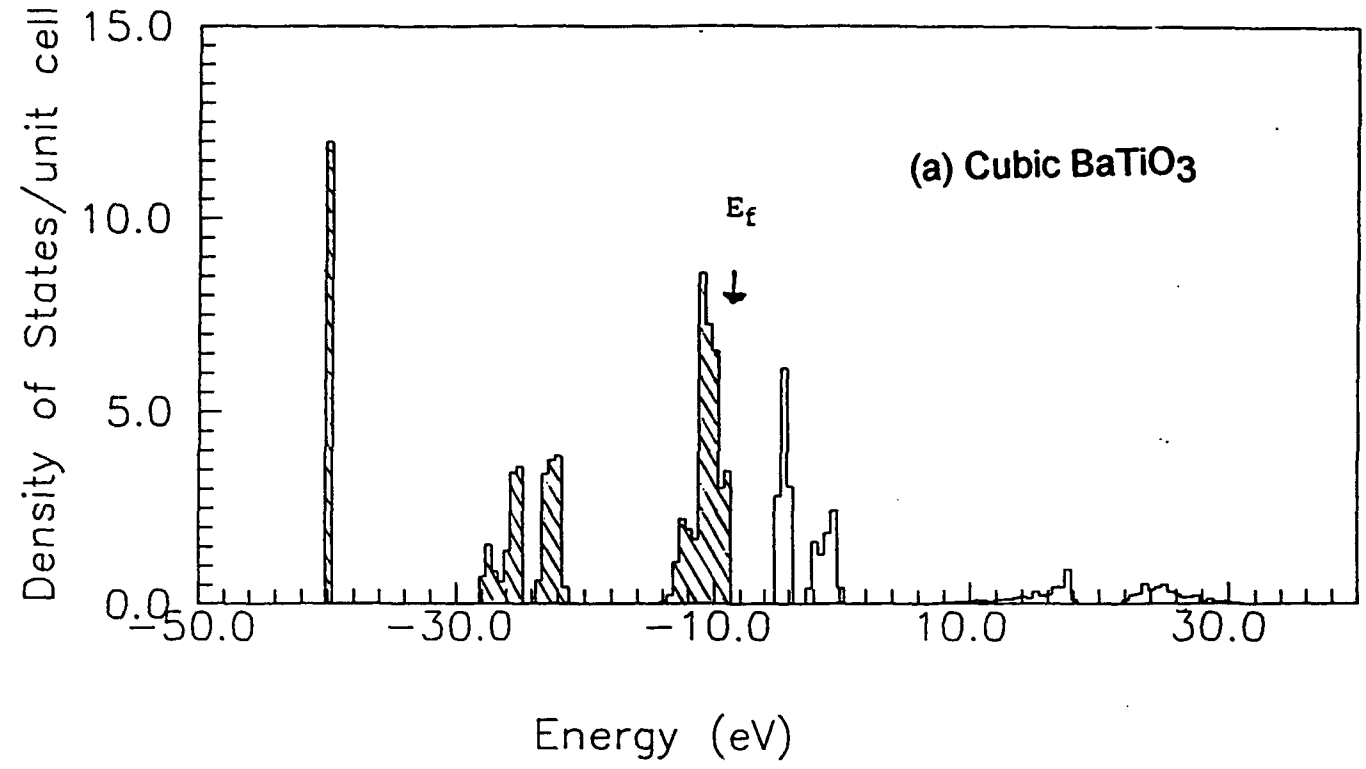
15.0
10.0
5.0
0.0
Density of States/unit cell
(a) Cubic BaTiO3
Ef
−50.0
−30.0
−10.0
10.0
30.0
Energy (eV)

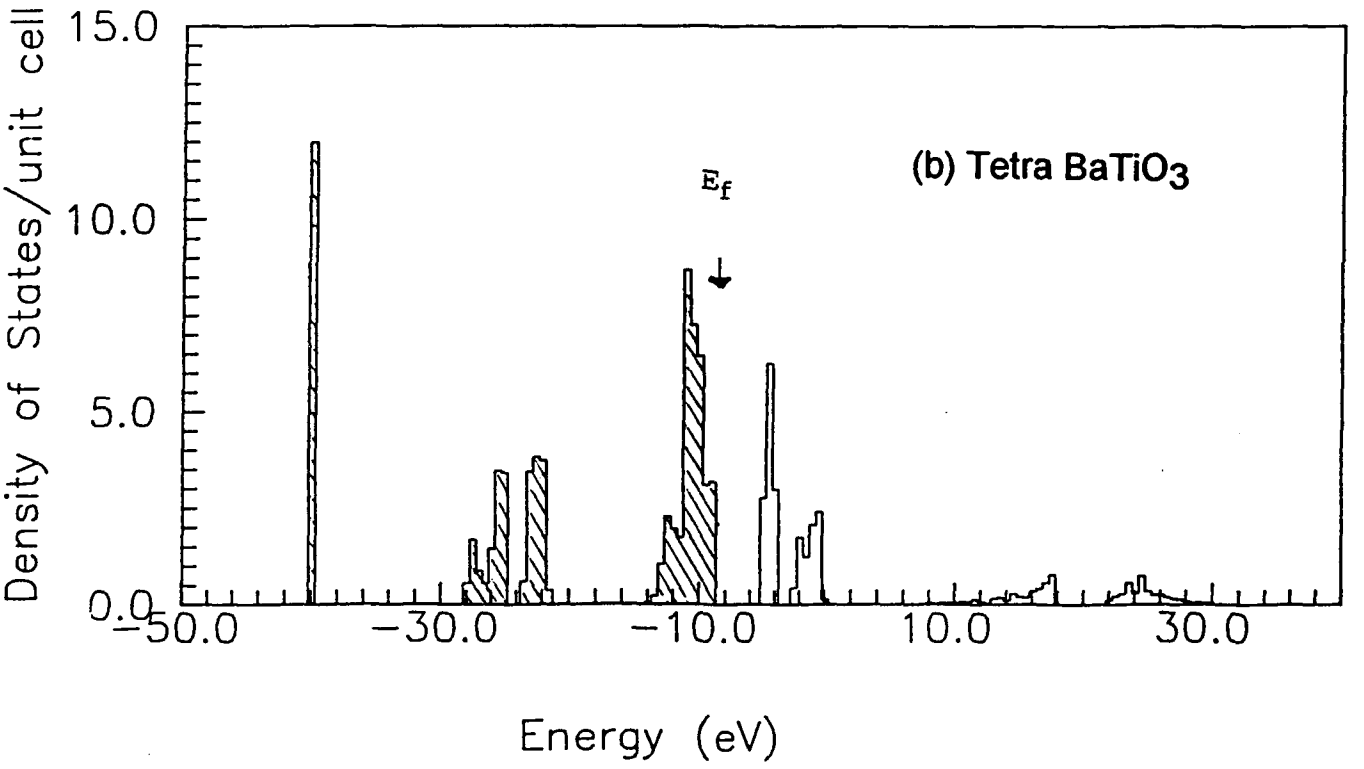
15.0
10.0
5.0
0.0
Density of States/unit cell
(b) Tetra BaTiO3
Ef
−50.0
−30.0
−10.0
10.0
30.0
Energy (eV)

Figure 1.

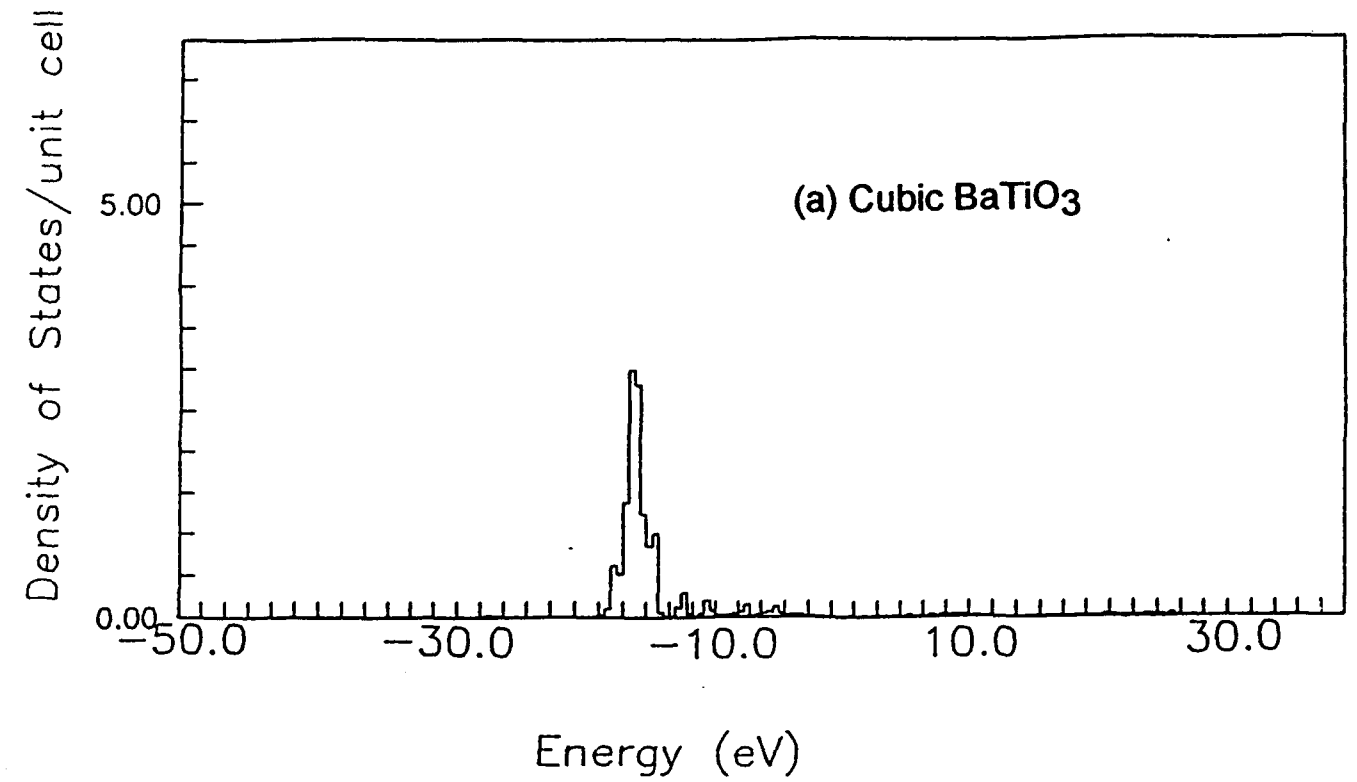
Density of States/unit cell
5.00
0.00
(a) Cubic BaTiO3
−50.0
−30.0
−10.0
10.0
30.0
Energy (eV)

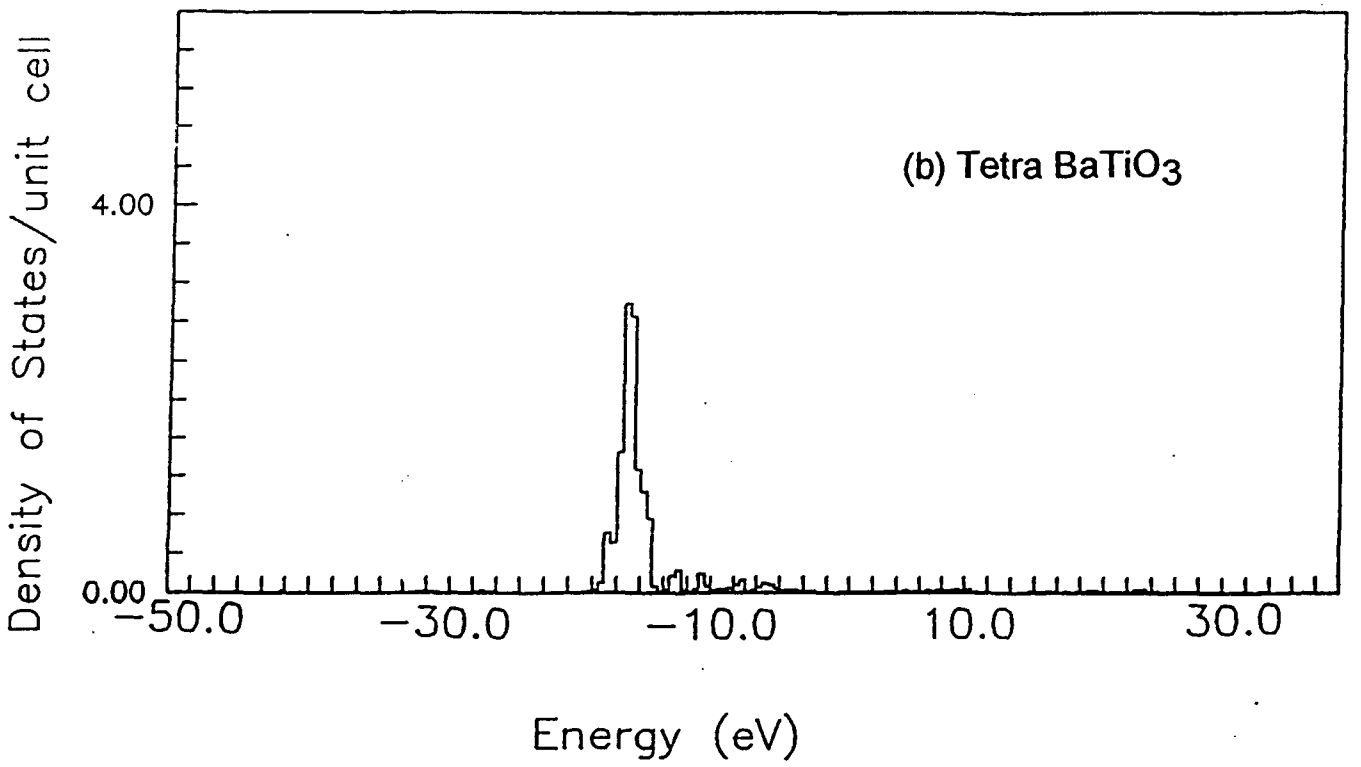
Density of States/unit cell
4.00
0.00
(b) Tetra BaTiO3
−50.0
−30.0
−10.0
10.0
30.0
Energy (eV)

Figure 2.

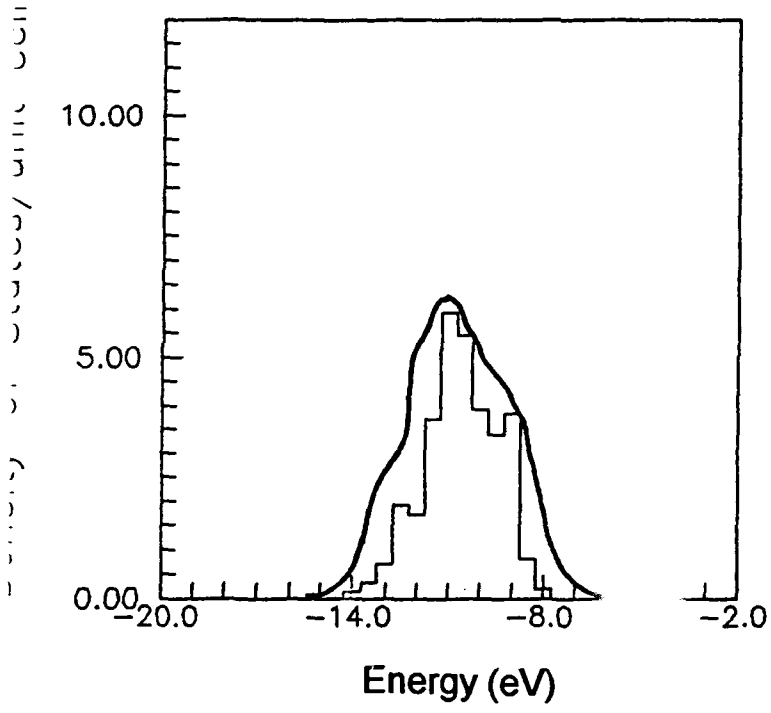

Cubic Barium titanate

Valence band

Figure 3.

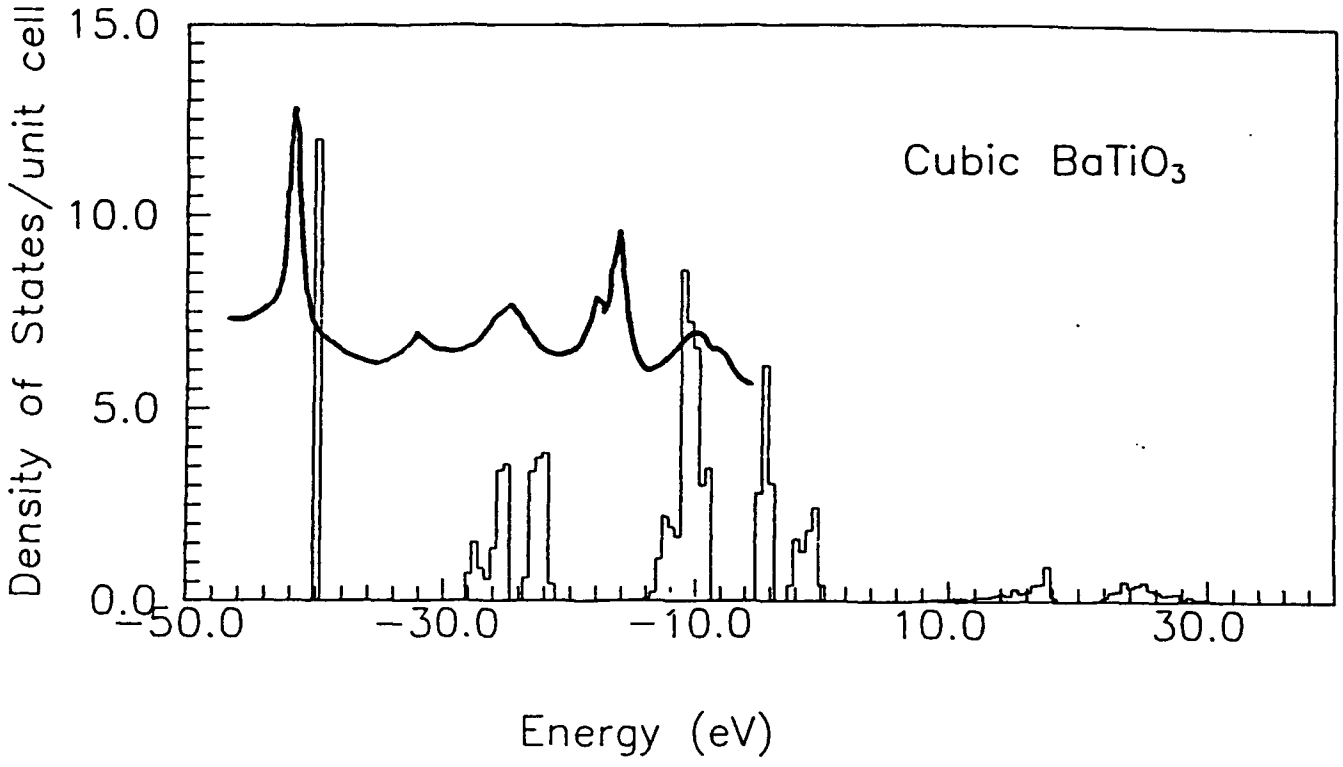
Density of States/unit cell
15.0
10.0
5.0
0.0
Cubic $BaTiO_3$
−50.0
−30.0
−10.0
10.0
30.0
Energy (eV)

Figure 4.

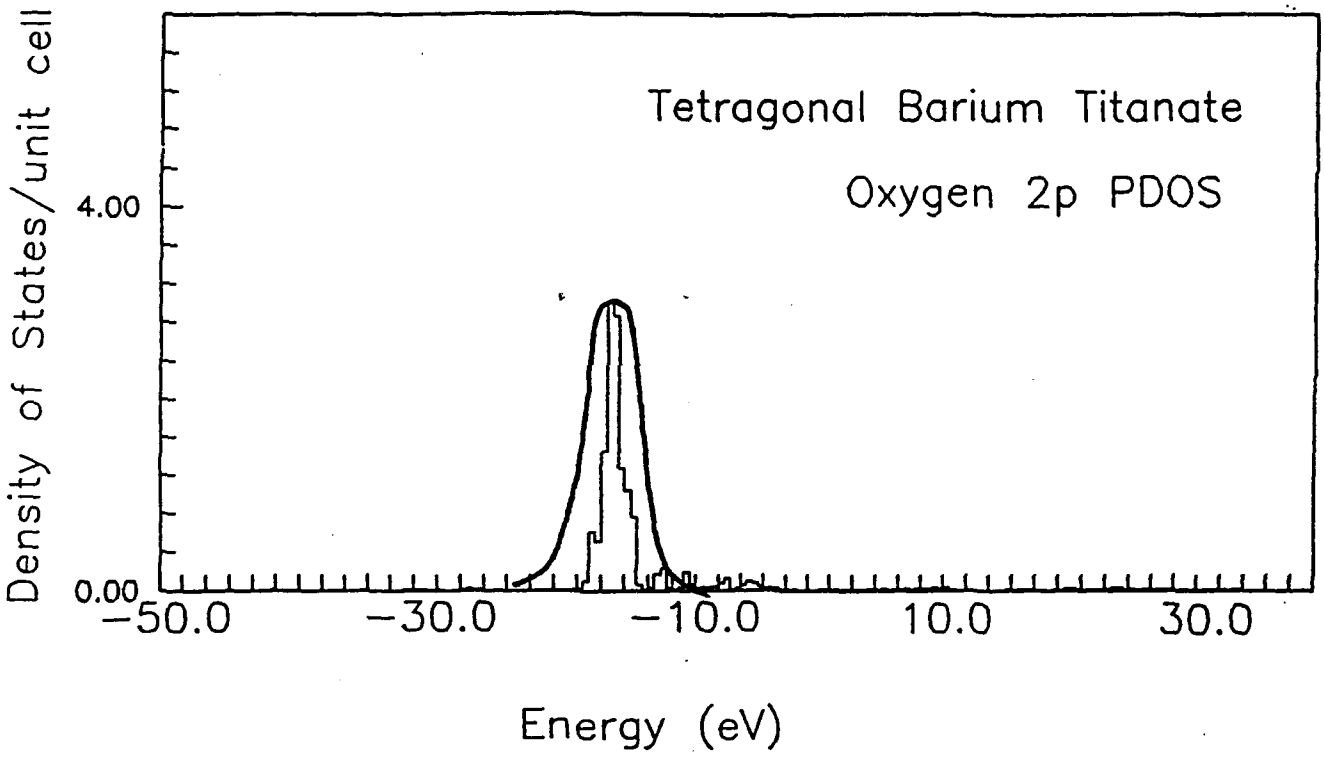
Tetragonal Barium Titanate
Oxygen 2p PDOS
Density of States/unit cell
4.00
0.00
−50.0
−30.0
−10.0
10.0
30.0
Energy (eV)

Figure 5.

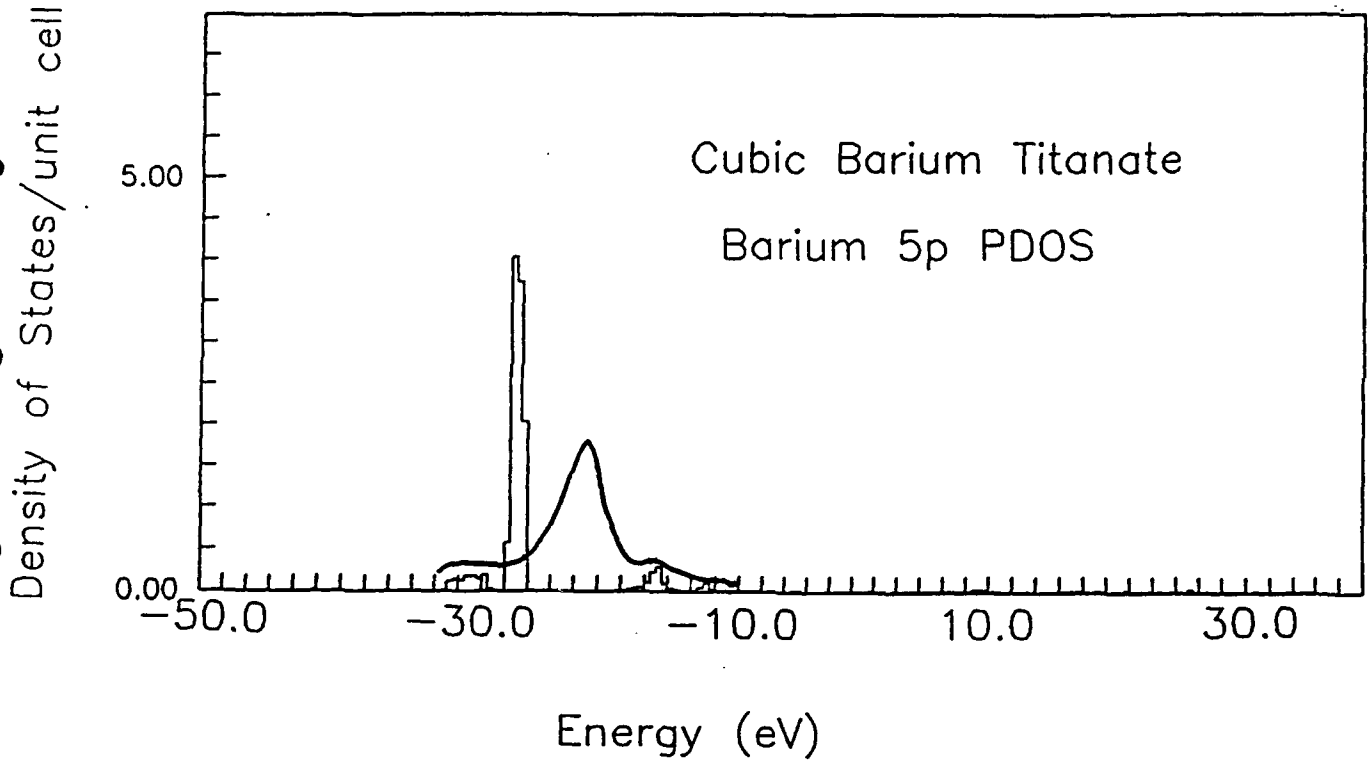
Cubic Barium Titanate
Barium 5p PDOS
Density of States/unit cell
5.00
0.00
−50.0
−30.0
−10.0
10.0
30.0
Energy (eV)

Figure 6.

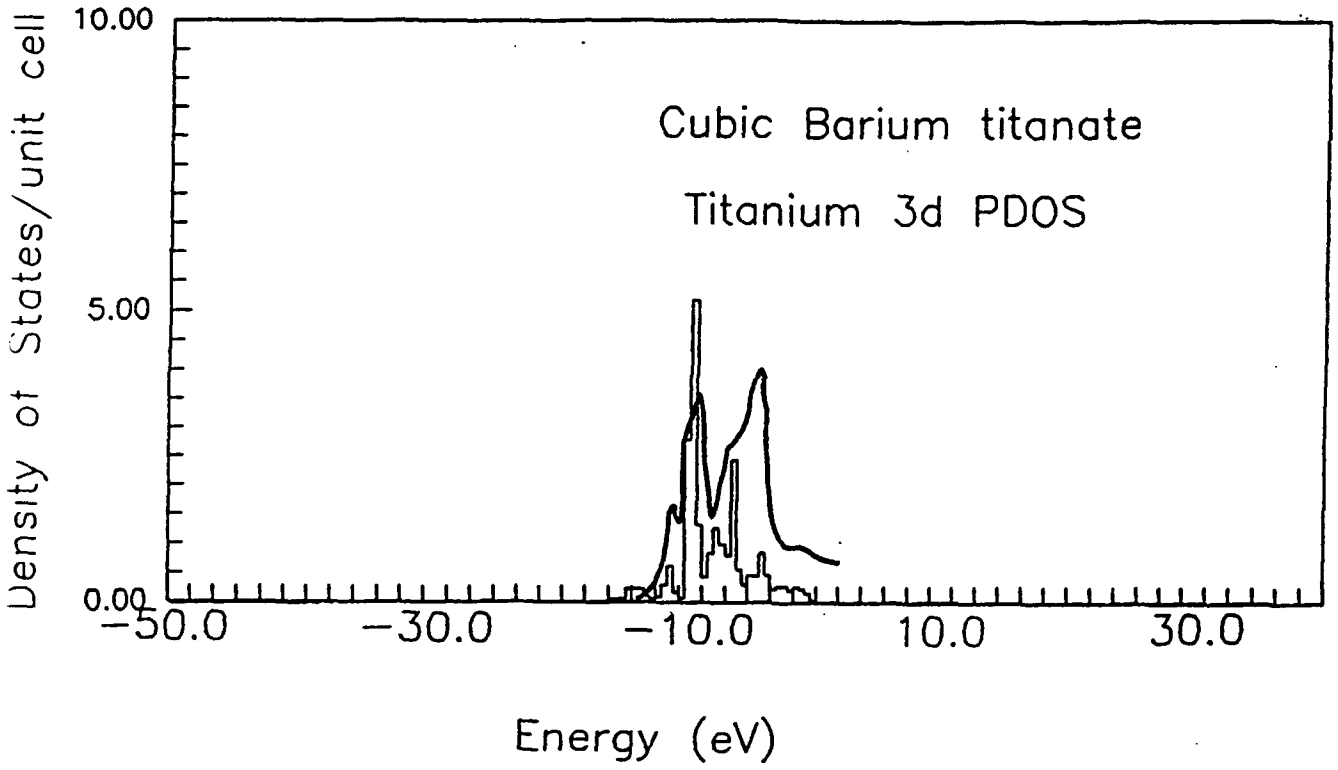
Cubic Barium titanate
Titanium 3d PDOS
Density of States/unit cell
10.00
5.00
0.00
−50.0
−30.0
−10.0
10.0
30.0
Energy (eV)

Figure 7.

// first draft. → Physical Review Letters.

X-Ray Thermal Diffuse Scattering Study of Soft Modes in Paraelectric $BaTiO_3$

N. Takesue and H. Chen
Department of Materials Science and Engineering,
University of Illinois at Urbana-Champaign,
Urbana, Illinois 61801, U. S. A.

Distribution of the x-ray thermal diffuse scattering intensities from the paraelectric $BaTiO_3$ has been observed as a function of temperature. The sheet of the diffuse scattering which had been observed previously was well reproduced on a (100) plane in a reciprocal lattice space, showing characterized intensity distribution from the TA and overdamped TO modes with the [100] polarization. The distribution and temperature dependence of the diffuse intensities also agreed with the results from the previous neutron inelastic scattering experiment. In addition, the phonon dispersion curves of the TA modes with a [100] polarization were first found out to be also anisotropic with the modes with other polarizations.

The two-dimmensional sheets of the diffuse scattering on {100} planes in a reciprocal lattice space were observed from $KNbO_3$ [1),2),4)] and $BaTiO_3$ [1)-3)] in the x-ray diffraction experiments. Because of their significant intensities it has been thought that the observed diffuse sheets might show a precursory effect which would play an important role on the ferroelectric phase transformation in those perovskite materials. There have been two theoretical models explaining the origin of the diffuse sheets; one is Hüller's model[5),6)] based upon the soft-optic dipole interaction and the other is R. Comes, M. Lambert and A. Guinier's model[1),2)] of the order-disorder type. Models were both suggested to reasonably produce the diffuse sheets on {100) planes.

The ferroelectric phase transformation was originally studied by W. Cochran[7)], based upon the lattice dynamics. It was mentioned that at least one of the TO modes must decrease its energy in proportional to $(T-T_0)$, where T_0 corresponds to the paraelectric Curie temperature. As a result, the anomaly of the low-frequency dielectric constant appears near the critical temperature. The neutron inelastic scattering experiments were then performed by Y. Yamada, G. Shirane and A. Linz[8)], and J. Harada, J. D. Axe and G. Shirane[9)], to observe how the actual vibrational modes in the paraelectric phase, which exists at temperature $T>T_C\approx130$ °C, are related to the subsequent ferroelectric phase transformation. It was clearly showed that the TO mode with the polarization along the <100>-type direction is overdamped[8),9),10),11)] with a significant temperature dependence[8)] of the scattering

intensity at small $\vec{q}$ around the zero neutron energy loss. Furthermore, there was a suprisingly strong anisotropy[9] between the uncoupled-phonon dispersion curves with the <100>-type and any other polarizations of the TO modes. The uncoupled dispersion curves were calculated from the experimental data by using the analytical approximation form expressing the phonon energy near $\vec{q}$=0 with the $\vec{q}$-dependent expansion coefficient $\Lambda_j(\hat{q})$ explicitly included as follows,

$$h^2\omega^2(j\vec{q})=h^2\omega^2(0)+\Lambda_j(\hat{q})|\vec{q}|^2+\cdots \qquad (1).$$

The expansion coefficient $\Lambda_j(\hat{q})$ for any q vector with the <100>-type polarization have low values all over the $\vec{q}$, while the one with aother polarization, for example , <110> steeply goes up. They concluded that due to this anisotropy between the dispersion curves, the diffuse sheets on the {100} planes might exist with the low values of the expansion coefficient reflected. The results of the neutron inelastic scattering experiments, whose feature is similar to one of Hüller's model, phenomenologically suggested the overdamped optic motion of atoms along the polarization directions <100> to make the predicted chain structure along the same <100> directions on which the motions of atoms are strongly correlated with each other[9].

We used a poled crystal of $BaTiO_3$ with size 4.1×2.8×1.0 mm^3 and a surface normal almost along a [100] direction. It has a quite small amount of impurities. In this study, the x-ray diffuse scattering measurement was made by using the synchrotron radiation source at National Synchrotron Light Source in Brookhaven National Laboratory. A wavelength here used is 1.1808 Å. The x-ray diffuse scattering measurement was successively done at 200, 150 and 135 °C on a cooling cycle. From abrupt change in an intensity of a Bragg peak the transition temepratures were defined as 132.5 and 129 °C on a heating and cooling cycles.

Intensity distribution of the sheet of the diffuse scattering on a (100) plane at 200, 150 and 135 °C is mapped in figures 1 (a), (b) and (c), respectively. In each figure there are two kinds of diffuse scattering distributed around a (400) and (410) reflections. We clearly see the sheet of the intensities around a (400) zone center reproduced at all the three temperatures. It is noticeable that at $|\vec{q}|$>about 0.25 the intensity distribution is quite flat and almost cicular, while it is considerably steep within $|\vec{q}|$=0.25 and elongated along [010] and [001] directions. On the other hand, distribution of the diffuse scattering around a (410) zone center is weaker than the other. Especially, there is almost no significant scattering at $|\vec{q}|$>about 0.25. Only the steep intensity distribution is recognized at $|\vec{q}|$<about 0.25. As mentioned by J. Harada and G. Honjo[3] in the previous paper, a reason is mostly related to a difference in static

crystal structure factors between a (400) and (410) reflections which measure the diffuse scattering intensities from the acoustic modes around each reflection.

The diffuse scattering intensities from the acoustic modes around a (400) and (410) reflections are each proportional to their static structure factors. They are expressed at each reflection as $F(400)=f_{Ba}+f_{Ti}+3f_O$ and $F(410)=f_{Ba}-f_{Ti}-f_O$, where f_{Ba}, f_{Ti} and f_O are atomic scattering factors of elements. We see that the structure factor of a (400) reflection is much larger than the other since an atomic scattering factor of a Ti atom is relatively large in all the elements of this substance and a difference of $4f_O$ can not be neglected. As a result, the intensity distribution is not significant around the (410) zone. Consequently, it is understood that the flat intensity distribution around a (400) reflection at $|\vec{q}|$>about 0.25 is caused by large contribution of the diffuse scattering intensities from the TA modes with the [100] polarization in the lowest branches. In fact, wee see continuously slight reductions of the diffuse scattering intensities of the flat and circular distribution with temperature decreased from 200 °C to 135 °C as shown in the figures. Since there is no significant temperature dependence of the frequencies of the TA modes along the [010] direction as concluded in the previous neutron inelastic scattering study[8], it well agrees with Warren's theory[12] shown by a factor of temperature T. The phonon dispersion curves of the TA modes with the [100] polarization along any $\vec{q}$ on the (100) plane must be quite flat at $|\vec{q}|$>about 0.25 with low energies and independent of temperature. Whereas it is already known that there is the strong anisotropy of the phonon dispersion curves between the TO modes with the <100>-type and the other polarizations as shown by the $\vec{q}$-dependent expansion coefficient $A_j(\hat{q})$[9], the flat and circular distribution of the diffuse scattering at $|\vec{q}|$>about 0.25 was also here found out to be due to anisotropy of the dispersion curves between the TA modes in $BaTiO_3$ with the <100>-type and the other polarizations. This new discovery of the anisotropy of the TA modes is quite similar to the results in the previous neutron inelastic scattering experiment about $KTaO_3$[13], from which the diffuse sheets were also observed in the x-ray diffraction experiment. However, the TA modes seem not to play an important role as a pretransitional effect for the ferroelectric phase transformation.

On the other hand, the steep intensity distribution at $|\vec{q}|$<about 0.25 results from strong contribution of the diffuse scattering intensities from the overdamped TO modes. As shown in figures 1, the steep intensity distribution of the diffuse scattering at all the three temperatures is elongated along the [010] and [001] directions. In the previous experiment of the neutron inelastic scattering[8], the similar intensity distribution of the highly damped TO modes with the [001] polarization was observed by Q scanning with the energy fixed to zero, giving narrow ridges of the neutron scattering intensities along the [100] and [010] directions. It corresponds to the intensity distribution at $|\vec{q}|$<about 0.25 in our measurement.

The intensity distribution from the overdamped TO modes well reproduced. Figures 2 shows cross-sectional intensity profiles at 200, 150 and 135 °C on the (100) plane along the [010] direction around the (400) zone center. The figure was extracted from the contour maps of figures 1 (a), (b) and (c). Since there is only a small temperature dependence due to the contribution of the diffuse scattering intensities from the TA mode, the profiles at k=0.3 through 0.5 are not shown in the figures. We see temperature dependences of the diffuse scattering intensities from the overdamped TO mode at k<about 0.25. As well as the neutron scattering intensities from the overdamped TO mode measured by E scanning with Q constsnt are increased with temperature lowered[8], the x-ray diffuse scattering intensities similarly behave as temperature is decreased from 200 °C to 135 °C. The change in the intensities is not so significant since the contribution from the TA mode giving high background intensities is reduced in proportional to T[12] as temperature is decreased and Debye-Waller factors, which usually indicate negative temperature dependences in the paraelectric region as is shown in a case of $PbTiO_3$[14], also lower the diffuse scattering intensities. In spite of these effect, the temperature dependence in the figure was well reproduced.

As mentioned above, in the previous neutron inelastic scattering experiment[9] it was concluded that Hüller's model[5],[6] reasonably agreed with the experimental results since the strong anisotropy as shown by the $\hat{q}$-dependent expansion coefficient $\Lambda_j(\hat{q})$ was found out, meaning that atoms in the substance optically vibrate strongly correlated with each other along the subsequent polar axis. Our observation of the distribution of the thermal x-ray diffuse scattering represented the characteristics of the results in the previous neutron inelastic scattering experiments. Especially, the intensity distribution from the overdamped TO mode was well reproduced, as well as the distribution of the sheet of the diffuse scattering. Furthermore, its temperature dependence is reasonably understood. Consequently, the study here supports Hüller's model of the dynamical atomic chain structure. The overdamped TO modes with the <100>-type polarization plays an important role as a precursory effect toward the subsequent ferroelectric phase transformation. Details will be described in a later paper to be published[15].

The present study is supported by Materials Research Laboratory in University of Illinois at Urbana-Champaign. We wish to thank Dr. Mario Maglione for providing the excellent single crystal of $BaTiO_3$. The experiment was made by using the synchrotron radiation source at MATRIX beam line X-18A at National Synchrotron Light Source in Brookhaven National Laboratory.

1) R. Comes, M. Lambert and A. Guinier, Acta Cryst. A26 (1970) 244.
2) R. Comes, M. Lambert and A. Guinier, Solid State Commun. 6 (1968) 715.
3) J. Harada and G. Honjo, J. Phys. Soc. Japan 22 (1967) 45.
4) M. Holma, H. Hong, M. Nelson and H. Chen, Mat. Res. Soc. Proc. 307 (1993) 293.
5) A. Hüller, Solid State Commun. 7 (1969) 589.
6) A. Hüller, Z. Physik 220 (1969) 145.
7) W. Cochran, Advan. Phys. 9 (1960) 387.
8) Y. Yamada, G. Shirane and A. Linz, Phys. Rev. 177 (1969) 848.
9) J. Harada, J. D. Axe and G. Shirane, Phys. Rev. B4 (1971) 155.
10) A. S. Barker, Phys. Rev. 145 (1966) 391.
11) M. Didomenico, S. P. S. Porto and S. H. Wemple, Phys. Rev. Letters 19 (1967) 855.
12) "X-Ray Diffraction", B. E. Warren, published by Addison-Wesley Publishing Company, Inc., Massachusetts (1969) 151.
13) R. Comes and G. Shirane, Phys. Rev. B5 (1972) 1886.
14) R. J. Nelmes, R. O. Piltz, W. F. Kuhs, Z. Tun and R. Restori, Ferroelectrics 108 (1990) 165.
15) N. Takesue and H. Chen, Phys. Rev. B. to be published.

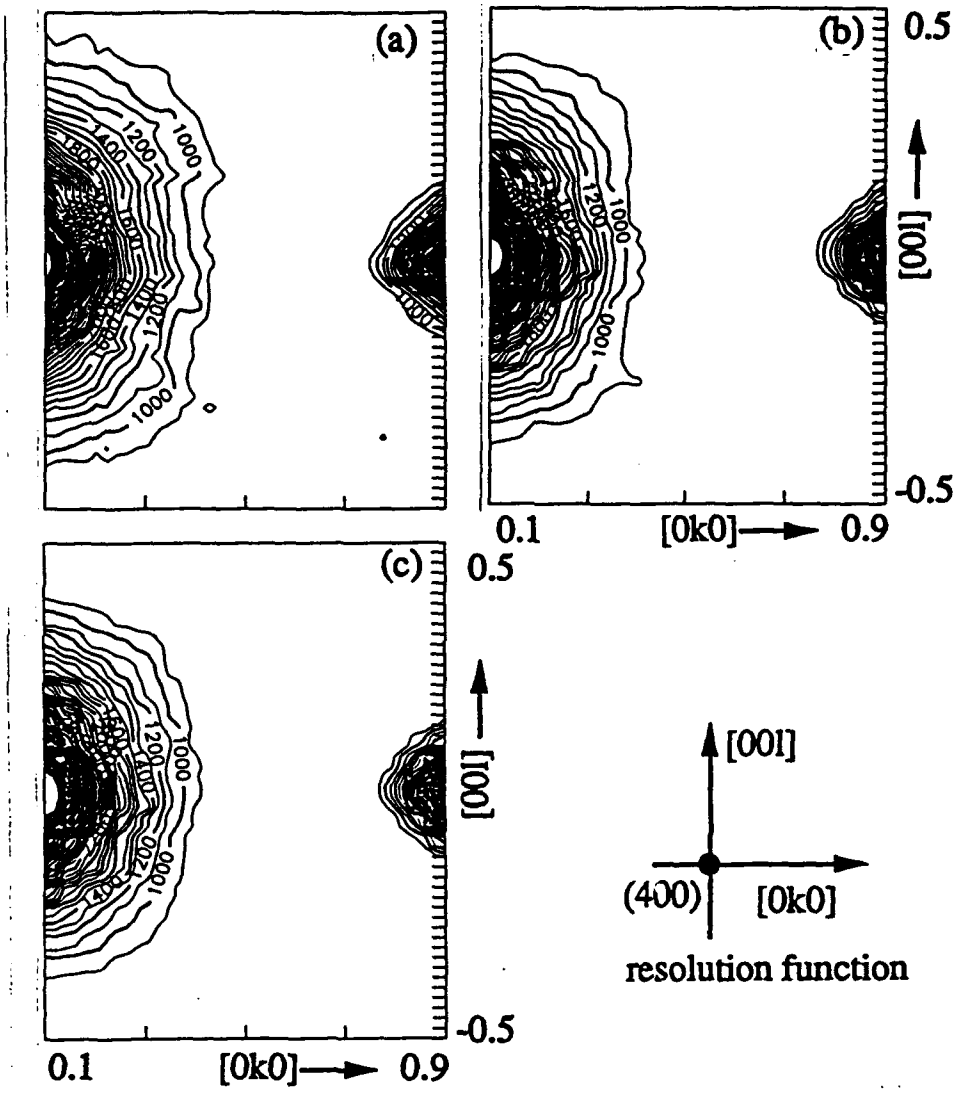

Figures 1. Contour maps of the intensity distribution of the x-ray diffuse scattering on the (100) plane at 200, 150 and 135 °C shown in (a), (b) and (c), rspectively. Figures clearly show the sheet of intensity around a (400) reflection on the plane. An approximate resolution function at a (400) reflection is indicated by a round-shaped mark above. A unit of the intensity is arbitrary.

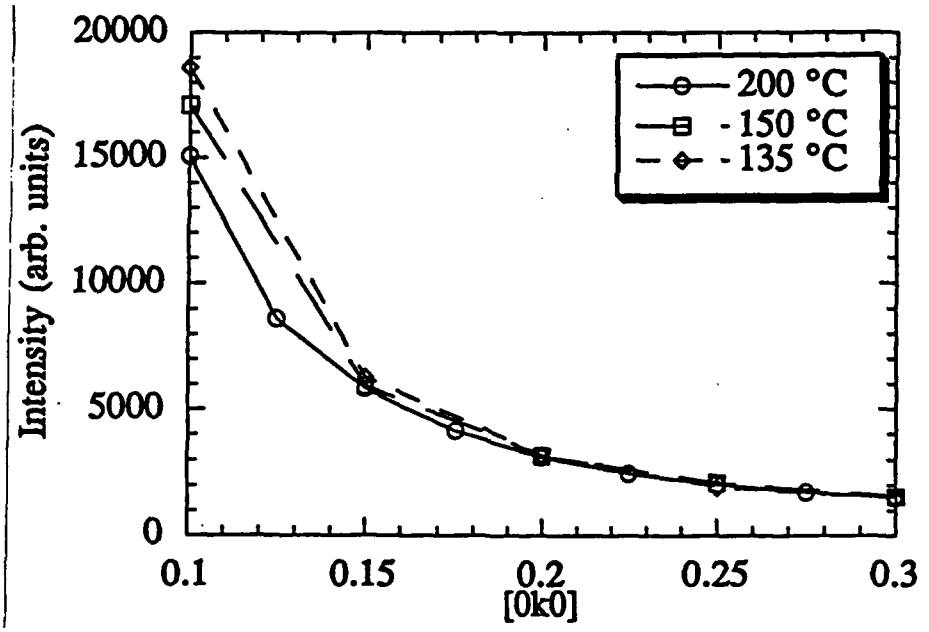

Figure 2. Temperature dependences of the diffuse scattering intensities from the overdamped TO mode around the (400) zone center. Intensity profiles at 200, 150 and 135 °C are cross sections of the contour maps of figures 1 (a), (b) and (c). They are all on the (100) plane along the [010] direction at l=0.

POTASSIUM NIOBATE ($KNbO_3$)

Elastic properties of orthorhombic $KNbO_3$ single crystals by Brillouin scattering

A. G. Kalinichev,[a] J. D. Bass, and C. S. Zha[b]
Department of Geology, University of Illinois at Urbana–Champaign, Urbana, Illinois 61801

P. D. Han and D. A. Payne
Department of Materials Science and Engineering, University of Illinois at Urbana–Champaign, Urbana, Illinois 61801

(Received 7 July 1993; accepted for publication 6 August 1993)

Brillouin light scattering was used to obtain elastic and piezoelectric constants for a single domain orthorhombic $KNbO_3$ single crystal at room temperature and pressure. More than 320 measurements of longitudinal and transverse acoustic wave velocities were obtained in 160 different crystallographic directions. An inversion of these data using the literature values for the dielectric permittivity of $KNbO_3$ resulted in the full set of elastic and piezoelectric constants for the material. It is suggested that the difference between piezoelectric constants obtained by high- and low-frequency methods could be explained by the high-frequency relaxation-type dispersion for the dielectric constant ϵ_{33} in the GHz region by analogy with $BaTiO_3$. The directional dependence of electromechanical coupling for longitudinal and transverse acoustic waves in $KNbO_3$ was analyzed. The obtained elastic constants were (in GPa): $C_{11}^E=224(4)$, $C_{22}^E=273(5)$, $C_{33}^E=245(5)$, $C_{44}^E=75(1)$, $C_{55}^E=28.5(5)$, $C_{66}^E=95(2)$, $C_{12}^E=102(5)$, $C_{13}^E=182(10)$, $C_{23}^E=130(6)$, where E denotes constant electric field strength.

I. INTRODUCTION

Potassium niobate $KNbO_3$ is an important ferroelectric material with the perovskite structure.[1–3] Similar to the more extensively studied isomorphous analog, $BaTiO_3$, it shows the same sequence of structural phase transformations on cooling from high temperature with the crystallographic symmetry being reduced from cubic →tetragonal→orthorhombic→rhombohedral. The mechanisms for the phase transformations (i.e., their displacive or order-disorder character) are still under discussion.[4–7]

Unlike tetragonal $BaTiO_3$, $KNbO_3$ is orthorhombic at room temperature, with space group Bmm2 and the crystallographic lattice parameters $a=5.695$ Å, $b=3.973$ Å, and $c=5.721$ Å.[8,9] The spontaneous polarization vector is parallel to the c axis (i.e., parallel to the [110] direction of the prototypic high-temperature cubic state). The dynamical properties of the orthorhombic phase have been studied by various techniques, including Raman,[4,6,7,10] infrared,[5] inelastic neutron,[11] and diffusive x-ray[12] scattering as well as dielectric[13,14] measurements. According to its symmetry, orthorhombic $KNbO_3$ has nine independent elastic and five piezoelectric constants.[15] The entire set of elastic constants was first calculated by Phatak *et al.*[12] from diffuse x-ray scattering data. Using dielectric measurements, Wiesendanger[13] later showed, that the values of Phatak *et al.*[12] were in error, as they contradicted the slopes of acoustic phonon branches,[11] differed considerably from stiffness constants in related materials, and violated stability criteria. Wiesendanger[13] determined seven of the nine elastic moduli and two piezoelectric constants. Three remaining piezoelectric constants were measured by Günter.[14] Both measurements were carried out in the kHz and MHz range of frequencies.

In this paper we present the first results for the complete set of elastic and piezoelectric constants for an orthorhombic $KNbO_3$ single crystal measured using the high frequency (7–50 GHz) Brillouin light scattering technique. We will also discuss the possible influence of the high-frequency relaxation on the electromechanical properties of this material.

II. EXPERIMENTAL

The $KNbO_3$ single crystals used in our study were grown by a modified Kyropoulos method,[16,17] using a {100} seed and pure chemicals of K_2CO_3 (99.99%) and Nb_2O_5 (99.99%). As-grown $KNbO_3$ crystals up to 30 ×30×10 mm in size were usually multidomain at room temperature due to phase transformations on cooling. Single domain $KNbO_3$ crystals were obtained by a poling process at 500 V/cm (dc) and 198 °C in silicone oil. The single domain crystals were colorless and transparent. X-ray analysis of the $KNbO_3$ crystals at room temperature gave orthorhombic lattice parameters $a=5.697$ Å, $b=3.971$ Å, and $c=5.722$ Å. Qualitative chemical analysis indicated the total impurity level was less than 100 ppm. These results were confirmed by quantitative electron probe microanalysis of the crystal studied, which yielded the homogeneity of almost 1:1 for the K:Nb atomic ratio at three different points in the crystal with no traces of other elements at the 0.2% level. Excellent optical homogeneity in single domain crystals was confirmed by Twyman–Green

[a]On leave from: Institute of Experimental Mineralogy, Russian Academy of Sciences, 142432 Chernogolovka, Moscow District, Russia.
[b]Present address: Geophysical Laboratory, Carnegie Institution of Washington, 5251 Broad Branch Rd., N. W. Washington, DC 20015-1305.

 0021-8979/93/74(11)/6603/6/$6.00

interference measurements, and the inhomogeneity of refractive indices was less than 10^{-6} for a $5\times5\times2$ mm $KNbO_3$ crystal.

The specimen chosen for the Brillouin measurements was a clear and colorless single crystal with dimensions of $0.3\times5\times1.6$ mm along the orthorhombic a, b, and c axis, respectively. The crystal faces were polished smooth with a 0.5-μm Al_2O_3 precision lapping film. Polishing was minimized because it tended to introduce a slight curvature to the sample surfaces, especially near the edges. The specimen was oriented using an x-ray diffractometer and determined to be single domain.

A full description of the Brillouin apparatus used in this study can be found elsewhere.[18,19] We present here mainly the experimental details specific to the data collection of $KNbO_3$.

The light from an Ar-ion laser with a wavelength of $\lambda=514.5$ nm was scattered from the crystal and collected in a 90° scattering geometry. The scattered light was analyzed by a six-pass tandem Fabry–Perot interferometer, detected by a photon counting photomultiplier, and was output to a multichannel scaler.

As is well known, Brillouin scattering occurs due to the inelastic interaction of light with acoustic phonons in the crystal. This results in a frequency shift $\Delta\omega$ of the incident light, which is related to the velocity of the acoustic phonon V_q propagating with the wave vector q by

$$V_q=\frac{\Delta\omega\lambda}{(n_i^2+n_s^2-2n_in_s\cos\theta)^{1/2}}, \tag{1}$$

where n_i and n_s are the refractive indices for the incident and scattered light, and θ is the scattering angle. The subscripts i and s refer to the directions of light inside the crystal which, in general, do not coincide with the directions of the incident and scattered light outside the crystal. As a result $\theta\neq90°$ despite the adopted 90° scattering geometry. The orientations for all surfaces of the crystal were measured using optical goniometry before the Brillouin measurements were made, so that the effects of refraction of the laser light at the sample boundaries could be calculated.[20,21]

The refractive indices of orthorhombic $KNbO_3$ single crystals at room temperature have been measured by several authors[22–24] with very good internal consistency. In the present work, values of $n_a=2.3337$, $n_b=2.3951$, and $n_c=2.2121$, reported recently by Zysset *et al.*[24] for light at wavelength $\lambda=514.5$ nm were used.

In order to reduce the amount of light scattered from the surfaces, to decrease the background noise in the spectra, and to minimize the effect of refraction on the phonon direction and scattering angles,[21] most measurements were carried out with the crystal immersed in oil (Cargille Standard Refractive Index Fluid) with a nominal refractive index of $n_D=1.535$. However, some of the measurements were carried out in air as well. We obtained very good consistency between these two sets of data, proving the reliability of the refraction correction procedures.[20,21]

A total of more than 320 measurements of longitudinal and transverse acoustic wave velocities were obtained in 160 different crystallographic directions. For most of the runs, the polarization of the incident and analyzed light was controlled by a pair of Glan-Thompson polarizers and a Fresnel Rhomb polarization rotator to help reduce the background noise and distinguish between different acoustic modes.

III. RESULTS AND DISCUSSION

The velocity V of a plane acoustic wave propagating in a direction q is related to the elastic properties of the crystal via the Christoffel equation:[25]

$$|\Gamma_{ik}-\delta_{ik}\rho V^2|=0, \tag{2}$$

where

$$\Gamma_{ik}=\{C^E_{ijkl}+[(e_{mij}q_m)(e_{nkl}q_n)/(\epsilon^S_{rs}q_rq_s)]\}q_mq_nq_jq_l, \tag{3}$$

and $\rho=4.62$ g/cm^3 is the density of $KNbO_3$. C^E_{ijkl}, e_{nkl}, and ϵ^S_{rs} are the elements of the elastic stiffness, piezoelectric stress, and dielectric permittivity tensors, respectively. The superscript E indicates the condition of constant electric field, while the superscript S indicates the condition of constant strain, or clamped permittivity.[15] The q_i's are the direction cosines of the direction of wave propagation.

In matrix notation, the nonvanishing constants for orthorhombic $KNbO_3$ (Bmm2) are[15] C^E_{11}, C^E_{22}, C^E_{33}, C^E_{44}, C^E_{55}, C^E_{66}, C^E_{12}, C^E_{13}, C^E_{23}, e_{15}, e_{24}, e_{31}, e_{32}, e_{33}, ϵ^S_{11}, ϵ^S_{22}, and ϵ^S_{33}. The piezoelectric stress coefficients e_{ij} are related to the more familiar piezoelectric strain coefficients d_{ij} by

$$e_{15}=d_{15}C^E_{55}, \tag{4a}$$

$$e_{24}=d_{24}C^E_{44}, \tag{4b}$$

$$e_{31}=d_{31}C^E_{11}+d_{32}C^E_{12}+d_{33}C^E_{13}, \tag{4c}$$

$$e_{32}=d_{31}C^E_{12}+d_{32}C^E_{22}+d_{33}C^E_{23}, \tag{4d}$$

$$e_{33}=d_{31}C^E_{13}+d_{32}C^E_{23}+d_{33}C^E_{33}, \tag{4e}$$

and the clamped dielectric constants ϵ^S_{ii} are related to the more easily measurable constant stress, or free dielectric constants ϵ^T_{ii} by

$$\epsilon_0\epsilon^S_{11}=\epsilon_0\epsilon^T_{11}-d_{15}e_{15}, \tag{5a}$$

$$\epsilon_0\epsilon^S_{22}=\epsilon_0\epsilon^T_{22}-d_{24}e_{24}, \tag{5b}$$

$$\epsilon_0\epsilon^S_{33}=\epsilon_0\epsilon^T_{33}-(d_{31}e_{31}+d_{32}e_{32}+d_{33}e_{33}), \tag{5c}$$

where $\epsilon_0=8.8542\times10^{-12}$ F/m is the dielectric permittivity of vacuum.

Equation (2) has, in general, three different solutions ρV_i^2, $i=1,2,3$, associated with one compressional and two shear waves propagating in a given direction. The measured velocities were inverted for a best fit set of elastic and piezoelectric constants by minimizing the sum of squares of differences between the measured velocities and those calculated from a trial set of constants using Eq. (2). The direct simplex method[26] of minimization was used, which allowed for rapid calculations with any number of measurements and any combination of fitting parameters to be

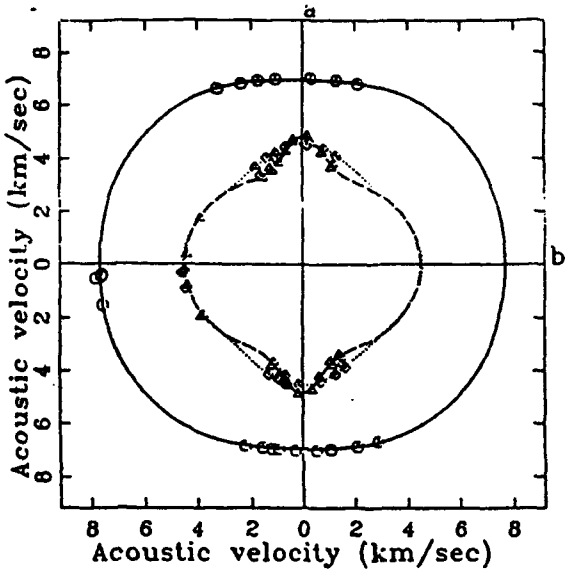

FIG. 1. Sound velocities in the *a-b* crystallographic plane. Best fit using the reported set of the elastic and piezoelectric constants. Symbols—experimental data, full line—compressional wave; dashed and dotted lines—shear waves polarized nearly prependicular and parallel to the plane, respectively

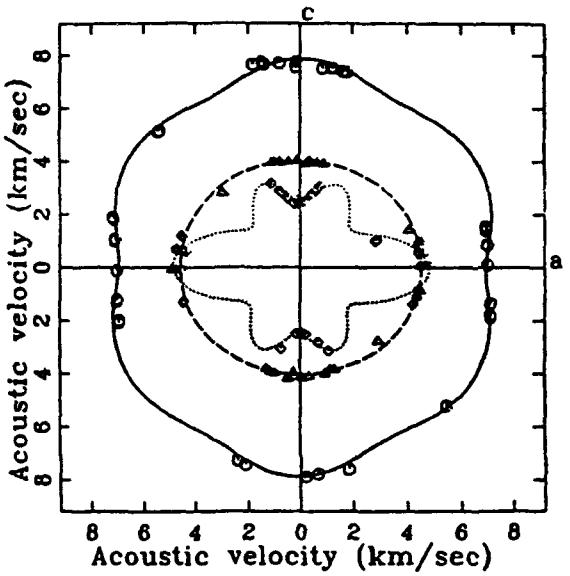

FIG. 3. Sound velocities in the *a-c* crystallographic plane. Best fit using the reported set of the elastic and piezoelectric constants. See Fig. 1 for the notation.

taken into consideration. Available data on elastic, piezoelectric, and dielectric constants[13,14] were used as a starting point for minimization.

The comparison of measured velocities with the computer-generated fit to the data is shown in Figs. 1–3 for the *a-b*, *b-c*, and *a-c* crystallographic planes, respectively. It should be noted that the discrepancies between measured and calculated velocities are slightly exaggerated on the plots, because all the data for waves directed within ±5° of the plane are projected on the corresponding

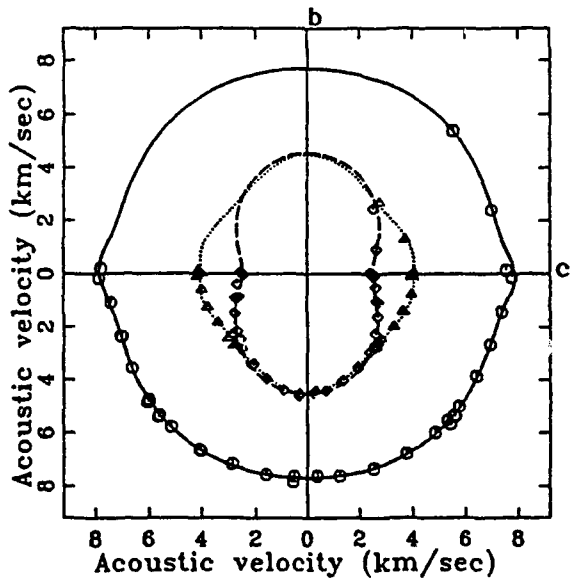

FIG. 2. Sound velocities in the *b-c* crystallographic plane. Best fit using the reported set of the elastic and piezoelectric constants. See Fig. 1 for the notation.

TABLE I. Elastic, piezoelectric, and dielectric constants of $KNbO_3$ at room temperature.

	This study	Literature[a]
	Elastic stiffness constants (GPa)	
C_{11}^E	224±4	226±2
C_{12}^E	273±5	270±2
C_{33}^E	245±5	
C_{44}^E	75±1.5	75.3±0.5
C_{55}^E	28.5±0.5	25.0±0.2
C_{66}^E	95±2	95.5±1
C_{12}^E	102±5	96±3
C_{13}^E	182±10	
C_{23}^E	130±6	
C_{33}^D	282±5	280±4
C_{44}^D	93±2	94±0.5
C_{55}^D	110±2	113±1
	Piezoelectric strain constants (10^{-11} C/N)	
d_{15}	19.2±0.5	21.5±0.5
d_{24}	15.5±0.5	15.9±0.5
d_{31}	2.7 to 4.8	0.98±0.2
d_{32}	−8.5 to −2.3	−1.95±0.2
d_{33}	−2.5 to +1.5	2.45±0.15
	Piezoelectric stress constant (C/m²)	
e_{15}	5.3±0.2	5.3±0.15
e_{24}	11.7±0.5	11.7±0.4
e_{31}	0.2 to 1.3	
e_{32}	−18.3 to −6.2	
e_{33}	−3.4±0.4	
	Dielectric constants	
ϵ_{11}^T		160±10
ϵ_{22}^T		1000±80
ϵ_{33}^T		55±5

[a]The data are from Ref. 13, except for d_{31} which are from Ref. 14.

planes. The results of the fitting procedure are given in Table I along with the values reported previously in the literature. The uncertainties reported in Table I combine experimental and computational uncertainties and are based on the root-mean-square deviation (RMSD) of the measured velocities from the best-fit model of0.11 km/s, as given by one standard deviation, $\pm 1\sigma$.

The overall agreement with the set of constants measured previously by Wiesendanger[13] using piezoelectric resonance method is remarkable. Minor differences can be attributed to the different types of crystal used in both studies. The so-called stiffened elastic constants, which are related to the unstiffened constants by

$$C_{55}^{D}=C_{55}^{E}+\frac{e_{15}^{2}}{\epsilon_{11}^{S}\epsilon_{0}}, \tag{6a}$$

$$C_{44}^{D}=C_{44}^{E}+\frac{e_{24}^{2}}{\epsilon_{22}^{S}\epsilon_{0}}, \tag{6b}$$

$$C_{33}^{D}=C_{33}^{E}+\frac{e_{33}^{2}}{\epsilon_{33}^{S}\epsilon_{0}}, \tag{6c}$$

have been measured along the crystallographic directions a, b, and c, respectively, and are also in good agreement with Wiesendanger's measurements.

The present set of measured velocities was found to be extremely insensitive to the variations of the three piezoelectric constants d_{31}, d_{32}, and d_{33} (or e_{31}, e_{32}, and e_{33}). Virtually the same quality of the fit (RMSD$\approx$0.11 km/s) can be achieved within the given error bars for all elastic, piezoelectric d_{15} and d_{24}, and dielectric constants with the three remaining piezoelectric constants being less resolved and varying within very broad limits, which are given in Table I for illustrative purposes only.

The poor resolution for these constants may be caused by the fact that they are all strongly dependent on the dielectric constant along the polar direction in the crystal, ϵ_{33}, [see Eqs. (5c) and (4c)–(4e)]. The dielectric constant ϵ_{33} of crystallographically similar $BaTiO_3$ is known to have high-frequency relaxation-type dispersion over the frequency range 10^7–10^{10} Hz.[27] Li *et al.*[28] have recently shown that this high-frequency relaxation is responsible for the difference between piezoelectric constants of $BaTiO_3$ measured by Brillouin light scattering technique and low-frequency methods. There are indications[10,27] that such relaxation exists for $KNbO_3$ crystals as well. However, direct measurements of dielectric permittivities of $KNbO_3$ in the GHz range of frequencies are required to resolve this problem. Alternatively, impurities in an amount of0.1 at. % may also significantly change the dielectric properties of $KNbO_3$.[29]

The effects of electromechanical coupling on the directional dependence of the compressional and shear moduli (ρV^2) in the a-b, b-c, and a-c crystallographic planes are demonstrated in Figs. 4–6, respectively. The $S1$ shear waves have displacements in the corresponding plane, while the $S2$ shear waves have displacements perpendicular to the plane. The dashed curves in the figures represent the same moduli with piezoelectricity ignored, i.e., calcu-

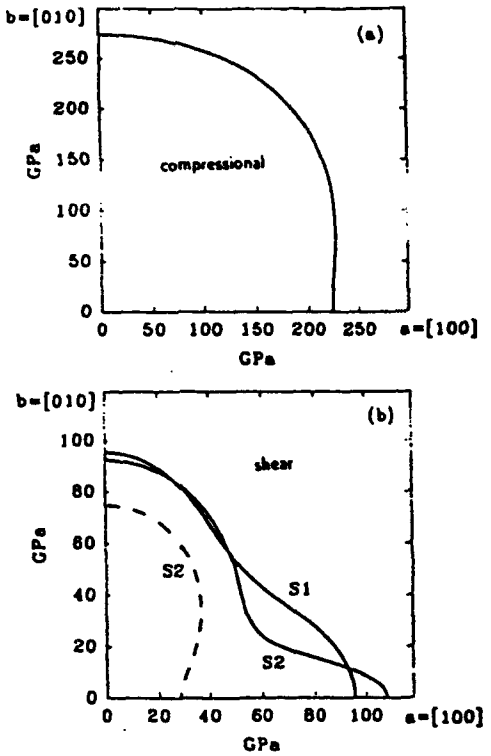

FIG. 4. Compressional (a) and shear (b) moduli ρV^2 in the a-b plane. The dashed curve is for the $S2$ shear mode with piezoelectricity ignored. The longitudinal and $S1$ shear modes are uncoupled to piezoelectricity.

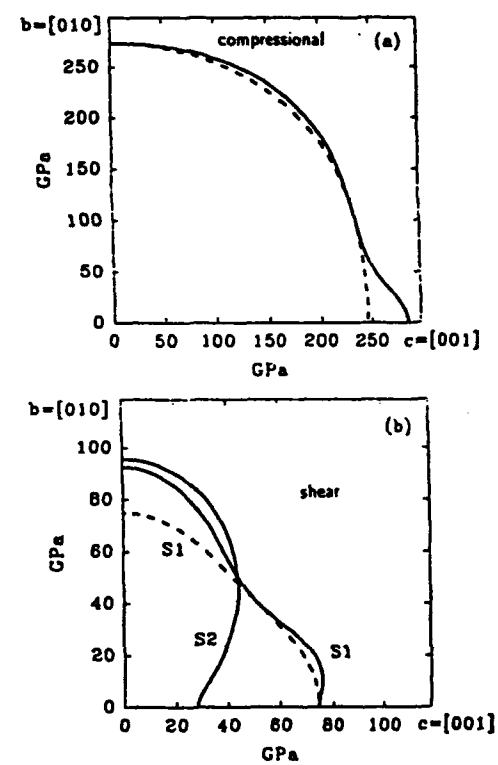

FIG. 5. Compressional (a) and shear (b) moduli ρV^2 in the b-c plane. The dashed curves are for piezoelectricity ignored. The $S2$ shear mode is uncoupled to piezoelectricity.

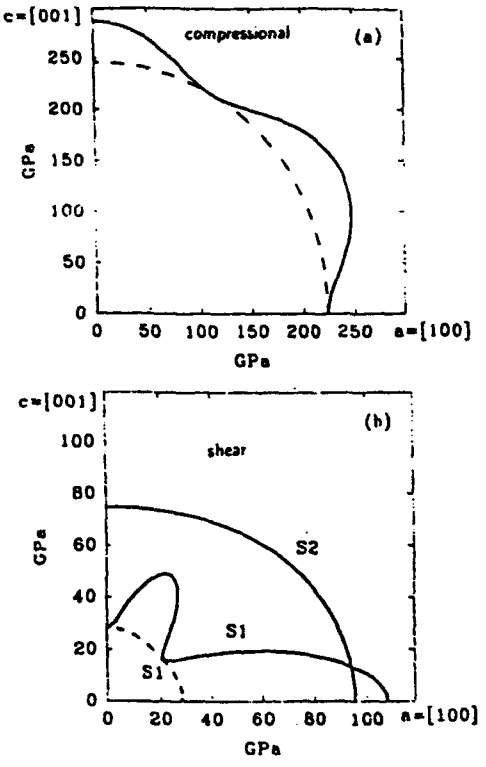

FIG. 6. Compressional (a) and shear (b) moduli ρV^2 in the a-c plane. The dashed curves are for piezoelectricity ignored. The $S2$ shear mode is uncoupled to piezoelectricity.

lated from the elastic constants only. It can be seen from these figures that, as in the case of $BaTiO_3$,[28] the electromechanical coupling has a maximum when the displacement is parallel to the c axis of electric polarization, and there is no coupling at all when the displacement is perpendicular to this axis.

About 75% of the shear energy is converted into electrical energy for the transverse wave propagating in the [100] direction [see Figs. 4(b) and 6(b)], while only about 20% of the shear energy is converted into electrical energy in the [010] direction [Figs. 4(b) and 5(b)]. These values are in good agreement with the electromechanical coupling constants (k_{ij}) of $KNbO_3$ found by Wiesendanger,[13] which are $k_{15}^2=0.77$ and $k_{24}^2=0.21$, respectively. About 14% of compressional energy is transformed into electrical energy for the longitudinal wave propagating in the [011] direction [Figs. 5(a) and 6(a)] which leads to the electromechanical coupling constant $k_{33}=0.37$. It is interesting to note that there is another maximum of electromechanical coupling in the direction $\approx$[102] in Fig. 6(b), when about 50% of the shear energy is transformed into electrical energy, and this maximum corresponds to a minimum of electromechanical coupling for the longitudinal wave in the same direction [Fig. 6(a)]. There is also a zero electromechanical coupling for the shear waves propagating approximately in the crystallographic directions [045] and [504] [see Figs. 5(b) and 6(b), respectively].

IV. CONCLUSIONS

The complete set of elastic constants for a single domain orthorhombic $KNbO_3$ single crystal at room temperature has been determined by a Brillouin light scattering technique using literature data for the dielectric permittivity of $KNbO_3$. The difference between piezoelectric constants obtained by low- and high-frequency methods suggests there may exist a high-frequency relaxation-type dispersion for the dielectric constant ϵ_{33} in the GHz range of frequencies, similar to that found earlier for analogous $BaTiO_3$ crystals. High frequency dielectric measurements for $KNbO_3$ are needed to resolve this problem.

The directional dependence of electromechanical coupling for longitudinal and transverse acoustic waves in $KNbO_3$ was analyzed. The coupling is at maximum when the displacement is parallel to the c (polar) orthorhombic axis and there is zero coupling when the displacement is perpendicular to this axis. Several other directions of wave propagation corresponding to extrema of electromechanical coupling have also been determined.

Note added in proof: After acceptance of this article, we became aware of the recent article by Zgonik *et al.*[30] who present a complete set of materials constants for $KNbO_3$ consistent with the available low-frequency measurements. Our results are generally in very good agreement with the suggested set of constants, except for those constants strongly dependent on ϵ_{33}, the dielectric constant along the polar direction in the crystal. The possible existence of relaxation-type dispersion for ϵ_{33} in the GHz range of frequencies, as discussed in the present article, may explain this disagreement.

ACKNOWLEDGMENTS

The study has been supported by the Air Force Office of Scientific Research through the University Research Initiative Program (AFOSR-90-0174) to J.D.B. and D.A.P. and the National Science Foundation through Grant No. EAR90-18676 to J.D.B.

[1] F. Jona and G. Shirane, *Ferroelectric Crystals* (Pergamon, New York, 1962).
[2] M. L. Lines and A. M. Glass, *Principles and Applications of Ferroelectrics and Related Materials* (Oxford University Press, Oxford, UK, 1977).
[3] *Ferroelectrics and Related Materials*, edited by G. A. Smolenskii (Gordon and Breach, New York, 1984).
[4] A. M. Quittet, J. L. Servoin, and F. Gervais, J. Phys. (Paris) 42, 493 (1981).
[5] M. D. Fontana, G. Metrat, J. L. Servoin, and F. Gervais, J. Phys. C 16, 483 (1984).
[6] M. D. Fontana, A. Ridah, G. E. Kugel, and C. Carabatos-Nedelec, J. Phys. C 21, 5853 (1988).
[7] T. P. Dougherty, G. P. Wiederrecht, K. A. Neison, M. H. Garrett, H. P. Jensen, and C. Warde, Science 258, 770 (1992).
[8] L. Katz and H. D. Megaw, Acta Cryst. 22, 639 (1967).
[9] A. W. Hewat, J. Phys. C 6, 2559 (1973).
[10] F. X. Winter, E. Wiesendanger, and R. Claus, Phys. Status Solidi B 64, 95 (1974).
[11] R. Currat, R. Gomes, B. Dorner, and E. Wiesendanger, J. Phys. C 7, 2521 (1974).

[12] S. D. Phatak, R. C. Srivastava, and E. C. Subbarao, Acta Cryst. A 28, 227 (1972).
[13] E. Wiesendanger, Ferroelectrics 16, 263 (1974).
[14] P. Günter, Jpn. J. Appl. Phys. 16, 1727 (1977).
[15] J. F. Nye, *Physical Properties of Crystals* (Oxford University Press, Oxford, UK, 1960).
[16] D. Z. Shen, Mater. Res. Bull 21, 1375 (1986).
[17] T. Fukuda and Y. Uematsu, Jpn. J. Appl. Phys. 11, 163 (1972).
[18] J. R. Sandercock, in *Topics in Applied Physics, Light Scatterings in Solids III*, Vol. 15, edited by M. Cardona and G. Gunterhodt (Springer, New York, 1982), pp. 173–206.
[19] J. D. Bass, J. Geophys. Res. 84, 7621 (1989).
[20] M. T. Vaughan, Ph.D. thesis, State University of New York at Stony Brook, 1979.
[21] M. T. Vaughan and J. D. Bass, Phys. Chem. Minerals 10, 62 (1983).
[22] E. Wiesendanger, Ferroelectrics 1, 141 (1970).
[23] Y. Uematsu, Jpn. J. Appl. Phys. 13, 1362 (1974).
[24] B. Zysset, I. Biaggio, and P. Günter, J. Opt. Soc. Am. B 9, 380 (1992).
[25] E. Dieulesaint and D. Royer, *Elastic Waves in Solids: Applications to Signal Processing* (Wiley, Chichester, 1980).
[26] J. A. Nelder and R. Mead, Comp. J. 7, 308 (1965).
[27] A. V. Turik and N. B. Shevchenko, Phys. Status Solidi B 95, 585 (1979).
[28] Z. Li, S.-K. Chan, M. H. Grimsditch, and E. S. Zouboulis, J. Appl. Phys. 70, 7327 (1991).
[29] V. K. Yanovskii, Sov. Phys. Solid State 22, 1284 (1980).
[30] M. Zgonik, R. Schlesser, I. Biaggio, E. Voit, J. Tscherry, and P. Günter, J. Appl. Phys. 74, 1287 (1993).

PRE-TRANSITIONAL BEHAVIOR IN CUBIC POTASSIUM NIOBATE

M. HOLMA*, H. HONG**, M. NELSON*** AND HAYDN CHEN**

*University of Illinois at Urbana-Champaign, Department of Physics, Urbana, IL 61801.
** University of Illinois at Urbana-Champaign, Dept. of Materials Sci. & Engr.,Urbana, IL 61801.
***University of Illinois at Urbana-Champaign, Materials Research Lab.,Urbana, IL 61801.

ABSTRACT

Pre-transitional behavior prior to the onset of the cubic-to-tetragonal phase transformation in $KNbO_3$ has been studied with synchrotron x-ray scattering at NSLS, Brookhaven National Lab. Measurements of the Thermal Diffuse Scattering (TDS), Grazing Incidence X-ray Scattering (GIXS), and precursor Bragg scattering have been performed at a series of temperatures on a single crystal sample in the cubic phase (T_c = 405 °C). The TDS was measured in the (001), (011) and (111) cubic planes. The GIXS was measured above, at and below the critical scattering angle of the sample. Based on localized soft mode theory, dynamic tetragonal fluctuations may be expected prior to the onset of the phase transition initiated by defects or surfaces. The GIXS data indicate that the tetragonal phase is apparent prior to the phase transition of the bulk - - consistent with the notion that nucleation originates from potent defect sites during a martensitic-like displacive transformation. The TDS intensity distribution is disk-shaped; arising from a localized, low energy transverse optic mode in the [100] directions extending out to the Brillouin zone boundary (reduced wave vector, q =0.5). Scans made in the (011) planes show TDS intensity extending out to a reduced wave vector of q ~ 0.2. Preliminary analysis indicates that a low energy transverse optic mode extends in the [011] direction as well. The TDS intensity decreases as the transition temperature is approached from above. Comparison of the TDS results with inelastic neutron scattering data will be made.

I. INTRODUCTION

The oxygen perovskite, potassium niobate, is known to undergo successive phase transitions from cubic to tetragonal to orthorhombic to rhombohedral structures.[1] Together with barium titanate, which undergoes the same set of successive phase transitions, an extensive number of studies have focussed on these ferroelectrics. The major objective is to investigate the physical origin of the phase transtions. In 1960, soft mode theory was proposed as a lattice dynamical model in that one or many normal modes of oscillation becomes increasingly unstable as the temperature is lowered.[2,3] The dynamic displacements become frozen in, resulting in the formation of a new structure. The symmetry of the new low temperature phase is a subgroup of the parent phase and there is a symmetry relation between the soft mode and the pattern of atomic displacements of the product phase. This model has found success with many materials, most notably $SrTiO_3$.

Many studies since then have displayed results inconsistent with some of the features of soft mode theory. In particular, an x-ray scattering study of $KNbO_3$ revealed diffuse sheets of intensity in the {100} reciprocal lattice planes.[4,5] The results suggested that a model

on local static disorder -- due to several possible statistical positions available to the center (Nb) ion -- was appropriate. More recent results indicate the existence of dynamic disorder in the Nb ions in the orthorhombic phase of $KNbO_3$ with highly anisotropic properties. [6] The results also suggest, in the case of $BaTiO_3$, that the appearance of a central peak and other anomalous behavior in neutron scattering and x-ray scattering studies as the phase transition is approached from above indicates evidence of precursor clusters of the product phase. The current work focusses on a quantitative study of the diffuse scattering in $KNbO_3$ and possible evidence for similar precursor behavior prior to the onset of the cubic to tetragonal phase transition.

II. EXPERIMENTAL RESULTS

The x-ray scattering measurements were made at beamline X14 at the NSLS using a wavelength of 1.512 Å on a single crystal sample of $KNbO_3$. Scans were made for seven temperatures above the phase transition temperature. The phase transition temperature was observed to occur at 405 °C (+/- 1°) on cooling. The measured lattice parameters agreed with previously reported values. [7] The sample was oriented with the [011] of the cubic axis normal to the surface and was heated from below. The sample temperature was monitored to within 1 degree and the thermal gradient calculated to be no more than 1 degree. The Thermal Diffuse Scattering was measured primarily from the 004 cubic Bragg peak but also from the 002, 022 and 030 cubic peaks. The Grazing Incidence X-ray Scattering was measured from 200 surface peak at grazing incidence angles of 0.15, 0.3 and 1.5 degrees. The data are presented for the angles of 0.3 and 1.5 which correspond to scattering from the top 250 Å and 2500 Å, respectively. Figures 1 and 2 show representative surface plots and contour plots of the TDS in the transverse configuration. The scans were obtained at a

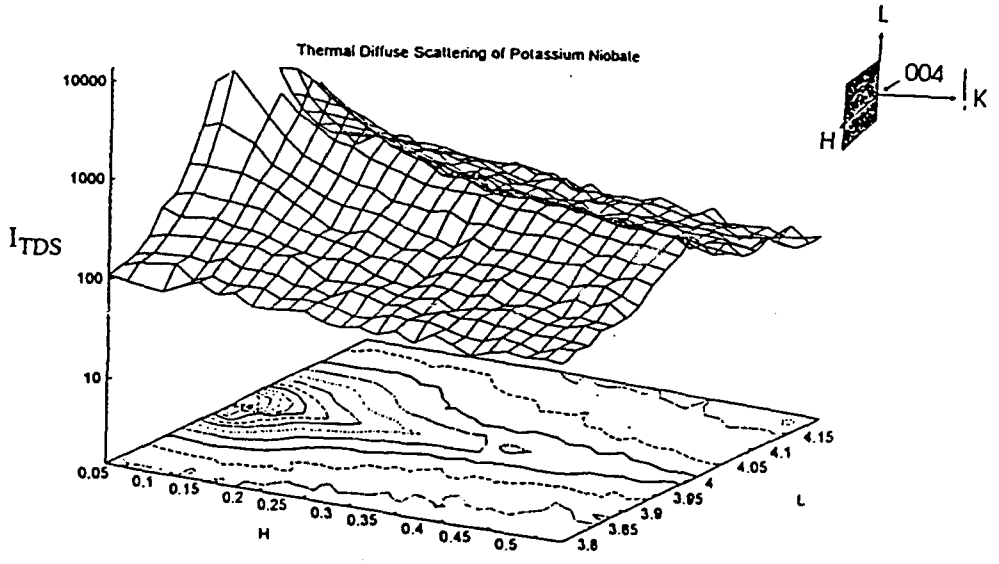

Figure 1. Thermal Diffuse Scattering of the (100) plane in the transverse configuration from the 004 Bragg peak.

Figure 2. Thermal Diffuse Scattering of the (010) plane in the transverse configuration from the 004 Bragg peak.

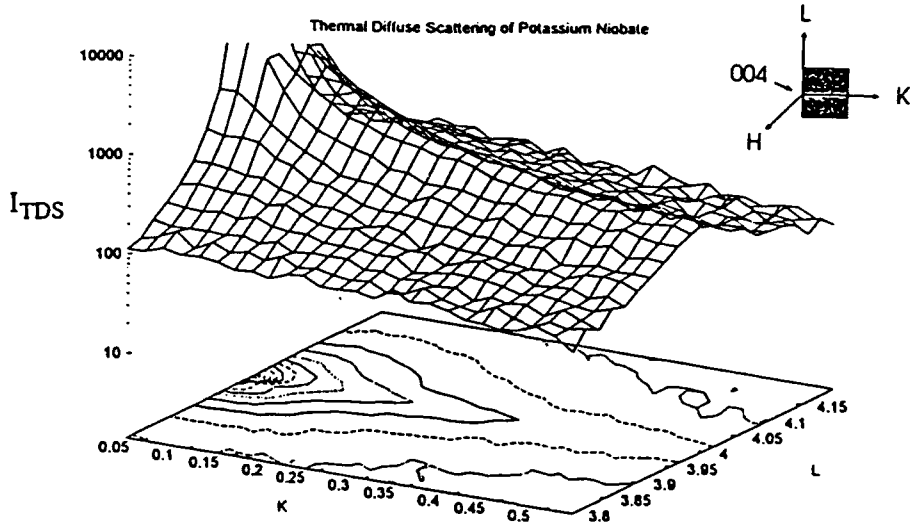

temperature of 409°C, corresponding to 4 degrees above the phase transition temperature. These scans were done from the 004 cubic Bragg peak with the net momentum transfer nearly perpendicular to the scattering vector. The scattering geometry is shown in the inset. The intensity distribution shown includes a first order correction to Bragg scattering, fitting the broadened peak with a gaussian distribution. The TDS intensity distribution, which arises from low energy transverse phonon modes, extends strongly to the zone boundary ($\mathbf{q} = 0.5$). The width of this intensity distribution, δq, is 0.075.

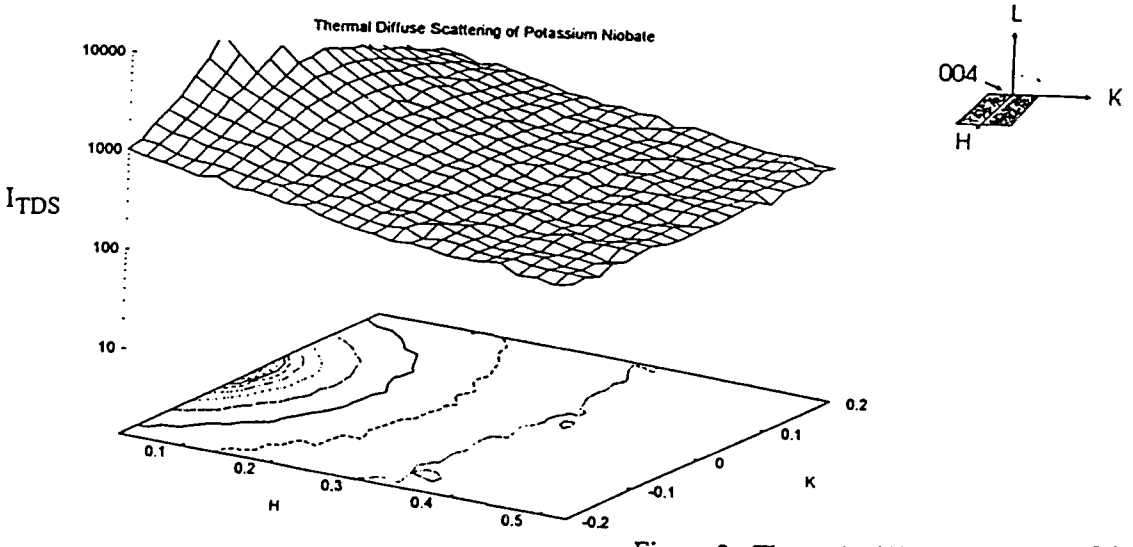

Figure 3. Thermal Diffuse Scattering of the (001) plane in the transverse configuration from the 004 Bragg peak.

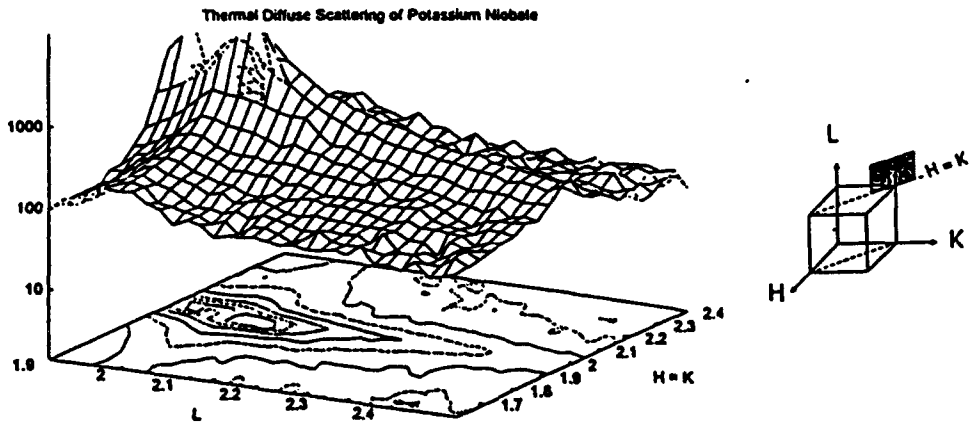

Figure 4. Thermal Diffuse Scattering of the (011) plane in the transverse configuration from the 022 Bragg peak.

Figure 3 shows a representive surface plot and contours for the purely transverse configuration (see inset). There is no structure in the intensity distribution, however the magnitude of the TDS scattering intensity is large for all values of momentum transfer. The contribution to the TDS in total is a disk-shaped sheet of intensity in the {100} reciprocal lattice planes. Figure 4 shows the contribution of two mutually perpendicular intensity distributions. The diffuse intensity versus temperature is plotted in Figure 5 for reduced wave vectors of $q = 0.15$, 0.25 and 0.45. The intensity of the diffuse sheet decreases as the transition temperature is approached from above. This is consistent with a low energy transverse phonon mode that stiffens into static displacements at the phase transition resulting in the new product structure.

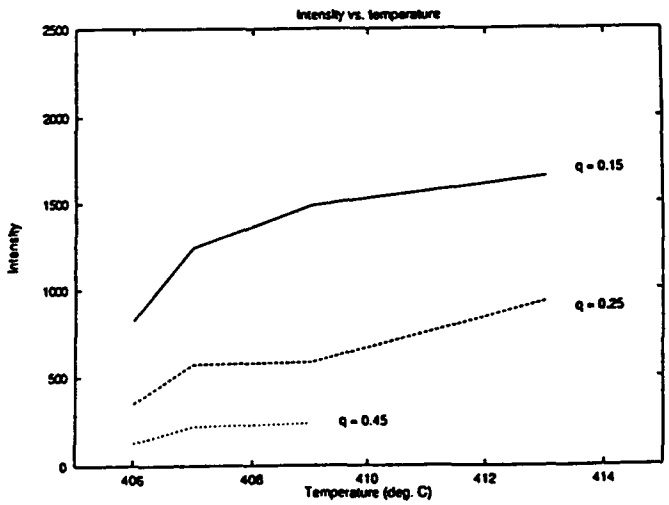

Figure 5. Diffuse scattering intensity versus temperature at reduce wave vectors , q; of 0.15, 0.25 and 0.4.

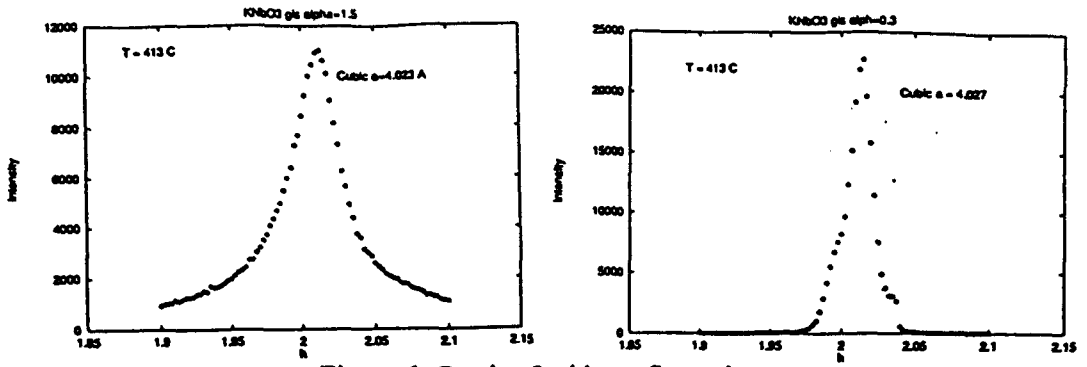

Figure 6. Grazing Incidence Scattering at angles α = 0.3 and α= 1.5 for T= 413°C.

The results for the GIXS are shown in Figures 6, 7 and 8 for three temperatures above the transition temperature. Well above the transition temperature (Figure 6) both the bulk scattering and surface scattering peaks correspond to the cubic phase only with measured lattice parameters of 4.023 Å and 4.027 Å respectively. A few degrees above the phase transition the main peaks correspond to the cubic phase, however the surface scattering peak displays a small satellite peak which may correspond to fluctuations of the tetragonal phase initiated from the surface. Just above the phase transition (Figure 8) the bulk scattering peak is cubic however the surface scattering displays the tetragonal phase.

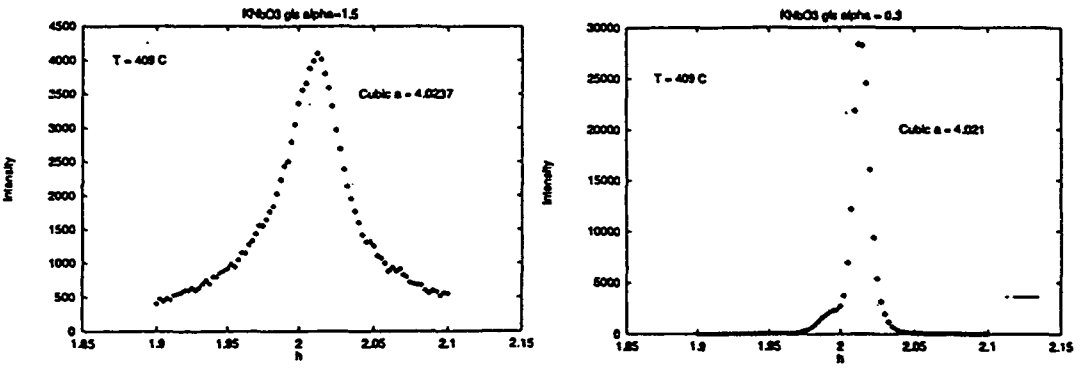

Figure 7. Grazing Incidence Scattering at angles α = 0.3 and α= 1.5 for T= 409°C.

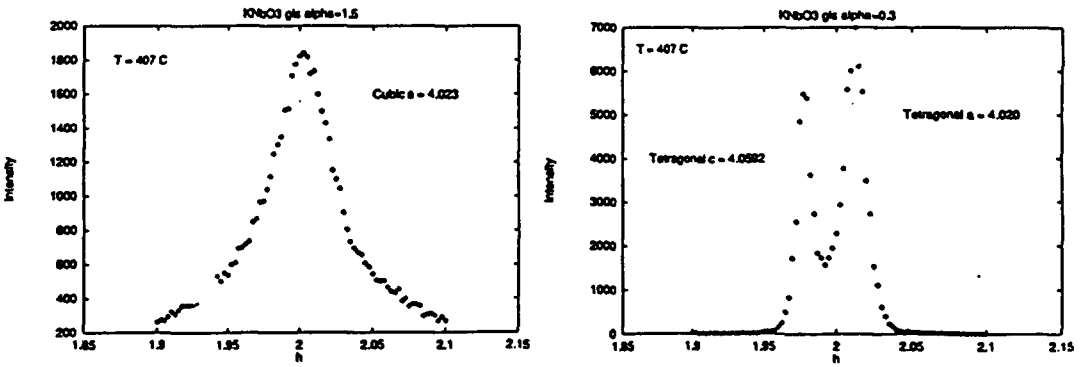

Figure 8. Grazing Incidence Scattering at angles α= 0.3 and α= 1.5 for T= 407°C.

III. DISCUSSION

The pre-transitional behavior of potassium niobate has been studied using synchrotron x-ray scattering. The measurements of the TDS indicate the existence of a low energy diffuse mode in the [100] directions. The intensity of the TDS decreases as the transition temperature is approached from above which is consistent with a stiffened soft mode corresponding to the static displacements of the new transformed phase. The inconsistency with soft mode theory occurs in the distribution of the TDS intensity. This peculiar type of disk-shaped intensity distribution indicates a small correlation length between phonon modes in real space. This behavior cannot be simply described in terms of first or second order TDS theory. The results of the GIXS provides evidence of precursor behavior related to the new product phase. Nucleation of the new product phase occurs at defect sites, interfaces and surfaces. In comparison, inelastic neutron scattering results (not shown)[8] support the conclusion of strongly anharmonic behavior in addition to evidence of disorder. The inelastic neutron scattering results show low energy transverse optic modes in the [100] directions only and strong broadening in energy and wave vector of phonon modes as the transition temperature is approached from above. These results suggest that a different model than soft mode theory is necessary, that includes anisotropic behavior and anharmonicity.

References

[1] F. Jona and G.Shirane, Ferroelectric Crystals. (Pergamon Press, New York,1962).

[2] W. Cochran, Adv. Phys. **9**, 387 (1960).

[3] P.W. Anderson in Fizika Dielectrikov, edited by G.I. Skanavi (Acad. Nauk SSR, Moscow, 1960).

[4] R. Comes, M. Lambert and A. Guinier, C. R. Acad. Sci. Paris **226**, 959 (1968).

[5] R. Comes, M. Lambert and A. Guinier, Sol. State Comm. **6**, 715 (1968).

[6] J. P. Sokoloff, L. L. Chase and D. Rytz, Phys. Rev. B **38**, 597 (1988).

[7] G. Shirane, H. Danner, A Pavlovic and R. Pepinsky, Phys. Rev. **93**, 672 (1954).

[8] M. Holma, R. Nicklow and H. Chen, Abstracts of 1992 ACA Meeting, Pittsburgh Diffraction Conference (Pittsburgh, PA, 1992).

ACKNOWLEGEMENTS

This research was supported by the Department of Energy/Materials Research Laboratory (DEFG02-91ER45439), the Air Force Office of Scientific Research-URI (AFSOR90-0174) and acknowledgements are also due to Dr. Pendi Han (UIUC) for providing the single crystal.

G. W. Bailey and C. L. Rieder, Eds., Proc. 51st Annual Meeting of the Microscopy Society of America

MICROSTRUCTURE AND PHASE TRANSFORMATION IN $KNbO_3$

Oludele O. Popoola and Waltraud M. Kriven

Department of Materials Science and Engineering, University of Illinois at Urbana-Champaign, 105 South Goodwin Avenue, Urbana IL 61801

$KNbO_3$ is a perovskite ferroelectric ceramic material with important electro optical and non linear optical properties [1 - 2]. It can be used in an optical parametric oscillator, secondary harmonic generator and photo refractive holographic storage devices. Its macroscopic properties depend on a number of inter-related features such as crystal structure, domain structure, defects and impurity content. $KNbO_3$ has four known solid phases with decreasing symmetry with temperature: Cubic $\xrightarrow{418^{\circ}C}$ Tetragonal $\xrightarrow{225^{\circ}C}$ Orthorhombic $\xrightarrow{-10^{\circ}C}$ Monoclinic. The paraelectric to ferroelectric transition occurs during the cubic to tetragonal transformation. The dielectric properties of $KNbO_3$ have been extensively studied and related to the various phase transformations. The aim of this investigation is to study the orthorhombic to tetragonal phase transformations using TEM.

Thin slices were cut from a flux grown crystal and mechanically polished to a thickness of 100 μm with a 1μm surface finish using diamond paste and isopropyl alcohol as the lubricant. Discs (3 mm in diameter) were then ultrasonically drilled, dimpled on one side to a thickness of about 50 μm, and mounted on Cu grids for support. Final perforation to electron transparency was achieved by argon ion beam milling under an accelerating voltage of 6 kV and a gun current not exceeding 1 mA. Under these conditions, no domain boundary motion, domain or defect (dislocations) nucleation was expected. Hot stage TEM experiments were performed on a Philips EM 420 using a single tilt specimen holder. The heating rate was about 10°C / minute. A dwell time of 20 minutes was allowed after each 50°C increment to allow for structural relaxation.

Figure 1a is a bright field (TEM) image of the domain configurations commonly observed in $KNbO_3$. The associated diffraction pattern (Figure 1b), taken across many boundaries, shows no spot splitting in [001] direction and contrast behavior similar to Friedel's law failure was frequently observed. These are characteristics of 180° domains. 90° domains, characterized by spot splitting in the [001] diffraction patterns are also frequently observed. On heating a [011] foil, the orthorhombic to tetragonal transformation started at 188°C and was completed at 192°C. The reverse transformation (i.e. tetragonal to orthorhombic) occured between 174°C and 167°C. In Figure 2, the microstructural modifications that took place during the transformation of an area containing 180° domains is seen. The transformation manifested itself by the disappearance of the domains at 192°C (Figure 2a). On subsequent cooling, many domain variants reappeared (Figure 2b). This behavior, observed during repeated experiments, indicated that the transformation had no microstructural reversibility. The diffraction patterns associated with Figures 2a and 2b are seen in Figure 3. The [011] orthorhombic direction changed to the [001] tetragonal without any tilting or rotation of the specimen. Although no orthorhombic / tetragonal phase boundary could be imaged due to the rapidity of the transformation, these two patterns were sufficient to establish the reversible orientation relation between the two phases. This relation was $[011]_O$ // $[001]_t$ and $(100)_O$ // $(100)_t$. Since the $(100)_t$ and the $(010)_t$ were interchangeable, two symmetry equivalent options at 90° to each other could be expected in the tetragonal phase, as observed in the microstructure (Figure 4).

References

1. S. A. Ingle and A. P. David, Ferroelectrics (1989) 97, 201.
2. T. Malis and H. Gleiter, J. Appl. Phys. (1976) 47, 12, 5195.
3. This research was supported by AFOSR-URI-90-0174.

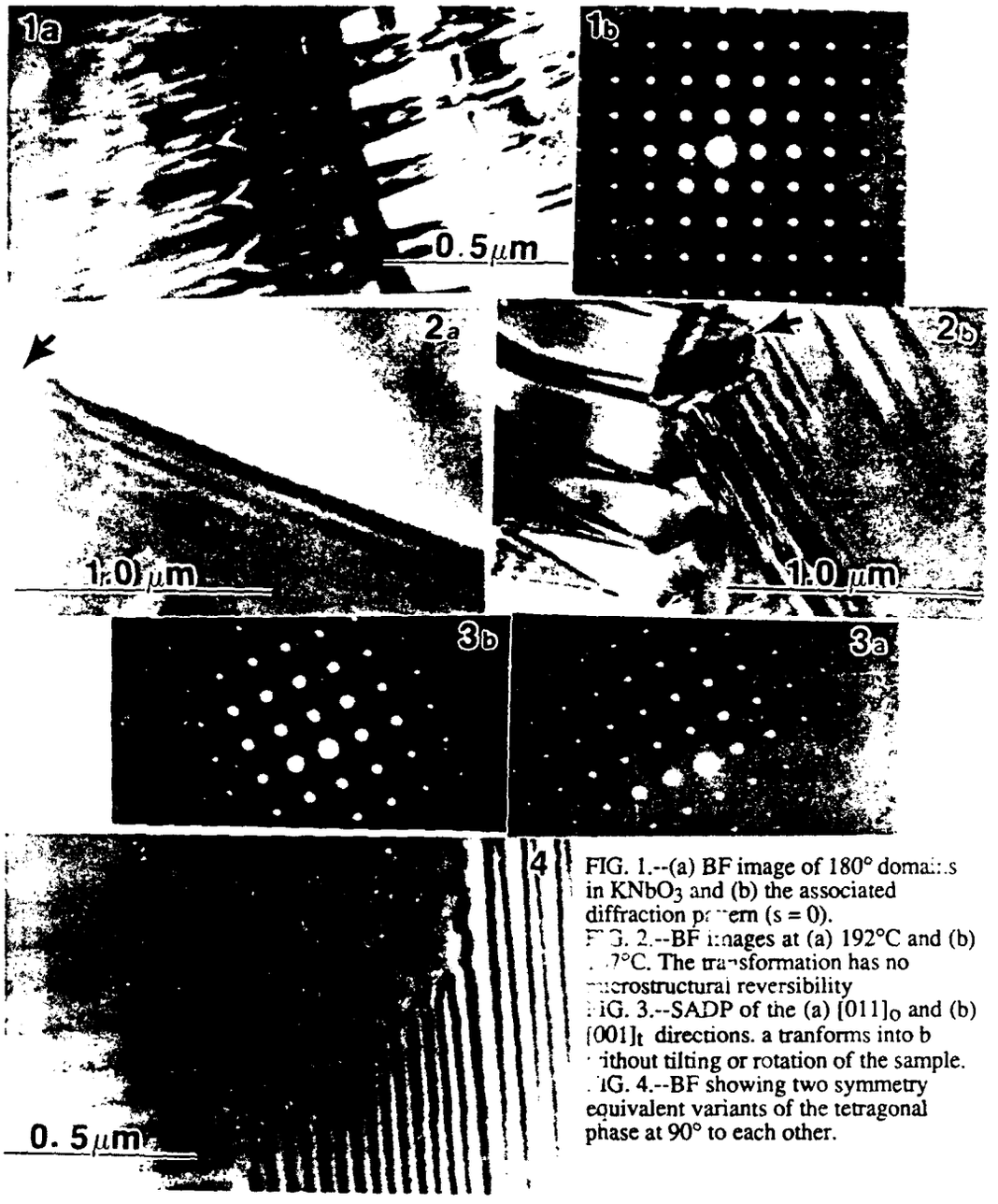

FIG. 1.--(a) BF image of 180° domains in $KNbO_3$ and (b) the associated diffraction pattern (s = 0).
FIG. 2.--BF images at (a) 192°C and (b) 207°C. The transformation has no microstructural reversibility
FIG. 3.--SADP of the (a) $[011]_O$ and (b) $[001]_t$ directions. a tranforms into b without tilting or rotation of the sample.
FIG. 4.--BF showing two symmetry equivalent variants of the tetragonal phase at 90° to each other.

Abstract Accepted for Int. Conf. on Solid-Solid Phase Transformations in Inorganic Materials, Pittsburgh, PA, July 17-22, 1994

Linear Chain Structure in Cubic $KNbO_3$‡

M. Holma* and HAYDN CHEN**

* Department of Physics, University of Illinois, Urbana, IL 61801, USA
** Department of Materials Science & Engineering, University of Illinois, Urban, IL 61801 USA

Among the ferroelectric perovskites, $BaTiO_3$ and $KNbO_3$ have received the most theoretical attention, and may be regarded as prototypical materials. As a function of ascending temperature both materials undergo rhombohedral to orthorhombic, to tetragonal and to cubic transitions, with all non-cubic phases being ferroelectric. Both systems were reported to show two-dimensional diffuse intensity sheets in the reciprocal space, indicating the presence of one-dimensional correlation in real space. In late sixties Comes, Lambert and Guinier proposed the eight-site static model which suggested the transitions are of order-disorder type. In this model, the potential energy surface has a maximum for the cubic perovskite structure and eight (degenerate) minima for the <111> displacements of the body-centered transition metal ion. In this picture, the relevant dynamics consist mainly of hopping among these eight minima. At low temperatures, only one of the minima is occupied, corresponding the rhombohedral phase, while at high temperatures the barriers between the minima are more easily surmounted leading to equal occupation of all eight sites and an average cubic structure. The cubic symmetry is broken as the temperature is lowered through preferential occupation of four sites lying in a plane in the tetragonal phase and two adjacent sites in the orthorhombic phase. Comes et al. also proposed the presence of a linear chain static structure for all three high-temperature phases in order to describe the two-dimensional intensity sheets observed in the diffraction pattern. The current investigation emphasizes the use of high-resolution synchrotron x-ray measurements to resolve the fine features associated with the 2D sheet intensity profile. Intensity simulation is performed to check against the static eight-site model as well as the dynamical model based upon a shallow, soft phonon branch. Inelastic neutron scattering was also performed to confirm the required flat soft phonon branch. Our results favor the dynamical model over the static one, although a combined effect from both cannot be totally ruled out.

‡ Research supported by the U.S. AFOSR URI grant No. 90-0174.

Accepted abstract for the International Conference on Solid to Solid Phase Transformations, Pittsburgh, PA July,1994.

Phase Transformations in Potassium Niobate Perovskite Ceramics

O. O. Popoola* and W. M. KRIVEN
Dept. of Materials Science and Engineering, University of Ilinois at Urbana-Champaign, 105, S. Goodwin Ave., Urbana, IL 61801, USA.
* Materials Systems Reliability Dept., Ford Research Laboratory, P. O. Box 2053, Dearborn, MI 48121-2053, USA.

Potassium niobate ceramics undergo the phase transformations:

Cubic (Pm3m) $\xrightarrow[425°C]{}$ Tetragonal (P4mm2) $\xrightarrow[234°C]{}$ Orthorhombic (Bmm2)

The cubic to tetragonal transformation is accompanied by a ferroelectric phase transition. In situ TEM studies reveal that this transformation starts (on cooling) at 438°C and ends at 410°C. It is preceeded by the appearance of stable microdomains at 440°C. These microdomains are arranged at 120°, 90°and 30° to each other. Ferroelectric domains nucleate at the intersection of these microdomains and grow during cooling. The transformed fraction is temperature dependent. This transformation is characterized by the reversible orientation relation:

$$\{110\}_c \,//\, \{110\}_t \text{ and } (001)_c \,//\, (001)_t.$$

The reverse transformation (on heating) starts at 418°C and does not show any microdomain formation once completed. The tetragonal to orthorhombic transformation occurs at exactly 234°C. Once initiated, the transformation front sweeps through the whole microstructure within seconds. The orientation relationship is:

$$[001]_t \,//\, [011]_o \text{ and } (100)_t \,//\, (100)_o.$$

While the cubic to tetragonal transformation occurs via a dilatational process, the tetragonal to orthorhombic transformation involves a shear mechanism. The details of these transformations will be presented.

DICALCIUM SILICATE (Ca_2SiO_4)

journal

Reprinted from the Journal of the American Ceramic Society, Vol. 75, No. 9, September 1992

J. Am. Ceram. Soc., 75 [9] 2407–19 (1992)

Phase Transformations in Dicalcium Silicate: II, TEM Studies of Crystallography, Microstructure, and Mechanisms

Youn Joong Kim,* Ian Nettleship,*,† and Waltraud M. Kriven*

Department of Materials Science and Engineering, University of Illinois at Urbana-Champaign, Urbana, Illinois 61801

The crystallography, microstructures, and phase transformation mechanisms in dicalcium silicate (Ca_2SiO_4) were studied by TEM. Three types of superlattice structures were observed in the α_L' and β phases. Almost all β grains were twinned and strained. Symmetry-related domain structures inherited from previous high-temperature transformations were observed in β grains. Both the $\alpha \rightarrow \alpha_H'$ and $\alpha_L' \rightarrow \beta$ transformations were considered to be ferroelastic, and spontaneous strains were calculated. In terms of the crystal structures, the major driving force for the $\beta \rightarrow \gamma$ transformation is proposed to be strains and cation charge repulsions in the β structure. This mechanism can be displacive, but it needs to overcome a comparatively high energy barrier.

I. Introduction

DICALCIUM SILICATE (Ca_2SiO_4) is a major component of portland cement that has been studied for a long time. However, considerable confusion and lack of understanding exist in the literature regarding the crystal structures and microstructures as well as transformation behavior between its polymorphs. As an orthosilicate, Ca_2SiO_4 has an unusually large number of polymorphs, viz., α, α_H', α_L', β, and γ. For comparison, olivine (Mg_2SiO_4), a typical orthosilicate mineral, has only one stable phase (the orthorhombic γ phase) throughout the entire temperature range, from room temperature to the melting point. Most microstructural studies of Ca_2SiO_4 have been limited to the stabilized β and α_L' phases, because of the difficulty in retaining solid samples of the other phases at room temperature. The dusting effect due to a large volume increase accompanying the $\beta \rightarrow \gamma$ transformation has been observed, but the transformation mechanism itself is poorly understood.

There are many different reports on the polymorphism, microstructures, and phase transformations in Ca_2SiO_4,[1] possibly due to (i) different macrostructures and microstructures of the starting materials, such as different grain sizes;[2,3] (ii) different chemistry of the starting materials, especially the presence of impurities;[4] and (iii) different processing conditions, in particular, cooling kinetics.[3] Nevertheless, five polymorphs of pure Ca_2SiO_4 have been widely observed, including the metastable, high-pressure β phase. Table I lists crystallographic data of each polymorph from the literature.[5-16] Several different choices of crystallographic axes have been used in describing these polymorphs, especially the orthorhombic structures. As a working model for this study, one space group is chosen for each polymorph, and these polymorphs are correlated to one another. Figure 1 schematically displays the geometries of these polymorphs and the reported lattice correspondences among them. Figure 1 shows the interchange of *b* and *c* axes between the two orthorhombic phases (α_L' and γ) and the monoclinic β phase. Since the *b* axis of the β phase is the highest symmetry axis in conventional crystallographic notation, which corresponds to the *c* axes of the other phases, there is actually no switching of axes by the transformation in this system.

The following points summarize some of the current problems in the crystal structures and microstructures that are relevant to this study:

(1) The crystal structure of α has not yet been firmly determined. Three space groups for the structure have been suggested: $P6_3/mmc$,[6] $P6_3mc$,[17] or $P\bar{3}m1$.[5]

(2) No report of a structural refinement of α_H' exists, but a space group of *Pmcn* has been assigned[5] based on high-temperature powder XRD data.

(3) Two superlattice models have been proposed for the α_L' structure referring to the α_H' lattice: (i) doubling of the *a* and *b* axes ($\times 2a, 2b$-type) with a space group *Pmcn*[5] and (ii) tripling of the *c* axis ($\times 3c$-type) with a space group $P2_1cn$.[11]

(4) Two different twinning modes of β-Ca_2SiO_4 have been reported: (i) both {100}-type and {001}-type twinning[18] or (ii) only {100}-type twinning.[13,19]

(5) The suggested transformation mechanisms among the polymorphs are generally (i) a semireconstructive mechanism between α and α_H';[17] (ii) an order–disorder transformation mechanism between α_H' and α_L';[17] (iii) a displacive, possibly martensitic mechanism between α_L' and β;[17,20] and (iv) a reconstructive[17] or displacive[21] mechanism for $\beta \rightarrow \gamma$.

The objective of this study is to address the above-listed problems through an in-depth TEM characterization of various Ca_2SiO_4 samples. The approach is to understand these problems as a part of the entire sequence of phase transformations in the Ca_2SiO_4 system. A special intention is to understand the $\beta \rightarrow \gamma$ transformation in terms of crystal structures and the mechanisms involved. It is an unusual, low- to high-symmetry transformation accompanied by a large volume increase (~12%) on cooling.

II. Experimental Methods

Three groups of samples were studied: (i) pellets of fine-grained, single-phase Ca_2SiO_4, sintered between 1300° and 1450°C for 1 min to 12 h;[22] (ii) pellets of Ca_2SiO_4, doped with 1 to 5 mol% Ba_2SiO_4 and sintered between 1300° and 1400°C for 1 to 3 h;[23] and (iii) composites of Ca_2SiO_4 (15 vol%) in an MgO matrix, sintered at 1600°C for 3 h,[24] and composites of Ca_2SiO_4 (10 vol%) in a $CaZrO_3$ matrix, sintered at 1600°C for 2 h.[25]

All pellets were examined by TEM (Model EM-430 (300 kV), Philips Instruments, Inc., Mahwah, NJ; Model EM-420 (120 kV), Philips Instruments, Inc., with EDS Model EDAX-9900, EDAX International, Inc., Prairie View, IL; Model EM-400T (120 kV), Philips Instruments, Inc.; and Model 600 (100 kV), Hitachi Instruments, Inc., Conroe, TX,

M. P. Harmer—contributing editor

Manuscript No. 196055. Received January 13, 1992; approved May 11, 1992.
Presented at the 93rd Annual Meeting of the American Ceramic Society, Cincinnati, OH, April 29 to May 2, 1991 (Basic Science Division, Paper Nos. 122-B-91 and 123-B-91). Also presented at Fall Symposium of the American Ceramic Society, Marco Island, FL, October 15–18, 1991 (Basic Science Division, Paper No. 10-BP-91F).
Supported by the U.S. Air Force Office of Scientific Research through a URI Grant No. AFOSR-90-0174.
*Member, The American Ceramic Society.
†Present address: Department of Materials Science and Engineering, University of Pittsburgh, Pittsburgh, PA 15261.

Table I. Crystallographic Data from the Literature for Ca_2SiO_4 Polymorphs

Polymorph (crystal system)*	Space group	Lattice parameters† a (Å)	b (Å)	c (Å)	β (deg)	T_{rxn} (°C)‡	Sample§	Reference
α	$P\bar{3}m1$	5.526		7.307		1500	Powder	5
	$P6_3/mmc$	5.579		7.150		RT	Single xl¶	6
α'_H	*Pmcn*	5.593	9.535	6.860		1250	Powder	5
	Pnma	6.748	5.494	9.261		1330	Powder	7
	?	11.227	6.865	19.110		1270	Powder	8
	Pcmn	9.49	5.59	6.85		1200	Powder	9
α'_L	*Pmcn*	11.184	18.952	6.837		1000	Powder	5
	?	11.207	6.849	18.952		1020	Powder	8
		11.150	6.820	18.822		770		
	Pcmn	9.48	5.59	20.49		1000	Powder	9
		9.41	5.53	20.43		800		
	Pmcn?	5.48	9.27	20.40		RT	Powder#	10
	$P2_1cn$	5.566	9.355	20.569		RT	Single xl**	11
	$Pna2_1$	20.863	9.500	5.601		RT	Single xl**	12
β	$P2_1/n$	5.554	6.813	9.421	93.60	650	Powder	5
		5.506	6.749	9.304	94.62	RT		
	?	5.544	6.802	9.419	93.28	720	Powder	8
		5.512	6.752	9.294	93.34	RT		
	$P2_1/n$	5.502	6.745	9.297	94.59	RT	Single xl	13
γ	*Pcmn*	5.085	6.773	11.237		RT	Powder	5
	Pbnm	5.091	11.371	6.782		RT	Single xl	14
	Pbnm	5.078	11.225	6.760		RT	Single xl	15
	Pbnm	5.081	11.224	6.778		RT	Single xl	16

*α is hexagonal, α'_H, α'_L, and γ are othorhombic and β is monoclinic. †1 Å = 10^{-1} nm ‡RT is room temperature. §xl is crystal, a is barium-stabilized Ca_2SiO_4, b is $Na_2P_2O_7$-stabilized Ca_2SiO_4, and c is strontium-stabilized Ca_2SiO_4.

with EDS Model TN-5500, Tracor Northern Co., Middletown, WI) to study the crystal structures, microstructures, and microchemistry. Ion-thinned foils (Model 600 dual ion miller, Gatan, Inc., Pleasanton, CA) were prepared from all specimens for TEM observation.

III. Results

(1) Overview

Of the five polymorphs of Ca_2SiO_4, α'_L, β, and γ were studied by TEM. The two types of superlattice for α'_L were both present: (i) the $\times 2a,2b$-type in composites of $Ca_2SiO_4/CaZrO_3$ and (ii) the $\times 3c$-type in Ba_2SiO_4-doped Ca_2SiO_4 samples. Twinned β grains were found throughout the samples, but all showed a superlattice structure that was not previously reported. Transformed γ grains retained in single-phase Ca_2SiO_4 samples showed the known γ crystal structure. Interfaces of α'_L/β, untwinned-β/twinned-β, and β/γ phases were identified and studied to establish lattice correspondences.

Untwinned, euhedral α'_L grains were found in Ba_2SiO_4-doped samples. In single-phase Ca_2SiO_4, twinned β grains were mostly euhedral, but their grain boundaries were highly strained. Most β grains showed {100} twinning, but some clearly showed {001} twinning. Two twinned domains coexisted in some β grains. Microcracks tended to develop along grain boundaries as the grain size increased at longer sintering times. β grains in composites sintered in the α region were also twinned. They were more elongated and strained as compared to those in the single-phase Ca_2SiO_4. High concentrations of defects and numerous microcracks were observed. In addition, symmetry-related domain structures of β grains were often observed. Large cracks were frequently present around the transformed γ grains. Whereas β grains were mostly twinned, γ grains were untwinned and strain-free, but the latter usually contained some planar defects.

(2) Crystallography

(A) α'_L Phase: Remnants of the untwinned α'_L phase surrounded by the twinned β domains were occasionally observed in composites of $Ca_2SiO_4/CaZrO_3$. Figure 2 illustrates one of

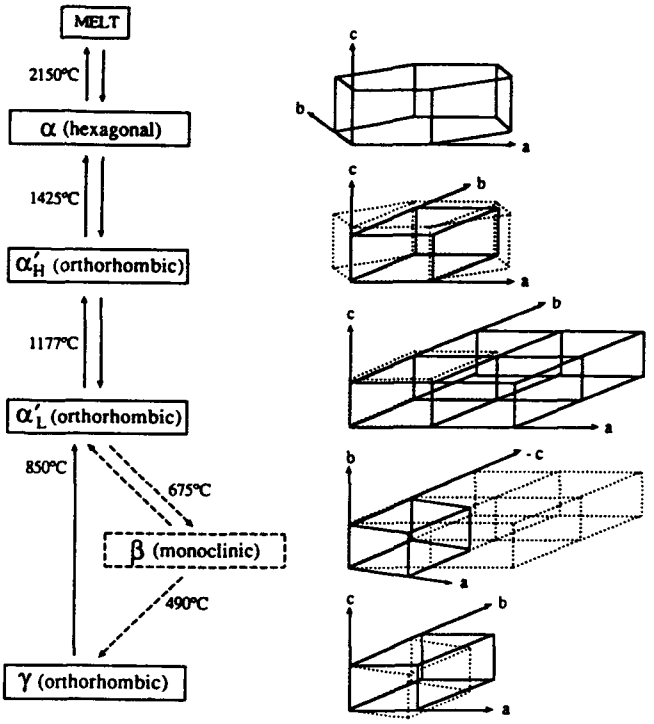

Fig. 1. Schematic diagram of the geometries and lattice correspondences for the five Ca_2SiO_4 polymorphs, including the metastable β phase.

these microstructures. The $[001]_{\alpha'_L}$ SADP indicated the presence of the $\times 2a,2b$-type superlattice of α'_L. Doubling of the {100} and {010} planes was evident by comparison with the corresponding $[010]_\beta$ SADP. By tilting the specimen along the *b* axis of α'_L, only a doubling of the {100} planes was detected. This was clearly displayed in the $[014]_{\alpha'_L}$ SADP compared to the corresponding $[021]_\beta$ SADP. The surrounding β domains were

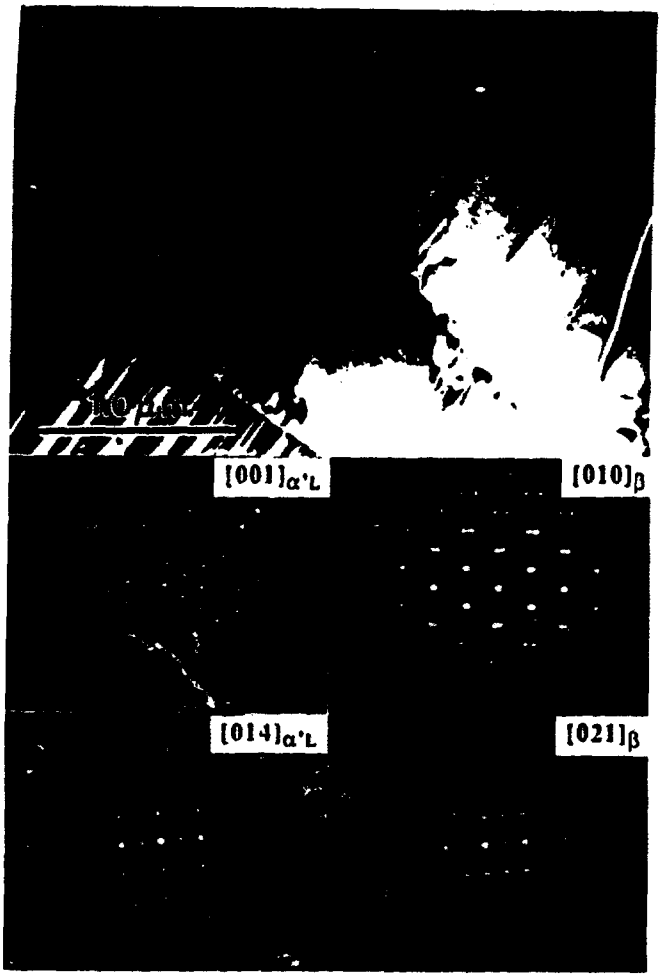

Fig. 2. Interfaces between the untwinned α_L' and the twinned β domains and the corresponding SADPs: $[001]_{\alpha_L'}$ vs $[010]_\beta$ and $[014]_{\alpha_L'}$ vs $[021]_\beta$ (from a Ca_2SiO_4-$CaZrO_3$ composite sintered at 1600°C for 2 h).

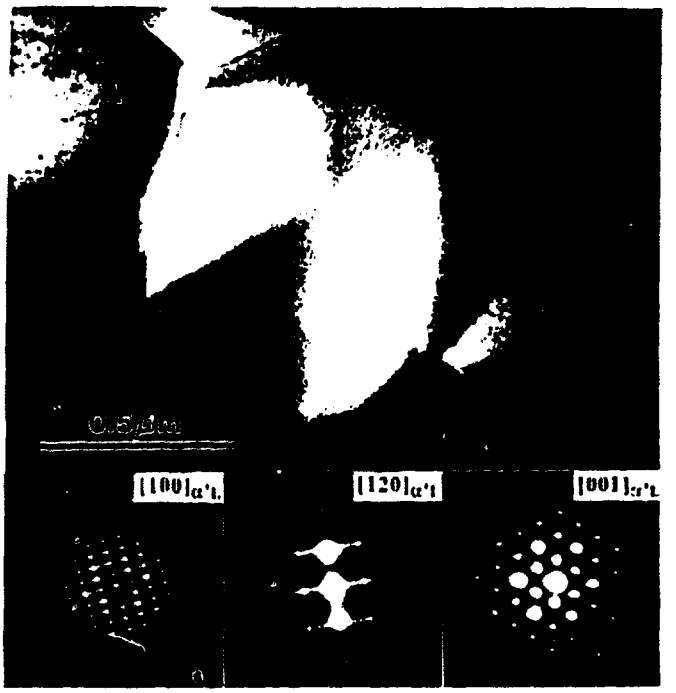

Fig. 3. Untwinned euhedral α_L' grains and the SADPs of the $\sqrt{3}c$-type α_L' superlattice: [100], [120], and [001] (from a Ba_2SiO_4-doped (5 mol%) Ca_2SiO_4 sample sintered at 1300°C for 3 h).

symmetrically related by a 120° rotation. These domain microstructures are explained in the next section.

SADPs from untwinned α_L' grains of a Ba_2SiO_4-doped specimen showed another type of superlattice reflections. In Fig. 3, the $[100]_{\alpha_L'}$ SADP clearly displayed a tripling of the {001} planes, that is, the $\sqrt{3}c$-type α_L' superlattice. These superlattice reflections were shown whenever the $\{001\}_{\alpha_L'}$ planes were in the reflecting condition, such as in the $[120]_{\alpha_L'}$. The $[001]_{\alpha_L'}$ SADP indicated the absence of the $\sqrt{2}a,2b$-type superlattice in this specimen.

(B) β Phase: The superlattice structure of β phase was totally unexpected, not only because it had not been reported before, but also because the β phase had been most extensively studied in the Ca_2SiO_4 system. β grains from all the available samples observed, however, showed superlattice reflections. In contrast to the superlattice reflections of α_L'—which were evident in SADPs of the principal zone axes, such as $[001]_{\alpha_L'}$ or $[100]_{\alpha_L'}$—those of β did not appear in SADPs of the principal zone axes, such as $[100]_\beta$, $[010]_\beta$, or $[001]_\beta$. However, when the specimens were tilted to intersect either the $\{10\bar{3}\}_\beta$ or $\{103\}_\beta$ planes, such as the $[311]_\beta$ or $[\bar{3}11]_\beta$ orientations, superlattice reflections were visible at the 1/3 positions along the $\langle 10\bar{3}\rangle_\beta^*$ or $\langle 103\rangle_\beta^*$ directions. Figure 4 displays the six major orientations showing these superlattice reflections.

(C) γ Phase: Solid samples of γ phase were normally not retainable because of the shattering effect of the large volume increase accompanying the β → γ transformation. However, a few transformed γ grains were retained among the β grains in some single-phase Ca_2SiO_4 samples. The SADPs from the γ

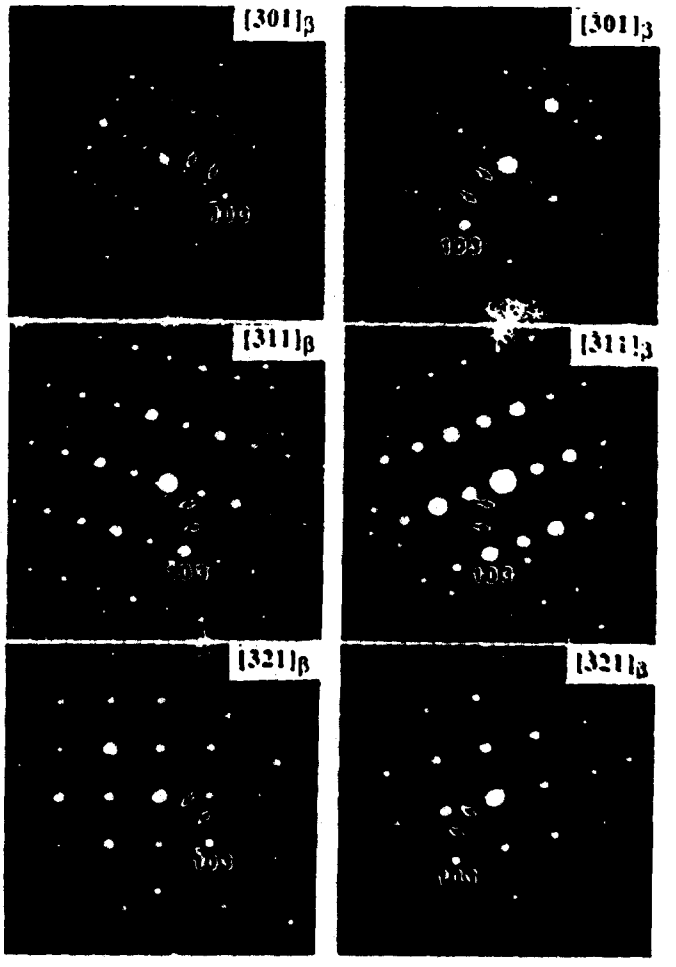

Fig. 4. [301] [311] [321] and $[\bar{3}01]$ $[\bar{3}11]$ $[\bar{3}21]$ SADPs of the β phase showing a tripling of both $\langle 103\rangle^*$ and $\langle 10\bar{3}\rangle^*$ (arrowed).

Fig. 5. Interface between the β phase and the transformed γ phase and the corresponding SADPs in two different orientations: $[001]_\beta$ vs $[010]_\gamma$ and $[011]_\beta$ vs $[011]_\gamma$.

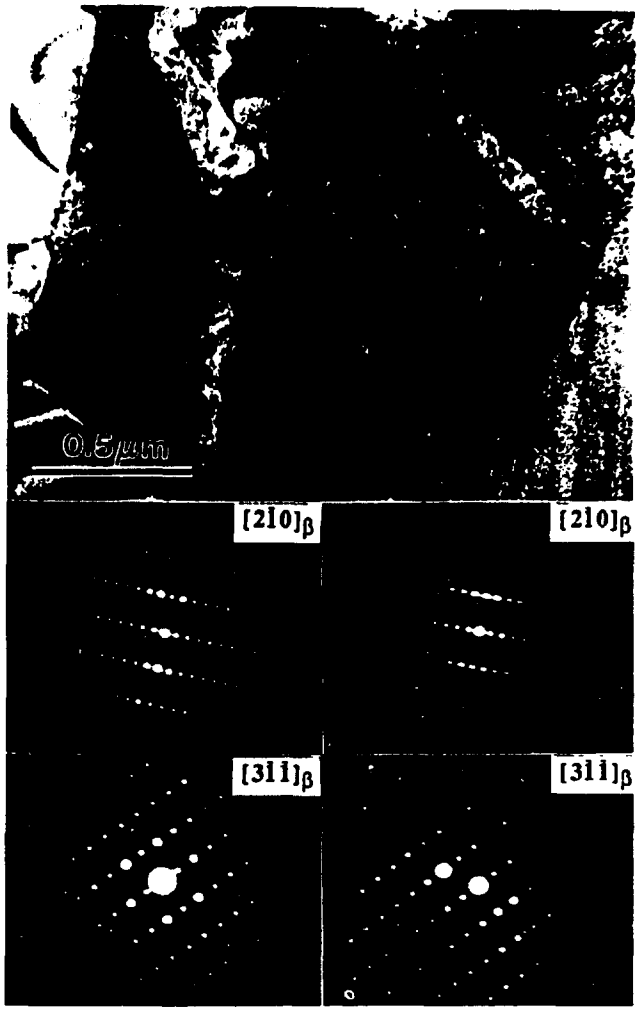

Fig. 6. Interface between the untwinned β phase and the (001)-twinned β phase. Corresponding $[2\bar{1}0]$ and $[3\bar{1}\bar{1}]$ SADPs are shown.

grains were consistent with the reported structure and the XRD results. Occasionally, the transformed γ phase and the untransferred β phase coexisted in a single grain, as shown in Fig. 5. The SADPs from these two parts showed the orientation relationship between the two phases to be $[001]_\beta \| [010]_\gamma$. The $[011]_\beta$ SADP obtained by tilting the same grain closely resembled the $[011]_\gamma$ SADP, except for the additional $\{100\}_\beta$-type twinned reflections.

(D) Interfaces and Lattice Correspondences: The interfaces between α_l' ($\times 2a,2b$) and β were sharp and straight, as shown in Fig. 2, and not noticeably strained or cracked. The following relationship was observed:

$$[001]_{\alpha_l'} \| [010]_\beta \text{ such that } (020)_{\alpha_l'} \| (00\bar{2})_\beta \text{ and } (200)_{\alpha_l'} \| (200)_\beta$$

As a result, a possible lattice correspondence could be

$$a_{\alpha_l'} \| a_\beta^*,\ b_{\alpha_l'} \| -c_\beta, \text{ and } c_{\alpha_l'} \| b_\beta$$

which agreed with previous single-crystal X-ray precession work.[26]

The interfaces between β and γ were also sharp but always showed some microcracks. The interface shown in Fig. 5 has the following relationship:

$$[001]_\gamma \| [010]_\beta \text{ such that } (010)_\gamma \| (00\bar{2})_\beta \text{ and } (100)_\gamma \| (200)_\beta$$

This result gave rise to a possible lattice correspondence:

$$a_\gamma \| a_\beta,\ b_\gamma \| -c_\beta, \text{ and } c_\gamma \| b_\beta$$

which also agreed with previous single-crystal X-ray precession work.[26]

The untwinned β phase had not been previously reported. However, several β grains containing an untwinned portion and a twinned portion were observed in this study. Figure 6 illustrates one such grain, in which both portions had similar orientations. As shown in the $[2\bar{1}0]_\beta$ SADP, the twinned portion typically had the {001}-type twinning instead of the more popular {100}-type twinning. The $[3\bar{1}\bar{1}]_\beta$ SADPs from both portions also showed the previously mentioned superlattice reflections.

(3) Microstructures

(A) α_l' Phase: The euhedral α_l' grains observed in 5-mol%-Ba_2SiO_4-doped samples (sintered at 1300°C for 3 h) were not twinned. Grain boundaries were well-defined and strain-free (Fig. 3). No apparent grain-boundary phases were noticed. EDS analyses showed barium peaks within grains, indicating that barium was in solid solution.

(B) β Phase: In single-phase Ca_2SiO_4, almost all euhedral β grains were twinned, and their grain boundaries were highly strained (Fig. 7(A)). Grain growth on longer sintering times gave rise to a development of microcracks along the grain boundaries (Fig. 7(B)). Both twin types, {100} and {001}, were observed, but the {100}-type was observed more frequently.

To study the relative populations of the two main twin types occurring in β, 100 grains were randomly chosen from various samples and examined by TEM. Grain sizes and average twin widths were also measured and correlated. The results showed that 87 grains were {100} twinned, and 13 grains were {001}

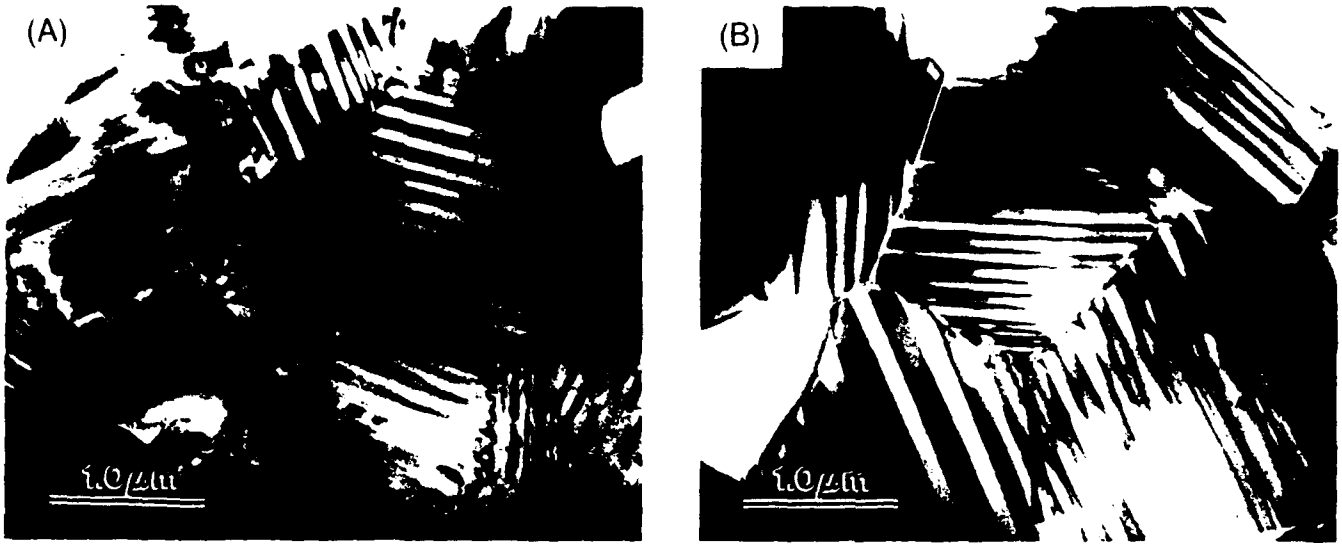

Fig. 7. Twinned euhedral β grains showing strains and microcracks along grain boundaries (from single-phase Ca_2SiO_4 samples sintered at 1400°C for (A) 1 and (B) 3 h).

twinned. The twin widths correlated positively with the grain sizes. For the same grain size, the twin width of the {001}-type was generally a little larger than that of the {100}-type (Fig. 8).

Several β grains from the pure Ca_2SiO_4, which experienced the $\alpha_l' \cdot\beta$ transformation, showed domain structures of the two twin types. Figure 9 shows a single grain composed of the two twin types that had the same [010] orientation. Twin lamellae at the interface terminated in wedges.

Samples from the composites that experienced the $\alpha \cdot\alpha_H'$ transformation displayed another type of domain structure of twinned β. Figure 10 shows a typical domain structure where three domains had the same [010] orientation but were related to one another by 120° rotations. Each domain was {100}-twinned and its twin lamellae were matched with the lamellae of the adjacent domains. The domain boundaries, however, were rather curved.

Euhedral β grains in single-phase Ca_2SiO_4 were internally strained and sometimes showed streaking in the SADPs. In composites, twinned β grains were more elongated and more internally strained. Figure 11 displays the internal strain of a β grain in one such composite that gave rise to two-directional streaking in the [010] SADP, both parallel and perpendicular to {200}*. Because of this internal strain, the grains were so unstable under the electron beam that amorphous ring patterns were rapidly produced (e.g., Fig. 10). Whereas the Ca_2SiO_4–MgO composites contained a higher concentration of defects, such as dislocations with β grains, the Ca_2SiO_4–$CaZrO_3$ composites contained numerous microcracks, both within and around β grains (Fig. 12).

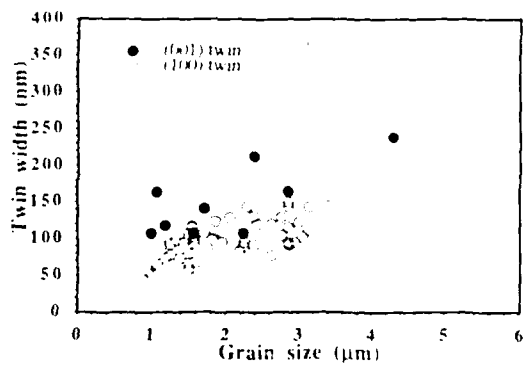

Fig. 8. Plot of grain sizes versus twin widths measured from β grains of various samples (○) {100}-twinned grains and (●) {001}-twinned grains).

(C) γ Phase: Frequently, γ grains in single-phase Ca_2SiO_4 were surrounded by large microcracks because of the large volume increase of the $\beta \cdot\gamma$ transformation (Fig. 13). Twinning in β grains disappeared during this transformation. γ grains usually showed a clear appearance without strain contrast and produced sharp SADPs. However, the γ grains contained some planar defects. These planar defects were possibly related to the previous twins in the β structure. Figure 14(A) shows apparent similarity between twin planes of the untransformed β part and a planar defect of the transformed γ part in a single grain. Figure 14(B) also indicates that twin lamellae in one grain tended to match across the neighboring grains (arrowed). The complex shapes and fringe patterns of planar defects in Fig. 14(C) suggested that the nature of the defect was related to faults formed by the detwinning process during the $\beta \cdot\gamma$ transformation.

IV. Discussion

(1) Crystallography

(A) α_l' Phase: This study has shown that two superlattices of α_l' are present independently. This is contrary to the previous suggestion that the high-temperature X-ray diffractograms of α_l' could be indexed in two ways, i.e., based either on the $\sqrt{2}a,2b$-type cell or on the $\sqrt{3}c$-type cell.[20] Calcium displacements have been suggested to be a possible origin for the $\sqrt{2}a,2b$-type superlattice.[5] The $\sqrt{3}c$-type superlattice in α_l' has been attributed to tilting or rotation of SiO_4 tetrahedra.[9] It is still uncertain as to whether there is any relationship between these superlattice types and their chemistry. However, this study and previous reports show some tendency for the $\sqrt{2}a,2b$-type in purer Ca_2SiO_4 and for the $\sqrt{3}c$-type in doped Ca_2SiO_4.

(B) β Phase: A tripling of both $\{10\bar{3}\}$ and {103} planes in β could have originated from the tripling of the *a* axis. Figure 15(A) shows this geometrical relationship. Since the $\alpha_l' \cdot\beta$ transformation involved the interchange of *b* and *c* axes, the superlattice structure occurring in β was not the same type as that occurring in α_l'. Considering that all of the solid samples studied should have experienced the $\alpha_l' \cdot\beta$ transformation, this superlattice may have originated from another unreported type of superlattice in α_l', i.e., the $\sqrt{3}a$-type. Alternatively, it could have formed during the $\alpha_l' \cdot\beta$ transformation.

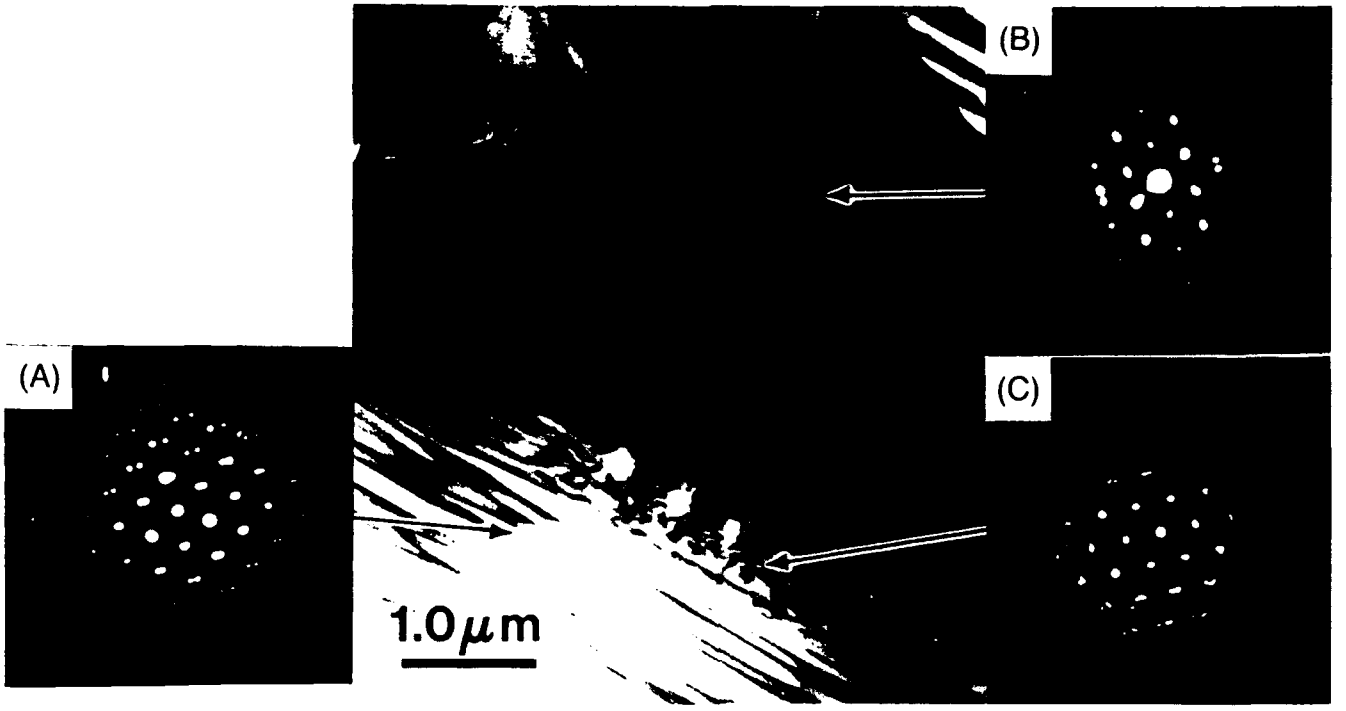

Fig. 9. Two twin domains of the β grains and SADPs from (A) (100)-twinned domain, (B) (001)-twinned domain, and (C) interface (from a single-phase Ca_2SiO_4 sample sintered at 1400°C for 12 h).

The (010) projection of the β structure in Fig. 15(B) displayed $\{10\bar{3}\}$ and $\{103\}$ planes, which may have been responsible for the superlattice reflections. In fact, both planes were closely related to the arrangements of silicon in SiO_4 tetrahedra and adjacent calcium. Being analogous to the $\times 3c$-type of α_L', systematic tilting of SiO_4 tetrahedra along the direction perpendicular to $\{10\bar{3}\}$ or $\{103\}$ planes may have been an origin of this threefold modulation. The lack of superlattice reflections along the a^* direction was possibly related to the predominant $\{100\}$ twinning or to systematic absences.

(C) γ Phase: The crystal structure of γ was well established. The diffraction data obtained from the γ phase correspond well to previous reports. No superlattice reflections were observed in γ-Ca_2SiO_4.

(2) Microstructures

(A) Intergranular Strains in β: The intergranular strains observed in single-phase β-Ca_2SiO_4 could be attributed to an anisotropic and large thermal expansion. From the lattice parameter data[5] given in Table I, the calculated thermal expansion coefficients of the β-Ca_2SiO_4 are

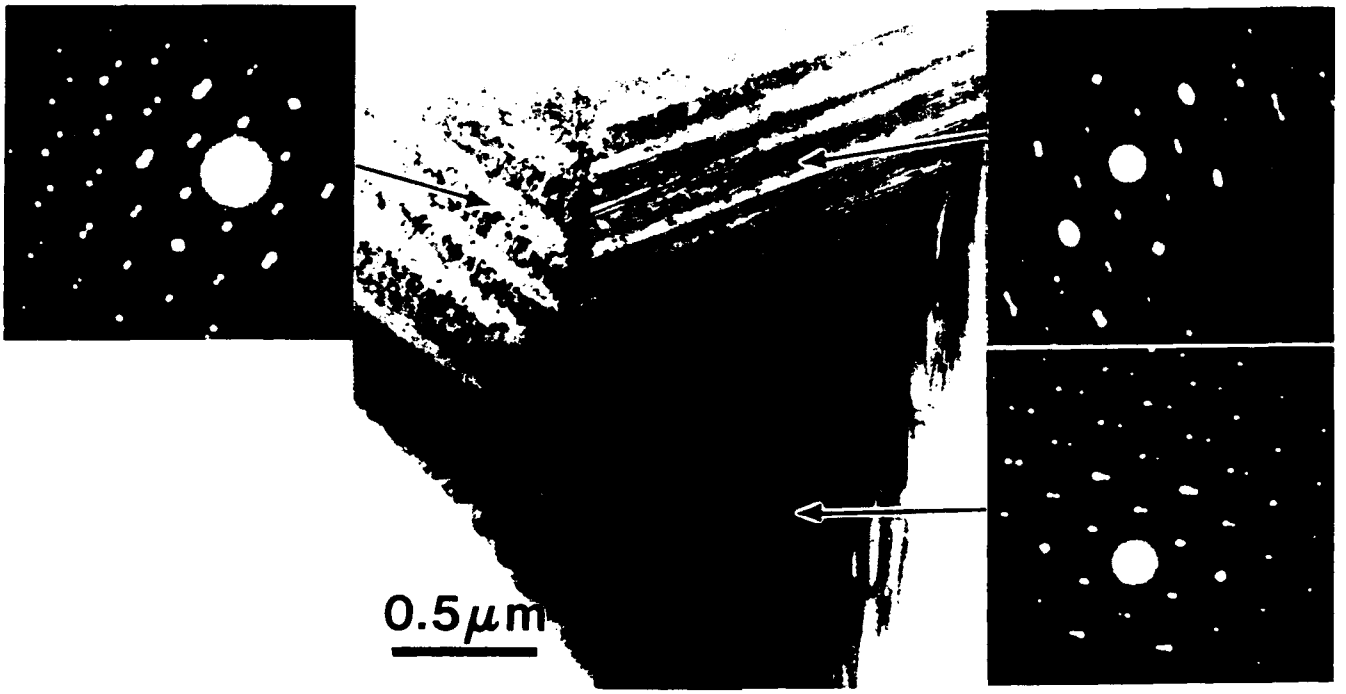

Fig. 10. Three domains related by 120° rotation along the *b* axis of β (from a Ca_2SiO_4/MgO composite sintered at 1600°C for 3 h).

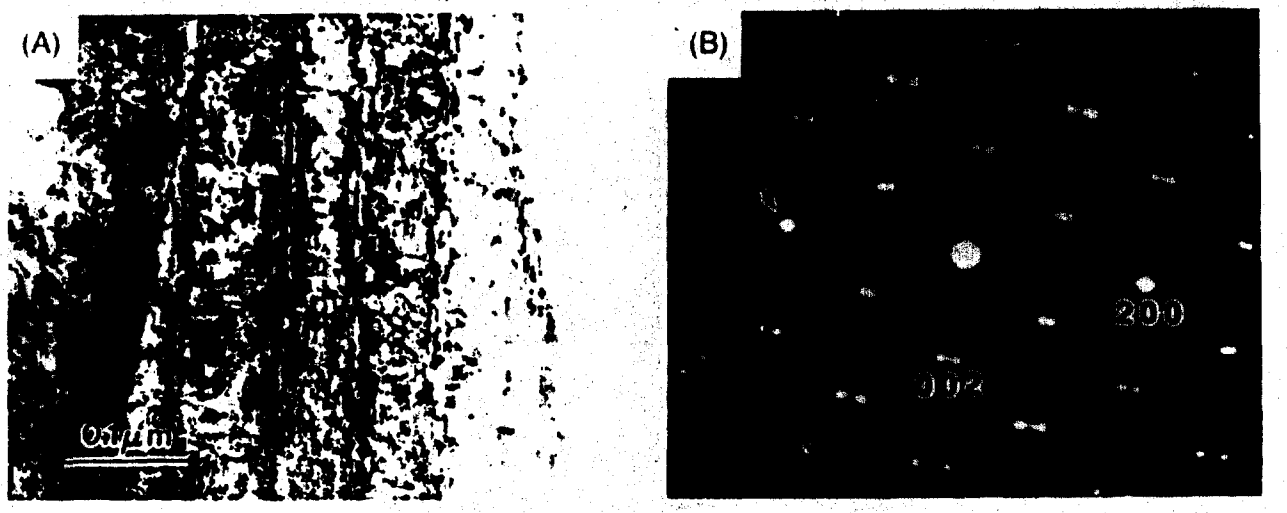

Fig. 11. (A) Strained and twinned β grain and (B) corresponding SADP showing two directional streaking (arrows), both parallel and perpendicular to [200]* (from a Ca_2SiO_4–MgO composite sintered at 1600°C for 3 h).

$$\alpha_a = 13.9 \times 10^{-6}\ ^\circ C^{-1}$$
$$\alpha_b = 15.2 \times 10^{-6}\ ^\circ C^{-1}$$
$$\alpha_c = 20.1 \times 10^{-6}\ ^\circ C^{-1}$$
$$\alpha_v \text{ (average)} = 16.4 \times 10^{-6}\ ^\circ C^{-1}$$
$$\alpha_v = 51.8 \times 10^{-6}\ ^\circ C^{-1}$$

This α_v value corresponds to the linear thermal expansivity of CaO polyhedra ($15 \times 10^{-6}\ ^\circ C^{-1}$). Since strains were accumulated as the grains grew, microcracks could easily be generated to release the strains. The intragranular strains were possibly related to the spontaneous strains produced by the ferroelastic transformations, which are discussed in the next section.

(B) Domain Structures in β. The domain structures observed in β grains of single phase Ca_2SiO_4 (Fig. 9) were probably related to the $\alpha' \rightarrow \beta$ transformation. The symmetry elements in α ({100} and {001} mirror planes in this case) were replaced by twin elements in β. Domain structures observed in β grains of composites (Fig. 10) could have been formed during the $\alpha \rightarrow \alpha_H$ (hexagonal–orthorhombic) transformation, when a symmetry element (three-fold rotation) was lost, producing three symmetry-related domains, as proposed by Groves.[7] All domains later experienced the $\alpha_H \rightarrow \beta$ transformation, producing {100}* twins within each domain. Figure 10 summarizes possible configurations of domain formations resulting from $\alpha \rightarrow \alpha_H$ and $\alpha_H \rightarrow \beta$ transformations. Figure 10(B) shows that there could be two possible shear mechanisms: (1) shearing along the a_β direction or along the b_β direction.

Based on lattice parameter data, the strain tensor components (ε_{ij}) of the transforms can be calculated as follows:

$$\varepsilon_{ij} = \begin{vmatrix} 0.012 & 0 & 0 \\ 0 & 0.002 & 0 \\ 0 & 0 & 0.055 \end{vmatrix} \quad \text{for } \alpha \rightarrow \alpha_H$$

$$\varepsilon_{ij} = \begin{vmatrix} 0.00010 & 0 & 0.031^* \\ 0 & 0.002^* & 0 \\ 0.031^* & 0 & 0.000^* \end{vmatrix}$$

for $\alpha \rightarrow \beta$ by [illegible] shear.

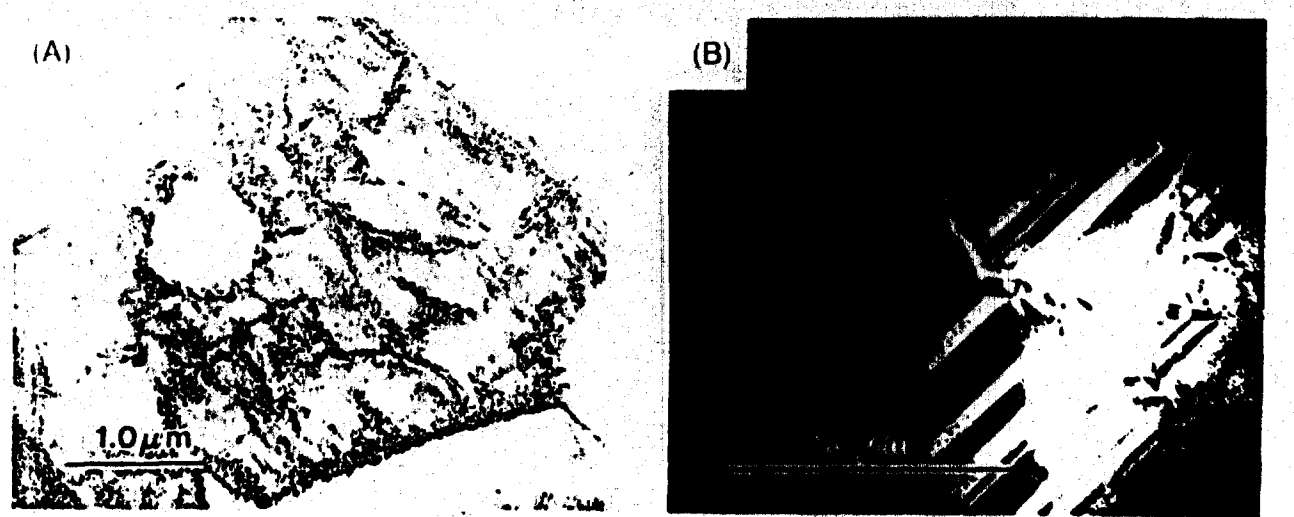

Fig. 12. [illegible]

Fig. 13. Transformed γ grain retained in β grains. Large cracks generated during the β→γ transformation (from single-phase Ca_3SiO_5 sample sintered at 1400°C for 3 h).

Fig. 14. (A) Planar defects developed in γ grains of single-phase Ca_3SiO_5 samples. Note the resemblance between the defect in transformed γ part and twin planes of the untransformed β part. (B) Twin lamellae in one grain tend to match those of the neighboring grain (arrows). (C) A magnified image of planar defect in (B) showing complicated fringe pattern.

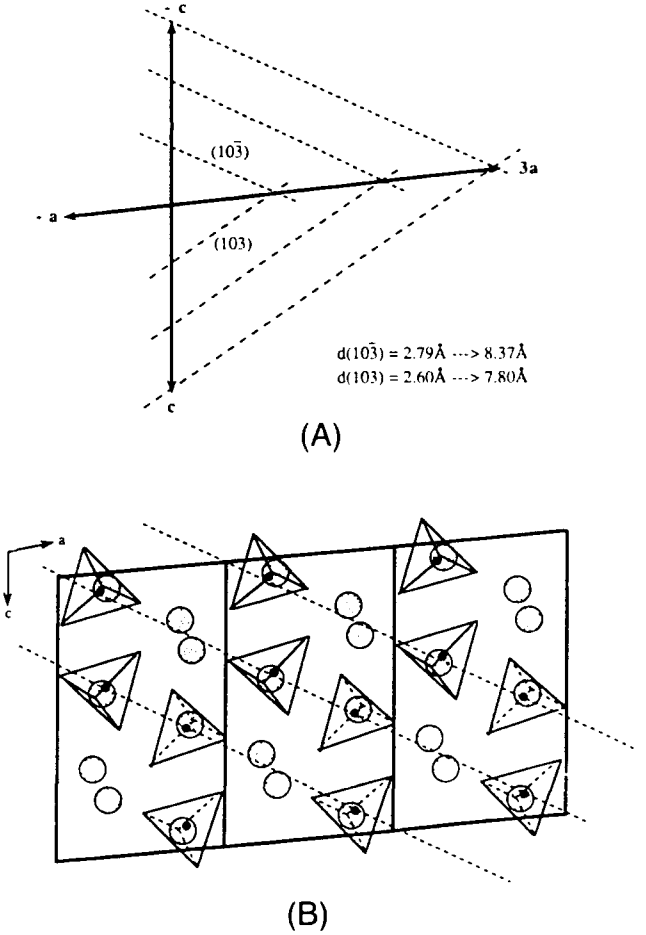

Fig. 15. (A) Geometrical explanation showing that the tripling of (10$\bar{3}$) and (103) planes may be due to the tripling of *a* axis of the β lattice. (B) (010) projection of the structure showing {10$\bar{3}$} planes that may be responsible for the mo[illegible] in the structure

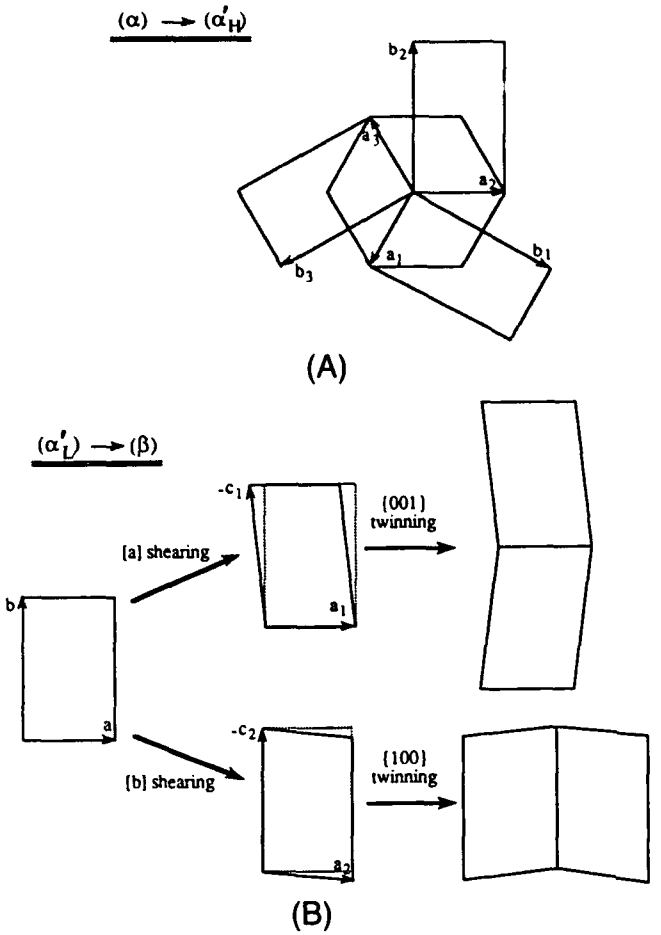

Fig. 16. *Schematic drawing of possible domains formed during the* $\alpha \rightarrow \beta$ transformation: (A) $\alpha \rightarrow \alpha'_H$ transformation and (B) $\alpha'_L \rightarrow \beta$ transformation.

$$\varepsilon_{ij} = \begin{bmatrix} 0.0087 & 0 & -0.0314 \\ 0 & 0.0012 & 0 \\ -0.0314 & 0 & -0.0030 \end{bmatrix}$$

for $\alpha'_L \rightarrow \beta$ by $[b_{\alpha'}]$ shearing

(C) Twinning in β: The twins observed in β grains belonged to the type of "twinning by reticular pseudomerohedry."[29] The predominent population of {100} twins over {001} twins in β grains was related to (i) shearing during the $\alpha'_L \rightarrow \beta$ (orthorhombic→monoclinic) transformation and (ii) formation of twins after the shearing. The shear-strain components ($\varepsilon_{13} = \varepsilon_{31}$) for the $\alpha'_L \rightarrow \beta$ transformation indicated that the $[a_{\alpha'}]$ shearing mechanism was slightly lower energy than the $[b_{\alpha'}]$ shearing mechanism. To release the strains, twin formation would be energetically favorable. As shown in Fig. 16(B), $\{001\}_\beta$ twinning would be a natural consequence of the $[a_{\alpha'}]$ shearing, whereas the $[b_{\alpha'}]$ shearing would lead to $\{100\}_\beta$ twinning. The coexistence of the untwinned and the twinned part (mainly {001}-type) in β grains (Fig. 6) supported this sequential development of twinned structures. It also suggested that the formation of the $\{001\}_\beta$ twin was energetically more difficult compared with that of the $\{100\}_\beta$ twin. A wider twin width of the $\{001\}_\beta$ twin for the same grain size (Fig. 8) suggested that the twin boundary energy of the $\{001\}_\beta$ twin was higher than that of the $\{100\}_\beta$ twin.[30]

(3) Phase Transformations

(A) Molar Volume Changes: Ca_2SiO_4 experienced considerable volume changes throughout the phase transformations. Referring to the lattice parameter data[5] in Table I and to some extrapolations to account for thermal expansions, a volume shrinkage of ~4.4% was estimated for the $\alpha \rightarrow \alpha'_H$ transformation (at ~1425°C). In the α′ region, the volume change was small and steady, involving a ~3.3% shrinkage from 1425° to 650°C. The $\alpha'_L \rightarrow \beta$ transformation (at ~650°C) was accompanied by a small volume shrinkage of 0.4%. If the β phase was to be retained down to room temperature, it would experience a significant amount of volume shrinkage (~3.1%). Therefore, the total volume decrease from α (at 1425°C) to β (at room temperature) was estimated to be as much as ~11.2%, which was unusually large for ceramic materials. In some sense, then, the large volume increase of ~12.3% during the $\beta \rightarrow \gamma$ transformation at room temperature could be a recovery process for the volume shrinkages accumulated on cooling from the α phase at 1425°C.

(B) Symmetry Changes and Ferroelastic Transformations: From a symmetry point of view,[31] a ferroic transformation requires a group–subgroup symmetry relationship between the parent phase and product phase. In addition, there should be a change in the domain system between the two phases to satisfy the criteria for a ferroelastic transformation.

Even though no direct studies of the α structure have been made to date, it is possible to deduce the symmetry of α from the data obtained in this study. Combining the established symmetry of β ($P2_1/n$; point group $2/m$) with the observed symmetry-related domain structures (threefold rotations along the *b* axis of β), a possible symmetry element along the *c* axis of α may be $6/m$. Since twin-related domain structures in β may be a result of the loss of previous mirror planes ({100} and {001} planes) during the $\alpha'_L \rightarrow \beta$ transformation, the point group of the α′-type structure (α'_L or α'_H, or both) is assumed to be *mmm*. In this case, a probable symmetry for the α phase may be $6/mmm$ as a point group and $P6_3/mmc$ as a space group. Actually, the most reliable structural studies of A_2BX_4-type compounds shows a space group of $P6_3/mmc$. This includes K_2SO_4[32] and Na_2SO_4,[33] which are believed to be isostructural with α-Ca_2SiO_4. Space group $P6_3/mmc$ is the highest possible symmetry (prototype) for A_2BX_4 polymorphs. This requires orientational disorder of the BX_4 tetrahedra along the *c* axis, which results in an additional mirror plane perpendicular to the axis.

If the α phase of Ca_2SiO_4 has a point symmetry of $6/mmm$ (hexagonal) and the α'_H phase has a point symmetry of *mmm* (orthorhombic), the $\alpha \rightarrow \alpha'_H$ transformation can be classified as ferroelastic, belonging to an Aizu species[34] $6/mmmFmmm$. In the case of K_2SO_4 and K_2SeO_4, this ferroelastic transformation has been directly proved to exist by movement of domain boundaries under an external stress.[35] A measure of ferroelasticity is usually expressed in terms of spontaneous strain (ε_s). Utilizing formulas given by Aizu,[36] the spontaneous strain generated by the $\alpha \rightarrow \alpha'_H$ (pseudoorthorhombic→orthorhombic) transformation could be approximated as

$$\varepsilon_S^2 = \left[\frac{1}{2}(\varepsilon_{11} - \varepsilon_{22})\right]^2 + \left[\frac{1}{2}(\varepsilon_{22} - \varepsilon_{33})\right]^2 + \left[\frac{1}{2}(\varepsilon_{33} - \varepsilon_{11})\right]^2$$

Following this equation, $\varepsilon_S \approx 0.046$, which is quite a large value.

If the $\alpha'_H \rightarrow \alpha'_L$ transformation were a disorder–order transformation without change of symmetry, the $\alpha'_L \rightarrow \beta$ (orthorhombic (*mmm*)→monoclinic ($2/m$)) transformation would also be ferroelastic, belonging to an Aizu species[34] $mmmF2/m$. ε_S for $mmm \rightarrow 2/m$ is simply expressed as[36]

$$\varepsilon_S = \sqrt{2}\,|\varepsilon_{13}|$$

Then, $\varepsilon_S \approx 0.044$, which is again quite a large value. The ferroelastic nature of the $\alpha' \rightarrow \beta$ transformation has also been reported for Sr_2SiO_4, with $\varepsilon_S = 0.033$.[37] Shift of domain walls caused by a lateral stress has been observed in twinned β-Sr_2SiO_4 crystals.

(C) Crystal Structure Changes: From a crystal structural point of view, the Ca_2SiO_4 structure is remarkably flexible to endure the large strains produced by the phase transformations.

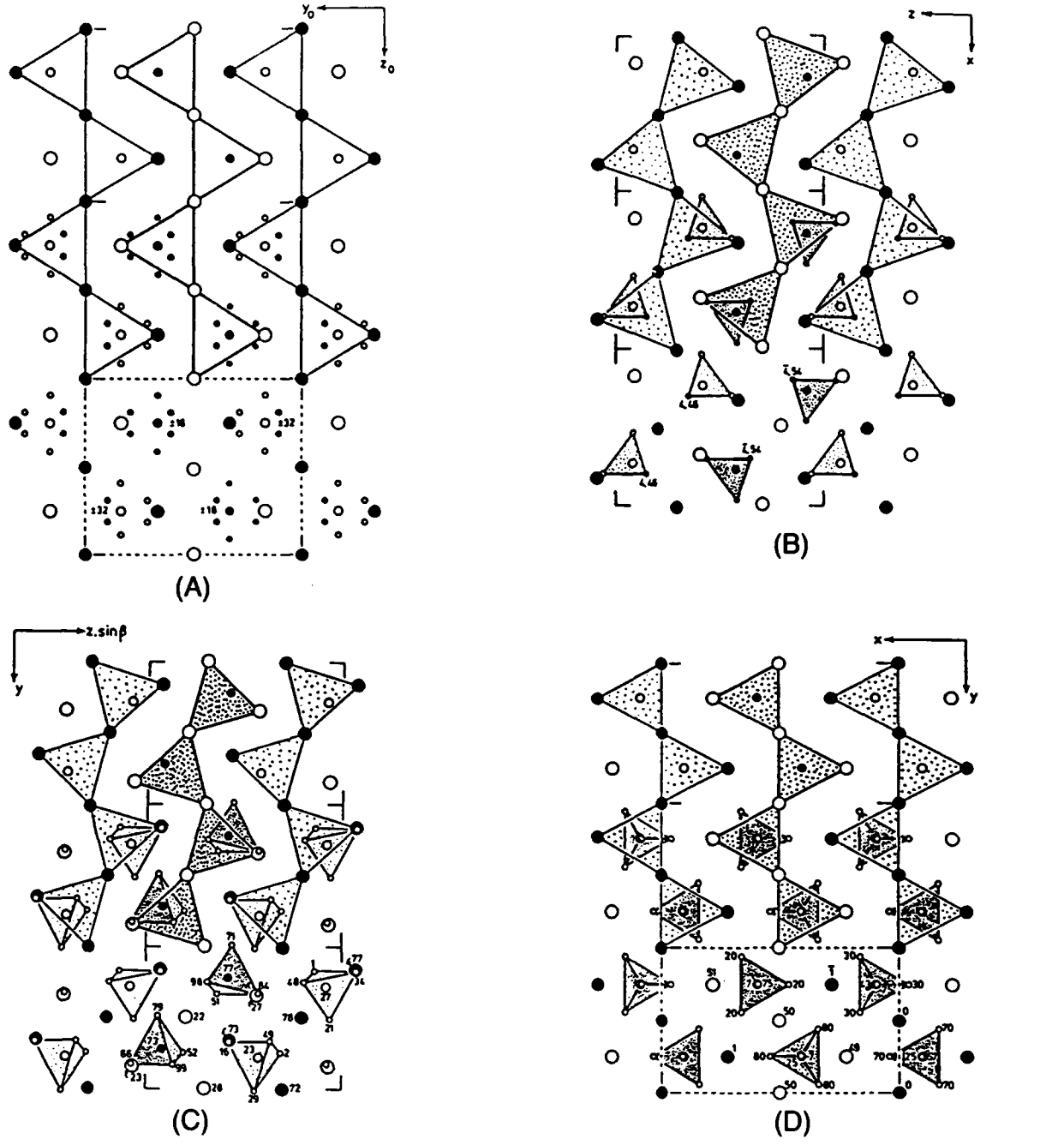

Fig. 17. Schematic projection of (A) α structure (from K_2SO_4), (B) α′ structure (from K_2SO_4), (C) β structure of Ca_2SiO_4, and (D) γ-structure of Ca_2SiO_4. Cation (Ca^{2+}) arrangements are emphasized. (After O'Keeffe and Hyde.[38])

One possible reason for this flexibility is that the structure is an inhomogeneous mixture of relatively large, but loosely-bonded CaO_x polyhedra and small, but rigid, SiO_4 tetrahedra. Furthermore, in this orthosilicate, the SiO_4 tetrahedra are not linked to one another and can easily be moved.

Figure 17 displays essential features of the sequence of Ca_2SiO_4 crystal structures in terms of the cation arrangements,[21,38] rather than the conventional view of an oxygen framework stuffed with cations. All the polymorphs of Ca_2SiO_4 have similar arrangements based on the Ca_2Si alloy structure.[38] They consist of regular, edge-linked trigonal prisms of calcium atoms with SiO_4 tetrahedra in the center. Although edge-linked calcium prisms have a linear arrangement in the α and γ structures, they have a kinked arrangement in the α′ and β structures. During the α→α′ transformation, collapse of the CaO_x polyhedra results in kinking of the calcium-prism arrangements and movement of SiO_4 tetrahedra to new positions. Subsequent tilting of the SiO_4 tetrahedra is a major change in the structure during the α′→β transformation. The kinked arrangement of the calcium prisms is straightened by the β→γ transformation.

From structural refinement data of Ca_2SiO_4, the cation–anion bond lengths and the nearest cation–cation bond distances have been calculated (Table II). Note that, while there are minor changes of Si–O bond lengths throughout the transformations, the changes of Ca–O bond lengths are significant. On cooling, the CaO_x polyhedra rapidly collapse because of the diminishing of the effective calcium vibration. The neighboring SiO_4 tetrahedra adjust their positions with respect to the CaO_x.

Comparison of the nearest bond distances between cations shows that the β structure has the shortest bond distances for both Ca–Ca and Si–Ca. Referring to ambient pressure data for nonbonded radii of silicon and calcium,[39] the ideal Ca–Ca distance is ~3.40 Å and the ideal Si–Ca distance is ~3.23 Å (1 Å = 10^{-1} nm). This means that the shortest Si–Ca bond distance in β (~2.97 Å) is too short to maintain the stability of the structure at ambient pressure. As a consequence, strong repulsive

Table II. Average Bond Lengths of Si–O and Ca–O and the Shortest Bond Distances between Silicon and Calcium Atoms for Ca_2SiO_4 Polymorphs

Polymorph	Bond length (Å)*					Reference
	Si–O	Ca–O	Ca–Ca	Si–Ca	Si–Si	
α	1.81(?)'	2.70(?)'	3.49	3.12	4.81	6
α_L'	1.63	2.63	3.48	3.13	4.39	11
β	1.63	2.50	3.43	2.97	4.11	13
γ	1.64	2.38	3.39	3.67	4.09	16

*1 Å = 10 ⁻¹ nm. 'Because of the uncertainty of one oxygen position (O(2)), these data may have significant errors.

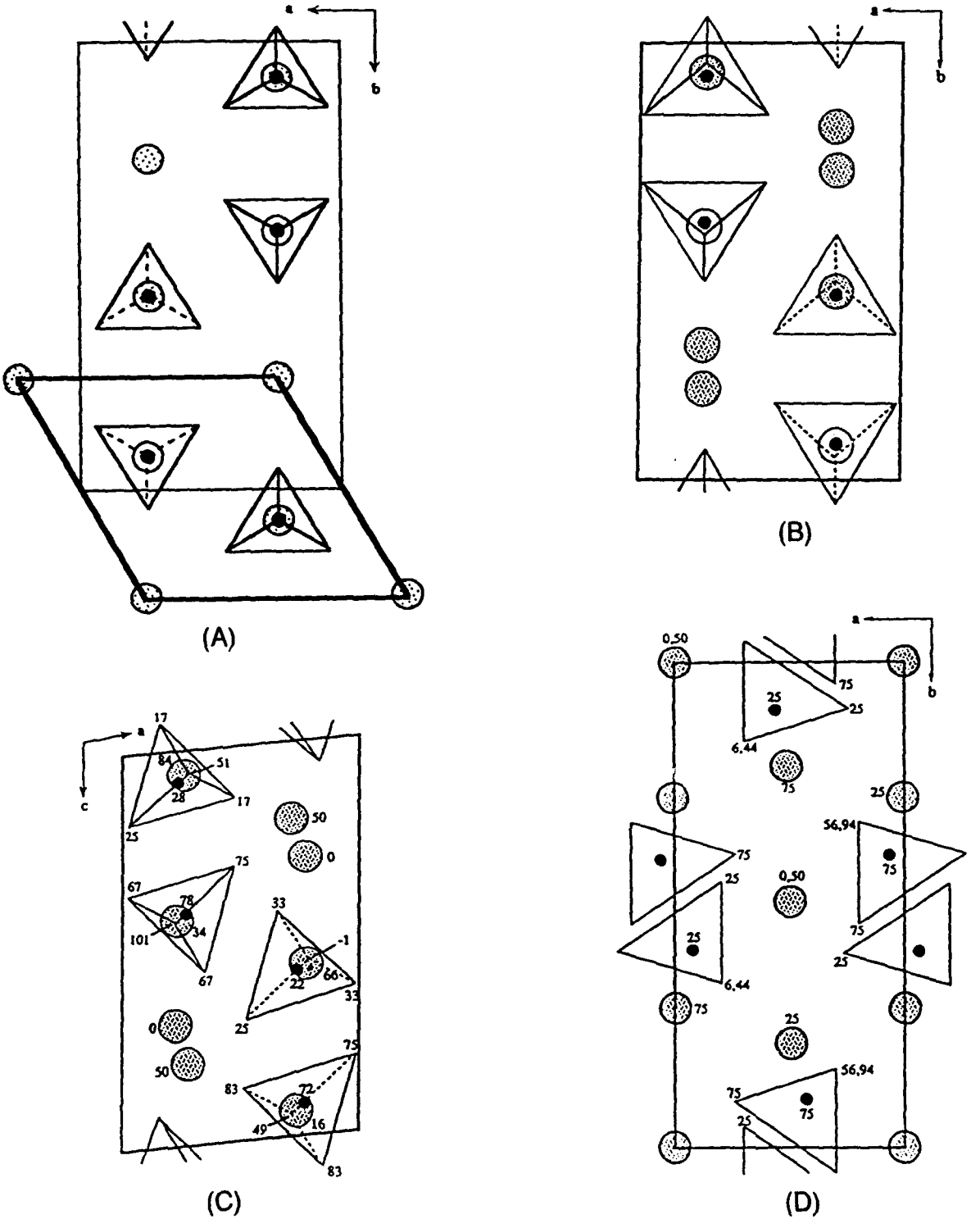

Fig. 18. *Conventional projections of* Ca_2SiO_4: (A) α structure, (B) α′ structure, (C) β structure, and (D) γ structure.

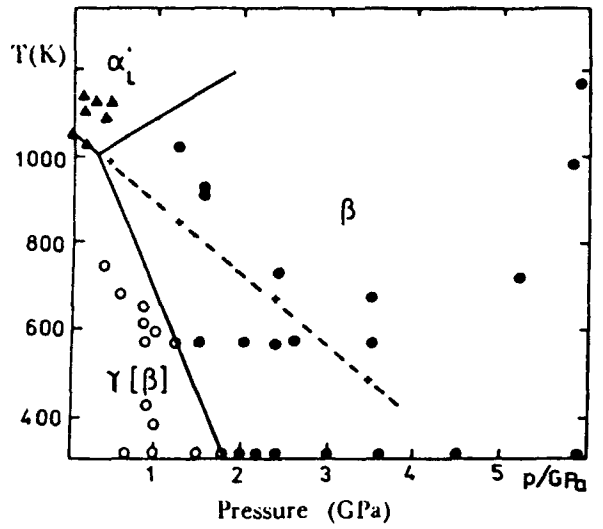

Fig. 19. *p–T* diagram of Ca_2SiO_4 determined by DTA, X-ray, and optical measurements. Metastable form is designated in square brackets. (After Hanic *et al.*[40])

forces are expected to be developed in the β structure. The modulated structures observed in both α′ and β may be related to some effective ways of calcium and SiO_4 arrangements to relieve such electrostatic repulsions between them.

Conventional projections of the Ca_2SiO_4 polymorphs in Fig. 18 illustrate that all of the α, α′, and β structures show close association of silicon atoms in SiO_4 tetrahedra with adjacent calcium atoms. However, in the γ structure, the silicon and calcium atoms are no longer closely associated because of large displacements of both the SiO_4 and calcium by the β→γ transformation. The displacements are not a simple shuffling movement of atoms, but involve a considerable amount of SiO_4 rotation. All major movements occur along the *b* axis of the γ structure. Compared with the α structure in a different projection (Figs. 17 (A) and (D)), the γ structure has silicon in a more balanced but distant position with respect to calcium. In other respects, the major configurations of both structures are very similar.

(D) Stability of β *Structure and* β→γ *Transformation*: From the crystal structure point of view discussed in the previous section, the β structure is expected to be unstable at ambient pressure because of the cation charge repulsions. As shown in Fig. 19, however, this structure has been reported to be more stable than both the γ structure and the α_L' structure at very high pressures.[40] For example, at 675°C, which is suggested to be the transformation temperature of α_L'→β, the β structure may be more stable than the γ structure only above 1 GPa. In this case, it is difficult to understand why the β phase always intervenes between α_L' and γ on cooling at ambient pressure. This observation implies that the structure should be in a highly stressed condition on cooling. One possible reason may be the influence of the spontaneous strain generated during the ferroelastic α_L'→β transformation. That is, the β structure is more suitable for accommodating the strain than the γ structure for certain temperature ranges. In this respect, the metastable β structure is inherently strained. This may be a reason why all the β grains observed in this study show intragranular strains.

Since the α→α_H' transformation also appeared to be ferroelastic, the β grains that experienced both α→α_H' and α_L'→β transformations should have a higher internal strain than the β grains that only experienced the α_L'→β transformation. This built-in strain may be a reason why (i) solid pellets of single-phase Ca_2SiO_4, which were sintered above the α→α_H' transformation temperature, could not be retained intact[22] and (ii) β grains in composites sintered above the α→α_H' transformation temperature showed higher intragranular strains, as well as a high concentration of defects and microcracks.

These large, built-in strains in the β structure and strong repulsive forces between silicon and calcium may be a possible reason why the β→γ transformation can occur instantaneously, despite the fact that the transformation necessarily involves the breaking of some oxygen bonds in the β structure. It suggests a reexamination of Buerger's classification[41] of displacive versus reconstructive transformation mechanisms. The higher symmetry and larger volume of the transformed γ phase are, therefore, probably related to the process of straightening of the β lattice to release strains and maximization of the volume to reduce charge repulsions.

V. Conclusion

From TEM studies of the Ca_2SiO_4 system, three types of superlattice structures were observed: (i) $\times 2a,2b$-type in α_L'; (ii) $\times 3c$-type in α_L'; and (iii) $\times 3a$-type in β. Almost all β grains were twinned and strained. Microcracks tended to develop along grain boundaries as the grain size increased. Some transformed γ grains coexisted with β grains, producing large intergranular microcracks. γ grains were strain free, but detwinning-related planar defects were usually present. The $\{100\}_\beta$ twinning occurred more favorably than did $\{001\}_\beta$ twinning. Two types of symmetry-related domain structures were observed in β grains: (i) two twin-related domains for samples that experienced the α_L'→β transformation and (ii) three 120° rotation-related domains for samples that experienced the α→α_H' transformation.

Based on symmetry considerations, both α→α_H' and α_L'→β appeared to be ferroelastic transformations. The α_L'→β transformation could be achieved by shearing along the a_α direction or along the b_α direction leading to $\{001\}_\beta$ or $\{100\}_\beta$ twinning, respectively. The β-Ca_2SiO_4 structure resulting from this sequence of ferroelastic transformations was inherently strained. This strained β structure was not stable at ambient pressure because of the strong electrostatic charge repulsions between silicon and calcium, which were too close to each other. In terms of the crystal structure, the major driving forces for the β→γ transformation, therefore, are considered to be the release of strains and charge repulsions in the β structure. The higher symmetry and larger volume of the transformed γ phase are probably related to the process of straightening of the β lattice to release strains and maximizing of the volume to reduce repulsions. The β→γ tranformation can be displacive in the sense of its instantaneous reaction, but needs to overcome a comparatively high energy barrier due to the breaking of some oxygen bonds in the β structure.

Acknowledgments: Dr. T. I. Hou and Mr. E. Mast are thanked for fabricating the composite samples used in this study. We acknowledge valuable discussions with Prof. A. H. Heuer of Case Western Reserve University. Use of the electron microscopy facilities at the Center for Microanalysis of Materials in the Materials Research Laboratory and at the Center for Electron Microscopy, both at the University of Illinois at Champaign-Urbana, is gratefully acknowledged.

References

[1]W. M. Kriven, "Possible Transformation Toughening Alternative to Zirconia: Crystallographic Aspects," *J. Am. Ceram. Soc.*, **71**, 1021–30 (1988).

[2]W. M. Kriven, C. J. Chan, and E. A. Barinek, "The Particle-Size Effect of Dicalcium Silicate in a Calcium Zirconate Matrix"; pp. 145–55 in Advances in Ceramics, Vol. 24A, *Science and Technology of Zirconia III*. Edited by S. Sōmiya, N. Yamamoto, and H. Yanagida. American Ceramic Society, Westerville, OH, 1988.

[3]C. J. Chan, W. M. Kriven, and J. F. Young, "Physical Stabilization of the β to γ Transformation in Dicalcium Silicate," *J. Am. Ceram. Soc.*, **75** [6] 1621–27 (1992).

[4]C. J. Chan, W. M. Kriven, and J. F. Young, "Analytical Electron Microscopic Studies of Doped Dicalcium Silicate," *J. Am. Ceram. Soc.*, **71**, 713–19 (1988).

[5]M. Regourd, M. Bigare, J. Forest, and A. Guinier, "Synthesis and Crystallographic Investigation of Some Belites"; pp. 44–48 in *Proceedings of the 5th International Symposium on the Chemistry of Cement*, Part I, Supplement Paper I-10 (Tokyo, Japan, 1968). Cement Association of Japan, Tokyo, Japan, 1969.

[6]S. Udagawa, K. Urabe, and T. Yano, "The Crystal Structure of α-Ca_2SiO_4," (in Jpn.), *Cem. Assoc. Jpn. Rev., Gen Meet., Tech. Sess.*, **31**, 26–29 (1977).

[7]G. Yamaguchi, Y. Ono, S. Kawamura, and Y. Soda, "Synthesis of the Modifications of Ca_2SiO_4 and the Determination of Their Powder X-ray Diffraction Patterns" (in Jpn.), *J. Ceram. Assoc. Jpn.*, **71**, 21–26 (1963).

[8]P. Barnes, C. H. Fentimen, and J. W. Jeffery, "Structurally Related Dicalcium Silicate Phases," *Acta Crystallogr., Sect. A: Cryst. Phys., Diffr., Theor. Gen. Crystallogr.*, **36**, 353–56 (1980).

[9]H. Saalfeld, "X-ray Investigation of Single Crystals of β-Ca_2SiO_4 (Larnite) at High Temperatures," *Am. Mineral.*, **60**, 824–27 (1975).

[10]I. Jelenic and A. Bezjak, "Electron Diffraction Evidence for Superstructures in α'-Modification of Dicalcium Silicate," *Cem. Concr. Res.*, **12**, 785–88 (1982).

[11]S. Udagawa, K. Urabe, T. Yano, K. Takada, and M. Natsume, "Studies on the Dusting of Ca_2SiO_4—The Crystal Structure of α_L'-Ca_2SiO_4" (in Jpn.), *Cem. Assoc. Jpn. Rev., Gen. Meet., Tech. Sess.*, **33**, 35–38 (1979).

[12]A. M. Il'inets and M. Ya. Bikbau, "Structural Mechanism of Polymorphic Transitions of Dicalcium Silicate, Ca_2SiO_4. Part II: Refinement of Crystal Structure of High-Temperature α_L' Modification of Dicalcium Silicate, Ca_2SiO_4," *Sov. Phys.—Crystallogr. (Engl. Transl.)*, **35**, 54–56 (1990).

[13]K. H. Jost, B. Ziemer, and R. Seydel, "Redetermination of the Structure of β-Dicalcium Silicate," *Acta Crystallogr., Sect. B: Struct. Crystallogr. Cryst. Chem.*, **33**, 1696–700 (1977).

[14]D. K. Smith, A. Majumdar, and F. Ordway, "The Crystal Structure of γ-Dicalcium Silicate," *Acta Crystallogr.*, **18**, 787–95 (1965).

[15]R. Czaya, "Refinement of the Structure of γ-Ca_2SiO_4," *Acta Crystallogr., Sect. B: Struct. Crystallogr. Cryst. Chem.*, **27**, 848–49 (1971).

[16]S. Udagawa, K. Urabe, M. Natsume, and T. Yano, "Refinement of the Crystal Structure of γ-Ca_2SiO_4," *Cem. Concr. Res.*, **10**, 139–44 (1980).

[17]W. Eysel and T. Hahn, "Polymorphism and Solid Solution of Ca_2GeO_4 and Ca_2SiO_4," *Z. Kristallogr.*, **131**, 322–41 (1970).

[18]C. M. Midgley, "The Crystal Structure of β-Dicalcium Silicate," *Acta Crystallogr.*, **5**, 307–12 (1952).

[19]G. W. Groves, "Twinning in β-Dicalcium Silicate," *Cem. Concr. Res.*, **12**, 619–24 (1982).

[20]G. W. Groves, "Portland Cement Clinker Viewed by Transmission Electron Microscopy," *J. Mater. Sci.*, **16**, 1063–70 (1981).

[21]J. Barbier and B. G. Hyde, "The Structures of the Polymorphs of Dicalcium Silicate, Ca_2SiO_4," *Acta Crystallogr., Sect. B: Struct. Sci.*, **41**, 383–90 (1985).

[22]I. Nettleship, K. Slavick, Y. J. Kim, and W. M. Kriven, "Phase Transformations in Dicalcium Silicate: I, Fabrication and Phase Stability of Fine-Grained β-Phase," *J. Am. Ceram. Soc.*, **75** [9] 2400–406 (1992).

[23]I. Nettleship, K. Slavick, Y. J. Kim, and W. M. Kriven, "Phase Transformations in Dicalcium Silicate: III, The Effects of Barium on the Stability of Fine-Grained α_L' and β"; unpublished work.

[24]E. S. Mast, "Development and Possible Use of Dicalcium Silicate in the Transformation Toughening of Magnesia"; M.S. Thesis. University of Illinois at Urbana-Champaign, 1990.

[25]T. I. Hou and W. M. Kriven, "Processing, Microstructures, and Mechanical Properties of Dicalcium Silicate–Calcium Zirconate Composites," to be published in *J. Am. Ceram. Soc.*

[26]S. Udagawa, K. Urabe, T. Yano, and M. Natsume, "Studies on the Phase Transitions of Ca_2SiO_4 by X-ray Single-Crystal Camera with a High-Temperature Apparatus" (in Jpn.), *J. Ceram. Assoc. Jpn.*, **88**, 285–91 (1980).

[27]R. M. Hazen and L. W. Finger, *Comparative Crystal Chemistry*; pp. 115–46. Wiley, New York, 1982.

[28]J. L. Schlenker, G. V. Gibbs, and M. B. Boison, "Strain-Tensor Component Expressed in Terms of Lattice Parameters," *Acta Crystallogr., Sect. A: Cryst. Phys., Diffr., Theor. Gen. Crystallogr.*, **34**, 52–54 (1978).

[29]J. W. Cahn, "Twinned Crystal," *Adv. Phys.*, **3**, 363–445 (1954).

[30]T. Roy and T. E. Mitchell, "Twin Boundary Energies in $YBa_2Cu_3O_{7-\delta}$ and La_2CuO_4," *Philos. Mag. A*, **63**, 225–32 (1991).

[31]V. K. Wadhawan, "Ferroelasticity and Related Properties of Crystals," *Phase Transitions*, **3**, 3–103 (1982).

[32]M. Miyake, H. Morikawa, and S.-I. Iwai, "Structural Reinvestigation of the High-Temperature Form of K_2SO_4," *Acta Crystallogr., Sect. B: Struct. Crystallogr. Cryst. Chem.*, **36**, 532–36 (1980).

[33]W. Eysel, H. H. Hofer, K. L. Keester, and Th. Hahn, "Crystal Chemistry and Structure of Na_2SO_4(I) and Its Solid Solutions," *Acta Crystallogr., Sect. B: Struct. Sci.*, **41**, 5–11 (1985).

[34]K. Aizu, "Possible Species of Ferromagnetic, Ferroelectric, and Ferroelastic Crystals," *Phys. Rev. B: Solid State*, **2**, 754–72 (1970).

[35]S. Shiozaki, A. Sawada, Y. Ishibashi, and Y. Takagi, "Hexagonal–Orthorhombic Phase Transition and Ferroelasticity in K_2SO_4 and K_2SeO_4," *J. Phys. Soc. Jpn.*, **43**, 1314–19 (1977).

[36]K. Aizu, "Determination of the State Parameters and Formulation of Spontaneous Strain for Ferroelastics," *J. Phys. Soc. Jpn.*, **28**, 706–16 (1970).

[37]M. Catti and G. Gazzoni, "The β ↔ α' Phase Transition of Sr_2SiO_4. II. X-ray and Optical Study, and Ferroelasticity of the β Form," *Acta Crystallogr. Sect. B: Struct. Sci.*, **39**, 679–84 (1983).

[38]M. O'Keeffe and B. G. Hyde, "An Alternative Approach to Nonmolecular Crystal Structures with Emphasis on the Arrangements of Cations," *Struct. Bonding (Berlin)*, **61**, 77–144 (1985).

[39]M. O'Keeffe and B. G. Hyde, "The Role of Nonbonded Forces in Crystals"; pp. 227–54 in *Structure and Bonding in Crystals*, Vol. 1. Edited by M. O'Keeffe and A. Navrotsky. Academic Press, New York, 1981.

[40]F. Hanic, J. Kamarad, J. Stracelsky, and I. Kapralik, "The *p–T* Diagram of Ca_2SiO_4," *Br. Ceram. Trans. J.*, **86**, 194–98 (1987).

[41]M. J. Buerger, "Phase Transformations," *Sov. Phys.—Crystallogr. (Engl. Transl.)*, **16**, 959–68 (1972). □

Journal of the European Ceramic Society 11 (1993) 291–298

Chemical Preparation and Phase Stability of Ca_2SiO_4 and Sr_2SiO_4 Powders

Ian Nettleship,* James L. Shull, Jr. & Waltraud M. Kriven

Department of Materials Science and Engineering, University of Illinois at Urbana-Champaign, Urbana, Illinois 61801, USA

(Received 29 January 1992; revised version received 23 June 1992; accepted 10 July 1992)

Abstract

A process has been developed to produce high surface area Ca_2SiO_4 and Sr_2SiO_4 powders using colloidal silica for the silicon precursor. This method was relatively straightforward and avoided the use of precipitation techniques and unstable alkoxides. Calcium carbonate and strontium carbonate were identified as intermediate compounds, and the silicates appeared to form by a low-temperature solid-state reaction. The effect of resin content and calcination conditions on the phase distribution and physical properties of the powders was examined. Finally, the sodium content of the colloidal silica was found to have a significant effect on the phase stability of β-Ca_2SiO_4 after calcination at 1400°C.

Es wurde ein Verfahren zur Herstellung von Ca_2SiO_4- und Sr_2SiO_4-Pulvern mit großer freier Oberfläche entwickelt. Als Silizium-haltiger Prekursor wurde Siliziumdioxid verwendet. Diese verhältnismäßig direkte Methode erspart die Anwendung von Ausscheidungstechniken und nicht stabiler Alkoxide. Kalziumkarbonat und Strontiumkarbonat konnten als intermediäre Verbindungen identifiziert werden. Die entsprechenden Silikate scheinen sich durch eine Festphasenreaktion bei tiefen Temperaturen zu bilden. Die Auswirkungen des Anteils an Binderharz und der Kalzinierungsbedingungen auf die Phasenverteilung und die physikalischen Eigenschaften der Pulver wurden genauer untersucht. Schließlich konnte gezeigt werden, daß der Natrium-Gehalt des kolloiden Siliziumdioxids einen beträchtlichen Einfluß auf die Stabilität der β-Ca_2SiO_4-Phase nach der Kalzinierung bei 1400°C ausübt.

Un procédé a été développé pour synthétiser des poudres de Ca_2SiO_4 et Sr_2SiO_4 présentant une surface spécifique élevée, avec de la silice colloïdale comme précurseur du silicium. Cette méthode est relativement directe et évite les techniques de précipitation et l'usage d'alcoolates instables. Les carbonates de calcium et de strontium ont été détectés en tant que composés transitoires et les silicates paraissent se former par réaction à l'état solide à basse température. Les auteurs rapportent l'influence de la teneur en résine et des conditions de calcination sur la distribution de phase et les propriétés physiques des poudres. Les résultats démontrent, enfin, que la stabilité de la phase β-Ca_2SiO_4 après calcination à 1400°C est influencée de façon significative par la teneur en sodium de la silice colloïdale.

1 Introduction

The polymorphism of dicalcium silicate (Ca_2SiO_4) has been well studied[1,2] because of the considerable importance of this compound in the cement and refractories industries. The currently accepted sequence of phase transformations is illustrated in Fig. 1. In most cases work on the material has been directed at avoiding the disruptive 12 vol.% expansion associated with the $\beta \rightarrow \gamma$ transformation, commonly referred to as 'dusting'. The α'_L- and β-phases are also important hydraulic phases in Portland cement, but the γ-phase is undesirable because it does not hydrate.

Dicalcium silicate powders have usually been fabricated by a high-temperature solid-state reaction between CaO and SiO_2. The kinetics of this reaction are slow, and temperatures of 1450°C and above are commonly used to drive the reaction to completion. The resulting powder is predominantly γ-phase after cooling to room temperature. Retention of the high-temperature polymorphs is achieved by the addition of stabilizing additives or impurities.[3]

The β-phase of Ca_2SiO_4 can also be retained after

* Present address: Department of Materials Science and Engineering, University of Pittsburgh, Pittsburgh, Pennsylvania 15261, USA.

Journal of the European Ceramic Society 0955-2219/93/$6.00 © 1993 Elsevier Science Publishers Ltd, England. Printed in

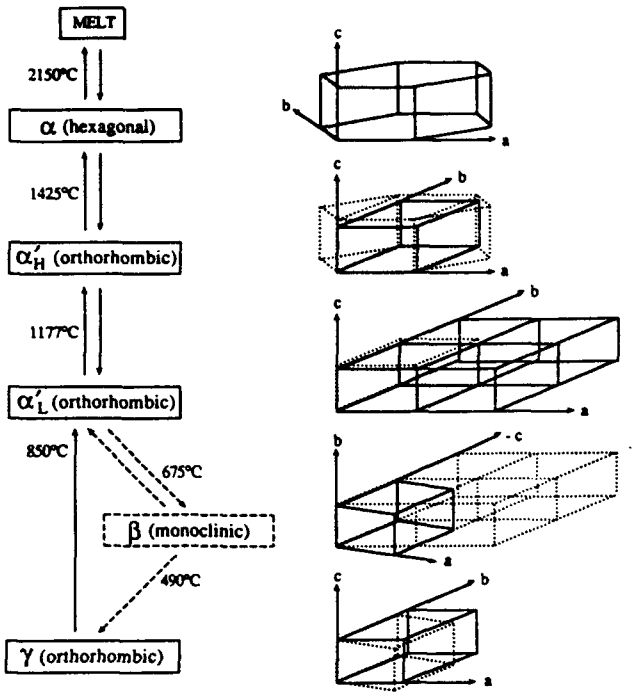

Fig. 1. The polymorphism of Ca_2SiO_4.

low-temperature heat treatment of γ-powders,[4] or by chemical preparation.[5] Both studies have linked the retention of the β-phase to a particle size effect on the $\beta \rightarrow \gamma$ transformation.

The chemical preparation route[5] involved either spray reacting or direct gelling of colloidal silica in the presence of $Ca(NO_3)_2$. This was an extension of the method used for the preparation of other silicates, as reviewed by Luth & Ingamells.[6] These chemical methods allowed preparation of β-Ca_2SiO_4 powders at temperatures as low as 750°C.[5] Powders of β-Ca_2SiO_4 have also been prepared by solid-state reaction of CaC_2O_4 and amorphous SiO_2 at 950°C in a CO_2 atmosphere.[7] The advantage of the latter method is that no corrosive salts, which produce acidic fumes on calcination, are used in the powder production. All the low-temperature methods already mentioned produced powders with higher surface areas than those produced by high-temperature calcination. Another advantage of the low-temperature routes is that the β-phase is retained and hence the powders are reactive in terms of their hydration behavior. Unfortunately, the nature of the chemical reactions that formed Ca_2SiO_4 has not been studied in detail and the physical properties, including the particle size, have not been fully reported, even though they are important to the hydration behavior.

Dicalcium silicate has recently been considered as a candidate for a possible alternative transformation toughener to zirconia.[8] This was based on the large volume change (12 vol.%) associated with the $\beta \rightarrow \gamma$ transformation. The desire to fabricate dense, polycrystalline Ca_2SiO_4 in order to study the transformation has also stimulated research into the preparation of high surface area Ca_2SiO_4 powders.

In comparison, Sr_2SiO_4 has been less well studied. The $\alpha' \rightarrow \beta$ transformation in this compound is structurally analogous to the $\alpha'_L \rightarrow \beta$ transformation in Ca_2SiO_4, but the transformation occurs at 90°C compared to 675°C for pure Ca_2SiO_4. This makes it easier to study the ferroelastic $\alpha' \rightarrow \beta$ type transformation in Sr_2SiO_4.[9,10] Consequently, fine Sr_2SiO_4 powders are required to process dense polycrystalline Sr_2SiO_4.

In this study a quick and comparatively easy method is reported for the chemical preparation of Ca_2SiO_4 and Sr_2SiO_4 powders. The method has previously been used to prepare Ca_2SiO_4 powders for incorporation into a calcium zirconate ($CaZrO_3$) matrix.[11] It involves a 'Pechini-type' process in which one of the constituents is colloidal. The effect of resin content and calcination conditions on the physical properties of the powder and the phase distribution are presented. The effect of the sodium content of the colloidal silica on the phase distribution of the Ca_2SiO_4 is also studied.

2 Experimental Procedures

A flow diagram detailing the preparation method is shown in Fig. 2. The resin content of the resulting gel is defined as follows:

$$\% \text{ resin content} = 100\, W_{resin}/(W_{oxide} + W_{resin})$$

where W_{oxide} is the weight of the oxide after calcination, calculated from the known weights of the precursors, and W_{resin} is the weight of resin added. In all cases the resin was composed of 60 wt% citric acid monohydrate and 40 wt% ethylene glycol.

Firstly, the calcium and strontium precursors, which were $Ca(NO_3)_2.4H_2O$ and $Sr(NO_3)_2$ respectively, were assayed and stored in desiccators. The

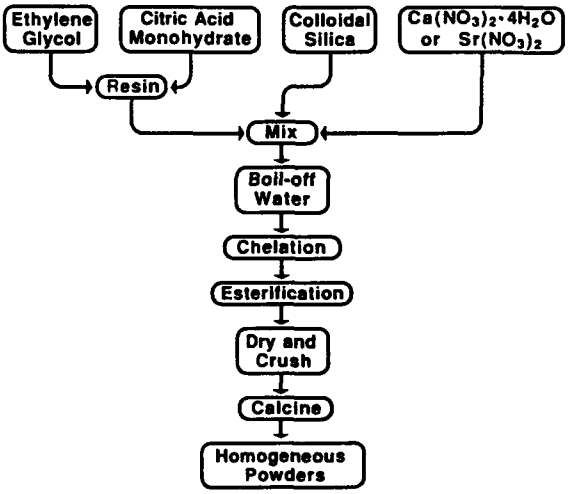

Fig. 2. Flow diagram showing the processing route for both Ca_2SiO_4 and Sr_2SiO_4 powders.

use of the hydrated nitrates, which can have variable moisture contents, did not affect the phase distributions obtained in the final powder. The required amount of the nitrate precursor was dissolved in water and then added to colloidal silica. In order to prevent flocculation of the silica, the pH of the colloidal silica was adjusted to below 1·5 with nitric acid prior to the addition of the nitrates. In this study, two colloidal silicas with different sodium contents were used. The first, which was designated Silica 1 (Ludox® SM, Du Pont Chemical Company), contained more sodium than the second, which was called Silica 2 (Ludox® AS-40, Du Pont Chemical Company). Silica 1 was used for all the Sr_2SiO_4 and Silica 2 was used for most of the Ca_2SiO_4 preparations. After the nitrate solutions and colloidal silica had been mixed, the resin was added and the mixture was heated. As the water boiled off, the gel formed without flocculation of the colloidal silica, and the viscosity increased. The remaining water then evaporated, expanding the gel into a foam. Finally the foam was dried and crushed before calcination at temperatures in the range 200°C to 1400°C.

Some of the crushed Ca_2SiO_4 gel was subjected to differential thermal analysis (DTA) and thermogravimetric analysis (TGA) while heating at 5°C/min, the same heating rate used for calcination. The phase distributions in the powders were evaluated by X-ray diffraction (XRD). This was after calcination for 1 min at temperatures in the range 200°C to 800°C and also after calcination for 1 h in the temperature range 800°C and 1400°C.

The effects of resin content and calcination conditions on the specific surface area and the particle size of the powders were determined by nitrogen adsorption (BET) and sedigraph techniques respectively. Some of the powders were also examined by SEM.

Finally, chemical analysis by plasma emission spectroscopy was performed on some Ca_2SiO_4 powders to check the calcium to silicon ratio, which was found to be in the range 2 to 2·1.

3 Results and Discussion

3.1 Phase development on calcination

Figure 3(a) shows the TGA results for a Ca_2SiO_4 gel containing 85% resin. The first major weight loss took place just above 250°C and could be correlated with the first low exothermic peak in the DTA curve of the same material, shown in Fig. 3(b). This was thought to be associated with the decomposition of the gel. The other major weight loss occurred at about 450°C and corresponded to a large exothermic DTA peak in Fig. 3(b). This was the stage at which the remainder of the gel decomposed and

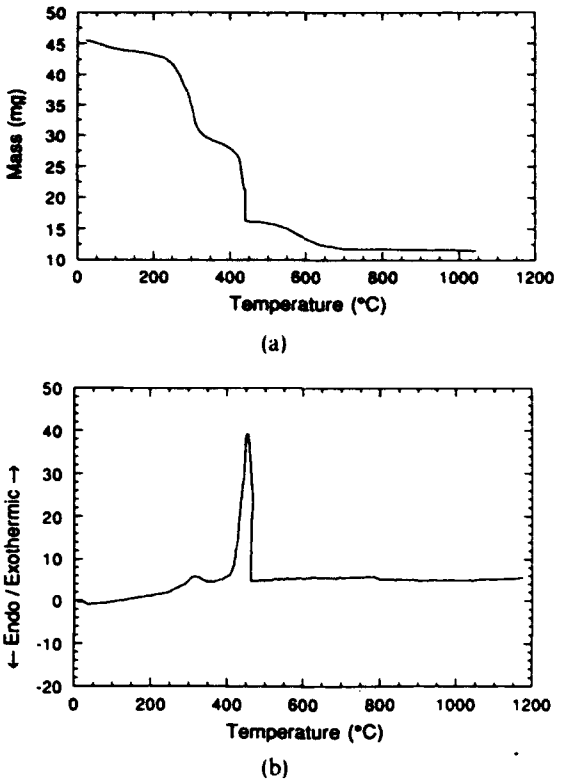

Fig. 3. (a) TGA and (b) DTA of a Ca_2SiO_4 gel containing 85% resin.

pyrolyzed. Further weight loss at higher temperatures was attributed to the removal of carbon formed during the pyrolysis. The thermal decomposition behavior of all the Ca_2SiO_4 and Sr_2SiO_4 gels in this study had the same characteristics as already described.

The phase distributions for the Ca_2SiO_4 gel containing 85% resin at different temperatures during the calcination are shown in Fig. 4(a). Each sample was heated at 5°C/min, held at the requisite temperature for 1 min and cooled. At temperatures below the pyrolysis stage the samples were X-ray amorphous, but after the pyrolysis at temperatures between 500°C and 650°C, the crystalline calcite phase of $CaCO_3$ could clearly be identified. As the temperature was increased, the amount of calcite appeared to diminish and the amount of Ca_2SiO_4 increased. By 700°C the sample was single phase α'_L-Ca_2SiO_4. When the calcination temperatures was increased to 800°C, the presence of β-Ca_2SiO_4 was observed. To further show that $CaCO_3$ was an intermediate compound, a sample of gel was calcined for 1 h at 600°C and then recalcined at 800°C. As can be seen in Fig. 4(b), after calcination at 600°C the only observable crystalline phase was $CaCO_3$, whereas after a second calcination at 800°C the sample was single phase β-Ca_2SiO_4. The exact nature of the reactions by which the $CaCO_3$ was removed and the Ca_2SiO_4 formed was unclear. Similar behavior was observed for the Sr_2SiO_4 gels with $SrCO_3$ being positively identified as an

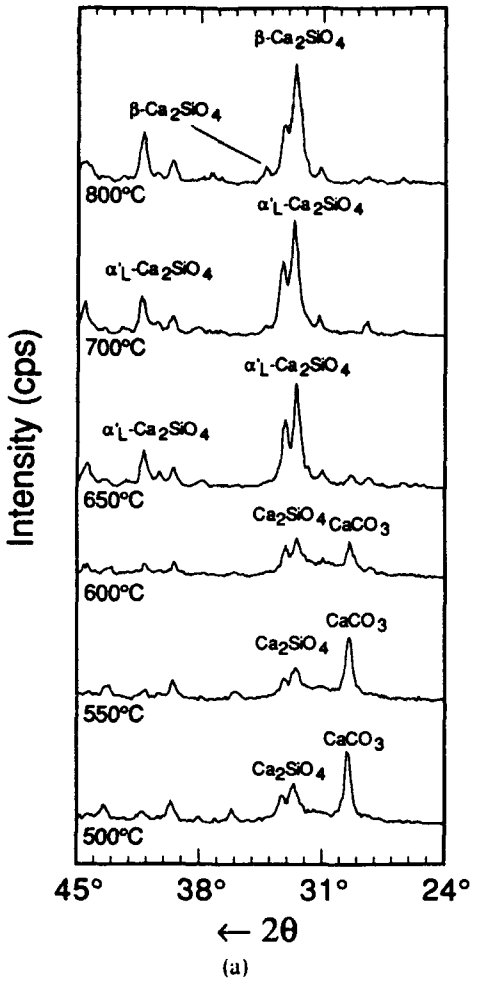

Fig. 4. (a) X-Ray diffraction traces showing the phase distribution in a Ca_2SiO_4 gel containing 85% resin, at different temperatures after the pyrolysis. Each sample was heated to temperature at 5°C/min and held at temperature for 1 min. (b) A comparison of X-ray diffraction traces of a Ca_2SiO_4 gel containing 85% resin, after calcination at 600°C for 1 h, and then after further calcination at 800°C for 1 h.

intermediate phase. Carbonates, specifically $BaCO_3$, have been identified during calcination of chemically derived powders in other studies.[12,13] They were intermediates in the formation of $BaTiO_3$, for example.

The phase distributions of Ca_2SiO_4 prepared with Silica 2 and calcined at high temperature are shown in Fig. 5(a). From 800°C to 1200°C the powders remained single phase β-Ca_2SiO_4, but the sample calcined at 1400°C showed single phase γ-Ca_2SiO_4. This could be attributed to enhanced grain growth at higher temperatures which decreased the stability of the β-phase. A particle size effect for this transformation in powders has been reported previously.[4,14-18]

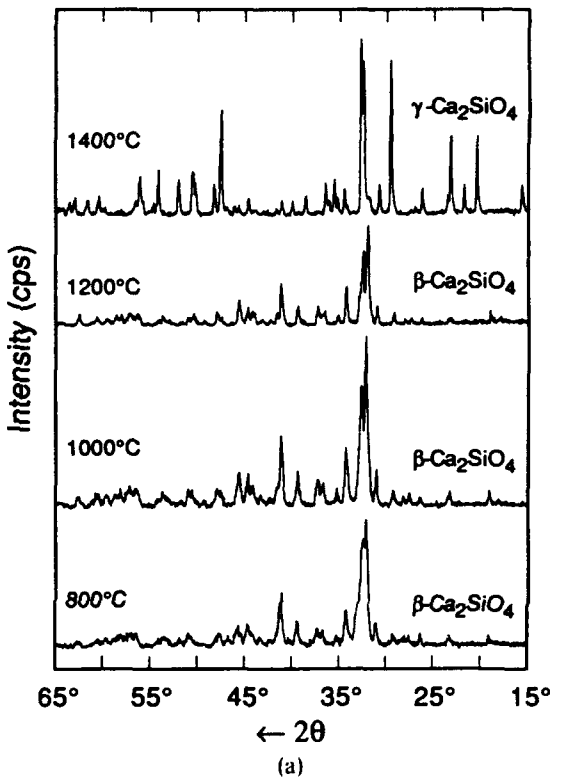

Fig. 5. X-Ray diffraction traces of (a) Ca_2SiO_4 (containing 85% resin) and (b) Sr_2SiO_4 (containing 90% resin) gels calcined for 1 h at temperatures in the range 800°C to 1400°C.

Figure 5(b) shows the development of the phase distribution for Sr_2SiO_4 prepared with Silica 1 and fired in the temperature range 800°C to 1400°C. The resin content was 90%. At 800°C the powder was single phase α' but as the temperature was increased β-phase was detected. The amount of β-phase increased with temperature until after 1400°C the sample was almost entirely β-phase.

The morphology of Sr_2SiO_4 powder calcined at 800°C for 1 h is shown in Fig. 6(a). The agglomerates were highly porous and comprised crystallites approximately 80 nm in size. Calcination at higher temperatures caused the agglomerates to densify and the crystallites to grow. Figure 6(b) shows powder calcined at 1400°C in which the agglomerates were dense and the grains were substantially larger than 1 μm. The SEM and X-ray diffraction results indicate a particle size dependence for the $\alpha' \rightarrow \beta$ transformation in Sr_2SiO_4.

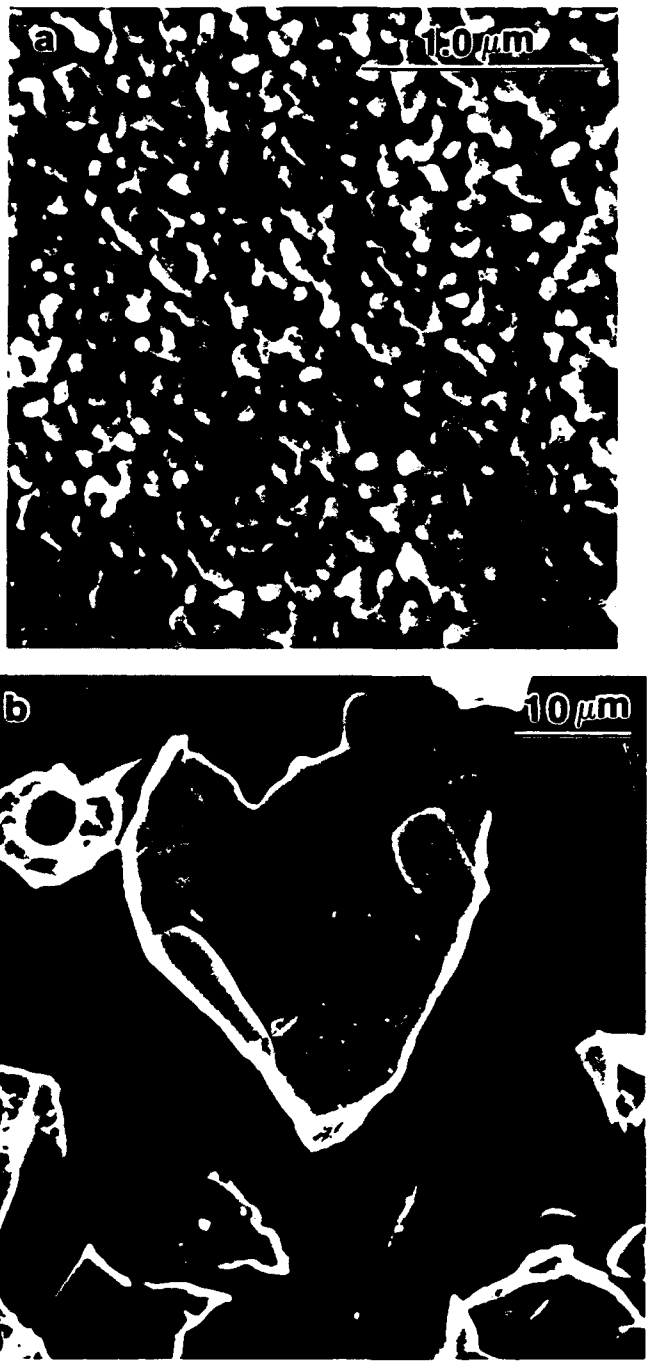

Fig. 6. SEM micrographs of Sr_2SiO_4 powder derived from a gel containing 90% resin calcined at (a) 800 C for 1 h (the individual crystallites have sintered together into highly porous agglomerates), and (b) 1400 C for 1 h (the agglomerates have fully sintered).

3.2 Effect of resin content

It is well known that the resin content can have an effect on the physical characteristics of powders produced by the Pechini process.[19] Hence the effect of resin content on the powders was investigated in this study. Resin contents from 50% to 93% were investigated and found to have no effect on the phase distribution in Ca_2SiO_4 for a specific calcination condition. In contrast, the resin content did affect the phase distributions in the Sr_2SiO_4 powders. Lower resin contents (50% and 70%) produced significant amounts of $SrCO_3$ or SrO along with $SrSiO_3$ after calcination at 800°C and 1000°C. This was attributed to strontium nitrate observed in the dried gels by X-ray analysis.

The presence of $Sr(NO_3)_2$ in the dried gels was attributed to incomplete chelation of the strontium ions during heating of the mixture and consequent precipitation of the nitrate. However, at the high resin contents required to obtain high surface area, this behavior was not observed.

Figure 7 shows DTA traces for Sr_2SiO_4 gels with different resin content. It can be seen that those gels which contained crystalline $Sr(NO_3)_2$ (50% and 70% resin) clearly exhibited a broad endotherm at approximately 650 C, which could be linked to the melting and decomposition of $Sr(NO_3)_2$. Such segregation would be a source of chemical inhomo-

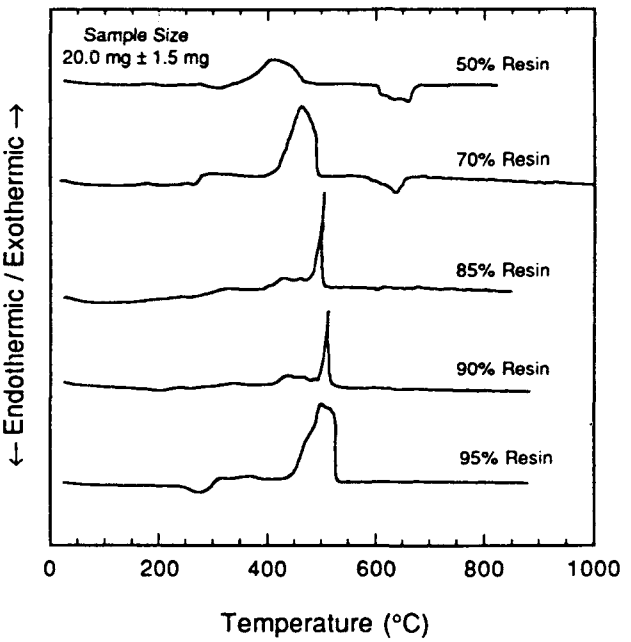

Fig. 7. DTA of Sr_2SiO_4 gels containing different resin contents.

geneity that could lead to the formation of SrO during calcination. It may also have been responsible for the retention of the $SrCO_3$ intermediate at temperatures above 700°C. In order to avoid reprecipitation of $Sr(NO_3)_2$ in the gels during drying, resin contents of 90% or above were used in the preparation of Sr_2SiO_4.

The physical characteristics of the powder were also affected by the resin content of the gel. Figure 8(a) shows the surface area of Ca_2SiO_4 powder as a function of calcination temperature for different resin contents. Above 1000°C, the resin content did not appear to have any significant effects on the surface areas of the powders. However, at lower temperatures the situation was very different. After calcination at 800°C the 85% and 93% resin contents showed the highest surface areas ($\sim 17\,m^2/g$), while the gels made without resin by direct casting of the colloidal silica in the presence of $Ca(NO_3)_2.4H_2O$ had the lowest surface area ($6\,m^2/g$). This increase in surface area with resin content was attributed to the extensive internal porosity seen in the powders made using high resin contents (Fig. 6(a)). When the calcination temperature was increased, sintering and grain growth of the powder agglomerates reduced the internal porosity (Fig. 6(b)) and led to lower specific surface areas.

Figure 8(b) displays the effect of resin content on the surface area of Sr_2SiO_4 powders. As was the case with Ca_2SiO_4, gels with higher resin contents produced powders with higher surface areas. This plot clearly showed that resin contents above 85% must be employed to produce high surface area powders.

The particle size of the powders was also affected by resin content. The results of different resin contents for Sr_2SiO_4 powders calcined at 800°C are shown in Fig. 9(a). The 50% and 70% resin contents gave powders with large median values of 20 μm and 11 μm respectively. Further increases in the resin content shifted the distributions to smaller particle sizes. The median value for 85% resin was about 6 μm and the largest particles in the distribution were approximately 20 μm. This trend to smaller sizes may have been due to the more violent pyrolysis in gels containing higher resin contents, leading to smaller, highly porous agglomerates. The highest resin contents used, including 90% and 95%, gave powders with the lowest median particle sizes. However, the largest particles in the distributions were of a similar size to the largest particles in the powders made from gels with 70% resin. Interestingly, both of the higher resin contents give bimodal distributions and 40% of the powder was submi-

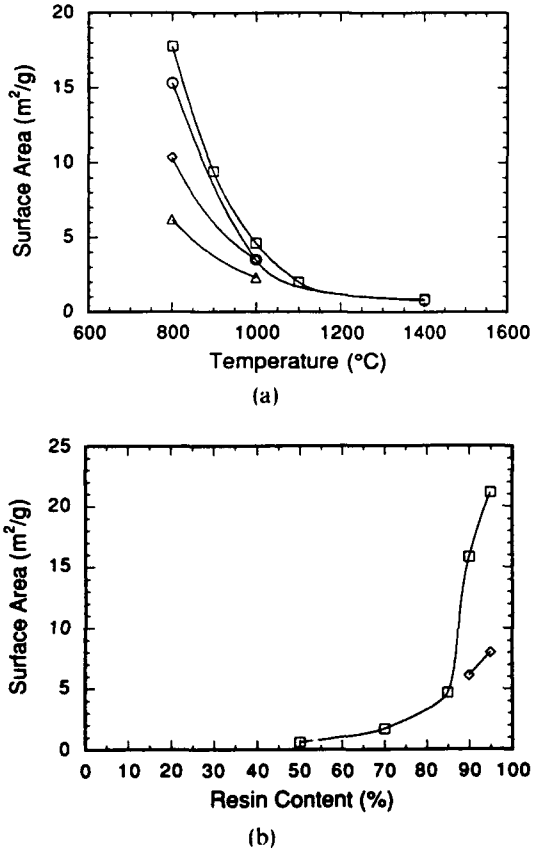

Fig. 8. (a) Surface areas of Ca_2SiO_4 powders containing different resin contents and calcined in the temperature range 800 C to 1400 C. (△) 0%, (◇) 50%, (□) 85%, and (○) 93% resin. (b) Effect of resin content on the surface area of Sr_2SiO_4 powders calcined at (□) 800 C and (◇) 1000 C for one hour.

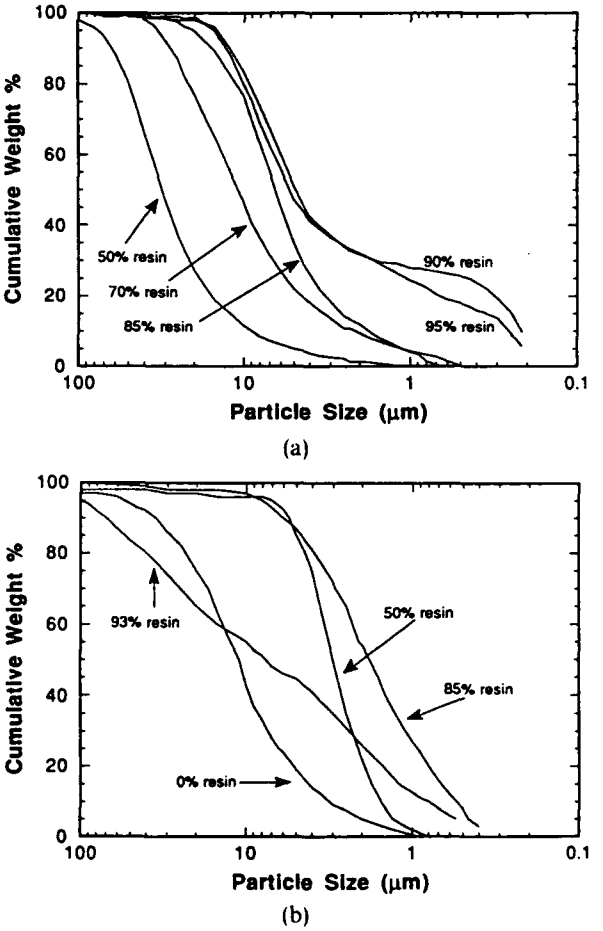

Fig. 9. Effect of resin content on particle size distribution of (a) Sr_2SiO_4 and (b) Ca_2SiO_4 powders calcined at 800 C for one hour.

cron. This biomodal characteristic was reproducible although difficult to explain.

Figure 9(b) shows the effect of resin content on the particle size of the Ca_2SiO_4 powders. The trend with resin content was not as systematic as in the Sr_2SiO_4 powders. With no resin, the distribution was wide. The 50% resin sample had a narrow distribution, between 10 μm and 1 μm with a median of approximately 2 μm. This was in contrast to the trend in Fig. 9(a), but may be explained by the fact that during calcination, the Ca_2SiO_4 gel with this resin content exploded at about 200°C. This was thought to be a consequence of the sudden and violent release of moisture, leading to smaller particles. When the resin content was increased to 85%, the particle size distribution shifted to smaller particle sizes. For this powder, the large particles were about 6 μm in size but there was also approximately 30% of submicron powder. Further increase in the resin content to 93% gave a very wide particle size distribution from submicron to 100 μm. This contrasted with the results for Sr_2SiO_4 using similar resin contents. In this case interagglomerate sintering was thought to have taken place during pyrolysis and calcination.

3.3 Effect of sodium on the phase distribution in dicalcium silicate powders

The phase distributions in Ca_2SiO_4 powders prepared with Silica 1 and Silica 2 were markedly different after calcination for 1 h at 1400°C. This was attributed to the difference in sodium content, since sodium is known to be a stabilizer for β-Ca_2SiO_4.[20] Calculation showed that Silica 2 would give Ca_2SiO_4 with 0·14 wt% Na_2O and Silica 1 would give Ca_2SiO_4 with 0·67 wt% Na_2O. Sodium was added in preparations of Ca_2SiO_4 with Silica 2 in the form of $NaNO_3$ dissolved with the $Ca(NO_3)_2.4H_2O$. In this way, powders containing up to 1 wt% Na_2O were prepared, and calcined at temperatures ranging from 800°C to 1500°C. The results of the phase analysis are shown in Table 1. All the powders exhibited β-phase after calcination at temperatures below 1400°C. However, after calcination at 1400°C, samples containing less than 0·5 wt% Na_2O transformed to γ-phase on cooling, while the other compositions remained β-phase.

Table 1. Phase distributions of Ca_2SiO_4 powders with different sodium contents, calcined for 1 h at various temperatures

Na_2O (wt%)	*800°C*	*1000°C*	*1200°C*	*1400°C*
0·14 (Silica 2)	β	β	β	γ
0·27	β	β	β	γ
0·41	—	—	β	γ
0·54	—	—	β	β
0·67 (Silica 1)	β	β	β	β
1·0	—	β	β	β

Consequently, there was evidence to suggest that the difference in phase distribution for samples prepared with Silica 1 and Silica 2 was due to the sodium content of these colloidal silica precursors.

4 Summary

A quick and relatively simple method for the preparation of both Ca_2SiO_4 and Sr_2SiO_4 powders of high surface area has been developed. The method avoided the use of unstable alkoxides and precipitation techniques. The powders so produced were very porous and friable and could easily be milled into submicron particle sizes.

The development of single phase powders at 700°C or above appeared to involve the formation of $CaCO_3$ or $SrCO_3$ as intermediate compounds. The desired silicate then developed by a low-temperature solid-state reaction between 500°C and 700°C. When the temperature was increased in this range, the silicate developed and the carbonates disappeared. The exact nature of the reaction was unknown.

Single phase powders of α'_L-, β- and γ-Ca_2SiO_4 could easily be produced by this route. The method has also been used to prepare single phase α'-powders of Sr_2SiO_4 for the first time.

The physical characteristics of the powders could be controlled by the resin content of the gel and the calcination conditions. In the case of Sr_2SiO_4, the resin content was also used to control chemical inhomogeneity caused by the reprecipitation of $Sr(NO_3)_2$ during drying of the gel. The effect of resin content on surface area was generally the same for both systems, but there were marked differences in how the resin content affected the particle size distributions.

Finally, the difference in the phase distributions observed in the Ca_2SiO_4 powders prepared with Silica 1 and Silica 2 was attributed to the difference in the sodium content of these colloidal silicas.

Acknowledgements

The authors wish to thank Mr Kyle E. Eckmann for help in preparing some of the dicalcium silicate and some of the X-ray analyses. This project was funded by the US Air Force Office of Scientific Research under grants AFOSR-89-0300 and URI AFOSR-90-0174. James L. Shull, Jr was supported by a US National Science Foundation Graduate Fellowship. The authors would also like to thank the Du Pont Chemical Company for supplying the colloidal silica used in this study. Use of the electron microscope facilities at the Center for Electron Microscopy at

UIUC is gratefully acknowledged. The plasma emission spectroscopy was performed by the staff of the Microanalytical Laboratory in the School of Chemical Sciences at UIUC.

References

1. Schwiete, H. E., Kronert, W. & Deckert, K., Existence range and stabilization of high temperature modification of dicalcium silicate. *Zement Kalk Gips*, **9** (1968) 359–66.
2. Midgley, H., The polymorphism of calcium orthosilicate. In *6th International Congress on the Chemistry of Cements*, Moscow, Suppl. Paper 1, 1974, pp. 1–16.
3. Pritts, I. M. & Daugherty, K. E., The effect of stabilizing agents on the hydration rate of β-C_2S. *Cement Concrete Res.*, **6** (1976) 783–96.
4. Chan, C. J., Kriven, W. M. & Young, J. F., Physical stabilization of the β to γ transformation in dicalcium silicate. *J. Am. Ceram. Soc.*, **75** (1992) 1621–27.
5. Roy, D. M. & Oyfesobi, S. O., Preparation of very reactive Ca_2SiO_4 powder. *J. Am. Ceram. Soc. Discussion and Notes*, **60** (1977) 178–80.
6. Luth, W. C. & Ingamells, C. O., Gel preparation of starting materials for hydrothermal experimentation. *Am. Mineral.*, **50** (1965) 255–8.
7. Kralj, D., Matkovic, B., Trojko, R., Young, J. F. & Chan, C. J., Preparation of dicalcium silicate at 950°C. *J. Am. Ceram. Soc.*, **69** (1986) C170–C172.
8. Kriven, W. M., Possible alternative transformation toughening to zirconia: Crystallographic aspects. *J. Am. Ceram. Soc.*, **71** (1988) 1021–30.
9. Catti, M., Gazzoni, G., Ivaldi, G. & Zanini, G., The $\beta \leftrightarrow \alpha'$ phase transition of Sr_2SiO_4. I: Order–disorder in the structure of the α' form at 383 K. *Acta Cryst.*, **B39** (1983) 674–9.
10. Catti, M. & Gazzoni, G., The $\beta \leftrightarrow \alpha'$ phase transition of Sr_2SiO_4. II: X-Ray and optical study, and ferroelasticity of the β form. *Acta Cryst.*, **B39** (1983) 679–84.
11. Hou, T. I. & Kriven, W. M., Mechanical properties and microstructures of $CaZrO_3$–Ca_2SiO_4 composites. *J. Am. Ceram. Soc.*, in press.
12. Chaput, I. F. & Boilet, J. P., Chemically derived barium titanate gels and ceramics. In *High Tech Ceramics, Materials Monograph*, Vol. 36(B), ed. P. Vincenzini. Elsevier, 1987, pp. 1459–68.
13. Phule, P. P. & Risbud, S. H., Sol–gel synthesis and characterization of $BaTi_4O_9$ and $BaTiO_3$ powders. In *Materials Research Society Symposium Proceedings*, Vol. 121, *Better Ceramics through Chemistry III*, ed. C. J. Brinker, D. E. Clark & D. R. Ulrich. Materials Research Society, Pittsburgh, USA, 1988, pp. 275–80.
14. Chromy, S., The inversion of the $\beta \rightarrow \gamma$ modification of dicalcium silicate. *Zement Kalk Gips*, **23** (1970) 382–9 (in German).
15. Gawlicki, M. & Nocon-Wczelik, W., Influence of thermal treatment on the transition of $\beta \rightarrow C_2S$. In *Proceedings of the 7th International Symposium on Chemistry of Cements*, Vol. II, Paris, 1980, pp. 161–5 (in French).
16. Shibata, S., Kishi, K., Asaga, K. & Daimon, M., Effect of thermal history on $\beta \rightarrow \gamma$ transformation of pure Ca_2SiO_4. *Yogyo-Kyokai-Shi.*, **91** (1983) 497–502 (in Japanese).
17. Gawlicki, M., The role of thermal treatment on dicalcium silicate polymorphic transitions. In *Proceedings of the 14th Conference on Silicate Industry and Silicate Science III*. Budapest, Hungary, 1985, pp. 67–73.
18. Kriven, W. M., Chan, C. J. & Barinek, E. A., The particle size effect of dicalcium silicate in a calcium zirconate matrix. In *Advances in Ceramics*, Vol. 24, *Science and Technology of Zirconia III*, ed. S. Somiya, N. Yamamoto & H. Yanagida. American Ceramic Society, Westerville, OH, 1988, pp. 145–55.
19. Lessing, P. A., Mixed-cation oxide powders via polymeric precursors. *Am. Ceram. Bull.*, **68** (1989) 1002–7.
20. Ghosh, S., Rao, P., Paul, A. K. & Raina, K., Review: The chemistry of dicalcium silicate mineral. *J. Mat. Sci.*, **14** (1979) 1554–66.

Proceedings of

The International Conference on

Martensitic Transformations

(ICOMAT-92)

20-24 July 1992
Monterey, California

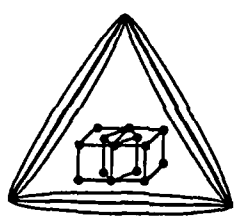

ICOMAT-92

Edited by C.M. Wayman and J. Perkins

Proceedings of the International Conference on Martensitic Transformations (1992)
Monterey Institute for Advanced Studies © 1993
Monterey, California, USA

TRANSFORMATION MECHANISMS IN DICALCIUM AND DISTRONTIUM ORTHOSILICATES

Y.J. Kim, J.L. Shull, B.N. Sun and Waltraud M. Kriven

University of Illinois
Department of Materials Science and Engineering
105 South Goodwin Avenue
Urbana, Illinois 61801 USA

ABSTRACT

The crystallography, microstructures and phase transformation mechanisms in dicalcium silicate (Ca_2SiO_4) and other orthosilicates have been studied. Both the α to α'_H and α'_L to β transformations in Ca_2SiO_4 are considered to be ferroelastic and spontaneous strains were calculated. Grinding-induced phase transformations occurred in $\alpha' \rightarrow \beta$ and $\beta \rightarrow \gamma$. Microstructures shown in the transformed β grains in Ca_2SiO_4 and Sr_2SiO_4 suggested that the $\alpha' \rightarrow \beta$ transformation is possibly martensitic. A single crystal study of β-Sr_2SiO_4 indicated a hysteresis in transformation temperatures of about 10°C (75°C for $\beta \rightarrow \alpha'$ and 65°C for $\alpha' \rightarrow \beta$). Hot-stage optical microscopy of Sr_2SiO_4 showed the rapid appearance or disappearance of β-twins upon transformation. In terms of the crystal structures, the major driving force for the β to γ transformation in Ca_2SiO_4 is proposed to be strains due to previous ferroelastic transformations and cation charge repulsions in the β structure. This mechanism can be displacive, but needs to overcome a comparatively high energy barrier due to the breaking of some oxygen bonds.

1. INTRODUCTION

Dicalcium silicate (Ca_2SiO_4) is a major component of portland cement. As an orthosilicate of the general formula of M_2SiO_4 (where M is a divalent cation), Ca_2SiO_4 has an unusually large number of polymorphs, *viz.*, α, α'_H, α'_L, β and γ. As the cation size in the M site increases, high temperature phases tend to be more stable. That is, α' and β in Sr_2SiO_4 and α' in Ba_2SiO_4 have been reported as stable phases. In contrast, the low-temperature orthorhombic γ phase is the only stable phase in the mineral olivine (Mg_2SiO_4) which has smaller cations in the M site. The schematic diagram in figure 1 compares the stable polymorphs in these four orthosilicates.

The crystal structures of Ca_2SiO_4-polymorphs have not yet been firmly determined except for the β and γ phases. The suggested transformation mechanisms among the polymorphs in Ca_2SiO_4 are generally: (i) a semi-reconstructive mechanism between α and α'_H [1]; (ii) an disorder-order transformation mechanism between α'_H and α'_L [1]; (iii) a displacive, possibly martensitic

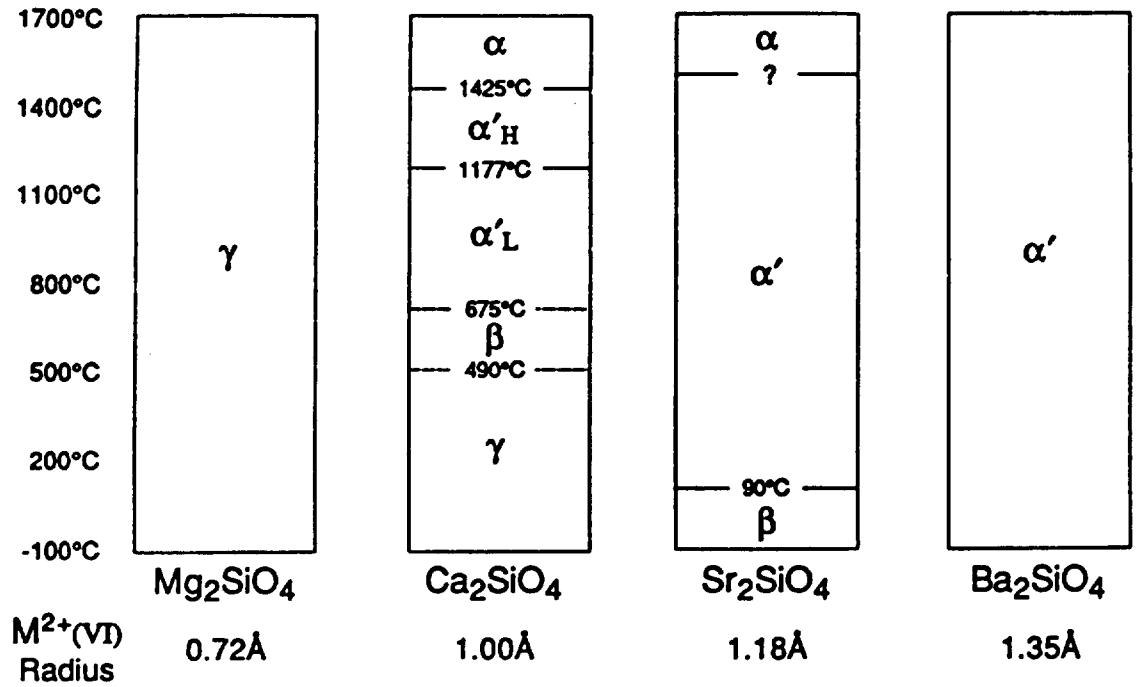

Figure 1. A schematic diagram comparing stable polymorphs and their transformation temperatures in different orthosilicates (M_2SiO_4).

mechanism between α'_L and β [1,2]; and (iv) a reconstructive [1], semi-reconstructive [3] or displacive [4] mechanism for β to γ.

The objective of this study was to understand the mechanisms of polymorphic phase transformations in these orthosilicates through structural and microstructural characterization of various ceramic samples primarily by TEM and optical microscopy. Two special intentions were to study (i) the mechanism of the β to γ transformation in Ca_2SiO_4, which is an unusual, low- to high-symmetry transformation accompanied by a large volume increase (~12%) on cooling; and (ii) the martensitic nature of the α' to β phase transformations in Ca_2SiO_4 and Sr_2SiO_4.

Ceramic samples studied were: (i) pure Ca_2SiO_4, sintered between 800 and 1500°C for 1 minute to 72 hours [5]; (ii) Ca_2SiO_4, doped with 1 to 5 mol% Ba_2SiO_4 and sintered between 800 and 1400°C for 1 to 3 hours [6]; and (iii) composites of Ca_2SiO_4 (15 vol%) in an MgO matrix, sintered at 1600°C for 3 hours and composites of Ca_2SiO_4 (10 vol%) in a $CaZrO_3$ matrix, sintered at 1600°C for 2 hours; (iv) pure Sr_2SiO_4, sintered betwen 900 and 1400°C for 1 to 5 hours; and (v) pure Ba_2SiO_4, sintered at 1400°C for 1 hour. All powders and pellets were examined by XRD, SEM and TEM to study crystal structures, microstructures and microchemistry. In addition, hot-stage optical microscopy of single crystals of β-Sr_2SiO_4 was conducted to study the $\alpha' \leftrightarrow \beta$ phase transformation.

2. PHASE TRANSFORMATIONS IN DICALCIUM SILICATE

A TEM study of the interfaces between Ca_2SiO_4-polymorphs resulted in the following possible lattice correspondences: [7]

$$\mathbf{a}_{\alpha'L} // \mathbf{a}^*_\beta,\ \mathbf{b}_{\alpha'L} // -\mathbf{c}_\beta \text{ and } \mathbf{c}_{\alpha'L} // \mathbf{b}_\beta,$$

$$\mathbf{a}^*_\beta // \mathbf{a}_\gamma,\ \mathbf{b}_\beta // -\mathbf{c}_\gamma \text{ and } \mathbf{c}_\beta // \mathbf{b}_\gamma$$

which agreed with previous single crystal X-ray precession work [8]. Almost all β grains were twinned and strained. Microcracks tended to develop along grain boundaries as the grain size increased. In pure Ca_2SiO_4 β grains were internally strained, and sometimes showed streaking in the SADP's. In composites, twinned β grains were usually elongated and internally more strained, giving rise to two directional streaking in the $[010]_\beta$ SADP, both parallel and perpendicular to $\{200\}_\beta^*$. Some transformed γ grains coexisted with β grains, producing large intergranular microcracks. γ grains were strain free, but detwinning-related planar defects were usually present. The $\{100\}_\beta$ twinning occurred more favorably than did $\{001\}_\beta$ twinning. Two types of symmetry-related domain structures were observed in β grains: (i) two twin-related domains for samples which had experienced the α'_L to β transformation; and (ii) three 120° rotation-related domains for samples which had experienced the α to α'_H transformation. XRD studies indicated that grinding-induced phase transformations occurred in both $\alpha'_L \rightarrow \beta$ and $\beta \rightarrow \gamma$.

Based on symmetry considerations deduced from microstructures of β-Ca_2SiO_4, the α (hexagonal, *6/mmm*) to α'_H (orthorhombic, *mmm*) transformation appeared to be ferroelastic. The spontaneous strain (ε_S) generated by this transformation was estimated to be 0.046. If the $\alpha'_H \rightarrow \alpha'_L$ were an disorder-order transformation without change of symmetry, the α'_L (orthorhombic, *mmm*) to β (monoclinic, *2/m*) transformation would also be ferroelastic and its spontaneous strain was estimated to be 0.044. Therefore, the β-Ca_2SiO_4 structure resulting from this sequence of ferroelastic transformations should inherently be strained.

From structural refinement data of Ca_2SiO_4, the cation-anion bond lengths and the nearest cation-cation bond distances were calculated. While the changes of Si-O bond lengths throughout the transformations are minor, the changes of Ca-O bond lengths are significant, indicating the rapid collapse of the CaO_x "cage" on cooling. Comparison of the nearest bond distances between cations show that the β structure has the closest bond distances for Si-Ca. Referring to ambient pressure data for nonbonded radii of Si and Ca [9], the ideal Si-Ca distance would be ~3.23 Å. This means that the nearest Si-Ca bond distance in β (~2.97 Å) is too close to maintain the stability of the structure at ambient pressure. As a consequence, strong repulsive forces are expected to develop in the β structure. This may be a reason why the β structure is unstable at ambient pressure. However, this structure was reported to be more stable than both the γ structure and the α'_L structure at very high pressures [10]. Conventional projections of the Ca_2SiO_4 polymorphs showed that all of the α, α' and β structures have close association of Si atoms in SiO_4 tetrahedra with adjacent Ca atoms. However, in the γ structure, they are no longer closely associated due to large displacements of both the SiO_4 and Ca by the β to γ transformation. The displacements are not a simple shuffling movement of atoms, but involve a considerable amount of SiO_4 rotation.

In terms of the crystal structure, the major driving forces for the β to γ transformation, therefore, are considered to be the release of strains inherited from previous high temperature transformations and Si-Ca charge repulsions in the β structure. The higher symmetry and larger volume of the transformed γ phase are probably related to the process of straightening of the β lattice to release strains and maximization of the volume to reduce repulsions. The β to γ transformation can be displacive in the sense of its instantaneous reaction, but needs to overcome a comparatively high energy barrier due to the breaking of some oxygen bonds in the β structure.

3. MODULATED STRUCTURES IN ORTHOSILICATES

From TEM studies of the Ca_2SiO_4 system, three types of superlattice structures were observed: (i) the x2$\underline{a}$,2$\underline{b}$-type in pure α'_L (space group, *Pmcn*; $\underline{a}<\underline{c}<\underline{b}$) (ii) the x3$\underline{c}$-type in α'_L doped with Ba_2SiO_4 and (iii) the x3$\underline{a}$-type in all β (space group, *P2₁/n*; $\underline{a}<\underline{b}<\underline{c}$). On the other hand, pure Sr_2SiO_4 showed incommensurate modulations in both α' and β phases: (i) $\mathbf{q} \approx 0.30\,\underline{c}^*_{\alpha'}$ and (ii) $\mathbf{q} \approx 0.30\,\underline{b}^*_\beta$. No significant changes of these modulation vectors were noticed in both Ca_2SiO_4 and

Sr_2SiO_4 samples sintered under different conditions. No modulation was observed in pure α'-Ba_2SiO_4.

Similar modulated structures were frequently reported from other orthorhombic A_2BO_4 compounds (β-K_2SO_4 type) which are believed to be isostructural with α'_L-Ca_2SiO_4 and α'-Sr_2SiO_4 [11]. Five different modulated phases were also reported in the Ba_2SiO_4-Ca_2SiO_4 system [12]. Modulated monoclinic phases were not common but a three-fold modulation was observed in monoclinic $[N(CH_3)_4]_2ZnCl_4$ [13]. These varieties of modulated phases in A_2BO_4 suggest the inherent instability of the orthorhombic structure which is an inhomogeneous mixture of relatively large, but loosely-bonded AO_x polyhedra and small, but rigid, BO_4 tetrahedra. These BO_4 tetrahedra are not linked to one another and can easily be moved and rotated. Actually, the origin of many modulated structures in A_2BO_4 compounds can be attributed to the three-fold rotation of BO_4 tetrahedra.

It is interesting to note the changes of modulated structures in α'-M_2SiO_4 as the size of M cations changes (Ba^{2+}: R ≈ 1.35Å, Sr^{2+}: R ≈ 1.18Å, Ca^{2+}: R ≈ 1.00Å): that is, no modulation in Ba_2SiO_4, incommensurate modulation in Sr_2SiO_4 and commensurate modulation in Ca_2SiO_4 (figure 2). This trend suggests that the modulated structures in α'-M_2SiO_4 are directly related to the stability of the MO_x polyhedra. Smaller cations in MO_x apparently destabilize the α' structure and produce modulations. As discussed before, the modulated structures observed in both α'_L and β in Ca_2SiO_4 may be related to some effective ways by which CaO_x and adjacent SiO_4 arrangements relieve electrostatic repulsions between Ca and Si atoms.

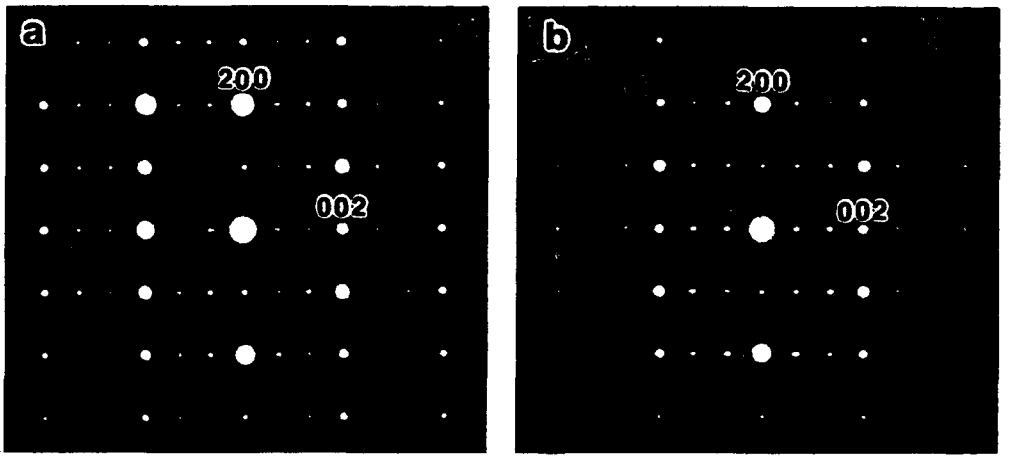

Figure 2. The [010] SADP's of orthorhombic (α') orthosilicates showing modulations along ζ^*: (a) pure Sr_2SiO_4 and (b) Ca_2SiO_4 doped with 5 mol% Ba_2SiO_4.

4. MARTENSITIC NATURE OF THE α'→β TRANSFORMATION

Microstructures shown in the transformed β grains in Ca_2SiO_4 and Sr_2SiO_4 suggest that the α'→β transformation is probably martensitic as well as ferroelastic. The development of β-laths which resembled β-twins were often observed in Sr_2SiO_4 (figure 3). These laths were possibly formed by a stress-induced martensitic transformation during TEM specimen preparation. Grinding-induced α'→β phase transformation was evident in both Ca_2SiO_4 and Sr_2SiO_4. Because of the similarity of the lattice dimensions as well as the low transformation temperature, the β→α'

transformation in Sr_2SiO_4 could be induced by electron beam heating of the twinned β phase. The lattice correspondence between α' and β was identical to that in Ca_2SiO_4.

For a more direct study, single crystals of β-Sr_2SiO_4 were grown using a flux melting technique [14]. DSC measurements of transformation temperatures indicated a hysteresis of ~10°C (75°C for β→α' and 65°C for α'→β). Hot-stage optical microscopy displayed changes in interference colors and the rapid appearance or disappearance of β-twins upon transformation (figure 4). Some crystals transformed in a series of sudden bursts with a propagating interface while others transformed in a single event. A few crystals fractured on, or shortly after undergoing the reverse α'→β transformation.

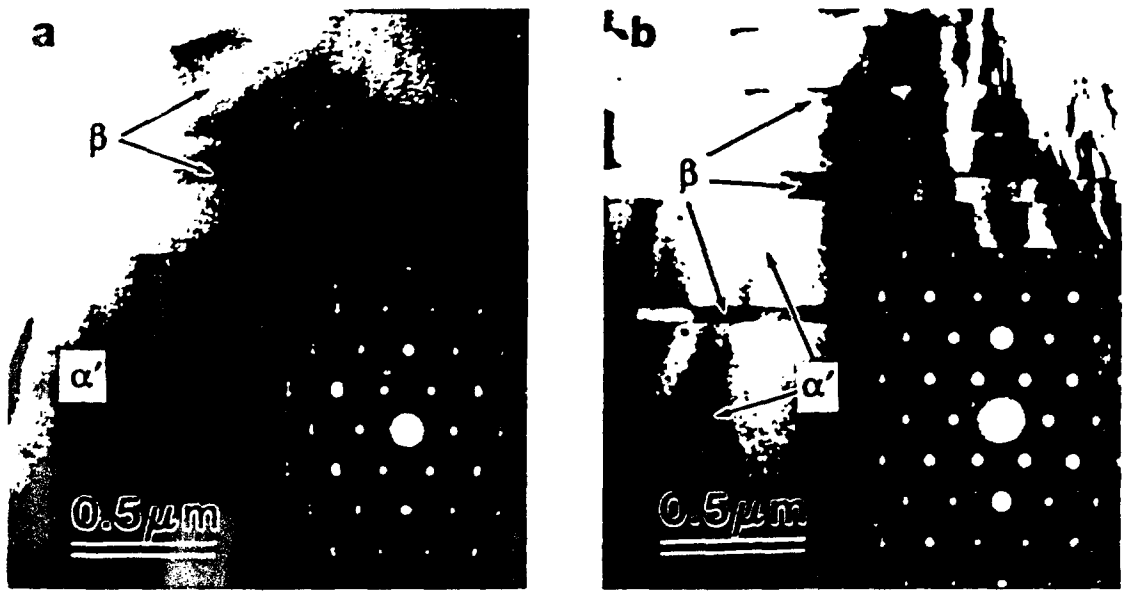

Figure 3. TEM micrographs displaying the resemblance of β-twins (a) with β-laths (b), both developed in the α' phase of Sr_2SiO_4. The $[001]_{\alpha'}$+$[010]_{\beta}$ SADP's are shown in the insets.

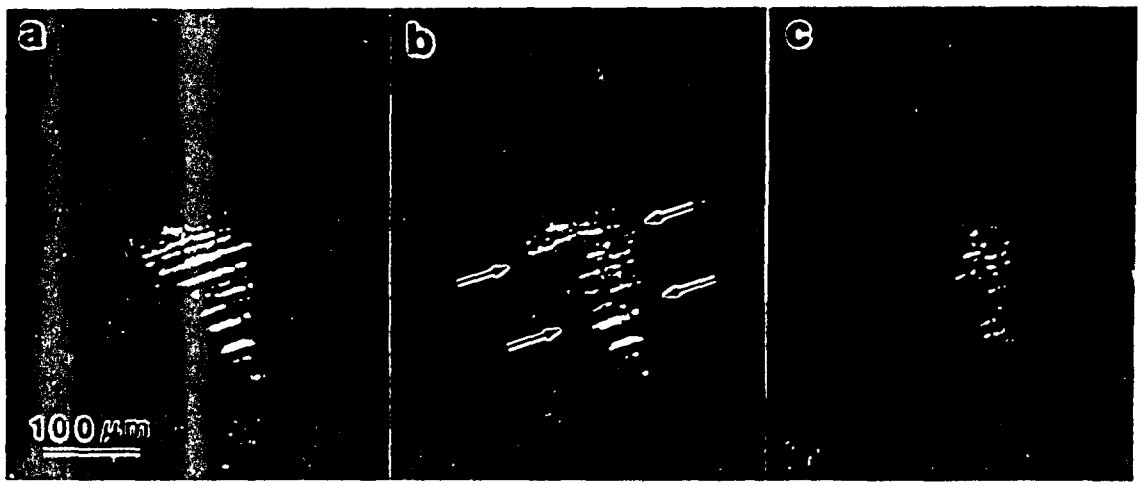

Figure 4. Transmitted light micrographs under crossed polars of the β→α' transformation at 73.6°C on heating in Sr_2SiO_4. The twinned β-crystal (a) transformed in a series of bursts via an interface (arrowed in b) to untwinned α' phase (c).

The $\alpha'_L \rightarrow \beta$ transformation in Ca_2SiO_4 was reported to occur instantaneously, but with a hysteresis of 25°C [15]. From an *in situ* hot-stage TEM study, Groves [16] observed the twinning-detwinning process by cooling and heating of Ca_2SiO_4 and suggested a martensitic mechanism for the $\alpha'_L \rightarrow \beta$ transformation. The great rapidity of the twin formation on cooling may indicate that this martensitic transformation did not require an additional lattice invariant shear strain to produce an invariant plain strain [16]. Martensitic calculation of the $\alpha'_L \rightarrow \beta$ transformation in Ca_2SiO_4 also showed that a small lattice invariant shear would be necessary and the choice of lattice invariant shear system had little effect on the results [17].

5. CONCLUSION

Both the α to α'_H and α'_L to β transformations in Ca_2SiO_4 are considered to be ferroelastic. The spontaneous strain (e_s) generated by these transformations was estimated to be ~0.046 for $\alpha \rightarrow \alpha'_H$ and ~0.044 for $\alpha'_L \rightarrow \beta$. The $\alpha' \rightarrow \beta$ transformations in Ca_2SiO_4 and Sr_2SiO_4 are also possibly martensitic. The hysteresis in transformation temperatures in Sr_2SiO_4 was about 10°C (75°C for $\beta \rightarrow \alpha'$ and 65°C for $\alpha' \rightarrow \beta$). The rapid appeareance or disappearance of β-twins upon transformation was observed in Sr_2SiO_4. In terms of the crystal structures, the major driving force for the β to γ transformation in Ca_2SiO_4 is proposed to be strains accumulated during previous higher temperature ferroelastic transformations and cation charge repulsions in the β structure. This mechanism can be displacive, but needs to overcome a comparatively high energy barrier due to the breaking of some oxygen bonds. The modulated structures observed in both α' and β in Ca_2SiO_4 and Sr_2SiO_4 appeared to be directly related to the instability of the CaO_x and SrO_x polyhedra and their interaction with adjacent SiO_4 tetrahedra.

ACKNOWLEDGEMENTS

This work was supported by the Air Force Office of Scientific Research through a URI Grant AFOSR-90-0174. J. L. Shull was supported under a National Science Foundation Graduate Fellowship.

REFERENCES

1. Eysel, W. and Hahn, T.: Z. Krist., 1970, 131, 322.
2. Groves, G. W.: J. Mat. Sci., 1981, 16, 1063.
3. Smith, D. K., Majumdar, A. and Ordway, F.: Acta Cryst., 1965, 18, 787.
4. Barbier, J. and Hyde, B. G.: Acta Cryst., 1985, B41, 383.
5. Nettleship, I., Slavick, K., Kim, Y. J. and Kriven, W. M.: J. Am. Ceram. Soc., 1992, 75[9], in press.
6. Nettleship, I., Slavick, K., Kim, Y. J. and Kriven, W. M.: J. Am. Ceram. Soc., submitted.
7. Kim, Y. J., Nettleship, I. and Kriven, W. M.: J. Am. Ceram. Soc., 1992, 75[9], in press.
8. Udagawa, S., Urabe, K., Yano, T. and Natsume, M.: J. Ceram. Assoc. Japan, 1980, 88, 285.
9. O'Keeffe, M. and Hyde, B. G.: Structure and Bonding in Crystals, (M. O'Keeffe and A. Navrotsky, eds.) Vol. 1, (Academic Press), 1981, p. 227.
10. Hanic, F., Kamarad, J., Stracelsky, J. and Kapralik, I.: Br. Ceram. Trans. J., 1987, 86, 194.
11. Tunistra, F. and van der Berg, A. J.: Phase Transitions, 1983, 3, 275.
12. Withers, R. L., Thompson, J. G. and Hyde, B. G.: Cryst. Rev., 1989, 2, 27.
13. Zuniga, F. J., Madariaga, G. and Perez-Mato, J. M.: Acta Cryst., 1989, B45, 462.
14. Catti, M., Gazzoni, G. and Ivaldi, G.: Acta Cryst., 1983, C39, 29.
15. Singh, N. B. and Rastogi, P.: Tonindustrie Zeitung, 1980, 104, 645.
16. Groves, G. W.: J. Mat. Sci., 1983, 18, 1625.
17. Kelly, P. M.: Martensitic Transformations, (B. C. Muddle, ed.) Pt. I, (Trans Tech Publications), 1990, 335.

"TEM Characterization of the α'and β Phases in Polycrystalline Distrontium Silicate (Sr_2SiO_4)," Y. J. Kim, J. L. Shull and W. M. Kriven. Proc. 50th Annual Meeting of the Electron Microscopy Society of America (EMSA). Edited by G. W. Bailey, J. Bentley and J. A. Small, pp 354-355 (1992).

TEM CHARACTERIZATION OF THE α' AND β PHASES IN POLYCRYSTALLINE DISTRONTIUM SILICATE (Sr_2SiO_4)

Y. J. Kim, J. L. Shull and W. M. Kriven

Department of Materials Science and Engineering, University of Illinois at Urbana-Champaign, Urbana, IL 61801

Two polymorphs, α' and β, are known to be major phases in pure distrontium silicate (Sr_2SiO_4) at atmospheric pressure.[1] Fully dense pellets were fabricated by sintering chemically prepared powders in the temperature range of 900° to 1400°C for 1 to 5 hours. Their phases and microstructures were studied by TEM. At lower sintering temperatures such as 900°C, the major phase was orthorhombic α' (space group, *Pmnb*). The euhedral α' grains had a size of about 1 μm diameter (Fig. 1a). As the sintering temperature increased, the amount of monoclinic β phase (space group, $P2_1/n$) tended to increase. These β grains were usually irregular and twinned on {100}β or {001}β planes. Concentration of the electron beam on the grains gave rise to a disappearence of twins (Fig. 1b).

SADP's from the α' grains showed an incommensurate modulation along the $\underline{b}^*$ direction. In the $[001]_{\alpha'}$ orientation, the modulation was almost commensurate, with satellite reflections located at ~1/3 of the principal reflections (Fig. 2a). When the specimen was tilted to the $[102]_{\alpha'}$ orientation, the number of satellite reflections increased (Fig. 2b). This modulation could be interpreted in several different ways, one of which suggested that the satellite reflections around {0*k*0} were extinct, when *k* is even, in the $[001]_{\alpha'}$ orientation. In this case the modulation vector, **q**, would be about 0.3 $\underline{b}^*$. A previous study reported $\mathbf{q} = 0.303 \pm 0.005\ \underline{b}^*$.[2] SADP's from the twinned β grains also showed a similar incommensurate modulation along the $\underline{b}^*$ direction. Fig. 3a shows the [100]β SADP, which is almost identical to the $[001]_{\alpha'}$ SADP except for the appearance of {010}β principal reflections in the former. The [110]β SADP of the same area (Fig. 3b) did not display any modulations, but {001}β twinned reflections were observed (arrowed). Because of complications and variations of the modulated structures of both the α' and β phases in samples processed under different conditions, further study is needed, particularly in conjunction with the transformation mechanism between the α' and β phases.

References

1. M. Catti *et al.*, Acta Cryst. (1983) B39, 674.
2. R. L. Wither *et al.*, J. Physics (1987) C20, 1653.
3. This research was supported by Air Force Office of Scientific Research through a URI Grant AFOSR-90-0174.

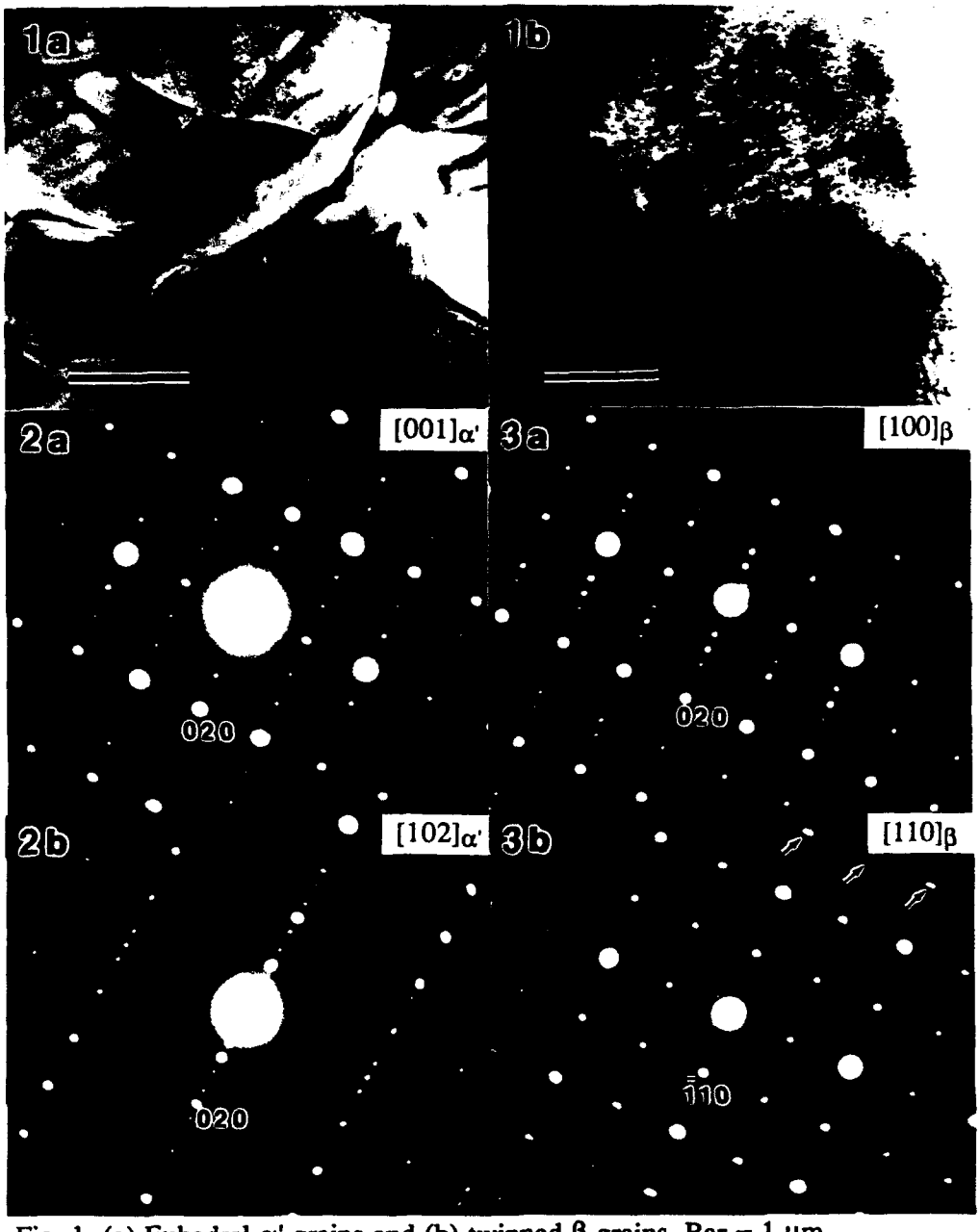

Fig. 1. (a) Euhedral α' grains and (b) twinned β grains. Bar = 1 μm.
Fig. 2. SADP's from an α' grain showing an incommensurate modulation: (a) $[001]_{\alpha'}$ and (b) $[102]_{\alpha'}$
Fig. 3. SADP's from a twinned β grain: (a) $[100]_{\beta}$ showing an incommensurate modulation and (b) $[110]_{\beta}$ with $\{001\}_{\beta}$ twinned reflections (arrowed).

A TEM STUDY ON THE DECOMPOSITION OF SYNTHETIC HILLEBRANDITE ($Ca_2SiO_4 \cdot H_2O$)

Youn Joong Kim and Waltraud M. Kriven

Department of Materials Science and Engineering, University of Illinois at Urbana-Champaign, Urbana, IL 61801

J. Materials Research, accepted

Abstract

The decomposition mechanism of hillebrandite ($Ca_2SiO_4 \cdot H_2O$) to larnite (β-Ca_2SiO_4) was studied by conventional and *in situ* hot-stage TEM methods. The hillebrandite structure is suggested to be a composition of parawollastonite ($CaSiO_3$) and portlandite ($Ca(OH)_2$) adjoining on {001} planes. The decomposed larnite fibers showed occasional bending and kinking as well as internal defects such as dislocations and domains. No transformation-related microstructures such as twinning were observed. The preferred orientations in the larnite fibers were not distinct. The decomposition route of hillebrandite in air and in a vacuum may be different. In air, the decomposed CaO from the portlandite layer directly participates in the process of SiO_4 chain breaking to form larnite. In the TEM this decomposed CaO is removed and reprecipitated, so that hillebrandite converts directly to parawollastonite. A possible lattice correspondence between hillebrandite (C_2SH) and larnite (β-C_2S) is proposed to be: $\underline{b}_{C_2SH}$ // $\underline{b}_{\beta\text{-}C_2S}$, $\underline{a}_{C_2SH}$ // $\approx [10\bar{2}]_{\beta\text{-}C_2S}$, and $\underline{c}_{C_2SH}$ // $\approx [401]_{\beta\text{-}C_2S}$.

I. INTRODUCTION

Hydrothermally produced hillebrandite ($Ca_2SiO_4 \cdot H_2O$) has recently been introduced as a new energy-saving source material for very reactive larnite (β-Ca_2SiO_4), which is a major ingredient of portland cement.[1] On heating in air, fibrous hillebrandite starts to decompose at about 500°C and produces fibrous β-Ca_2SiO_4. A high specific surface area (about 7 m^2/g) and chemical purity without any chemical stabilizers are major characteristics of β-Ca_2SiO_4 produced from this hillebrandite.[1]

Although the structure of hillebrandite has not been refined, our previous transmission electron microscopy (TEM) study on the structure and microstructures of the synthetic hillebrandite revealed their close similarity to those of the mineral wollastonite ($CaSiO_3$).[2] As in wollastonite, hillebrandite fibers showed their fiber axes to be aligned to the b axis, which is the single chain direction of SiO_4 tetrahedra ("dreierketten"), and a prominent stacking disorder perpendicular to this axis. The decomposition of synthetic hillebrandite to β-Ca_2SiO_4 has been investigated by thermogravimetric analyses (TGA), differential thermal analyses (DTA), powder x-ray diffraction (XRD), ^{29}Si nuclear magnetic resonance (NMR) and TEM.[1,3] However, the TEM result was still very preliminary in establishing the decomposition mechanism. On the other hand, a considerable number of TEM studies on β-Ca_2SiO_4 produced by conventional or chemical methods have been reported.[4,5]

It was our purpose to investigate the decomposition mechanism of hillebrandite using mainly conventional and *in situ* hot-stage TEM techniques. A special interest was to find the structural relationship between hillebrandite and β-Ca_2SiO_4. A comparative study on microstructures in β-Ca_2SiO_4 produced by

the decomposition of hillebrandite with those produced by conventional or chemical methods was also attempted.

II. EXPERIMENTAL PROCEDURE

Powders of synthetic hillebrandite prepared by Ishida *et al.*[1] were used in this study. Two different TEM experiments were performed. First, three batches of the as-received powders were furnace-heated for 1 hour at 500°, 600°, and 700°C in air, respectively. Each batch of powders was dispersed ultrasonically in alcohol. A formvar-supported holey copper grid was dipped into the solution and dried. Hitachi 600 operated at 100 kV and Philips EM-420 operated at 120 kV microscopes were used for conventional TEM studies. These solutions were also examined by XRD (Siemens, operated at 30 kV - 30 mA) to check the degree of decomposition and the existence of preferred orientations at different temperatures. Second, *in situ* TEM studies of the as-received hillebrandite powders were carried out using double-tilt heating stages with Philips EM-420 and AEI EM-1200 (operated at 200 kV, Argonne National Laboratory) transmission electron microscopes. Severe electron beam damage of hillebrandite was minimized by using low beam currents and long exposure times.

III. RESULTS

III.1. Furnace-heated Powders

In spite of the previous decomposition study on synthetic hillebrandite that reported the decomposition started at about 500°C and was completed at about

660°C[1], TEM examination of all the furnace-heated powders in this study, including the 700°C-heated one, showed a considerable amount of undecomposed hillebrandite. This hillebrandite had characteristic fibrous forms whose widths usually ranged from 0.1 μm to 0.4 μm, as reported before[2]. In selected area diffraction patterns (SADP's), distinct streaking due to stacking disorder perpendicular to the fiber axis was present. Such a fiber from the 700°C-heated sample displayed strong strain contrast as well as characteristic linear defects along the fiber axis (Fig. 1a). The [001] SADP (Fig. 1b) clearly indicates that the fiber was still undecomposed hillebrandite. Its extinction condition and weak streaking parallel to the $\underline{a}^*$ direction reflected the characteristic stacking disorder in hillebrandite, as in the case of wollastonite.[2,6]

In addition to hillebrandite, there were two new phases observed in the furnace-heated powders (Figs. 2 and 3). The fibrous morphology and the [001] SADP's of both phases resembled those of hillebrandite. Coexistence of the new phase with hillebrandite was often reflected by extra spots along the $\underline{a}^*$ directions together with the hillebrandite spots.

One of these new phases had a larger d-spacing of about 9.89 Å (the corresponding spot is arrowed in Fig. 2a) than the largest d-spacing of hillebrandite, where $d_{200} \approx 8.30$ Å, along the $\underline{a}^*$ direction. No d-spacing values of both hillebrandite and β-Ca_2SiO_4 exactly matched this value. In addition, there was a weak but distinct reflection at the {020} position of hillebrandite (d-spacing ≈ 3.63 Å; arrowed in Fig. 2a) which is extinct in pure hillebrandite. The corresponding image shown in Fig. 2b suggests that this fiber is composed of alternating bands of hillebrandite and the new phase in contact on the {200} plane of hillebrandite. This phase was occasionally observed in specimens taken from both the 500°C- and 600°C-heated powders, and even from the unheated powders,

but not from the 700°C-heated powders. We designated this new phase as "the L phase" ("L" for larger) for further description.

The [001] SADP of the other new phase was also very similar to those of hillebrandite and the L phase (Fig. 3a). However, it had a smaller d-spacing of about 7.64 Å (the corresponding spot is arrowed in Fig. 3a) than the largest d-spacing of hillebrandite, where $d_{200} \approx 8.30$ Å, along the $\underline{a}^*$ direction. No d-spacing values of both hillebrandite and β-Ca_2SiO_4 matched this value. The corresponding image of the heated fiber apparently contains a band of this new phase (arrowed in Fig. 3b) within the undecomposed hillebrandite. It was aligned in the same direction with the hillebrandite fiber and had a thickness of ≈ 150 Å. This phase was not observed in specimens taken from both the 500°C- and 600°C-heated powders, but occasionally observed in specimens from the 700°C-heated powders. We designated this new phase as "the S phase" ("S" for smaller) for further description.

Fully decomposed hillebrandite, that is, β-Ca_2SiO_4 was not observed in specimens taken from the 500°C-heated powders, but infrequently observed from the 600°C-heated powders, and more frequently observed from the 700°C-heated powders. Throughout the decomposition process, the fibrous morphology of hillebrandite generally remained, but with some modifications. Figs. 4a and 4b illustrate two morphological changes in β-Ca_2SiO_4: (i) bending of fibers which was repeatedly observed and (ii) kinking or knotting of fibers. In addition, the decomposition process also changed the internal microstructure of hillebrandite. Instead of the characteristic linear defects in hillebrandite as shown in Fig. 1b, β-Ca_2SiO_4 fibers have many defects such as dislocations (Fig. 4c) and domain microstructures within a fiber (Fig. 4d). Partly because of this high defect concentration, and partly because of the low crystallinity of β-Ca_2SiO_4 fibers, most SADP's of β-Ca_2SiO_4 appeared as quite diffuse reflections. However, the

transformation-related microstructures such as twinning or modulated structures, which were prevalent in β-Ca_2SiO_4 formed by conventional or chemical methods,[4,5] were not detected in this decomposed powder.

In contrast to the hillebrandite fibers which lay mostly on the {001} cleavage planes, there were no distinct preferred orientations in the β-Ca_2SiO_4 fibers. Examination of 20 individual β-Ca_2SiO_4 fibers resulted in the following orientations. Within ±10° of tilting, β-Ca_2SiO_4 could be oriented to [101] (4 fibers), [100] (3 fibers), [201] (2 fibers), [001] (2 fibers), [210] (1 fiber), [110] (1 fiber), [011] (1 fiber), and [010] (1 fiber). Among the other 5 fibers, 4 fibers could be oriented to [100] and 1 fiber to [101] with a larger tilting of about ±30°. SADP's of two frequently observed orientations, [100] and [101], are shown in Figs. 5a and 5b.

The XRD results for these powders can be summarized as follows: (i) The as-received powder showed some weak peaks that did not belong to hillebrandite. The phases responsible for these peaks were not positively identified; (ii) At 500°C, β-Ca_2SiO_4 peaks were moderate and hillebrandite peaks were weak. Low peak intensities and high background suggested a low crystallinity of both hillebrandite and β-Ca_2SiO_4, and the possible existence of amorphous phases; (iii) The peak intensity of β-Ca_2SiO_4 became stronger and sharper as the heating temperature increased from 600° to 700°C. However, weak intensities of hillebrandite were still present in specimens from the 700°C-heated powders; (iv) Any preferred orientations in β-Ca_2SiO_4 were not clearly detectable.

III.2. *In Situ* TEM Study

Direct observation of the decomposition process was attempted by *in situ* TEM heating of several hillebrandite fibers up to 900°C in a vacuum. The

average heating rate was usually about 3°C/min. Since the thermocouple was attached to the heating furnace, the real specimen temperature was uncertain. No internal standard was used to calibrate the temperature. As seen in Figs. 6a and 6b, the unheated fiber showed the characteristic [001] SADP and microstructures of hillebrandite. At 500°C extra spots started to appear along the $\underline{a}^*$ direction (a spot near the $(200)_{\text{hillebrandite}}$ is arrowed in Fig. 6c). Examination of the d-spacings of these extra spots revealed that they were the same as those of the S phase mentioned above. They were a little diffuse and weaker than the {200}-type reflections of hillebrandite at 500°C, but intensified more and more as the temperature increased (Fig. 6e and 6g). At 800°C the {200}-type reflections of hillebrandite completely disappeared and only the extra spots were present (Fig. 6i). No change in the SADP was observed at 900°C (Fig. 6k). Another change in the SADP at 500°C (Fig. 6c) was the appearance of diffuse rings. These rings were more diffused and weakened as the heating temperature increased, but still remained at 900°C.

Characteristic microstructures of hillebrandite, such as linear defects and strain contrast, shown in Fig. 6b, still remained at 500°C (Fig. 6d), but were not apparent at 600°C (Fig. 6f). The overall microstructures of the samples from 600°C to 900°C were very similar. They were relatively featureless and showed disturbed strain contrast (Figs. 6h, 6j, and 6l). However, there was one major change in morphology at 700°C: a lateral shrinkage of the fiber of about 8% occurred. This shrinkage was commonly observed from several fibers, even though the amount of lateral shrinkage was variable, ranging from 6% to 23%. It was interesting to observe precipitation and growth of the cube-like crystallites outside the fiber during the heating experiment. The crystallites appeared at the same time when the reflections of the S phase appeared. They grew as the intensity of the S reflections increased (Figs. 6c to 6k). It was uncertain as to

whether these crystallites were products of decomposition or some kinds of contaminants.

In order to observe direct decomposition to β-Ca_2SiO_4, one fiber which was a mixture of hillebrandite and the L phase was deliberately chosen from the 600°C furnace-heated powders. *In situ* heating of this fiber, however, resulted in almost the same trend of variation as those of the hillebrandite fiber described above. The spots of the L phase were weak at 500°C and completely disappeared at 600°C. Instead, the spots of the S phase appeared at 600°C and intensified as the temperature increased. At 800°C the hillebrandite spots completely disappeared and only the spots of the S phase remained. Variation of microstructures including the cube-like precipitates outside the fiber, were similar to those of the S phase described above.

Throughout this *in situ* TEM study, our attempts to convert the hillebrandite fibers to the β-Ca_2SiO_4 fibers were mostly not successful, except only in a few cases. As a example of the successful cases, Fig. 7 displays the images and SADP's of a fiber which was unheated (7a and 7b), and heated to 700°C in the TEM (7c and 7d). Unfortunately the unheated fiber was not exactly in the zone axis but considerably off from the [001] zone axis. Compared to that, the heated one was exactly in the [101] zone axis of β-Ca_2SiO_4. Additional reflections shown in SADP's indicated that this fiber was not a single grain. From the corresponding images, a slight movement (rotation) and lateral shrinkage were detectable. Other fibers which were completely converted to β-Ca_2SiO_4 by heating at 700°C had drifted and were bent so severely that an unambiguous determination of orientation relationship was not possible.

IV. DISCUSSION

IV.1. Structural Relationship

In order to study the decomposition mechanism in terms of the structural change from hillebrandite to larnite (β-Ca_2SiO_4), it is necessary to have reliable information about the crystal structures of both materials. Unfortunately, there has been no report on the structural refinements of hillebrandite, whereas the structure of β-Ca_2SiO_4 has been well studied[7,8]. It is possible, however, to deduce the hillebrandite structure qualitatively, based on powder XRD, electron diffraction and microstructural data for hillebrandite. Our previous TEM study[2] strongly indicated a similarity of the structure and microstructures between hillebrandite and wollastonite, especially monoclinic parawollastonite. In terms of chemistry, hillebrandite ($Ca_2SiO_4 \cdot H_2O$) is an exact compound of wollastonite ($CaSiO_3$) and portlandite ($Ca(OH)_2$).

Lattice Geometry

Table 1 lists the crystallographic data of parawollastonite[9], portlandite[10], hillebrandite[11] and larnite[8] from the literature. Comparison of the lattice geometries among them gives rise to the following results:

(1) The hillebrandite structure could be a composition of parawollastonite and portlandite adjoining on the {001} planes. The length of the a and b axes of hillebrandite and parawollastonite are very to close each other. The length of the c axis of hillebrandite, 11.788 Å, is close to the sum of the c axes of parawollastonite and portlandite: 7.066 Å + 4.906 Å = 11.972 Å. Similar relationship can be applied to their unit volumes ($V_{Z=1}$): 118.4 Å^3 *versus* 66.29 Å^3 +

54.82 $Å^3$ = 121.11 $Å^3$. The symmetry of parawollastonite and hillebrandite is the same (#14, $P2_1/a$).

(2) Larnite also has the same space group symmetry (#14), but the lattice was described in a different crystallographic orientation ($P2_1/n$) (Fig. 8), where the b axis is common; the a axis is parallel to the c axis of $P2_1/a$; and the c axis is parallel to the $[\bar{1}0\bar{1}]$ direction of $P2_1/a$.[12]

Atomic Structures

To compare the atomic structures, Fig. 9 displays the [001] and [010] projections of parawollastonite and the [010] projections of portlandite and larnite, based on their structural refinement data.[8-11] For clarity, the Si-O bonds (*i.e.*, SiO_4 tetrahedra) and O-H bonds are marked. The relative ionic size of each element is not strictly applied and the Ca^{2+} size is exaggerated for emphasis and the O^{2-} size was minimized. The solid lines indicate the projected unit cell of each structure.

In the [001] projection of parawollastonite, the single-chains of SiO_4 tetrahedra ("dreierketten") running parallel to the b axis are directly noticeable. If the hillebrandite structure is a simple composition of parawollastonite and portlandite on {001} planes, the prominent {001} cleavage of hillebrandite probably results from the inherent cleavage plane of portlandite, dividing the OH layers (designated in Fig. 9c).

On the other hand, direct comparison of the [010] projections between parawollastonite and larnite provides several important pieces of information related to the decomposition of hillebrandite to larnite:

(1) In parawollastonite, all Ca atoms form the Ca layers, but in larnite only half of the Ca atoms form the Ca layers. The other half

of the Ca atoms in larnite are located directly above and below the SiO_4 tetrahedra.

(2) Assuming that the Ca layers in both structures are parallel to each other, their lattice correspondence is estimated from the projected unit cells of parawollastonite ($CaSiO_3$ or abbreviated to CS) and larnite (β-Ca_2SiO_4 or abbreviated to β-C_2S) such that:

$$\underline{b}_{CS} \,//\, \underline{b}_{\beta\text{-}C_2S},\ \underline{a}_{CS} \,//\, \approx [10\bar{2}]_{\beta\text{-}C_2S},\ \text{and}\ \underline{c}_{CS} \,//\, \approx [401]_{\beta\text{-}C_2S}$$

(3) The Ca atoms not forming the layers in larnite are so close to the SiO_4 tetrahedra[5] that they should have strong bonding with the oxygen atoms of SiO_4.

If the hillebrandite structure is a composition of parawollastonite and portlandite, then the lattice correspondence deduced above between parawollastonite and larnite should also be true for hillebrandite and larnite.

However, a more quantitative determination of the hillebrandite structure in three dimensions, including the exact positions of atoms on the contact plane of parawollastonite and portlandite, is quite difficult without more direct experimental data. It is even not certain whether hillebrandite really has its own structure or not. Instead of the fixed structure suggested above, hillebrandite may be composed of several layers of wollastonite and several layers of portlandite in a stoichimetric manner such that the total number of both layers is the same.

IV.2. Decomposition Mechanism

Decomposition of Portlandite

Considering the proposed structure of hillebrandite, its decomposition process is expected to be closely related to the decomposition of portlandite

($Ca(OH)_2$). Quite extensive studies have been done on the decomposition of portlandite[13-18] and its isostructural material, particularly brucite($Mg(OH)_2$)[19-22]. In general, three decomposition steps have been proposed[16]: (i) formation of H_2O molecules from OH^- ions; (ii) elimination of the H_2O molecules from the structure of the hydroxide; and (iii) transformation of the hydroxide structure into the oxide structure. The decomposition temperature of portlandite is reported to be about 450°C in air and about 230°C in a vacuum of 10^{-6} mm Hg.[14] Before any loss of water, a contraction of the layers was observed and the resulting distortion and disorientation of the layers to accommodate the newly created defects was reported.[16,17]

The decomposition of portlandite by electron beam heating showed two stages of change in terms of SADP's[13]: (i) at the initial stage the spots of $Ca(OH)_2$ split into two sets; (ii) on further heating one set of spots belonging to $Ca(OH)_2$ disappeared and the other set belonging to CaO remained. The decomposed CaO showed a topotactic relationship with the undecomposed $Ca(OH)_2$. Formation of a porous microstructure was noticed in the decomposed CaO[15,18], but studied in more detail for the decomposed MgO using TEM[19,21,22].

Basically two different mechanisms responsible for the porous microstructure in MgO have been proposed. The first mechanism, so-called the homogeneous mechanism, involves two stages of microstructural generation[19]: (i) a small shrinkage of the basal plane due to the homogeneous formation of H_2O molecules from OH^- ions, which causes a maze of cracks in the crystal; and (ii) a collapse of the basal plane that results in the formation of porous, microcrystalline MgO. The second mechanism is related to a nucleation and growth process to form the microstructure of MgO.[21,22] MgO nuclei formed coherently with the $Mg(OH)_2$ matrix introduce large strains and cause extensive

fissuring of the matrix before all water was expelled. This second mechanism well explains the small crystallite size of MgO as well as the observed shift of MgO spots in SADP's, which indicates a gradual decrease of the Mg-Mg distance during the decomposition process.

Decomposition of Hillebrandite

Although the decomposition mechanism of hillebrandite is expected to resemble the portlandite decomposition, there must be some differences, since hillebrandite fibers inherently have a different structure and microstructure from those of portlandite. The characteristic SiO_4 chains and numerous linear defects parallel to the fiber axis may constrain the real decomposition behavior of hillebrandite fibers. The wide range of decomposition temperature, which was previously reported as 500° ~ 660°C[1], but which appeared to be much wider in this study, may reflect the inhomogeneous nature of the decomposition process.

While the decomposition of portlandite produces microcrystalline CaO as a final step, the decomposition of hillebrandite requires one more important step. In hillebrandite, the decomposed CaO from portlandite is expected to directly participate in the process of SiO_4 chain breaking to form larnite. In this case the bridging oxygens of SiO_4 should first be released and form independent SiO_4 tetrahedra with the supply of oxygens from the decomposed portlandite layers. As seen in the [010] projection of the larnite structure (Fig. 9d), the strong bonding between Ca and O in larnite seems to reflect this decomposed CaO that participates in the SiO_4 chain breaking process. Due to the Si-O bond breaking, the hillebrandite decomposition needs to overcome a high energy barrier. In addition, the stoichmetric requirement, Ca:Si = 2:1, seems to also limit the range and completion of the decomposition process for individual fibers. The presence

of undecomposed hillebrandite, the L phase, the S phase and larnite in the furnace-heated powders illustrates the complexity of the real process.

The L Phase

The [001] SADP and the image shown in Fig. 2 suggest that the structure of the L phase should be very similar to the hillebrandite structure having the same fiber b axis. Surveying candidates from different calcium silicate hydrates results in one possible phase whose structure is still unknown but the chemistry is known as $Ca_2SiO_4 \cdot$ 2-4 H_2O. The positions and intensities of the major XRD peaks (JCPDS #11-211) generally resemble those of hillebrandite[11] and the largest d-spacing listed is 9.8 Å which is close to the observed value, 9.89 Å.

This phase may be accidentally formed during the synthetic process, or formed by further hydration of hillebrandite in air later. The occurrence of this phase in the unheated sample and the disappearance of this phase at 600°C by *in situ* TEM heating support this idea. However, precipitation of the H_2O-rich L phase along the linear defects of hillebrandite on heating is also possible, considering the presence of this phase in specimens taken from the 500°C- and 600°C-heated powders and the availability of water molecules from the decomposed portlandite at this temperature.

The S Phase

The [001] SADP and the image shown in Fig. 3 suggest that the structure of the S phase is also similar to the hillebrandite structure. Since this phase has been observed in specimens taken from powders furnace-heated at 700°C, the S phase should be a dehydrated phase or at least a H_2O-poor calcium silicate phase. The distinct lateral shrinkage of the fiber at 700°C observed from the *in situ* TEM study suggests that the dehydration is accompanied possibly by a distortion or rearrangement of the previous lattice. The gradual development of the S phase at

the expense of hillebrandite strongly indicates a nucleation and growth process, probably along the linear defects in hillebrandite (refer to Fig. 3d). Among the H_2O-poor calcium silicate hydrates, however, no compound shows a close match to this S phase. The dellaite, $6CaO \cdot 3SiO_4 \cdot H_2O$, which is known to be a stable phase above 800°C at moderate water pressure[23], would be a good candidate. But the reported d-spacing of dellaite does not match well with the experimental data of the S phase.

Surprisingly enough, parawollastonite matches as one possible phase for the S phase, because its [001] SADP is similar to that of hillebrandite and the d-spacing of the (200) plane is about 7.7 Å, which is close to the observed value of 7.64 Å. Two supporting pieces of evidence for this identification are: (i) no further changes in SADP and morphology occurs even at 900°C-heating, which indicates that the S phase is stable above 800°C; (ii) the simultaneous appearance of the cube-shaped crystallites and the S phase, and their simultaneous growth with increasing temperature (Fig. 6). If these crystallites are CaO formed from the decomposition of the portlandite layer in hillebrandite, the appearance and growth of both wollastonite and CaO should be simultaneous. However, since the chemistry of the S phase and the crystallite phase have not been examined, this identification is still tentative.

Larnite from the Synthetic Hillebrandite

The previous XRD study[14] clearly indicates that the decomposition temperature of portlandite in a vacuum is much lower than in air. The same trend is expected for the decomposition of hillebrandite. Our experimental results, however, are contrary to this expectation, even though the *in situ* TEM results are difficult to generalize. There are two possible explanations for this discrepancy. First, the decomposition route in air and in a vacuum may be

different. In air, the decomposed CaO from portlandite directly participates in the formation of larnite. On the other hand, in the TEM this decomposed CaO is removed and reprecipitated, so that hillebrandite converts directly to parawollastonite. Second, there may be a microstructural change upon the decomposition of the portlandite layer, which inhibits the decomposition of hillebrandite to larnite. Considering the porous microstructures of the decomposed CaO and MgO, a plausible microstructure is strain-related microcracking of the hillebrandite matrix, although no direct evidence is available. It is frequently reported that a smaller grain size tends to prevent the expected phase transformations in material.[4,24] In this case the S phase should be a H_2O-poor dicalcium silicate phase with microcracks. Further investigation is needed to test these possibilities.

The morphology and microstructures of larnite should reflect its decomposition process. The fibrous forms in larnite suggest that the overall structural integrity of hillebrandite was not severely modified by decomposition, even though the silica chains were broken. As expected from the [010] projections of parawollastonite and larnite shown in Fig. 9, however, the decomposition of hillebrandite to larnite is probably not exactly topotactic. The theoretically expected lattice correspondence, shown in the [010] stereoprojection of Fig. 10, predicts the c axis of hillebrandite to be approximately parallel to the [401] direction of larnite. This requires about 13° clockwise rotation of the hillebrandite structure along the b axis. Although the experimentally observed orientations of larnite (refer to the Results section) are scattered, they have some tendency to lie on the plane perpendicular to the [401] orientation. The scatterring of data is probably due to the drifting and bending of hillebrandite fibers during the heating.

Numerous internal defects in larnite may also originate from this structural change, especially from the breaking process of silica chains in hillebrandite. Alternatively, these defects may be a remnant of microstructures produced during the decomposition process of portlandite mentioned above.

These microstructures of the fibrous larnite (β-Ca_2SiO_4) are obviously different from the microstructures of the equiaxial β-Ca_2SiO_4 formed by conventional or chemical methods.[4,5] The lack of transformation-related microstructures such as twinning indicates the low temperature synthesis of larnite without any polymorphic transformations. The presence of domain microstructures within the larnite fiber, shown in Fig. 3D, may reflect the inherent, ferroelastic nature of β-Ca_2SiO_4, which was studied in more detail in β-Ca_2SiO_4 formed by conventional or chemical methods.[5]

V. CONCLUSION

The decomposition mechanism of hillebrandite ($Ca_2SiO_4 \cdot H_2O$) was studied mainly by conventional and *in situ* hot-stage TEM methods. Furnace-heating of hillebrandite fibers at 700°C in air mostly resulted in larnite (β-Ca_2SiO_4) fibers which showed occasional bending and kinking as well as internal defects such as dislocations and domains. In contrast to the hillebrandite fibers which lay mostly on the {001} cleavage planes, the preferred orientations in the larnite fibers were not distinct.

The *in situ* TEM heating study to observe the direct convertion from hillebrandite to larnite was mostly unsuccessful. Instead of larnite, *in situ* heating sometimes produced another phase whose structure is similar to the hillebrandite structure but has a smaller d-spacing for the (200) plane, $\approx$ 7.64 Å, than that of

hillebrandite, ≈ 8.30 Å. This phase was stable even at 900°C heating. Tentative identification of this phase is parawollastonite.

Based on the theoretical consideration and the experimental results, the hillebrandite structure is suggested to be a composition of parawollastonite ($CaSiO_3$) and portlandite ($Ca(OH)_2$) adjoining on the {001} planes. Therefore, the hillebrandite decomposition is also suggested to be closely related to the portlandite decomposition. In hillebrandite, the decomposed CaO from the portlandite layer is expected to directly participate in the process of SiO_4 chain breaking to form larnite. A possible lattice correspondence between hillebrandite (C_2SH) and larnite (β-C_2S) is proposed to be:

$$\underline{b}_{C2SH} // \underline{b}_{\beta\text{-}C2S},\ \underline{a}_{C2SH} // \approx [10\bar{2}]_{\beta\text{-}C2S},\ \text{and}\ \underline{c}_{C2SH} // \approx [401]_{\beta\text{-}C2S}.$$

The decomposition route of hillebrandite in air and in a vacuum may be different. In air, the decomposed CaO from the portlandite layer directly participates in the formation of larnite. In the TEM this decomposed CaO is removed and reprecipitated, so that hillebrandite converts directly to parawollastonite.

The microstructures of the fibrous larnite formed by decomposition of hillebrandite are obviously different from the microstructures of the equiaxial larnite formed by conventional or chemical methods. The lack of transformation-related microstructures such as twinning indicates the low temperature synthesis of larnite without any polymorphic transformations.

ACKNOWLEDGEMENTS

This research was supported by the US Air Force Office of Scientific research under grant number AFOSR-URI-90-0174. We are grateful to Drs. T. Mitsuda and H. Ishida who provided us their synthetic hillebrandite powders. A

part of our *in situ* TEM heating experiments were done by generous support from the electron microscopy facility in the Argonne National Laboratory, Chicago, Illinois. The use of TEM facilities at the Center for Microanalysis of Materials in the Materials Research Laboratory at the University of Illinois at Urbana-Champaign is also gratefully acknowledged.

REFERENCES

1. H. Ishida, K. Mabuchi, K. Sasaki, and T. Mitsuda, J. Am. Ceram. Soc., **75**, 2427 (1992).

2. Y. J. Kim and W. M. Kriven, J. Mater. Res., **8**, [8] 2948 (1993).

3. N. A. Torpov, Kh. S. Nikogosyan, and A. I. Boikova, Zh. Neorg. Khim., **4**, 1159 (1959).

4. C. J. Chan, W. M. Kriven and J. F. Young, J. Am. Ceram. Soc., **75**, 1621 (1992).

5. Y. J. Kim, I. Nettleship, and W. M. Kriven, J. Am. Ceram. Soc., **75**, 2407 (1992).

6. H.-R. Wenk, W. F. Müller, N. A. Liddell, and P. P. Phakey (eds.), *Electron Microscopy in Mineralogy* (Springer, Berlin, Heidelberg, New York, 1976), p. 324.

7. C. M. Midgley, Acta Cryst., **5**, 307 (1952).

8. K. H. Jost, B. Ziemer and R. Seydel, Acta Cryst., B**33**, 1696 (1977).

9. F. J. Trojer, Zeit. für Krist., **127**, 291 (1968).

10. W. R. Busing and H. A. Levy, J. Chem. Phys., **26**, 563 (1957).

11. L. Heller, Mineral. Mag., **30**, 150 (1953).

12. N. F. M. Henry and K. Lonsdale (eds.), *International Tables for X-ray Crystallography V. I* (The International Union of Crystallography, 1952).

13. S. Chatterji and J. W. Jeffery, Min. Mag., **35**, 867 (1966).

14. N. H. Brett, Min. Mag., **37**, 244 (1969).

15. D. Beruto, L. Barco, A. W. Searcy, and G. Spinolo (1980), J. Am. Ceram. Soc., **63**, 439 (1980).

16. O. Chaix-Pluchery, J. Bouillot, D. Ciosmak, J. C. Niepce, and F. Freund, J. Solid State Chem, **50**, 247 (1983).

17. O. Chaix-Pluchery, J. Pannetier, J. Bouillot, and J. C. Niepce, J. Solid State Chem, **67**, 225 (1987).

18. D. Beruto, M. G. Kim, and A. W. Searcy, High Temperatures-High Pressures, **20**, 25 (1988).

19. J. F. Goodman, Pro. Roy. Soc., A**247**, 346 (1958).

20. M. C. Ball and H. F. W. Tayler, Min. Mag., **32**, 754 (1961).

21. R. S. Gordon and W. D. Kingery, J. Am. Ceram. Soc., **49**, 654 (1966).

22. M. G. Kim, U. Dahmen, and A. W. Searcy, J. Am. Ceram. Soc., **70**, 146 (1987).

23. D. M. Roy, Am. Min., **43**, 1009 (1958).

24. W. M Kriven, J. Am. Ceram. Soc., **71**, 1021 (1988).

Table 1. Crystallographic data for major materials investigated in this study.

Mineral Name	Para-wollastonite	Portlandite	Hillebrandite	Larnite
Chemical Formula	$CaSiO_3$	$Ca(OH)_2$	$Ca_2SiO_4 \cdot H_2O$	Ca_2SiO_4
Space Group	*P2₁/a*	*P$\bar{3}$m1*	*P2₁/a*	*P2₁/n*
#Formular Unit (Z)	12	1	12	4
Lattice Parameters	a = 15.426 Å b = 7.320 Å c = 7.066 Å β = 94.40° V = 795.53 Å^3 $V_{Z=1}$ = 66.29 Å^3	a = 3.592 Å c = 4.906 Å V = 54.82 Å^3	a = 16.588 Å b = 7.267 Å c = 11.788 Å β = 90.23° V = 1420.97 Å^3 $V_{Z=1}$ = 118.4 Å^3	a = 5.502 Å b = 6.745 Å c = 9.297 Å β = 94.59° V = 343.91 Å $V_{Z=1}$ = 85.98 Å^3
Reference	9	10	11	12

Figure Captions

FIG. 1. (a) Morphology and (b) the [001] SADP of an undecomposed hillebrandite fiber taken from the 700°C furnace-heated sample.

FIG. 2. A new phase occurring with hillebrandite from the 600°C furnace-heated powders: (a) The [001] SADP and (b) the corresponding image of a fiber. Along the a* direction, one of the extra spots near the $(200)_{hillebrandite}$ is arrowed in (a). A weak reflection at the (020) position of hillebrandite is also arrowed in (a).

FIG. 3. A new phase occurring with hillebrandite from the 700°C furnace-heated powders: (a) the [001] SADP and (b) the corresponding image of a fiber Along the a* direction, one of the extra spots near the $(200)_{hillebrandite}$ is arrowed in (a). A band of a new phase within the undecomposed hillebrandite is also arrowed in (b).

FIG. 4. Microstructures of β-Ca_2SiO_4 fibers: (a) bending and (b) kinking or knotting of fibers as well as (c) dislocations and (d) domains within a fiber.

FIG. 5. SADP's of β-Ca_2SiO_4 fibers in two orientations, (a) [100] and (b) [101], which are frequently observed.

FIG. 6. The [001] SADP's and the corresponding images from the *in situ* TEM heating study of a hillebrandite fiber heated up to 900°C ((a) to (l)). A newly appeared spot near the $(200)_{hillebrandite}$ in the SADP's and a cube-like precipitate in the images are arrowed.

FIG. 7. The images and SADP's of a fiber which is unheated, (a) and (b), and 700°C-heated inside the TEM, (c) and (d).

FIG. 8. Two different lattice choices for space group symmetry (#14): (a) $P2_1/a$ (b) $P2_1/n$. Note the interchange of the a and c axes.

FIG. 9. (a) The [001] and (b) [010] projections of parawollastonite; (c) the [010] projections of portlandite; and (d) the [010] projections of larnite. The Si-O bonds and O-H bonds are marked. The Ca^{2+} size is exaggerated for emphasis and the O^{2-} size was minimized. The solid lines indicate the projected unit cell of each structure.

FIG. 10. The [010] stereoprojection showing the theoretically expected lattice correspondence between hillebrandite (open square) and larnite (solid square).

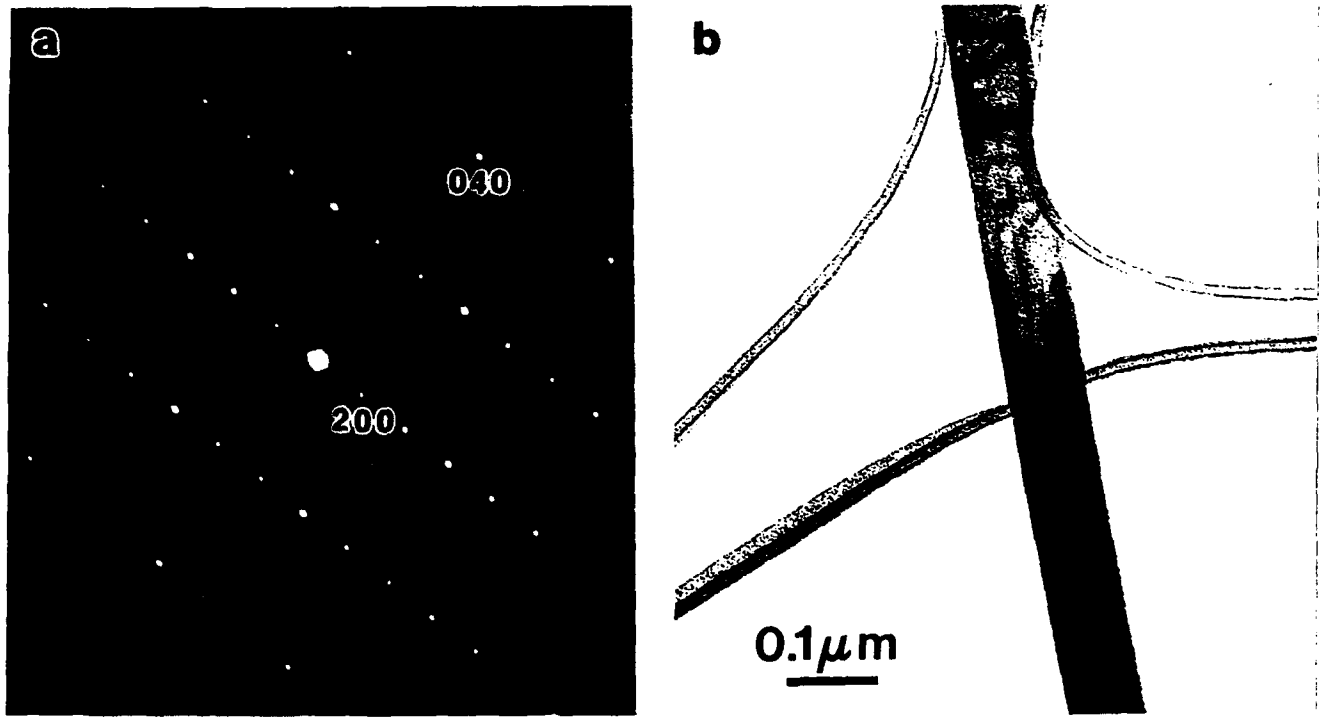

FIG. 1. (a) Morphology and (b) the [001] SADP of an undecomposed hillebrandite fiber taken from the 700°C furnace-heated sample.

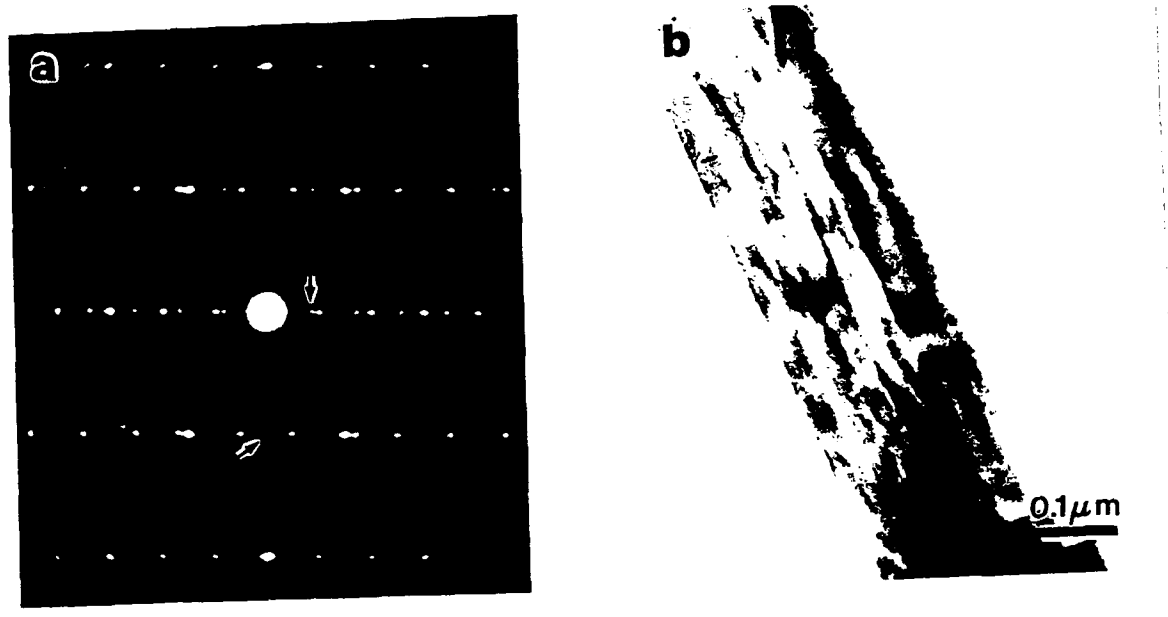

FIG. 2. A new phase occurring with hillebrandite from the 600°C furnace-heated powders: (a) The [001] SADP and (b) the corresponding image of a fiber. Along the a* direction, one of the extra spots near the (200)hillebrandite is arrowed in (a). A weak reflection at the (020) position of hillebrandite is also arrowed in (a).

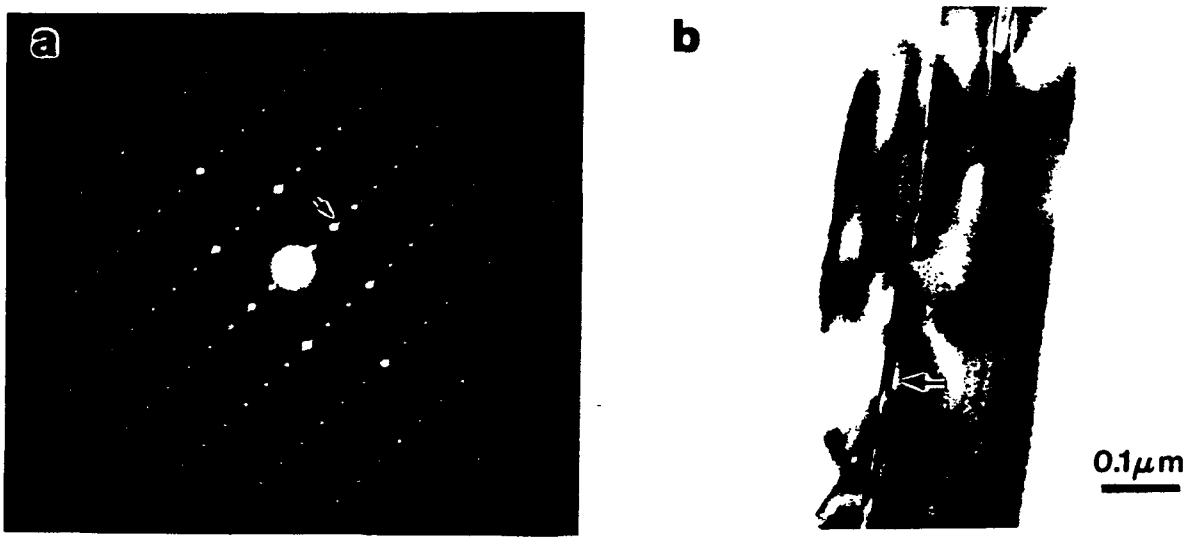

FIG. 3. A new phase occurring with hillebrandite from the 700°C furnace-heated powders: (a) the [001] SADP and (b) the corresponding image of a fiber Along the a* direction, one of the extra spots near the (200)hillebrandite is arrowed in (a). A band of a new phase within the undecomposed hillebrandite is also arrowed in (b).

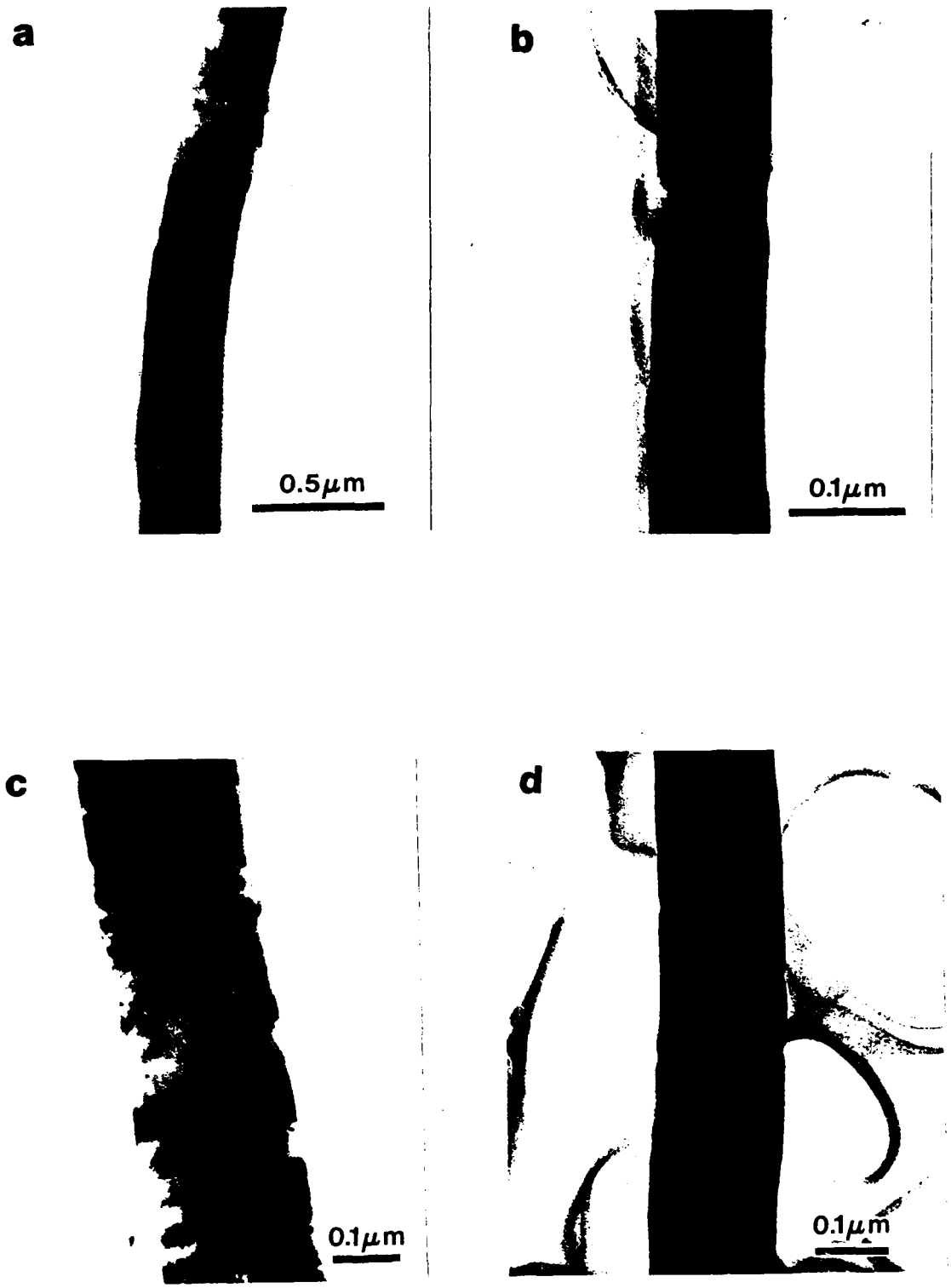

FIG. 4. Microstructures of β-Ca_2SiO_4 fibers: (a) bending and (b) kinking or knotting of fibers as well as (c) dislocations and (d) domains within a fiber.

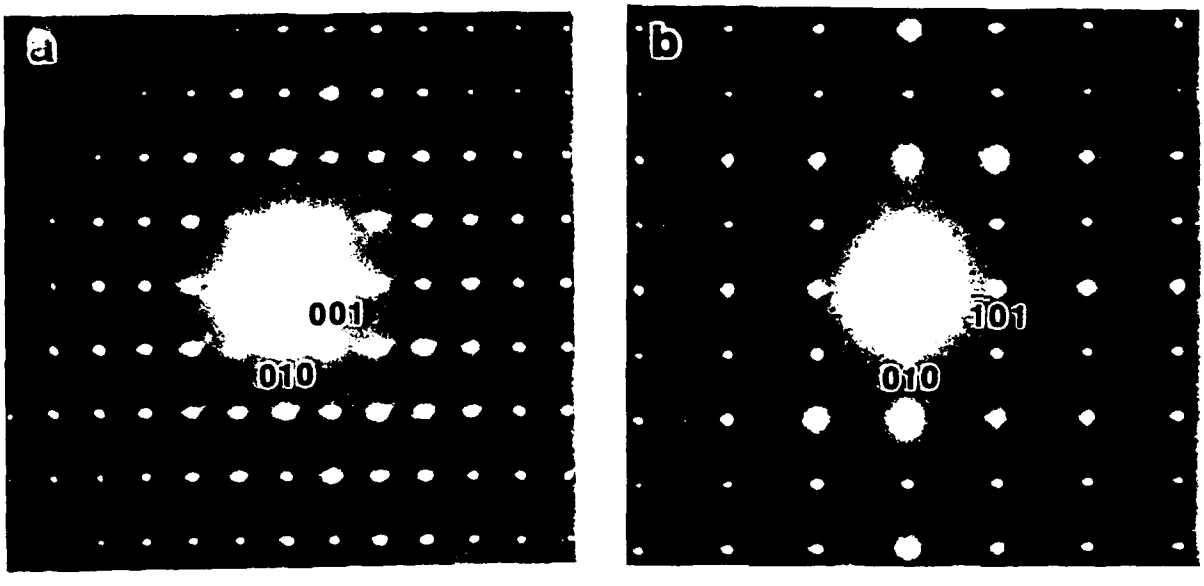

FIG. 5. SADP's of β-La_2SiO_4 fibers in two orientations, (a) [100] and (b) [101], which are frequently observed.

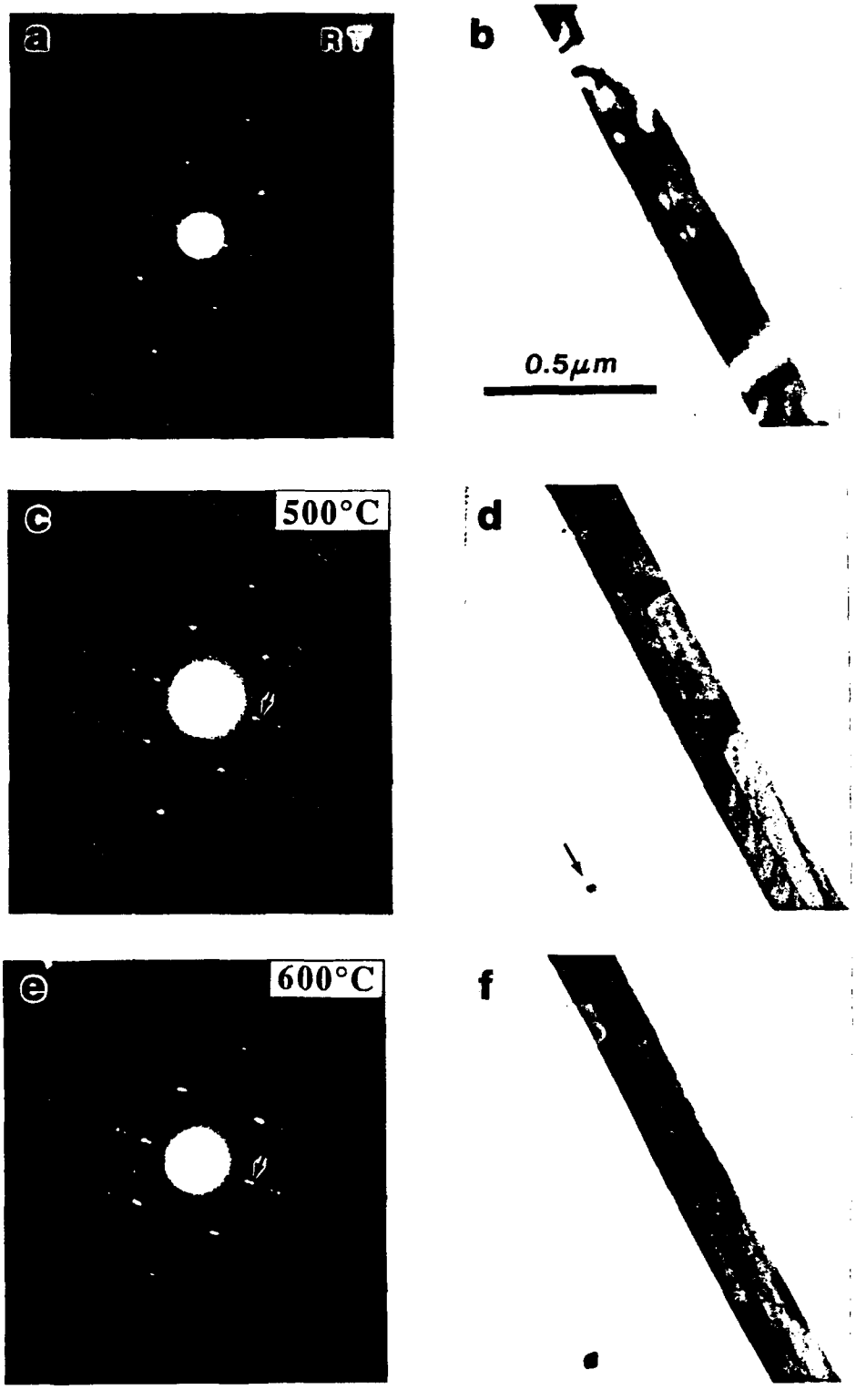

FIG. 6. The [001] SADP's and the corresponding images from the *in situ* TEM heating study of a hillebrandite fiber heated up to 900°C ((a) to (l)). A newly appeared spot near the (200)hillebrandite in the SADP's and a cube-like precipitate in the images are arrowed.

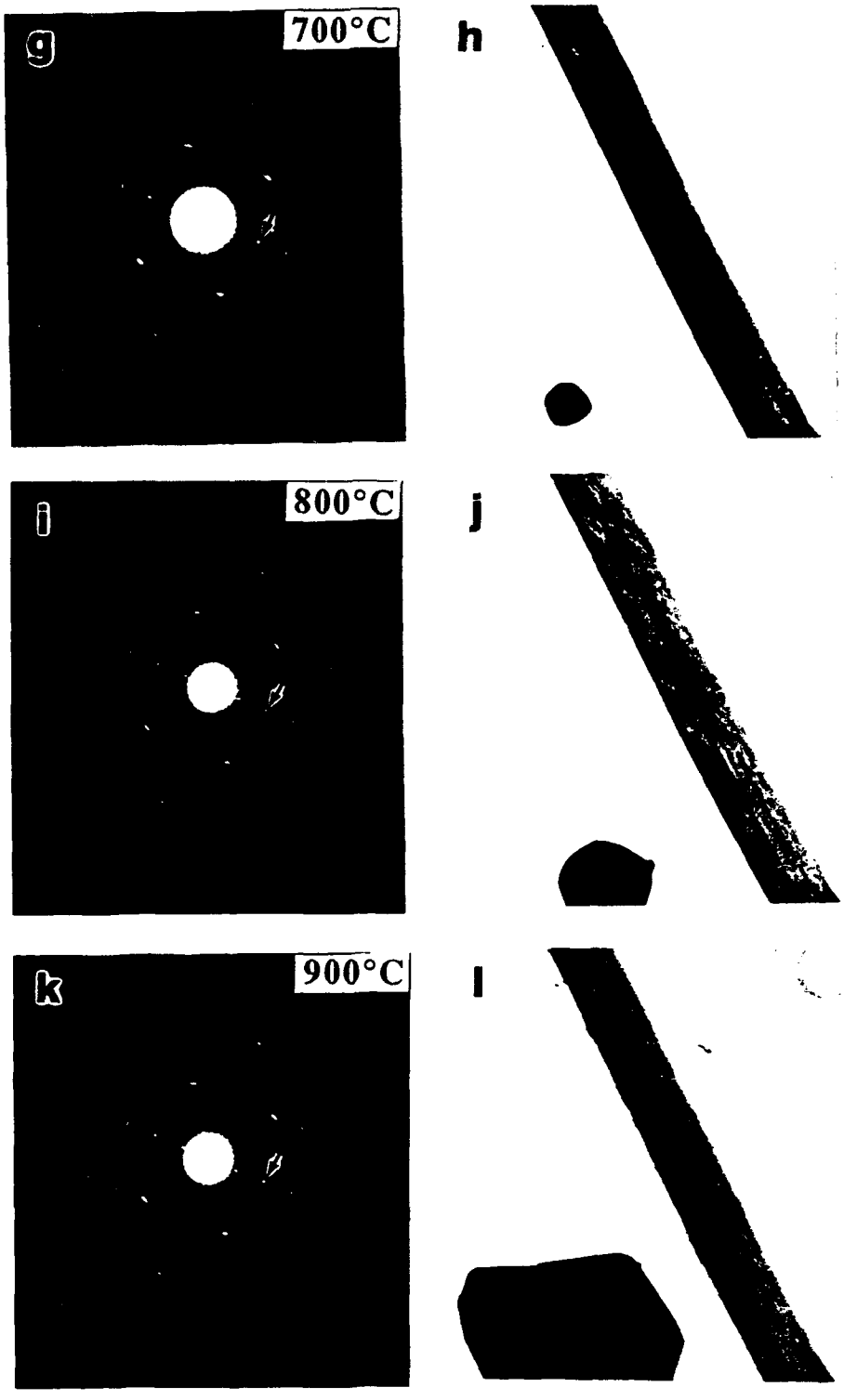

FIG. 6. The [001] SADP's and the corresponding images from the *in situ* TEM heating study of a hillebrandite fiber heated up to 900°C ((a) to (l)). A newly appeared spot near the (200)hillebrandite in the SADP's and a cube-like precipitate in the images are arrowed.

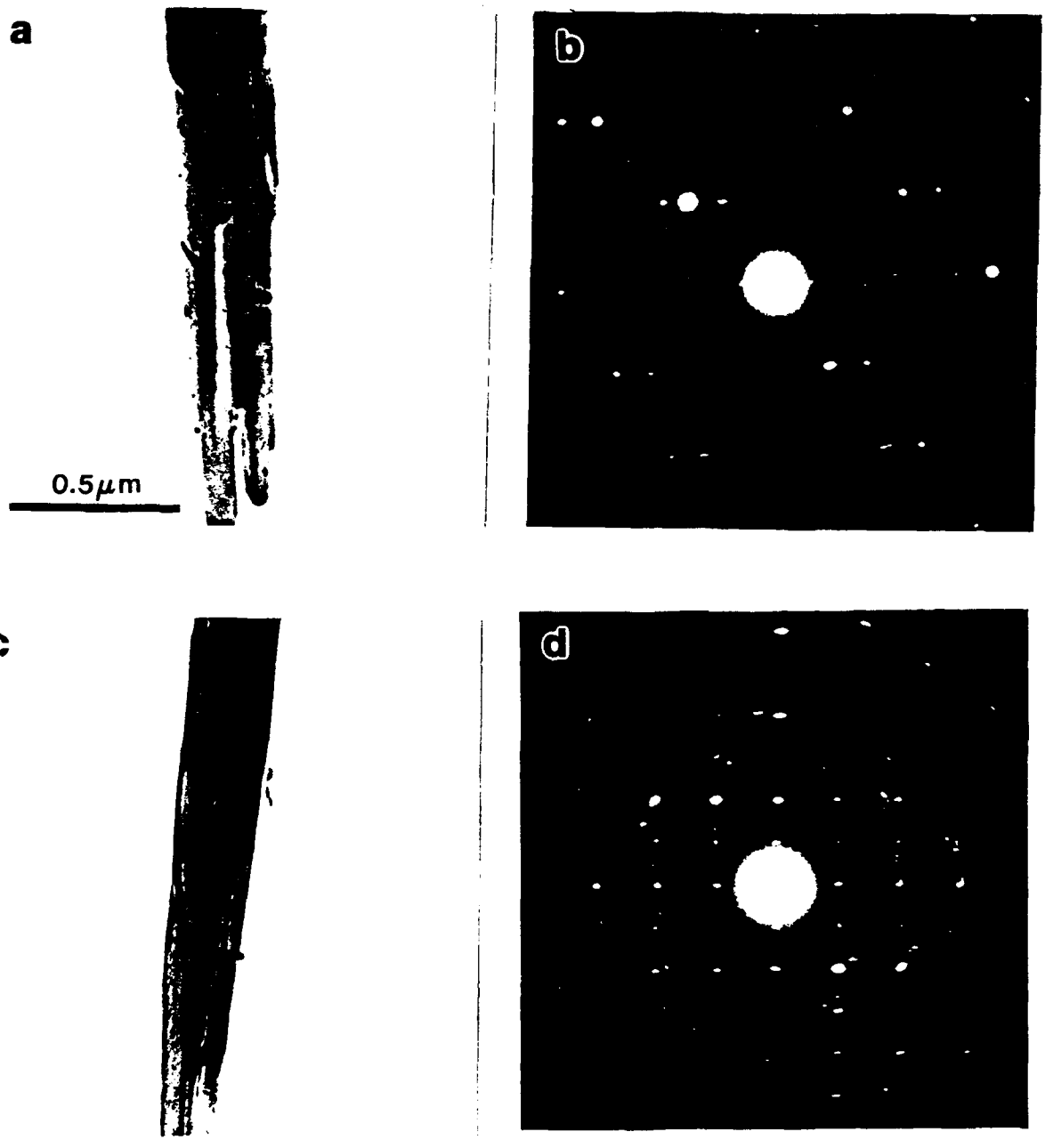

FIG. 7. The images and SADP's of a fiber which is unheated, (a) and (b), and 700°C-heated inside the TEM, (c) and (d).

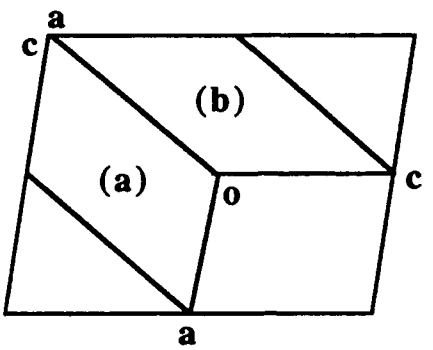

FIG. 8. Two different lattice choices for space group symmetry (#14): (a) $P2_1/a$ (b) $P2_1/n$. Note the interchange of the a and c axes.

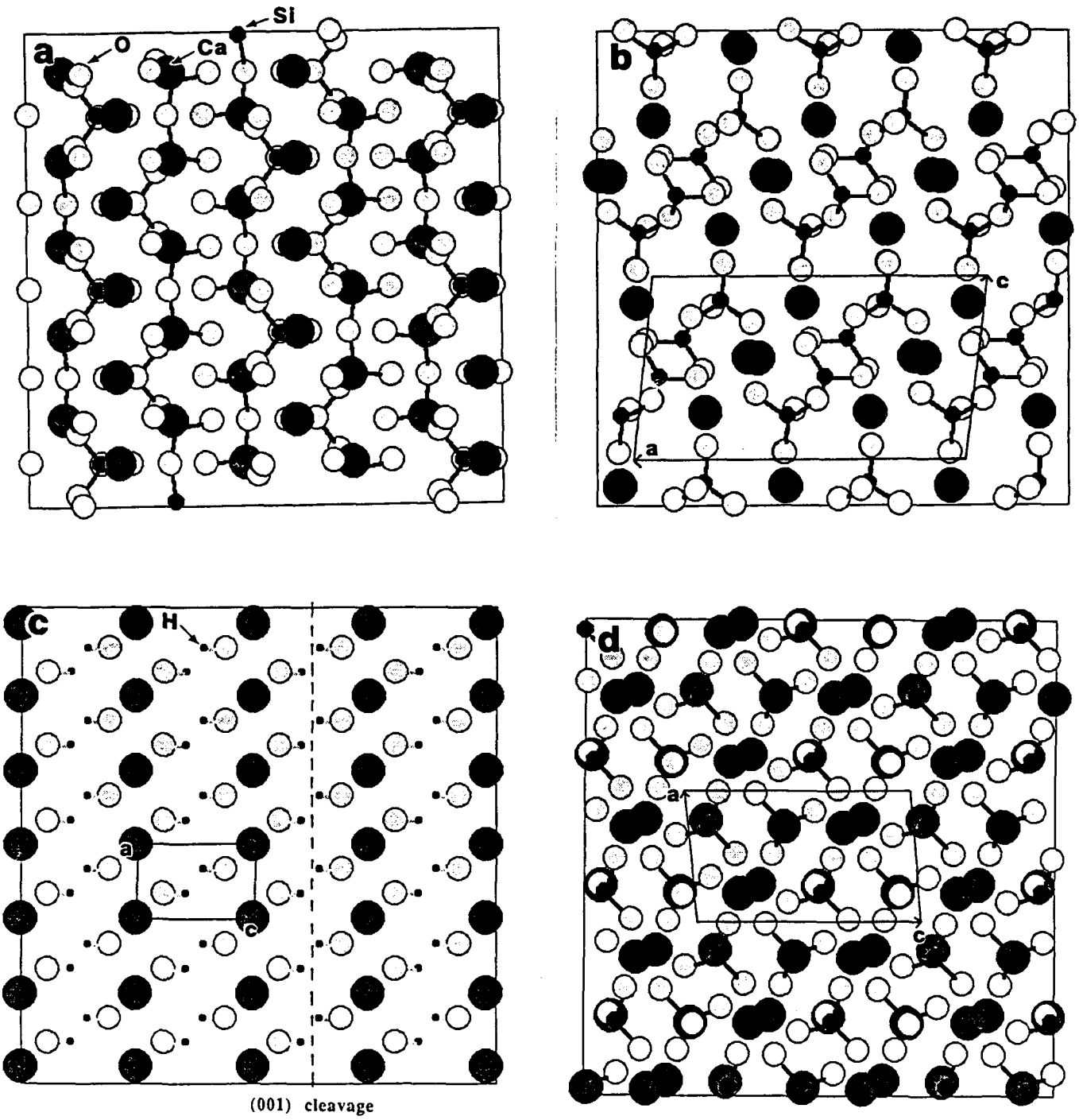

FIG. 9. (a) The [001] and (b) [010] projections of parawollastonite; (c) the [010] projections of portlandite; and (d) the [010] projections of larnite. The Si-O bonds and O-H bonds are marked. The Ca^{2+} size is exaggerated for emphasis and the O^{2-} size was minimized. The solid lines indicate the projected unit cell of each structure.

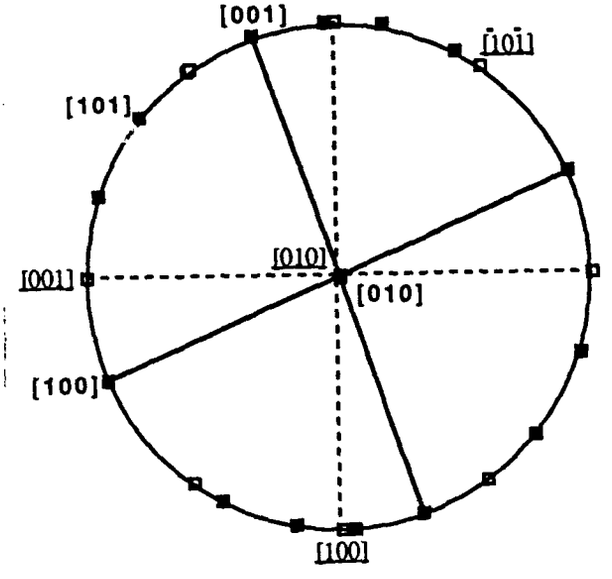

FIG. 10. The [010] stereographic projection showing the theoretically expected lattice correspondence between hillebrandite (open squares) and larnite (solid squares).

NICKEL SULFIDE (NiS)

Proceedings of

The International Conference on

Martensitic Transformations

(ICOMAT-92)

20-24 July 1992
Monterey, California

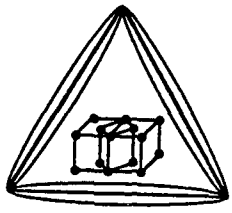

ICOMAT-92

Edited by C.M. Wayman and J. Perkins

Proceedings of the International Conference on Martensitic Transformations (1992)
Monterey Institute for Advanced Studies © 1993
Monterey, California, USA

THE ALPHA TO BETA TRANSFORMATION IN STOICHIOMETRIC NICKEL SULFIDE

B. Kim, Chen-Chia Chou and C. Marvin Wayman

University of Illinois
Department of Materials Science and Engineering
1304 West Green Street
Urbana, Illinois 61801 USA

ABSTRACT

The forward (alpha to beta) and reverse transformation characteristics of NiS have been studied using the hot-stage x-ray diffraction, hot stage optical microscopy, dilatometry, and electrical resistivity measurements. The hot-stage x-ray diffraction patterns confirmed the structural change-from beta to alpha during the heating cycle and alpha to beta during the cooling cycle. The structural change of NiS was observed as surface relief through hot stage optical microscopy. Both the dilatometry and resistivity measurements revealed a large hysteresis, spanning a temperature range of approximately 200° C. The shape of the hysteresis resembled those found in martensitic materials and shape memory alloys. Also, from the dilatometry measurements, the volume change associated with the transformation was calculated to be approximately 4.7%. All experimental results appear to fit the characteristics of a martensitic transformation.

1. INTRODUCTION

In the Ni-S binary system, many compounds exist at various compositions. At 35.33 weight percent sulfur, the compound NiS is the stable phase, where the atomic ratio for nickel to sulfur is 1:1. The low temperature phase is the beta phase, commonly called millerite. This phase has a rhombohedral crystal structure, with three nickel and three sulfur atoms per unit cell. The structure of millerite was first recognized by Alsen [1] and Kolkmeijer & Moesveld [2]. The high temperature phase is the alpha phase, and it has a hexagonal crystal structure with two nickel atoms per unit cell. Millerite has an unusual five-fold coordination of the Ni atoms by S atoms, whereas alpha NiS has a six-fold coordination of the Ni atoms by S atoms. The five-fold coordination requires less bonding energy to form than the six-fold coordination, which is the reason why millerite is the stable phase in nature [3].

It was reported that "artificially made" stoichiometric NiS transforms from beta to alpha at approximately 396° C during heating [4]. The forward transformation occurs during cooling at approximately 350° C [4]. This transition is first order, exhibiting considerable hysteresis which spans a temperature range of approximately 50 degrees. The volume change accompanying the transformation is approximately 4% [5]. There is a volume increase during the forward inversion and a volume decrease during the reverse. Due to the large volume discrepancy, micro-cracks are introduced during the transformations. These may be undesirable for potential practical applications. Besides the volume change, there are also changes in electrical and magnetic properties during the transformation [6].

Recently, NiS ceramics became of interest to many people because of its reversible transformation at a relatively low temperature span. It was suggested that this material can be used as a transformation toughener in composites based on its temperature conversion from beta to alpha NiS at 379° C [7]. It is believed that NiS has many of the characteristics of zirconia, commonly used as a transformation toughener for composite materials. By now, the mechanism of transformation toughening with zirconia is somewhat well understood. The constrained zirconia particles in a ceramic undergo a martensitic transformation due to stress fields close to the crack tips. As the zirconia particles absorb the

energy, energy-deficient crack tips no longer propagate through the matrix. If NiS can perform the same functions as zirconia, it will have many applications, which is the main reason for studying this compound.

In order to determine whether NiS is a potential candidate for a transformation toughener, basic mechanisms of the transformation must be understood. The first condition NiS must meet is that it has to undergo a martensitic transformation. Secondly, this martensitic transformation must be able to be produced from induced stress. Up to date, no one has studied and identified the NiS transformation mechanism. Therefore, in order to elucidate this, the following experiments were performed: (a) hot stage x-ray diffraction, (b) optical hot stage microscopy, (c) electrical resistivity measurements and (d) dilatometry measurements.

2. EXPERIMENTAL PROCEDURE

Equal atomic ratios of Ni and S powders were sintered in evacuated quartz tubes. For most runs, 3 mm (I. D.) by 1.5 mm (wall thickness) quartz tubes were used. The wall thickness was crucial because high vapor pressures of sulfur during sintering can explode the tube. Furthermore, the atmosphere in the tube was minimized in order to control the loss of sulfur through vaporization. In general, the charge was sintered at 700° C for 48 hrs, 1000° C for 2 hrs, and 900° C for 96 hrs, successively. Slow furnace cooling was utilized to obtain beta NiS. For alpha NiS, the temperature was first reduced to 700° C and left at that temperature for 24 hours, followed by a quench in cold water. After each sample was sintered, a powder x-ray diffraction test was performed to determine the nature of the specimen. In most cases, only a single phase was present.

A Philips x-ray diffractometer unit with a copper target was used at 40 kV and 10 mA for powder NiS x-ray diffraction. Specimens were scanned at a rate of 5 deg./min in the 2θ range of 15 to 65 degrees. For hot stage x-ray diffraction experiments, a Rigaku unit was used in conjunction with a hot stage. A diffusion pump vacuum system was attached to the hot stage to avoid possible oxidation during heating cycles. Parameters were similar to the ones described previously. The temperature range of thermal cycling was from 25° C to 400° C. The heating rate was approximately 10 deg./min.

For hot stage optical microscopy, one polished slice (approx. 3 mm X 3 mm X 0.05 mm) was put in the hot stage at a time, which was set up with a Nikon microscope. The Nomarski interference contrast system on the Nikon microscope was utilized in order to see the surface relief, as specimens were heated and cooled through the transformation temperatures. The heating rate was approximately 30 deg./min, whereas the cooling rate was approximately 10 deg./min. For viewing the specimen in the hot stage, a magnification of 100 times was normally used. For experimental procedures on electrical resistivity and dilatometry measurements, see reference [8].

3. RESULTS & DISCUSSION

3.1 Hot Stage X-Ray Diffraction

Figure 1 illustrates the results from heating and cooling cycles for alpha NiS,the high temperature phase. The alpha phase was "frozen" by quenching in cold water from 750° C after sintering. The thermal cycle spanned a temperature range of 25° C to approximately 400° C. At room temperature, only alpha peaks were present during the 2θ scanning from 15 to 60 degrees. At approximately 200° C, some beta peaks were observed, and at the same time, alpha peaks decreased in intensity. Since alpha NiS is unstable at this temperature, the presence of beta peaks is not a surprise. In nature, the five-fold coordination in beta NiS requires less bonding energy to form than the six-fold coordination in alpha NiS, which is the reason why millerite is the stable phase at temperatures such as 200° C. Upon further heating, beta peaks started to disappear while alpha peaks were increasing in intensity. The alpha peaks at 400° C were almost identical to those at 25° C, which indicated that the retained phase at room temperature was a single phase alpha NiS. With increasing temperatures, the free energy barrier was overcome, enabling the change from a five-fold into a six-fold coordination. The main driving force in this case is the thermal energy. During the cooling cycle, both alpha and beta peaks were observed. Even at room temperature, x-ray diffraction readings showed both alpha and beta peaks. This was caused by an "improper" cooling rate. When a proper cooling rate (less than 10° C/min) was used, only beta peaks were obtained at room temperature.

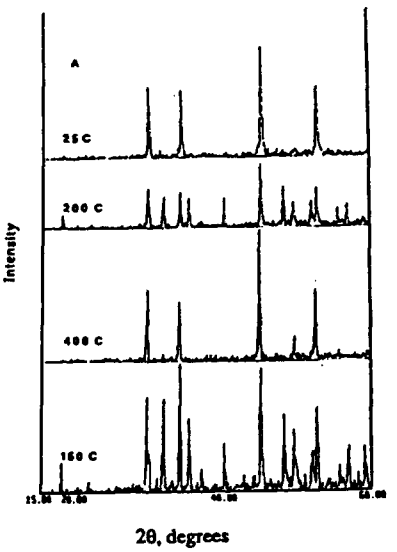

Fig. 1 - Hot stage x-ray results from heating and cooling cycles for alpha NiS.

For NiS, the cooling rate from 400° C must be about 10° C/min or lower if the forward transformation is to occur. At cooling rates greater than 30° C/min, alpha NiS will be retained at room temperature. This behavior is not common in martensitic materials because they normally transform athermally. According to Cohen [9], "A martensite transformation cannot be suppressed by quenching: the fastest cooling rates hitherto achieved (approx. 18,000° C/sec.) have shown no indication of being able to avoid the reaction or of appreciably lowering the temperature, M_s, at which it starts." For instance, martensite transformations rapidly come to a halt when the rate of cooling or heating is brought to zero, and the transformation process is resumed only if the temperature change is resumed. Surprisingly, some iron alloys, such as Fe-C-Mn [10] and Fe-Ni-Mn-C [11] follow C-curve behavior where the martensitic reaction can actually be suppressed by fast cooling. Moreover, a substantial amount of martensite can be formed isothermally on holding at the quenching temperature. Like these alloys, a slow cooling rate is required for NiS in order for the forward reaction to occur. Therefore, the possibility of classifying as a martensitic transformation for NiS is not ruled out.

3.2 Hot Stage Optical Microscopy

The phase transformation behavior was also investigated using in-situ hot stage optical microscopy. With the aid of Nomarski interference contrast, it is possible to see very minute roughness changes during transformations. At an appropriate grain orientation, phase fronts were seen passing swiftly through the whole grain, or sometimes the new phase nucleated and grew scatteringly in the matrix (they showed different contrast) and surface upheavals were revealed. In Fig. 2, photomicrographs of beta NiS (specimen #33) during thermal cycling in the hot stage are illustrated. All were taken using polarized light. Figure 2A shows three large grains of beta NiS at room temperature. Upon heating, surface relief began to appear at 381° C, as shown in Fig. 2B. This one showed clear variants within a single grain. With further heating, the microstructure began to appear dull and almost monochrome, as shown in Fig. 2C. In this figure, micro-cracks are illustrated, which were caused by a large volume change during the reverse transformation. By comparing with the hot stage x-ray results, it was concluded that the microstructure shown in Fig. 2C was alpha NiS. During cooling, a change in the microstructure was noted at 311° C, where indications of beta NiS were observed. Figure 2D illustrates a photomicrograph taken at 221° C, which resembles that in Fig. 2A. Specimen #33 was thermally cycled four times, and the results were very consistent; complete reversibility was always noted during thermal cycling.

More surface reliefs are shown in Fig. 3, which were the direct result of beta to alpha transformation during heating. As shown in Fig. 3 and Fig. 2B, clear cut variants are illustrated, indicating that well defined habit planes were present during the transformation. However, it was not common to see this behavior in all transformations. In fact, it was only about 20% of the time that results such as Fig. 3 and Fig. 2B were observed. During the other 80%, surface relief such as those at the bottom of Fig. 2C were observed. This phenomenon resulted because in order to see clear-cut variants in NiS, the grain orientation must have a special relation to the viewing direction. This can be further explained by analyzing Fig. 2B. As mentioned previously, this photomicrograph contained three large grains of beta NiS prior to thermal cycling. Although, these grains are from the same sample, the morphology of each is very different. The grain to the far right shows well defined variants, whereas the grain near the bottom does not show prominent surface relief. Without "correct" grain orientations, well defined crystallographic features are not observed in the microstructure.

3.3 Interference Microscopy

Figure 4A illustrates a large grain containing two bands of surface relief as a result of beta to alpha transformation. In this photomicrograph, alpha NiS surface relief is shown as dark bands within a light beta NiS grain. This was taken as soon as the first surface relief started to appear, in order to isolate the parent and product phase. Unlike the others, the initial transformation temperature was found to be 361° C, which is somewhat lower. The interference micrograph corresponding to part of Fig. 4A is shown in Fig. 4B. The fringe pattern in Fig. 4B indicates that both surface reliefs have the same tilt due to same habit plane variant. The displacement between the parent and product phase is shown by zig-zag fringes. A definite fringe shift can be seen, which appears to be characterized as an invariant-plane strain [12]. These characteristics are commonly found in typical martensites. In Fig. 4A, the scratches (shown as white lines) running perpendicular to the beta NiS grain were not affected by surface relief. If the scratches were deflected at the surface relief interface, then this would indicate shearing in the perpendicular direction to the the viewing direction. It is clear that the zig-zag fringe behavior in Fig. 4B confirms tilting. From these findings, it can be said that shearing must have occurred approximately in the direction parallel to the viewing direction.

3.4 Electrical Resistivity Measurements

Figure 5 illustrates the results from electrical resistivity measurements during the first, third, and seventh thermal cycles of beta NiS. The unit for resistance is arbitrary. After the seventh thermal cycle, the specimen fractured and no more data was obtained. Forward and reverse transformations were characterized by a sharp increase and decrease in resistivity, respectively. During the first heating cycle, two sharp transition points were noted. There was a sharp increase in resistance starting at 350° C and a sharp decrease starting at about 385° C. Moreover, during the first cooling cycle, there was a sharp decrease in resistance starting at 330° C.

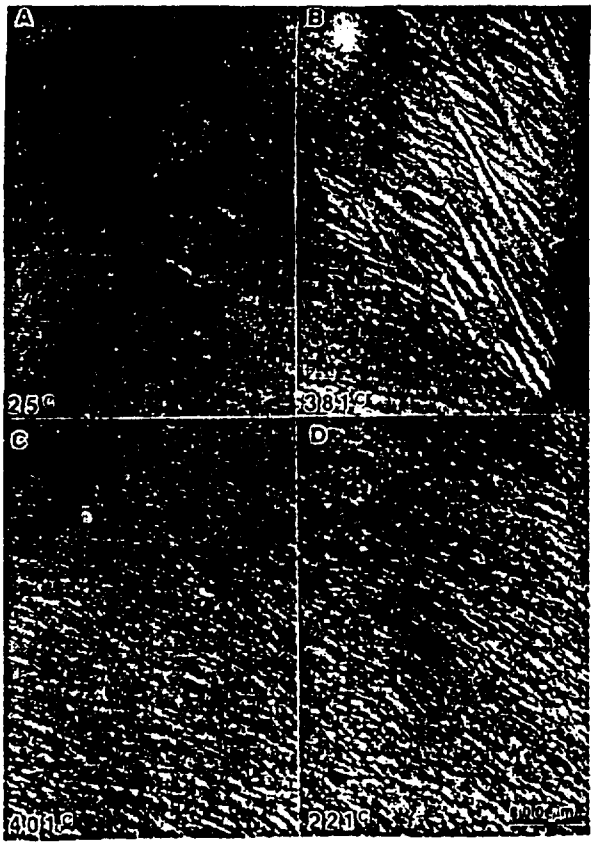

Fig. 2 - Photomicrographs of beta NiS during thermal cycling in the hot stage.

Fig. 3 - Photomicrograph of beta NiS during thermal cycling, illustrating alpha surface relief.

During heating cycle #3, there was a sharp decrease in the resistance starting at 385° C, which still remained the same. However, during cooling cycle #3, there was a sharp increase in the resistance starting at 298° C. Compared to first thermal cycle results, thermal conditioning of beta NiS increased the gap between the upper and lower transition points. Furthermore, thermal conditioning had an effect on the disappearance of the transition point at 350° C which was noted during heating cycle #1. Analysis of this beta NiS transition point will be discussed in the next section on dilatometry.

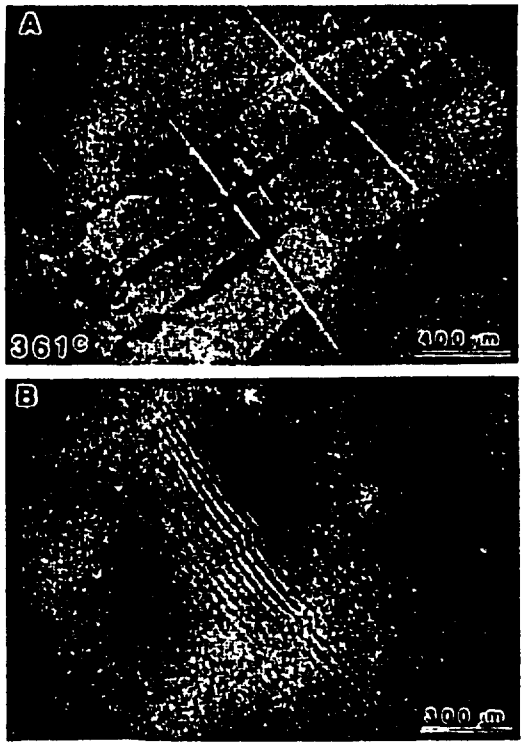

Fig. 4 - (A) Photomicrograph of alpha surface relief; (B) Interference micrograph of part in A.

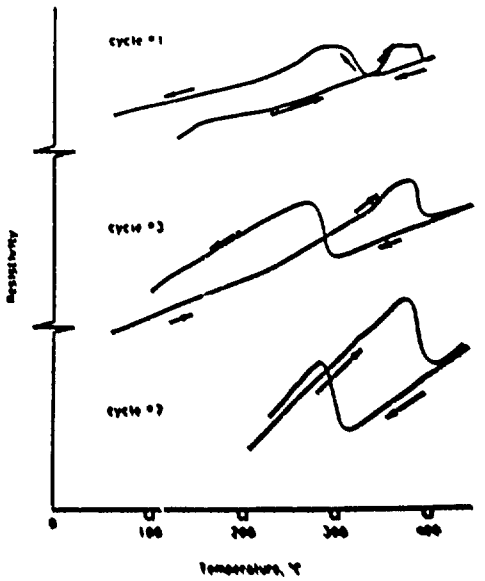

Fig. 5 - Electrical resistivity results of beta NiS, illustrating the effects of thermal cycling.

which is an indication of diffusionless process; (iv) the transformation process is clearly first order. All these microstructural features fall within the classification scheme for martensitic transformations. Although the general characteristics appear to fit the requirements for a martensitic transformation in the present experiment, more detail and quantitative results such as the crystallography of microstructures between the two phases are needed for a clear classification in the future.

4. CONCLUSIONS

In an effort to understand the mechanism of the alpha (high temperature) to beta (low temperature) transformation in NiS, the following experiments were performed: a) hot stage x-ray diffraction, b) hot stage optical microscopy, c) electrical resistivity measurements and d) dilatometry measurements. Hot stage x-ray diffraction confirmed the structural changes involved in forward (cooling) and reverse (heating) transformations in NiS. Thermal cycling of beta NiS showed reversibility of the transformations. The beta to alpha structural change of NiS was observed as surface relief through hot stage optical microscopy. The relief was the direct result of the beta to alpha transformation during heating. With the aid of a Nomarski interference contrast system, prominent surface relief was observed which corresponds to self-accommodating variants. Through interference microscopy, definite fringe shifts were seen, which appear to be characterized as an invariant-plane strain. Reversibility of the forward and reverse transformations was observed using polarized light for both alpha and beta NiS. Resistivity and dilatometry measurements produced large inverted S-shaped hysteresis loops, spanning temperature ranges of greater than 100 degrees. The angular mismatch between the hexagonal and rhombohedral structures evidently results in a large hysteresis loop. These inverted S-shaped hysteresis loops are found in martensitic materials. Assuming that the forward and reverse transformations in NiS are martensitic, A_s, A_f, M_s, and M_f temperatures are noted. Dilatometry measurements showed that the volume change associated with the transformation was 4.67%. All experimental results described in this paper appear to fit the characteristics of a martensitic transformation.

ACKNOWLEDGEMENT

The project is supported by Air Force Office of Scientific Research under contract: AFOSR-90-0174.

REFERENCES

1. Alsen, N.: Geol. For. Forth. Stockholm, 1925, 47, 19.
2. Kolkmeijer, N. H. and Moesveld, A. L. Th.: Zeits. Krist., 1931, 80, 91.
3. Grice, J. D.: Crystal structures of the Tantalum Oxide Minerals Tantalite and Wodginite and of Millerite NiS, (University of Manitoba, Winnipeg), 1973.
4. Kullerud, G. & Yund, R. A.: J. Petroleum, 1962, 3, 126.
5. Hsiao, C. C.: Fracture, 1977, 1, 987.
6. Jellinek, F., Sulfides in Inorganic Sulfur Chemistry, (Elsevier, Amsterdam), 1970.
7. Kriven, W. M.: J. Am. Ceram. Soc., 1988, 12, 1021.
8. Kim, B.: The Alpha to Beta and Reverse Transformation in NiS Ceramic, (University of Illinois, Urbana), 1992.
9. Cohen, M.: Phase Transformations in Solids, (John Wiley and Sons, New York), 1951.
10. Kurdyumov, G. P. and Maksimova, O. P.: Koklady Akad. Nauk S. S. S. R., 1948, 61, 83, 1950, 73, 95.
11. Cech, R. E. and Hollomon, J. H.: Trans. Amer. Inst. Min. Met. Eng., 1953, 197, 685.
12. Clark, H. M. and Wayman, C. M.: Phase Transformations, (American Society for Metals), 1970.
13. Kim, Y. D. and Wayman, C. M.: Scripta Metallurgica et Materialia, 1990, 24, 245.

Pittsburgh Plate and Glass Company (PPG). The exact processing conditions of both sets of samples were unknown.

Experimental Techniques

The inclusions in bulk glass samples, just visible to the naked eye, were examined optically by polarized light microscopy using a Leco Neophot instrument. They were then removed from the glass by cutting thin slices of glass with a diamond saw, marking the glass with a diamond pen and carefully crushing the glass up to them. Several inclusions were lost or broken in the process. Two inclusions that adhered well to the surface of the fractured glass were prepared for SEM observation by coating with vacuum-evaporated carbon.

To prepare samples for TEM, the inclusions were embedded in Eponate 12 epoxy resin. The embedding mixture formulation included 5.0 mL Eponate 12, 1.0 mL dodecanyl succinic anhydride, 4.0 mL nadic methyl anhydride, and 2.0 mL tri-[dimethyl amino ethyl] phenol. Embedding the samples was accomplished by first polymerizing shallow blanks of the mixture in a silicone mold, then placing the stone on the blank, filling the mold with the mixture, and then repolymerizing for 48 h. Using a razor blade, the casting was trimmed to a pyramid having an approximately 0.5 × 0.5 mm square face, the center of which contained the embedded particle. Sections approximately 900 Å thick were then cut using a Reichert OM U2 ultramicrotome equipped with a diamond knife. The cutting speed was 1 mm/s. The sections were recovered onto 400-mesh copper TEM grids, air-dried, and coated with a thin film of vacuum-evaporated carbon in readiness for TEM. TEM was performed using a Philips EM 420 instrument operated at 120 KeV, in conjunction with an EDAX 9900 system equipped with an Si-Li X-ray detector. Single crystal and polycrystalline selected area diffraction (SAD) patterns were obtained using a large objective aperture and analyzed.

Experimental Results

Microstructures

The results obtained on the samples from Dr. Swain are presented in Figs. 1–3. Figure 1 shows an inclusion within a bulk glass. This transmitted polarized light optical micrograph revealed the strain field around the inclusion. In this particular case, no inhomogeneity with localized strain could be seen. Although the particle was about 250 μm in diameter, no cracks were observed around it, suggesting that the particle had not transformed or that the extent of transformation was not sufficient to induce fracture. A scanning electron micrograph of an inclusion located at the fracture surface is shown in Fig. 2. This inclusion, about 200 mm in diameter, adhered strongly to the

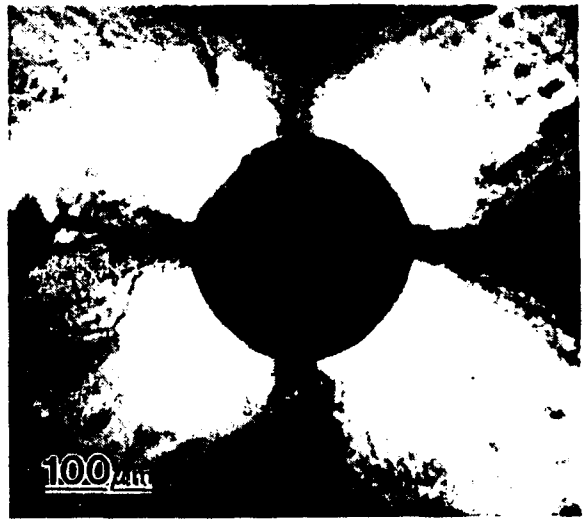

Fig. 1. Polarized light micrograph of a nickel sulfide stone embedded in t bulk plate glass showing birefringence around the embedded stone.

Fig. 2. Scanning electron micrograph of an inclusion at the fracture origin the tempered plate glass. The particles strongly adhered to the surface.

Ceramic Science and Eng. Proceedings
14 [3-4] 284-294 (1993)

Microstructural Investigation of Fracture-Initiating Nickel Sulfide Inclusions in Glass

O.O. POPOOLA, J.J. COOPER, AND W.M. KRIVEN

Department of Materials Science and Engineering
University of Illinois at Urbana-Champaign
Urbana, IL 61801

Transmission electron microscopy (TEM) was used to investigate the microstructure and the microchemistry of nickel sulfide inclusions in plate glass. TEM samples from inclusions recovered from both fracture surfaces and bulk glass were prepared by ultramicrotomy. The inclusions were polycrystalline and contained predominantly $Ni_{1-x}S$ phases. Traces of Ni_3S_2 and Ni_7S_6 were also found. Electron diffraction analyses showed that the inclusions on the fracture surfaces were β-NiS, while those from the unfractured bulk glasses were α-NiS. These results confirmed the hypothesis that the volume increase associated with the α-to-β transformation in NiS caused fracture. The glass processing conditions determined the microstructure of the inclusions.

Introduction

The spontaneous fracture of thermally toughened plate glass has been attributed to the presence of nickel sulfide inclusions.[1-3] These inclusions, typically 150 μm in diameter, were formed as a result of the chemical reactions between sodium sulfate (Na_2SO_4) and a nickel compound in the presence of a reducing agent during glass manufacture. Their small size has limited the methods available for characterizing them. Using scanning electron microscopy (SEM) and energy dispersive spectroscopy (EDS), Bradt[4] found them to be composed of nickel and sulfur and noted that it was probable that the stones were polycrystalline and not single phase. Hsiao[5] examined a small stone from a fracture surface and identified both α-NiS and β-NiS by X-ray diffraction; similar findings were reported by Ballantyne.[6] A study of sulfide inclusions in plate glass by electron probe microanalysis (EPMA)[1] identified sulfide stones of various compositions, including Ni_3S_2 and $Ni_{1-x}S$. Two alternative explanations for the fracture-initiating behavior of the nickel sulfide stones have been proposed. Many workers suggested that on cooling, the phase transformation of the α-NiS to β-NiS, which is accompanied by a 4% volume increase, is responsible for the fracture of the thermally tempered plate glass.[6] The transformable phases that may produce significant volume changes in the Ni-S system (thereby causing fracture) are $Ni_{1-x}S$, Ni_3S_2, and Ni_7S_6.[8] Table I lists their characteristics, where $\Delta V = (V_2 - V_1)/V_1$, and V_1 is the molar volume of the parent phase.

In all cases the extent of volume change is dependent on the transformation temperature and the stoichiometry. The high-temperature phases can be metastably retained down to low temperatures by stoichiometry offsets, impurity additions, and rapid quenching. The metastably retained phases have been found to transform with time at room temperature.[2,5] A detailed analysis of the strain field around the inclusions showed that a critical size of 60 μm was needed for fracture to occur.[5,7] For an inclusion 200 μm in diameter, a partial α-to-β transformation resulting in a 2% volume increase was found to generate sufficiently high internal stress to initiate fracture viscoelastically[5] in a fully tempered plate glass.

An alternative explanation was that the instantaneous fracture may be attributed to the thermal expansion mismatch between the particles and the glass matrix. A study of the glass with additions of nickel sulfide impurities[8] concluded that the fracture-initiating stones were not necessarily the NiS compound, and that the cause of fracture was the thermal expansion mismatch between the nickel sulfide phases and the glass matrix. For example, it is known[9] that pentlandite, $(Fe,Ni)_9S_8$, a naturally occurring mineral, has an unusually large coefficient of thermal expansion.

Although some optical and scanning electron microscopy studies of these stones have been performed,[2,10-12] the essential microstructural features (phase identification, grain sizes, twinning, etc.) needed to understand the nature of the phase transformations are yet to be determined. The inclusions are generally too small for X-ray analyses, and analytical electron microprobe results are only indicative of overall compositions. The aim of this communication is to report the results of a TEM investigation of these inclusions. Two sets of samples were studied. The first, supplied by Dr. M. Swain, consisted of fractured and bulk glasses obtained from the Commonwealth Scientific Investigation and Research Organization (CSIRO) in Melbourne, Australia. The second set, supplied by Dr. A. Mishra, were bulk glasses made by the

Table I. Transformable Nickel Sulfur Compounds

Compound	Low-Temperature Phase	High-Temperature Phase	Transformation Temperature (°C)	Volume Change (ΔV) (%)
Ni_3S_2	Rhomb, *R3m*	Cubic, *F43m*	565	3 to −6.5
Ni_7S_6	Ortho, *C222*	Ortho, *Bmmb*	397	≈30
$Ni_{1-x}S$	Rhomb, *R3m*	Hex, $P6_3/mmc$	282–379	2.3 to 4

Fig. 3. (*a*) Transmission electron micrographs of ultramicrotomed inclusion from CSIRO showing slivers of nickel sulfide. The sample underwent a significant deformation during specimen preparation. (*b*) Ultramicrotomy—induced chatter. Note that there was no contrast variation across the boundaries. (*c*) Microstructure showing the grain boundaries (arrowed), confirming the polycrystalline nature of the inclusions. (*d*) Internally twinned sliver.

Fig. 3. (Cont'd.)

glass matrix and could be readily seen at the fracture origin. Its surface was very rough and had numerous cracks.

A low magnification, bright-field TEM micrograph of the ultramicrotomed section is shown in Fig. 3(*a*). It consisted of many slivers separated by cracks. This indicated that extensive deformation occurred during ultramicrotomy. Other microstructural features are shown in Fig. 3(*b–d*). Figure 3(*b*) shows the characteristic chatter morphology of ultramicrotomed samples, readily identifiable by the absence of contrast variations across the boundaries. Figure 3(*c*) shows the polycrystalline nature of the inclusions. Apart from the fine chatter and knife scratches, the grain boundaries can readily be identified (see arrows). Figure 3(*d*) shows an internally twinned sliver. The twin width was about 0.01 μm. Contrast variation across the twin boundaries was clearly visible. Some of the twin boundaries contained cracks. The microstructure of the inclusions recovered from the PPG glass is shown in Fig. 4. These inclusions were also polycrystalline and extensively faulted.

Electron Diffraction Analyses

Figure 5 summarizes the electron diffraction analyses from all of the samples. The sample recovered from the fracture surface contained predominantly β-NiS (Fig. 5(*a,b*)) with traces of α-NiS. A few grains of Ni_3S_2 and Ni_7S_6 were also observed as evidenced by the large aperture SAD pattern shown in Fig. 5(*c*). Apart from Ni_3S_2 and Ni_7S_6 impurities, the inclusions in the unfractured bulk glasses contained the α-NiS phase. No β-NiS phase was identified in these samples. EDS analyses from all the samples showed Ni and S peaks, with occasional traces of Fe. Most of the analyses lay between $Ni_{60}S_{40}$ and $Ni_{50}S_{50}$. Compositional variations were observed both within and between samples. Table II summarizes the results obtained for all cases.

Discussion

The use of ultramicrotomy to prepare the tiny stones for TEM observations was of mixed advantage. It enabled semiquantitative, microchemical analyses, which could not otherwise have been performed, and allowed the observation of the microstructure of the stones. However, it induced permanent strain damage that produced streaks and distorted the diffraction patterns, thus rendering their interpretation difficult. This investigation showed that the microstructure of the inclusions depended on the glass processing conditions. The samples supplied by Dr. Swain were polycrystalline with occasionally twinned grains, while those from PPG were highly faulted crystals. These microstructural differences could affect the transformability of the metastably retained α-NiS.

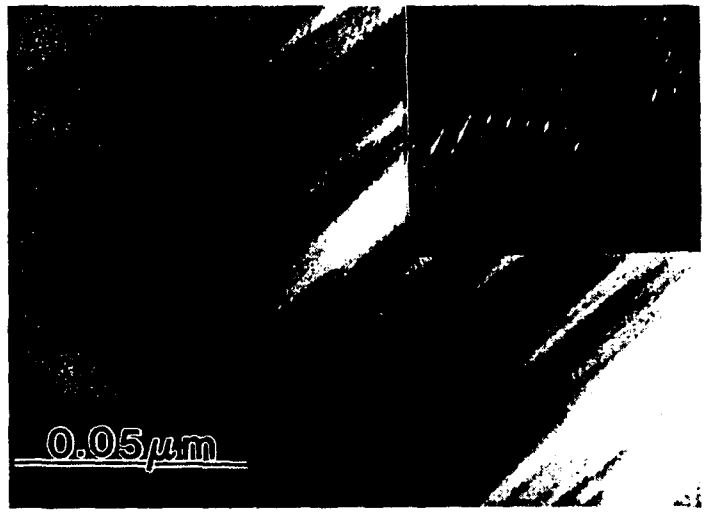

Fig. 4. The microstructure of the inclusion from the PPG bulk glass specimen showing extensive faults. The sample was polycrystalline and the associated diffraction pattern (insert) showed streaks.

EDS analysis, although not sufficiently quantitative to allow outright identification of phases, confirmed that the composition of the stones was indeed nickel sulfide. The variation in Ni:S ratio observed both within and between samples was believed to indicate the presence of various nickel sulfide compounds, which strongly suggested that the stones were polycrystalline and not single phase. The identification of regions of pure nickel or nickel oxide by EDS supported this conclusion. This polycrystallinity was confirmed by TEM bright-field images.

The microcrystalline ring diffraction patterns observed in large aperture SAD patterns provided further evidence of the presence of various nickel sulfide phases in the stones from different glass samples. Analysis of the stones from bulk glass clearly showed that α-NiS was the major phase in this sample. The same type of results from the stone found at the fracture origin indicated just as clearly that β-NiS was the major phase present in these fracture-initiating stones. These results were consistent with the hypothesis that fracture of the glass occurred as a result of the α-to-β transformation in NiS. There are several possible scenarios for the fracture of the glass as a result of phase transformation within the stone. The rough surface of the stone provided inhomogeneities at the particle/glass interface, which would be the most likely site for nucleation at flaws.

Acknowledgments

This work was supported by the Air Force Office of Scientific Research under grant number AFOSR-89-0300. Use of the electron microscope facilities at the Center for Microanalysis of Materials in the Materials Research Laboratory at UIUC is gratefully acknowledged. Thanks are due to Dr. M. Swain of the University of Sydney, Australia, and Dr. A. Mishra of the Pittsburgh Plate and Glass Co. for supplying the glass samples.

References

[1]H. Tabuchi, *10th International Congress on Glass*, Ceramic Society of Japan, Kyoto, Japan, July 1974.
[2]R. Wagner, *Glastech. Berichte* (in French) 50, 296 (1977).
[3]L. Merker, *Glastech. Berichte* (in German) 47, 116 (1974).
[4]R.C. Bradt, *Alfred University Fractography Conference*, August 1986.
[5]C.C. Hsiao, *Fracture 1977, Vol. 3.* ICF4, Waterloo, Canada.
[6]E.R. Ballantyne, CSIRO Division of Building Research Report, Melbourne, 1961.
[7]A.G. Evans, *J. Mater. Sci.*, 9, 1145 (1974).
[8]Internal Report, St. Gobain Glass Industries, France.
[9]V. Rajamani and C.T. Prewitt, *Am. Mineral.*, 60, 39 (1974).
[10]M.V. Swain, *J. Mater. Sci.*, 16, 151 (1981).
[11]O.O. Popoola, J.J. Cooper, B.P. Jakstys, and W.M. Kriven, *MRS Proc.*, 254, 271 (1992).
[12]J.J. Cooper, O.O. Popoola, and W.M. Kriven; p. 186 in *Proceedings of the International Ceramic Conference.* Edited by J.M. Bannister. CSIRO Publications, 1992.
[13]J.J. Cooper, M.S. Thesis, University of Illinois, 1992.
[14]T.K. Gupta, F.F. Lange, and J.H. Bechtol, *J. Mater. Sci.*, 13, 1464 (1978).
[15]J.S. Nadeau and J.J. Dickerson, *J. Am. Ceram. Soc.*, 63 [9–10] 517 (1980).
[16]D. Bunis, *Science of Ceramics, Vol. 1.* Edited by G.H. Stewart. Academic Press, New York, 1962. P. 315.

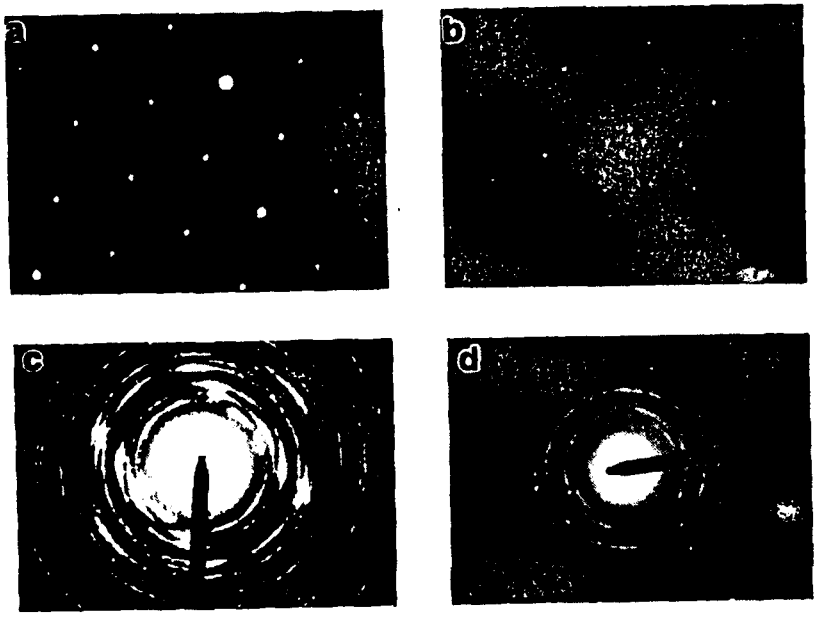

Fig. 5. SAD patterns from nickel sulfide inclusions in plate glass: (*a*) [0001] α-NIS obtained from CSIRO bulk glass; (*b*) [0001] β-NiS obtained from the inclusion at the fracture surface of CSIRO broken glass; (*c*) β-NiS ring pattern obtained from the same inclusion as in (*b*); (*d*) α-NiS polycrystalline ring pattern obtained from PPG bulk glass.

Table II. Principal Phases Detected in Nickel Sulfide Inclusions

Sample	Fracture Origin	Swain's Bulk Glass	Mishra's Bulk Glass
Phases identified	β-NiS, traces of α-NiS	α-NiS; no β-NiS, nickel oxide, or nickel	α-Nis, no β-NiS

The stresses generated by the volume increase (2–4%, depending on the precise composition and lattice parameters) accompanying the phase transformation are postulated to be the driving force for nucleation and propagation of the transformation. Since the stones were polycrystalline, transformation was possible within each α-NiS grain. Transformation may have occurred grain by grain over time depending on grain size, twin width, and temperature. If transformation were gradual, nucleation and growth of the critical flaw may have been gradual also, with each additional increment of transformation stress causing either a new nucleation event or propagation of the existing microcrack(s). The α-to-β transformation in NiS does not appear to be stress inducible. Repeated mechanical polishing, under various loads, of both fine- and coarse-grained surfaces of the α phase did not produce any X-ray detectable β phase.[13] Instantaneous stress buildup resulting from spontaneous transformation caused by autocatalysis could thus be ruled out.

It appeared unlikely that the fracture was caused by thermal expansion mismatch between the particles and the glass matrix. Studies of Al_2O_3-toughened glasses showed that for large particles, thermal expansion mismatch caused weakening, whereas for small particles strengthening occurred.[14–16] The weakening/toughening transition, considering only thermal expansion mismatch, was found to occur for an inclusion size of 40 μm. The calculations of Evans et al.[7] showed that the mechanical stresses generated as a result of the α-to-β transformation in a 60-μm NiS inclusion were enough to cause spontaneous fracture of plate glass. The fact that particles larger than 150 μm randomly dispersed in the glass did not necessarily cause fracture negates the thermal expansion mismatch hypothesis.

Field observation[10] *of the failure of the plate glass windows indicated a* dependence on ambient temperature, with more window failures recorded from the hotter side of buildings. A time dependence of failure is also implied by the variable time to failure of the various windows. These observations would be consistent with either hypothesis for the role of the phase transformation. Calculation of the total stresses generated by complete transformation of particles[6] indicated that the stresses for particles above a critical size would be sufficient to cause failure of the glass matrix. However, gradual relaxation and residual stress activity in the glass matrix surrounding the polycrystalline stone, combined with thermal cycling due to ambient temperature fluctuations, seems to be a likely mechanism of nucleation of the α-to-β transformation leading to fracture.

Conclusion

Small, spherical, silver-colored stones found in plate glass were analyzed microchemically and were found to contain nickel and sulfur in ratios between Ni and $Ni_{50}S_{50}$ (at%). The stones were polycrystalline and possibly polyphasic. Compositions appeared to vary from stone to stone, with some compositions being less harmful to the glass than others. Electron diffraction allowed the identification of α-NiS in unfractured glass and β-NiS in fractured glass. The results were consistent with the hypothesis that the α-to-β transformation in NiS played a role in initiating fracture in tempered plate glass containing nickel sulfide stones.

YTTRIM BARIUM COPPER OXIDE ($YBa_2Cu_3O_{6+x}$)

Physica C 212 (1993) 470–477
North-Holland

PHYSICA C

Concentration-dependent oxygen diffusivity in $YBa_2Cu_3O_{6+x}$
I. Argon annealing studies

John R. LaGraff [1] and David A. Payne
Department of Materials Science and Engineering, Materials Research Laboratory, Science and Technology Center for Superconductivity, University of Illinois at Urbana-Champaign, Urbana, IL 61801, USA

Received 8 February 1993

Electrical resistance measurements were used to follow the isothermal in-diffusion characteristics in $YBa_2Cu_3O_{6+x}$ (YBCO) as a function of the initial oxygen content, x, at temperatures ranging from 650–708°C. Prior to the determination of oxygen in-diffusion rates, the initial oxygen contents in both polycrystalline and single crystal specimens were controlled by out-gassing in argon for different periods of time. An increasing dependence of the chemical diffusivity with decreasing initial oxygen content was observed which was typical of a vacancy diffusion mechanism. However, the magnitude of the dependence (and comparison with tracer diffusion studies) suggested that other factors (e.g., correlation effects or the thermodynamic factor) were responsible for the concentration dependence. The results are important for the development of atomic diffusion models for the oxygen mobility in YBCO.

1. Introduction

The overall oxygen content and ordered configurations in YBCO are known to strongly influence both the superconducting and normal-state properties [1,2]. Consequently, measurements of the chemical diffusivity $\tilde{D}$ of oxygen in YBCO are important for the predetermination of the proper temperatures and times required for the processing of YBCO with fixed oxygen contents for specific property requirements. In addition, knowledge of the chemical diffusivity of oxygen, in conjunction with tracer diffusion D^* measurements [3,4], will assist in establishing the fundamental diffusion mechanisms active in YBCO over different temperature ranges and oxygen non-stoichiometries. In this (Part I) and subsequent papers [5,6], electrical resistance measurements are reported as a function of oxygen content in order to examine the diffusion kinetics as a function of concentration in single crystal and polycrystalline YBCO. We discuss the implications these results have on the development of a diffusion model.

Conflicting oxygen diffusion concentration dependences have been reported primarily for polycrystalline specimens by tracer diffusion [3,4,7], internal friction [8], electrical resistance [9], and thermogravimetric measurements [10]. Rothman et al. [4] reported no oxygen partial pressure dependence of the tracer diffusivity, D^*, at 400°C and 600°C suggesting that D^* was not a function of the vacancy concentration at least within an experimental uncertainty of a factor of two. Other tracer diffusion measurements [7], however, reported an *increasing* diffusivity with increasing oxygen content. Thermogravimetric analysis suggested a similar dependence in $\tilde{D}$ which was attributed to a compositional dependence of the enthalpy of motion term in the self-diffusivity [10]. On the other hand, an electrical resistance study [9] reported activation energies for oxygen in-diffusion, ranging from 0.5–1.3 eV as the oxygen content x varied from 0.62–1.0, which suggested that the diffusivity would *decrease* with increasing oxygen content. No dependence was reported for oxygen out-diffusion on the concentration [9]. Internal friction measurements [8] also deter-

[1] Present address: Department of Chemistry and Materials Research Laboratory, University of Illinois at Urbana-Champaign, Urbana, IL 61801, USA.

mined an activation energy for oxygen migration which decreased as the oxygen content decreased below $x=0.75$. Models predicted a concentration-dependent diffusivity which should *increase* with *decreasing* oxygen content for all x [11,12].

It is evident that a clear consensus regarding the influence of oxygen concentration on the chemical diffusivity has not yet emerged; consequently, the underlying diffusion mechanisms are still unknown. In this and subsequent papers [5,6], resistance measurements during oxygen in-diffusion are reported which indicate an *increasing* chemical diffusivity with *decreasing* oxygen content in both the orthorhombic and tetragonal phase regions of YBCO. In this paper (Part I), the initial overall oxygen contents in the specimens were established by out-gassing in argon for different periods of time. In Part II [5], controlled oxygen partial pressures were used to uniquely set the initial and final oxygen concentrations in YBCO specimens during in-diffusion and out-diffusion. The use of different oxygen partial pressures also allowed for the estimation of equilibrium defect chemistry. In Part III [6], the concentration-dependent diffusion results will be discussed in relation to other reported diffusion measurements and models in order to develop an oxygen diffusion mechanism(s) for YBCO.

2. Experimental

Electrical resistance measurements have been used by others to make diffusion measurements in NiO and CoO [13,14] since they provide a sensitive probe to small changes in the concentration of the diffusing species. Electrical measurements are also ideal for monitoring the oxygen content in YBCO [9,15,16] especially in small single crystals [17–20] where a low mass precludes the use of other techniques (e.g., thermogravimetric analysis). In addition, repeated measurements are possible on a single specimen which removes some of the sample-to-sample variation that can occur in tracer diffusion studies. Measurements were made in both orthorhombic (650°C) and tetragonal (708°C) phase regions for the single crystals and at 708°C in polycrystalline specimens. Sample preparation was described previously [18] and specimen characteristics are summarized in table 1. Superconducting transition temperatures were determined from SQUID susceptibility measurements in a field of 10 G (table 1). Impurity analyses were determined by an inductively coupled plasma emission technique.

Four gold wire leads (0.002 inch, Be-modified) were attached by silver paste to the corners of the rectangular crystals or along the length of rectangular polycrystalline bars (fig. 1). The specimens were subsequently mounted inside the hot-stage of an optical microscope. The annealed electrodes had contact resistances of less than $\sim 1\ \Omega$ and were periodically tested for space charge build-up and overall integrity in both positive and negative DC potentials. The electrical resistance was monitored by a computer-controlled Stanford SR530 lock-in amplifier with a measuring AC current of 1.86 mA at 564 Hz. the ambient gases (argon or oxygen) were scrubbed for water vapor and carbon dioxide by passing through a column containing CaO and $CaSO_4$. The resistance was recorded every 30–60 s during out-diffusion and between 8 and 15 s during in-diffusion. A typical resistance experiment contained at least a thousand data points which were subsequently used for data analysis. The small chamber volume ($\sim 50\ cm^3$) of the hot-stage assembly ensured rapid purging of the gas and re-establishment of equilibrium for the new has mixture.

The initial oxygen content x of the YBCO specimens was established by out-gassing in argon for different times. The YBCO specimen was first equilibrated in 100% oxygen at the desired temperature until the resistance remained constant for at least 24 h. Upon introduction of argon, the resistance increased linearly (e.g., fig. 2) until, after long times, the resistance saturated as x approached zero. By measuring the resistance of a YBCO specimen as a function of oxygen partial pressure at a fixed temperature [5], it was possible to construct calibration curves (fig. 3) relating the oxygen content, x, to the overall sample resistance, R, from the following expression:

$$R=R_0 \exp[a(6+x)]\ . \qquad (1)$$

For crystal C1 at 708°C the maximum (3.4 Ω) and minimum (0.132 Ω) resistances corresponded to 6.0 and 6.6 oxygens per unit cell, respectively [21], where $R_0=4.456\times10^{14}\ \Omega$ and $a=-5.42$ (fig. 3).

Table 1
Sample characteristics

Selected specimen	T_c	Specimen size (mm^3)	Electrical resistivities [a]	Impurity content [b]
Crystal C1 [c]	90 K	1×1×0.05	100 μΩ cm (25°C) 1–10 mΩ cm (600–780°C)	Fe: 0.0012(1) Al: 0.0049(3) Zr: 0.0001(1)
Crystal C2 [d]	90 K	2×1.5×0.5	100 μΩ cm (25°C) 1–10 mΩ cm (600–780°C)	Fe: 0.0036(2) Al: 0.0010(2) Zr: 0.020(1)
Polycrystal S2	92 K	4.65×1.50×0.95	3–30 mΩ cm (350–780°C)	Fe: 0.0018(1) Al: 0.0000(3) Zr: 0.0033(4)

[a] Ref. [20].
[b] Impurity analysis determined by an inductively coupled plasma (ICP) method. Values are in atomic fractions per formula unit of YBCO.
[c] Grown in an alumina crucible.
[d] Grown in an yttria-stabilized zirconia (YSZ) crucible.

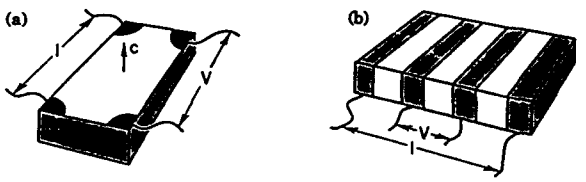

Fig. 1. Electrical four-point probe configurations for, (a) single crystal (*c*-axis indicated) and (b) polycrystalline YBCO. The current and voltage leads are labeled *I* and *V*, respectively.

During the argon anneal, the resistance increased with increasing time, with a corresponding decrease in the overall oxygen content (fig. 2). Halting the argon anneal after different periods of time (5 min to 20 h) established the initial value of the resistance and hence the initial overall oxygen content for crystal C1 prior to in-diffusion (eq. (1)). The reproducibility was excellent as indicated by the identical slopes of the resistance change with time (dR/dt) during each out-diffusion run (i.e., the slope in fig. 2). The recovery of the initial resistance (R=0.132(5) Ω; 100% oxygen) between each run indicated the absence of any irreversible phase decomposition or any significant kinetic de-mixing [22,23]. Following the argon anneal, isothermal oxygen in-diffusion measurements were made by re-introducing oxygen into the hot-stage. Variations in the diffusion kinetics were subsequently correlated to the initial average values of x. This technique did not ensure a constant oxygen concentration profile across the specimen (unless diffusion was surface-reaction limited [19]); however, it was extremely versatile and enabled diffusion kinetics to be measured for a large number of different values of x.

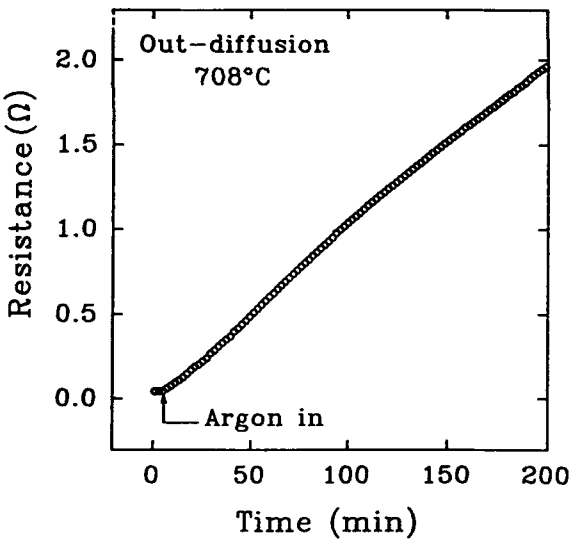

Fig. 2. The electrical resistance as a function of time during oxygen out-diffusion in an argon ambient for single crystal C1 at 708°C. The crystal was initially in equilibrium with 100% oxygen. As the resistance increased, the overall oxygen content decreased.

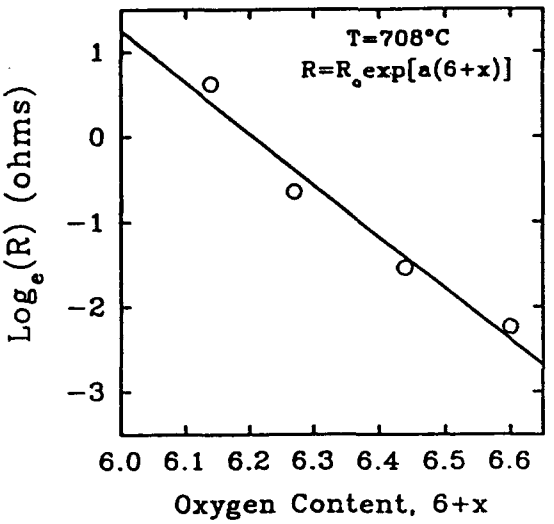

Fig. 3. Calibration curve (see eq. (1)) for the dependence of the electrical resistance as a function of oxygen content at 708°C for crystal C1.

3. Results and discussion

Figure 4(a) shows several in-diffusion curves for crystal C1 at 708°C after several different starting resistances. The non-linear behavior implies a non-standard diffusion process at the onset of in-diffusion. Assuming that a single diffusion mechanism characterized by a constant diffusion coefficient was active in tetragonal YBCO, one would expect the normalized resistance curves to be identical regardless of the initial oxygen content of the crystal. In fig. 4(b), however, the normalized resistances reveal a systematic variation in their functional form which depends upon the initial oxygen content of the YBCO crystal. This indicates a fundamental change in the chemical diffusivity of oxygen with concentration.

Characteristic relaxation times, τ, were obtained by fitting the resistance data to the long-time solution ($n=0$) for three-dimensional diffusion into a rectangular solid

$$\frac{\ln(R(0))-\ln(R(t))}{\ln(R(0))-\ln(R(\infty))} = 1-\left(\frac{8}{\pi^2}\right)^3 \sum_{n=0}^{\infty} \frac{1}{(2n+1)^2} \exp\left(\frac{-(2n+1)^2 t}{\tau}\right), \quad (2)$$

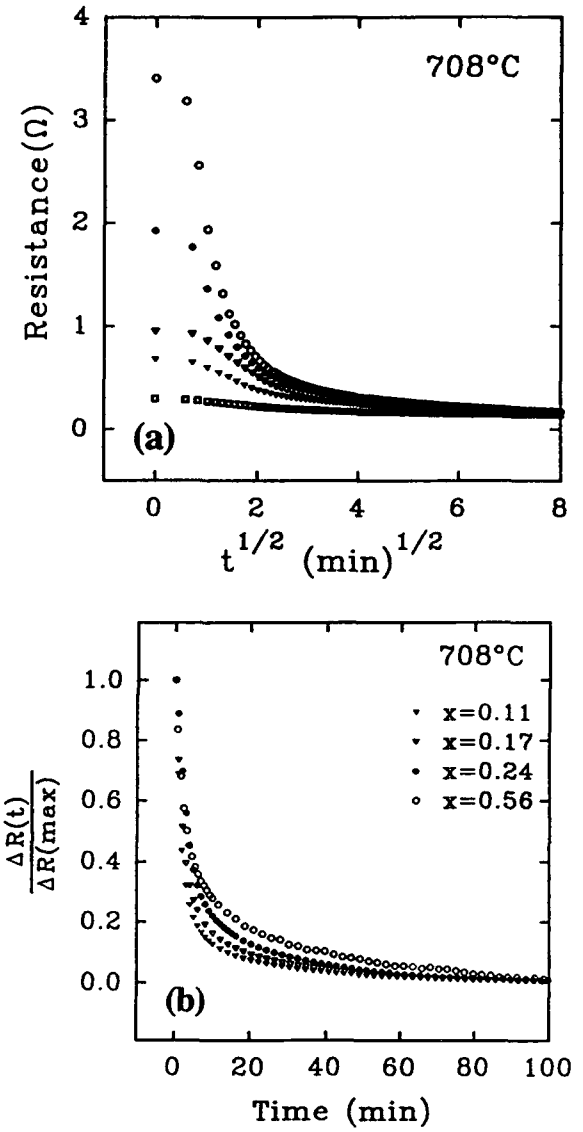

Fig. 4. (a) Resistance as a function of the square-root of time for oxygen in-diffusion from different initial resistance states (i.e., oxygen contents). (b) Normalized resistance from several curves in (a) showing different functional forms for the in-diffusion isotherms as a function of initial oxygen content.

where $R(0)$ is the resistance at the beginning of in-diffusion, $R(t)$ the resistance as a function of time, and $R(\infty)$ the eventual saturation resistance [20]. The exponential dependence of the resistance on the oxygen concentration was indicated in eq. (1) and has been described elsewhere [20]. Figure 5 shows

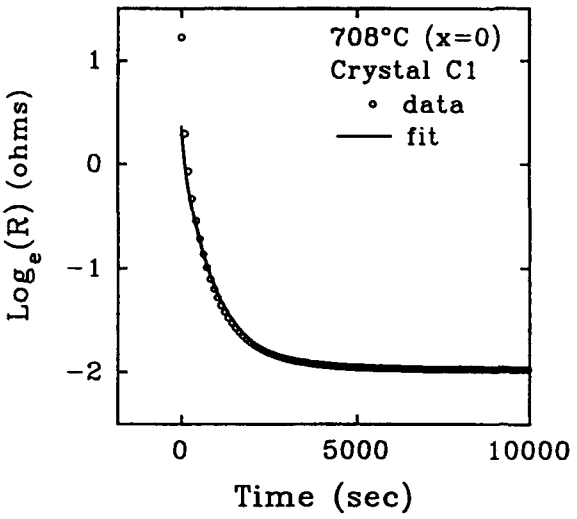

Fig. 5. Experimental data (open circles) during in-diffusion for the fully deoxygenated ($x=0$) crystal C1 at 708°C and the fit (solid line) to eq. (2).

a typical curve fit ($n=0$) for in-diffusion in crystal C1 which had an initial oxygen content of $x\sim 0$.

For both tetragonal and twinned orthorhombic crystals of dimensions $a\times b\times c$, the in-plane diffusivity $\tilde{D}_{ab}$ is

$$\tilde{D}_{ab}=\frac{1}{\pi^2\tau}\left(\frac{1}{a^2}+\frac{1}{b^2}+\frac{1}{\beta c^2}\right)^{-1}, \qquad (3)$$

where β is the anisotropy ratio between $\tilde{D}_{ab}$ and the c-axis diffusivity, $\tilde{D}_c$. The anisotropic tracer diffusivity, $\beta=D^*_{ab}/D^*_c\sim 10^4$–$10^6$ (ref. [4]) suggests that oxygen exchange will occur almost entirely at the edges of a single crystal; i.e., it will be a two-dimensional process and the third term in eq. (3) may be neglected. Characteristic relaxation times are given in fig. 6(a) as a function of the initial oxygen content for crystal C1. As a first approximation, diffusivities were calculated from eq. (3) using the relaxation times in fig. 6(a), the crystal dimensions ($1\times 1\times 0.05$ mm^3), and an anisotropy ratio β greater than 10^3 (fig. 6(b)). Figure 6 indicates a four-fold decrease in τ (or increase in $\tilde{D}_{ab}$) with decreasing concentration from 6.6 to 6.0 oxygen per unit cell. It should be noted that eqs. (2) and (3) were developed for a constant diffusion coefficient and, therefore, the diffusivities calculated in this paper

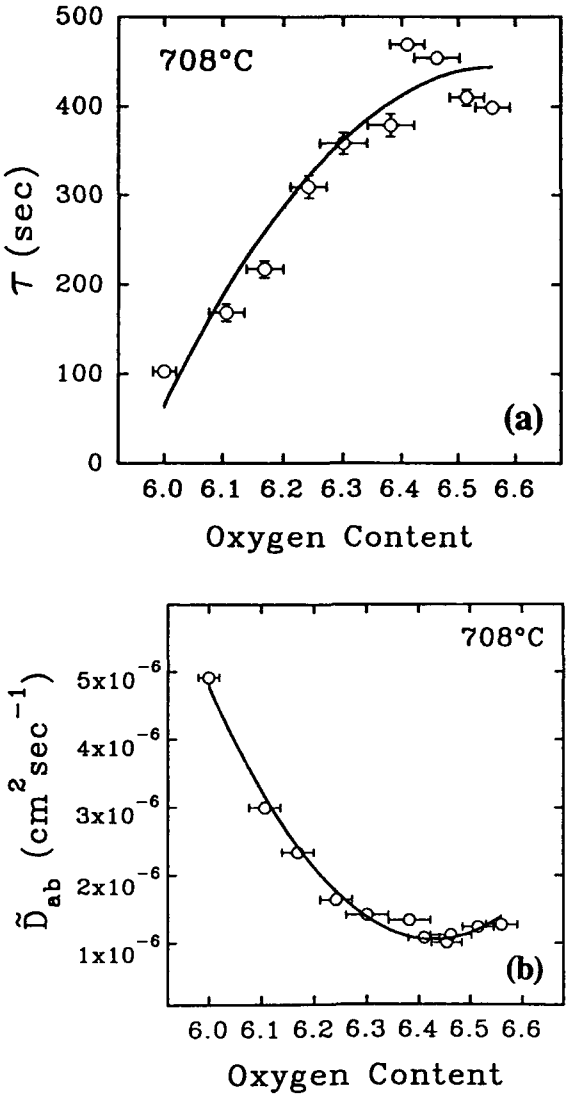

Fig. 6. (a) Relaxation times for crystal C1 determined from fig. 3 as a function of the initial oxygen contents (eq. (2)). (b) Calculated chemical diffusion coefficients (eq. (3)) for oxygen in-diffusion as a function of the initial oxygen content for crystal C1 ($a=b=0.1$ cm).

should be regarded as average values between different oxygen concentrations.

A similar analysis was carried out for crystal C2 at 650°C and 708°C, at temperatures which correspond to the orthorhombic and tetragonal phases, respectively, when in equilibrium with 100% oxygen. Figure 7 shows the diffusivities determined from eqs.

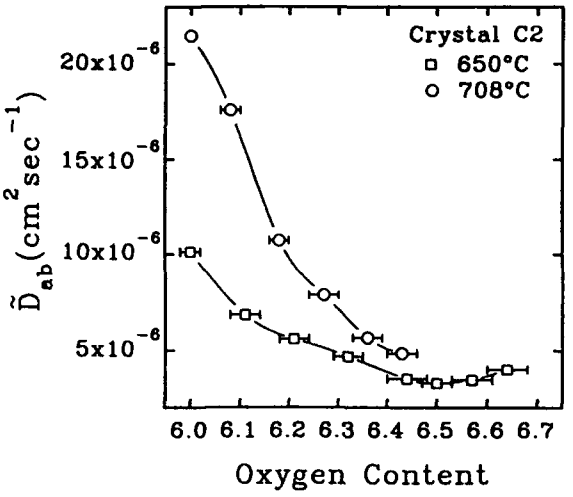

Fig. 7. Chemical diffusion coefficients (eq. (3)) for crystal C2 at 650°C and 708°C as a function of the initial overall oxygen content ($a=0.2$ cm, $b=0.15$ cm).

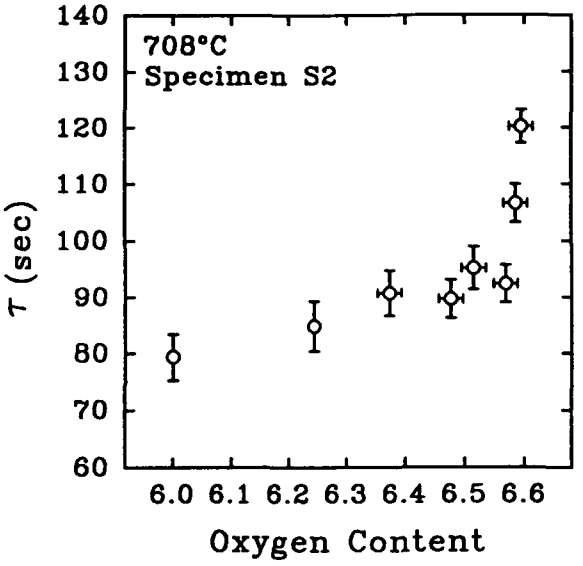

Fig. 8. Relaxation times for polycrystalline specimen S2 during oxygen in-diffusion as a function of the initial oxygen content.

(2) and (3) as a function of the initial overall oxygen content. The chemical diffusivities increased with decreasing oxygen content at both temperatures similar to the behavior of crystal C1 at 708°C (fig. 6(b)).

Diffusion measurements were also carried out on a polycrystalline specimen S2 at 708°C (fig. 8) after annealing in argon. Relaxation times were determined from a one-dimensional form of eq. (2) written as

$$\frac{\ln(R(0))-\ln(R(t))}{\ln(R(0))-\ln(R(\infty))} = 1-\left(\frac{8}{\pi^2}\right)\sum_{n=0}^{\infty}\frac{1}{(2n+1)^2}\exp\left(\frac{-(2n+1)^2 t}{\tau}\right). \quad (4)$$

Figure 8 indicates the relaxation times were more rapid than for single crystals and they decreased with decreasing oxygen content over a narrower oxygen concentration range. The different functional forms of $\tilde{D}$ (or τ) with x between single crystals (figs. 6 and 7) and polycrystals (fig. 8) suggest that extrinsic microstructural factors influence diffusion in polycrystalline specimens [20].

A concentration-dependent *chemical* diffusion coefficient has been inferred from reports of activation energies which varied with oxygen content and temperature [9,10]. In this study, however, the kinetics of oxygen diffusion were determined as a direct function of the oxygen content at constant temperature. Values of $\tilde{D}$ for crystals were found to change by about a factor of four (figs. 6 and 7) over the range of oxygen non-stoichiometry, x, available at the measurement temperatures. This large change cannot simply be explained by factors within the expression for the self-diffusivity,

$$D^* = \tfrac{1}{4} f N_v a^2 \nu , \quad (5)$$

where f is the correlation coefficient N_v the vacancy availability factor, a the jump distance, and ν the jump frequency. Tracer diffusion studies have reported a concentration-independent D^* within an experimental uncertainty of a factor of two, suggesting that the terms in eq. (5) are either weakly dependent on the oxygen content or have compensating compositional dependences [3,4].

The observed concentration dependence in figs. 6–8 is more likely to arise from the non-ideal behavior of oxygen defects in YBCO (i.e., defect–defect interactions). The relationship between the chemical $\tilde{D}$ and tracer D^* diffusivities can be written as

$$\tilde{D}=D^*\left(1+\frac{\partial \ln \gamma}{\partial \ln x}\right), \qquad (6)$$

where the term in brackets is the thermodynamic factor which contains the oxygen activity, γ, and the concentration, x. In an ideal solution (often in the dilute limit), the activity γ is unity for all concentrations and the tracer diffusion and chemical diffusion coefficients are equal. The reported values of $\tilde{D}$ are generally larger than D^*, suggesting a significant contribution of the thermodynamic factor to the rate of oxygen diffusion in a chemical potential gradient. Measurements [10,24,25] and models [12,26] suggest that $\partial \ln \gamma/\partial \ln x$ can be as large as 1000, especially at low temperatures and high oxygen contents, and also may be concentration-dependent at constant temperature. Reports of slower in-diffusion than out-diffusion in single crystals [20] is also consistent with a diffusivity which depends on the oxygen content [27].

The benefit of using single crystal specimens was evident in the comparison of the functional forms of the change in diffusivities (relaxation times) with oxygen content (figs. 6 and 7) when compared with polycrystals (fig. 8). The most striking feature of fig. 8 is the rapid drop of the relaxation times over a narrow range of oxygen content. This was attributed to extrinsic microstructural effects in which the influence of highly oxygenated shells introduced high conductivity pathways in polycrystalline YBCO [20].

Knowledge of the effective diffusion length for a specific specimen is required before an accurate determination of the diffusion coefficient can be made from eq. (3). In the case of electrical resistance measurements of single crystals the lengths may not necessarily be the external crystal dimensions and, consequently, the values of the chemical diffusivities indicated in figs. 6(b) and 7 should be taken as estimates of the upper limits. It is possible that the effective diffusion lengths are actually less than the sample dimensions or that there is a contribution of c-axis diffusion to the overall diffusion rate. The possibility of such a systematic error in the values of $\tilde{D}$ does not detract from the important information concerning oxygen diffusion mechanisms contained in the *relative* change of $\tilde{D}$ (or τ) with oxygen concentration. This is illustrated in fig. 9 for a Log–Log plot of $\tilde{D}_{ab}$ as a function of the anisotropy ratio, $\beta=D^*_{ab}/D^*_c$, for the two extremes of x in fig. 6(b). By changing the effective diffusion lengths, the curves would shift in an identical manner. If there was a significant contribution of c-axis diffusion $\tilde{D}_c$ to the oxygen in-diffusion rates, β would be smaller, resulting in lower diffusivities calculated from eq. (3) (figs. 6 and 7). For comparison purposes, the tracer diffusivity at 700°C was reported to be $\sim 10^{-9}$ cm^2/s (ref. [4]).

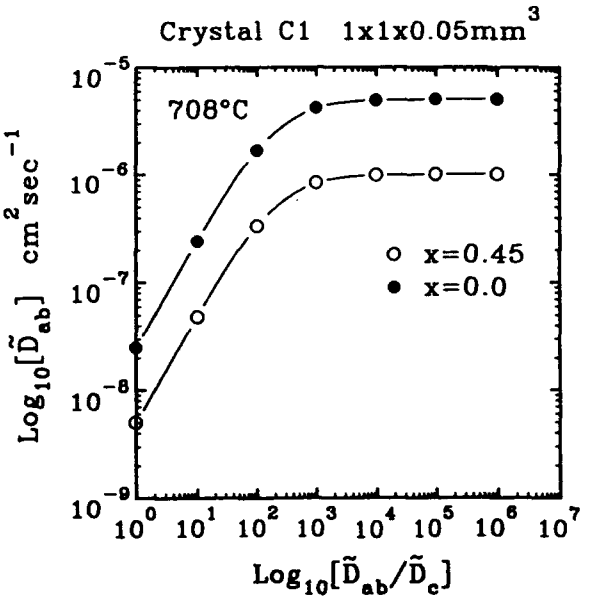

Fig. 9. Dependence of the *ab*-plane chemical diffusivity on the anisotropy ratio, $\beta=D^*_{ab}/D^*_c$, for crystal C1 at 708°C. The large diffusivities, $\tilde{D}$, by comparison with tracer diffusion coefficients, suggest that the thermodynamic factor accounts for the observed concentration dependence in $\tilde{D}$.

4. Conclusion

In summary, the kinetics for chemical diffusion of oxygen were measured by monitoring the relaxation of the electrical resistance during in-diffusion, while systematically varying the initial overall oxygen content in YBCO specimens. The chemical diffusion coefficient for in-diffusion was found to increase with decreasing initial overall oxygen content, the latter determined from out-gassing in argon for different times. The concentration dependence for the chem-

ical diffusivity, and the lack of one in reported tracer diffusion studies [3,4], indicates that a simple vacancy model does not fully describe the observed behavior. This suggests that the diffusion mechanism depends on other factors such as the thermodynamic factor. Further studies of $\tilde{D}$ and D^* as a function of oxygen stoichiometry will lead to an increased understanding of the diffusion mechanisms.

Acknowledgements

The research was supported by the United States Air Force Office of Scientific Research through a University Research Initiative (URI-41318) on Phase Transformation Studies in Ceramics, and by the National Science Foundation (DMR 88-09854) through the Science and Technology Center for Superconductivity. We thank T.P. McCarthy of the School of Chemical Sciences for impurity analyses.

References

[1] R.J. Cava, A.W. Hewat, E.A. Hewat, B. Batlogg, M. Marezio, K.M. Rabe, J.J. Krajewski, W.F. Peck and L.W. Rupp, Physica C 165 (1990) 419.
[2] B.W. Veal, H. You, A.P. Paulikas, H. Shi, Y. Fang and J.W. Downey, Phys. Rev. B 42 (1990) 4770.
[3] S.J. Rothman, J.L. Routbort and J.E. Baker, Phys. Rev. B 40 (1989) 8852.
[4] S.J. Rothman, J.L. Routbort, U. Welp and J.E. Baker, Phys. Rev. B 44 (1991) 2326.
[5] J.R. LaGraff and D.A. Payne, Physica C 212 (1993) 478 (this issue).
[6] J.R. LaGraff and D.A. Payne, Physica C 212 (1993) 487 (this issue).
[7] Y. Ikuma and S. Akiyoshi, J. Appl. Phys. 64 (1988) 3915.
[8] J.L. Tallon and M.P. Staines, J. Appl. Phys. 68 (1990) 3998.
[9] K.N. Tu, N.C. Yeh, S.I. Park and C.C. Tsuei, Phys. Rev. B 39 (1989) 304.
[10] K. Kishio, K. Suzuki, T. Hasegawa, T. Yamamoto, K. Kitazawa and K. Fueki, J. Solid State Chem. 82 (1989) 192.
[11] J.S. Choi, M. Sarikaya, I.A. Aksay and R. Kikuchi, Phys. Rev. B 42 (1990) 4244.
[12] E. Salomons and D. deFontaine, Phys. Rev. B 41 (1990) 11159.
[13] J.B. Price and J.B. Wagner, Z. Phys. Chem. Neue Folge 49 (1966) 257.
[14] R. Farhi and G. Petot-Ervas, J. Phys. Chem. Solids 39 (1978) 1169.
[15] J. Park, P. Kostic and J.P. Singh, Mater. Lett. 6 (1988) 393.
[16] G. Ottaviani, C. Nobili, F. Nava, M. Affronte, T. Manfredini, F.C. Matacotta and E. Galli, Phys. Rev. B 39 (1989) 9069.
[17] A.T. Fiory, S. Martin, L.F. Schneemeyer, R.M. Fleming, A.E. White and J.V. Waszczak, Phys. Rev. B 38 (1988) 7129.
[18] J.R. LaGraff, P.D. Han and D.A. Payne, Physica C 169 (1990) 355.
[19] J.R. LaGraff, P.D. Han and D.A. Payne, Phys. Rev. B 43 (1991) 441.
[20] J.R. LaGraff and D.A. Payne, Phys. Rev. B 47 (1993) 3380.
[21] T.B. Lindemer, J.F. Hunley, J.E. Gates, A.L. Sutton, J. Brynestad, C.R. Hubbard and P.K. Gallagher, J. Am. Ceram. Soc. 72 (1989) 1775.
[22] P.K. Gallagher, G.S. Grader and H.M. O'Bryan, Solid State Ionics 32-33 (1989) 1133.
[23] M. Martin, Mater. Sci. Rep. 7 (1991) 1.
[24] P. Meuffels, R. Naeven and H. Wenzl, Physica C 161 (1989) 539.
[25] O. Porat, I. Reiss and H.L. Tuller, Physica C 192 (1992) 60.
[26] H. Bakker, J.P.A. Westerveld, D.M.R. LoCascio and D.O. Welch, Physica C 157 (1989) 25.
[27] J. Crank and M.E. Henry, Trans. Faraday Soc. 45 (1949) 636.

Physica C 212 (1993) 478–486
North-Holland

PHYSICA C

Concentration-dependent oxygen diffusivity in $YBa_2Cu_3O_{6+x}$
II. Oxygen partial pressure studies

John R. LaGraff [1] and David A. Payne

Department of Materials Science and Engineering, Materials Research Laboratory, Science and Technology Center for Superconductivity, University of Illinois at Urbana-Champaign, Urbana, IL 61801, USA

Received 8 February 1993

Electrical resistance measurements were used to determine the equilibrium resistivity characteristics and the oxygen diffusion behavior in $YBa_2Cu_3O_{6+x}$ (YBCO) as a function of oxygen partial pressure at temperatures ranging from 450–850°C. The equilibrium resistivity values depended on the oxygen partial pressures as $n = \partial \mathrm{Log}\rho / \partial \mathrm{Log}[P(O_2)]$, where n ranged from approximately $-\frac{1}{6}$ up to $-\frac{1}{4}$ from low to high temperatures. A clear p-type to n-type transition was observed near 750°C for an oxygen content of 6.1 ($x=0.1$). Values of the oxygen exponent, n, for single crystal YBCO at 650°C and 708°C were similar to those for polycrystalline specimens. Measurements of the time-dependent resistivity behavior between different oxygen partial pressures yielded diffusion kinetics between well-established boundary values of the oxygen content, x. In single crystal specimens, the chemical diffusivity for oxygen in-diffusion was observed to increase with decreasing oxygen content. The kinetic data for the polycrystalline specimens between 450–850°C also depended on the oxygen concentration; however, the temperature dependence was non-Arrhenius.

1. Introduction

The carrier concentration in YBCO, which is important for regulating the superconducting properties [1,2], is established during thermal processing and cooling. As the lattice incorporates more oxygen, the carrier concentration increases and the superconducting properties generally improve. Consequently, an understanding of the oxygen chemical diffusion behavior and the high temperature equilibrium transport properties of YBCO are important for optimizing ceramic processing. In this paper (Part II), the simultaneous measurement of equilibrium electrical transport properties and time-dependent resistivity characteristics (i.e., oxygen diffusion) are reported as a function of different oxygen partial pressures. The results yield information on the defect chemistry and on the concentration-dependent diffusion kinetics.

In fully oxygenated YBCO the conductivity depends primarily on the hole-concentration, $[h^{\cdot}]$, according to

$$\sigma = [h^{\cdot}] e \mu_p , \tag{1}$$

where μ_p is the hole mobility and, e the electron charge. The temperature dependence of the conductivity is contained within the mobility and carrier density terms. The resistivity ρ in fully oxygenated YBCO increases linearly from the superconducting transition temperature, T_c, to approximately 300–500°C [3–5]. At higher temperatures, oxygen loss occurs, with a concomitant reduction in hole carriers. This leads to thermally activated resistivity–temperature characteristics typical of a p-type semiconductor. To a first approximation, one may describe the influence of the oxygen stoichiometry on the electron hole content according to an interstitial model which can be written in Kroger–Vink notation as [6]

$$O_i'' + 2h^{\cdot} \rightleftarrows \tfrac{1}{2}O_2 + V_i , \tag{2}$$

where O_i'' represents a doubly negatively charged oxygen interstitial, $h^{\cdot}$ a compensating electron hole, and

[1] Present address: Department of Chemistry and Materials Research Laboratory, University of Illinois at Urbana-Champaign, Urbana, IL 61801, USA.

V_i a "vacant" interstitial site. The corresponding mass-action equation is written as

$$\frac{[V_i]}{[O_i'']\,[h^{\cdot}]^2} = P(O_2)^{-1/2} K'' \exp(\Delta H/kT)\,, \qquad (3)$$

where $P(O_2)$ is the oxygen partial pressure and ΔH the enthalpy of the oxidation reaction. This ideal solution model would lead to a $P(O_2)^{1/6}$ dependence for the hole concentration, $[h^{\cdot}]$. Substitution of this dependence into the conductivity equation (eq. (1)) yields an inverse dependence of the electrical resistivity on the oxygen partial pressure, i.e., $n = \partial \mathrm{Log}\,\rho / \partial \mathrm{Log}[P(O_2)] = -\frac{1}{6}$ for an interstitial model.

The equilibrium defect chemistry for YBCO has been studied primarily by electrical conductivity and thermoelectric power (Seebeck effect) measurements [7–28]. The electrical conductivity yields information about the carrier-mobility product, while the thermoelectric power, in principle, enables one to distinguish between the carrier concentration and the carrier mobility. Most studies are in good qualitative agreement. The general findings include: values for the oxygen partial pressure exponent, n, from the electrical resistivity between -0.25 and -0.5; a large and rapidly changing thermoelectric power indicative of a change from metallic to semiconducting behavior, and a negative thermoelectric power at high temperatures and low oxygen partial pressures suggesting a further transition from p-type to n-type semiconducting behavior.

Previously (Part I) [29], a concentration-dependent chemical diffusivity was reported for oxygen in-diffusion in which the oxygen content x was established by out-gassing YBCO specimens in argon. In this paper (Part II), oxygen partial pressures were used to firmly establish the initial and final oxygen contents during in- and out-diffusion measurements. The diffusion measurements revealed an increasing diffusivity with decreasing oxygen content as before [29]. The use of controlled $P(O_2)$ also allowed for the simultaneous measurement of the equilibrium resistivity characteristics (i.e., defect chemistry) for YBCO specimens. In Part III [30], the equilibrium defect chemistry, concentration-dependent diffusion behavior, and other reported experimental and theoretical studies will be compared in order to develop an oxygen diffusion model in YBCO.

2. Experimental

Details of the specimen characteristics and electrical resistance measurements were described previously (Part I) [29]). Measurements were made in both the orthorhombic (650°C) and tetragonal (708°C) phase regions for single crystals (when in equilibrium with 1 atm O_2) and from 450–850°C for polycrystalline specimens. (In large single crystals below 600°C, the kinetics were prohibitively slow for diffusion measurements.) Equilibrium times, estimated from diffusivity calculations and experimentally determined by monitoring for constant resistance, were as long as 30 h at low temperatures (450°C) for polycrystalline specimens and also in single crystals ($T > 600$°C) which had longer diffusion lengths. In order to unequivocally establish a constant oxygen concentration across a YBCO specimen, diffusion experiments were carried out after bringing the specimen to equilibrium in controlled oxygen partial pressures (O_2/Ar) of 1, 0.1, 0.01, 0.001 atm, or pure argon. Subsequently, the oxygen partial pressure was either increased to monitor the oxygen in-diffusion or decreased for out-diffusion. Using the data of Lindemer et al. [31], the oxygen partial pressures were directly related to the oxygen content of the specimen and hence the initial and final values of x were known for each diffusion experiment. Figure 1 shows a typical series of time-dependent resistance curves for crystal C2. The data were obtained at constant temperature (708°C) as the oxygen partial pressure was decreased from 1 atm to 0.1, 0.01, and 0.001. Equilibrium resistance values, used in the defect chemistry analysis, allowed for the construction of calibration curves which related the time-dependent resistance behavior to the overall oxygen content.

The characteristic relaxation times, τ, were obtained by fitting the resistance data to the long-time solution ($n = 0$) for three-dimensional diffusion into a rectangular solid

$$\frac{\ln(R(0)) - \ln(R(t))}{\ln(R(0)) - \ln(R(\infty))} = 1 - \left(\frac{8}{\pi^2}\right)^3 \sum_{n=0}^{\infty} \frac{1}{(2n+1)^2} \exp\left(\frac{-(2n+1)^2 t}{\tau}\right), \qquad (4)$$

V_i a "vacant" interstitial site. The corresponding mass-action equation is written as

$$\frac{[V_i]}{[O_i''][h^{\cdot}]^2} = P(O_2)^{-1/2} K'' \exp(\Delta H/kT), \quad (3)$$

where $P(O_2)$ is the oxygen partial pressure and ΔH the enthalpy of the oxidation reaction. This ideal solution model would lead to a $P(O_2)^{1/6}$ dependence for the hole concentration, $[h^{\cdot}]$. Substitution of this dependence into the conductivity equation (eq. (1)) yields an inverse dependence of the electrical resistivity on the oxygen partial pressure, i.e., $n = \partial \mathrm{Log}\rho / \partial \mathrm{Log}[P(O_2)] = -\frac{1}{6}$ for an interstitial model.

The equilibrium defect chemistry for YBCO has been studied primarily by electrical conductivity and thermoelectric power (Seebeck effect) measurements [7–28]. The electrical conductivity yields information about the carrier-mobility product, while the thermoelectric power, in principle, enables one to distinguish between the carrier concentration and the carrier mobility. Most studies are in good qualitative agreement. The general findings include: values for the oxygen partial pressure exponent, n, from the electrical resistivity between -0.25 and -0.5, a large and rapidly changing thermoelectric power indicative of a change from metallic to semiconducting behavior, and a negative thermoelectric power at high temperatures and low oxygen partial pressures suggesting a further transition from p-type to n-type semiconducting behavior.

Previously (Part I) [29], a concentration-dependent chemical diffusivity was reported for oxygen in-diffusion in which the oxygen content x was established by out-gassing YBCO specimens in argon. In this paper (Part II), oxygen partial pressures were used to firmly establish the initial and final oxygen contents during in- and out-diffusion measurements. The diffusion measurements revealed an increasing diffusivity with decreasing oxygen content as before [29]. The use of controlled $P(O_2)$ also allowed for the simultaneous measurement of the equilibrium resistivity characteristics (i.e., defect chemistry) for YBCO specimens. In Part III [30], the equilibrium defect chemistry, concentration-dependent diffusion behavior, and other reported experimental and theoretical studies will be compared in order to develop an oxygen diffusion model in YBCO.

2. Experimental

Details of the specimen characteristics and electrical resistance measurements were described previously (Part I) [29]). Measurements were made in both the orthorhombic (650°C) and tetragonal (708°C) phase regions for single crystals (when in equilibrium with 1 atm O_2) and from 450–850°C for polycrystalline specimens. (In large single crystals below 600°C, the kinetics were prohibitively slow for diffusion measurements.) Equilibrium times, estimated from diffusivity calculations and experimentally determined by monitoring for constant resistance, were as long as 30 h at low temperatures (450°C) for polycrystalline specimens and also in single crystals ($T > 600$°C) which had longer diffusion lengths. In order to unequivocally establish a constant oxygen concentration across a YBCO specimen, diffusion experiments were carried out after bringing the specimen to equilibrium in controlled oxygen partial pressures (O_2/Ar) of 1, 0.1, 0.01, 0.001 atm, or pure argon. Subsequently, the oxygen partial pressure was either increased to monitor the oxygen in-diffusion or decreased for out-diffusion. Using the data of Lindemer et al. [31], the oxygen partial pressures were directly related to the oxygen content of the specimen and hence the initial and final values of x were known for each diffusion experiment. Figure 1 shows a typical series of time-dependent resistance curves for crystal C2. The data were obtained at constant temperature (708°C) as the oxygen partial pressure was decreased from 1 atm to 0.1, 0.01, and 0.001. Equilibrium resistance values, used in the defect chemistry analysis, allowed for the construction of calibration curves which related the time-dependent resistance behavior to the overall oxygen content.

The characteristic relaxation times, τ, were obtained by fitting the resistance data to the long-time solution ($n=0$) for three-dimensional diffusion into a rectangular solid

$$\frac{\ln(R(0)) - \ln(R(t))}{\ln(R(0)) - \ln(R(\infty))} = 1 - \left(\frac{8}{\pi^2}\right)^3 \sum_{n=0}^{\infty} \frac{1}{(2n+1)^2} \exp\left(\frac{-(2n+1)^2 t}{\tau}\right), \quad (4)$$

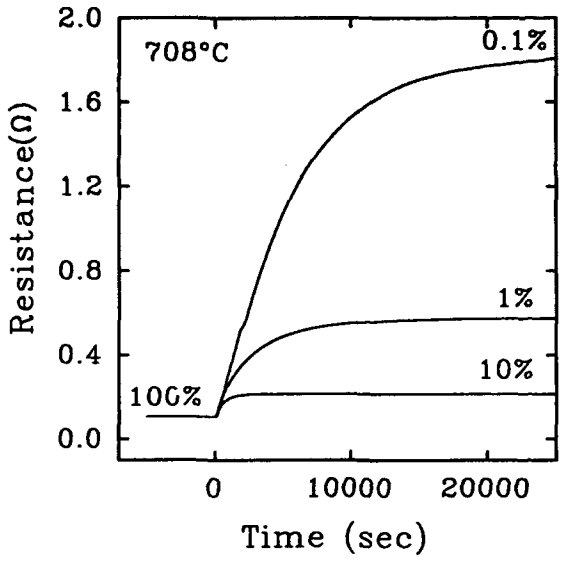

Fig. 1. Time-dependent electrical resistance for crystal C2 during oxygen out-diffusion between 1 atm of oxygen and increasingly lower oxygen partial pressures. Equilibrium values of the resistivity were used in the defect chemistry analysis, while the calculated relaxation times yielded information on the diffusion kinetics between established oxygen concentrations.

where the terms were previously defined [29]. The in-plane diffusivity $\tilde{D}_{ab}$ is [29]

$$\tilde{D}_{ab}=\frac{1}{\pi^2\tau}\left(\frac{1}{a^2}+\frac{1}{b^2}+\frac{1}{\beta c^2}\right)^{-1}, \qquad (5)$$

where β is the anisotropy ratio between $\tilde{D}_{ab}$ and the c-axis diffusivity, $\tilde{D}_c$. The use of eqs. (4) and (5) and controlled oxygen partial pressures enabled one to determine the diffusion kinetics between different oxygen concentrations. Values of $\tilde{D}_{ab}$ calculated in this paper should be considered average values between two different oxygen concentrations as eqs. (4) and (5) were developed for constant diffusion coefficients. Results for equilibrium defect chemistry are presented first, followed by concentration-dependent diffusion measurements.

3. Results and discussion

3.1. Defect chemistry

Resistivity characteristics were determined as a function of the oxygen partial pressure from 450–850°C for rectangular bars of polycrystalline YBCO and at 650°C and 708°C for single crystals. The resistivity as a function of temperature for a particular polycrystalline specimen S2 is given in fig. 2(a) which reveals a clear p–n transition near 750°C, $P(O_2)=0.001$ ($x=0.11$). The behavior is indicative of a change from p-type conductivity to n-type which has been reported previously by other groups [8–12]. An Arrhenius plot of the resistivity data from fig. 2(a) reveals several different activation energies (fig. 2(b), table 1) as determined from the relation

$$R=R_0\exp(E/kT)\,. \qquad (6)$$

Values of the activation energy ranged between 0.2–0.8eV (table 1). Figure 3 is a Log–Log plot of the resistivity versus oxygen partial pressure with the corresponding best linear fits. The slopes $n=\partial\mathrm{Log}\,\rho/\partial\mathrm{Log}[P(O_2)]$ vary from approximately -0.1 at 450°C to less than $-\frac{1}{2}$ at higher temperatures and lower oxygen partial pressures. (The slopes were not completely linear at high temperatures suggesting non-ideal oxygen solute behavior.) For comparison, fig. 4 is a similar plot for a single crystal specimen, C2, at 650°C and 708°C with slopes, n, of -0.38 and -0.41, respectively. The similarity in exponents between single crystal and polycrystalline YBCO (figs. 3 and 4) suggests that microstructural features (i.e., boundaries, second phases, etc.) and crystal anisotropy were not significant in affecting the measurement of high temperature equilibrium transport properties in polycrystalline YBCO [7–28]. Comparison of measured activation energies and oxygen exponents with values reported in the literature also served as an indicator of sample quality and consistency.

The results presented in figs. 1–4 were generally in good agreement with other studies [7–28] on the high-temperature equilibrium defect chemistry and conduction mechanisms reported for YBCO. The similarities include: oxygen partial pressure exponents, n, for the electrical resistivity decreasing from -0.1 to -0.6 as temperature increased, and a p-type to n-type transition near 6.1 oxygen which agreed with the results of Porat et al. [12], but not with Yoo [9] who reported a transition near 6.35. In general, oxygen exponents near $-\frac{1}{2}$ in the tetragonal phase and $-\frac{1}{4}$ in the orthorhombic phase have been reported [7–10,14]. There is unfortunately still little

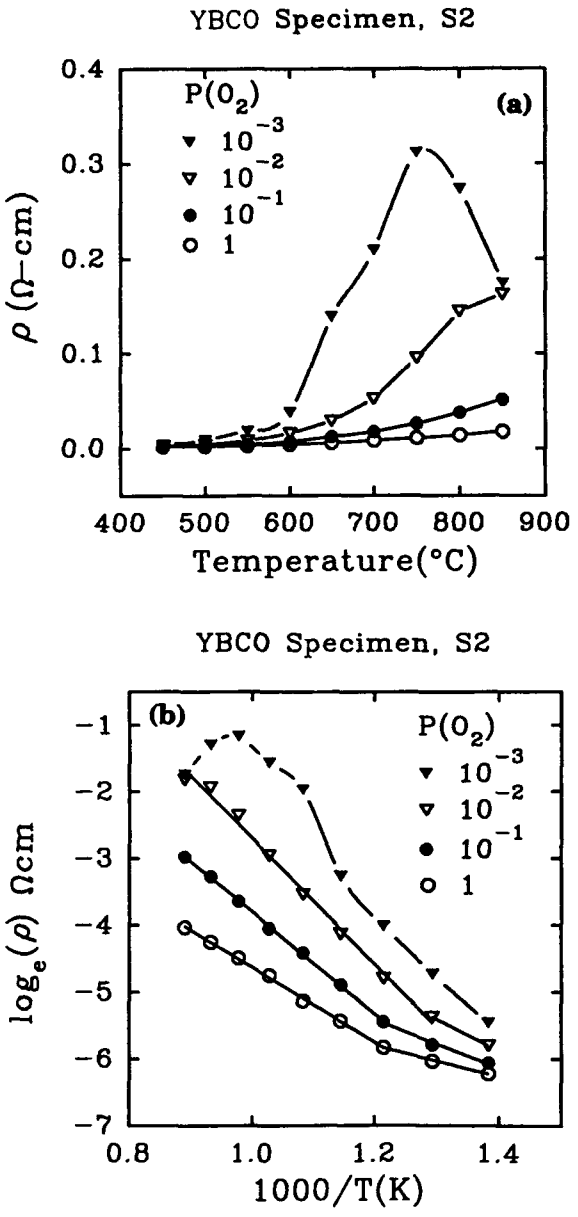

Fig. 2. (a) Values of the equilibrium resistivity for different oxygen partial pressures (0.001–1 atm) for polycrystalline YBCO (specimen S2) as a function of temperature between 450–850°C. A resistivity maximum occurs near 750°C for an oxygen partial pressure of 0.001 atm (oxygen content $x=0.11$) which corresponds to a change from primarily p-type to n-type conductivity. (b) Arrhenius plot of the equilibrium resistivity data for specimen S2 from fig. 2(a). The resistance curves were not characterized by a single activation energy over the entire temperature range (see table 1).

Table 1
Activation energies for the temperature-dependence of the electrical resistivity as a function of temperature (eq. (6) and fig. 2(b))

$P(O_2)$ (atm)	T (°C)	E (eV)
1	450–550	0.20(3)
	550–850	0.48(4)
0.1	450–550	0.31(2)
	550–850	0.65(4)
0.01	450–500	0.41(1)
	500–850	0.81(5)
0.001	450–600	0.80(3)

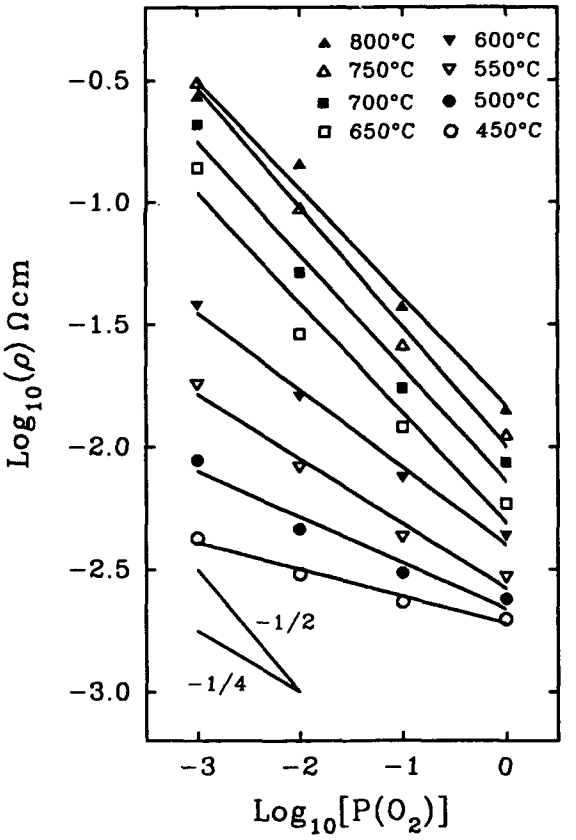

Fig. 3. Log–Log plots of the equilibrium resistivity values vs. oxygen partial pressure for different temperatures for polycrystalline YBCO with corresponding linear curve fits. The oxygen exponents, $n \simeq \partial \mathrm{Log}\,\rho / \partial \mathrm{Log}[P(O_2)]$ (eqs. (2) and (3)) vary from approximately -0.1 to -0.6 from 450–800°C. Non-linear oxygen dependences at higher temperatures suggest non-ideal solute behavior.

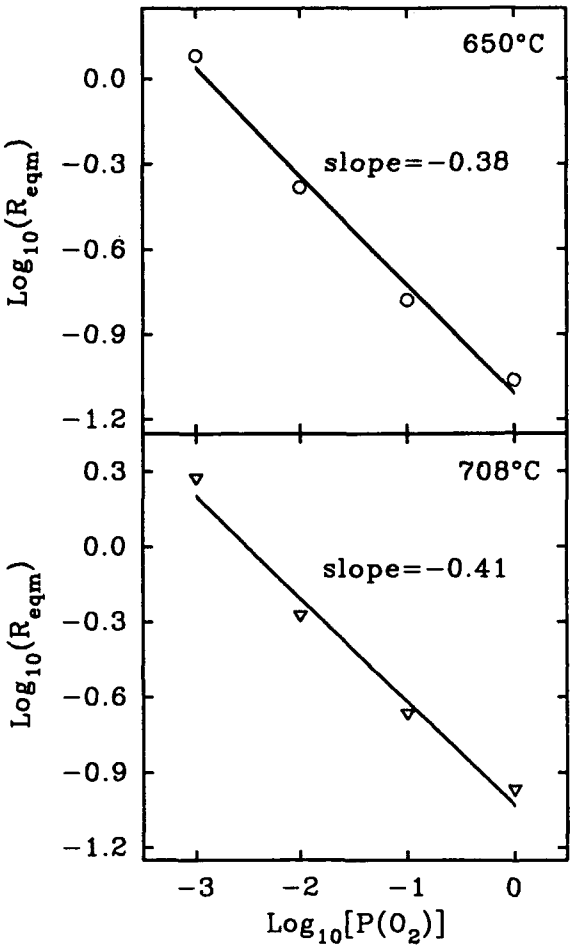

Fig. 4. Log–Log plot of the equilibrium resistance value vs. oxygen partial pressure at 650°C and 708°C for a single crystal specimen (C2).

consensus on which models are appropriate for the complete description of the defect chemistry for YBCO. Chang et al. [14] have suggested that a vacancy-filling model yields the best fit to their reported conductivity data typical of an ideal solute behavior of oxygen in YBCO.

There are two major features of YBCO which complicate the development of a defect model to describe oxygen: one, there exist two distinct copper sites and, two, oxygen does not appear to behave as an ideal solute in YBCO. Infrared measurements by Schlesinger et al. [32] and calculations by Friedmann et al. [33] suggest that the room temperature conductivity of *fully* oxygenated YBCO is shared almost equally between the ordered chain planes and the CuO_2 sheets. As oxygen is disordered it has two limiting effects on the conductivity: one, it removes effective hole carriers from the CuO_2 planes and, two, it increases the scattering of that portion of the conductivity carried by the CuO chains. These two distinct copper sites, each possessing its own oxygen stoichiometry dependent conduction mechanism, will make it difficult to develop an equilibrium defect model for YBCO. Also, defect–defect interactions are evident in the copper–oxygen chain formation in orthorhombic material [34] and chain fragments [35] in tetragonal YBCO suggesting that one no longer has a dilute solution of non-interacting oxygen interstitials (or oxygen vacancies). It is outside the scope of this paper to propose a detailed defect model, but the overall similarity of the data in figs. 1–4 with reported results [7–28] will allow some general conclusions to be made as regards the oxygen diffusion mechanisms (Part III) [30].

3.2. Diffusion measurements

In order to unambiguously verify a constant oxygen distribution across a YBCO specimen at the beginning and end of a diffusion experiment, studies were carried out on polycrystalline and single crystal specimens using different oxygen partial pressures ranging from 0.001 to 1 atm. Figure 5 shows the chemical diffusivities, $\tilde{D}$, for oxygen in-diffusion (eqs. (4) and (5)) for crystal C2 at 650°C and 708°C as a function of the initial oxygen content, while table 2 contains the initial and final x values for each diffusion experiment and the diffusion coefficients. As observed for the out-gassing in argon experiments (Part I) [29], $\tilde{D}$ for in-diffusion increased as the initial oxygen content decreased. However, the values of $\tilde{D}$ differ somewhat from those measured by out-gassing in argon [29], which may reflect the two different techniques used to establish the initial oxygen contents.

The relaxation times for oxygen in-diffusion and out-diffusion in a polycrystalline specimen did not exhibit the typical Arrhenius temperature-dependent behavior (fig. 6, table 3). The out-diffusion relaxation times from 1 atm of oxygen to partial pressures of 0.1, 0.01, and 0.001 atm reveal an increasing

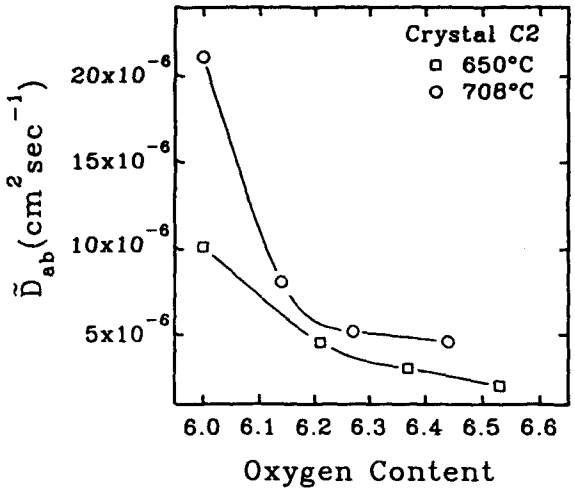

Fig. 5. Chemical diffusivity at 650°C and 708°C for crystal C2 as a function of the initial oxygen content (a=0.15 cm, b=0.2 cm).

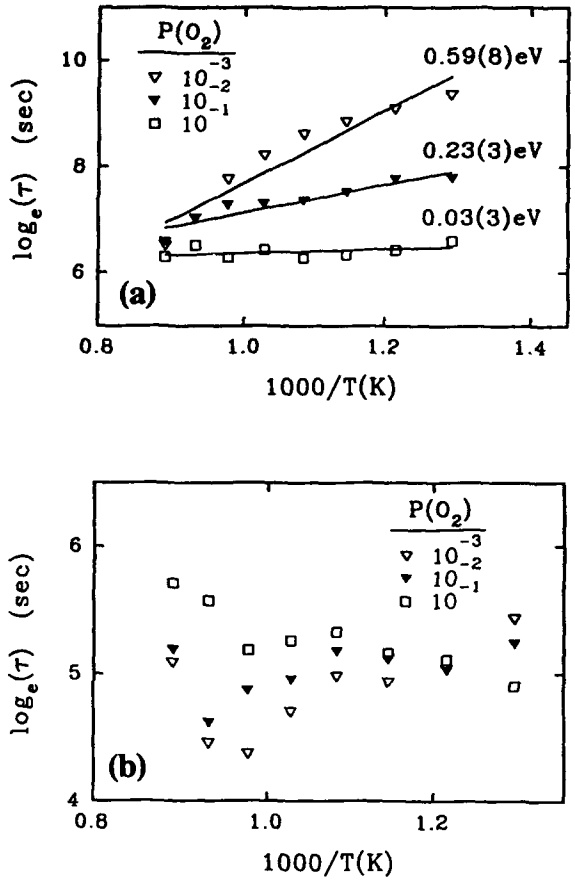

Fig. 6. Relaxation times for (a) oxygen out-diffusion and (b) oxygen in-diffusion for polycrystalline YBCO (S2) between different oxygen partial pressures (table 3).

diffusivity with increasing temperature. As a first approximation, activation energies were determined at each partial pressure (fig. 6(a)). The activation energy for out-diffusion to an oxygen partial pressure of 0.001 atm was 0.59(8) eV which was identical (within experimental error) with the activation energy determined during out-diffusion in argon in a previous study [36]. As $\Delta P(O_2)$ decreased (i.e., the Δx became smaller), the activation energies decreased to almost 0 eV (fig. 6(a)). The different activation energies with different Δx were indicative of a concentration-dependent diffusivity. In light of the

Table 2
Diffusion coefficients for oxygen in-diffusion and out-diffusion for crystal C2. The initial (i) and final (f) oxygen contents, $6+x$, were established by equilibration in different oxygen partial pressures. (Diffusion lengths: a=0.2 cm, b=0.15 cm)

T (°C)	$(6+x)_i$	$(6+x)_f$	$\tilde{D}$ (cm^{2}s^{-1})	
			In-diffusion	Out-diffusion
650°C	6.53	6.70	$2.05(1)\times10^{-6}$	$1.00(1)\times10^{-6}$
	6.37	6.70	$3.06(3)\times10^{-6}$	$2.8(1)\times10^{-7}$
	6.21	6.70	$4.56(4)\times10^{-6}$	$9.4(1)\times10^{-8}$
	~6.0	6.70	$10.1(2)\times10^{-6}$	[a]
708°C	6.44	6.60	$4.63(3)\times10^{-6}$	$1.88(3)\times10^{-6}$
	6.27	6.60	$5.19(5)\times10^{-6}$	$4.02(2)\times10^{-7}$
	6.14	6.60	$8.1(1)\times10^{-6}$	$2.05(3)\times10^{-7}$
	~6.0	6.60	$21.1(6)\times10^{-6}$	[a]

[a] A linear change in the resistance during out-diffusion in low $P(O_2)$ precludes the determination of a relaxation time.

equilibrium resistivity results and the well-behaved out-diffusion behavior in polycrystalline specimens of YBCO, it is surprising that the corresponding oxygen in-diffusion relaxation times exhibited such an unusual temperature-dependent behavior (fig. 6(b), table 3). At most temperatures, the relaxation times show an increasing diffusivity with lower initial values of x as previously reported in Part I [29] and now in fig. 5. The unusual temperature-dependence for in-diffusion in polycrystalline specimens was attributed to high conductivity shells which formed during oxygen in-diffusion [36]. The shell effects are minimized or non-existent during out-diffusion in polycrystalline specimens (fig. 6(a)) and for both in- and out-diffusion in single crystal specimens (fig. 5 and refs. [29] and [36]).

Comparison of the diffusion coefficients in tables 2 and 3 would suggest that, in general, the calculated diffusivities were smaller (i.e., slower) for out-diffusion than in-diffusion. As was shown previously [36], however, electrical resistance measurements are more susceptible to high-conductivity shell effects during in-diffusion than out-diffusion. In fact, single crystal specimens exhibit a long resistance tail during the final stages of in-diffusion which indicated that in-diffusion, especially during the latter stage, was intrinsically slower than out-diffusion [36]. The apparently slower out-diffusion shown in tables 2 and 3 was a result of eqs. (4) and (5) not fitting the resistive tail at long times during in-diffusion for single crystal specimens.

The use of controlled oxygen partial pressures to

Table 3
Relaxation times for oxygen in-diffusion in polycrystalline specimen S2. The initial (i) and final (f) oxygen contents, $6+x$, were established by equilibration in different oxygen partial pressures

T (°C)	$(6+x)_i$	$(6+x)_f$	τ (s)	
			In-diffusion	Out-diffusion
450°C	6.92	6.96	366(12)	1 240(20)
	6.80	6.96	332(16)	3 340(53)
	6.67	6.96	312(12)	10 137(62)
500°C	6.83	6.92	135(8)	734(10)
	6.69	6.92	188(11)	2 401(16)
	6.50	6.92	228(7)	11 622(113)
550°C	6.75	6.87	166(8)	618(10)
	6.56	6.87	152(5)	2 338(16)
	6.38	6.87	154(3)	8 883(119)
600°	6.63	6.79	175(5)	561(18)
	6.45	6.79	166(5)	1 816(16)
	6.28	6.79	139(4)	6 974(60)
650°C	6.53	6.70	206(6)	530(13)
	6.37	6.70	177(4)	1 558(12)
	6.21	6.70	145(4)	5 510(41)
700°C	6.45	6.62	193(5)	613(15)
	6.28	6.62	142(3)	1 450(13)
	6.15	6.62	110(2)	3 650(18)
750°C	6.39	6.55	179(4)	538(5)
	6.23	6.55	130(3)	1 440(10)
	6.11	6.55	79(1)	2 341(11)
800°C	6.32	6.49	263(6)	677(8)
	6.18	6.49	101(2)	1 112(11)
	6.08	6.49	86(2)	1 124(42)[a]
850°C	6.26	6.44	302(6)	542(12)
	6.13	6.44	179(3)	719(29)
	6.05	6.44	162(2)	669(20)[a]

[a] The p-type to n-type conductivity transition is evident in the resistance data which yielded poor fits to eq. (2).

establish the boundary values of x for each diffusion experiment allowed for the corroboration of the concentration dependences observed in the argon annealing experiments (Part I) [29]. Both techniques revealed an increasing diffusivity during in-diffusion with decreasing values of x. Differences in the actual values of the diffusivities and the magnitude of the concentration-dependence observed in Part I and II were attributed to the different techniques used to establish the oxygen concentration, namely, argon annealing versus controlled oxygen partial pressures. In Part III [30], factors which may account for the observed concentration-dependence will be proposed.

4. Conclusion

In summary, high-temperature electrical resistance measurements in controlled oxygen partial pressures allow for the simultaneous measurement of equilibrium transport properties and oxygen diffusion kinetics. The oxygen exponents for electrical resistance, n, were found to decrease from -0.1 to -0.6 with increasing temperature. A clear p-type to n-type semiconductor transition was observed near 750°C and an oxygen content of 6.1. The Log–Log dependence of the electrical resistance with oxygen partial pressure became increasingly non-linear at higher temperatures indicating non-ideal solute behavior. Consequently, there was some argument whether one can use ideal solution mass-action equations to describe the equilibrium defect chemistry of a highly defective and non-stoichiometric compound such as YBCO. The diffusion coefficients for oxygen in-diffusion were found to increase with decreasing oxygen content in single crystal YBCO. Polycrystalline YBCO also revealed concentration-dependent diffusion kinetics; however, the temperature-dependence was non-Arrhenius, especially for in-diffusion.

Acknowledgements

The research was supported by the United States Air Force Office of Scientific Research through a University Research Initiative (URI-41318) on Phase Transformations Studies in Ceramics and by the National Science Foundation (DMR 88-09854) through the Science and Technology Center for Superconductivity.

References

[1] R.J. Cava, A.W. Hewat, E.A. Hewat, B. Batlogg, M. Marezio, K.M. Rabe, J.J. Krajewski, W.F. Peck and L.W. Rupp, Physics C 165 (1990) 419.
[2] B.W. Veal, H. You, A.P. Paulikas, H. Shi, Y. Fang and J.W. Downey, Phys. Rev. B 42 (1990) 4770.
[3] A.T. Fiory, M. Gurvitch, R.J. Cava and G.P. Espinosa, Phys. Rev. B 36 (1987) 7262.
[4] J.R. LaGraff, P.D. Han and D.A. Payne, Physica C 169 (1990) 355.
[5] J.R. LaGraff, P.D. Han and D.A. Payne, Phys. Rev. B 43 (1991) 441.
[6] F.A. Kroger and H.J. Vink, Solid State Phys. 3 (1956) 307.
[7] A. Mehta and D.M. Smyth, Non-Stoichiometric Compounds Surfaces, Grain Boundaries, and Structural Defects (Kluwer Academic, Dordrecht, 1989) p.509.
[8] G.M. Choi, H.L. Tuller and M.J. Tsai, Non-Stoichiometric Compounds Surfaces, Grain Boundaries, and Structural Defects (Kluwer Academic, Dordrecht, 1989) p.451.
[9] H.I. Yoo, J. Mater. Res. 4 (1989) 23.
[10] M.Y. Su, S.E. Dorris and T.O. Mason, J. Solid State Chem. 75 (1988) 381.
[11] J. Nowotny, M. Rekas and W. Weppner, J. Am. Ceram. Soc. 73 (1990) 1040.
[12] O. Porat, I. Riess and H.L. Tuller, Physica C 192 (1992) 60.
[13] M. Ould Die, C. Picard, P. Gerdanian, B. Poumellec and B. Touzelin, Solid State Commun. 74 (1990) 483.
[14] E.K. Chang, A. Mehta, D.J.L. Hong and D.M. Smyth, Ferroelectrics 102 (1990) 309.
[15] P.P. Freitas and T.S. Plasket, Phys. Rev. B 37 (1988) 3657.
[16] J. Genossar, B. Fisher, I.O. Lelong, Y. Ashkenazi and L. Patlagan, Physica C 157 (1989) 320.
[17] G. Sageev Grader, P.K. Gallagher and E.M. Gyorgy, Appl. Phys. Lett. 51 (1987) 1115.
[18] P.P. Freitas and T.S. Plaskett, Phys. Rev. B 36 (1987) 5723.
[19] D.J. Vischjager, A.A. van Zomeren, J. Schoonman, I. Kontoulis and B.C.H. Steele, Solid State Ionics 40–41 (1990) 810.
[20] J. Maier, P. Murugaraj and G. Pfundtner, Solid State Ionics 40–41 (1990) 802.
[21] H.L. Tuller and E. Opila, Solid State Ionics 40–41 (1990) 790.
[22] J. Nowotny and M. Rekas, J. Am. Ceram. Soc. 73 (1990) 1048.
[23] J. Nowotny and M. Rekas, J. Am. Ceram. Soc. 73 (1990) 1054.

[24] D.J.L. Hong and D.M. Smyth, J. Am. Ceram. Soc. 74 (1991) 1751.
[25] J. Nowotny and M. Rekas, J. Am. Ceram. Soc. 74 (1991) 1753.
[26] J. Molenda, A. Stoklosa and T. Bak, Physica C 175 (1991) 555.
[27] P. Gerdanian, M. Ould Die and C. Picard, Phys. Rev. B 43 (1991) 11337.
[28] Z. Gao, Z. Hou, B. Du, D. Zhang, G. Wang, C. Wang and C. Zhu, Physica C 167 (1990) 49.
[29] J.R. LaGraff and D.A. Payne, Physica C 212 (1993) 470 (this issue).
[30] J.R. LaGraff and D.A. Payne, Physica C 212 (1993) 487 (this issue).
[31] T.B. Lindemer, J.F. Hunley, J.E. Gates, A.L. Sutton, J. Brynestad, C.R. Hubbard and P.K. Gallagher, J. Am. Ceram. Soc. 72 (1989) 1775.
[32] Z. Schlesinger, R.T. Collins, F. Holtzberg, C. Feild, S.H. Blanton, U. Welp, G.W. Crabtree, Y. Fang and J.Z. Liu, Phys. Rev. Lett. 65 (1990) 801.
[33] T.A. Friedmann, M.W. Rabin, J. Giapintzakis, J.P. Rice and D.M. Ginsberg, Phys. Rev. B 42 (1990) 6217.
[34] D. deFontaine, L.T. Willie and S.C. Moss, Phys. Rev. B 36 (1987) 5709.
[35] P.A. Rikvold, M.A. Novotny and T. Aukrust, Phys. Rev. B 43 (1991) 202.
[36] J.R. LaGraff and D.A. Payne, Phys. Rev. B 47 (1993) 3380.

Physica C 212 (1993) 487–496
North-Holland

PHYSICA C

Concentration-dependent oxygen diffusivity in $YBa_2Cu_3O_{6+x}$
III. Diffusion mechanisms

John R. LaGraff [1] and David A. Payne
Department of Materials Science and Engineering, Materials Research Laboratory, Science and Technology Center for Superconductivity, University of Illinois at Urbana-Champaign, Urbana, IL 61801, USA

Received 8 February 1993

In this paper, aspects of diffusion theory are discussed which could account for the reported concentration-dependent chemical diffusion coefficients previously reported [Physica C 212 (1993) 470, 478 (this issue)]. These factors include correlation effects, the thermodynamic factor, the type of mechanism (i.e., vacancy or interstitial), and the different types of fundamental atomic jumps. It is proposed that defect interactions are primarily responsible for a concentration-dependent $\tilde{D}$. Examination of jump pathways in orthorhombic YBCO indicate that diffusion along the copper–oxygen chain direction (along the *b*-axis) is more favorable if, (1) the oxygen starts at the end of a chain and, (2) the adjacent chain is empty of oxygen. Intrachain diffusion (along the *a*-axis) between two copper–oxygen chains is more slow and depends on the oxygen concentration.

1. Introduction

It is expected that diffusion in a highly defective solid such as YBCO cannot be completely described by a simple random walk model. The many ordered oxygen superstructures which exist in YBCO [1–3] suggest that the detailed mechanism for oxygen diffusion will be quite complex. The local environment that a diffusing oxygen ion or atom will experience varies from completely ordered copper–oxygen chains and {110} thin walls in the orthorhombic structure ($x \sim 1$) to individual oxygen ions in the low oxygen limit ($x \sim 0$) of tetragonal YBCO. It is the purpose of this paper (Part III) to assimilate the experimental results reported previously on the concentration-dependent chemical diffusion coefficient (Parts I and II) [4,5] with other reported studies [6–27] in order to examine possible mechanism(s) describing oxygen diffusion in YBCO. Fundamental oxygen jumps available to a mobile oxygen anion will be semi-quantitatively evaluated with an oxygen interaction model [1]. These oxygen interactions are expected to contribute to the correlation coefficient and the thermodynamic factor (i.e., non-ideal solute behavior).

The complexity inherent in developing an oxygen diffusion model for YBCO is exemplified in the difficulty in establishing a reference structure. One possible reference structure is the oxygen deficient $YBa_2Cu_3O_6$ in which the O(1) and O(5) sites would both be considered interstitial sites [28]. If fully ordered $YBa_2Cu_3O_7$ is the reference structure, then the vacant O(5) sites are, in fact, interstitials, while the O(1) oxygen reside on normal lattice sites. An O(1)→O(5) oxygen jump would then create a Frenkel defect, while an oxygen anion hopping from an O(5) site to an O(5) site would be typical of an interstitial diffusion mechanism (fig. 1). A collinear or non-collinear interstitialcy mechanism would occur when an interstitial O(5) oxygen displaced an O(1) oxygen to another O(5) interstitial site (fig. 1), while a direct O(1)→O(1) intrachain jump would be typical of a vacancy mechanism. As the lattice loses more oxygen, and the oxygen configurations become more varied the possible jumps available to an oxygen anion may become more complex. In section 2, the diffusion literature is briefly reviewed. Section 3 discusses factors which account for

[1] Present address: Department of Chemistry and Materials Research Laboratory, University of Illinois at Urbana-Champaign, Urbana, IL 61801, USA

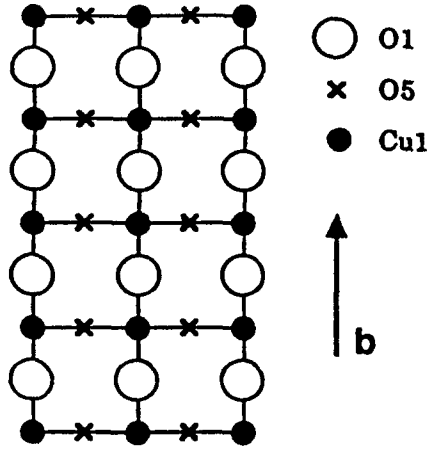

Fig. 1. The ideally ordered copper oxygen chain plane in YBCO. The O(5) positions are interstitial sites, while the O(1) positions are normal lattice sites.

observed concentration dependence in the chemical diffusion coefficient, $\tilde{D}$, while section 4, examines fundamental diffusive jumps available to an oxygen anion in orthorhombic YBCO.

2. Literature survey

Fundamental oxygen diffusion behavior has been measured in YBCO by tracer diffusion techniques [6–10] and internal friction measurements [11–18]. Rothman et al. [6,7] used secondary ion mass spectroscopy (SIMS) to measure ^{18}O profiles in both polycrystalline and twinned and untwinned single crystal YBCO. Major findings, include [6,7]

(1) the diffusivity was not a function of oxygen partial pressure within a factor of two implicating either a concentration-independent D^* or two different factors in the diffusion coefficient possessing opposite and nearly equal compositional dependences;

(2) the Arrhenius behavior of the diffusivities suggested a single diffusion mechanism over all temperatures from 300–850°C described by the Arrhenius expression of the form $D^* = 1.4\times10^{-4}\exp(-0.97(5)\ \text{eV}/kT)\ \text{cm}^2/\text{s}$, and

(3) diffusivities were found to be highly anisotropic with $D_a^* \sim 10^{-2} D_b^*$ and $D_c^* \sim 10^{-4}$–$10^{-6} D_{ab}^*$.

Oxygen diffusion in YBCO is expected to be highly anisotropic for two reasons. First, the lattice has either tetragonal or orthorhombic symmetry such that diffusion is described by two or three independent diffusion coefficients aligned with the crystallographic axes. Second, the mobile oxygen ions are located almost exclusively on the O(1) and O(5) sites associated with the copper–oxygen chain plane, hence, diffusion in the *c*-direction is expected to be extremely slow in comparison with the *ab*-plane directions. Furthermore, the anisotropy between the *a*- and *b*-directions strongly suggests that oxygen diffusion is faster along the chains than perpendicular to the chains [7]. Bredikhin et al. [10] have measured activation energies of ~1.27 eV and 2.3 eV in the *ab*-plane direction and the *c*-direction, respectively. This suggests that as the temperature increases, the anisotropy D_{ab}^*/D_c^* should decrease. In fact D_{ab}^*/D_c^* was found to vary from approximately 10^4 to 10^2 from 400°C to 800°C (ref. [10]).

Self-diffusion coefficients of oxygen in YBCO as a function of both frequency and temperature have been determined from internal friction studies which are assumed to be relatively independent of the microstructure [11–18]. In YBCO the atomic motions which give rise to a loss peak are considered to be O(1)→O(5) jumps. Xie et al. [11] reported that $D = 3.5\times10^{-4}\exp(-1.03\ \text{eV}/kT)\ \text{cm}^2\text{s}^{-1}$ while Tallon and Staines [12] measured $D = 1.8\times10^{-4}\exp(-1.07\ \text{eV}/kT)\ \text{cm}^2\text{s}^{-1}$ which are in close agreement with the tracer diffusion studies of Rothman et al. [6,7]. Differences between the activation energies determined by internal friction measurements and tracer-diffusion experiments should allow one to determine the enthalpy of formation of a vacancy (section 3).

Few models have been proposed to describe oxygen diffusion in YBCO. Rothman et al. [7] suggest that oxygen can only be added to or removed from the ends of ordered chains and will proceed with little hindrance down the open channels between the chains (a series of O(5)→O(5) jumps) before attachment to the end of another chain. This model has been supported by theoretical work which reported an activation energy for motion in the *b*-direction of nearly zero [24]. This mechanism would account for the concentration-independent tracer diffusivity and for the anisotropy between D_a^* and D_b^* (ref. [7]); however, it does not describe diffusion in the tetragonal structure which lacks *long-range*

ordered chains. (Randomly arranged short chain fragments have been theoretically predicted [25].) While the tracer diffusion studies [6,7] suggest a concentration-*independent* oxygen diffusivity in YBCO, the internal friction [12], chemical diffusion [4,5,19,20], and modeling [21,22] studies all suggest a concentration-*dependent* diffusivity. In the following section, factors are examined which may be responsible for a concentration-dependent $\tilde{D}$.

3. Concentration-dependent chemical diffusion

3.1. Vacancy diffusion

A vacancy diffusion mechanism often gives rise to a concentration-dependent diffusivity according to the expression

$$D^* = \alpha f \Gamma N_v a^2 , \tag{1}$$

which contains terms for the correlation coefficient, f, the mean jump frequency, Γ, the vacancy fraction, N_v, the jump distance, a, and a geometric factor, α. ($\alpha = \frac{1}{4}$ for diffusion on a square lattice.) If one considers the O(1) and O(5) sites equivalent, then the vacancy availability factor, N_v, in eq. (1) can be written in terms of the oxygen content as $N_v = (2-x)/2$. This term alone, however, could not account for the approximately four-fold change in $\tilde{D}$ with initial oxygen content [4,5]. Evaluation of the ratio $N_v(x=0)/N_v(x=1)$, predicts a maximum possible enhancement of only 2 over the concentration range $0<x<1$. Theoretically, tracer diffusion measurements should be able to detect such a contribution of N_v towards the oxygen diffusion coefficient in YBCO; however, studies [6,7] are reported only within an experimental uncertainty of a factor of two. More precise measurements will be needed before one can definitively rule out a vacancy diffusion mechanism.

Further evidence against a vacancy diffusion mechanism includes a comparison of activation energies reported in tracer diffusion and internal friction studies [6–18]. The activation energy from tracer diffusion measurements, Q_{tracer}, for a vacancy diffusion model will contain two terms for the enthalpies of formation, ΔH_v, and migration, ΔH_m,

$$Q_{\text{tracer}} = \Delta H_v + \Delta H_m , \tag{2}$$

whereas the activation energy from internal friction measurements, Q_{IF}, will contain only one term for migration

$$Q_{\text{IF}} = \Delta H_m . \tag{3}$$

Theoretically, the difference in these two energies should yield the enthalpy of vacancy formation, $\Delta Q = Q_{\text{tracer}} - Q_{\text{IF}} = \Delta H_v$. However, the similarity in activation energies (~ 1 eV) measured by both tracer measurements [6,7] and by internal friction studies [11–18] suggests that ΔH_v for an oxygen vacancy is extremely small or zero ($\Delta H_v < 0.1$ eV). For most cases of interest, the vacancy availability factor, N_v, in eq. (1) can be assumed to be approximately 1 across the entire range of non-stoichiometry and, hence, does not contribute significantly to a concentration-dependent $\tilde{D}$.

3.2. Interstitial diffusion

In the limit of completely ordered and oxygenated YBCO ($x \sim 1$), oxygen may diffuse by an interstitial mechanism. Ideal solution mass-action equations (see Part II) [5] often do not completely describe the electrical transport properties of a highly disordered material. However, they may serve as an initial reference point in describing the defect chemistry for YBCO. At lower temperatures (450–550°C) the oxygen partial pressure exponents relating $P(O_2)$ to the isothermal resistivities, $\partial \operatorname{Log} \rho / \partial \operatorname{Log}[P(O_2)]$, were on the order of -0.1 to -0.25 (ref. [5]). These are close to an expected $-\frac{1}{6}$ (-0.17) dependence predicted by an interstitial model [5]

$$O_i'' + 2h^{\cdot} \rightleftarrows \tfrac{1}{2}O_2 + V_i , \tag{4}$$

where the terminology was given previously [5]. The vacant O(5) sites in YBCO are interstitial sites with reference to the completely ordered $YBa_2Cu_3O_7$ structure (fig. 1); hence, the diffusion model of Rothman et al. [7] may describe oxygen diffusion by an interstitial mechanism through successive $O(5) \rightarrow O(5)$ jumps. Consequently, at high oxygen concentrations, the tracer diffusivity would be independent of the concentration as reported [6,7]. If the model of Rothman et al. [7] is valid, one would

expect the disordering of oxygen from the O(1) to the O(5) sites to eventually block the interstitial rows. This would lead to a decrease in D^* as x decreases initially from $x=1$.

3.3. Correlation coefficient

In orthorhombic YBCO, oxygen anion jumps have been predicted to be strongly correlated [22,23]. Therefore, a candidate for a concentration-dependent diffusivity can be found in the correlation coefficient, f, in the expression

$$D^*=\alpha f a^2 \nu . \tag{5}$$

The correlation coefficient accounts for the fact that atomic jumps are often not strictly random [29]. If there is a greater than even chance that a diffusing atom will return to the site from which it just left, the jumps are correlated and f will become less than one. Correlation effects are often evident in curved Arrhenius plots according to the expression [29]

$$Q=H-k\frac{\mathrm{d}\ln f}{\mathrm{d}(1/T)}, \tag{6}$$

where Q is the measured activation energy for diffusion and H is the enthalpy for an atomic jump found in the jump frequency, ν. The absence of curvature reported by Rothman et al. [6,7] does not rule out correlation effects because, as mentioned previously, there was a factor of two experimental uncertainty.

One possible cause for correlated jumps includes oxygen defect interactions which occur in highly disordered materials such as YBCO. For example, in tetragonal YBCO, an oxygen anion may prefer to be a part of a chain (fig. 2(b)) rather than be by itself (fig. 2(a)). Consequently, jumps which place an oxygen on an O(1) site with another next nearest neighbor (nnn) O(1) oxygen are more probable and, hence, will be correlated. It has been suggested that $f\to 0$ as jumps become highly correlated in the oxygen ordered orthorhombic structure, while $f\to 1$ for the tetragonal structure [23]. However, oxygen interactions are still expected to occur in macroscopically tetragonal YBCO and may result in biased atomic jumps. Consequently, the expected chain fragments (or clusters) in the tetragonal phase could result in concentration-dependent correlation coefficients less than 1. Measurements of the correlation coefficient have not been reported.

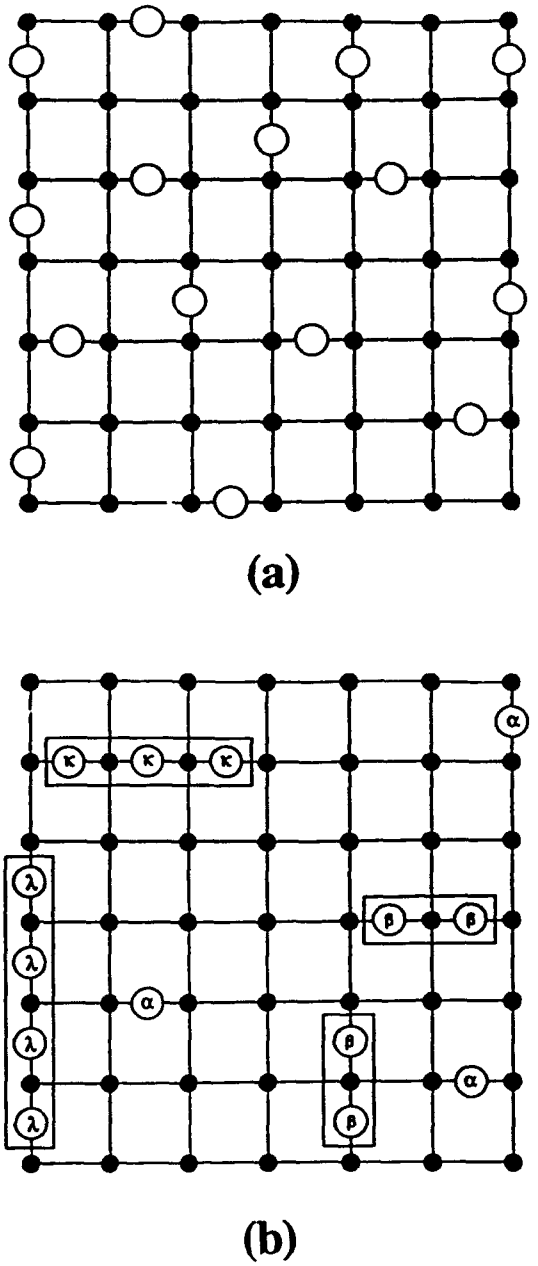

Fig. 2. (a) Randomly arranged oxygen anions in tetragonal YBCO. (b) Randomly arranged chain fragments or defect clusters in tetragonal YBCO.

3.4. Defect interactions and the thermodynamic factor

Orthorhombic YBCO has one-dimensional copper–oxygen chains which form when oxygen atoms order on the O(1) sites leaving the O(5) sites essentially vacant [28]. The chains disorder above ~700°C in pure oxygen to yield macroscopically tetragonal YBCO. Theoretical oxygen–oxygen interaction models suggest that short-range oxygen ordering in the form of chain fragments exist in tetragonal YBCO [1,2,25]. Randomly arranged chain fragments would still give equal occupancies for the O(1) and O(5) sites and macroscopic tetragonal symmetry. The change from tetragonal to orthorhombic symmetry in YBCO can then be viewed as the gradual coalescence and long-range ordering of these fragments at the transformation temperature. This ordering in YBCO would suggest a non-ideal solute behavior in YBCO across the entire range of oxygen nonstoichiometry, x, which is typical of a highly defective solid. Consequently, oxygen interactions are expected to influence oxygen mobility characteristics and are the prime candidates for a concentration-dependent chemical diffusivity.

The influence of ordered copper–oxygen chain structures on the oxygen diffusion behavior is evident in the reported diffusion anisotropy between the a and b crystallographic directions ($D_a^* \sim 0.01 D_b^*$) (ref. [7]) and from computer simulations [26]. (This anisotropy was reported to have completely disappeared at 650°C [30].) A purely random distribution of oxygen ions in the tetragonal structure (fig. 2(a)) may result in unfavorable atomic coordinations (e.g., three-fold coordinated copper in YBCO). Therefore, some degree of defect ordering in the form of short chain fragments [1,2,25] of four-fold coordinated Cu(1) ions is to be expected in tetragonal YBCO (fig. 2(b)). The length of these chain fragments will increase as both the temperature decreases and the oxygen concentration increases [1,2,25]. Consequently, there are several types of oxygen defects expected in tetragonal YBCO: lone oxygen anions (labeled as α in fig. 2(b)) and oxygen chain fragments of length two (β), three (κ), four (λ), etc. These chain fragments or defect clusters may have interaction and mobility dynamics which depend not only on temperature, but also on oxygen concentration. Clusters may behave as "lone" defects capable of diffusing as a whole through a solid, or their participation may be more indirect as in providing a source or sink for oxygen ions which could diffuse individually from one cluster to another. In YBCO, both of these processes may occur simultaneously.

If indeed, D^* is concentration-independent as reported [6,7], then a concentration-dependent $\tilde{D}$ (Parts I and II) [4,5] cannot be due to either the vacancy availability factor, the correlation coefficient, or the jump distance (eq. (1)). Therefore, the only remaining possibility would be a concentration-dependent thermodynamic factor $\partial \ln \gamma / \partial \ln x$ in the expression

$$\tilde{D} = D^* \left(1 + \frac{\partial \ln \gamma}{\partial \ln x} \right), \tag{7}$$

where γ is the activity coefficient of oxygen. The measured chemical diffusivities in YBCO have generally been larger than values reported for tracer or self-diffusivities. This suggests a significant contribution from the thermodynamic factor to the enhancement of the chemical diffusivity (eq. (7)). For example, $\tilde{D}$ for oxygen in YBCO, at an initial concentration of ~6.4 at 708°C, was of the order of 10^{-6} $cm^2 s^{-1}$ (refs. [4] and [5]) while D^* was reported to be approximately 10^{-9} $cm^2 s^{-1}$ at 700°C (ref. [6]). Consequently, the thermodynamic factor may be as large as 1000 (eq. (7)).

The thermodynamic factor contains the oxygen activity coefficient which should be unity at infinite dilution and may be expected to decrease as the solute concentration increases due to electrostatic interactions between oxygen anions and the lattice. The effective oxygen concentration would be lowered because the ions are associated into ordered configurations. Consequently, the measured oxygen partial pressure surrounding the system would be less than expected for the actual oxygen content in the material. The thermodynamic factor can theoretically be measured from the relationship between the oxygen content of a YBCO specimen and the surrounding oxygen partial pressure according to [20].

$$\frac{\partial \ln \gamma}{\partial \ln x} = \frac{1}{2} \frac{\partial \ln P(O_2)}{\partial \ln x}. \tag{8}$$

Large thermodynamic factors have been measured directly [20,27] and predicted theoretically [22,23]. A concentration-dependent oxygen activity would be evident in a curved plot of $\ln[P(O_2)]$ versus $\ln(x)$. If one examines such plots in refs. [20,27,31], a curvature is apparent; hence, a concentration-dependence is expected in both the thermodynamic factor and $\tilde{D}$ (eq. (7)).

4. Diffusion pathways

The fundamental jump mechanism(s) for an oxygen ion in YBCO has not been clearly established. The many ordered oxygen structures from $0<x<1$ suggest that the paths available for atomic jumps may also vary with oxygen concentration. In other words, the jump distance, a, in eq. (1) may vary with oxygen concentration, hence giving rise to the concentration-dependence in $\tilde{D}$ [4,5,19,20]. Inspection of eq. (1) reveals that a two-fold change in the jump distance with concentration would result in a four-fold change in the diffusion characteristics. However, evidence for such a large change in jump distance, a, with concentration has not been seen in tracer diffusion measurements [6,7].

In this section, the possible two-dimensional [32] jump pathways will be examined for two of the ordered oxygen structures, namely the Ortho I ($x\sim1$) and Ortho II ($x\sim0.5$) structures. Doping studies [33] (e.g, Fe, Al, F etc.) indicate that it is possible to have 7 to 8 anions per unit cell in YBCO. This clearly demonstrates that there is physical room for an oxygen anion on the O(5) site, suggesting that it will be primarily the electrostatic charge of the oxygen ion, rather than its size, which will control fundamental diffusive jumps in YBCO. For this reason, the oxygen ordering model of deFontaine et al. [1] was used to semi-quantitatively examine the energetics of particular diffusive jumps in YBCO. The oxygen anions with a net negative charge will repel each other when brought to nearest neighbor (nn) sites (i.e., O(1) and O(5)) or nnn sites between two chains (i.e., two intrachain O(1) sites) as denoted by V_1 and V_3, respectively (fig. 3). The most favorable site interaction occurs when two nnn O(1) sites are part of a single chain and are bridged by a Cu(1) copper cation as denoted by the V_2 parameter in fig.

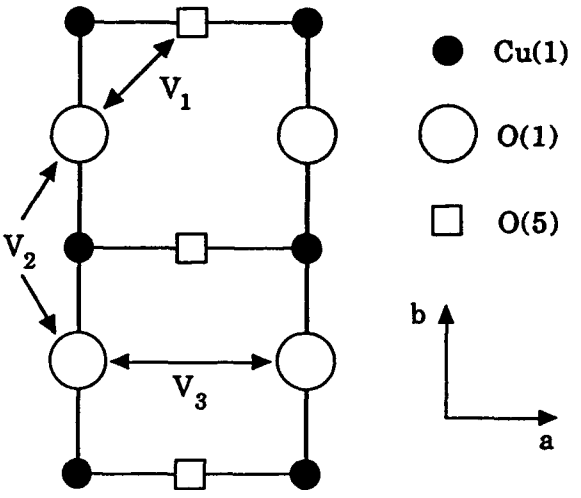

Fig. 3. Site interaction parameters V_1, V_2, V_3 between chain plane oxygen sites, $V_2<0<V_3<V_1$ (after ref. [1]).

3. This attractive interaction between oxygen anions favors chain formation. Sterne and Willie [34] reported interaction potentials of $V_1=0.38$ eV, $V_2=-0.13$ eV, and $V_3=0.06$ eV which can be used to estimate the increase in energy, ΔE, associated with different oxygen configurations encountered during oxygen jumps. Estimates are made in the following two sections. (Note: these ΔE's are *not* activation energies as they do not represent the typical inter-site saddle potentials one normally considers for diffusion.)

4.1. Diffusion in the Ortho I structure

In the ideal orthorhombic structure ($x=1$), the only jump sites available to an O(1) oxygen are the four nn O(5) positions (denoted by x's in fig. 4(a)). This jump is unfavorable as the diffusing oxygen anion would now have three nn oxygens and the energy of the system would be raised by $\Delta E_{15}=(3V_1-2V_3-2V_2)=1.18$ eV>0. Estimates of ΔE are listed in table 1. The oxygen ion would most likely prefer to return to its original chain site, thus, making this type of jump correlated (fig. 4(a)). Motion of an O(1) oxygen becomes more probable when a nnn O(1) oxygen vacancy is created, which results in two distinct O(5) sites labeled a and b in fig. 4(b). If the

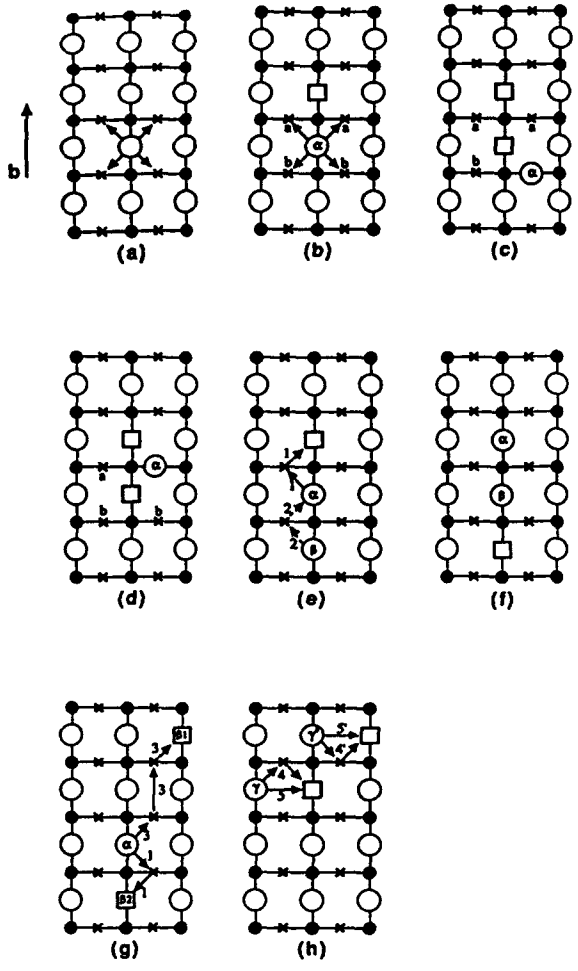

Fig. 4. (a) Four highly correlated jumps available to an O(1) oxygen in Ortho I YBCO. (b) An oxygen anion is more likely to make an interchain jump if it belongs to the end of a chain. (c) A jump to the b-site is energetically less favorable than (d) a jump to the a-site. (e, f) Suggested interchain diffusion mechanism in Ortho I YBCO (path 1, 2). (g) A series of O(5)→O(5) hops is energetically unfavorable (path 3). (h) Proposed interchain diffusion mechanisms for Ortho I YBCO.

Table 1
Configuration energies for an oxygen anion during diffusion based on the interaction parameters in ref. [33].

Ortho I		Ortho II	
ΔE (eV)	Fig.	ΔE (eV)	Fig.
$\Delta E_{15}=1.18$	4(a)	$\Delta E_{11}=0.26$	5(a)
$\Delta E_{15}^{a}=0.67$	4(b, d)	$\Delta E_{15}=0.64$	5(a)
$\Delta E_{15}^{b}=1.05$	4(b, c)	$\Delta E_{15}^{a}=0.51$	5(b, d)
$\Delta E_{55}=1.52$	4(g)	$\Delta E_{15}^{a'}=0.13$	5(b, c)
		$\Delta E_{55}=0.76$	5(f)

Note: The subscripts refer to the O(1) and O(5) sites. The superscripts differentiate the oxygen sites according to the local oxygen environment as identified in figs. 4 and 5.

Oα atom hops to the b site, it will have *three* nn oxygens and the energy is raised by $\Delta E_{15}^{b}=3V_1-2V_3-V_2=1.05$ eV (fig. 4(c)). However, a jump to the a site will result in *two* nn oxygens with an increase in energy of only $\Delta E_{15}^{a}=2V_1-2V_3-V_2=0.67$ eV (fig. 4(d)). The relation between the energies is simply $0<\Delta E_{15}^{a}<\Delta E_{15}^{b}<\Delta E_{15}$ (table 1). In other words, the jump shown in fig. 4(d) is energetically more favorable. Therefore, one can envisage diffusion in the *b*-direction (fig. 4(e)) in which Oα jumps to the nnn vacant O(1) site along the chain by following path 1; subsequently, the Oβ oxygen may proceed along path 2 (fig. 4(e) and (f)). This mechanism for diffusion along the *b*-direction is more likely than the model proposed by Rothman et al. [7] (fig. 4(g), path 3). The model of Rothman et al. [7] consisted of an oxygen hopping from the end of one chain onto an O(5) site, followed by a series of O(5)→O(5) jumps until it comes to the end of another chain represented by β1 (path 3). In accordance with a side interaction model, this diffusion pathway would be energetically unfavorable. Jumps from O(5)→O(5) sites between two fully ordered chains would place the diffusing oxygen ion between four nn O(1) anions; an increase in energy of $\Delta E_{55}=4V_1=1.52$ eV. Hence, a jump to the nnn O(1) oxygen vacancy, β2, is more probable (path 1 in fig. 4(g)).

Two types of intrachain jumps are possible in the Ortho I structure as represented by oxygen γ and γ′ (fig. 4(h)). Oxygen Oγ has two nnn O(1) oxygen while γ′ is at the end of a copper–oxygen chain with only one nnn O(1) site. Oγ has two possible pathways to the vacant site; first, it can first jump to an O(5) site (path 4) or, second, it can jump directly to the O(1) site (path 5). Motion of the Oγ, however, will result in the formation of two new chain ends which raises the energy of the system. In general, it should be easier for an oxygen anion to initiate a hop, if it is at the end of a chain (Oγ′), than

if it is part of a chain (Oγ) (fig. 4(h)). Diffusion of Oγ' can proceed by both
(1) an intrachain jump along either an O(1)→O(1) or O(1)→O(5)→O(1) path (fig. 4(h)) or,
(2) an interchain jump as shown previously (fig. 4(e) and (f)). Motion of both Oγ and Oγ' would result in a net diffusive flux in the *a*-direction. The in-plane anisotropy $D_b^*/D_a^* \sim 100$ near 300°C suggests that intrachain motion of oxygen is less likely than the interchain hopping shown in fig. 4(e) and (f). However, as more vacant O(1) sites appear, intrachain hopping could become more pronounced with a corresponding decrease in D_b^*/D_a^*. Since intrachain diffusion would require oxygen vacancies on neighboring chains, the *a*-axis diffusivity is expected to be concentration-dependent.

4.2. Diffusion in the Ortho II structure

The ideal Ortho II structure consists of alternating *full* copper–oxygen chains and *empty* chains (fig. 5(a)). This structure has a more open environment for a diffusing O(1) oxygen anion (fig. 5(a)) and provides two possible jump sites; an O(1)→O(5) hop (path 1) or a direct O(1)→O(1) hop (path 2). The jump to the O(5) site would change the energy by $\Delta E_{15} = V_1 - 2V_2 = 0.64$ eV > 0 while the intrachain hop to the neighboring O(1) site would change the energy by $\Delta E_{11} = -2V_2 = 0.26$ eV (table 1). Since $\Delta E_{11} < \Delta E_{15}$, the O(1)→O(1) jump is more favorable. In fig. 5(b) a single O(1) oxygen has been removed from a full chain resulting in two types of O(5) sites labeled a and a'. An Oα oxygen hopping to an a' site would change its energy by $\Delta E_{15}^{a'} = -V_2 = 0.13$ eV (fig. 5(c)) while a hop to the a site would change the energy by $\Delta E_{15}^{a} = -V_2 + V_1 = 0.51$ eV (fig. 5(d)). In other words, $\Delta E_{15}^{a'} < \Delta E_{15}^{a}$, and the a' jump is expected to be more probable (fig. 5(c)). Consequently, one can envisage *b*-direction diffusion occurring in a manner similar to the Ortho I structure (fig. 5(e) and (f)) in which an oxygen atom at the end of a chain would make an O(1)→O(5)→O(1) jump (fig. 5(e)) resulting in net diffusion in the *b*-direction. The neighboring empty chain, however, makes the O(5)→O(5) diffusion model of Rothman et al. [7] energetically more probable (fig. 5(f)) than in the Ortho I structure (fig. 4(g)). An oxygen residing in an O(5) site during diffusion in the Ortho II structure would have at most two nn O(1) oxygen anions ($\Delta E_{55} = 2V_1 = 0.76$ eV) by comparison with four nn oxygens ($\Delta E_{55} = 4V_1$) in the Ortho I structure (table 1). Intrachain jumps in the Ortho II structure are considered to occur by either multiple O(1)→O(5)→O(1) hops (path 1–2), O(1)→O(1) hops (path 3), or a combination of the two (fig. 5(g)). If the Oα oxygen hops to the O(5) site along path 1, it has two equivalent sites available for its next jump; first, a jump back to the full chain by path 1 or 1' or, second, Oα can jump to one of two O(1) sites in the empty chain (e.g., path 2).

Although rather simplistic, the above evaluation of the energies associated with possible jump pathways indicate that the local environment for a diffusing oxygen atom in orthorhombic YBCO can become quite varied and complex. Mixtures of ortho I and Ortho II structures could give rise to a variety of different jump pathways. The above discussion also emphasizes the fact that until the fundamental diffusive jump(s) can be determined in YBCO, a complete diffusion model cannot be developed. The lower energies for basic oxygen jumps in the Ortho II structure suggest that diffusion in highly oxygenated Ortho I material would be greatly facilitated by completely empty chains randomly dispersed in the lattice. The inability to achieve complete oxygenation of YBCO (i.e., $x = 1$) may then be a result of the difficulty of oxygen diffusing through the lattice, once most of these empty chains are isolated from the surface.

5. Conclusion

The observed concentration-dependence for the chemical diffusivity of oxygen in YBCO is proposed to be a result of defect–defect interactions. Consequently, the thermodynamic factor, which is a measure of the oxygen activity as a function of oxygen content, is considered to be most likely responsible for a concentration-dependent chemical diffusivity. Defect–defect interactions are expected to be evident in correlation effects. It is also possible that randomly oriented chain fragments or defect clusters exist in tetragonal YBCO. Examination of various oxygen diffusi[illegible]mps predicts that oxygen will dif-

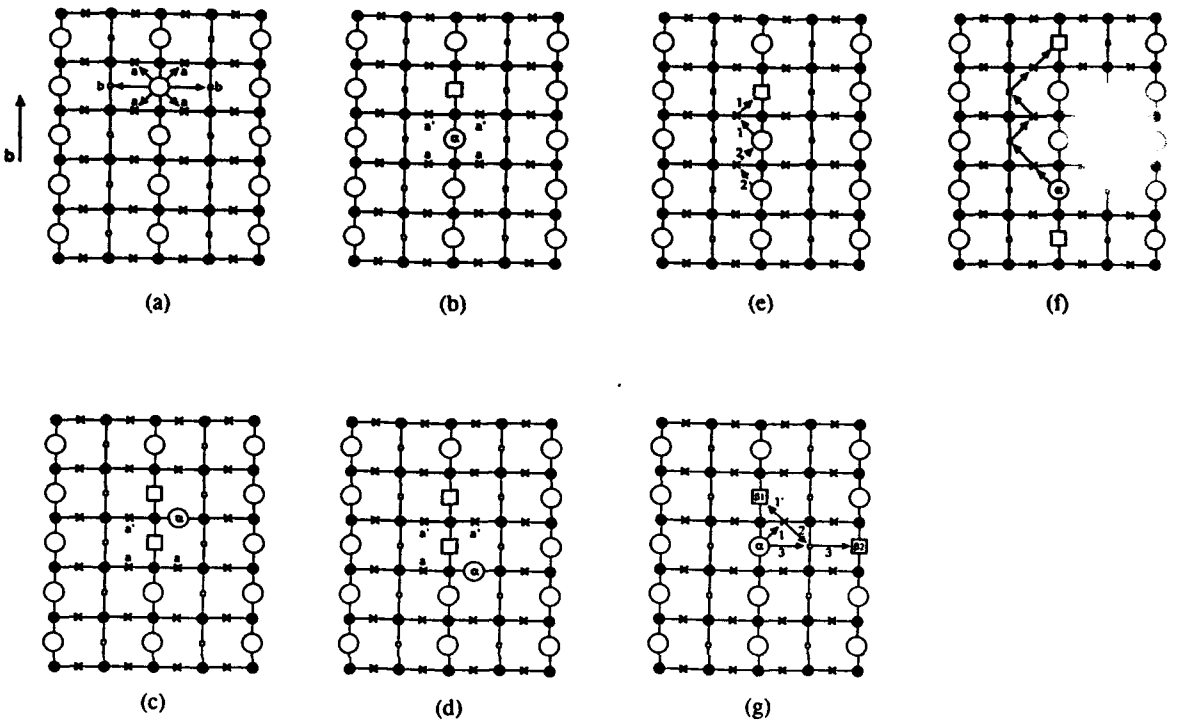

Fig. 5. (a) There are two distinct jump sites available to an O(1) anion in the Ortho II structure. (b) An oxygen anion is more likely to make an interchain jump if it belongs to the end of a chain. (c) A jump to the a'-site is energetically more favorable than (d) a jump to the a-site. (e) Suggested interchain diffusion mechanism in Ortho II YBCO. (f) Proposed diffusion mechanism for the more open Ortho II structure. (g) Intrachain diffusion pathways.

fuse more rapidly in the *b*-direction (along the copper–oxygen chains) when the anion is originally at the end of a chain and the adjacent chain is missing. Intrachain diffusion (*a*-axis) is expected to be slower and to depend on oxygen concentration.

Acknowledgements

The authors wish to thank S.J. Rothman and J.L. Routbort for helpful comments on this manuscript. The research was supported by the United States Air Force Office of Scientific Research through a University Research Initiative (URI-41318) on Phase Transformations Studies in Ceramics and by the National Science Foundation (DMR 88-09854) through the Science and Technology Center for Superconductivity.

References

[1] D. deFontaine, G. Ceder and M. Asta, Nature (London) 343 (1990) 544.
[2] S. Semenovskaya and A.G. Khachaturyan, Phys. Rev. Lett. 67 (1991) 2223.
[3] R. Beyers et al., Nature (London) 340 (1989) 619.
[4] J.R. LaGraff and D.A. Payne, Physica C 212 (1993) 470 (this issue).
[5] J.R. LaGraff and D.A. Payne, Physica C 212 (1993) 478 (this issue).
[6] S.J. Rothman, J.L. Routbort and J.E. Baker, Phys. Rev. B 40 (1989) 8852.
[7] S.J. Rothman, J.L. Routbort, U. Welp and J.E. Baker, Phys. Rev. B 44 (1991) 2326.
[8] Y. Ikuma and S. Akiyoshi, J. Appl. Phys. 64 (1988) 3915.
[9] S. Tsukui, T. Yamamoto, M. Adachi, Y. Shono, K. Kawabata, N. Fukuoka, S. Nakanishi, A. Yanase and Y. Yoshioka, Jpn. J. Appl. Phys. 30 (1991) L973.
[10] S.I. Bredikhin, G.A. Emel'chenko, V.Sh. Shechtman, A.A. Zhokhov, S. Carter, R.J. Chater, J.A. Kilner and B.C.H. Steele, Physica C 179 (1991) 286.

[11] X.M. Xie, T.G. Chen and J. Huang, Phys. Status Solidi A 110 (1988) 415.
[12] J.L. Tallon, A.H. Schuitema and N.E. Tapp, Appl. Phys. Lett. 52 (1988) 507.
[13] X.M. Xie, T.G. Chen and Z.L. Wu, Phys. Rev. B 40 (1989) 4549.
[14] J.L. Tallon and M.P. Staines, J. Appl. Phys. 68 (1990) 3998.
[15] J.R. Cost and J.T. Stanley, J. Mater. Res. 6 (1991) 232.
[16] G. Cannelli, R. Cantelli, F. Cordero, M. Ferretti and F. Trequattrini, Solid State Commun. 77 (1991) 429.
[17] Y. Mi, R. Schaller, S. Sathish and W. Benoit, Phys. Rev. B 44 (1991) 12575.
[18] G. Cannelli, M. Canali, R. Cantelli, F. Cordero, S. Ferraro, M. Ferretti and F. Trequattrini, Phys. Rev. B 45 (1992) 931.
[19] K.N. Tu, N.C. Yeh, S.I. Park and C.C. Tsuei, Phys. Rev. B 39 (1989) 304.
[20] K. Kishio, K. Suzuki, T. Hasegawa, T. Yamamoto, K. Kitazawa and K. Fueki, J. Solid State Chem. 82 (1989) 192.
[21] J.S. Choi, M. Sarikaya, I.A. Aksay and R. Kikuchi, Phys. Rev. B 42 (1990) 4244.
[22] E. Salomons and D. deFontaine, Phys. Rev. B 41 (1990) 11159.
[23] H. Bakker, J.P.A. Westerveld, D.M.R. LoCascio and D.O. Welch, Physica C 157 (1989) 25.
[24] M. Ronay and P. Nordlander, Physica C 153–155 (1988) 834.
[25] P.A. Rikvold, M.A. Novotny and T. Aukrust, Phys. Rev. B 43 (1991) 202.
[26] J.V. Andersen, H. Bohr and O.G. Mouritsen, Phys. Rev. B 42 (1990) 283.
[27] P. Meuffels, R. Naeven and H. Wenzl, Physica C 161 (1989) 539.
[28] O1 and O5 represent the O(1) and O(5) sites. See J.D. Jorgensen, M.A. Beno, D.G. Hinks, L. Soderholm, K.J. Volin, R.L. Hitterman, J.D. Grace, I.K. Schuller, C.U. Serge, K. Zhang and M.S. Kleefisch, Phys. Rev. B 36 (1987) 3608 for site designations.
[29] J.R. Manning, Phys. Rev. Lett. 1 (1958) 365.
[30] S. Tsukui et al. Proc. Int. Conf. on Diff. in Mater. (1993), to be published.
[31] O. Porat, I. Riess and H.L. Tuller, Physica C 192 (1992) 60.
[32] It has been suggested that diffusion may also take place through the apical O(4) oxygen sites situated immediately above and below the Cu(1) site in the (001) direction. See M. Islam, Supercond. Sci. Technol. 3 (1990) 531.
[33] For example, J.M. Tarascon, L.H. Greene, P. Barboux, W.R. McKinnon, G.W. Hull, T.P. Orlando, K.A. Delin, S. Foner and E.J. McNiff, Phys. Rev. B 36 (1987) 8393;
J.M. Tarascon, P. Barboux, P.F .Miceli, L.H. Greene, G.W. Hull, M. Eibschutz and S.A. Sunshine, Phys. Rev. B 37 (1988) 7458;
J.R. LaGraff, E.C. Behrman, J.A.T. Taylor, F.J. Rotella, J.D. Jorgensen, L.Q. Wang and P.G. Mattocks, Phys. Rev. B 39 (1989) 347.
[34] P. Sterne and L.T. Willie, Physica C 162–164 (1989) 223.

Chemical diffusion of oxygen in single-crystal and polycrystalline $YBa_2Cu_3O_{6+x}$ determined by electrical-resistance measurements

John R. LaGraff and David A. Payne
Department of Materials Science and Engineering and Materials Research Laboratory, University of Illinois at Urbana-Champaign, Urbana, Illinois 61801
(Received 7 February 1992; revised manuscript received 24 June 1992)

Isothermal electrical-resistance measurements were used to monitor oxygen diffusion kinetics in both single-crystal and polycrystalline $YBa_2Cu_3O_{6+x}$ between 350 and 780 °C. Distinctions are made between intrinsic diffusion behavior and microstructure-dependent properties. An activation energy of 0.4(1) eV was determined for oxygen in-diffusion in dense polycrystalline material from 400 to 780 °C, and 1.10(6) eV for single crystals between 600 and 780 °C. Below 600 °C, the activation energies for out-diffusion in porous and dense polycrystalline specimens were determined to be 0.5(1) eV and 0.6(1) eV, respectively. The lower activation energy in polycrystalline specimens was attributed to (i) shell effects at either grain boundaries or the specimen surface in which the rapid formation of a highly oxygenated skin created short-circuit pathways for current flow, and (ii) high-diffusivity pathways along grain boundaries. Measurements on single crystals reveal that the intrinsic rate of oxygen in-diffusion was comparable to, if not slower, than out-diffusion, which was contrary to measurements on polycrystalline specimens. This type of behavior was attributed to the formation of a highly oxygenated shell during in-diffusion which behaved as both (i) a high-conductivity pathway and (ii) a barrier to bulk oxygen in-diffusion. The use of single crystals enabled these effects to be clearly distinguished.

I. INTRODUCTION

Oxygen stoichiometry has a profound effect on the superconducting, normal state, and structural properties of $YBa_2Cu_3O_{6+x}$ (YBCO).[1,2] Consequently, an understanding of the chemical diffusion of oxygen $\tilde{D}$ is important for the processing of YBCO with specific property requirements in all of its requisite forms (e.g., bulk, melt-textured, single-crystal, thin-film, wire, etc.). Fundamental oxygen diffusion behavior has been reported by tracer-diffusion techniques[3–5] and internal friction measurements,[6–9] however, it is the chemical diffusion of oxygen, under a concentration gradient, which is most important for the processing of YBCO. The oxygen chemical diffusion coefficient is measured under a gradient in the chemical potential, which is most often achieved through changes in oxygen partial pressure surrounding the specimen, or changes in temperature. $\tilde{D}$ is related to the tracer or self-diffusivity D^* by the equation[10]

$$\tilde{D}=D^*\left[1+\frac{\partial \ln\gamma}{\partial \ln c}\right], \tag{1}$$

where the term in brackets is the thermodynamic enhancement factor containing the solute activity γ and concentration c of the diffusing species. In an ideal solution (often in the dilute limit), the activity γ is unity for all concentrations and the tracer-diffusion and chemical diffusion coefficients are equal. In the YBCO system, however, a significant contribution of the thermodynamic factor [Eq. (1)] is expected from studies of oxygen partial pressure as a function of oxygen concentration.[11,12] These results explain why values of $\tilde{D}$ reported for YBCO have generally been greater than the tracer or self-diffusivities.

The two most common techniques used to measure $\tilde{D}$ in YBCO are electrical-resistance measurements,[13–31] and thermogravimetric analysis,[12,30,32–36] which monitor the electron-hole content and mass, respectively, associated with oxygen exchange. Other techniques include solid-state electrochemical measurements,[37–41] gas volumetry,[42,43] *in situ* neutron diffraction,[43,44] differential scanning calorimetry,[45] IR spectroscopy,[35] and positron annihilation.[46] The remarkable agreement found in the tracer- and self-diffusivity studies[3–9] with regards to diffusion coefficients and activation energies is unfortunately lacking in the chemical diffusion studies.[13–46] In addition to the more complex situation for chemical diffusion (e.g., solute activities), these discrepancies can be attributed to different sample microstructures and experimental techniques.

In this paper, we report electrical-resistance measurements of oxygen diffusion kinetics in single-crystal and polycrystalline YBCO. A particular advantage of the electrical-resistance method, in addition to its extreme sensitivity to small changes in oxygen content, Δx, is the ability to make repeated measurements on a single specimen. This ensures high reproducibility by removing sample-to-sample variance, which enables subtle changes in oxygen diffusion behavior to be more readily distinguished. All of these factors make resistance measurements especially suitable for monitoring diffusion kinetics in single crystals of YBCO whose small mass precludes the use of thermogravimetric analysis. However, one is measuring a response that is attributed to the dynamic change in the carrier concentration and associated scattering processes and, thus, assumptions must be made

on the relationships between oxygen content, electron-hole concentration, and the overall resistance of the specimen.

YBCO is principally an electronic conductor with extremely low oxygen anion transference numbers (10^{-9} to 10^{-7} in Refs. 23 and 37). The electrical conductivity σ for majority hole carriers can be written as

$$\sigma=[h^{\cdot}]\mu e \ , \tag{2}$$

where $[h^{\cdot}]$ is the hole concentration, μ is the hole mobility, and e is the electron charge. Isothermal measurements allow the mobility term to be neglected and thus an increase in the resistance is largely a consequence of a decrease in the hole concentration as oxygen leaves the system according to the defect relation[14,23]

$$O_O^x+2h^{\cdot}\rightleftarrows V_O^{\cdot\cdot}+\tfrac{1}{2}O_2 \ , \tag{3}$$

where $V_O^{\cdot\cdot}$ denotes a doubly ionized (positive) vacant O(1) chain oxygen site, and O_O^x is the neutral occupied O(1) site. Defect models in a highly defective and nonstoichiometric compound such as YBCO are expected to be more complex. Theoretically, Eq. (3) describes a dilute solution of noninteracting oxygen anions and should be regarded as a first approximation of the relationship between the majority carriers and the oxygen content in YBCO.

Resistance measurements require that assumptions be made concerning the actual distribution of oxygen within the specimen, i.e., a diffusion mechanism must be assumed. The change in resistance with time $\Delta R(t)$ of YBCO is proportional to the change in oxygen content $\Delta x(t)$ according to the relation

$$\left[\frac{\ln R(t)-\ln R(0)}{\ln R(\infty)-\ln R(0)}\right]\equiv\left[\frac{x(t)-x(0)}{x(\infty)-x(0)}\right]\equiv\alpha(t) \ , \tag{4}$$

where $R(0)$ is the resistance at the beginning of in- or out-diffusion, $R(t)$ the resistance as a function of time, $R(\infty)$ the eventual saturation resistance, and $\alpha(t)$ the fractional change in resistance (or oxygen content). The resistance change during oxygen diffusion in rectangular bars of polycrystalline YBCO can be fit to the equation for one-dimensional diffusion into a plane[47]

$$\alpha(t)=1-\frac{8}{\pi^2}\sum_{n=0}^{\infty}\frac{1}{(2n+1)^2}\exp\left[\frac{-(2n+1)^2t}{\tau}\right] \ , \tag{5}$$

where the relaxation time τ is related to the chemical diffusivity $\tilde{D}$ by the expression

$$\tilde{D}=\frac{L^2}{\pi^2\tau} \ , \tag{6}$$

and L is the effective diffusion length. The large anisotropy in the tracer diffusivities[5] of YBCO suggests that oxygen exchange in single crystals will occur primarily at the edges of the thin platelets (i.e., it will be a two-dimensional process). This in turn can be represented by the two-dimensional analogue of Eq. (5) in which the presummation term is replaced by $64/\pi^4$ and the effective diffusion length L in Eq. (6) is replaced by

$$L^2=(1/L_a^2+1/L_b^2)^{-1}$$

where L_a and L_b are the crystal dimensions in the ab plane.

It is evident that, in addition to the measurement of accurate relaxation times, one must also choose an appropriate effective diffusion length L to estimate reliable diffusivities [Eq. (6)]. Unfortunately, this is often the most difficult step in interpreting the results of chemical diffusion studies especially in YBCO. Not only does the effective diffusion length depend on microstructural features such as grain size and connected porosity, but quite possibly on the experimental technique. For example, heterogeneous oxygen distributions may lead to shell effects, especially during in-diffusion. These shells may behave as short-circuit pathways for electrical current thus yielding resistances that are not representative of the bulk oxygen content.[27,28,30] With these motivations in mind, a study of the chemical diffusion behavior in both single-crystal and polycrystalline YBCO was undertaken to distinguish between intrinsic oxygen diffusion rates, and those influenced—if not dominated—by such factors as grain size, bulk density, and short-circuit pathways for current flow, which can occur in polycrystalline ceramic superconductors.

II. EXPERIMENTAL

A. Sample preparation

The authors have experience in the growth of doped and undoped single crystals of YBCO and have prepared and measured over 30 batches. Large single crystals of various sizes (up to $10\times10\times2$ mm^3) were grown in either alumina or yttria-stabilized zirconia crucibles by a standard self-flux technique described elsewhere.[13] Resistance measurements were made on many of these crystals during oxygen diffusion, and the results were found to be consistent from crystal to crystal, and from batch to batch.[13–18] The authors report here extensive resistance

TABLE I. Data for single crystals and polycrystalline YBCO specimens.

Specimen type	T_c	Specimen size (mm^3)	Grain size (mm)	Bulk density
Crystal $C1$	90 K	$1\times1\times0.05$		
Crystal $C2$	90 K	$2\times1.5\times0.5$		
Polycrystal $S1$	92 K	$4.85\times2.05\times0.50$	$1.1(2)\times6(1)$	75(5)%
Polycrystal $S2$	92 K	$4.70\times1.55\times0.90$	$2.8(4)\times19(3)$	95(5)%

measurements on two representative crystals, which serve to illustrate the general observations. The two twinned crystals had dimensions of approximately $1\times1\times0.05$ and $2\times1.5\times0.5$ mm^3 (hereafter referred to as $C1$ and $C2$, respectively) with the c axis oriented in the thin direction (Table I). The critical temperatures, T_c (onset), from superconducting quantum interference device (SQUID) susceptibility measurements were 90 K for both crystals with a transition width (10–90%) of 1 K.

YBCO powder was prepared by a standard mixed-oxide route as described previously.[48] Polycrystalline specimens of different grain sizes and bulk densities were obtained by pressing pellets at 24 MPa and then sintering for 24 h in oxygen at temperatures from 950 to 980 °C. We report here data on the two extremes in bulk densities as means of illustrating the influence of microstructure on the oxygen diffusion behavior as measured by the electrical resistance method. The bulk densities of specimens #1 ($S1$) and #2 ($S2$) were ~75(5) and ~95(5) %, respectively. The acicular grains had average dimensions of $\sim1.1(2)\times6(1)$ and $\sim2.8(4)\times19(3)$ μm for specimens $S1$ (porous) and $S2$ (dense), respectively (Fig. 1, Table I). Following a one week anneal at 500 °C in oxygen, x-ray analysis (scan rate, 1° 2θ/min; Cu $K\alpha$ radiation, 20 mA and 45 mV) indicated that the polycrystalline specimens were "phase-pure" and orthorhombic. SQUID susceptibility measurements yielded broad transitions (<2 K) with onset critical temperatures of 92 K. The pellets were subsequently sectioned into rectangular bars and polished to a 1 μm finish prior to resistance measurements. At least two bars were measured from each pellet and consistent results were obtained.

B. Electrical-resistance measurements

Measurements of electrical resistance during oxygen in-diffusion and out-diffusion were made by a computer-controlled four-point probe ac technique, while the specimen was simultaneously mounted in the hot stage of an optical microscope.[13,14] The applied ac current was kept constant at 1.86 mA (564 Hz) by a Stanford Research Systems SR530 lockin amplifier. Four gold wires (0.1% Be addition, 2 mil) were attached with silver paste to the corners of the (001) face of the single crystals and along the length of rectangular ceramic bars cut from the ceramic pellets. After annealing at 600° for several hours, the contacts had resistances of one ohm or less and had ohmic characteristics. Contact integrity was checked periodically throughout the measurements in both positive and negative dc currents. In order to further ascertain sample quality and contact integrity, resistivities were estimated from the geometry of polycrystalline specimens and by Montgomery's technique[49] for single crystals at various temperatures. The resistivities (ρ_{ab}) of the crystals were on the order of 100–200 $\mu\Omega$ cm at room temperature and 1–10 mΩ cm from 600–780 °C (100% oxygen). The bulk resistivities of the ceramic specimens were typically on the order of 3–30 mΩ cm from 350–780 °C. These values are in good agreement with those cited in the literature.[50]

Isothermal oxygen out-diffusion and in-diffusion was monitored by resistance measurements for single crystals

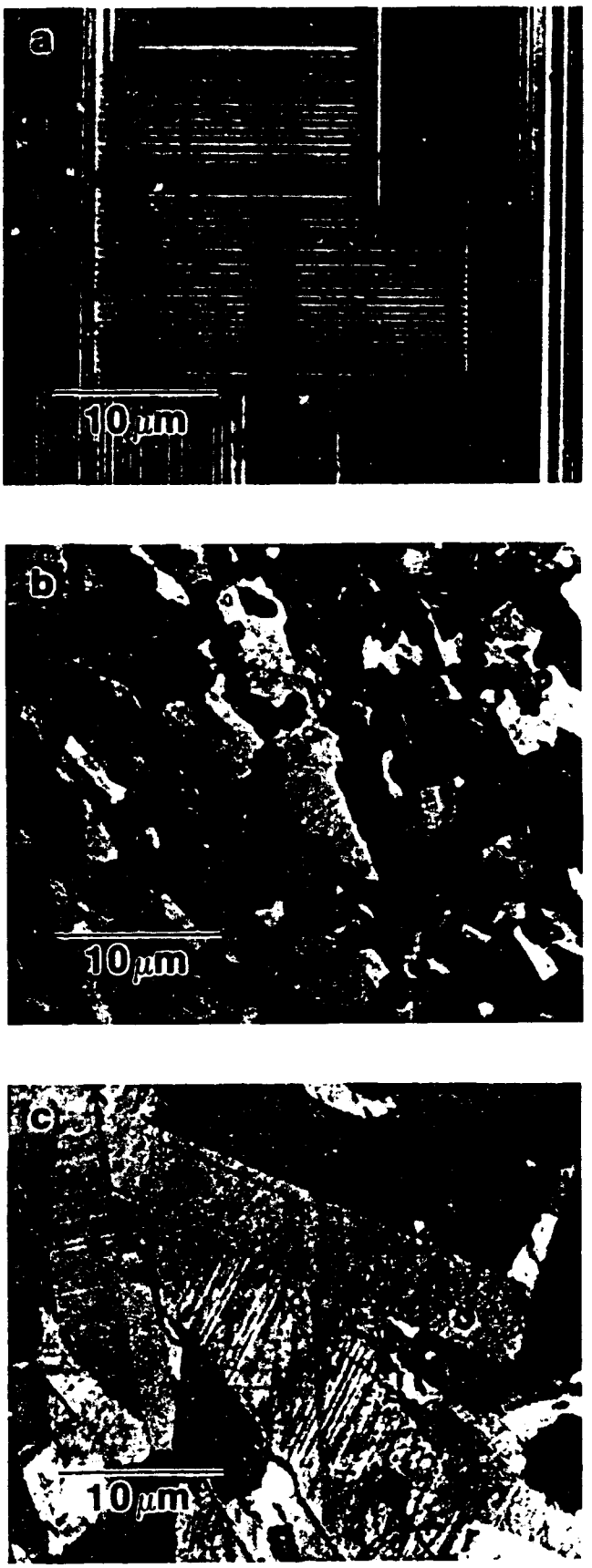

FIG. 1. Optical photomicrographs under cross-polarized reflected light of (a) single-crystal, (b) *porous*, fine-grain polycrystalline specimen $S1$, and (c) *dense*, coarse-grain polycrystalline specimen $S2$.

from 600–780 °C and for polycrystalline specimens from 350–780 °C. Resistance measurements in single crystals were prohibitively slow below 600 °C due to slow oxygen diffusion kinetics. (Several weeks are required to establish equilibrium in crystals.) The specimen was initially annealed in oxyge ' at the measurement temperature until equilibrium was established (> 36 h for crystals) as determined from calculations and by monitoring for constant resistance. Oxygen out-diffusion studies were carried out by introducing argon into the hot stage and recording the resistance increase of the specimen as a function of time. Following the argon anneal, oxygen was reintroduced into the system and the resistance decrease associated with oxygen in-diffusion was recorded. Water vapor and CO_2, which can degrade YBCO,[51] were removed from the ambient by a scrubbing column that contained CaO and $CaSO_4$. The strain accompanying the ferroelastic tetragonal-orthorhombic (TO) phase transformation was accommodated by the formation of {110} twin boundaries.[52] These transformation twins were clearly visible under polarized reflected light [see Fig. 1(a)] and enabled the phase transformation to be observed in an optical microscope during the resistance measurements.[13,14] Observation of the twin networks indicated that the crystal retained the orthorhombic structure below ~700 °C, and the tetragonal form above ~700 °C, when in equilibrium with pure oxygen. The crystal was driven isothermally through the orthorhombic-tetragonal (OT) transformation below ~700 °C by switching between oxygen and argon gases, however, no anomalies were observed in the measured resistance values.

III. RESULTS AND DISCUSSION

A. In-diffusion

Normalized resistance isotherms during oxygen in-diffusion for YBCO single crystals reveal a change in functional form as the temperature increased [e.g., crystal *C*2 in Fig. 2(a)]. Relaxation times during in-diffusion for crystals *C*1 and *C*2 were determined by fitting the data to the two-dimensional analogue of Eq. (5). An Arrhenius plot of the normalized relaxation times for crystals *C*1 and *C*2 yielded an activation energy for in-diffusion of 1.10(6) eV from 600–780 °C [Fig. 2(b)]. A similar analysis for dense polycrystalline material *S*2 yielded an activation energy of ~0.4(1) eV for in-diffusion from 400–780 °C [Fig. 2(c)]. (The rate of resistance change during in-diffusion for specimen *S*1 was too rapid for reliable determinations of relaxation time.) The activation energy (~0.4 eV) for in-diffusion from 400–780 °C in *dense*, large-grain specimen *S*2 [Fig. 2(c)] was similar to the values reported by Tu *et al.*[27] (~0.5 eV) from 210–360 °C and by Ottaviani *et al.*[28] (~0.4 eV) from 215–315 °C for the early stages of in-diffusion. These low values in comparison with single-crystal data (~1.10(6) eV) suggests either grain-boundary diffusion or the formation of a highly oxygenated conductive shell region,[27,28,30] the latter obscuring intrinsic in-diffusion behavior. Both Tu *et al.*[27] and Ottaviani *et al.*[28] measured in-diffusion activation energies of ~1.3 and 0.9 eV, respectively, for the latter stages of in-diffusion suggesting that the activation energy of ~1.10 eV for single crystals [Fig. 2(b)] was more representative of bulk oxygen in-diffusion.

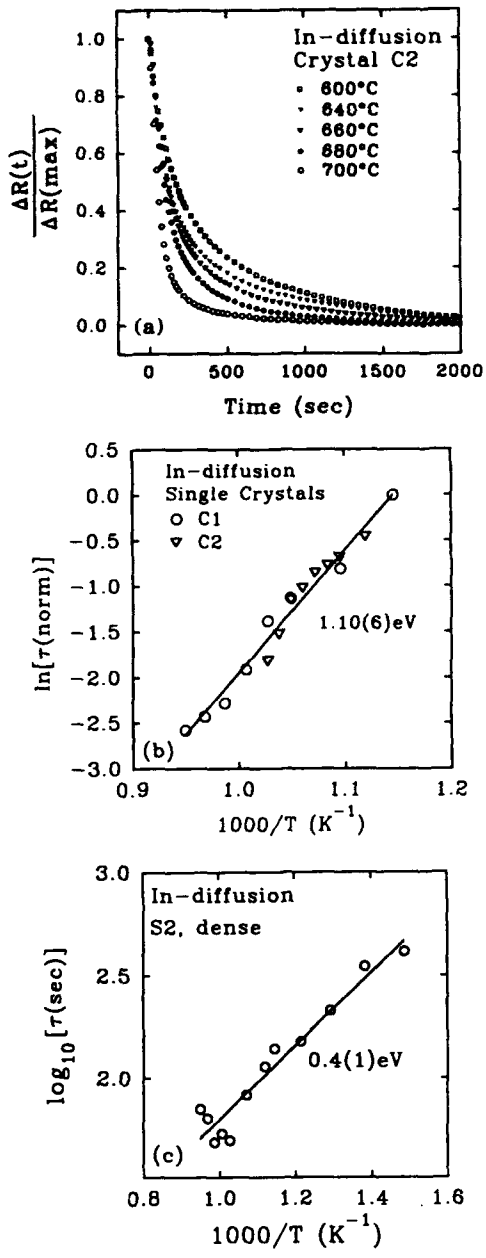

FIG. 2. (a) Normalized in-diffusion resistance isotherms from 600–700 °C in crystal *C*2 reveal a change in functional form with temperature. (b) An Arrhenius plot of normalized relaxation times for oxygen in-diffusion into *C*1 and *C*2 crystals suggests a single mechanism with an activation energy of 1.10(6) eV. (c) An Arrhenius plot of the relaxation times for oxygen in-diffusion into *dense*, coarse-grain polycrystalline specimen *S*2 from 400–780 °C. The low activation energy (0.4(1) eV) in comparison with single crystals (~1.10(6) eV) suggests that the formation of a highly oxygenated, highly conductive shell may mask intrinsic in-diffusion behavior.

B. Out-diffusion

The rate of resistance change during out-diffusion for the porous specimen *S*1 increased with temperature from

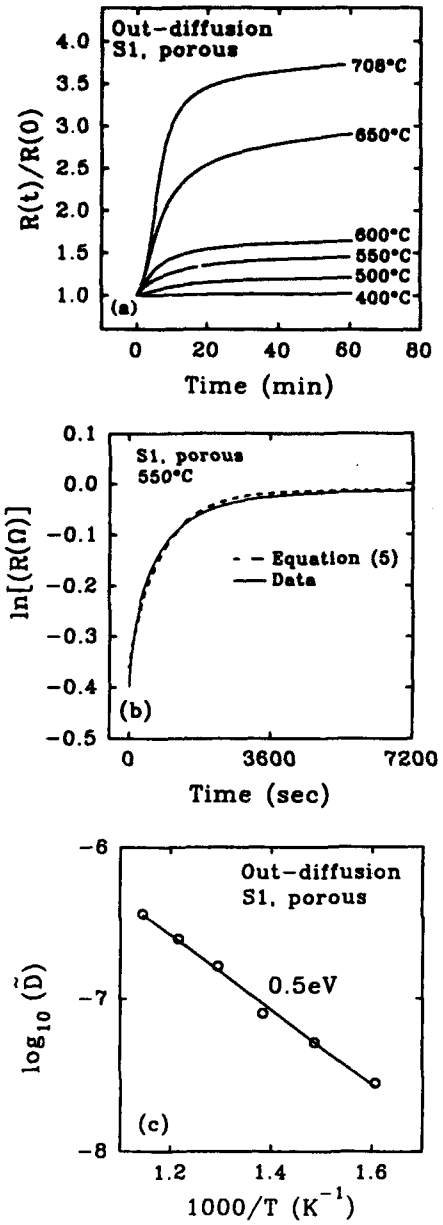

FIG. 3. (a) Resistance as a function of time for oxygen out-diffusion for *porous*, fine-grain specimen *S*1. (b) Resistance as a function of time for oxygen out-diffusion at 550°C and the corresponding fit to Eq. (5). (c) Arrhenius plot of the chemical diffusivities for oxygen out-diffusion below 600°C for the *porous*, fine-grain specimen *S*1. The diffusivities were estimated from Eq. (6) with an effective diffusion length equal to the specimen thickness ($L = 0.05$ cm).

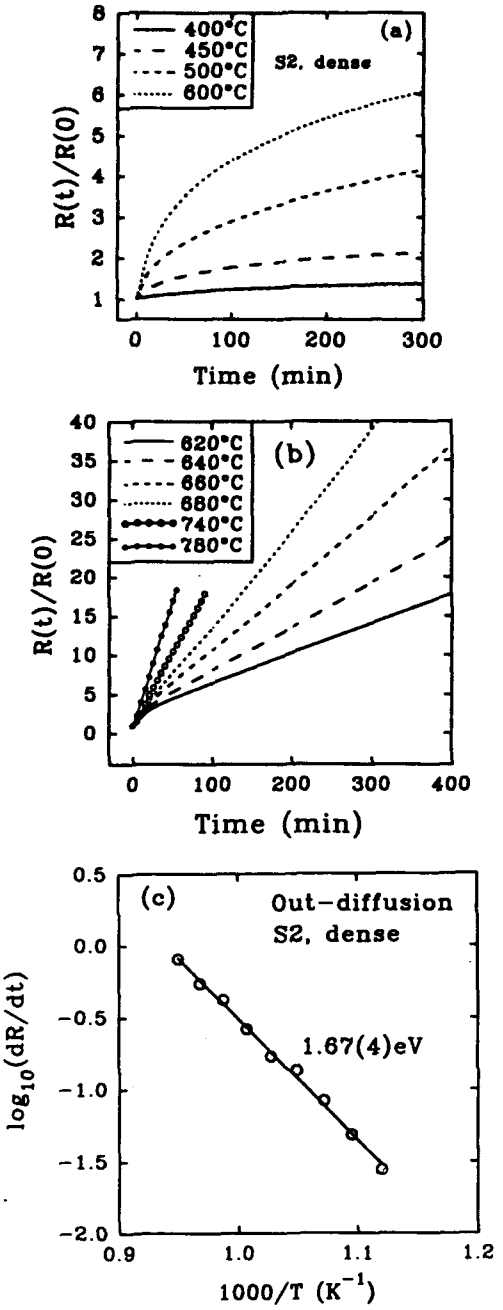

FIG. 4. Resistance increase during oxygen out-diffusion for *dense*, coarse-grain specimen *S*2 at temperatures (a) below 600°C and (b) above 600°C. There appears to be a crossover from diffusion-controlled to surface-limited out-diffusion behavior near 600°C. (c) Temperature dependence of $\log_{10}(dR/dt)$ for oxygen out-diffusion for *dense*, coarse-grain specimen *S*2.

400–708°C [Fig. 3(a)]. The resistance behavior was well described by a one-dimensional diffusion equation [Eq. (5)] [e.g., Fig. 3(b)]. The effective diffusion length L needed to accurately calculate $\tilde{D}$ [Eq. (6)] theoretically ranges from the average grain size to the external dimensions of the specimen depending on both porosity and the contribution of grain-boundary diffusion. As a first approximation, $\tilde{D}$ for *S*1 were estimated by using the thinnest sample dimension ($L \sim 0.05$ cm) as the effective diffusion length [Eq. (6)], which yielded an Arrhenius equation of the form

$$\tilde{D} = (2.6(5) \times 10^{-4}\ \text{cm}^2/\text{sec}) \exp\left[\frac{-0.5\ \text{eV}}{kT}\right] \quad (7)$$

from 350–600°C [Fig. 3(c)]. The connected porosity of specimen *S*1 in conjunction with the possibility of fast grain-boundary diffusion suggests that the average grain size could control the effective diffusion length. Howev-

TABLE II. Activation energies for oxygen diffusion in single-crystal and polycrystalline YBCO.

Specimen type	E (eV)	Temperature range	Comments[a]
Crystal $C1,C2$	1.10	600–780°C	ID
Polycrystal $S1$	0.5	350–600°C	OD,GB,SE
(porous, 75%; 6 μm)			
Polycrystal $S2$	0.6	400–600°C	OD,GB,SE
(dense, 95%; 19 μm)	1.67	600–780°C	OD,SRC
	0.4	400–780°C	ID,SE

[a]Key: OD (out-diffusion), ID (in-diffusion), SRC (surface-reaction controlled), GB (grain-boundary diffusion), SE (shell effects).

er, the Arrhenius expression obtained using $L=6$ μm (Table I) had a prefactor of 10^{-8} cm^2/sec, which was unreasonably small. The values of $\tilde{D}$ for $S1$ determined from Eq. (7) should, however, be interpreted as upper limits [Fig. 3(c)].

Out-diffusion curves for the dense, coarse-grain specimen $S2$ are shown in Figs. 4(a) and 4(b) both below and above 600°C, respectively. The resistance increase accompanying out-diffusion was linear with time above 600°C [Fig. 4(b)] but had exponential forms below 600°C [Fig. 4(a)]. This suggests a crossover from diffusion-limited to surface reaction-limited diffusion near 600°C during out-diffusion in an argon atmosphere. A similar crossover was observed during out-diffusion in argon for single crystals near 600°C,[18] but not in porous specimens (e.g., $S1$). Below 600°C, several days would have been required to obtain saturation resistances for the dense YBCO specimens (e.g., $S2$). Consequently, dense specimens were not completely deoxygenated below 600°C, which precluded the calculation of reliable relaxation times. The activation energy, however, for out-diffusion for $S2$ was determined from a constant resistance cut made through Fig. 4(a) to obtain characteristic times τ' at each temperature. These were fit to the standard expression

$$\tau'=\tau_0'\exp\left[\frac{E_0}{kT}\right] \tag{8}$$

yielding an activation energy of $E_0=0.6(1)$ eV (Table II). Within experimental error, this value was identical to the value (0.5(1) eV) obtained for the porous specimen $S1$ [Fig. 3(c)].

The activation energy for out-diffusion below 600°C in both dense and porous polycrystalline specimens (0.5–0.6 eV) was lower than the activation energies for $\tilde{D}$ for crystals [e.g., Fig. 2(b)] and reported for oxygen tracer diffusion ($\sim$1 eV).[3–5] This suggests a high-diffusivity pathway such as grain boundaries or external surfaces. Evidence for grain-boundary diffusion was also observed in dynamic heating experiments with single-crystal and polycrystalline specimens.[13,16] The resistance behavior of orthorhombic YBCO ($x\approx 1$) was metallic and increased linearly with temperature in pure oxygen up to approximately 350°C for polycrystalline ceramics[16] and up to 500°C for single crystals.[13,16] Above these temperatures appreciable oxygen out-diffusion occurred and the resistance increased more rapidly. This suggests that near 350°C grain-boundary diffusion becomes active in polycrystalline material, while significant bulk diffusion does not occur until close to 500°C. Internal friction measurements[53] have observed a Debye-like damping peak near 530°C, which was attributed to basal plane oxygen hopping at the onset of bulk lattice diffusion. The above discussion suggests that optimum oxygen incorporation will occur near 500°C where appreciable lattice diffusion would lead to an equilibrium oxygen content of approximately 6.9 (Ref. 54). Below 500°C, however, grain-boundary diffusion dominates and additional incorporation of oxygen into the bulk becomes extremely slow. This may explain the difficulty in achieving complete oxygenation (i.e., $x=1$) in YBCO especially in single crystals and in large dense polycrystalline specimens at reduced temperatures.

C. Surface-controlled out-diffusion

Above 600°C, out-diffusion of oxygen in single-crystal and dense polycrystalline specimens was assumed to be surface-reaction limited as suggested by the linear change of resistance with time, dR/dt [e.g., Fig. 4(B)]. The rate of oxygen out-diffusion was directly proportional to the change in carrier concentration dR/dt, which enabled the activation energy for out-diffusion to be calculated from,[14,27]

$$\left[\frac{dR}{dt}\right]=B_0\exp\left[\frac{-E_0}{kT}\right], \tag{9}$$

where B_0 is the preexponential factor and E_0 the activation energy. Analysis of linear out-diffusion isotherms (dR/dt) for dense polycrystalline specimen $S2$ [Fig. 4(b)] as a function of temperature from 600–780°C yielded a single activation energy of 1.67(4) eV [Fig. 4(c)].

The linear resistance behavior during oxygen out-diffusion for single crystals[14] and for *dense* polycrystalline specimens above 600°C [e.g., Fig. 4(b)] was similar to the behavior reported[27] below 440°C in polycrystalline specimens. However, most electrical conductivity studies on polycrystalline material exhibit an exponential increase in resistance during oxygen out-diffusion typical of a standard diffusion controlled process [for example, Refs. 21, 23, 25, 28, 30, and Fig. 3(a)]. Linear out-diffusion behavior was observed in polycrystalline material with high bulk density and coarse-grain size [e.g., specimen $S2$; Fig. 4(b)] suggesting that connected porosity or fine-grain size

gives rise to the nonlinear out-diffusion behavior reported in other studies[21,23,25,28,30] and observed in specimen $S1$ above 600 °C [Fig. 3(a)].

At this point, it is important to consider extrinsic factors that might be responsible for the linear resistance behavior during oxygen out-diffusion. These include, (i) a surface impurity film formed during preparation or, (ii) phase decomposition at the surface during out-diffusion measurements. It has been suggested[4] that a surface film on YBCO samples, which develops during sample preparation, impedes oxygen exchange. However, in this study, the rectangular bars obtained from polycrystalline pellets were polished, and crystals were cut or fractured from much larger crystals, which exposed fresh (100)/(010) surfaces for oxygen exchange. Consequently, an impurity film formed during specimen synthesis was not responsible for the surface barrier for out-diffusion.

Phase decomposition (ii) at temperatures above 600 °C could have resulted in surface-reaction limited oxygen out-diffusion. There were, however, several observations that make this possibility unlikely. Linear resistance behavior was not observed during oxygen out-diffusion in the porous specimen, $S1$ [Fig. 3(a)], which by virtue of the larger internal and external surface area should make the material more susceptible to phase decomposition. Irreversible phase decomposition in $S1$ should lead to drift in the equilibrium resistance values $R(\infty)$ for repeated diffusion anneals. However, $R(\infty)$ in both polycrystalline and single-crystal specimens was always regained between successive diffusion runs suggesting that, if a secondary phase developed during out-diffusion in argon, it was thermodynamically reversible. A recent paper[55] suggested that the reversible formation of $YBa_2Cu_4O_8$ at the YBCO grain surface during out-diffusion gave rise to a surface barrier for out-diffusion. However, it is difficult to ascribe an explicable source for the additional Ba and Cu content. Also, $YBa_2Cu_4O_8$ formation is usually favored in high oxygen overpressures and should not form, while YBCO is undergoing reduction.

In addition, x-ray analysis, optical microscopy, and Auger analysis were used in an attempt to detect any surface phase present. X-ray diffraction did not detect impurity phases in any of the specimens even after numerous diffusion experiments. *In situ* observation of the (001) face of single crystals in an optical microscope did not reveal changes in features that may accompany phase decomposition during oxygen diffusion (e.g., tarnishing, pitting, etc.). In order to detect possible trace impurities, however, semiquantitative chemical analysis of YBCO crystal surfaces and near-surface composition was determined on a PHI model 660 Scanning Auger microscope, which could be operated in a sputter mode. Both (001) and (100/010) surfaces of as-grown crystals were found to have trace amounts of zirconia and carbon, which disappeared immediately upon sputtering. The Y-Ba-Cu-O ratio was essentially constant from the surface into the near-surface region. Crystal $C2$ was examined after one month of diffusion measurements and after an additional two months at 600 °C. The (001) surface was found to have slightly excess barium along with carbon and zirconium, however, the near surface region was entirely Y-Ba-Cu-O. The (100/010) surfaces were found to have more excess barium than the (001) surface, and carbon and zirconia were found to penetrate further into the near-surface region (<50 nm) before a constant Y-Ba-Cu-O ratio was obtained. As suggested by diffusion anisotropy, the (100/010) surfaces of a YBCO crystal were more reactive than the (001) surface during oxygen exchange. Although surface phases were not detected by x-ray analysis or observed by optical microscopy, Auger analysis detected trace impurities at the (100/010) surfaces of crystals.

D. Intrinsic diffusion rates: influence of microstructure

There is still some controversy surrounding the intrinsic rates of oxygen in-diffusion and out-diffusion in YBCO. Thermogravimetric analysis (TGA) has reported in-diffusion to be both faster[33] and equal[12] to out-diffusion. Most electrical-resistance studies, however, report *faster* in-diffusion than out-diffusion in polycrystalline material,[19,21,23,27] however, a study on single crystals reported *slower* in-diffusion than out-diffusion.[15] It is possible that the relative rates of in- and out-diffusion may depend on both the temperature of the measurement and the specimen's microstructure. A study[42] reported that the relative rates of in- and out-diffusion vary with temperature, becoming nearly identical at higher temperatures. Correspondingly, the influence of microstructure on the measured activation energies and chemical diffusivities was supported, for example, by a TGA study,[34] which reported the activation energy for oxygen diffusion to be greater for a polycrystalline pellet (~ 1.5 eV) than a loose powder (~ 1.2 eV). The reported discrepancies on diffusion rates in electrical-resistance measurements may also be due the formation of a highly oxygenated, highly conductive shell region during in-diffusion. The influence of a highly oxygenated shell will now be discussed with relation to its extrinsic effect on electrical-resistance measurements and its intrinsic effect on oxygen diffusion rates.

The influence of microstructure on the resistance behavior of YBCO during oxygen out- and in-diffusion is exemplified in Figs. 5 and 6. During out-diffusion in argon at 708 °C, the resistance of single-crystal $C1$ increased linearly with time typical of a surface-reaction controlled process [Fig. 5(a)]. Oxygen in-diffusion was initiated by exchange from argon to oxygen and was evident in the resulting resistance change, which first decreased rapidly and then more slowly with time [Fig. 5(a)]. If out-diffusion was driven to completion at 708 °C, it took more than 24 h for crystal $C1$ to reach a saturation resistance. Examination of dense polycrystalline YBCO [e.g., $S2$ in Fig. 1(c)], revealed that the resistance increase during out-diffusion was also linear [Fig. 5(c)] and, if taken to completion, saturated in ~ 24 h. Similar times for saturation for out-diffusion in crystal $C1$ and dense polycrystal $S2$, together with nearly identical effective diffusion lengths ($L \sim 0.9-1.0$ mm, Table I), suggests that oxygen out-diffusion in dense polycrystalline

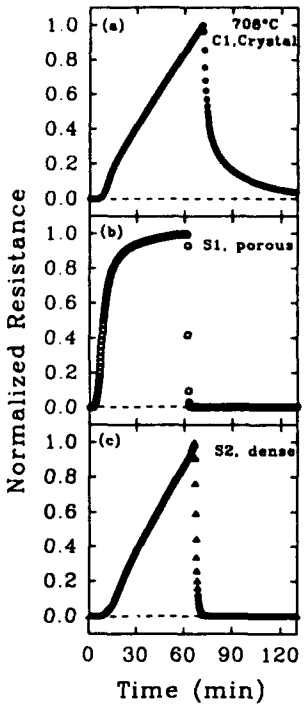

FIG. 5. Normalized resistance as a function of time for oxygen out-diffusion and in-diffusion at 708 °C for (a) single-crystal $C1$, (b) *porous*, fine-grain specimen $S1$, and (c) *dense*, coarse-grain specimen $S2$ (see Fig. 1). The resistance increased during oxygen out-diffusion and decreased for oxygen in-diffusion in all specimens, however, the functional forms are noticeably different. Note that in (a) the initial resistance was still not regained after a 1 h oxygen anneal, which suggests that oxygen in-diffusion was intrinsically slower than out-diffusion.

YBCO was not significantly affected by grain-boundary diffusion or shell effects. However, introducing connected porosity into YBCO [e.g., $S1$ in Fig. 1(b)] led to a non-linear increase in resistance during out-diffusion [Fig. 5(b)], which if driven to completion, saturated after

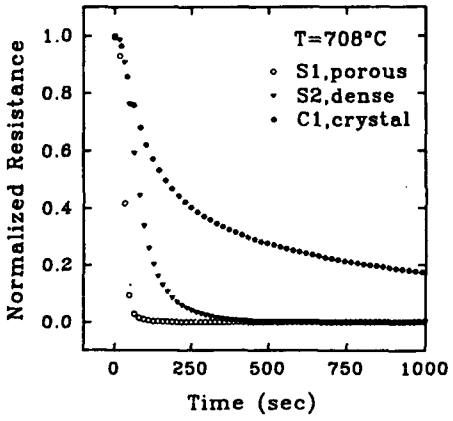

FIG. 6. Normalized resistance for oxygen in-diffusion at 708 °C in polycrystalline and single-crystal YBCO. The difference in functional form between *porous* $S1$ and *dense* $S2$ polycrystalline specimens suggests that grain size and/or bulk density influenced the in-diffusion kinetics.

~3 h. This nonlinear behavior, and rapid saturation in $S1$ in comparison with single crystals and dense polycrystalline $S2$, was attributed to the connected porosity in $S1$, which made more internal surface area available for oxygen exchange and, also, shortened the diffusion pathway, L.

Measurements on several single crystals indicated that the intrinsic rate of oxygen in-diffusion was comparable to, if not slower than, the rate of out-diffusion [e.g., Fig. 5(a)].[15] This was in contradiction to reports[19,21,23,27] for extremely fast in-diffusion for polycrystalline specimens [e.g., Figs. 5(b) and 5(c)]. As a means of illustrating these discrepancies, the resistance behavior during oxygen in-diffusion for $C1$, $S1$, and $S2$ (Fig. 5) are shown for smaller time increments in Fig. 6. A clear difference is seen in the rate of resistance decrease between porous and dense specimens indicating that connected porosity will, as expected, increase the rate of oxygen in-diffusion (Fig. 6). In addition, the equilibrium resistance $R(\infty)$ value upon oxygen in-diffusion was recovered more quickly for polycrystalline specimens compared with the crystal, which incorrectly suggests that oxygen in-diffusion was more rapid than out-diffusion [Figs. 5(b), 5(c), and 6].

The apparent rate of oxygen in-diffusion was more rapid in $S2$ in comparison with single-crystal $C1$ even though the effective diffusion lengths were similar (Fig. 6 and Table I). One possibility, for such apparently faster in-diffusion for $S2$ was that it had a greater surface area (approximately 100×) than the small crystal (Table I). In addition, oxygen exchange would occur primarily at the edges of a platelet single crystal due to the highly anisotropic D^*.[5] However, if the larger surface area for $S2$ was the only cause for rapid in-diffusion, then the rate of out-diffusion in $S2$ should have been, correspondingly, much faster than in crystal $C1$. The apparent rapid in-diffusion for $S2$ was therefore attributed to shell effects in which the formation of an initial highly oxygenated surface layer caused a short-circuit pathway for current flow. This gave a measured overall resistance that was not representative of the bulk oxygen content. Consequently, reports of faster in-diffusion than out-diffusion in polycrystalline YBCO, especially as determined from electrical-resistance measurements, are most likely due to extrinsic factors.[19,21,23,27]

There are several possibilities for the slow recovery of the equilibrium resistance $R(\infty)$ during in-diffusion in single crystals [e.g., Fig. 5(a)], including, (i) slow oxygen ordering kinetics, (ii) reversible phase decomposition and, (iii) slower in-diffusion than out-diffusion. The existence of a series of oxygen superlattice structures from $0.3 < x < 0.8$ (Ref. 56) and of room-temperature oxygen mobility[57–60] suggests that the effective hole density not only depends on the total oxygen content but also on the local coordination and ordering of oxygen.[61] Consequently, the slow recovery of $R(\infty)$ in Fig. 5(a) could be due to time-dependent ordering behavior (i). However, at high temperatures (e.g., $\gtrsim 600$ °C), the kinetics of oxygen ordering are expected to be rapid in comparison with the time scale of the diffusion measurement and should not greatly influence the effective carrier concentration. If reversible phase decomposition (ii) did occur during out-

diffusion in argon, then the slow recovery of the equilibrium resistance during in-diffusion may be due to the new phase slowly reverting back to YBCO. However, as discussed in Sec. III C, thermodynamically reversible phase decomposition (ii) appears to be unlikely.

The intrinsic rates of oxygen in- and out-diffusion (iii) were more clearly distinguished in single-crystal specimens [e.g., Fig. 5(a)]. The surface area to volume ratio for single crystals was much less than polycrystalline specimens, consequently, a highly conductive layer around a crystal's edge would have less of an effect on the overall resistance. Upon inspection of Fig. 5(a), the intrinsic rate of in-diffusion appears slower than out-diffusion for single crystals (iii). This type of behavior has been observed at all temperatures (600–780 °C) and for other crystals we have measured regardless of the length of the initial argon anneal. It is suggested that upon oxygenation, a crystal will quickly form a highly oxygenated layer around its edges, which coarsens with time, thus, leading to increasingly slower in-diffusion rates [e.g., Fig. 5(a)]. Oxygen diffusion through this layer would be hindered by several factors; a lower concentration of oxygen vacancies in comparison with the bulk; and, in the orthorhombic structure, ordered oxygen regions and twin boundaries. Both Monte Carlo simulations[62] and reported anisotropy in the tracer-diffusion coefficients[5] ($\tilde{D}_b \approx 100\tilde{D}_a$) sugges s that ordered regions impede oxygen diffusion. In addition, the observation of an increasing chemical diffusivity $\tilde{D}$ with decreasing oxygen content at 708 °C (Ref. 17) is to be expected when in-diffusion is intrinsically slower than out-diffusion.[63]

Reports[19,21,23,27] of faster in-diffusion than out-diffusion by electrical-resistance measurements did not satisfactorily address the possibility that shell effects may lead to different apparent rates. As means of illustration, series and parallel resistor models for cubic grains can be used as a first approximation to illustrate the influence of time-varying heterogeneous oxygen concentration distributions on a sample's overall resistivity characteristics during oxygen exchange. The overall resistivity ρ_t of a sample during the initial stages of oxygen in-diffusion can be modeled by a parallel resistor network

$$\frac{1}{\rho_t} = \frac{1}{\rho_b} + \frac{2x_{gb}}{3\rho_{gb}} , \tag{10}$$

where ρ_b and ρ_{gb} are the resistivities of the bulk and of the shell, respectively, and x_{gb} the volume fraction of the shell for cubic grains. Likewise, a simple series model may describe out-diffusion:

$$\rho_t = \rho_b + \frac{x_{gb}\rho_{gb}}{3} . \tag{11}$$

At 700 °C, the resistivities of fully oxygenated and deoxygenated dense YBCO polycrystals were approximately 10 and 1000 mΩ cm, respectively. Consequently, during in-diffusion $\rho_{gb} = 10$ mΩ cm and $\rho_b = 1000$ mΩ cm, while during out-diffusion the values of ρ_{gb} and ρ_b were interchanged. Figure 7 shows the change in overall resistivity versus the effective thicknesses of shells x_{gb} of highly oxygenated and deoxygenated material during in- and out-diffusion, respectively. Even assuming that the rates of in- and out-diffusion are equal, there was a considerably more rapid decrease in resistivity during in-diffusion than a resistivity increase during out-diffusion. In other words, a *deoxygenated* shell formed during out-diffusion would have a lesser effect on the overall rate of resistance change in comparison to an equally thick *oxygenated* shell formed during in-diffusion. The influence of oxygen in- and out-diffusion on the resistance behavior in YBCO is probably more complex than described by Eqs. (10)–(11), however, these models serve as a simple illustration of how measurements of resistance characteristics during oxygen diffusion may lead to different apparent rates of oxidation and reduction.

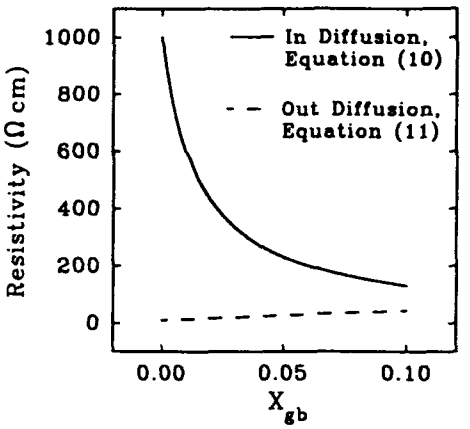

FIG. 7. The possible influence of heterogeneous oxygen distributions on the rate of resistance change for oxygen in- and out-diffusion as estimated from parallel and series resistor models [Eqs. (10) and (11)]. x_{gb} is the effective volume of the shell for cubic grains.

IV. CONCLUSION

In summary, the study of the time-dependent electrical characteristics of single-crystal and polycrystalline YBCO during oxygen in- and out-diffusion has allowed for intrinsic diffusion characteristics to be distinguished from those that are influenced by extrinsic microstructure effects. Diffusion rates and activation energies were found to be dependent on microstructure under certain conditions, which accounts for the many apparent discrepancies reported in the literature for chemical oxygen diffusion in YBCO superconductors. In-diffusion in dense YBCO specimens had an activation energy of 0.4 eV from 400–780 °C, while oxygen out-diffusion in dense and porous material had an activation energy of 0.5–0.6 eV below 600°. These low energies, in comparison with those determined from tracer diffusivities (~1 eV) and from measurements on single crystals, suggests high-diffusivity pathways along internal surfaces (e.g., grain boundaries) or external surfaces. In addition, the rate of oxygen in-diffusion was observed to be comparable to, if not *slower*, than out-diffusion in single crystals of YBCO at all measurement temperatures (600–780 °C) with an activation energy of 1.10(6) eV.

The formation of a highly oxygenated shell during oxygen in-diffusion had two major effects on the electrical resistance of YBCO specimens. One, the shell behaved as a highly conductive, short-circuit pathway yielding resistances that were not representative of the bulk, particularly in polycrystalline specimens. This extrinsic effect made the rate of in-diffusion appear to be much faster than out-diffusion in polycrystalline specimens when first examined by resistance measurements. Simple parallel and series resistor models were used to illustrate this effect. Two, a highly oxygenated shell also behaves as a barrier to further oxygen in-diffusion. A lower concentration of oxygen vacancies and/or more ordered oxygen regions in this shell would make oxygen diffusion through the layer increasingly slower. The use of single-crystal specimens enabled the intrinsic effect of the diffusion barrier for the highly oxygenated shell region to be more clearly distinguished from the extrinsic effect of high-conductivity pathways.

ACKNOWLEDGMENTS

The authors greatly appreciate the assistance of their colleagues P. D. Han and A. Asthana, and the use of facilities in the Materials Research Laboratory at the University of Illinois. Auger analysis was carried out by Dr. Zhengkui Xu. The authors would also like to thank S. J. Rothman and J. L. Routbort for helpful discussions. The project was supported by the Air Force Office of Scientific Research, Grant No. URI-41318, through a University Research Initiative on Phase Transformations in Ceramics and by the National Science Foundation, Grant No. DMR 88-09854, through the Science and Technology Center for Superconductivity.

[1]R. J. Cava, A. W. Hewat, E. A. Hewat, B. Batlogg, M. Marezio, K. M. Rabe, J. J. Krajewski, W. F. Peck, and L. W. Rupp, Physica C **165**, 419 (1990).

[2]J. D. Jorgensen, B. W. Veal, A. P. Paulikas, L. J. Nowicki, G. W. Crabtree, H. Claus, and W. K. Kwok, Phys. Rev. B **41**, 1863 (1990).

[3]For a recent review, see S. J. Rothman and J. L. Routbort, in *Diffusion in Materials*, edited by A. L. Laskar *et al.* (Kluwer, Dordecht, 1990), p. 393.

[4]S. J. Rothman, J. L. Routbort, and J. E. Baker, Phys. Rev. B **40**, 8852 (1989).

[5]S. J. Rothman, J. L. Routbort, U. Welp, and J. E. Baker, Phys. Rev. B **44**, 2326 (1991).

[6]X. M. Xie, T. G. Chen, and J. Huang, Phys. Status Solidi A **110**, 415 (1988).

[7]X. M. Xie, T. G. Chen, and Z. L. Wu, Phys. Rev. B **40**, 4549 (1989).

[8]J. L. Tallon and M. P. Staines, J. Appl. Phys. **68**, 3998 (1990).

[9]G. Cannelli, R. Cantelli, F. Cordero, M. Ferretti, and F. Trequattrini, Solid State Commun. **77**, 429 (1991).

[10]P. G. Shewmon, *Diffusion in Solids* (Williams, Jenks, OK, 1983).

[11]P. Meuffels, R. Naeven, and H. Wenzl, Physica C **161**, 539 (1989).

[12]P. Kishio, K. Suzuki, T. Hasegawa, T. Yamamoto, K. Kitazawa, and K. Fueki, J. Solid State Chem. **82**, 192 (1989).

[13]J. R. LaGraff, P. D. Han, and D. A. Payne, Physica C **169**, 355 (1990).

[14]J. R. LaGraff, P. D. Han, and D. A. Payne, Phys. Rev. B **43**, 441 (1991).

[15]J. R. LaGraff, P. D. Han, and D. A. Payne, in *Defects in Materials*, edited by P. D. Bristowe, J. E. Epperson, J. E. Griffith, and Z. Liliental-Weber, MRS Symposia Proceedings No. 209 (Materials Research Society, Pittsburgh, 1991), p. 801.

[16]J. R. LaGraff and D. A. Payne, in *Physics and Materials Science of High-Temperature Superconductors II*, edited by R. Kossowsky, B. Raveau, and S. Patapis (Kluwer, Dordecht, 1992), pp. 225–246.

[17]J. R. LaGraff and D. A. Payne (unpublished).

[18]J. R. LaGraff, Ph.D. thesis, University of Illinois at Urbana-Champaign, 1992.

[19]K. N. Tu, S. I. Park, and C. C. Tsuei, Appl. Phys. Lett. **51**, 2158 (1987).

[20]S. I. Park, C. C. Tsuei, and K. N. Tu, Phys. Rev. B **37**, 2305 (1988).

[21]G. Sageev Grader, P. K. Gallagher, J. Thomson, and M. Gurvitch, Appl. Phys. A **45**, 179 (1988).

[22]K. N. Tu, C. C. Tsuei, S. K. Park, and A. Levi, Phys. Rev. B **38**, 772 (1988).

[23]J. Park, P. Kostic, and J. P. Singh, Mater. Lett. **6**, 393 (1988).

[24]K. N. Tu, N. C. Yeh, S. I. Park, and C. C. Tsuei, Phys. Rev. B **38**, 5118 (1988).

[25]A. T. Fiory, S. Martin, L. F. Schneemeyer, R. M. Fleming, A. E. White, and J. V. Waszczak, Phys. Rev. B **38**, 7129 (1988).

[26]N. C. Yeh, K. N. Tu, S. I. Park, and C. C. Tsuei, Phys. Rev. B **38**, 7087 (1988).

[27]K. N. Tu, N. C. Yeh, S. I. Park, and C. C. Tsuei, Phys. Rev. B **39**, 304 (1989).

[28]G. Ottaviani, C. Nobili, F. Nava, M. Affronte, T. Manfredini, F. C. Matacotta, and E. Galli, Phys. Rev. B **39**, 9069 (1989).

[29]Y. Song, X. D. Chen, J. R. Gaines, and J. W. Gilje, J. Mater. Res. **5**, 27 (1990).

[30]C. Nobili, G. Ottaviani, M. C. Rossi, and M. Sparpaglione, Physica C **168**, 549 (1990).

[31]K. Yamamoto, B. M. Lairson, J. C. Bravman, and T. H. Geballe, J. Appl. Phys. **69**, 7189 (1991).

[32]P. K. Gallagher, Adv. Ceram. Mater. **2**, 632 (1987).

[33]T. Umemura, K. Egawa, M. Wakata, and K. Yoshizaki, Jpn. J. Appl. Phys. **28**, L1945 (1989).

[34]L. T. Shi and K. N. Tu, Appl. Phys. Lett. **55**, 1351 (1989).

[35]Y. Zhao, T. Shi, S. Hu, and L. Xie, Mater. Lett. **8**, 83 (1989).

[36]T. B. Tang and W. Lo, Physica C **174**, 463 (1991).

[37]D. J. Vischjager, P. J. Van Der Put, J. Schram, and J. Schoonman, Solid State Ionics **27**, 199 (1988).

[38]E. J. M. O'Sullivan and B. P. Chang, Appl. Phys. Lett. **52**, 1441 (1988).

[39]J. MacManus, D. Fray, and J. Evetts, Physica C **162-164**, 143 (1989).

[40]Y. Scolnik, E. Sabatani, and D. Cahen, Physica C **174**, 273 (1991).

[41]J. MacManus, D. J. Fray, and J. E. Evetts, Physica C **190**, 511 (1992).

[42]E. Ruckenstein and A. K. Mallick, Mater. Lett. **7**, 122 (1988).

[43]H. F. Poulsen, N. H. Andersen, and B. Lebech, Physica C **173**, 387 (1991).

[44]S. Jantsch, J. Ihringer, J. K. Maichle, W. Prandl, S.

Kemmler-Sack, R. Kiemel, S. Losch, W. Schafer, M. Schlichenmaier, and A. W. Hewat, J. Less-Common. Met. **150**, 167 (1989).

[45]B. A. Glowacki, R. J. Highmore, K. F. Peters, A. L. Greer, and J. E. Evetts, Supercond. Sci. Technol. **1**, 7 (1988).

[46]H. Hermes, M. Forster, and H. E. Schaefer, Phys. Rev. B **43**, 10 399 (1991).

[47]J. Crank, *The Mathematics of Diffusion* (Clarendon, Oxford, 1975).

[48]J. R. LaGraff, E. C. Behrman, J. A. T. Taylor, F. J. Rotella, J. D. Jorgensen, L. Q. Wang, and P. G. Mattocks, Phys. Rev. B **39**, 347 (1989).

[49]H. C. Montgomery, J. Appl. Phys. **42**, 2971 (1971); L. J. van der Pauw, Philips Res. Rep. **16**, 187 (1961).

[50]For example, U. Welp, S. Fleshler, W. K. Kwok, J. Downey, Y. Fang, G. W. Crabtree, and J. Z. Liu, Phys. Rev. B **42**, 10 189 (1990); T. A. Friedmann, M. W. Rabin, J. Giapinzakis, J. P. Rice, and D. M. Ginsberg, Phys. Rev. B **42**, 6217 (1990); G. Sageev Grader, P. K. Gallagher, and E. M. Gyorgy, Appl. Phys. Lett. **51**, 1115 (1987); P. P. Freitas and T. S. Plaskett, Phys. Rev. B **36**, 5723 (1987).

[51]Y. Gao, K. L. Merkle, C. Zhang, U. Balachandran, and R. B. Poeppel, J. Mater. Res. **5**, 1363 (1990); W. K. Lee and A. S. Nowick, J. Mater. Res. **5**, 1855 (1990); E. A. Cooper, A. K. Gangopadhyay, T. T. Mason, and U. Balachandran, J. Mater. Res. **6**, 1393 (1991).

[52]J. R. LaGraff and D. A. Payne, Ferroelectrics **130**, 87 (1992).

[53]J. L. Tallon, A. H. Schuitema, and N. E. Tapp, Appl. Phys. Lett. **52**, 507 (1988).

[54]T. B. Lindemer, J. F. Hunley, J. E. Gates, A. L. Sutton, J. Brynestad, C. R. Hubbard, and P. K. Gallagher, J. Am. Ceram. Soc. **72**, 1775 (1989).

[55]L. T. Shi and K. N. Tu, Appl. Phys. Lett. **59**, 2040 (1991).

[56]R. Beyers, B. T. Ahn, G. Gorman, V. Y. Lee, S. S. P. Parkin, M. L. Ramirez, K. P. Roche, J. E. Vazquez, T. M. Gur, and R. A. Huggins, Nature (London) **340**, 619 (1989); D. de Fontaine, G. Ceder, and M. Asta, *ibid.* **343**, 544 (1990).

[57]I. Poberaj, D. Mihailovic, and S. Bernik, Phys. Rev. B **42**, 393 (1990).

[58]B. W. Veal, H. You, A. P. Paulikas, H. Shi, Y. Fang, and J. W. Downey, Phys. Rev. B **42**, 4770 (1990).

[59]B. W. Veal, A. P. Paulikas, H. You, H. Shi, Y. Fang, and J. W. Downey, Phys. Rev. B **42**, 6305 (1990).

[60]J. D. Jorgensen, S. Pei, P. Lightfoot, H. Shi, A. P. Paulikas, and B. W. Veal, Physica C **167**, 571 (1990).

[61]G. Cedar, R. McCormick and D. de Fontaine Phys. Rev. B **44**, 2377 (1991).

[62]J. V. Andersen, H. Bohr, and O. G. Mouritsen, Phys. Rev. B **42**, 283 (1990).

[63]J. Crank and M. E. Henry, Trans. Faraday Soc. **45**, 636 (1949).

CHEMICAL DIFFUSION OF OXYGEN IN $YBa_2Cu_3O_{6+x}$

JOHN R. LaGRAFF and DAVID A. PAYNE
Department of Materials Science and Engineering and Materials Research Laboratory,
The University of Illinois at Urbana-Champaign,
Urbana, IL 61801,
USA

ABSTRACT. Chemical diffusion of oxygen has been measured in both single crystal and polycrystalline $YBa_2Cu_3O_{6+x}$ in order to distinguish between intrinsic diffusion behavior and extrinsic characteristics which depend on microstructure. Isothermal electrical resistance measurements were used to monitor the dynamics of oxygen diffusion from 350-780°C under both oxidizing and reducing conditions. Measured activation energies depended on sample morphology, temperature, and whether in-diffusion or out-diffusion of oxygen was occurring. Below 600°C, the activation energies for out-diffusion in porous (~75%) and dense (~95%) polycrystalline material were found to be 0.5(1)eV and 0.6(1) eV, respectively. These low energies suggest a high diffusivity pathway such as a grain boundary. Polycrystalline material exhibited a change in functional form for out-diffusion near 600°C in both dense and porous samples which was attributed to a change from primarily grain boundary diffusion to significant bulk lattice diffusion. Above 600°C, oxygen out-diffusion in *dense* polycrystalline and single crystal $YBa_2Cu_3O_{6+x}$ was found to be surface-reaction controlled. The activation energies for out-diffusion in the dense material were 1.93(6)eV and 1.7(1)eV above and below ~700°C; and in the single crystal 1.6(1)eV and 1.00(4)eV above and below ~680°C. Oxygen in-diffusion was found to have activation energies of 0.4(1)eV from 400-780°C in dense polycrystalline material and 1.16(6)eV in single crystal material from 600-780°C. The lower activation energy in the polycrystalline material may be due to percolation effects in which the rapid formation of a highly oxygenated shell masks intrinsic diffusion behavior.

R. Kossowsky et al. (eds.), Physics and Materials Science of High Temperature Superconductors, II, 225–246.

1. Introduction

The oxygen content plays an important role in determining both normal-state and superconducting properties of $YBa_2Cu_3O_{6+x}$ (for example, see Ref. [1]) and serves to illustrate the importance of the defect state in achieving superconductivity in other oxide materials [2]. The properties of other oxide superconductors have also been found to depend to some extent on the oxygen content of the specimen [3]. In $YBa_2Cu_3O_{6+x}$ the critical temperature and electron hole density approach their maximum values as the oxygen content increases towards seven anions per unit cell. Studies of the chemical diffusion of oxygen are thus extremely important with respect to processing the material with optimal superconducting properties. The fully oxygenated (orthorhombic) state ($x \approx 1$) of $YBa_2Cu_3O_{6+x}$ consists of oxygen atoms ordered on the O(1) chain sites which form one-dimensional copper-oxygen rows or chains (Figure 1). As x decreases, oxygen is both removed from O(1) sites and disordered from O(1) sites onto normally vacant O(5) chain sites until both sites are equally occupied and the material becomes tetragonal. This orthorhombic-tetragonal transformation is an order-disorder structural phase transformation which occurs near an oxygen content of 6.4-6.5 oxygen per unit cell [4], and whose equilibrium transformation temperature, T_0, is determined by the partial pressure of oxygen in equilibrium with the material (e.g., ~700°C in 100% oxygen). The strain accompanying this structural transformation is accommodated by the formation of {110} twin walls (Figure 1) [5]. Theoretical models [6] have suggested that different ordered oxygen superstructures may exist between the ideal orthorhombic ($x \approx 1$) and tetragonal ($x \approx 0$) structures. Transmission electron microscopy [7] and neutron diffraction [8] studies have indeed confirmed the existence of intermediate oxygen ordered phases including the orthorhombic-II (OII) structure which has every other copper-oxygen chain absent.

The crystal structure of $YBa_2Cu_3O_{6+x}$ depends on both the oxygen content and degree of ordering which suggests that the kinetics of the orthorhombic-tetragonal phase transformation will depend strongly on oxygen diffusion behavior [9-12]. Therefore, in addition to the temperature and oxygen partial pressure dependencies for the *equilibrium* transformation, one must also consider the heating and cooling rates and grain (or crystal) size effects (e.g., diffusion length) when considering the *kinetics* of the transformation. A complete knowledge of oxygen diffusion behavior in $YBa_2Cu_3O_{6+x}$ should facilitate an understanding of the kinetics and mechanism of the orthorhombic-tetragonal phase transformation in addition to elucidating on fundamental diffusion mechanisms.

The purpose of this paper is to summarize our findings in the area of oxygen diffusion in $YBa_2Cu_3O_{6+x}$, and compare our results with the literature in order to develop common trends [13]. The range of reported diffusion coefficients and activation energies may be attributed to many differing factors, including, experimental methodologies chosen and the preparation of specimens with different microstructures. Several questions

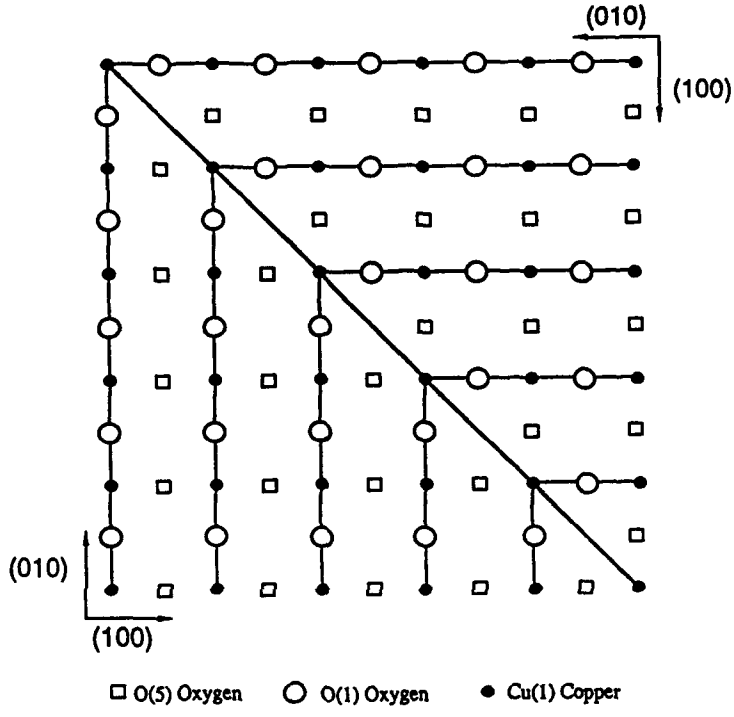

Figure 1. An idealized {110} twin boundary in $YBa_2Cu_3O_{6+x}$ as viewed in the **a-b** plane. Twin boundaries form in order to relieve the strain accompanying the tetragonal to orthorhombic phase transformation (from Ref. [5]).

still remain to be answered; is the diffusivity dependent on the oxygen concentration? Are there different diffusion mechanisms active in the orthorhombic and tetragonal structures? Is grain boundary diffusion significant? Is oxygen out-diffusion surface-reaction controlled? Does oxygen behave as an ideal solute in $YBa_2Cu_3O_{6+x}$? Will correlation effects occur in certain temperature and oxygen concentration ranges? In addressing some of these questions, the authors hope the reader will gain an understanding of the complexities and issues that remain to be resolved with regard to the mobility of oxygen in $YBa_2Cu_3O_{6+x}$.

1.1. TRACER OR SELF DIFFUSION

Fundamental oxygen diffusion behavior has been measured by both tracer diffusion techniques [13-15] and internal friction measurements [16-19]. Rothman et al. [13-15] have used secondary ion mass spectroscopy (SIMS) to measure ^{18}O profiles in both polycrystalline and single crystal

$YBa_2Cu_3O_{6+x}$. The tracer diffusivities D* followed a standard Arrhenius-type equation of the form $D^* = 1.4x10^{-4}$ exp (-0.97(5)eV/kT) cm^2/sec over the temperature range 300-850°C. They observed no break near the orthorhombic-tetragonal (OT) transformation, nor did they observe any oxygen partial pressure dependence of D* (i.e., the diffusivity appeared to be independent of the oxygen content). Using single crystal specimens, the tracer diffusivities were found to be highly anisotropic with $D^*_a \sim 10^{-2} D^*_b$ and $D^*_c \sim 10^{-4}$-$10^{-6} D^*_{ab}$ [15]. This anisotropy strongly suggests that oxygen diffusion is both limited primarily to the chain plane and is faster along the chains than perpendicular to the chains.

Internal friction measurements as a function of both frequency and temperature have been used to determine the self-diffusion coefficients of $YBa_2Cu_3O_{6+x}$ [16-19]. Internal friction measures the fundamental motion of atoms in response to an applied stress and are assumed to be relatively independent of microstructure. In $YBa_2Cu_3O_{6+x}$ these atomic motions are considered to be O(1)-O(5) jumps (see Figure 1) whose characteristic relaxation times under stress often follow Arrhenius-type behavior allowing both the activation energy for the atom jumps and the self-diffusion coefficients to be calculated. Xie et al. [17] has found $D = 3.5x10^{-4}$ exp (-1.03eV/kT) cm^2/sec while Tallon and Staines [18] measured $D = 1.8x10^{-4}$ exp (-1.07eV/kT) cm^2/sec both of which are in close agreement with the tracer diffusion studies of Rothman et al. [13-15] However, the internal friction studies [17,18] observe a concentration dependent diffusivity and a break near the OT transformation.

Room temperature oxygen diffusion was first observed by Raman spectroscopy [20]. Subsequent studies by Veal et al. [21,22] and Jorgensen et al. [23] confirmed room temperature oxygen mobility by measuring the dependence of the critical temperature with aging time in oxygen deficient $YBa_2Cu_3O_{6+x}$. This aging effect was attributed to oxygen ordering as chains developed involving fundamental O(1)-O(5)-O(1) jumps. Assuming that this aging effect was thermally activated, Veal et al. [22] calculated an activation energy for oxygen jumps of 0.96eV which is also in good agreement with the tracer diffusion studies [13-15] and the internal friction measurements [16-18].

1.2. CHEMICAL DIFFUSION

Measurements of the dynamic change in oxygen content as a function of temperature and oxygen partial pressure enable the chemical diffusivities $\tilde{D}$ to be calculated in $YBa_2Cu_3O_{6+x}$ (for example, Ref. [12]). The chemical diffusivity is related to the tracer or self-diffusivity by the equation [24]

$$\tilde{D} = D^* \left(1 + \frac{\partial \ln \gamma}{\partial \ln c}\right) \qquad (1)$$

where the term in brackets is the thermodynamic factor containing the oxygen activity, γ, and concentration, c. In an ideal solution (often in the dilute limit), the activity γ is unity for all concentrations and the tracer-diffusion and chemical diffusion coefficients are equal. Some of the higher values of $\tilde{D}$ than D^* reported in the literature suggest that oxygen may not behave as an ideal solute in $YBa_2Cu_3O_{6+x}$.

The two most common techniques used to monitor the dynamics of oxygen motion in $YBa_2Cu_3O_{6+x}$, including estimations of $\tilde{D}$, are electrical resistance measurements [9,10,25-38], which monitor the hole content, and thermogravimetric analysis [36,39-44], which directly measures weight change. Other techniques include gas volumetry [45,46], in-situ neutron diffraction [46,47], impedance spectroscopy [48], differential scanning calorimetry [49], solid state electrochemical measurements [50-52], IR spectroscopy [53], and positron annihilation [54]. When comparing the chemical diffusivities and activation energies in these studies the remarkable agreement found for tracer and self-diffusivities is now unfortunately lacking. The chemical diffusion coefficient is measured under a chemical potential gradient, most often affected by changes in either the oxygen partial pressure surrounding the specimen or in the temperature, and appears to be influenced by both microstructure and experimental methodology.

Thermogravimetric analysis is the most direct way to measure the change in the oxygen content as one is directly measuring weight change, however, relatively large samples (>1.5 mm^3) are needed to obtain precise measurements especially for small changes in x. Also, drift and buoyancy effects can complicate analysis. Electrical resistance measurements provide a sensitive probe to small changes in oxygen content especially in small crystals whose size precludes the use of thermogravimetric analysis [9,10,38]. However, one is measuring a response that is attributed to dynamic change in the carrier concentration and associated scattering processes. Thus, assumptions must be made on the relationship between the oxygen content and the hole concentration. Furthermore, inhomogeneous oxygen distributions may lead to percolation effects in polycrystalline material which would yield resistances that are not representative of the bulk oxygen content [33,24,36]. However, percolation effects can be minimized by using single crystal specimens which provide much less available surface area for near-surface diffusion [9,10,38].

$YBa_2Cu_3O_{6+x}$ is principally an electronic conductor with an extremely low oxygen ion transference numbers (10^{-9} to 10^{-7}; Ref. [29] and [48]). The electrical conductivity, σ, for majority hole carriers can be written in familiar form as $\sigma = [h^{\bullet}]\mu e$ where $[h^{\bullet}]$ is the hole concentration, μ hole mobility, and e electron charge. Isothermal measurements allow the mobility term to be neglected and thus an increase in the resistance is largely a consequence of a decrease in the hole concentration as oxygen

leaves the system according to the defect relation [10,29]

$$O_O^x + 2h^\bullet \quad \rightleftarrows \quad V_O^{\cdot\cdot} + \tfrac{1}{2}O_2 \qquad (2)$$

where a doubly ionized (positive) vacant O(1) chain oxygen site is denoted by $V_O^{\cdot\cdot}$, O_O^x is the neutral occupied O(1) site, and $h^\bullet$ an electron hole.

There is still some controversy surrounding the intrinsic rates of oxygen in-diffusion and out-diffusion in $YBa_2Cu_3O_{6+x}$. Most resistance measurements report *faster* in-diffusion than out-diffusion in polycrystalline material [25,27,29,33], while studies on single crystals report *slower* in-diffusion than out-diffusion [38]. Thermogravimetry (TGA) has reported in-diffusion to be both faster [41] and equal [40] to each other. Both TGA [40] and resistance [33] studies have reported that the chemical diffusivity depends on the oxygen content although with opposite compositional dependencies! Kishio et al. [40] observed an *increasing* diffusivity with increasing oxygen content which was attributed to a compositional dependence of the enthalpy of motion term in the tracer diffusivity. On the other hand, Tu et al. [33] have calculated oxygen in-diffusion activation energies ranging from 0.5-1.3eV as the oxygen content x varied from 0.62-1.0 which suggests that the diffusivity will *decrease* with increasing oxygen content. (Oxygen out-diffusion was reported to be independent of the oxygen content.) Internal friction measurements [18] also suggest a decreasing diffusivity with increasing oxygen content as shown by a decreasing activation energy for $x<0.75$. Needless to say, further investigations are required. Combined TGA and resistance studies [34,36] have shown that electrical properties continue to vary even though the sample weight remains constant, which suggests that oxygen ordering (and not content) is varying the effective carrier concentration. However, TGA measurements may not be able to detect very small changes in x which occur during the latter stages of both in-diffusion and out-diffusion. A TGA study [42] reported that the activation energy for out-diffusion was greater in a polycrystalline pellet (~1.5eV) by comparison with powders (~1.2eV), suggesting that density or microstructure can influence the activation energies and diffusivities by controlling the amount of free-surface area per unit volume and consequently the effective diffusion length.

It is a general consensus that in-diffusion is a standard diffusion-controlled process, however, several studies have suggested that out-diffusion is interface-controlled [10,25,33]. A surface activation barrier to oxygen out-diffusion can also be inferred from Veal et al.'s studies [21,22] of room temperature oxygen mobility. Below a certain temperature oxygen cannot escape the sample, however, it is still sufficiently mobile within the lattice and orders with time to increase the effective hole density. This suggests that a surface barrier to oxygen diffusion exists. Diffusion kinetics are expected to depend on the microstructure, however, there has been relatively few reports in the literature on a systematic identification of

factors which are most important. For example, one would expect that a small grain size, with sufficient porosity, would greatly lower the effective diffusion length.

1.3. OXYGEN DIFFUSION MODELS

The many ordered oxygen superstructures which exist in $YBa_2Cu_3O_{6+x}$ suggest that the detailed mechanism for oxygen diffusion will be quite complex. The local environment that a diffusing oxygen atom will experience varies from completely ordered copper-oxygen chains and {110} twin walls in the ideal orthorhombic structure ($x \approx 1$) to disordered individual oxygen atoms in the tetragonal structure. Thus, one may expect the diffusion mechanisms to also vary between the ordered orthorhombic and the disordered tetragonal structures. Rothman et al. [15] suggest that oxygen can only be added to or removed from the ends of ordered chains and will proceed with little hindrance down the open channels along the b-axis between chains (see Figure 1). This would account for the lack of a concentration dependence on the tracer diffusivity. Needless to say, this mechanism would not be dependent on the number of oxygen vacancies nor would one expect it to adequately describe diffusion in the tetragonal structure which lacks ordered chains.

Theoretical models by Bakker et al. [55] and Salomons and deFontaine [56] predict that the thermodynamic factor in equation (1) could be on the order of 100 or more which suggests that oxygen behaves as a highly non-ideal solute in $YBa_2Cu_3O_{6+x}$. Large thermodynamic factors are supported in the literature by large values of $\tilde{D}$ compared with measured D^* [29,40,41,50]. The tracer diffusivity in equation (1) can be written in terms of a correlation factor, f, as [24]

$$D^* = \gamma f N_v a^2 \nu \tag{3}$$

where γ is a geometric term, N_v the vacancy availability factor, a, jump distance, and ν the jump frequency. The correlation factor accounts for the fact that atoms do not necessarily diffuse by a random walk process unless f is equal to one. As f becomes less than one, there is a greater than even chance that a diffusing atom will return to the site from which it just left (i.e., the atom jumps are correlated). Bakker et al. [57] have suggested that $f \rightarrow 1$ in the highly disordered tetragonal structure due to the random arrangement of oxygen atoms and vacancies, while $f \rightarrow 0$ as oxygen becomes more ordered in the orthorhombic structure.

Theoretical models [55-58] also predict a break in the Arrhenius behavior of $\tilde{D}$ or D^* at the orthorhombic-tetragonal transformation with lower activation energies expected in the tetragonal structure. The break has been observed experimentally for oxygen out-diffusion [38], however, the measured activation energy is always greater in the tetragonal

structure [36,38,46]. A concentration dependent diffusivity has been predicted [56,58] and observed experimentally [18,33,40] although no clear consensus exists on the exact concentration dependence. For example, Salomons and deFontaine [56] predict a minimum in $\tilde{D}$ and D^* near x=0.5 with the diffusivity increasing with oxygen content for x>0.5 and increasing with decreasing oxygen content for x<0.5. However, Choi et al. [58] report an increasing diffusivity with decreasing oxygen content for all x.

2. Experimental

2.1. SAMPLE PREPARATION

Large single crystals with critical temperatures of 90K were grown by standard self-flux techniques in zirconia crucibles as described elsewhere [9]. $YBa_2Cu_3O_{6+x}$ powder was prepared by the mixed oxide route [59], pressed into pellets and sintered in oxygen at different temperatures (950-980°C) and times in order to achieve a range of grain sizes and bulk densities. The oxygen annealed polycrystalline pellets had broad critical temperatures from 90-92K as measured by SQUID magnetometry. Rectangular bars were cut from two of the pellets. Specimen #1 (here after referred to as S1) was porous (bulk density~75(5)%) with high aspect ratio grains of average dimensions ~1.1(2) by 6(1) μm. Specimen #2 (S2) had a bulk density of ~95(5)% with grains 2.8(4) by 19(3) μm in dimension (Table I).

2.2. RESISTANCE MEASUREMENTS

Electrical resistance measurements were made by a computer-controlled four-point probe technique that allowed one to monitor the kinetics of oxygen in-diffusion and out-diffusion in $YBa_2Cu_3O_{6+x}$ specimens [9,10,38]. A Stanford Research Systems SR530 Lock-in amplifier was used to apply a constant ac current of 1.86mA at a frequency of 564Hz. The specimens were simultaneously mounted in the hot-stage of an optical microscope in order

Table I. Sample characteristics for porous (S1) and dense (S2) polycrystalline $YBa_2Cu_3O_{6+x}$.

Specimen Type	T_c	Specimen Size (mm^3)	Grain Size (μm)	Bulk Density
Polycrystal S1	92K	4.85x2.05x0.50	1.1(2) x 6(1)	75(5)%
Polycrystal S2	92K	4.70x1.55x0.90	2.8(4) x 19(3)	95(5)%

to observe the (de)twinning behavior associated with the orthorhombic-tetragonal phase transformation. Gold wires were attached to the specimens with silver paste whose contact integrities were checked periodically for ohmic behavior and under both positive and negative DC currents. Oxygen in-diffusion and out-diffusion were monitored by isothermal resistance measurements from 350-780°C upon switching between oxygen and argon atmospheres, respectively. A scrubbing column containing CaO and $CaSO_4$ was used to remove water vapor and CO_2 from the gas.

3. Results and Discussion

3.1. IN-DIFFUSION AND OUT-DIFFUSION

When using electrical resistance measurements to monitor oxygen diffusion it is assumed that the change in resistance with time $\Delta R(t)$ is proportional to the change in oxygen content $\Delta x(t)$ according to the following relation

$$\left(\frac{R(t) - R(0)}{R(\infty) - R(0)}\right) \equiv \left(\frac{x(t) - x(0)}{x(\infty) - x(0)}\right) \equiv \alpha \tag{4}$$

where R(0) is the resistance at the beginning of in-diffusion or out-diffusion, R(t) the resistance as a function of time, $R(\infty)$ saturation resistance, and α fractional change in resistance (or oxygen content). Out-diffusion below 600°C in polycrystalline $YBa_2Cu_3O_{6+x}$ and in-diffusion in both polycrystalline and single crystal specimens were found to obey two types of rate equations. One, an Avrami-type rate equation (written here for out-diffusion) of the form [60]

$$\alpha = 1 - \exp\left[-(t/\tau)^n\right] \tag{5}$$

where τ is the relaxation time for the process and n, a characteristic exponent, which can depend on the diffusion geometry and temperature. Secondly, the first two terms (n=0,1) for diffusion in a plane given by [61]

$$\alpha = 1 - \frac{8}{\pi^2} \sum_{n=0}^{\infty} \frac{1}{(2n+1)^2} \exp\left(\frac{-(2n+1)^2 t}{\tau'}\right) \tag{6}$$

The relaxation time τ' in equation (6) is different from that in equation (5) and can be used to estimate the chemical diffusivity $\tilde{D}$ from $\tau' = L^2/\tilde{D}\,\pi^2$, where L is the effective diffusion length of the specimen (see Ref. [62] for a

discussion of estimated coefficients $\tilde{D}$). The Arrhenius behavior of the relaxation times in both equations obey the following equation:

$$\tau = \tau_o \exp\left(\frac{E}{kT}\right) \tag{7}$$

yielding activation energies E which are identical regardless of whether τ is taken from equation (5) or (6).

The activation energies for oxygen out-diffusion below 600°C in both, porous (S1) and dense (S2) polycrystalline material, were 0.5(1)eV and 0.6(1)eV, respectively (Table II) [62]. These activation energies are lower than those calculated by tracer diffusion [13-15] and internal friction [16-18] measurements and may represent a high diffusivity pathway such as a grain boundary (to be discussed in a later section). Oxygen out-diffusion above 600°C in the dense specimen (S2) was found to be surface-reaction controlled and will be analyzed in the following section. In the porous specimen (S1), out-diffusion above 600°C was too rapid to yield a reasonable fit to equations (5) or (6).

The oxygen in-diffusion analogues of equations (5) and (6) in combination with equation (9) yield activation energies of 0.4(1)eV from 400-780°C in the dense polycrystalline specimen S2 and 1.16(6)eV from 600-780°C in the single crystal form (Table II). The Avrami exponent n (equation (5)) for in-diffusion in single crystal $YBa_2Cu_3O_{6+x}$ was approximately 1/2, which is typical for diffusion into the edges of a plate [63]. Dense polycrystalline $YBa_2Cu_3O_{6+x}$ had n values of ~3/2, typical of in-diffusion into a sphere [63] which may be attributed to diffusion into randomly oriented grains of isotropic distribution. (In-diffusion was too rapid in the porous specimen S1 for a reasonable fit to equations (5) or (6).) The low activation energy (~0.4eV) for in-diffusion in S2 suggests that percolation effects attributed to the formation of highly oxygenated shells may mask intrinsic in-diffusion behavior. Electrical resistance measurements could therefore be monitoring the lower resistance of highly oxygenated grain boundaries, or the specimen's surface, and not the bulk resistance. Single crystals do not appear to exhibit such artifacts.

3.2. SURFACE-CONTROLLED OUT-DIFFUSION

Above 600°C, out-diffusion of oxygen in single crystal specimens and *dense* polycrystalline specimens was assumed to be surface-reaction limited [33], as suggested, by the linear change of resistance with time (see Figure 2). This was qualitatively confirmed by hot-stage optical microscopy which showed that a tetragonal single crystal (i.e., one which is oxygen deficient, $x<0.4$) slowly absorbed oxygen over a 24 hour period at 400°C to become orthorhombic as indicated by the appearance of twin boundaries. However, switching the surrounding gas to reducing conditions (argon) did not remove the twin boundaries even after a ~140 hour anneal suggesting that

Table II. Comparison of activation energies for oxygen diffusion in $YBa_2Cu_3O_{6+x}$ for single crystals, polycrystals, powders, and thin films. When available, the bulk density is given in percent (%) and the average grain size in microns (μm).

Specimen Type	E (eV)	Temperature Range	Comments†	Ref.
Single Crystal	1.0-1.2	600-680°C	ER, OD, SRC	[10],[38]
	1.6	680-780°C	ER, OD, SRC	[38]
	1.16	600-780°C	ER, ID	[38]
Polycrystal S1 (porous, 75%; 6μm)	0.5	350-600°C	ER, OD, GB, PE	[62]
Polycrystal S2 (dense, 95%; 19μm)	0.6	400-600°C	ER, OD, GB, PE	[62]
	1.7	600-700°C	ER, OD, SRC	[62]
	1.9	700-780°C	ER, OD, SRC	[62]
	0.4	400-780°C	ER, ID, PE	[62]
Polycrystal (porous; 10μm)	1.7	370-440°C	ER, OD, SRC	[33]
	0.5-1.3	210-360°C	ER, ID, CD	[33]
	1.52	dynamic heating	TGA, ID	[42]
Polycrystal (porous, 75%; 10-20μm)	0.4	215-315°C	ER, ID	[34]
Polycrystal (dense, 98%; 50μm)	1.38-1.81	550-850°C	TGA, OD, CD	[40]
Polycrystal (dense)	0.74	~700-960°C	TGA, ID	[41]
	0.5	~600-860°C	TGA, OD	
Powder, 9μm	1.3	~360-450°C	TGA, OD	[44]
Powder	1.25	dynamic heating	TGA, ID	[42]
Thin Film (0.4μm)	1.17	320-435°C	ER, ID	[27]
Thin Film	1.2	~400-600°C	ER, ID	[37]
Polycrystal (dense, 99%)	0.97	300-850°C	TD	[15]
Polycrystal	1.03	400-650°C	IF, CD	[17]
Polycrystal (dense, 85%)	1.07	27-827°C	IF, CD	[18]

†*Key:*
OD (out-diffusion)
ID (in-diffusion)
SRC (surface-reaction controlled)
GB (grain boundary diffusion)
PE (percolation effects?)
ER (electrical resistance)
TGA (thermogravimetry)
TD (tracer diffusion)
IF (internal friction)
CD (concentration dependence)

oxygen could not readily leave the crystal. This was confirmed by electrical resistance measurements at 400°C. The resistance of a reduced sample decreased immediately as oxygen was absorbed into the material at 400°C. However, switching of the gas to reducing conditions (argon) did not result in any increase in resistance up to 48 hours. Both of these observations suggest that oxygen can enter the lattice at these temperatures, however, it is "locked" into the interior by a surface energy barrier.

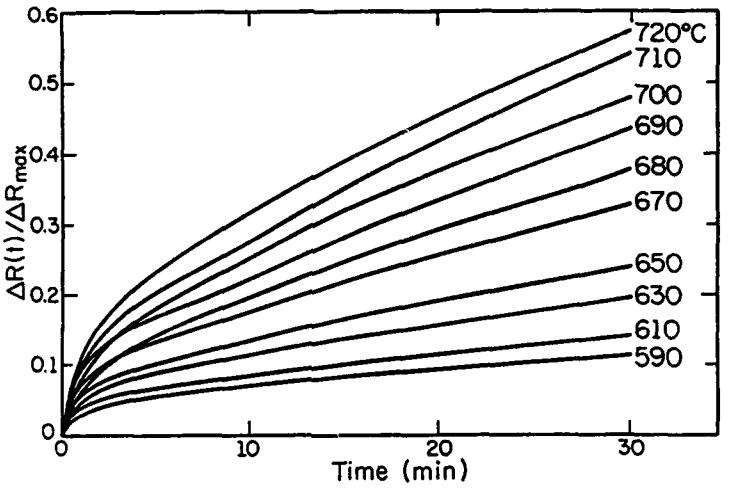

Figure 2. Resistance as a function of time for oxygen out-diffusion in single crystal $YBa_2Cu_3O_{6+x}$ from 590-720°C. The linear increase in the *resistance suggests a surface-reaction* controlled out-diffusion process (from Ref. [10]).

The different mechanisms for oxygen in-diffusion and out-diffusion are also evident in the (de)twinning dynamics of the orthorhombic-tetragonal phase transformation as observed by optical microscopy in single crystals [10]. Below 700°C, the crystal structure of $YBa_2Cu_3O_{6+x}$ can transform isothermally on switching from a pure oxygen atmosphere to reducing conditions [9,10,38]. Since oxygen in-diffusion is a standard diffusion-controlled process, one expects a non-uniform oxygen distribution across a crystal with the edges richer in oxygen content than the interior. When the oxygen content exceeds ~0.4, these edge regions will become orthorhombic as shown by the appearance of twin boundaries and these twinned regions will advance into the crystal upon further oxygen in-diffusion. This has been experimentally observed by hot-stage optical microscopy for single crystal [10] and polycrystalline [11] specimens. On the other hand, oxygen out-diffusion is a surface-reaction controlled process [33] and one expects a constant oxygen content across the width of the crystal. As the oxygen content is reduced below ~0.4, twin boundaries would disappear simultaneously across the entire crystal. Again, this has been experimentally observed by hot-stage optical microscopy [10].

Out-diffusion in single crystal and dense polycrystalline $YBa_2Cu_3O_{6+x}$ above 600°C was assumed to be directly proportional to the linear rate of change of the isothermal resistance curves. Figure 2 reveals several isothermal out-diffusion resistance curves for single crystal $YBa_2Cu_3O_{6+x}$ from 590-720°C. After the initial rapid rise in resistance at the onset of out-diffusion, resistance increases linearly with time with slope

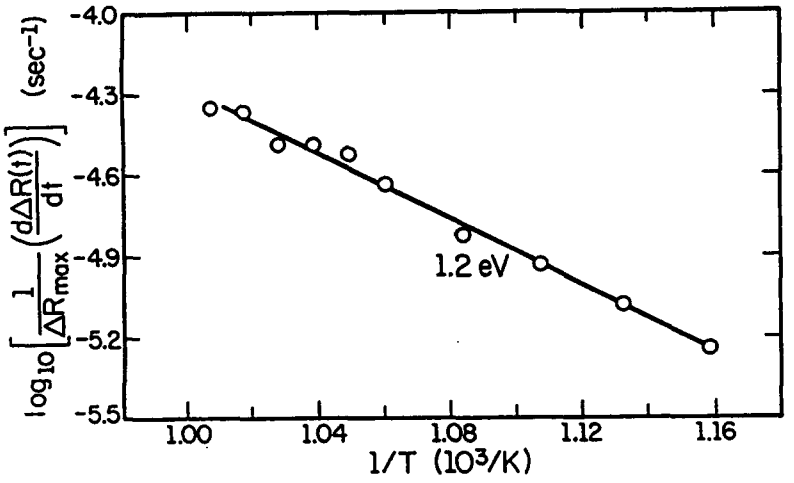

Figure 3. Arrhenius plot from equation (8) of the slopes (dR/dt) of the linear regions in Figure 4 yielding an activation energy for out-diffusion of 1.2(1)eV from 590-720°C (from Ref. [9]).

dR/dt. The resistance change during oxygen out-diffusion was assumed to be directly proportional to the carrier concentration and hence, oxygen content (see equation (4)) and allows one to calculate the activation energy E_o for out-diffusion from the equation [33]

$$\left(\frac{dR}{dt}\right) = B_0 \exp\left(\frac{-E_o}{kT}\right) \tag{8}$$

where B_0 is a constant. Figure 3 is an Arrhenius-type plot of the slopes in Figure 2 using equation (8) which yields an activation energy for out-diffusion of 1.2(1)eV between 590-720°C (Table II) [10].

The extension of isothermal resistance measurements for out-diffusion up to 780°C in both single crystal and polycrystalline $YBa_2Cu_3O_{6+x}$ suggests a change in out-diffusion mechanisms near 680-700°C. Figure 4 is a plot of the slope of the linear regions for oxygen out-diffusion in single crystal $YBa_2Cu_3O_{6+x}$ as a function of temperature. Arrhenius analysis (equation (8)) of the linear slopes (dR/dt) as a function of temperature for several different isotherms (600-780°C) indicates two different regimes for oxygen out-diffusion behavior in the single crystal, one above and one below ~680°C. The activation energies from region I (600-680°C) and II (680-780°C) were determined to be 1.00(4)eV and 1.6(1)eV, respectively. The activation energies for the dense polycrystalline material were 1.93(6)eV and 1.7(1)eV above and below ~700°C. The break in the rates of oxygen out-diffusion occurs remarkably close to the orthorhombic-tetragonal transformation temperature and it is tempting to associate each activation

THIS
PAGE
IS
MISSING
IN
ORIGINAL
DOCUMENT

238 Fig 4

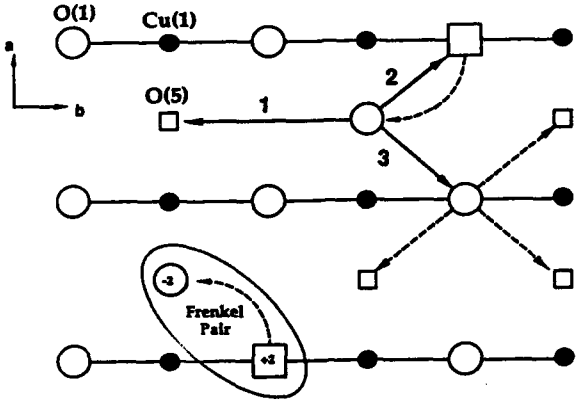

Figure 5. Possible diffusion pathways along the CuO chains in orthorhombic $YBa_2Cu_3O_{6+x}$ as viewed normal to the a-b plane. In addition to the possible formation of Frenkel pairs, two types of diffusion mechanisms are indicated: (1) interstitial and (2) interstitialcy mechanisms. The possibility of these two types of mechanisms may explain the change in activation energies near 680-700°C. Above these temperatures only the tetragonal structure exists and a vacancy mechanism is appropriate.

where the oxygen vacancy, $V_O^{\cdot\cdot}$, is associated with the O(1) site and the doubly negative oxygen interstitial, O_i'', with the O(5) site. Slow cooling of $YBa_2Cu_3O_{6+x}$ would be required to minimize the number of Frenkel pairs frozen into the structure at low temperatures. The initial formation of Frenkel pairs would not alter the total oxygen content, nevertheless, they would change the local coordination of chain copper cations and, also, destroy long-range ordering, both of which could decrease the hole concentration [21-23].

An interstitial oxygen, O_i'', can potentially jump to one of two sites. One, it can jump to a neighboring unoccupied interstitial O(5) site along pathway 1 (Figure 5) typical of an interstitial mechanism and, two, it can displace an O(1) oxygen into an interstitial site along either pathway 2 or 3 (interstitialcy mechanism). Oxygen diffusion in the orthorhombic structure could then be thought of as a combination of interstitial and interstitialcy diffusion. In the tetragonal structure the O(5) and O(1) sites are equivalent and diffusion would only appear to proceed by a vacancy mechanism.

When oxygen begins to leave the orthorhombic crystal, there are three possible reactions which could occur at the surface,

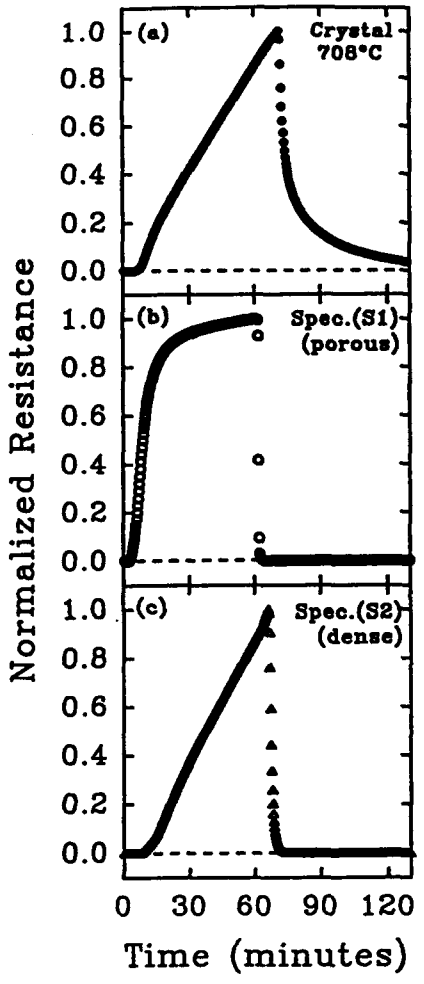

Figure 6. Normalized resistance as a function of time for both oxygen out-diffusion and in-diffusion at 708°C for (a) single crystal $YBa_2Cu_3O_{6+x}$, (b) *porous* fine-grain specimen S1, and (c) *dense* coarse-grain specimen S2. Note that in (a) the initial resistance is still not regained after a one hour oxygen anneal which suggests that oxygen in-diffusion is intrinsically slower than out-diffusion.

and observations of slower oxygen in-diffusion in *tetragonal* $YBa_2Cu_3O_{6+x}$ up to 780°C suggests that oxygen in-diffusion was indeed intrinsically slower than out-diffusion unless oxygen tends to order even in the supposedly disordered tetragonal structure [62].

Figure 6 illustrates the inherent problems in interpreting the diffusion of oxygen in polycrystalline material without considering important micro-structural features such as grain size, grain boundaries,

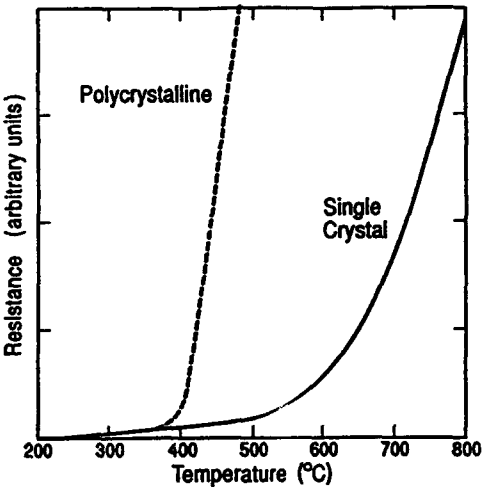

Figure 7. The influence of microstructure on the temperature dependence of resistance for initially oxygenated polycrystalline and single crystal $YBa_2Cu_3O_{6+x}$. The deviation from linear metallic-type resistance behavior due to appreciable oxygen out-diffusion occurs near 350°C and 500°C, respectively, which suggests the onset of grain boundary diffusion near 350°C and bulk lattice diffusion near 500°C (adapted from Ref. [9]).

and porosity. These factors can complicate the choosing of an effective diffusion length, thus, leading to the variations in chemical diffusion coefficients and activation energies reported in the literature (Table II). Polycrystalline material has a larger surface-area to volume ratio than single crystals, and often connected porosity, which may lead to apparently faster oxygen in-diffusion than out-diffusion. These faster rates of in-diffusion in polycrystalline specimens suggest that electrical measurements may be sensitive to percolation effects in which a highly oxygenated shell forms around individual grains or the specimen's surface during in-diffusion and behaves as a short circuit pathway for current flow. However, in single crystal $YBa_2Cu_3O_{6+x}$ these percolation effects would be minimized allowing one to observe the intrinsically slower rates of oxygen in-diffusion.

During initial oxygen incorporation, the formation of a highly oxygenated shell which coarsens with time will lead to increasingly slower in-diffusion rates. Oxygen diffusion through this shell could be hindered by several factors: a low concentration of oxygen vacancies; and, in the orthorhombic structure, ordered oxygen regions and twin boundaries. The existence of a-b anisotropy in the tracer diffusivity ($\tilde{D}_b \approx 100\tilde{D}_a$) [15] and Monte Carlo simulations [64] suggest that ordered oxygen regions may impede oxygen diffusion which could explain intrinsically slower in-diffusion than out-diffusion.

3.5. GRAIN BOUNDARY DIFFUSION

The resistance of orthorhombic $YBa_2Cu_3O_{6+x}$ (x≈1) is metallic and increases linearly with temperature in pure oxygen up to approximately 350°C in polycrystalline ceramics [33] and up to 500°C in single crystals (Figure 7) [9]. Above these temperatures, appreciable oxygen out-diffusion occurs, and the resistance increases more rapidly. This suggests that near 350°C, grain boundary diffusion becomes active in polycrystalline material while bulk diffusion does not occur until close to 500°C. Internal friction measurements [65] have observed a Debye-type damping peak near 530°C which was attributed to basal plane oxygen hopping and may also indicate the onset of bulk lattice diffusion. The activation energy for out-diffusion below 600°C in both dense and porous polycrystalline specimens has been found to be of the order of 0.5-0.6eV (Table II). These values are lower than the activation energy for tracer diffusion (~1eV), which suggests a high diffusivity pathway, such as, a grain boundary. A change in functional form near 600°C has been observed in the out-diffusion resistance curves of both porous and dense polycrystalline specimens (Table II) [62]. This temperature may indicate the point at which lattice diffusion dominates.

If grain boundary diffusion is rapid enough, then the boundaries will become saturated with the diffusing species, and will serve as an oxygen source or sink for diffusion into or out of the interior of the grain. Thus, both single crystal and polycrystalline diffusion data should be in

agreement if the grain size is used as the effective diffusion length. However, by using the grain size as the effective diffusion length in polycrystal S2 for in-diffusion yielded diffusivities which were 2-3 orders of magnitude smaller than reported tracer diffusivities [14,62]. This discrepancy may indicate that the actual diffusion length may fall somewhere between the grain size and specimen thickness depending on the amount of connected porosity. The lower activation energy (Table II) for in-diffusion in polycrystal S2 (0.4eV) compared with the single crystal (1.16eV) suggests that percolation effects may mask intrinsic in-diffusion behavior in polycrystalline material [62].

4. Conclusions

In summary, the study of single crystal and polycrystalline $YBa_2Cu_3O_{6+x}$ has allowed for intrinsic diffusion behavior to be distinguished from that which is influenced by microstructure. Diffusion characteristics were found to be dependent on the microstructure under certain conditions, which could explain the many apparent discrepancies for chemical diffusion in the literature. Whereas there appears to be close agreement between tracer diffusion studies, internal friction measurements, and room temperature mobility, there are wide discrepancies in the measurement of chemical diffusivities and activation energies most likely due to different experimental techniques, varying microstructures, and difficulty in choosing an appropriate diffusion length.

Oxygen out-diffusion was observed to proceed by two different mechanisms in single crystal $YBa_2Cu_3O_{6+x}$ above and below 680°C, with calculated activation energies of 1.6(1) eV and 1.00(4) eV, respectively. In dense polycrystalline material, this break occurred at a higher temperature (700°C) with activation energies of 1.93(6)eV and 1.7(1)eV above and below 700°C. These two mechanisms were not necessarily associated with the orthorhombic or tetragonal structures, but may instead be due to the natural tendency for oxygen to order below 680-700°C regardless of the oxygen content. The low activation energies of 0.6(1)eV and 0.5(1)eV for oxygen out-diffusion below 600°C in dense and porous material, respectively, and for in-diffusion in the dense material (0.4(1)eV) suggests a high diffusivity pathway such as grain boundary diffusion or percolation effects. Both processes may complicate the selection of an appropriate diffusion length for the calculation of $\tilde{D}$. The higher activation energies for oxygen out-diffusion above 600°C in dense material (1.7eV and 1.9eV) and single crystals (1.0eV and 1.7eV) suggests that grain boundary diffusion and/or percolation effects were not significant at these temperatures.

Oxygen in-diffusion was observed to be slower than out-diffusion in single-crystal $YBa_2Cu_3O_{6+x}$ at all measurement temperatures (600-780°C) with an activation energy of 1.16(6)eV. This was contrary to the diffusion rates observed in polycrystalline ceramic specimens, in which electrical

measurements of in-diffusion appeared to proceed at a faster rate than out-diffusion. Faster in-diffusion in *polycrystalline* material can be attributed to the formation of thin conductive layers of highly oxygenated material at grain boundaries or at the specimen's surface, which behave as percolation paths for electrical transport. Intrinsically slower in-diffusion in *single crystals* can be attributed to the increasingly slower diffusion through a highly oxygenated shell which coarsens with time. A low concentration of oxygen vacancies and/or ordered oxygen regions would make oxygen diffusion extremely slow through the shell.

Acknowledgements. The authors greatly appreciate the technical assistance of P.D. Han and A. Asthana, and the use of the facilities in the Materials Research Laboratory at the University of Illinois. The authors would also like to thank S.J. Rothman, J.L. Routbort, U. Welp, and J.E. Baker for a copy of their manuscript (Ref. [15]) prior to review. This project was supported by the Air Force Office of Scientific Research (Grant No. URI-41318) through a University Research Initiative on phase transformations in ceramics and by the National Science Foundation (Grant No. DMR 88-09854) through the Science and Technology Center for Superconductivity.

References.

[1] R.J. Cava, A.W. Hewat, E.A. Hewat, B. Batlogg, M. Marezio, K.M. Rabe, J.J. Krajewski, W.F. Peck, and L.W. Rupp, *Physica C* **165**, 419 (1990).

[2] For a recent review see, J.D. Jorgensen, *Physics Today* **44**, 34 (1991).

[3] For example, E. Sonder, B.C. Chakoumakos, and B.C. Sales, *Phys. Rev. B* **40**, 6872 (1989); M.R. Presland, J.L. Tallon, R.G. Buckley, R.S. Liu, and N.E. Flower, *Physica C* **176**, 95 (1991); C. Martin, A. Maignan, J. Provost, C. Michel, M. Hervieu, R. Tournier, and B. Raveau, *Physica C* **168**, 8 (1990); J.Horn, H.C. Semmelhacl, H. Borner, B. Lippold, U. Boehnke, M. Wurlitzer, and M. Krotzsch, *Physica C* **170**, 343 (1990); A. Maignan, C. Martin, M. Huve, J. Provost, M. Hervieu, C. Michel, and B. Raveau, *Physica C* **170**, 350 (1990); M. Nagoshi, T. Suzuki, Y. Fukuda, K. Terashima, Y. Nakanishi, M. Ogita, A. Tokiwa, Y. Syono, and M. Tachiki, *Phys. Rev. B* **43**, 10445 (1991); Y. Yokoyama, T. Katayama, H. Oyanagi, Y. Hasumi, and Y. Nishihara, *Jap. J. Appl. Phys.* **30**, L272 (1991); D. Kovatcheva, P. Strobel, B. Souletie, and A.W. Hewat, *Physica C* **174**, 280 (1991); A. Maignan, T. Rouillon, D. Groult, J. Provost, M. Hervieu, C. Michel, B. Raveau, R.S. Liu, and P.P. Edwards, *Physica C* **177**, 461 (1991).

[4] J.D. Jorgensen, B.W. Veal, A.P. Paulikas, L.J. Nowicki, G.W. Crabtree, H. Claus, and W.K. Kwok, *Phys. Rev. B* **41**, 1863 (1990); J.D. Jorgensen, M.A. Beno, D.G. Hinks, L. Soderholm, K.J. Volin, R.L. Hitterman, J.D. Grace, I.K. Schuller, C.U. Serge, K. Zhang, and M.S. Kleefisch, *Phys. Rev. B* **36**, 3608 (1987).

[5] J.R. LaGraff and D.A. Payne, *Ferroelectrics: Special Issue on Ferroelectricity, Structural Instability, and High-Temperature Superconductivity* , (in press, 1991).

[6] L.T. Willie and D. de Fontaine, *Phys. Rev. B* **37**, 2227 (1988); D. de Fontaine, M.E. Mann, and G. Ceder, *Phys. Rev. Lett.* **63**, 1300 (1989); D. de Fontaine, G. Ceder, and M. Asta, *Nature* **343**, 544 (1990).

[7] M.A. Alario-Franco, J.J. Capponi, C. Chaillout, J. Chenavas, and M. M. Marezio, *Mater. Res. Soc. Symp. Proc.* **99**, 41 (1988); D. Shi and D.W. Capone, *Appl. Phys. Lett.* **53**, 159 (1988); R. Beyers, B.T. Ahn, G. Gorman, V.Y. Lee, S.S.P. Parkin, M.L.

Ramirez, K.P. Roche, J.E. Vaxquez, T.M. Gur, and R.A. Huggins, *Nature* **340**, 619 (1989).
[8] R. Sonntag, D. Hohlwein, T. Bruckel, and G. Collin, *Physi. Rev. Lett.* **66**, 1497 (1991).
[9] J.R. LaGraff, P.D. Han, and D.A. Payne, *Physica C* **169**, 355 (1990).
[10] J.R. LaGraff, P.D. Han, and D.A. Payne, *Phys. Rev. B* **43**, 441 (1991).
[11] D. Shi, *Phys. Rev. B* **39**, 4299 (1989).
[12] N. Hudakova and P. Diko, *Physica C* **167**, 408 (1990).
[13] For a recent review see, S.J. Rothman and J.L. Routbort, in *Diffusion in Materials*, eds. A.L. Laskar et al., p.393, Kluwer Academic Publishers (1990).
[14] S.J. Rothman, J.L. Routbort, and J.E. Baker, *Phys. Rev. B* **40**, 8852 (1989).
[15] S.J. Rothman, J.L. Routbort, U. Welp, and J.E. Baker, *Phys. Rev. B* (In press, 1991).
[16] X.M. Xie, T.G. Chen, and J. Huang, *Phys. Stat. Sol. (a)* **110**, 415 (1988).
[17] X.M. Xie, T.G. Chen, and Z.L. Wu, *Phys. Rev. B* **40**, 4549 (1989).
[18] J.L. Tallon and M.P. Staines, *J. Appl. Phys.* **68**, 3998 (1990).
[19] G. Cannelli, R. Cantelli, F. Cordero, M. Ferretti, and F. Trequattrini, *Solid State Commun.* **77**, 429 (1991).
[20] I. Poberaj, D. Mihailovic, and S. Bernik, *Phys. Rev. B* **42**, 393 (1990).
[21] B.W. Veal, H. You, A.P. Paulikas, H. Shi, Y. Fang, and J.W. Downey, *Phys. Rev. B* **42**, 4770 (1990).
[22] B.W. Veal, A.P. Paulikas, H. You, H. Shi, Y. Fang, and J.W. Downey, *Phys. Rev. B* **42**, 6305 (1990).
[23] J.D. Jorgensen, S. Pei, P. Lightfoot, H. Shi, A.P. Paulikas, and B.W. Veal, *Physica C* **167**, 571 (1990).
[24] P.G. Shewmon, *Diffusion in Solids*, J. Williams Book Co. (1983).
[25] K.N. Tu, S.I. Park, and C.C. Tsuei, *Appl. Phys. Lett.* **51**, 2158 (1987).
[26] S.I. Park, C.C. Tsuei, and K.N. Tu, *Phys. Rev. B* **37**, 2305 (1988).
[27] G. Sageev Grader, P.K. Gallagher, J. Thomson, and M. Gurvitch, *Appl. Phys. A* **45**, 179 (1988).
[28] K.N. Tu, C.C. Tsuei, S.I. Park, and A. Levi, *Phys. Rev. B* **38**, 772 (1988).
[29] J. Park, P. Kostic, and J.P. Singh, *Mater. Lett.* **6**, 393 (1988).
[30] K.N. Tu, N.C. Yeh, S.I. Park, and C.C. Tsuei, *Phys. Rev. B* **38**, 5118 (1988).
[31] A.T. Fiory, S. Martin, L.F. Schneemeyer, R.M. Fleming, A.E. White, and J.V. Waszczak, *Phys. Rev. B* **38**, 7129 (1988).
[32] N.C. Yeh, K.N. Tu, S.I. Park, and C.C. Tsuei, *Phys. Rev. B* **38**, 7087 (1988).
[33] K.N. Tu, N.C. Yeh, S.I. Park, and C.C. Tsuei, *Phys. Rev. B* **39**, 304 (1989).
[34] G. Ottaviani, C. Nobili, F. Nava, M. Affronte, T. Manfredini, F.C. Matacotta, and E. Galli, *Phys. Rev. B* **39**, 9069 (1989).
[35] Y. Song, X.D. Chen, J.R. Gaines, and J.W. Gilje, *J. Mater. Res.* **5**, 27 (1990).
[36] C. Nobili, G. Ottaviani, M.C. Rossi, and M. Sparpaglione, *Physica C* **168**, 549 (1990).
[37] K. Yamamoto, B.M. Lairson, J.C. Bravman, and T.H. Geballe, *J. Appl. Phys.* **69**, 7189 (1991).
[38] J.R. LaGraff, P.D. Han, and D.A. Payne, in *Defects in Materials*, eds. P.D. Bristowe, J.E. Epperson, J.E. Griffith, and Z. Liliental-Weber, Mat. Res. Soc. Symp. Proc. **209**, 801 (1991).
[39] P.K. Gallagher, *Adv. Ceram. Mater.*. **2**, 632 (1987).
[40] K. Kishio, K. Suzuki, T. Hasegawa, T. Yamamoto, K. Kitazawa, and K. Fueki, *J. Solid State Chem.* **82**, 192 (1989).
[41] T. Umemura, K. Egawa, M. Wakata, and K. Yoshizaki, *Jap. J. Appl. Phys.* **28**, L1945 (1989).
[42] L.T. Shi and K.N. Tu, *Appl. Phys. Lett.* **55**, 1351 (1989).
[43] Y. Zhao, T. Shi, S. Hu, and L. Xie, *Mater. Lett.*. **8**, 83 (1989).
[44] T.B. Tang and W. Lo, *Physica C* **174**, 463 (1991).
[45] E. Ruckenstein and A.K. Mallick, *Mater. Lett.*. **7**, 122 (1988).
[46] H.F. Poulsen, N.H. Andersen, and B. Lebech, *Physica C* **173**, 387 (1991).
[47] S. Jantsch, J. Ihringer, J.K. Maichle, W. Prandl, S. Kemmler-Sack, R. Kiemel, S. Losch, W. Schafer, M. Schlichenmaier, and A.W. Hewat, *J. Less-Comm. Met.* **150**, 167 (1989).
[48] D.J. Vischjager, P.J. Van Der Put, J. Schram, and J. Schoonman, *Solid State Ionics* **27**, 199 (1988).
[49] B.A. Glowacki, R.J. Highmore, K.F. Peters, A.L. Greer, and J.E. Evetts, *Supercon. Sci. Technol.* **1**, 7 (1988).

[50] E.J.M. O'Sullivan and B.P. Chang, *Appl. Phys. Lett.* **52**, 1441 (1988).
[51] J. MacManus, D. Fray, and J. Evetts, *Physica C* **162-164**, 143 (1989).
[52] Y. Scolnik, E. Sabatani, D. Cahen, *Physica C* **174**, 273 (1991).
[53] Y. Zhao, T. Shi, S. Hu, and L. Xie, *Mater. Lett.* **8**, 83 (1989).
[54] H. Hermes, M. Forster, and H.E. Schaefer, *Phys. Rev. B* **43**, 10399 (1991).
[55] H. Bakker, J.P.A. Westerveld, and D.O. Welch, *Physica C* **153-155**, 848 (1988).
[56] E. Salomons and D. deFontaine, *Phys. Rev. B* **41**, 11159 (1990).
[57] H. Bakker, J.P.A. Westerveld, D.M.R. Lo Cascio, and D.O. Welch, *Physica C* **157**, 25 (1989).
[58] J.S. Choi, M. Sarikaya, I.A. Aksay, and R. Kikuchi, *Phys. Rev. B* **42**, 4244 (1990).
[59] J.R. LaGraff, E.C. Behrman, J.A.T. Taylor, F.J. Rotella, J.D. Jorgensen, L.Q. Wang, and P.G. Mattocks, *Phys. Rev. B* **39**, 347 (1989).
[60] M. Avrami, *J. Chem. Phys.* **8**, 212 (1940).
[61] J. Crank, *The Mathematics of Diffusion*, Clarendon Press, Oxford (1975).
[62] J.R. LaGraff and D.A. Payne, (unpublished).
[63] R.H. Doremus, *Rates of Phase Transformations*, Academic Press, Orlando (1985).
[64] J.V. Andersen, H. Bohr, and O.G. Mouritsen, *Phys. Rev. B* **42**, 283 (1990).
[65] J.L. Tallon, A.H. Schuitema, and N.E. Tapp., *Appl. Phys. Lett.* **52**, 507 (1988).

Ferroelectrics, 1992, Vol. 130, pp. 87–105
Reprints available directly from the publisher
Photocopying permitted by license only

OXYGEN STOICHIOMETRY AND MOBILITY EFFECTS ON DOMAIN WALL MOTION IN FERROELASTIC $YBa_2Cu_3O_{7-\delta}$

JOHN R. LAGRAFF and DAVID A. PAYNE

Department of Materials Science and Engineering, Materials Research Laboratory and the Science and Technology Center for Superconductivity, The University of Illinois at Urbana-Champaign, Urbana, Illinois 61801 U.S.A.

(Received February 12, 1991; in final form July 15, 1991)

The purpose of this paper is to examine the interrelationship between oxygen stoichiometry and mobility with ferroelastic properties in $YBa_2Cu_3O_{7-\delta}$. Changes in oxygen stoichiometry, δ, affect the orthorhombic-tetragonal phase transformation behavior and consequently can be expected to directly affect the ferroelastic domain structure and switching properties. A free energy formulation is used to derive an expression for the energy γ_T of a {110} twin wall in $YBa_2Cu_3O_{7-\delta}$ in terms of the spontaneous strain, coercive stress, and twin wall separation. An upper limit of 40 mJ/m^2 was estimated. Ferroelastic viscosity, η, of $YBa_2Cu_3O_{7-\delta}$ was assumed to be an activated process which depends on both the diffusivity and concentration of oxygen according to the relation $\eta = \eta_0(0.6-\delta)\exp(-E/kT)$ for $\delta < 0.6$. Two types of domain reorientation mechanisms are proposed, a cooperative shear process of oxygen along a twin wall and a stress-assisted short-range oxygen hopping process in the bulk of the domain, both of which are expected to be strongly dependent upon the oxygen content and mobility.

Keywords: Superconductor, ferroelastic, $YBa_2Cu_3O_{7-\delta}$, oxygen diffusion, phase transformation, domains

INTRODUCTION

There are many interesting features of $YBa_2Cu_3O_{7-\delta}$ in addition to the remarkable superconducting properties. $YBa_2Cu_3O_{7-\delta}$ is a ferroelastic (and possibly ferroelectric[1]) which exhibits domain (twin) structures reminiscent of the more familiar perovskite ferroics, e.g., $BaTiO_3$, $Bi_4Ti_3O_{12}$, etc. The ferroelastic phase transformation in $YBa_2Cu_3O_{7-\delta}$, however, is controlled by the oxygen content which allows for the transformation to be driven not only by changes in temperature but also by varying the partial pressure of oxygen isothermally.[2-4] An understanding of twinning dynamics and domain structure in $YBa_2Cu_3O_{7-\delta}$ has several fundamental and technologically important consequences. The multidomain nature of most single crystal $YBa_2Cu_3O_{7-\delta}$ makes certain physical property measurements difficult to determine as the **a**–**b** anisotropy cannot be deconvoluted. This problem can be alleviated by the application of a suitably applied uniaxial stress directed along either the **a** or **b** axis which results in single domain crystals at appropriate temperatures.[5-10] The measurement of fundamental anisotropic properties[11] may contribute to a more complete understanding of the superconducting mechanism. Twin (domain)[12] boundaries have been reported to act as weak flux pinning sites[13] which give rise to larger critical current densities under applied magnetic fields. Thus the ability to tailor twin boundary densities, and possibly wall thicknesses, through applied mechanical stress would be desirable. Twin boundaries may also serve as high

diffusivity pathways for oxygen incorporation[14] which would be important in the manufacture of ceramics with optimum properties. The relatively large chemical diffusivities of oxygen ($D \sim 10^{-6}$–10^{-7} cm^2/sec)[10] at elevated temperatures (500–800°C) also make these materials potential candidates as "smart" materials, namely as oxygen sensors. $YBa_2Cu_3O_{7-\delta}$ is electrically conductive in which case oxygen sensors fabricated from this material would not require bulky electrodes or reference cells. The possibility of introducing a single twin wall into a crystal by a suitably applied uniaxial stress and the ability to manipulate twin wall thicknesses by appropriate oxygen annealing treatments could lead to the formation of individual weak links or Josephson junctions for device applications.

Many technologically important ferroelectric materials are simultaneously ferroelastic. Consequently, their domain structure and switching behavior depend not only on spontaneous strain, but also on spontaneous polarization and the subsequent depolarization and dipolar energies at domain walls. However, elastic effects can be so large as to be the controlling influence on domain configurations in many ferroelectrics. Grain size greatly influences domain wall separation due to clamping stresses from neighboring grains and consequently controls the switching behavior in polycrystalline $BaTiO_3$. $YBa_2Cu_3O_{7-\delta}$ is a pure ferroelastic and serves as an excellent prototype material with which to study purely stress-related domain dynamics and structure. This could have important implications in understanding aging behavior and domain switching in other ferroic systems.

It is the purpose of this paper to review some fundamental considerations of ferroelasticity in $YBa_2Cu_3O_{7-\delta}$ including comparisons with other ferroic materials. The interrelationship between oxygen diffusion and ferroelasticity will be discussed in relation to domain (twin) structure and dynamics. The paper begins with a brief review of ferroelasticity, including prototype symmetries and spontaneous strain formulation, followed by a discussion of ferroelastic behavior in $YBa_2Cu_3O_{7-\delta}$. The latter will include an estimation of the {110} twin wall energy and a discussion of proposed mechanisms for domain wall mobility and reorientation.

FERROELASTIC $YBa_2Cu_3O_{7-\delta}$

Prototype Symmetry and Orientation States

It is well known that, ferroelastics are materials which exist in two or more energetically equivalent orientation states in the absence of an external applied stress field.[15] In addition, it must be theoretically possible to switch from one state to another through the application of a suitably applied uniaxial stress. In the absence of an external field, the orientation states, S_i, of ferroelectrics and ferromagnets differ in one or more components of spontaneous polarization, P_s, and spontaneous magnetization, M_s, respectively. In an analogous fashion, ferroelastics differ in one or more components of spontaneous strain, ε_s.[15] These three types of materials are grouped into a class of materials known as ferroics. A ferroic phase transformation occurs between the prototype phase and the ferroic phase and is accompanied by a change in the point group symmetry leading to the onset or disappearance of certain state parameters such as spontaneous strain, polarization, or magnetization.

The phase in which all state parameters are zero is defined as the prototype

phase. The prototype has the highest supergroup symmetry attainable by a given crystal structure through a small structural displacement and thus there is ideally no rupture or reconstructive rearrangement of chemical bonds in a ferroic phase transformation. The point group symmetry of the prototype phase should enable the prediction of all orientation states possible in the lower symmetry ferroic phases.[16] In ferroic materials the domain structure and finite switching times for the orientation states leads to hysteresis between the relevant state parameter and the corresponding driving potential. Ferroelectrics exhibit hysteresis in polarization versus electric field, ferromagnets in magnetization versus applied magnetic field, and ferroelastics in strain versus applied uniaxial stress.

According to Aizu[16] the number of theoretically permissible orientation states, n, in a ferroic crystal can be determined by symmetry considerations and equals the order of the prototype point group divided by the order of the ferroic point group. The number of symmetry operations (F-operations) lost in the ferroic phase transformation will determine the number and orientation of all the crystallographically permissible orientation states in the ferroic phase. These lost symmetry operations will map all of the different orientation states, S_i, onto one another. For example, if a mirror plane is lost in the ferroic phase transformation, it will map two different orientation states onto each other. $YBa_2Cu_3O_{7-\delta}$ belongs to the ferroelastic Aizu species 4/mmmFmmm.[15] The prototype phase (tetragonal; 4/mmm) has an order of 16 while the ferroic species (orthorhombic; mmm) has an order of 8 which predicts two (16/8 = 2) possible orientation states, S_1 and S_2.

Domains and Switching

Energetically equivalent orientation states (domains) are formed to minimize the free energy of a ferroic crystal. The formation of ferroelastic domains acts as a stress-accommodating mechanism as the crystal is cooled through a ferroic phase transformation. The equilibrium size of the average domain width, d, is determined by the minimum free energy of the domain walls which includes the elastic deformation energy and the twin wall energy, γ_T.[17] (One must also consider depolarization and dipolar energies at domain walls in insulating ferroelectrics.) Elastic deformation energy is caused by spontaneous deformation from the symmetry reduction of the crystal upon cooling through a ferroic transformation and by clamping of the crystal either externally in single crystals or by the surrounding grains in polycrystalline ceramics.

In general, the switching of orientation states in ferroic materials proceeds by three steps. First, nucleation of domains at crystal faces (and, possibly, at internal defects) due to the lower activation energies at surfaces and interfaces. Second, domain growth throughout the bulk. Third, sideways growth or expansion of domain walls, probably due to continuous nucleation along domain walls. These three processes may proceed simultaneously in different parts of a crystal or crystallite. The critical coercive stress, σ_c, of a ferroelastic can be defined as the minimum stress needed to introduce a new orientation state in a crystal which is comprised entirely of a different orientation state.[18] The coercive stress is directly analogous with the coercive field, E_c, in ferroelectrics.

Spontaneous Strain

Spontaneous polarization, P_s, and spontaneous magnetization, M_s, can be defined as the displacement of electric or magnetic charge and are easily seen to go to zero in the prototypic state for a ferroelectric or ferromagnetic crystal. However, defining a spontaneous strain, $\varepsilon_{(s)}$, in a ferroelastic crystal so that it goes to zero in the prototypic state is somewhat more subtle. The normal strain tensor of a material cannot be used to represent the spontaneous strain tensor of a ferroelastic because it does not necessarily equal zero in the prototype state due to induced thermal expansion effects. In defining spontaneous strain, the following requirements must be satisfied:[15]

1) Spontaneous strain should be independent of the rectangular coordinate system and be the same in all the orientation states of the ferroelastic phase.

2) Spontaneous strain should be zero over all temperatures in the prototypic phase.

The n orientation states of a ferroelastic crystal can be represented by S_1, S_2, . . . S_n. The spontaneous strain tensor, $\varepsilon_{(s)}(S_i)$, for a given orientation, S_i, can be written as,[15]

$$\varepsilon_{(s)}(S_i) = \varepsilon(S_i) - \frac{1}{n}\sum_{k=1}^{n} \varepsilon(S_k) \; (i = 1, 2, \ldots, n) \tag{1}$$

where, $\varepsilon(S_i)$ is the strain tensor for the orientation state, S_i and the second term is defined as the mean strain tensor, ε_m. The magnitude of the spontaneous strain tensor is simply written as,[15]

$$\varepsilon_s^2 = \sum_{i=1}^{3}\sum_{j=1}^{3} \varepsilon_{(s)ij}^2 \tag{2}$$

where $\varepsilon_{(s)ij}$ are the ij^{th} elements of $\varepsilon_{(s)}(S_i)$.

Spontaneous Strain in $YBa_2Cu_3O_{7-\delta}$

$YBa_2Cu_3O_{7-\delta}$ undergoes a 4/mmmFmmm ferroelastic phase transformation at ~700°C in pure oxygen[19] with the onset of spontaneous strain. The tetragonal to orthorhombic phase transformation results in the formation of energetically equivalent domains with (110) and $(1\bar{1}0)$ twin walls. These are so called W-walls[20] or crystallographically prominent planes which are expected to be strain-free. If two ferroelastic domains, S_1 and S_2, are separated by a W-wall, the spontaneous strain tensor of say S_1 can be mapped onto S_2 by the symmetry associated with the W-wall.

The spontaneous strain tensor for both orientation states is written from Equation (1) and the orthorhombic strain tensor as,

$$\varepsilon_{(s)}(S_i) = \pm\begin{pmatrix} w & 0 & 0 \\ 0 & -w & 0 \\ 0 & 0 & 0 \end{pmatrix} \tag{3}$$

where $w = \frac{1}{2}(\varepsilon_{11} - \varepsilon_{22})$ and ε_{11} and ε_{22} are the strains in the **a** and **b** directions

of the orthorhombic material. The magnitude of the spontaneous strain is written from Equations (2) and (3) as,[15]

$$\varepsilon_s = \sqrt{2}|w| \tag{4}$$

or in terms of the **a** and **b** lattice parameters,

$$\varepsilon_s = \sqrt{2}\left|\frac{\mathbf{a} - \mathbf{b}}{\mathbf{a} + \mathbf{b}}\right| \tag{5}$$

In the tetragonal prototypic phase, $\varepsilon_{11} = \varepsilon_{22}$ (i.e., the **a**-axis and **b**-axis are indistinguishable), and from inspection of Equation (3), the spontaneous strains in both orientation states are now equal and zero. Also note from Equation (5) that the magnitude of the spontaneous strain is the same in both orientation states of orthorhombic $YBa_2Cu_3O_{7-\delta}$. The requirements for defining the spontaneous strain have now been satisfied.[15]

The magnitude of the spontaneous strain in $YBa_2Cu_3O_{7-\delta}$ can be calculated from the appropriate lattice parameters at various temperatures (and hence oxygen contents) in equilibrium with 100% oxygen (Figure 1(a)).[19] The spontaneous strain also varies at room temperature in samples which were quenched from 520°C after annealing in controlled oxygen partial pressures (Figure 1(b)).[21] The spontaneous strain is nearly constant below 600°C (Figure 1(a)). However, stress induced detwinning has not been observed below 300–400°C, which suggests that there are additional factors, aside from the structural distortion, which must be overcome to enable twin wall motion.

Switching Stress

By neglecting any second-order ferrobielastic effect,[6,18] the free energy difference between the two orientation states, S_1 and S_2, for $YBa_2Cu_3O_{7-\delta}$ at constant temperature can be written as,

$$\Delta G = -\Delta\varepsilon_{(s)ij}\sigma_{ij} \tag{6}$$

The optimum stress state σ_{ij} required to switch from state S_1 to S_2 will give the maximum reduction of free energy, ΔG which is simply,

$$\Delta G = G_2 - G_1 = 2w(\sigma_{11} - \sigma_{22}) \tag{7}$$

where G_1 and G_2 are the free energies of S_1 and S_2, respectively. Below the orthorhombic-tetragonal phase transformation in $YBa_2Cu_3O_{7-\delta}$ the **a**-axis contracts and the **b**-axis expands relative to the tetragonal prototype. Consequently, ε_{11} is negative, ε_{22} is positive, and w is negative (Equation (3)). The optimum stress state (the minimum ΔG) will occur when $\sigma_{11} = 0$ and $\sigma_{22} = \sigma_{applied}$ (i.e., a compressive stress, $\sigma_{applied}$, is directed along the **b**-axis). Figure 2 is a schematic diagram for domain wall motion in a $YBa_2Cu_3O_{7-\delta}$ crystal under the application of a uniaxial stress. Orientation state S_1 is favored and will grow at the expense of orientation state S_2.

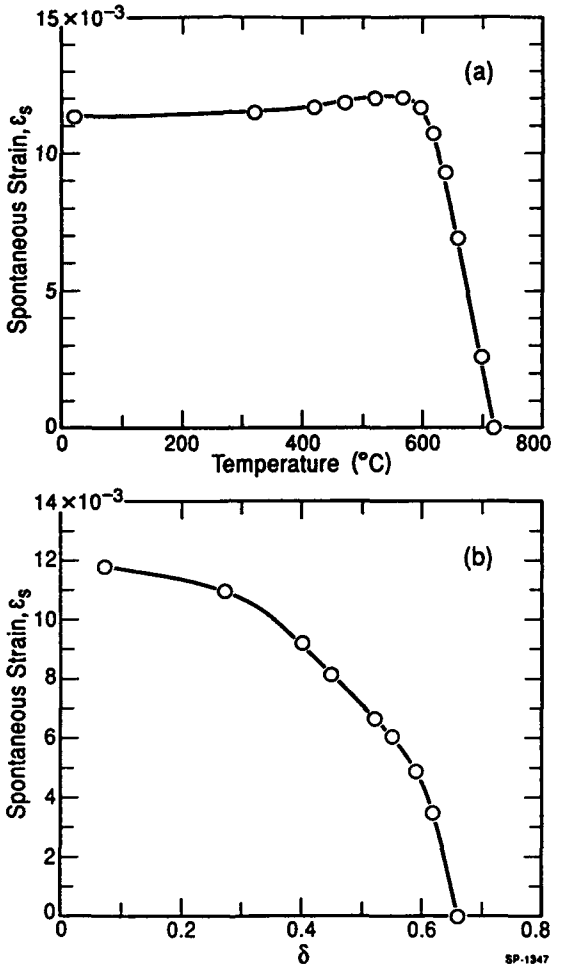

FIGURE 1 Spontaneous strain in ferroelastic $YBa_2Cu_3O_{7-\delta}$ as a function of (a) temperature and oxygen content when in equilibrium with 100% oxygen (Reference 19) and (b) oxygen vacancy content, δ, at room temperature following quenches from 520°C in controlled partial pressures of oxygen (Reference 21).

Orthorhombic-Tetragonal Phase Transformation

The orthorhombic-tetragonal transformation in $YBa_2Cu_3O_{7-\delta}$ is known to be an order-disorder structural phase transformation which occurs near an oxygen content of 6.4–6.5 oxygen per unit cell,[19,21] and whose transformation temperature, T_0, is determined by the partial pressure of oxygen surrounding the material. The oxygen content also plays an important role in determining other normal-state and superconducting properties of $YBa_2Cu_3O_{7-\delta}$ (for example, see Reference 22). The fully oxygenated (orthorhombic) state ($\delta \approx 0$) consists of oxygen atoms ordered on the O(1) chain sites, thereby forming one-dimensional copper-oxygen rows or chains (Figure 3). As δ increases, oxygen is both removed from O(1) sites and disordered from O(1) sites onto normally vacant O(5) chain sites until they are equally occupied

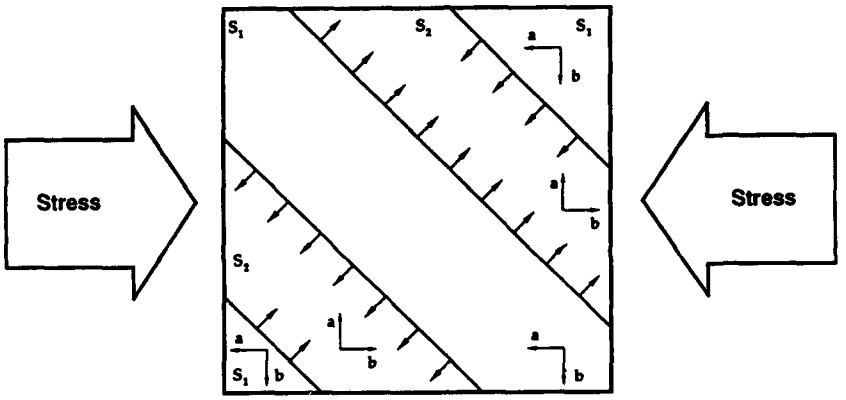

FIGURE 2 Lateral motion of twin boundaries under the influence of an applied uniaxial stress in which orientation state S_1 grows at the expense of S_2.

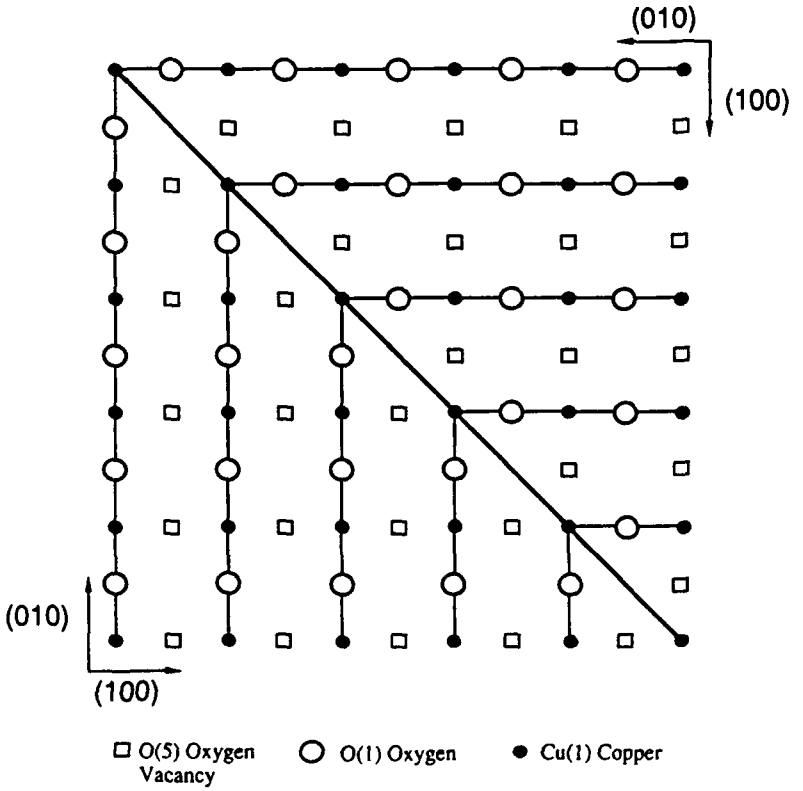

FIGURE 3 An idealized {110} twin boundary in $YBa_2Cu_3O_{7-\delta}$ as viewed in the **a**–**b** plane. The twin boundary separates two different orientation states (domains) which differ in the direction of spontaneous strain. Twin boundaries form in order to relieve the strain accompanying the tetragonal to orthorhombic phase transformation.

and the material becomes tetragonal. Theoretical models[23] first suggested that intermediate oxygen-ordering states may exist between the ideal orthorhombic ($\delta \approx 0$) and tetragonal ($\delta \approx 1$) structures. One such ordered state is the orthorhombic-II (OII) structure which has every other copper-oxygen chain absent. Subsequent transmission electron microscopy[24] and neutron diffraction[25] studies have indeed confirmed the existence of the OII structure in addition to other intermediate oxygen ordered phases.

The strong dependence of the crystal structure on the oxygen content suggests that the kinetics of the orthorhombic-tetragonal phase transformation will depend strongly on oxygen diffusion behavior.[2,3,26,27] Thus, in addition to the temperature and oxygen partial pressure dependencies for the equilibrium transformation, one must also consider other parameters such as heating and cooling rates and grain (or crystal) size effects (i.e., the diffusion length) when considering the kinetics of the transformation. The strain accompanying the orthorhombic-tetragonal phase transformation leads to the formation of twin walls which separate the material into ordered domains and, according to the symmetry operations lost at the transformation, makes $YBa_2Cu_3O_{7-\delta}$ a pure ferroelastic.[15] A complete knowledge of oxygen diffusion behavior in $YBa_2Cu_3O_{7-\delta}$ would facilitate an understanding of the kinetics and mechanism of the orthorhombic-tetragonal phase transformation and subsequently would elucidate on the mechanism for ferroelastic detwinning.

Upon cooling through the transformation temperature, T_0, orthorhombic microdomains are formed within a tetragonal matrix. These orthorhombic regions can have one of two different twin orientations—(110) or ($1\bar{1}0$) walls—and coarsen with time and decreasing temperature often giving rise to a characteristic "tweed" structure.[28,29] Shi[26] has proposed a two-step tranformation process. Initally, a rapid martensitic-shear type mechanism leads to twin boundary formation. Further domain growth proceeds more slowly and is limited by long range oxygen diffusion behavior. Eventually twin boundaries interact and local regions of strain or variable oxygen content will determine which domains grow at the expense of others. Observations of domain wall memory effects in $YBa_2Cu_3O_{7-\delta}$ crystals[3] suggest that lattice defects either control local strain regions or serve as nucleation sites for initial twin formation.

Ferroelastic Domains

The ferroelastic character of the orthorhombic-tetragonal transformation in $YBa_2Cu_3O_{7-\delta}$ has been supported by several detwinning (switching) studies.[5-10] The orientations of the twin walls in the $YBa_2Cu_3O_{7-\delta}$ material are of the {110} type and are determined from both the symmetry elements lost in the transformation and from spontaneous strain compatibility requirements at the twin wall.[20] In practice, however, four orientation states are usually observed[30] with ~90° orientated twin walls. Shuvalov *et al.*[31] consider the symmetry laws[15,16] of "ideal twinning" to be only a first approximation to the orientation states often observed in real ferroelastics. They noted that the angles between identical crystallographic directions in neighboring domains are not always the same as the angles expected between ideal orientation states. In addition, these angles are often observed to vary with temperature or pressure. These small deviations (or rotations) from ideal

orientations lead to the concept of suborientational domain states.[31] Boulesteix[32] has used a similar approach to explain the origin of the four different orientation variants observed in $YBa_2Cu_3O_{7-\delta}$.

Across the twin boundary in $YBa_2Cu_3O_{7-\delta}$, the **a**–**b** plane is rotated ~90°, so that the **b**-axis of one domain is almost perpendicular to the **b**-axis in a neighboring domain (Figure 3). Assuming a coherent twin wall, the angle θ between equivalent crystallographic axes in neighboring domains can be determined from the expression $\theta = 2 \tan^{-1} (\mathbf{a}/\mathbf{b})$. The lattice parameters of fully oxygenated $YBa_2Cu_3O_{7-\delta}$ are approximately $\mathbf{a} = 3.82$ Å and $\mathbf{b} = 3.88$ Å which results in $\theta = 89°$, close to a value (89.1°) determined by experiment.[10] Twin walls of the (100) variety, in which the **c**-axes in adjacent domains are rotated by 90°, have also been observed in $YBa_2Cu_3O_{7-\delta}$.[33] These, however, are probably growth twins as they do not disappear above the orthorhombic-tetragonal transformation. (100) twins would probably impede oxygen uptake as oxygen diffusion is extremely slow in the **c**-direction.[34] They may also impede {110} domain wall formation and movement.[33]

Wadhawan[35,36] suggests a hypothetical m3m prototypic symmetry to account for the different {110}, {100}, {113}, and {001} twin boundaries which have been reported in $YBa_2Cu_3O_{7-\delta}$. The point group m3m has an order of 48 which suggests three possible orientation states in the tetragonal phase. By assuming a m3m prototypic point group, a room temperature spontaneous strain of ~0.31 was calculate ef-erence 36) which is unreasonably large. However, if a tetragonal prototyp n-metry of 4/mmm is considered, only the occurrence of {110} twin walls c e predicted and a room temperature spontaneous strain of ~0.011 was calcu. d (Figure 1(a)). This is a more reasonable value when compared with other ferroelastic materials.[15] Thus, the authors believe that the vast majority of observed twin structures and domain switching characteristics can be accounted for by the 4/mmm prototypic symmetry.

Twin Wall Characteristics

Jou and Washburn[37] have proposed a model in which several atomic layers close to a twin boundary may be oxygen-deficient due to a balance between coulombic repulsive forces of neighboring oxygen anions across a twin boundary, the stress state of the boundary, and the chemical potential. Oxygen vacancy ordering near twin boundaries could explain slight variations in θ observed at the boundaries and, also, the difficulty in achieving complete oxygenation ($\delta = 0$). Variable oxygen content near twin boundaries is probably temperature dependent and could account for suborientation states observed in the material.[30] The high concentration of vacancies may also enable {110} twin boundaries to behave as high diffusivity paths for oxygen diffusion.[14]

Twin wall thicknesses may influence wall mobilities and also control oxygen diffusion behavior. Zhu *et al.*[38] have estimated twin boundary thicknesses, t, from electron diffraction patterns and the equation,

$$t = A\left(\frac{R_{110}}{l_{st}}\right) d_{110} \tag{8}$$

where R_{110} is the distance from the transmitted spot to the (110) diffraction spot,

l_{st} the length of the streak at the transmitted spot due to the twin boundary density, d_{110} the (110) lattice spacing, and A a constant depending on the experimental conditions and the twin density contribution. They estimated a twin wall thickness of 10–15 Å (2–3 unit cells) for fully oxygenated $YBa_2Cu_3O_{7-\delta}$ and found that this thickness could increase by the addition of specific dopants or the variation of oxygen stoichiometry.[38] For example, oxygen removal both decreased the average twin boundary separation and increased the boundary thickness. Optimal flux pinning and weak link behavior may occur when the twin boundary thickness is of the same length scale as the coherence length.[39] It is well known that the addition of dopants[40] and variations in oxygen stoichiometry[19,21] modify the orthorhombic strain and it is thus a reasonable assumption that they may also change the twin wall energy. This may allow twin wall densities and boundary thicknesses to be "tailored" for specific applications which depend on domain characteristics.

Sarikaya *et al.*[41] have proposed a model to predict the equilibrium twin separation, d, in $YBa_2Cu_3O_{7-\delta}$ as,

$$d^2 = \frac{2E_T}{\Omega}\left(\frac{a}{\Delta a}\right)^2 \tag{9}$$

where E_T is the twin boundary formation energy per unit lateral length, Ω the shear modulus, and $\Delta a/a$ the strain. As the oxygen stoichiometry is reduced, the orthorhombic strain will decrease and one expects the average twin spacing to increase if the twin wall energy remains relatively constant. Indeed, larger twin spacings have been observed by Shaw *et al.*[29] for decreasing oxygen content, however, others[38,42] have reported smaller twin spacings under similar conditions. The latter observations suggest that the twin wall energy may vary with oxygen content.

Shi *et al.*[42] report average twin spacings of 1500 Å, 800 Å, and 300 Å for oxygen contents of 6.98, 6.62, and 6.55, respectively, which according to Equation (9), can happen only if lower oxygen stoichiometry reduces the twin wall formation energy term E_T faster than the orthorhombic strain. The formation energy, E_T, contains terms for both the energy per unit area of a twin boundary, γ_T, and the lateral size, L, of a twin colony composed of a single variant,

$$E_T = \gamma_T L \tag{10}$$

This suggests that the observations of decreasing twin boundary separation with increasing oxygen deficiency[38,42] could be due to either (or both) a decrease in the twin boundary interface energy, γ_T, or to a decrease in the size of the twin colonies, L. More quantitative evidence is needed to resolve the discrepancies observed[29,38,42] in twin separation as a function of oxygen content. This would entail determining the individual dependencies of the twin wall energy, size of twin colonies, and twin separation distance on the oxygen content.

Not only can the transformation strain be compensated for by the creation of surface energy at the twin boundaries (i.e., γ_T), but it can also be accommodated at the edge of a single variant twin network (often a grain boundary) which would effectively lower the twin boundary energy, E_T, in Equation (10). If this accommodation energy is significant, the twin separation, d, would be expected to depend on the size of the twin network, L, to the one-half power (i.e., $d \propto \sqrt{L}$).[43,44] (Such a dependence can be seen by substituting Equation (10) into (9).) Indeed, obser-

vations for polycrystalline[29,45] and thin film[46] $YBa_2Cu_3O_{7-\delta}$ have shown this square-root dependence of twin boundary separation on grain size and film thickness, respectively.

A crystal comprised of a single twin variant would not be constrained by either the surrounding grains as in the polycrystalline specimen or the underlying substrate as in a thin film and the twin separation may not exhibit a $\sqrt{L}$ dependence. With this assumption, a first-order approximation of the {110} twin wall energy per unit area, γ_T, in $YBa_2Cu_3O_{7-\delta}$ can be estimated by assuming that the energy associated with the minimum stress (i.e., the coercive stress, σ_c) needed to detwin a crystal will be balanced by the total interface energy ($\gamma_T d^{-1}$) associated with the twin walls where d^{-1} is simply the total area of twins per unit volume of crystal. In other words, accommodation energies and the subsequent dependence of twin separation on L are assumed to be absent. Combining Equations (4) and (7) yields the twin boundary energy as

$$\gamma_T = \Delta G d = \sqrt{2}\varepsilon_s \sigma_c d \tag{11}$$

The lack of experimental values for σ_c as a function of temperature and oxygen content does not allow exact values of γ_T to be calculated, but upper limits can be estimated from switching stresses reported in the literature. Giapinzakis *et al.*[5] report the lowest applied stresses (25 MPa) required to achieve domain switching at 450°C. Assuming a spontaneous strain of 0.011 (Figure (1a)) and an average

TABLE I

A comparison of the ferroelastic domain characteristics of {110} twins in $YBa_2Cu_3O_{7-\delta}$ and 90° twins in $BaTiO_3$.
(180° twins in $BaTiO_3$ are not ferroelastic.)

	$YBa_2Cu_3O_{7-\delta}$	$BaTiO_3$
Prototypic Phase	4/mmm [(a)]	m3m
Ferroic Phase	mmm	4mm
Lattice Parameters, (Å)	a = 3.823 [(b)] b = 3.887	a = 3.992 [(c)] c = 4.036
Spontaneous Strain, ε_s	11.7×10^{-3} [(d)]	8.98×10^{-3} [(c)]
Wall Thickness (Å)	10-30 [(e)]	50-100 [(f)]
Wall Energy (mJ/m^2)	<40 [(d)]	2-4 [(f)]

(a) A hypothetical prototypic phase m3m has been proposed in Ref. [36].
(b) After Ref. [19].
(c) After Ref. [18].
(d) This paper.
(e) After Ref. [38].
(f) These are for 90° twin walls. After Ref. [47].

twin separation of 1000 Å[38] yields a value of ~40 mJ/m² for the twin wall energy. This is an order of magnitude greater than 2–4 mJ/m² for ferroelastic 90° domain walls in $BaTiO_3$ (Table I).[47] (180° walls are not ferroelastic.) The value of the wall energy estimated from Equation (11) for $YBa_2Cu_3O_{7-\delta}$ is in fact expected to be lower once reliable coercive stresses are measured. Again, it should be noted that Equation (11) assumes that the transformation energy is entirely compensated for by the formation of surface energy at the twin boundaries. However, as mentioned previously, strain can also be accommodated at the edge of a single variant twin network which would lead to a dependence of the twin separation on the grain size, L, as seen by others.[29,45] Equation (11) neglects the size of the twin colony, L, which is a reasonable assumption in an uncontrained single crystal comprised of only one twin variant.

deFontaine *et al.*[23] have used an Ising model with next-nearest neighbor (nnn) anisotropic interactions to succesfully model the different ordered oxygen configurations observed in $YBa_2Cu_3O_{7-\delta}$. Assuming the ideally coherent twin boundary (see, Figure 3) deFontaine *et al.*[48] derived an expression for the energy of a boundary per unit cell as $E_b = 4(V_1 - V_2 - V_3)$ where V_1 is the effective interaction between two nearest neighbor oxygen (i.e., the O(1) and O(5) sites in Figure (3)), V_2 the nnn interaction between two O(1) oxygen separated by a copper atom, and V_3 the nnn interaction between two O(1) oxygen in neighboring chains. Using values of 27.6 mRy, −9.6 mRy, and 4.4 mRy for V_1, V_2, and V_3, respectively,[49] and the expression for the twin boundary energy per unit area, $\gamma_T = E_b (c\sqrt{a^2 + b^2})^{-1}$ yields a value of ~450 mJ/m². This value seems quite large in comparison to the 40 mJ/m² estimated in this paper. This suggests that significant lattice relaxation and oxygen vacancies due to unfavorable nearest neighbor oxygen interactions may occur in the vicinity of a twin boundary. In other words, the boundary is not ideally coherent. However, the proposed expression should serve as a good starting point in developing an atomistic model to describe twin boundary characteristics.

The energy of a {110} twin boundary has been estimated by two groups using two different models. Roy and Mitchell[45] assume that the transformation strain is balanced by both the interface energy γ_T and the accommodation energy at the end of twin boundaries. From the slope of a plot of the average twin separation, d, as a function of the square root of the size of the twin colony, $\sqrt{L}$, they estimated an energy of ~2.8 mJ/m² at room temperature which seems reasonable in light of the energy of a 90° twin wall in $BaTiO_3$ (Table I) and falls below the upper limit of ~40 mJ/m² estimated from Equation (11). Dislocation theory was used by Bioko *et al.*[50] to estimate the energy of so-called elastic twins; those which do not extend through an entire grain. A twin boundary energy of ~1000 mJ/m² was obtained which seems quite large. The estimate of Boiko *et al.*[50] relies on the twin separation to length ratio (d/L) obtained from twenty-five twins observed by optical microscopy in several polycrystalline samples. As they point out, however, their samples vary in grain size which has been shown by others[29,45] to influence twin geometries. Further studies are needed to clarify the actual influence of the oxygen content and grain size on the twin characteristics. Also, studies on both polycrystalline and single crystal $YBa_2Cu_3O_{7-\delta}$ would help separate intrinsic twin characteristics from those which are influenced by the clamping stresses in a polycrystalline specimen.

Detwinning Mechanisms

One major difference between $YBa_2Cu_3O_{7-\delta}$ and most ferroelastics is the mechanism by which domain reorientation occurs. Traditional ferroelastics require small structural distortions on the order of 0.1 Å to impart domain reorientation, consequently no bonds are broken. In $YBa_2Cu_3O_{7-\delta}$, however, domain wall motion appears to occur by large jumps (~2.7 Å) of oxygen anions which requires both the breaking of bonds and sufficient oxygen mobility. Figure 4 demonstrates how oxygen may cooperatively shear (or jump) along a twin boundary under the application of an applied stress, thus imparting a lateral motion to a twin boundary (see also Figure 2). This motion involves a 2.7 Å jump of individual O(1) anions to the vacant O(5) sites which also advance the twin wall 2.7 Å. Thus, a strong dependence is expected between ferroelastic domain wall motion and the diffusivity and concentration of oxygen.

Rudyak[51] has developed a phenomenological model to describe domain switching properties in both ferroelectric and ferroelastic materials in terms of a viscosity coefficent η which contains the intrinsic switching properties of a given material without making any assumptions about the underlying microscopic mechanisms. This model has been successfully used to describe such phenomena as the time dependence of spontaneous strain (or polarization), the shapes of hysteresis curves, and the temperature dependence of coercive stresses (or fields) in a wide variety of ferroelastic (and ferroelectric) materials including order-disorder types such as triglycine sulphate (TGS), $KH_3(SeO_3)_2$, and gadolinium molybdate (GMO) (see Reference 51, and references contained within). This suggests that Rudyak's vis-

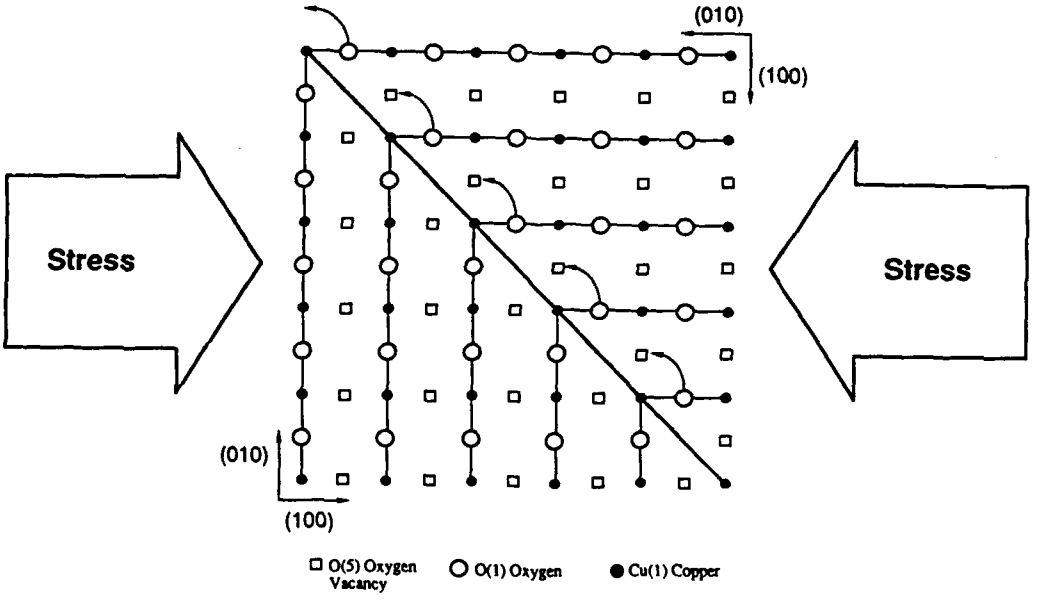

FIGURE 4 Cooperative shear mechanism for twin wall migration under the application of a uniaxial stress. At a given temperature and applied stress one would expect more facile wall motion (i.e., a lower ferroelastic viscosity) if a few oxygen atoms were removed from near the twin wall.

cosity model[51] may also be appropriate in describing the switching properties of $YBa_2Cu_3O_{7-\delta}$ whose ferroelastic transformation is of the order-disorder variety.[19,21]

The attainment of equilibrium of a ferroelastic under a constant applied stress σ can be written in scalar form as,[51]

$$\varepsilon = \varepsilon_s \left[1 - \exp\left(\frac{-\sigma t}{\eta}\right) \right] \tag{12}$$

where ε is the total macroscopic strain (which should be zero in a multidomain single crystal), ε_s the spontaneous strain of an individual orientation state, t time, and η the ferroelastic viscosity coefficient which is a measure of fundamental internal frictions and a function of temperature. Thus, with increasing time, the total strain of an initially multidomain material will approach the spontaneous strain of a single domain, ε_s (i.e., it will approach a single domain configuration). This is analogous to poling in ferroelectrics where the macroscopic polarization of a crystal approaches that of the spontaneous polarization of a single domain under the application of an applied electric field. Equation (12) reveals that if the applied stress increases or the ferroelastic viscosity decreases, the switching time should also decrease. Furthermore, according to Equation (12), there should be no threshold or coercive stress. Instead, domain wall velocities, v, would become infinitely small as the applied stress approaches zero. Similarly, domain wall mobilities ($\nu = v/\sigma$) vary with time at constant temperature under a constant applied stress, σ, according to the following exponential function,[51]

$$\nu = \nu_0 \exp\left(\frac{-\sigma t}{\eta}\right) \tag{13}$$

where ν_0 is the initial mobility which is a function of domain width, spontaneous strain, and η. Wall mobilities control hysteresis loops and consequently the switching behavior of ferroics, whose velocities are limited by impurities, imperfections, and intrinsic frictions or viscosities.[51] An understanding of domaain wall mobilities in $YBa_2Cu_3O_{7-\delta}$ may assist in developing a clearer understanding of similar processes in traditional ferroic materials.

The stress required to induce domain wall motion will not only depend on the spontaneous strain state of the material, but also on the short-range mobility of oxygen anions. Thus, the coercive stress will depend on both temperature and the number of O(1) oxygen vacancies present. Recent reports [52,53] of short range oxygen mobility at room temperature (and below) suggests that ferroelastic detwinning may be possible at these temperatures given sufficient stress, O(1) oxygen vacancy concentration, and time. Room temperature oxygen mobility occurs without loss of oxygen[53] suggesting a surface energy barrier for oxygen diffusion.[2,54] This should enable these materials to be detwinned without loss of oxygen at low enough temperatures (<300–400°C). The dependence of domain wall motion on oxygen mobility suggests that ferroelastic detwinning is also an activated process. Thus it may be difficult to measure actual coercive stresses due to the possibility of extremely slow oxygen migration and consequently slow domain wall motion.

In a fully oxygenated crystal, the number density of O(1) oxygen anions per unit area of twin boundary is calculated at $1.57 \times 10^{18}/m^2$. In order to advance a unit

area of twin wall one fundamental step (2.7 Å), this many oxygen atoms must jump to the O(5) sites (see Figure 4). The removal of oxygen will effectively reduce the total number of oxygen anions which must cooperatively shear to advance a twin boundary and one expects the ferroelastic viscosity to be reduced. This can be seen qualitatively in Figure 4 by removing a few oxygen from near the twin wall.

In $YBa_2Cu_3O_{7-\delta}$ the fundamental frictions affecting the ferroelastic viscosity coefficent η may arise from potential energy barriers due to overlapping repulsive forces as oxygen anions move through the lattice, the coulombic repulsion of neighboring oxygen anions across the twin wall (Figure 4), and local strain fields in the vicinity of a wall or the intersection of two walls. Switching times should decrease as oxygen is removed from $YBa_2Cu_3O_{7-\delta}$, as this would both reduce the local strain fields near the twin wall and the coulombic repulsion forces between adjacent oxygen anions and would effectively reduce the ferroelastic viscosity, η. One expects η to be a function of both temperature and oxygen content; increasing with decreasing temperature and increasing oxygen content.

One potential limitation of Rudyak's viscosity model[51] is that it is based on a linear approximation in which the viscosity, η, is assumed to be independent of the applied mechanical stress, σ_{appl}, which may not necessarily be valid over a wide range of σ (i.e., $\eta = \eta(\sigma_{appl})$). This suggests that, if ferroelasticity is intimately associated with the oxygen content, then the ferroelastic viscosity η may vary depending on both the amount and mobility of oxygen. Inspection of Figure 1(a) reveals that the spontaneous strain does not vary much below ~600°C, but does decrease monotonically with decreasing oxygen content. For switching to occur in $YBa_2Cu_3O_{7-\delta}$, not only must this structural strain be reversed, but temperatures must also be sufficiently high to allow appreciable oxygen mobility. Thus, one may assume that the ferroelastic viscosity η is an activated process which depends on the oxygen diffusivity and the vacancy content, δ, and can be written for $0 < \delta < 0.6$ as,

$$\eta = \eta_0 (0.6 - \delta) \exp\left(\frac{-E}{kT}\right) \tag{14}$$

where η_0 is a pre-exponential factor, E the activation energy for short-range oxygen jumps, k Boltzmann's constant, and T temperature. Thus, as one increases the temperature and oxygen vacancy content, the ferroelastic viscosity will decrease (Equation 14) with a corresponding increase in the wall mobility (Equation 13). Measurements of η as a function of applied stress, oxygen content, and temperature from Equations (12) and (14) should allow for the estimation of the fundamental activation energy for oxygen shear along the twin wall to be estimated. One may expect this value to be close to 1 eV which is the activation energy for a single oxygen jump as measured by tracer diffusion,[34] room temperature oxygen mobility,[52] and internal friction[55] measurements.

As oxygen stoichiometry is reduced towards 6.4 (i.e., the orthorhombic-tetragonal transformation point, $\delta = 0.6$), twin boundaries are observed to thicken[38] which may be due to oxygen vacancy clustering.[37] The ideal picture of cooperative shear of oxygen anions along a sharp coherent twin boundary may not be valid in this oxygen range. Jumps may occur more *en masse* at distances further from the twin boundary due to the larger concentration of oxygen vacancies. The mechanism

for domain reorientation may no longer result from twin wall motion by a cooperative shear process, but instead by a stress-assisted short-range hopping process of oxygen in the bulk of unfavorably aligned domains. A sharp coherent twin boundary should lead to a lower activation energy for short-range oxygen migration in comparison with the bulk and, consequently, a cooperative shear of oxygen anions along the boundary is to be expected. As the twin boundary becomes more diffuse at higher temperatures and/or lower oxygen contents, the difference in activation energy for an oxygen jump along the boundary and in the bulk of the domain should become less. One would then expect stress-associated short-range oxygen jumps in regions away from the boundary.

The observation of lateral motion of twin boundaries under an applied stress supports a cooperative shear of oxygen anions along the twin boundary.[6,10] However, detailed studies of twin wall motion at elevated temperatures by varying oxygen contents have yet to be reported. Under these experimental conditions, a stress-assisted short-range oxygen hopping process in the bulk of a domain should be evident as a "melting" of the twin walls. It is also quite possible that both of these mechanisms occur simultaneously. This raises the possibility of critical stresses, temperatures and oxygen contents for which domain reorientation mechanisms may change from a cooperative shear process to a stress-assisted diffusion mechanism.

CONCLUSIONS

In conclusion, one can appreciate that $YBa_2Cu_3O_{7-\delta}$ is a unique material, being simultaneously a superconductor, a ferroelastic, and possibly an oxygen sensor. The standard symmetry laws of ferroelastics can be used to define the prototype symmetry (4/mmm), the number (2) of orientation states, and twin wall orientation, {110}, in $YBa_2Cu_3O_{7-\delta}$. Ferroelastic phenomenon in $YBa_2Cu_3O_{7-\delta}$ is influenced by the oxygen stoichiometry and mobility; both of which depend on temperature, partial pressure of oxygen, rate of heating and cooling, and kinetics of oxygen migration. Twin boundary separation and thickness depend on the oxygen content, while domain reorientation behavior should depend on both the content and mobility.

An expression was derived to estimate the energy of a {110} twin wall as a function of spontaneous strain, coercive stress, and twin wall separation. An upper limit of 40 mJ/m^2 was calculated. The spontaneous strain, ε_s, as a function of temperature and oxygen content was calculated from available lattice parameter data and found to be almost independent of temperature below ~600°C. Room temperature detwinning has not been observed in $YBa_2Cu_3O_{7-\delta}$, even though the spontaneous strain is comparable to that at higher temperatures. This suggests that sufficient oxygen mobility is required for ferroelastic domain wall motion which would be typical of an activated process which depends on the diffusivity and concentration of oxygen. Since the activation energies for oxygen diffusion are expected to be lower near the twin boundaries of $YBa_2Cu_3O_{7-\delta}$, a cooperative-shear domain reorientation mechanism under the application of an applied stress seems reasonable. However, the relatively large oxygen jump distances (~2.7 Å) and variable oxygen

contents also make a stress-assisted short-range oxygen hopping process in all regions of a domain conceivable under certain conditions (i.e., different stresses, temperatures, and oxygen contents).

Many issues remain to be resolved regarding both the static and dynamic aspects of twin walls in $YBa_2Cu_3O_{7-\delta}$. This will require measurements of twin geometries in both polycrystalline and single crystal specimens at various temperatures and in controlled oxygen partial pressures in order to elucidate on available models of twin boundary formation. Systematic studies of the actual detwinning process, which includes the measurement of coercive stresses, ferroelastic viscosities, and twin boundary mobilities as a function of temperature in controlled oxygen partial pressures, are still needed in order to determine the role of oxygen content and mobility on switching behavior.

Thus, ferroelasticity and the subsequent domain structure must be properly characterized and understood in order to interrelate the effects on the physical properties of $YBa_2Cu_3O_{7-\delta}$. This may enable the engineering of domain characteristics through chemical doping, applied stresses, or varying oxygen stoichiometry in order to design a material with specific property requirements. An investigation of ferroelastic behavior in $YBa_2Cu_3O_{7-\delta}$ could also lead to a more complete understanding of domain dynamics and switching behavior in other ferroelectric-ferroelastic systems (e.g., $BaTiO_3$).

ACKNOWLEDGEMENTS

The authors gratefully acknowledge the technical assistance of P. D. Han and helpful suggestions from anonymous reviewers. This work was supported by the Air Force Office of Scientific Research (Grant No. URI-41098) through a University Research Initiative on phase transformations in ceramics and the National Science Foundation (Grant No. DMR 88-09854) through the Science and Technology Center for Superconductivity at the University of Illinois.

REFERENCES

1. S. K. Kurtz, J. R. Hardy and J. W. Flocken, *Ferroelectrics*, **87**, 29 (1988); O. F. Schilling, *Mater. Lett.*, **8**, 57 (1989); D. Mihailovic and A. J. Heeger, *Solid State Commun.*, **75**, 319 (1990).
2. J. R. LaGraff, P. D. Han and D. A. Payne, *Phys. Rev., B*, **43**, 441 (1991).
3. J. R. LaGraff, P. D. Han and D. A. Payne, *Physica C.*, **169**, 355 (1990).
4. J. R. LaGraff, P. D. Han and D. A. Payne, in *Defects in Materials*, eds. P. D. Bristowe, J. E. Epperson, J. E. Griffith and Z. Liliental-Weber, Proc. Mat. Res. Soc. Symp. **209**, 801 (1991); L. R. LaGraff and D. A. Payne, in Physics and Materials Science of High-Temperature Superconductivity II, eds. R. Kossowsky, B. Raveau and S. Patapis, Proc. NATO Advanced Study Institute, Kluwer Academic Publishers, The Netherlands (in press, 1991).
5. J. Giapintzakis, D. M. Ginsberg and P. D. Han, *J. Low Temp. Phys.*, **77**, 155 (1989).
6. H. Schmid, E. Burkhardt, B. N. Sun and J. P. Riviera, *Physica C.*, **157**, 555 (1989).
7. D. L. Kaiser, F. W. Gayle, R. S. Roth and L. J. Swartzendruber, *J. Mater. Res.*, **4**, 745 (1989).
8. T. Hatanaka and A. Sawada, *Ferroelectrics*, **105**, 57 (1990).
9. L. Dorosinskii, B. Farber, M. Indenbom, V. Nikitenko, A. Polyanskii and V. Vlasko-Vlasov, *Ferroelectrics*, **111**, 321 (1990).
10. J. R. LaGraff, P. D. Han and D. A. Payne (unpublished).
11. Z. Schlesinger, R. T. Collins, F. Holtzberg, C. Feild, S. H. Blanton, U. Welp, G. W. Crabtree, Y. Fang and J. Z. Lui, *Phys. Rev. Lett.*, **65**, 801 (1990); T. A. Freidmann, M. W. Rabin, J. Giapintzakis, J. P. Rice and D. M. Ginsberg, *Phys. Rev. B.*, **42**, 6217 (1990); U. Welp, R. Bhadra, J. Z. Liu and M. Grimsditch, *Physica C.*, **161**, 345 (1989).

12. Twin wall and domain wall can be used to describe the {110} boundaries in $YBa_2Cu_3O_{7-\delta}$ and are used relatively interchangably throughout the paper. In a more rigorous fashion, a twin wall relates two crystallographic parts of a crystal through a symmetry operation associated with the boundary such as a mirror plane or a n-fold rotation axis. In other words, operating on a section of the crystal through the symmetry associated with the twin wall would generate the neighboring crystallographic orientation state. Domain walls, however, separate two different ferroic orientation (domain) states and these two states are not necessarily related by a simple symmetry operation at the boundary. For example, wavy domain walls often observed in $BaTiO_3$ or ferromagnets do not exhibit any long-range symmetry behavior along the wall (i.e., there exists no symmetry operation associated with the wall which when applied to one domain will generate the neighboring domain). For ferroic crystals, in general, twin walls are always domain walls, but domain walls are not necessarily twin walls.
13. L. J. Swartzendruber, A. Roitburd, D. L. Kaiser, F. W. Gayle and L. H. Bennett, *Phys. Rev. Lett.*, **64**, 483 (1990); W. K. Kwok, U. Welp, G. W. Crabtree, K. G. Vandervoort, R. Hulscher and J. Z. Liu, *Phys. Rev. Lett.*, **64**, 966 (1990).
14. J. S. Choi, M. Sarikaya, I. A. Aksay and R. Kikuchi, *Phys. Rev. B.*, **42**, 4244 (1990).
15. K. Aizu, *J. Phys. Soc. Jap.*, **28**, 706 (1970).
16. K. Aizu, *Phys. Rev. B.*, **2**, 754 (1970).
17. G. Arlt, *Ferroelectrics*, **91**, 3 (1989).
18. V. K. Wadhawan, *Phase Trans.*, **3**, 3 (1982).
19. J. D. Jorgensen, M. A. Beno, D. G. Hinks, L. Soderholm, K. J. Volin, R. L. Hitterman, J. D. Grace, I. K. Schuller, C. U. Serge, K. Zhang and M. S. Kleefisch, *Phys. Rev. B.*, **36**, 3608 (1987).
20. J. Sapriel, *Phys. Rev. B.*, **12**, 5128 (1975).
21. J. D. Jorgensen, B. W. Veal, A. P. Paulikas, L. J. Nowicki, G. W. Crabtree, H. Claus and W. K. Kwok, *Phys. Rev. B.*, **41**, 1863 (1990).
22. R. J. Cava, A. W. Hewat, E. A. Hewat, B. Batlogg, M. Marezio, K. M. Rabe, J. J. Krajewski, W. F. Peck and L. W. Rupp, *Physica C.*, **165**, 419 (1990).
23. L. T. Willie and D. deFontaine, *Phys. Rev. B.*, **37**, 2227 (1988); D. deFontaine, M. E. Mann and G. Ceder, *Phys. Rev. Lett.*, **63**, 1300 (1989); D. deFontaine, G. Ceder and M. Asta, *Nature*, **343**, 544 (1990).
24. M. A. Alario-Franco, J. J. Capponi, C. Chaillout, J. Chenavas and M. M. Marezio, *Mater. Res. Soc. Symp. Proc.*, **99**, 41 (1988); D. Shi and D. W. Capone, *Appl. Phys. Lett.*, **53**, 159 (1988); R. Beyers, B. T. Ahn, G. Gorman, V. Y. Lee, S. S. P. Parkin, M. L. Ramirez, K. P. Roche, J. E. Vaxquez, T. M. Gur and R. A. Huggins, *Nature*, **340**, 619 (1989).
25. R. Sonntag, D. Hohlwein, T. Bruckel and G. Collins, *Phys. Rev. Lett.*, **66**, 1497 (1991).
26. D. Shi, *Phys. Rev. B.*, **39**, 4299 (1989).
27. N. Hudakova and P. Diko, *Physica C.*, **167**, 408 (1990).
28. G. Van Tendeloo, D. Broddin, H. W. Zandergen and S. Amelinckx, *Physica C.*, **167**, 627 (1990).
29. T. M. Shaw, S. L. Shinde, D. Dimos, R. F. Cook, P. R. Duncombe and C. Kroll, *J. Mater. Res.*, **4**, 248 (1989).
30. H. Schmid, E. Burkhardt, E. Walker, W. Brixel, M. Clin, J. P. Rivera, J. L. Jorda, M. Francois and K. Yvon, *Z. Phys. B.*, **72**, 305 (1988).
31. L. A. Shuvalov, E. F. Dudnik and S. V. Wagin, *Ferroelectrics*, **65**, 143 (1985).
32. C. Boulesteix, *Phase Trans.*, **14**, 41 (1989).
33. H. W. Zandbergen, R. Gronsky, M. Y. Chu, L. C. DeCjonghe, C. F. Holland and A. Stacy, *Physica C.*, **166**, 255 (1990).
34. S. J. Rothman, J. L. Routbort and J. E. Baker, *Phys. Rev. B.*, **40**, 8852 (1989); S. J. Rothman, J. L. Routbort, U. Welp and J. E. Baker, *Phys. Rev. B.*, **44**, 2326 (1991).
35. V. K. Wadhawan, *Ferroelectrics*, **97**, 171 (1989).
36. V. K. Wadhawan, M. S. Somayazulu and P. U. M. Sastry, *Phys. Rev. B.*, **38**, 2509 (1988).
37. C. J. Jou and J. Washburn, *J. Mater. Res.*, **4**, 795 (1989).
38. Y. Zhu, M. Suenga, Y. Xu, R. L. Sabatini and A. R. Moodenbaugh, *Appl. Phys. Lett.*, **54**, 374 (1989).
39. U. Welp, W. K. Kwok, G. W. Crabtree, K. G. Vandervoort and J. Z. Liu, *Appl. Phys. Lett.*, **57**, 84 (1990).
40. For example, J. R. LaGraff, E. C. Behrman, J. A. T. Taylor, F. J. Rotella, J. D. Jorgensen, L. Q. Wang and P. G. Mattocks, *Phys. Rev. B.*, **39**, 347 (1989).
41. M. Sarikaya, R. Kikuchi and I. A. Aksay, *Physica C.*, 152, 161 (1988).
42. D. Shi, J. G. Chen, M. Xu, H. E. Kourous, Y. Fang, Y. H. Li and M. S. Boley, *Supercond. Sci. Technol.*, **3**, 457 (1990).
43. A. G. Khachaturyan and G. A. Shatalov, *Sov. Phys. JETP*, **29**, 557 (1969).
44. B. Horovitz, G. R. Barsch and J. A. Krumhansl, *Phys. Rev. B.*, **43**, 1021 (1991).
45. T. Roy and T. E. Mitchell, *Phil. Mag. A.*, **63**, 225 (1991).

46. S. K. Steiffer, E. M. Zielinski, B. M. Lairson and J. C. Bravman, *Appl. Phys. Lett.*, **58**, 2171 (1991).
47. M. E. Lines and A. M. Glass, "Principles and Applications of Ferroelectrics and Related Materials," Clarendon Press, Oxford (1977).
48. D. deFontaine, L. T. Wille and S. C. Moss, *Phys. Rev. B.*, **36**, 5709 (1987).
49. P. Sterne and L. T. Wille, *Physica C.*, **162–164**, 223 (1989).
50. Y. Boiko, H. Jaeger, M. Aslan, K. Schulze and G. Petzow, *Mater. Lett.*, **11**, 207 (1991).
51. V. M. Rudyak, *Ferroelectrics*, **48**, 131 (1983).
52. B. W. Veal, H. You, A. P Paulikas, H. Shi, Y. Fang and J. W. Downey, *Phy. Rev. B.*, **42**, 4770 (1990).
53. J. D. Jorgensen, S. Pei, P. Lightfoot, H. Shi, A. P. Paulikas and B. W. Veal, *Physica C.*, **167**, 571 (1990).
54. K. N. Tu, N. C. Yeh, S. I. Park and C. C. Tsuei, *Phys. Rev. B.*, **39**, 304 (1989).
55. X. M. Xie, T. G. Chen and Z. L. Wu, *Phys.Rev. B.*, **40**, 4549 (1989); J. L. Tallon and M. P. Staines, *J. Appl. Phys.*, **68**, 3998 (1990).

OXYGEN IN-DIFFUSION AND OUT-DIFFUSION IN SINGLE CRYSTAL $YBa_2Cu_3O_{7-\delta}$

JOHN R. LaGRAFF, PENGDI HAN, AND DAVID A. PAYNE
Department of Materials Science and Engineering and Materials Research Laboratory, The University of Illinois at Urbana-Champaign, Urbana, IL 61801.

ABSTRACT

Isothermal resistance measurements were used to monitor oxygen in-diffusion and out-diffusion in single crystal $YBa_2Cu_3O_{7-\delta}$ from 600-780°C. Measurements on single crystals reveal that oxygen out-diffusion is intrinsically faster than in-diffusion, which is contrary to the rates observed in other studies for polycrystalline ceramics. Oxygen out-diffusion measurements suggest two different mechanisms, one above and one below ~680°C, which have activation energies of 1.57±0.06eV and 1.00±0.04eV, respectively. Calculation of relaxation times for oxygen in-diffusion into initially tetragonal $YBa_2Cu_3O_{7-\delta}$ suggest a single mechanism from 600-780°C with an activation energy of 1.16±0.06eV.

INTRODUCTION

The oxygen stoichiometry of $YBa_2Cu_3O_{7-\delta}$ can be monitored at high temperatures and at different oxygen partial pressures by electrical resistance measurements which directly monitor the hole concentration [1-10]. The resistance of orthorhombic $YBa_2Cu_3O_{7-\delta}$ (δ=0) is metallic and increases linearly with temperature up to approximately 350°C in ceramics [4] and up to 500°C in single crystals [9]. Above these temperatures appreciable oxygen out-diffusion occurs and the resistance increases more rapidly. This is largely a consequence of a decrease in the hole concentration as oxygen leaves the system according to a defect relation [3,9],

$$O_O^x + 2h^{\bullet} \rightleftarrows V_O^{\bullet\bullet} + \frac{1}{2}O_2 \qquad (1),$$

where $V_O^{\bullet\bullet}$ denotes a doubly ionized (positive) vacant O(5) oxygen site, O_O^x is the neutral occupied O(1) chain site, and $h^{\bullet}$ an electron hole.

In-situ resistance measurements as a function of temperature and P_{O_2} have been used to monitor the kinetics of oxygen in-diffusion and out-diffusion [2-4,10]. Oxygen diffusion has been found to depend strongly on the sample type (ceramic or single crystal) [2-6,8-10] and structure (orthorhombic or tetragonal) [4-6]. It has been reported for ceramic specimens that oxygen in-diffusion is much faster than out-diffusion [2-4]. It is the purpose of this paper to report oxygen diffusion behavior in single crystal $YBa_2Cu_3O_{7-\delta}$ in both the orthorhombic and tetragonal structures, and to measure the intrinsic rates of oxygen in-diffusion and out-diffusion.

Mat. Res. Soc. Symp. Proc. Vol. 209. ©1991 Materials Research Society

EXPERIMENTAL

Large single crystals of various sizes were grown by a standard self-flux technique described elsewhere [9]. The critical temperature, T_c (onset), from SQUID susceptibility measurements was 90K for the annealed crystal with a transition width of <1K. Resistance measurements were made on a crystal whose dimensions were approximately 1x1x0.05 mm^3 with the c-axis oriented in the thin direction. Four-circle x-ray diffraction analysis yielded lattice parameters of a=3.82Å, b=3.89Å, c=11.68Å. Oxygen in-diffusion and out-diffusion were monitored in-situ by a standard four-point probe ac technique with the crystal mounted in the hot-stage of an optical microscope [9,10]. Four gold wires were attached to the corners of the a-b face of the crystal with silver paste and these contacts retained their integrity throughout the measurements. The ambient gas could easily be switched from reducing (100% argon) to oxidizing (100% oxygen) conditions. Water vapor and CO_2, which can degrade $YBa_2Cu_3O_{7-\delta}$ [11], were removed from the ambient by a scrubbing column containing CaO and $CaSO_4$.

Isothermal oxygen out-diffusion and in-diffusion were monitored by resistance measurements at temperatures of 600, 640, 680, 700, 720, 740, 760, and 780°C. Initially, the crystal was annealed in oxygen until equilibrium was established as indicated by a constant resistance for at least three hours. Oxygen out-diffusion studies were then carried out by introducing argon into the hot-stage and measuring the resistance of the crystal as a function of time. After a one hour argon anneal, oxygen was reintroduced into the system and the in-diffusion resistance behavior was recorded. At temperatures below ~700°C, the orthorhombic-tetragonal phase transformation was monitored with an optical microscope by observing the appearance or disappearance of twin boundaries.

RESULTS

Oxygen in-diffusion was observed to be slower than oxygen out-diffusion at all temperatures (600-780°C). Figure 1 shows a typical resistance curve for oxygen in- and out-diffusion at 720°C. The introduction of argon into the hot-stage for one hour results in a linear increase in resistance as oxygen leaves the crystal, which suggests a linear dependence of resistance with the oxygen content. This linear dependence is also typical of a surface-reaction controlled process [4,10]. The

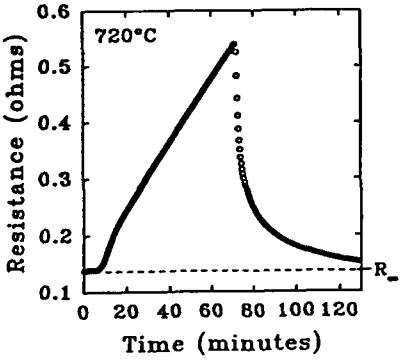

Figure 1. Resistance as a function of time for both oxygen out-diffusion and in-diffusion at 720°C. The resistance increases during oxygen out-diffusion and decreases for oxygen in-diffusion. Note that the initial resistance (R_∞) is still not regained after a one hour oxygen anneal which suggests that oxygen in-diffusion is intrinsically slower than out-diffusion.

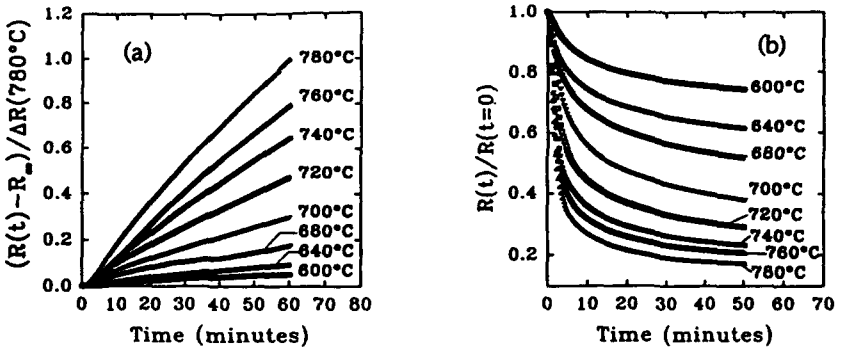

Figure 2. Normalized isothermal resistance curves for (a) oxygen out-diffusion and (b) oxygen in-diffusion from 600-780°C.

introduction of oxygen causes a rapid decrease in resistance attributed to a sudden adsorption of oxygen back into the crystal (Figure 1). The starting resistance, however, is not regained after a one hour oxygen anneal suggesting that oxygen in-diffusion in $YBa_2Cu_3O_{7-\delta}$ is in fact intrinsically slower than out-diffusion. This is contrary to the rates observed in bulk ceramic specimens [2-4]. This type of behavior was observed at all temperatures (600-780°C) and in all crystals that the authors have measured.

Figure 2(a) shows the normalized isothermal resistance behavior of oxygen out-diffusion during one hour argon anneals from 600-780°C. The corresponding oxygen in-diffusion isotherms are given in Figure 2(b). The strain accompanying the tetragonal-orthorhombic phase transformation is usually accommodated by the formation of {110} twin boundaries. These transformation twins are clearly visible under polarized reflected light and enable one to monitor the phase transformation in an optical microscope. Observation of the twin networks

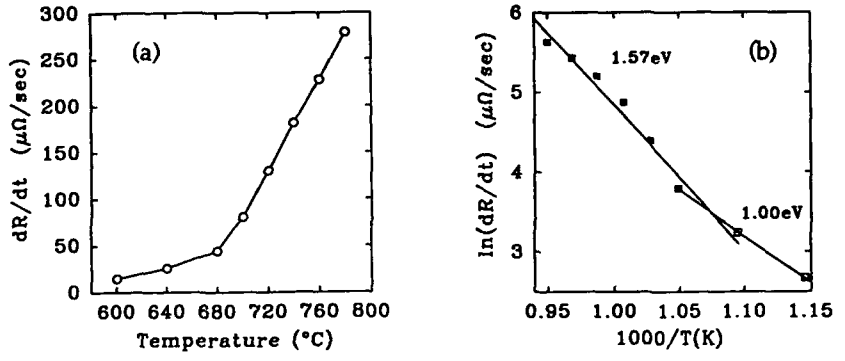

Figure 3. (a) The rate of change of resistance (dR/dt) from the linear regions of the oxygen out-diffusion isotherms (Figure 2(a)) suggests two different regimes for oxygen out-diffusion, one above and one below ~680°C. (b) An Arhennius plot of dR/dt (Equation 2) yields activation energies for oxygen out-diffusion of 1.57eV and 1.00eV above and below 680°C.

indicated that when the crystal was in equilibrium with oxygen it retained its orthorhombic form at 700°C and below, and its tetragonal form above 700°C. After the one hour argon anneal the crystal was tetragonal at all temperatures indicating that the orthorhombic-tetragonal phase transformation had taken place at those temperatures below 700°C. No anomalous resistance behavior was observed near the orthorhombic-tetragonal transformation.

Analysis of the linear slopes ($d\Delta R/dt$) of Figure 2(a) as a function of temperature (Figure 3(a)) suggests two different regions for oxygen out-diffusion behavior, one above and one below ~680°C. Assuming that the resistance change during oxygen out-diffusion is directly proportional to the carrier concentration allows one to calculate the activation energy for out-diffusion in both of these regions [4,10],

$$\left(\frac{d\Delta R}{dt}\right) = B_o \exp\left(\frac{-E}{kT}\right) \quad (2),$$

where B_o is a constant, E is the activation energy, k Boltzmann constant, and T absolute temperature. The activation energies from region I (600-680°C) and II (680-780°C) were determined to be 1.00±0.04eV and 1.57±0.06eV, respectively (Figure 3(b)).

The in-diffusion isotherms from Figure 2(b) were each fit to an equation of the form,

$$\left(\frac{R(t)-R_\infty}{R(0)-R_\infty}\right) = \exp\left(-(t/\tau)^n\right) \quad (3),$$

where oxygen was reintroduced into the crystal at time, t=0, R(t) is the resistance after a time, t, has elapsed, R_∞ the equilibrium resistance ($t=\infty$) in oxygen, τ relaxation time, and n an exponent. The calculated relaxation times and exponents are listed in Table I. Assuming that the relaxation time, τ, is inversely proportional to the diffusivity allows one to calculate the activation energy during the initial stages of oxygen in-diffusion from,

$$\tau = \tau_o \exp\left(\frac{E_i}{kT}\right) \quad (4).$$

The activation energy for early oxygen in-diffusion into initially tetragonal $YBa_2Cu_3O_{7-\delta}$ from 600-780°C was calculated to be 1.16±0.06eV.

DISCUSSION AND SUMMARY

The functional forms of oxygen in- and out-diffusion in single crystal $YBa_2Cu_3O_{7-\delta}$ are similar to those measured by the authors in a previous study from 590-720°C [10] and by others in ceramic specimens [2-6]. The most notable difference, however, is that the measured oxygen in-diffusion rate is slower than out-diffusion in single crystals (Figure 1) and faster than out-diffusion in polycrystalline ceramics [2-4]. Ottaviani et al. [5] suggest that the initial fast decrease in resistance for oxygen in-diffusion is due to either the formation of a thin conductive layer at the grain boundaries or to transformed orthorhombic regions which occupy a significant portion of each grain. Additional oxygen adsorption into the core of the crystal or grain would have a much less pronounced effect on

T (°C)	Initial Resistance, R_∞ (ohms)	Relaxation Time, τ (minutes)	n
600	0.77	43.5(2)	0.439(2)
640	0.93	19.4(1)	0.517(2)
680	1.09	14.01(6)	0.556(2)
700	1.26	10.9(2)	0.583(9)
720	1.39	6.5(1)	0.58(1)
740	1.49	4.4(1)	0.56(1)
760	1.57	3.8(1)	0.58(1)
780	1.64	3.30(8)	0.65(1)

Table I. Selected data from isothermal oxygen in-diffusion anneals (Figure 2). The initial resistances, R_∞, are for equilibrium conditions in oxygen at each temperature. The relaxation time, τ, for oxygen in-diffusion from Equation 3 decreases with increasing temperature, while the exponents, n, remain essentially constant.

the resistance behavior. Observations of twinning dynamics upon oxygen in-diffusion in ceramic [12] and single crystal [10] $YBa_2Cu_3O_{7-\delta}$, support the formation of a shell of twinned material around a core that is initially oxygen deficient (i.e., tetragonal). This would lead to the formation of a low conductivity percolation path along the grain boundaries for a ceramic specimen which could explain the measurement of apparently faster rates of oxygen in-diffusion than out-diffusion. The surface area to volume ratio in single crystal specimens is much smaller than polycrystalline ceramics, consequently, a thin conductive layer around the crystal would have a less pronounced effect on the overall resistance.

Nobili et al. [6] report that the resistance of a ceramic specimen continues to decrease even though thermogravimetric analysis (TGA) indicates no more oxygen uptake. They suggest that, upon oxygenation, a tetragonal material will begin to form small regions of ordered oxygen which will lead to an increase in the hole concentration even though the oxygen content remains constant. If such a model is correct, the slow decrease in resistance at 720°C (Figure 1) would suggest the formation of ordered oxygen precursor regions prior to the normal tetragonal-orthorhombic transformation point (~700°C in 100% oxygen). It is quite possible, however, that the slow decrease of resistance with time in single crystals is indeed a consequence of very slow oxygen incorporation into the bulk of the crystal. TGA measurements on large single crystals would help to resolve this issue.

In the present study, the extension of isothermal resistance measurements up to 780°C allowed for the distinction between two different regimes for oxygen out-diffusion to be clearly made, one above and one below ~680°C. The respective activation energies of 1.00 and 1.57eV suggest two different mechanisms for oxygen out-diffusion. It is tempting to associate each activation energy with one of the crystal structures (orthorhombic or tetragonal). It should be noted, however, that if the two measured activation energies were each associated directly with either the orthorhombic or tetragonal structure, one would expect a transition from one mechanism to another as the crystal transformed structures during an isothermal anneal. The crystal structure transformed during oxygen out- and in-diffusion between 600-700°C as observed by optical microscopy, however, no concurrent change in the resistance curves was detected (Figure 2). The change in out-diffusion mechanisms near 680°C may instead be due to the activation of different defect mechanisms which are not necessarily associated with any one particular crystal structure.

The relaxation time, τ, for oxygen in-diffusion is inversely proportional to the chemical diffusivity, D, and is a function of both temperature and starting oxygen content, 7-δ. As temperature increases, the jump frequency of oxygen increases, more oxygen vacancies are created, and the relaxation time decreases (Table I). Optical microscopy indicated that the crystal was in its tetragonal form at the start of oxygen in-diffusion at all temperatures, consequently, the in-diffusing oxygen initially encountered the tetragonal phase. This may explain the apparent single mechanism for the early stages of oxygen in-diffusion from 600-780°C. The crystal transformed from tetragonal to orthorhombic crystal symmetry below 700°C, however, there were no measurable differences in the functional forms of the in-diffusion resistance isotherms above or below 700°C.

In summary, oxygen in-diffusion was observed to be slower than out-diffusion in single-crystal $YBa_2Cu_3O_{7-\delta}$ at all temperatures. This was contrary to the diffusion rates observed in polycrystalline ceramic specimens, in which in-diffusion occurs at an apparently faster rate than out-diffusion. This difference can be attributed to the formation in ceramics of thin conductive layers at the grain boundaries which behave as a percolation path for electrical conductivity. Oxygen out-diffusion was observed to proceed by two different mechanisms above and below 680°C with calculated activation energies of 1.57±0.06eV and 1.00±0.04eV, respectively. These two mechanisms were not necessarily associated with the orthorhombic or tetragonal structures. Early oxygen in-diffusion into initially tetragonal $YBa_2Cu_3O_{7-\delta}$ proceeded by a single mechanism with an activation energy of 1.16±0.06eV.

ACKNOWLEDGEMENTS

The authors greatly appreciate helpful discussion with Gerald P. Wirtz and the use of the facilities in the Materials Research Laboratory. This project was supported by the Air Force Office of Scientific Research (Grant No. URI-41098) through the University Research Initiative on phase transformations in ceramics and by the National Science Foundation (Grant No. DMR 88-09854) through the Science and Technology Center for Superconductivity.

REFERENCES

[1] M. Gurvitch and A.T. Fiory, Phys. Rev. Lett. **59**, 1337 (1987).
[2] G. Sageev Grader, P.K. Gallagher, J. Thomson, and M. Gurvitch, Appl. Phys. A **45**, 179 (1988).
[3] J. Park, P. Kostic, and J.P. Singh, Mater. Lett. **6**, 393 (1988).
[4] K.N. Tu, N.C. Yeh, S.I. Park, and C.C. Tsuei, Phys. Rev. B **39**, 304 (1989).
[5] G. Ottaviani, C. Nobili, F. Nava, M. Affronte, T. Manfredini, F.C. Matacotta, and E. Galli, Phys. Rev. B **39**, 9069 (1989).
[6] C. Nobili, G. Ottaviani, M.C. Rossi, and M. Sparpaglione, Physica C **168**, 549 (1990)
[7] J. Nowotny, M. Rekas, and W. Weppner, J. Am. Ceram. Soc. **73**, 1040 (1990).
[8] A.T. Fiory, S. Martin, L.F. Schneemeyer, R.M. Fleming, A.E. White, and J.V. Waszczak, Phys. Rev. B **38**, 7129 (1988).
[9] J.R. LaGraff, P.D. Han, and D.A. Payne, Physica C **169** , 355 (1990).
[10] J.R. LaGraff, P.D. Han, and D.A. Payne, Phys. Rev. B **43**, 441 (1991).
[11] W.K. Lee and A.S. Nowick, J. Mater. Res. **5**, 1855 (1990).
[12] D. Shi, Phys. Rev. B **39**, 4299 (1989) .

Resistance measurements and oxygen out-diffusion near the orthorhombic-tetragonal phase transformation in single-crystal $YBa_2Cu_3O_{7-\delta}$

J. R. LaGraff, P. D. Han, and D. A. Payne
Department of Materials Science and Engineering and Materials Research Laboratory, The University of Illinois at Urbana-Champaign, Urbana, Illinois 61801
(Received 13 August 1990)

Isothermal resistance measurements and hot-stage optical microscopy were used to simultaneously follow the loss of oxygen and the disappearance of the twin structure in single-crystal $YBa_2Cu_3O_{7-\delta}$ from 590–720 °C. Oxygen out-diffusion was found to follow surface-reaction-limited conditions with an activation energy of 1.2 ± 0.1 eV. Although the crystal was driven through the orthorhombic-tetragonal phase transformation during the isothermal anneals, no anomalous resistance behavior was observed. This suggests that previous observations of anomalous resistance behavior in bulk ceramics may not be intrinsic to $YBa_2Cu_3O_{7-\delta}$. The difference between oxygen in-diffusion and out-diffusion kinetics is discussed in relation to the twin structure observed near the orthorhombic-tetragonal phase transformation.

INTRODUCTION

The degree of oxygen nonstoichiometry, δ, plays an important role in determining the normal-state and superconducting properties of $YBa_2Cu_3O_{7-\delta}$. Normal-state electrical resistance measurements of bulk ceramics at elevated temperatures depend directly on δ,[1–20] which in turn, is a function of temperature and oxygen partial pressure.[21,22] Most electrical measurements on single crystals have been carried out at temperatures (<300 K) where the oxygen defect state has already been predetermined by the processing parameters.[23–26] Electrical measurements above 300 °C, where oxygen becomes mobile, have been confined primarily to bulk ceramic specimens[1–20] with only a few reports on single crystals.[27–29] This is most likely due to the long times required to achieve homogeneous oxidation of large single crystals, which makes accurate determinations of δ more difficult. It is the purpose of this paper to report high temperature (590–720 °C) isothermal resistance measurements of oxygen out-diffusion kinetics in the vicinity of the orthorhombic-tetragonal phase transformation for single crystal $YBa_2Cu_3O_{7-\delta}$.

The orthorhombic-tetragonal transformation is known to be an order-disorder structural phase transformation driven by the oxygen nonstoichiometry parameter δ and its subsequent dependence on temperature and partial pressure of oxygen.[21,22] The fully oxygenated (orthorhombic) state ($\delta\approx0$) consists of oxygen atoms ordered on the O(1) sites thereby forming one-dimensional copper-oxygen chains. As δ increases, oxygen is both removed from the material and disordered from O(1) sites onto normally vacant O(5) sites. Early structural studies (for example, see Ref. 22) treated the orthorhombic-tetragonal phase transformation as a discrete process which occurred near $\delta\approx0.5$ where the occupancies of the O(1) and O(5) sites are equal and the material becomes tetragonal. However, observations of intermediate oxygen-ordering states between the ideal orthorhombic ($\delta\approx0$) and tetragonal ($\delta\approx1$) structures,[30] and theoretical models of oxygen ordering,[31] suggest that the orthorhombic-tetragonal phase transformation is more of an evolutionary process controlled by the oxygen diffusion kinetics.[29,32,33] Thus, in addition to the temperature and oxygen partial pressure dependencies for the transformation, one must also consider other parameters such as heating and cooling rates and grain (or crystal) size effects. Anomalies in the temperature dependence of resistivities have been reported for bulk ceramics[2–11] at the orthorhombic-tetragonal transformation, while others have not reported any anomalies.[12–20] Probable causes of these anomalies include the sudden gain or loss of oxygen near the orthorhombic-tetragonal transformation[34] or the appearance and disappearance of twin boundaries.[8,29] In a previous paper, anomalies were reported by the authors near the orthorhombic-tetragonal transformation in single crystal $YBa_2Cu_3O_{7-\delta}$, which were detected by a sensitive "bridge" electrode configuration.[29] The resistance anomaly manifest itself not as a change in slope as has been reported,[2–11] but as fine structure (or noise) near the transition.

In this paper a p-type electrical conduction model[11] is used for the range of δ studied. A simple defect equation can be written in Kroger-Vink notation as

$$O_O^x + 2h^{\cdot} \leftrightarrows V_O^{\cdot\cdot} + \tfrac{1}{2}O_2 , \qquad (1)$$

where $V_O^{\cdot\cdot}$ denotes a doubly ionized (positive) vacant O(5) chain oxygen site, O_O^x is the neutral occupied O(1) chain site, and $h^{\cdot}$ an electron hole. The hole conductivity σ_p can be written in its standard form as $\sigma_p = pe\mu_p$ where p is the hole concentration, e is the charge of the hole, and μ_p is the hole mobility. The transference number for oxygen ions has been calculated from experiment to be $\sim10^{-9}$,[11] thus, one can assume that all of the current is carried by electron holes and not oxygen ions. More ela-

borate models which also account for simultaneous *n*-type conduction or hopping polarons have been reviewed (and proposed) by Nowotny *et al.*[35] At low oxygen concentrations ($\delta \sim 0.7$) there is a *p-n* transition[5] in which the dominant charge carriers change from holes to electrons. The above defect equation, however, serves as a good first approximation in relating the effect of oxygen stoichiometry δ to the electronic resistance behavior of the $YBa_2Cu_3O_{7-\delta}$ material under normal operating conditions.

Resistivity values for $YBa_2Cu_3O_{7-\delta}$ single crystals are highly anisotropic with the room temperature out-of-plane resistivity ρ_c being 30 (Ref. 24) to 110 (Ref. 25) times greater at room temperature than the in-plane resistivity ρ_{ab}. The in-plane resistivity behavior (ρ_{ab}) is characteristically metallic with a linear temperature dependence from T_c to 500 °C (Refs. 27 and 29) and a ρ_a/ρ_b anisotropy of 2.2.[26] The out-of-plane resistivity (ρ_c) behavior exhibits characteristic semiconducting behavior with a negative temperature coefficient.[23–25] Not surprisingly, the diffusion of oxygen above 500 °C in single crystals is also found to be highly anisotropic[27,36] due to oxygen vacancies, required for oxygen diffusion, being localized near the copper-oxygen chains in both the a and b directions.

Oxygen diffusion kinetics determined from normal-state electrical measurements have been reported by a number of groups.[2,11,14,17–20] Surprisingly, oxygen in-diffusion has been observed to occur at a faster rate than oxygen out-diffusion.[2,11,14,17,19] Oxygen in-diffusion was found to strongly depend on δ, while oxygen out-diffusion was independent of δ.[2,17–20] Resistivity is generally linear (metallic) up to ~300–400 °C in bulk ceramics (for example, see Ref. 2) and ~500 °C (Refs. 27 and 29) in single crystals. Above these temperatures, a stronger than linear temperature dependence is seen in the resistance which is attributed to oxygen out-diffusion. The difference between these onset temperatures for single crystals and polycrystalline ceramics is attributed to the lower surface-area to volume ratios in single crystals.[29] The increase in resistivity upon heating may not only be due to a change in carrier concentration as oxygen leaves the material, but may be due to either a temperature or oxygen concentration dependence of the mobility. Therefore, in this paper, isothermal resistance measurements were specifically carried out so that any temperature dependence of the mobility term during a given anneal could be neglected. Also, complete oxidation of the crystal does not have to be assumed since the rate of oxygen out-diffusion is reported to be independent of δ.[12,17–20]

The purpose of this study was to investigate the high-temperature (590–720 °C) isothermal resistance behavior of a $YBa_2Cu_3O_{7-\delta}$ single crystal under different ambient conditions. This enabled the diffusion kinetics of oxygen to be monitored and the activation energy for oxygen out-diffusion to be calculated. Hot-stage optical microscopy simultaneously recorded the twin patterns allowing any correlations to be made between the resistance characteristics and the twin behavior near the orthorhombic-tetragonal phase transformation.

EXPERIMENTAL PROCEDURE

Sample preparation

Large single crystals of $YBa_2Cu_3O_{7-\delta}$ were grown by a self-flux method as described elsewhere.[29] The crystal chosen for resistance measurements was rectangular with dimensions of approximately $1 \times 1.4 \times 0.05$ mm.[3] Four-circle x-ray diffraction on a representative annealed crystal indicated that it was single phase, twinned, and had lattice parameters of $a = 3.818$ Å, $b = 3.886$ Å, $c = 11.68$ Å. The critical temperature T_c (onset), from SQUID susceptibility measurements, was determined to be 90 K for a crystal annealed for 14 days in oxygen at 500 °C (Fig. 1). The twinned state and surface quality of the crystals was also confirmed by optical microscopy using reflected light under crossed polars (Fig. 2).

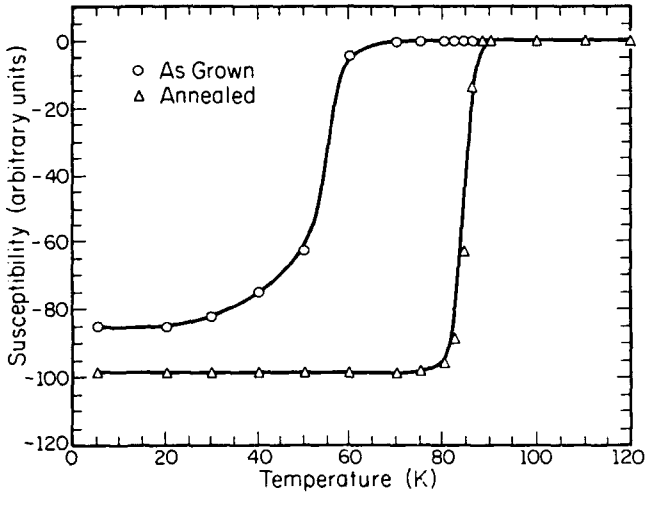

FIG. 1. Magnetic susceptibility of an as-grown and an annealed (14 days, 500 °C in oxygen) $YBa_2Cu_3O_{7-\delta}$ single-crystal; T_c (onset) is 90 K.

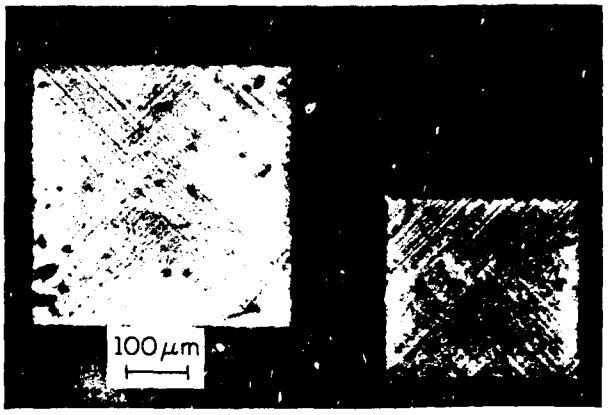

FIG. 2. Optical micrograph viewed under cross-polarized reflected light of two heavily twinned $YBa_2Cu_3O_{7-\delta}$ crystals.

Resistance measurements

Electrical resistance measurements were made by a standard ac four-point probe method in the hot-stage of an optical microscope. This allowed for *in situ* observations of twin configurations as the crystal progressed through the orthorhombic-tetragonal phase transformation. A constant current of 2 mA (564 Hz) was supplied by a computer-controlled Stanford Research Systems SR530 Lock-in amplifier with a resolution of 10 nanovolts. Four gold wire leads (2 mil) were attached to the corner positions of an (001) surface of the crystal using silver paste. The crystal was then heated to 650 °C, cooled to 500 °C, and annealed in oxygen for 12 hrs. The electrodes remained ohmic with a contact resistance of less than one ohm throughout the studies. The crystal was placed on an Al_2O_3 disk and the assembly was then mounted in the hot-stage optical microscope. A commercial scrubber containing phosphorus pentoxide was used to remove water vapor from the ambient gas, which could readily by cycled between reducing (argon) and oxidizing (100% oxygen) conditions. All measured resistance values were across the a-b plane.

Isothermal resistance experiments were carried out in both oxygen and argon. Isothermal oxygen out-diffusion was monitored by annealing the crystal in argon for one hour at temperatures of 590, 610, 630, 650, 670, 680, 690, 700, 710, and 720 °C. These temperatures were chosen so that the crystal would be driven through the orthorhombic-tetragonal transformation in all but the 710-°C and 720-°C argon anneals. Prior to each run, the crystal was annealed in oxygen for 4–10 hrs at the desired temperature. The length of this anneal was determined by monitoring the resistance until it remained constant for at least one hour. (Fig. 3 illustrates a typical resistance curve for oxygen in-diffusion). Due to the long times required for fully oxygenating large single crystals, a constant resistance does not necessarily indicate equilibrium has been attained, but instead that oxygen diffusion has become extremely slow. Complete oxygenation of the crystal does not need to be obtained, however, in order to measure the oxygen out-diffusion kinetics since the later has been found to be independent of δ.[2,17–20] The twin patterns were recorded *in situ* on an optical microscope with a photographic record system in order to monitor the orthorhombic-tetragonal transformation.

RESULTS

Estimates of the time required for oxygenation were made from $L^2 \cong 4Dt$ where L was the half-width of the crystal in the a-b direction, D the diffusivity calculated from $D = D_0 \exp(-E/kT)$, and t the time. Using reported values[2] for the preexponential coefficient $D_0 = 0.035$ cm^2/sec and activation energy for oxygen in-diffusion $E = 1.3$ eV, one can estimate the times required for fully oxygenating a 1-mm^2 crystal. These range from approximately 5 to 50 hr between 720 °C and 590 °C, respectively. Since oxygen out-diffusion has been found to be independent of δ,[2,17–20] complete equilibrium conditions ($\delta = 0$) are not necessary at the onset of the argon anneal. Between 590 °C and 700 °C, the structure at the onset of the argon anneals was orthorhombic as revealed by the characteristic twin structures in the optical microscope. Above 700 °C no twins were visible and the starting structure was assumed to be tetragonal.

Experimental data for a typical oxygen out-diffusion isotherm is given in Fig. 4 for a crystal annealed for 1 h in argon at 650 °C. Out-diffusion isotherms from 590 to 720 °C as a function of time in argon are illustrated in Fig. 5. After an initial sharp increase in resistance, the isotherms increased linearly for the remainder of the 1-hr anneal time. The onset of linearity did not correspond to the orthorhombic-tetragonal phase transformation as indicated by the loss of twin patterns. The total resistance change after one hour, and the rate of resistance change

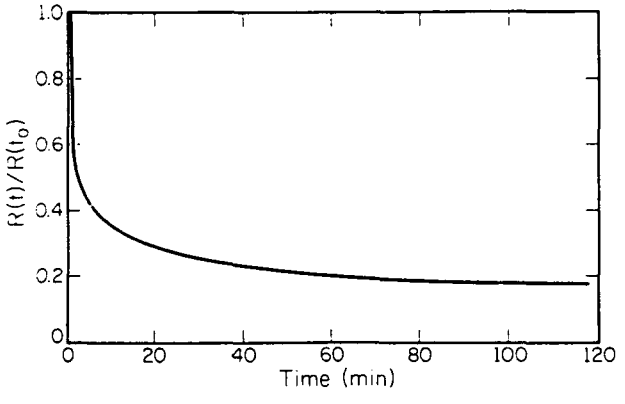

FIG. 3. Oxygen in-diffusion behavior at 650 °C after the crystal was annealed for one hour in argon. The shape of the curve suggests that oxygen is rapidly adsorbed into the crystal edges which then act as a barrier to further oxygen diffusion into the bulk of the crystal. Resistance curves of this type were used to monitor oxygen uptake prior to argon anneals.

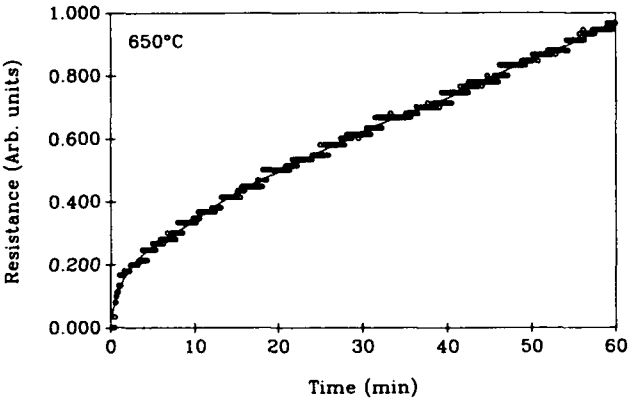

FIG. 4. Experimental data of resistance during a 1-hr argon anneal at 650 °C for a $YBa_2Cu_3O_{7-\delta}$ single crystal. After an initial rapid increase, the resistance increased linearly for the duration of the anneal. This linear behavior is characteristic of surface controlled oxygen out-diffusion.

TABLE I. Selected data from isothermal argon anneals. The start and end for argon anneals is indicated by t_0 and t_f, respectively. The total resistance change after a 1-hr anneal in argon was found to increase with temperature as expected. The change in resistance as a function of time ($d\Delta R/dt$) is taken from slopes in Fig. 5(b). The crystal was driven through the orthorhombic-tetragonal phase transformation by oxygen out-diffusion at most of the temperatures, but no anomalies were observed in the resistance curves (Fig. 5).

T (°C)	Total resistance change $[R(t_f)-R(t_0)]$ (mΩ)	Rate of resistance change $(d\Delta R/dt)$ ($\mu\Omega$/sec)	Twinned t_0	Twinned t_f
590	32.0	5.7	Yes	Yes
610	42.5	8.3	Yes	No
630	57.0	11.7	Yes	No
650	75.0	15.0	Yes	No
670	109.5	23.2	Yes	No
680	126.5	29.8	Yes	No
690	142.5	32.3	Yes	No
700	152.5	32.5	Yes	No
710	183.5	43.0	No	No
720	197.0	44.3	No	No

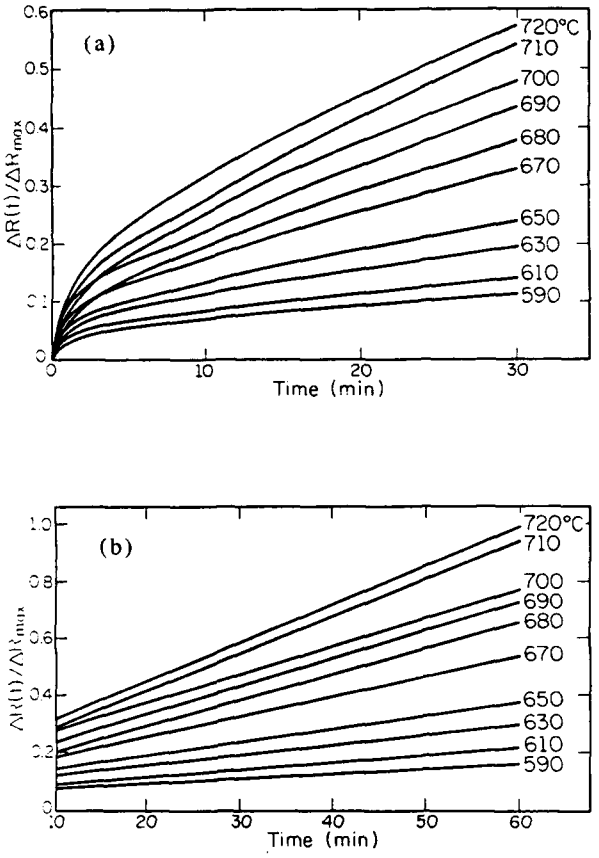

FIG. 5. Resistance change (ΔR), as a function of time, normalized to the total resistance change after a 1-hr argon anneal at 720°C (ΔR_{max}) showing (a) the initial increase in resistance and (b) the linear resistance behavior of the oxygen out-diffusion curves observed during the remainder of the anneal. Although the orthorhombic-tetragonal phase transformation occurred during anneals at most of these temperatures (see Table I), no significant anomalies were observed in the resistance curves.

in the linear portion of the isotherms, are listed in Table I. The initial (t_0) and final (t_f) twin states at each temperature were recorded by optical microscopy.

The dynamic resistance change as a function of time is introduced by a method proposed by Tu *et al.*[2] and is written as

$$\left[\frac{d\Delta R}{dt}\right]=B_0\exp\left[\frac{-E}{kT}\right], \tag{2}$$

where R is resistance, t time, B_0 a constant, E the activation energy for oxygen out-diffusion, k Boltzmann's constant, and T, absolute temperature. An Arrhenius-type plot of $\log_{10}(d\Delta R/dt)$, taken from the linear regions of Fig. 5, as a function of reciprocal temperature gives an activation energy for oxygen out-diffusion of 1.2±0.1 eV (Fig. 6).

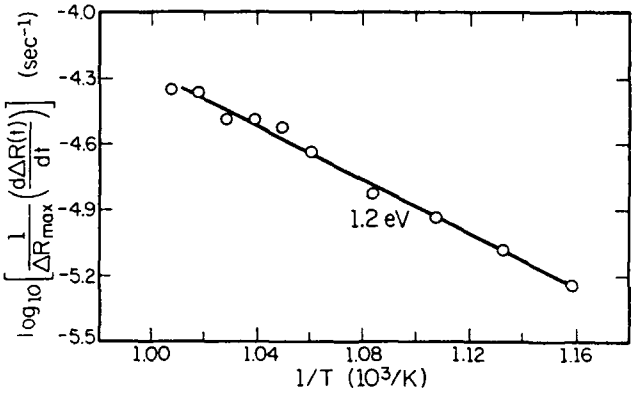

FIG. 6. Arrhenius-type plot of resistance data for isothermal argon anneals. The rate of resistance change ($d(\Delta R)/dt$) at each temperature was obtained from the slopes of Fig. 5(b) (see Table I). The activation energy for oxygen out-diffusion was calculated from the slope to be 1.2±0.1 eV.

A typical oxygen in-diffusion isotherm after a 1-hr argon anneal at 650 °C is shown in Fig. 3. Oxygen is rapidly adsorbed in the first few minutes as indicated by the rapid decrease in resistance. (Resistance curves similar to Fig. 3 were monitored to determine the length of the oxygen anneal required prior to each isothermal anneal in argon.) The orthorhombic-tetragonal transformation was observed to occur in cross-polarized light in all but the 590-°C, 710-°C, and 720-°C heat treatments (Table I). At 590 °C, the crystal remained orthorhombic throughout the anneal, although with sufficient time, one would expect the transformation to eventually occur.[21,22] At 710 °C and 720 °C the crystal appeared to remain in the tetragonal state for the duration of the anneal (Table I). Although the orthorhombic-tetragonal transformation occurred during the 1-hr argon anneal at all other temperatures (610–700 °C), no anomalies in the resistance curves were observed (Figs. 4 and 5).

Twins were observed to fade and disappear simultaneously across the entire crystal on annealing in argon (i.e., oxygen out-diffusion). Upon oxidation, however, twinning was observed to first nucleate at the crystal edges and then grow stepwise into the bulk. This indicated that different types of oxygen diffusion occurred between oxygen in-diffusion and out-diffusion, as will be discussed in the following section. Twinning behavior of this type was reported earlier by the authors for other crystals.[29]

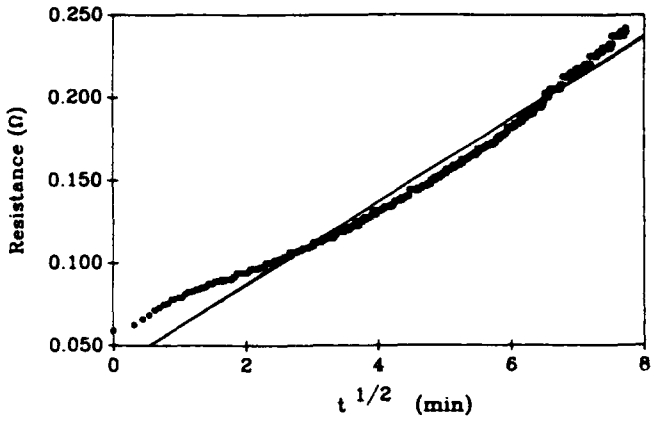

FIG. 7. Resistance vs square root of time for a 1-hr argon anneal at 710 °C. The nonlinear behavior indicates lack of compliance with diffusion-controlled oxygen out-diffusion from single crystal $YBa_2Cu_3O_{7-\delta}$.

DISCUSSION

Oxygen diffusion kinetics

The initial sharp increase in resistance on annealing in argon (Fig. 4) suggests rapid deoxygenation at crystal edges. A large concentration of oxygen vacancies ($\delta \rightarrow 1$) within this layer (as compared with the bulk) would be expected. Oxygen must then diffuse to the surface, combine into molecular oxygen, and desorb from the crystal surface. Since diffusion to the surface is rapid,[2] the layer controls further out-diffusion of oxygen and leads to a linear resistance behavior (Figs. 4 and 5) characteristic of surface-controlled reactions.

Several studies have observed that oxygen in-diffusion is much faster than oxygen out-diffusion,[2,11,14,17,19] which possibly suggests that different diffusion mechanisms occur for both processes. A plot of normalized resistance versus the square root of time did not yield a linear fit (Fig. 7) as reported by Fiory *et al.*[27] This further suggests that oxygen out-diffusion is not diffusion limited[11,27] but is indeed surface-reaction limited[2,17,19] The calculated activation energy of 1.2±0.1 eV for oxygen out-diffusion (Fig. 6) is substantially lower than 1.7±0.1 eV calculated for bulk ceramics.[2,17,19] This difference is attributed primarily to the highly anisotropic nature of oxygen diffusion in the material, with diffusivities several orders of magnitude smaller in the out-of-plane (c axis) than in the in-plane (a-b axes) directions.[36] A bulk ceramic material with randomly oriented grains would be expected to have a higher activation energy for oxygen out-diffusion. Studies on grain-oriented bulk ceramics would help to resolve this issue.

The sudden decrease in resistance in Fig. 3 corresponds to a rapid indiffusion of oxygen and can be explained by the rapid formation of a surface layer with high oxygen content. This layer coarsens with time and impedes further indiffusion of oxygen into the bulk. Measured activation energies for oxygen indiffusion as a function of oxygen concentration range from 0.38 eV at $\delta = 0.4-1.3$ eV at $\delta = 0$.[2,17] This difference is most likely due to a decrease in oxygen vacancies required for oxygen diffusion and, possibly, to the increase in oxygen ordering, as δ approaches zero. The long times required to obtain fully oxygenated single crystals prohibits the ready calculation of oxygen in-diffusion kinetics which strongly depend on δ.

Orthorhombic-tetragonal phase transformation

The lack of any anomalous behavior near the orthorhombic-tetragonal transformation in the resistance curves in Figs. 4 or 5 for single crystal $YBa_2Cu_3O_{7-\delta}$ suggests that the resistance anomalies observed by others[2-11] in bulk ceramics may not be intrinsic, but instead may be due to extrinsic factors like grain-boundary strain which accompanies the change in symmetry at the transformation. This may spatially alter local grain boundary structures which could alter the conductivity characteristics in the sample. Also, impurities or additional phases, which often segregate to grain boundaries, may contribute to anomalous measurements. Anomalies in resistance, which were attributed to twin boundary kinetics, have been observed previously by the authors[29] in single crystal $YBa_2Cu_3O_{7-\delta}$ through the use of more sensitive probe configurations than the ones used in the present study.

Since oxygen in-diffusion is relatively rapid and diffusion controlled, one expects a nonuniform concentration profile across the crystal.[2,19] The tetragonal-orthorhombic phase transformation would then first occur in regions where $\delta \sim 0.5$ (i.e., near the crystal edges). This would nucleate twin boundaries which have

been observed to extend into regions of $\delta > 0.5$ as reported by Shi.[32] The twin boundaries, however, were not observed to advance into the crystal at a steady rate, but spontaneously appeared in an almost stepwise fashion toward the center over a period of time. On the otherhand, the out-diffusion of oxygen is surface-reaction controlled, so one expects a constant oxygen concentration profile across the crystal except at the edges. Thus, as δ approached 0.5, twinning would simultaneously disappear across the entire sample. There would be no stepwise disappearance of twins. The authors have previously observed[29] a gradual loss of twinning across the entire crystal upon dynamic heating in argon. Retwinning, on the other hand, has been observed to nucleate at crystal edges and grow stepwise toward the center of the crystal. This lends support to Shi's model[32] of a martensitic-shear transformation, which forms the twin boundaries, followed by the further diffusion of oxygen into the sample which coarsens the orthorhombic phase and nucleates other twin regions. Since this type of twinning behavior has not been unambiguously seen in all crystals that the authors have studied, further work is needed to clarify the model.

CONCLUSION

In conclusion, oxygen out-diffusion in single crystal $YBa_2Cu_3O_{7-\delta}$ was found to be surface-reaction limited as shown by the linear behavior of resistance with time during isothermal argon anneals. The activation energy for oxygen out-diffusion was calculated to be 1.2 ± 0.1 eV which is lower than the value reported for polycrystalline $YBa_2Cu_3O_{7-\delta}$. This difference is attributed to the highly anisotropic nature of oxygen diffusion in the material. Differences in observed twin patterns upon cycling through the orthorhombic-tetragonal phase transformation were attributed to the different mechanisms of oxygen in-diffusion and out-diffusion. (In-diffusion is diffusion controlled and out-diffusion is surface-reaction limited.) No anomalous resistance behavior was observed near the orthorhombic-tetragonal transformation which suggests that observed anomalies in the literature may not be intrinsic to $YBa_2Cu_3O_{7-\delta}$, but may be due to impurities or additional phases at grain boundaries or to residual stresses at grain boundaries resulting from transformational strain.

ACKNOWLEDGMENTS

The authors wish to thank Joyce McMillan for the x-ray measurements and A. Asthana and T. A. Friedmann for helpful discussions. The use of facilities in the Materials Research Laboratory is greatly appreciated. This project was supported by the Air Force Office of Scientific Research Grant No. (URI-41098) through a University Research Initiative on phase transformations in ceramics and by the National Science Foundation (Grant No. DMR 88-09854) through the Science and Technology Center for Superconductivity.

[1]P. P. Freitas and T. S. Plaskett, Phys. Rev. B **37**, 3657 (1988).
[2]K. N. Tu, N. C. Yeh, S. I. Park, and C. C. Tsuei, Phys. Rev. B **39**, 304 (1989).
[3]G. Sageev Grader, P. K. Gallagher, and E. M. Gyorgy, Appl. Phys. Lett. **51**, 1115 (1987).
[4]A. T. Fiory, M. Gurvitch, R. J. Cava, and G. P. Espinosa, Phys. Rev. B **36**, 7262 (1987).
[5]H. I. Yoo, J. Mater. Res. **4**, 23 (1989).
[6]F. Munakata, K. Shinohara, H. Kanesaka, N. Hirosaki, A. Okada, and M. Yamanaka, Jpn. J. Appl. Phys. **26**, L1292 (1987).
[7]M. Gurvitch and A. T. Fiory, Phys. Rev. Lett. **59**, 1337 (1987).
[8]P. P. Feitas and T. S. Plaskett, Phys. Rev. B **36**, 5723 (1987).
[9]T. K. Chaki and M. Rubinstein, Phys. Rev. B **36**, 7259 (1987).
[10]T. Ohtani, T. Okudo, A. Tamaki, and T. Ueda, Jpn. J. Appl. Phys. **27**, L61 (1988).
[11]J. Park, P. Kostic, and J. P. Singh, Mater. Lett. **6**, 393 (1988).
[12]J. Park and H. G. Kim, Jpn. J. Appl. Phys. **27**, L191 (1988).
[13]S. Yamaguchi, K. Terabe, A. Imai, and Y. Iguchi, J. Appl. Phys. **27**, L220 (1988).
[14]G. Sageev Grader, P. K. Gallagher, J. Thomson, and M. Gurvitch, Appl. Phys. A **45**, 179 (1988).
[15]J. Nowotny, M. Rekas, and W. Weppner, J. Am. Ceram. Soc. **73**, 1040 (1990).
[16]S. I. Park, C. C. Tsuei, and K. N. Tu, Phys. Rev. B **37**, 2305 (1988).
[17]K. N. Tu, C. C. Tsuei, S. I. Park, and A. Levi, Phys. Rev. B **38**, 772 (1988).
[18]K. N. Tu, N. C. Yeh, S. I. Park, and C. C. Tsuei, Phys. Rev. B **38**, 5118 (1988).
[19]N. C. Yeh, K. N. Tu, S. I. Park, and C. C. Tsuei, Phys. Rev. B **38**, 7087 (1988).
[20]G. Ottaviani, C. Nobili, F. Nava, M. Affronte, T. Manfredini, F. C. Matacotta, and E. Galli, Phys. Rev. B **39**, 9069 (1989).
[21]J. D. Jorgensen, B. W. Veal, A. P. Paulikas, L. J. Nowicki, G. W. Crabtree, H. Claus, and W. K. Kwok, Phys. Rev. B **41**, 1863 (1990).
[22]J. D. Jorgensen, M. A. Beno, D. G. Hinks, L. Soderholm, K. J. Volin, R. L. Hitterman, J. D. Grace, I. K. Schuller, C. U. Serge, K. Zhang, and M. S. Kleefisch, Phys. Rev. B **36**, 3608 (1987).
[23]K. Murata, K. Hayashi, Y. Honda, M. Tokumoto, H. Ihara, M. Hirabayashi, N. Terada, and Y. Kimura, Jpn. J. Appl. Phys. **26**, L1941 (1987).
[24]S. W. Tozer, A. W. Kleinsasser, T. Penney, D. Kaiser, and F. Holtzberg, Phys. Rev. Lett. **59**, 1768 (1987).
[25]S. J. Hagen, T. W. Jing, Z. Z. Wang, J. Horvath, and N. P. Ong, Phys. Rev. B **37**, 7928 (1988).
[26]T. A. Friedmann, M. W. Rabin, J. Giapintzakis, J. P. Rice, and D. M. Ginsberg, Phys. Rev. B **42**, 6217 (1990).
[27]A. T. Fiory, S. Martin, L. F. Schneeymeyer, R. M. Fleming, A. E. White, and J. V. Waszczak, Phys. Rev. B **38**, 7129 (1988).
[28]M. Gurvitch, A. T. Fiory, L. S. Schneemeyer, R. T. Cava, G. P. Espinosa, and J. V. Waszczak, Physica C **153-155**, 1369 (1988).
[29]J. R. LaGraff, P. D. Han, and D. A. Payne, Physica C **169**, 355 (1990).

[30]M. A. Alario-Franco, J. ¹. Capponi, C. Chaaillout, J. Chenavas, and M. M. Marezio, Mater. Res. Soc. Symp. Proc. **99**, 41 (1988); D. Shi and D. W. Capone, Appl. Phys. Lett. **53**, 159 (1988); R. Beyers, B. T. Ahn, G. Gorman, V. Y. Lee, S. S. P. Parkin, M. L. Ramirez, K. P. Roche, J. E. Vazquez, T. M. Gür, and R. A. Huggins, Nature (London) **340**, 619 (1989).

[31]L. T. Willie and D. de Fontaine, Phys. Rev. B **37**, 2227 (1988); D. de Fontaine, M. E. Mann, and G. Ceder, Phys. Rev. Lett. **63**, 1300 (1989); D. de Fontaine, G. Ceder, and M. Asta, Nature (London) **343**, 544 (1990).

[32]D. Shi, Phys. Rev. B **39**, 4299 (1989).

[33]N. Hudakova and P. Diko, Physica C **167**, 408 (1990).

[34]C. J. Jou and J. Washburn, J. Mater. Res. **4**, 795 (1989).

[35]J. Nowotny, M. Rekas, and W. Weppner, J. Am. Ceram. Soc. **73**, 1054 (1990).

[36]S. J. Rothman, J. L. Routbort, and J. E. Baker, Phys. Rev. B **40**, 8852 (1989).

PHASE TRANSFORMATIONS AND TWINNING

G. W. Bailey and C. L. Rieder, Eds., Proc. 51st Annual Meeting of the Microscopy Society of America

PHASE TRANSFORMATIONS IN CERAMICS

W. M. Kriven

Department of Materials Science and Engineering, University of Illinois at Urbana-Champaign, Urbana, Illinois, 61801

The study of phase transformations in ceramic has received limited coverage in ceramic text books[1], other than for example, ferroelectric transformations, (e.g., in barium titanate), zirconia and amorphous to crystalline transformations in glass. While Newnham[2] has comprehensively reviewed the crystal chemistry of "ferroic" (ferroelectric, ferroelastic or ferromagnetic) ceramics, the success of "transformation toughening" as a mechanism for reducing the brittleness of ceramics has stimulated the search for other potential transformation tougheners alternative to zirconia.[3]

While phase transformations have been widely studied in metals over the past 50 years, caution needs to be exercized in transplanting conventional wisdom from metals to ceramics. The differences in bonding in ceramics (mixed covalent and ionic), can lead to profound differences in crystal structures and transformation mechanisms. An alternative approach which has been particularly helpful in our work is that of Hyde et al.,[4,5] which empasizes cation arrangements, into the interstices of which, the anions are inserted, rather than the inverse perspective of putting cations into a packed anion array. The aim of this abstract is to list known examples of non-perovskite - type transformations which generally have significant volume and/or unit cell shape changes (Table 1).

Judicious use of such transformations in ceramic composites may have beneficial effects on the mechanical properties of composites. Alternatively, a better understanding of the precise crystallography of the transformation mechanisms may lead to their application as new types of large-force actuator materials. When coupled with conventional perovskite transformations currently used in "smart" or adaptive ceramics they could produce a more powerful mechanical response. In the case of martensitic transformations which proceed with the speed of sound, the response times are comparable with current sensor and actuator materials.

In addition to those compounds listed in Table 1, other reports of displacive phase transformations in ceramics include: a tetragonal to monoclinic-like transformation in zircon ($ZrSiO_4$) on heating at 827 °C;[6] a $\beta \rightarrow \gamma$ transformation in Li_3PO_4 at ≈340°C[7]; a monoclinic to rhombohedral transformation in the NaSiCON type, $LiSn_2(PO_4)_4$[8]; as well as transformations in aluminium titanate (Al_2TiO_5), barium orthotitanate (Ba_2TiO_4) and cerium pyrosilicate ($CeSiO_4$).

References

1. W. D. Kingery,et al., Introduction to Ceramics, 2nd Ed, John Wiley and Sons Publ. (1975).
2. R. E. Newnham, Crystal Chemistry of Non-Metallic Materials, Springer-Verlag (1975).
3. W. M. Kriven, J. Am. Ceram. Soc. 71 [12] (1988) 1021-1030.
4. M. O'Keeffe and B. G. Hyde, Structure and Bonding 61, Springer Verlag, (1985) 77.
5. B. G. Hyde and S. Andersson, Inorganic Crystal Structures, John Wiley and Sons, 1989.
6. Z. Mursic, T. Vogt and F. Frey, Acta Cryst B48 (1992) .
7. C. Ibarra-Ramirez et al., J. Mater. Sci. 20 (1985) 812.
8. J. Angenault et Al., J. Mater. Sci. Lett. 11 (1992) 1705.
10. This was supported by the US Air Force Office of Scientific Research, Grant AFOSR-URI-90-0174.

Table 1. Examples of First Order Displacive Transformations in Ceramics

Compound	Crystal Symmetries	Transformation Temperature (T_o on cooling)	Volume Change (ΔV)	Unit Cell Shape Change(°)
ZrO_2	tetragonal→ monoclinic	950	(+)4.9% (R.T.)	9
Ln_2O_3 (type)	monoclinic→ cubic	600–2200	(+)10%	10
Ca_2SiO_4 (K_2SO_4-type)	monoclinic→ orthorhombic	490	(+)12%	4.6
Sr_2SiO_4 (K_2SO_4-type)	orthorhombic → monoclinic	90	0.2%	2
NiS	rhombohedral → hexagonal	379	(+)4%	—
$2Tb_2O_3 \cdot Al_2O_3$ (type)	orthorhombic → monoclinic	1070	(+)0.67%	18.83
$PbTiO_3$	cubic→ tetragonal	445	(+)1%	0
$KNbO_3$	tetragonal → orthorhombic	225	~0%	0
$LuBO_3$	hexagonal → rhombohedral	1310	(+)8%	—
$MgSiO_3$ ($CaSiO_3$-type) ($FeSiO_3$-type)	orthorhombic → monoclinic	865	(-)5.5%	18.3
$YNbO_4$ ($LnNbO_4$-type)	tetragonal → monoclinic	900	(-) 1.8%	4.53
$LnBO_3$(type)	hexagonal → hexagonal	550–800	(-)8.2%	—

(Invited overview paper). Accepted abstract for the International Conference on Solid to Solid Phase Transformations, Pittsburgh, PA July,1994.

Displacive and Martensitic Transformations in Ceramics

W. M. KRIVEN
Dept. of Materials Science and Engineering, University of Illinois at Urbana-Champaign, 105 S. Goodwin Ave., Urbana, IL 61801, USA.

The study of phase transformations in ceramics has received limited attention, other than, for example, ferroelectric transformations (e.g., barium titanate), zirconia and amorphous to crystalline transformations in glass. The success of "transformation toughening" as a mechanism for reducing the brittleness of ceramics has stimulated interest in transformations involving non-perovskite crystal structures. However, while phase transformations have been widely studied in metals over the past 50 years, caution needs to be exercized in transplanting conventional wisdom from metals to ceramics. The differences in bonding in ceramics, being mixed *covalent and ionic, can lead to profound* differences in crystal structures and transformation mechanisms. An alternative approach of Hyde et al. which has found to be helpful, is to focus on cation arrangements (derived from metals or intermetallics), into the interstices of which, anions (e.g. oxygen) are inserted. Complex structures can be visualized as groupings of flexible or rigidly bound polyhedra.

The state of knowledge on known, non-perovskite transformations which generally have significant volume (both positive and negative) and/or unit cell shape changes will be presented. Documented cases of martensitic transformation mechanisms in ceramics will be discussed. Quantitative examples of ferroelastic transformations will be reviewed, while displacive transformations exhibiting martensitic characteristics will be summarized.

TWINNING IN STRUCTURAL CERAMICS

Waltraud M. Kriven
Department of Materials Science and Engineering
University of Illinois at Urbana-Champaign
Urbana, IL 61801

Abstract

(In preparation)

"Twinning in Structural Ceramics, " W. M. Kriven. (invited review paper) in Twinning in Advanced Materials, Edited by M. H. Yoo and M. Wuttig. Published by The Minerals, Metals and Materials Society (TMS), Warrendale , PA.(1994), in preparation.

This work was supported by the U.S. Air Force Office of Scientific Research under Grant number AFOSR URI 90 1074. I am happy to acknowledge valuable discussions with my graduate student, J. L. Shull.

Introduction

According to the comprehensive treatise of Cahn[1], twins may be classified into three types: (1) Growth twins which can produce a variety of configurations depending on the chemistry, crystallography and conditions of the growth process. (2) Thermal and transformation twins which are formed in the solid state within one crystal structure, or during the change from one crystal structure to another. In both cases, they are a response to a change in the thermal environment of the crystal . (3) Mechanical twins which on the other hand, are a response to an applied stress or strain, giving rise to deformation accommodation. While (2) and (3) are intimately related, it is worthwile to keep in mind that transformation twins involve a change in crystal structure.

In the case of a transformation from high symmetry to lower symmetry, a mirror plane in the parent often becomes a twin plane in the product due to loss of a symmetry element. These then, are natural candidates to become transformation twins in the product. For example, in the case of a martensitic mechanism, these could be lattice invariant shear (LIS) twin systems[2]. An alternative way to produce transformation twins is by the generation of "symmetry equivalent options" which are apparently twin related in the product phase, if the product phase has sufficiently high symmetry. For example, in the cubic to tetagonal transfomation in perovskites, such as barium titanate ($BaTiO_3$), the three crystallographically equivalent $[a]_c$ axes become the six physically distinguishable $[c]_t$ axes (considering + and - polarizing directions). This leads to domains in the product phase which may happen to lie in apparent twin orientation to one another in the product phase. A similar example in mineralogy is the cubic to tetragonal transformation in leucite ($KAlSiO_6$)[3.]

Related to symmetry equivalent options and martensitic crystallography, it is possible for twin related variants to arise, which in themselves have undergone LIS slip or twinning. In the latter case, each variant is internally twinned. Basinski and Christian[4] analyzed such a configuration where variants share a common habit plane but have opposite shape changes, thereby avoiding accumulation of long range stress fields. The path to shape memory crystallography[5,6] is then clear, where cooperative configurations of twin related variants whose net macroscopic shape change is minimized or zero.

The difference between transformation twins and mechanical deformation twins has clearly been illustrated by Birnbaum and Read[7-11] in the case of AuCd metal alloys undergoing a β (bcc) to β' (orthorhombic, space group D^2) or β'' (tetragonal, point group 4/m, m, m) structures. LIS transformation twinning occurred on $(111)_{\beta'}$ and $(011)_{\beta''}$, and these could be made to move under an applied stress[8]. No yield point was observed for the transformation twin boundary motion. On release of the stressing load, the twin boundaries moved back to their original positions, thus behaving "pseudo-elastically" under an applied stress. After a relatively high value of yield stress of the order of 10^8 - 10^9 dynes cm^{-2}, however, mechanical twins of the type $(111)_{\beta'}$ were formed, accompanied by a sharp drop in load and audible clicking[7,9]. They replaced regions of the LIS transformation twins and increased in width and number as the stressing load was further increased. On gradual release of applied stress the mechanical twins disappeared suddenly, again accompanied by audible clicks and sharp increases in load. Similar twin boundary motion under an applied load has also been observed in metallic hydrides[11].

The aim of this paper is to review the occurrence of the different types of twinning in ceramics, in particular those associated with the mechanical behavior of structural ceramics. In this context, ferroelasticity and ferroelastic transformations are of interest. Ferroelastic domain switching has been demonstrated to be a toughening mechanism in ceramics, while ferroelastic transformations can lead to ferroelasticity, as well as involve significant spontaneous strains which can be stored in ceramic microstructures.

Ferroelasticity and Ferroelastic Transformations

Ferroelasticity can be more easily understood in the context of the more familiar phenomena of ferroelectricity and ferromagnetism (figure 1). Ferroic crystals in general are those which contain two or more orientation states or domains which can be switched by the application of suitable force or field[3]. Ferroelectric materials exhibit a hysteresis curve (figure 1a) in which there is a spontaneous polarization (P_i) in the absence of an applied electric field. This is known as "poling" and results in alignment of polar domains in the direction of the polarizing field. Similarly, in ferromagnetic materials, a spontaneous residual magnetization (M_i) is formed on application of a suitably coercive magnetic field (figure 1b). Aizu[12] introduced the term "ferroelasticity" to describe the mechanical analogue which gives a hysteresis loop between strain and applied stress (figure1c). A coercive stress (σ_c) induces a spontaneous strain (ε_i), which defines the deformation of a crystal at zero stress, relative to a prototypic structure. Specifically, Aizu[12] defined ferroelasticity as:

> "A crystal is said to be ferroelastic, when it has two more (orientation) states in the absence of mechanical stress and can be shifted from one to another of these states by a mechanical stress; here any two of the states are identical or enantiomorphous in crystal structure and different with respect to mechanical strain tensor at null stress."

Unfortunately, it has been pointed out by Lieberman [13] that ferroelasticity may be a misnomer in the sense that the spontaneous strain induced by the coercive stress in not trully "elastic." On the contrary, the behavior is more plastic in nature. However since ferroelasticity, as defined above, has been the currently accepted terminology for the past twenty five years[14-16], new terminology will not be introduced here.

Figure 1 - Comparison of hysteresis curves for ferroic materials

Ferroelastic crystals differ from ferroelectric or ferromagnetic crystals in that they do not require a non-centrosymmetric point group. However, spontaneous strain must be defined relative to a higher symmetry structure known as a prototype which contains all of the point group symmetry elements belonging to the ferroic crystal[17]. Ferroelastic crystals have a group → subgroup relationship with the prototypic structure.

A ferroelastic transformation involves a transformation from a prototypic structure to a ferroic subgroup structure which has a decrease in point group symmetry. The transformation also involves a change in crystal system according to the commonly accepted definition of Wadhawan[16]. It is interesting to note that a phase corresponding to the structure of the prototype need not actually exist. In some cases the crystal melts or decomposes before the prototypic phase becomes stable. A sequence of ferroic phases may be traced back to the same prototype, but one ferroic phase cannot be the prototype for another ferroic phase. An example of this is seen in dicalcium silicate ($CaSiO_4$) where there are two sequential ferroelastic transformations[18]. The first phase to appear from the melt (α) has hexagonal symmetry which transforms ferroelastically to orthorhombic α' phase at 1425°C. At 675°C, a second ferroelastic transformation occurs between the orthorhombic α' and monoclinic β phase. The high temperature hexagonal α phase in this example is prototypic to both of the ferroic α' and β phases.

Domains and Domain Switching

A domain is a contiguous region of a crystal which has the same orientation state. They are derived from symmetry related options in the parent phase. A crystal or grain is able to minimize its energy by developing a domain structure containing an optimum number and orientation of domains. When an external stress is applied, the crystal reorients itself through domain wall movement so as to minimize its free energy[16]. This process of domain switching is one where a compressive stress on a crystal makes one domain (S_1) more energetically favorable to another (S_2). The domain wall between them moves so as to better accommodate the strain and lower the free energy of the crystal. The generation of symmetry equivalent options and domain switching is schematically drawn in figures 2 and 3.

Figure 2 - Generation of ferroic domains from symmetry equivalent options of the parent crystal structure. E.g., tetragonal domains derived from cubic ZrO_2, or $BaTiO_3$.

Figure 3 - A compressive stress applied along the $[c]_t$ axis converts the $[c]_t$ axis of domain S_2 into the $[a]_t$ axes of domains S_1 and S_3.

Ferroelastic domain switching in K_2SO_4-type inorganic crystals (including K_2SeO_4, NH_4SO_4 and NH_4BeF_4) has been studied and reviewed by Shiozaki et al.[19]. The high temperature hexagonal (I) prototype produced three orthorhombic domains, related as shown in the $[c]_I$ // $[c\}_{II}$ projection of figure 6. The transformation occurred at 587°C, producing 120° twins on $(011)_{II}$ and $(031)_{II}$ twin planes. Shiozaki et al.[19] grew single domain crystals of K_2SO_4 and denoted them as domain I. They compressed them in a direction corresponding to the $[b]_I$ direction in figure 4. When an external stress was applied at room temperature, no other twinned domains were formed and the crystals fractured. However, when an external stress was applied at 300°C or above, new domains (II and III of figure 6) appeared at the crystal edges and moved through the crystals. The higher the temperature, the smaller was the critical stress (X_c) required to nucleate the new domains. For example at 350°C, X_c was ~50 kgw cm^{-2}, while at 470°C, it was only ~10 kgw cm^{-2}. The observations in K_2SO_4-type inorganic compounds therefore, indicate that ferroelastic domain switching is a viable way to avoid fracture in ceramics at high temperatures.

Figure 4 - The three ferroelastic domains of orthorhombic K_2SO_4 derived from the hexagonal prototype, both in [c] axis projections, after Shiozaki et al.[19].

Ferroelastic Domain Switching as a Toughening Mechanism

The mechanical properties of PZT and $BaTiO_3$ were examined by Pohanka et al.[20-23] and the ferroic tetragonal phases were seen to have higher fracture energy and hence toughness that the cubic para phases. Toughening mechanisms were attributed to microcracking , ferroelstic twinning and twin all motion. Pisarenko, Cushko and Kovalev[21] recognized the toughening effect of stress-induced domain reorientation near a crack tip in piezoelectric ceramics of lead zirconate titanate (PZT) and barium titanate. They reasoned that the poling of ferroelectric domains was also coupled with a resultant elastic anisoptropy which should give rise to fracture toughness anisotropy, as was observed. Virkar and Matsumoto [21-25] developed the phenomenon of ferroelastic domain switching as a toughening mechanism for non electrical ceramics, and demonstrated it in tetragonal zirconia ceramics [21-28]. They pointed out that the area enclosed by the hystersis loop represented the mechanical energy dissipated in a single cycle[21]. In zirconia, ferroelastic domains appeared during the cubic to tetragonal transformation at ~2200°C, where [c] axes were elongated relative to [a] axes, by an amount depending on the composition of CeO_2, Y_2O_3 or other stabilizer added, and hence on lattice parameters. It was hypothesized that during grinding of a polycrystalline pellet, some domains were oriented such that the applied tensile stress would stretch the $[a]_t$ axes into $[c]_t$ axes, while other domains were oriented such that a compressive stress along $[c]_t$ axes converted them into $[a]_t$ axes. Thus rotations of axes by 90° were effected.

Experimentally observations by X-ray diffractometry were made on CeO_2 or Y_2O_3 doped zirconia polycrystalline pellets[21-24] as well as pseudo (twinned) single crystals transformed from the cubic phase[25,26]. The domain switching phenomenon was detected under application of grinding, tensile (~400MPa) or compressive stresses. The change in texture as seen by XRD is schematically illustrated in Fig. 5 (after ref 21). Systematic uniaxial compression experiments on 3 mol % Y_2O_3 doped ZrO_2 (3Y-TZP) pseudo single crystals coupled with Vickers indentations and TEM dark fielding experiments were unequivocally able to confirm ferroelastic domain switching as a toughening mechanism[26]. A particularly clear demonstration of this was provided by Vickers indentation tests on mechanically poled, pseudo single crystal samples of 3Y-TZP and of gadolinium molybdate (GMO)[26-28]. In PSZ for example[28], a compressive load tended to align $[c]_t$ axes in a plane perpendicular to the coercive force as schematically depicted in figure 6. During subsequent indentation, the $[c]_t$ axis domains parallel to the crack surfaces reoriented themselves to be perpendicular to the crack surfaces. This crack energy dissipating mechanism by domain reorientation gave an apparent higher toughness (shorter cracks) in this direction as compared to the other radial crack direction (longer cracks).

In GMO ($Gd_2(MoO_4)_3$) single crystal specimens polished on (100), (010) and (001) faces, domain walls were of the {110} type [28]. The cubic to orthorhombic β' phase tranformation occured at 159°C, where the $[a]_{\beta'}$ axis was slightly shorter than the $[b]_{\beta'}$ axis. Vickers indentations were introduced under a 200g load, so that radial cracks would be aligned along $[a]_{\beta'}$ and $[b]_{\beta'}$ directions in the ferroelastic product phase. From the geometry of a mode I crack, it was anticipated that tensile stresses would emanate in a direction perpendicular to the crack plane. Any $[a]_{\beta'}$ axes experiencing the tensile stresses were expected to reorient to become the longer $[b]_{\beta'}$ axes. Such a domain switching process would cost energy from the crack, giving an apparent higher toughness in this

direction. Experimentally, the indentation toughnesses measured from crack lengths were measured to be ~1.2 MPa $m^{-1/2}$ for cracks propagating along the $[b]_{\beta'}$ axis, and ~0.42 MPa $m^{-1/2}$ for cracks propagating along the $[a]_{\beta'}$ axis. Thus, cracks propagating along the $[b]_{\beta'}$ axis had a tensile stress in the $[a]_{\beta'}$ axis direction of the specimen, causing domain reorientation to align the longer $[b]_{\beta'}$ axes to the stress field, thereby giving a higher toughness value. Conversely, cracks propagating along the $[a]_{\beta'}$ axis had tensile forces in the $[b]_{\beta'}$ axes of the specimen which were already in the optimum orientation and so did not dissipated any crack energy, giving rise to a lower toughness in that direction. The K_{1c} of radial cracks placed along $<110>_{\beta'}$ directions was 0.55 MPa $m^{-1/2}$ consistent with the the expectance of no ferroelastic switching. Similar behavior was expected in the chemically analogous terbium molybdate (TMO or $Tb_2(MoO_4)_3$) and dysprosium molybdate (DMO or $Dy_2(MoO_4)_3$). The indentation fracture toughness of hot pressed polycrystalline TMO and DMO pellets of grain size ~6 μm was measured as a funtion of temperature up to 300°C. It was observed that the toughness gradually decreased from room temperature to the Curie (transformation) temperature of ~160°C, and remained essentially constant in the high temperature cubic phase. The room temperature toughness was approximatedly twice that of the high temperature cubic phase where no ferroelastic activity was possible.

Bulk fracture toughness measurements were made on 3Y-TZP to compare the ferroelastic materials with fully doped cubic ZrO_2. The toughnesses of Y_2O_3 doped ZrO_2 pseudo single crystals at 1200°C and room temperature were ~12 and ~8 MPa.$m^{1/2}$ respectively[24], while polycrystalline samples typically had toughness values of ~7.7 MPa.$m^{1/2}$. In comparison, fully doped cubic ZrO_2 pellets had a toughness of 2.4 MPa.$m^{1/2}$ Thus for comparable polycrystalline specimens, a threefold increase in toughness was realizable. The ferroelastic toughening effect was also demonstrated in lead zirconate titanate (PZT) having a Zr:Ti ratio of 0.54:0.46, where tetragonal domains (with c/a = 1.019) were produced from the high temperature cubic phase[26]. At room

temperature the tetragonal toughness was measured as 1.85 MPa.$m^{1/2}$, while the cubic high temperature toughness was only 1.0 MPa $m^{1/2}$.
A theoretical formulation was developed to predict the ferroelastic contribution to the toughness[24-27] in which:

$$K_c = K_c^o$$

where

K_c^o = fracture tughness in absence of ferroelasticity
εs = switching strain
= coercive stress
= Elastic modulus
= Poisson's ratio ~ 0.25

This equation predicted a K_{Ic} for 3 mole % Y_2O_3 stabilized ZrO_2 of 6.1 MPa.$m^{1/2}$ as compared to the 7.7 MPa.$m^{1/2}$ measured for this material. Ferroelastic toughening has also been demonstrated in bismuth vanadate ($BiVO_4$) [29]. Single crystals showed domain nucleation and propagation under compressive loading, and domain generation during fracture, the latter leading to R-curve behavior.

Ceramic Examples with Non-Orthogonal Symmetry

References

1. R. W. Cahn. "Twinned Crystals," Adv. in Physics, 3 (12) (1954), 363-445.

2. C. M. Wayman, "Introduction to the Crystallography of Martensitic Transformations," (New York, NY: The Macmillan Company, 1964), 76-97.

3. Andrew Putnis, Introduction to Mineral Sciences, (Cambridge, UK: Cambridge University Press, 1992), 223-228.

4. Z. S. Basinski and J. W. Christian, "The Cubic to Tetragonal Transformation in Maganese-Copper Alloys," J. Inst. Metals, 80 (1951/52) 659-666.

5. T. Saburi and C. M. Wayman, "Crystallographic Similarities in Shape Memory Martensites," Acta Metall., 27 (1979) 979-995.

6. T. Saburi, S. Nenno and C. M. Wayman, "Shape Memory Mechanisms in Alloys," Proc. Int. Conf. Martensitic Transformations, ICOMAT 1979 (Cambridge, Massachusetts, USA, 1979), 619-632.

7. H. K. Birnbaum and T. A. Read, Mechanical Twinning in the AuCd β' Phase," Trans. Metall. Soc. of AIME, 218 (1960) 381-382.

8. H. K. Birnbaum and T. A. Read, Stress Induced Twin Boundary Motion in AuCd β′ and β ′′ Alloys," Trans. Metall. Soc. of AIME, 218 (1960) 662-669.

9. H. K. Birnbaum, "Twin Accommodation in Au Cd β′ Alloys," Trans. Metall. Soc. of AIME, 215 (1959) 508-509.

10. H. K. Birnbaum, "Stabilization Phenomena in Beta-Phase Au-Cd Alloys," Trans. Metall. Soc. of AIME, 215 (1959) 786-792.

11. H. K. Birnbaum, "Mechanical Properties of Metal Hydrides," J. Less-Common Metals, 104 (1984) 31-41.

12. K. Aizu, "Determination of the State Parameters and Formulation of Spontaneous Strain for Ferroelastics," J. Physical Society of Japan, 28 (1970) no. 3:706-716.

13. D. S. Lieberman, point of discussion at Syposium on Twinning in Advanced Materials at ASM Annual Fall Meeting in Pittsburgh, PA, Sept 18-21 1993.

14. K. Aizu, "Possible Species of Ferromagnetic, Ferroelectric and Ferroelastic Crystals," Physical Review B, 2 (1970) no. 3:754-772.

15. K. Aizu, "Phenomological Lattice-Dynamical Theory of Ferroelasticity," J. Physics and Chemistry of Solids, 32 (1971) 1959-1969.

16. V. K. Wadhawan, "Ferroelasticity and Related Properties of Crystals," Phase Transitions, 3 (1981) 3-103.

17. K. Aizu, "The Concepts 'Prototype' and 'Prototypic Phase' -- Their Difference and Others," J. Phys. Soc. Japan, 44 (1978) no. 2:683.

18. Y. J. Kim, I. Nettleship and W. M. Kriven, "Phase Transformations in Dicalcium Silicate:II, TEM Studies of Crystallography, Microstructure and Mechanisms," J. Am. Ceram. Soc., 75 (1992) no. 9:2407-2419.

19. S. Shiozaki, A. Sawada, Y. Ishibashi and Y. Takagi, "Hexagonal-Orthorhombic Phase Transition and Ferroelasticity in K_2SO_4 and K_2SeO_4," J. Phys. Soc. Japan, 443 (1977) no. 4:1314-1319.

20. R. C. Pohanka, S. W. Freiman and B. A. Bender, " Effect of Phase Transformation on the Fracture Behavior of $BaTiO_3$," J. Am. Ceram. Soc., 61, (1978) no: 72-75.

21.

22.

23. G. G. Pisarenko, V. M. Chushko and S. P. Kovalev, J. Am. Ceram. Soc., 68 (1985) no. 5: 259-265.

24. A. V. Virkar and R. L. K. Matsumoto, "Ferroelastic Domain Switching as a Toughening Mechanism in Tetragonal Zirconia," J. Am. Ceram. Soc., 69 (1986) no. 10: C224-C226.

25. A. V. Virkar, R. L. Matsumoto, "Toughening Mechanism in Tetragonal Zirconia (TZP) Ceramics," Adv. in Ceramics, 24 (1986) 653-662.

26. K. Mehta, J. F. Jue and A. V. Virkar, "Grinding-Induced Texture in Ferroelastic Tetragonal Zirconia," J. Am. Ceram. Soc., 73 (1990) no. 6: 1777-1779.

27. J. F. Jue and A. Virkar, "Fabrication, Microstructural Characterization and Mechanical Properties of Polycrystalline t′-Zirconia," J. Am. Ceram. Soc., 73 (1990) no. 12: 3650-3657.

28. G. V. Srinivasan, J.F. Jue, S. Y. Kuo and A. V. Virkar, "Ferroelastic Domain Switching in Polydomain Tetragonal Zirconia Single Crystals," J. Am. Ceram. Soc., 72 (1989) no. 11: 2098-2103.

29. C. J. Chan, F. F. Lange, M. Ruhle, J. F. Jue and A. V. Virkar, "Ferroelastic Domain switching in Tetragonal Zirconia Single Crystals - Microstructural Aspects," J. Am. Ceram. Soc., 74 (1991) no. 4: 807-813.

30. K. Mehta and A. V. Virkar, "Fracture Mechanisms in Ferroelectric-Ferroelastic Lead Zirconate Titanate (Zr:Ti = 0.54:0.46) Ceramics," J. Am. Ceram. Soc., 73 (1990) no. 3: 567-574.

31. A. Virkar, J. F. Jue, P. Smith, K. Mehta and K. Prettyman, "The Role of Ferroelasticity in Toughening of Brittle Materials," Phase Transitions, 35 (1991) 27-46.

32. T. L. Baker, K. T. Faber and D. W. Readey, "Ferroelastic Toughening in Bismuth Vanadate," J. Am. Ceram. Soc., 74 (1991) no. 7: 1619-1623.

OTHER RELATED TOPICS OR JOINT CO-AUTHORSHIPS

J. Phys. Chem. Solids Vol. 52, No. 5, pp. 731–734, 1991
Printed in Great Britain.

0022-3697/91 $3.00 + 0.00

CALCULATION OF THE *K*-ABSORPTION EDGE AND ITS CHEMICAL SHIFT OF COMMON METALS

MICHIHIDE KITAMURA† and HAYDN CHEN
Department of Materials Science and Engineering, University of Illinois at Urbana-Champaign, Urbana, IL 61801, U.S.A.

(*Received* 27 *September* 1990; *accepted* 2 *January* 1991)

Abstract—Self-consistent field calculations are systematically carried out for common metals Cr, Mn, Fe, Co, Ni, Cu and Zn atoms and ions in order to understand the *K*-absorption edge and its chemical shift. It is found that: (1) a transition state introduced by Slater is very useful to predict the absorption edge energy; (2) there is a linear correlation between the absorption edge chemical shift and the cation charge of a crystal; and (3) the present model is applicable to ionic bonded crystals but is not very good for covalent ones.

Keywords: *K*-absorption edge, chemical shift, common metals, self-consistent calculation.

INTRODUCTION

It is well known that the energy of the *K*-absorption edge of an element depends on the degree of ionicity of that element and its local structure. One of the authors (HC) has previously measured [1] the positions of *K*-absorption edge of Fe in several crystalline compounds including $Fe_{0.885}O$, $Fe_{0.905}O$, Fe_3O_4, Fe_2O_3, and α-Fe metal, and those of two amorphous solids: oxide glass ($[Na_20.2SiO_2]_{0.8}[Fe_2O_3]_{0.2}$) and metallic glass ($Fe_{36}Cr_{32}Ni_{14}P_{12}B_6$). It was demonstrated that there is a definite linear correlation between the *K*-absorption edge chemical shift and the effective coordination charge, which is defined as $\eta = Z - (1 - f_i)n$, where Z is the valence, f_i is the degree of ionicity, and n is the coordination number. This linear correlation is proposed by Batsanov [2], which physical meaning is obvious: it represents the charge that appears at the periphery of the atom as a result of participation in the chemical bonding of its own electrons (Z) and the electrons received from the neighboring atoms [$(1 - f_i)n$], which compensate for the positive charge. On the other hand, one of the authors (MK) studied the X-ray Absorption Near-Edge Structure (XANES) by means of a multiple-scattering (MS) theory utilizing a muffin-tin (MT) potential approximation, and found that the overall profile of the absorption spectra is well explained by this approach [3–9].

In the present paper, we calculate the *K*-absorption edge energy and its chemical shift on the basis of the atomic nature, instead of using the MS calculation within the MT approximation. The aim of this paper is to present a theoretical guide line for the *K*-absorption edge and its chemical shift in several common metals, since no such theoretical and systematic considerations are available in the literature.

† Permanent address: Department of Electrical and Electronic Engineering, Utsunomiya University, Utsunomiya 321, Japan.

THEORETICAL BACKGROUND

The energy of the absorption edge is given by the energy difference between the initial core and the final states for the *K*-absorption process, whose two states are, of course, eigenstates of the Schrödinger equation $[-\nabla^2 + V_{cry}(r)]\ \psi(r) = E\psi(r)$. Here, the crystal potential $V_{cry}(r)$ consists of a spherical term $V_s(r)$ and a non-spherical term $V_{ns}(r)$. Due to the fact that the $V_{ns}(r)$ term is usually small as compared with the term $V_s(r)$, hereafter we will consider only the spherical term as the crystal potential, which corresponds to the MT potential approximation. The spherical potential $V_s(r)$ [$= V_{cry}(r)$] is thus written as [5]:

$$V_{cry}(r) = V_c^{(s)}(r) - 6\alpha_{ex}[3\rho^{(s)}(r)/8\pi]^{1/3}, \tag{1a}$$

$$V_c^{(s)}(r) = V_c^{(at)}(r) + (2r)^{-1}\sum_{z\neq 0} R_z^{-1} \times \int_{Rz-r}^{Rz+r} r_z w(r_z)\,dr_z + \sum_{z\neq 0} 2\delta q_z/R_z, \tag{1b}$$

$$\rho^{(s)}(r) = \rho^{at}(r) + (2r)^{-1}\sum_{z\neq 0} R_z^{-1} \times \int_{Rz-r}^{Rz+r} r_z \rho^{at}(r)_z\,dr_z, \tag{1c}$$

$$w(r_z) = V_c^{at}(r_z) - 2\delta q_z/r_z, \tag{1d}$$

$$V_c^{at}(r_z) = -2Z_z/r_z + U(r_z), \tag{1e}$$

$$\nabla^2 U(r_z) = -8\pi\rho^{at}(r_z), \tag{1f}$$

where α_{ex} is the Schwartz's exchange parameter [10], δq_α denotes the value of charge transfer at the α-th atoms and is defined by

$$\sum_{n\lambda} \omega_{n\lambda}^{(\alpha)} - Z_\alpha.$$

Z_α and $\omega_{n\lambda}^{(\alpha)}$ are the atomic number of the α-th atom and the occupation number for the orbital specified by $n\lambda$, respectively. Here, it should be emphasized that, according to our experience based upon the XANES calculation using a MS theory, the contribution of the second term in eqns (1b) and (1c) to the crystal potential is small as compared with the other terms. While the crystal potential highly depends upon the structure and the charges of the atoms surrounding the absorbing atom, the second term in eqns (1b) and (1c) does not strongly depend on the ionicity factor [5, 6]. Therefore, in studying the absorption edge chemical shift as an effect of the ionicity, this second term may be omitted. Hence, the Schrödinger equation to be solved is given as

$$[-\nabla^2 + V_{cry}(r)]\psi_j(r; q, s) = E_j(q, s)\psi_j(r; q, s), \quad (2a)$$

$$V_{cry}(r) = V_c^{st}(r) - 6\alpha_{ex}[3\rho^{st}(r)/8\pi]^{1/3} + \sum_{\alpha \neq 0} 2\delta q_\alpha / R_\alpha \quad (2b)$$

where symbols q and s are the suffixes to indicate the charge and the crystal structure. Here, it is noted that the Madelung term

$$\sum_{\alpha \neq 0} 2\delta q_\alpha / R_\alpha$$

is not a function of distance r. Thus, the energy eigenvalue $E_j(q, s)$ is given by

$$\epsilon_j(q) + \sum_{\alpha \neq 0} 2\delta q_\alpha / R_\alpha.$$

The $\epsilon_j(q)$ is the energy eigenvalue for the quantum state $|j\rangle$ of the Schrödinger equation for the isolated atom or isolated ion for a given charge q.

Consequently, the energy of the absorption edge, E_{edge}, due to the transition from $|i\rangle$ to $|f\rangle$ is given by $E_{edge}(q) = \epsilon_f(q) - \epsilon_i(q)$, because the Madelung term does not depend on the quantum number. This result means that in order to understand the absorption edge and the chemical shift due to the change of the charge of an ion, it is sufficient to solve the Schrödinger equation for the isolated atom or ion.

CALCULATION

The self-consistent-field (SCF) calculations following a prescription of Herman and Skillman [11] using Schwarz's exchange parameter were carried out for isolated Cr, Mn, Fe, Co, Ni, Cu and Zn atoms and ions. These common metals are very important elements in the study of chemistry and solid state physics. Moreover, in order to take into account the effect of a core hole due to the K-absorption, a concept of the transition state introduced by Slater [12] was adopted in the present calculation. In a previous work [4] by one of us (MK) concerning the K-XANES of diamond, it has already been found that Slater's transition state must be used in order to more accurately predict the K-absorption edge.

According to the concept of Slater's transition state, the electron configuration of the K-absorption of the M^{q+} ion (M = Cr, Mn, Fe, Co, Ni, Cu and Zn) is $1S^{1.5}2S^2 2P^6 3S^2 3P^6 3d^x 4S^y 4P^{0.5}$, and the energy of the K-absorption edge is given by the energy difference between $4P$ and $1S$ states. Here, the occupation numbers of electrons x and y for the $3d$ and $4S$ orbitals are, for example, given as follows: For the cation charge $q = 0, 1, 2, 3$, $(x, y) = (5, 1)$, $(5, 0)$, $(4, 0)$ and $(3, 0)$ for the Cr ion; $(x, y) = (5, 2)$, $(5, 1)$, $(5, 0)$ and $(4, 0)$ for the Mn ion; $(x, y) = (6, 2)$, $(6, 1)$, $(6, 0)$ and $(5, 0)$ for the Fe ion; $(x, y) = (7, 2)$, $(7, 1)$, $(7, 0)$ and $(6, 0)$ for the Co ion; $(x, y) = (8, 2)$, $(8, 1)$, $(8, 0)$ and $(7, 0)$ for the Ni ion; $(x, y) = (10, 1)$ $(10, 0)$, $(9, 0)$ and $(8, 0)$ for the Cu ion; and $(x, y) = (10, 2)$, $(10, 1)$ $(10, 0)$ and $(9, 0)$ for the Zn ion.

RESULTS AND DISCUSSION

The calculated energies of the K-absorption edge are tabulated in Table 1 together with the experimental values [13] for M = Cr, Mn, Fe, Co, Ni, Cu and Zn atoms. From this table, it is found that the K-absorption edge energies calculated by using Slater's transition state are in good agreement with the experimental data. This result verifies again that the Slater's transition state is very useful for the understanding of the adsorption process.

The calculated K-absorption edge chemical shifts, with respect to the metallic state, are tabulated in Table 2, and plotted in Fig. 1, as a function of the cation charge q for various metals. From this figure the following observations are obtained.

(1) The chemical shift increases linearly with the increasing q value.

(2) There exists a critical value q_c at which a gradient change in the charge dependence of the

Table 1. Calculated and experimental [13] energies in units of eV of the K-absorption edge for Cr, Mn, Fe, Co, Ni, Cu and Zn atoms. The deviation (in %) between the experiment and the calculation is also indicated by the value inside the parentheses. The first column shows the energies calculated by using Slater's transition state (T.S.) and the second one those calculated by using the ground state (G.S.) which is also obtained from the SCF calculation

	T.S.	G.S.	Experiment
Cr	5960.49 (0.47)	5826.79 (2.71)	5988.8
Mn	6506.26 (0.48)	6365.16 (2.64)	6537.6
Fe	7070.61 (0.57)	6923.45 (2.64)	7111.2
Co	7658.78 (0.66)	7505.69 (2.64)	7709.54
Ni	8270.99 (0.73)	8110.82 (2.65)	8331.65
Cu	8897.03 (0.93)	8734.34 (2.74)	8980.3
Zn	9565.36 (0.99)	9392.51 (2.78)	9660.7

Table 2. M^{q+} K-absorption edge chemical shift calculated in units of eV as a function of the charge q for M = Cr, Mn, Fe, Co, Ni, Cu and Zn ions

q	0.5	1.0	1.5	2.0	2.5	3.0	3.5
Cr	0.14	1.35	3.57	8.06	12.06	18.41	23.11
Mn	0.99	1.82	2.06	3.91	7.10	13.33	19.43
Fe	0.74	2.14	2.89	4.10	10.84	13.52	18.99
Co	1.02	2.21	3.41	4.24	9.02	14.40	19.92
Ni	0.31	0.93	2.33	3.06	8.95	14.25	18.58
Cu	2.38	3.87	7.24	11.30	16.96	22.17	
Zn	−0.57	0.19	1.36	2.37	7.96	14.33	19.91

chemical shift occurs. This q_c value is 1 for Cr and Cu ions, and is 2 for Mn, Fe, Co, Ni and Zn ions.

(3) For all the systems considered, the gradients of the linear lines shown in Fig. 1 in the region $q > q_c$ are larger than those when $q < q_c$.

(4) The charge dependence of the chemical shift is nearly the same for Mn, Fe, Co and Ni ions (Fig. 1h).

It is clear that the value q_c corresponds to the occupation number of electrons on the $4S$ oribital of the neutral atom. Results (4) are borne out from the fact that Mn, Fe, Co, and Ni are $3d$ transition metals of the same $4S$ electron configuration. Moreover, results (3) can be understood because the $3d$ orbital electrons are more localized than the $4S$ electrons. Therefore, the effect of the change of the occupation number in the $3d$ orbital states on the K-absorption edge energy is larger than that of the $4S$ orbital state.

It is fruitful to compare the calculated chemical shifts with the experimental values. Some of the experimental measurements, in units of eV, are tabulated in Table 3 and shown in Fig. 1, together with the predicted cation charges $q(=Zf_i)$ based upon our current calculation. The charges of Mn, Fe, Co and Ni ions obtained by using the experimental chemical shifts and our calculation show reasonably good agreement with the formal charge of the respective ions, except for the case of Fe_2O_3. The discrepancy in this case is probably due to the fact that a certain degree of covalent bonding exists because the calculated ionicity by Levine [17] is 0.667 for Fe_2O_3, thereby giving a cation charge of 2.0. On the contrary, the predicted charges for Cu and Zn using the experimental K-absorption edge chemical shift information are significantly different from the formal charges for Cu_2O, CuO $KZnF_3$, ZnTe, ZnSe, ZnS and ZnO crystals. In the case of $KZnF_3$, a negative (−0.5 eV) chemical shift was measured, in contradiction with a predicted positive value. We believe that the charge of Zn ion does not exceed a value of 2, so that the chemical shift of the Zn K-absorption edge is about 1 eV or less within the present model. Such a small chemical shift might be difficult to measure, so that it is not unreasonable to question the accuracy of the measurement in this case. The charges predicted in the case of zinc chalcogenides ZnTe, ZnSe, ZnS and ZnO, however, exceed a value of 2. This is a serious problem. We suspect that these zinc chalcogenides crystallize by the SP^3 hybridized covalent bonding so

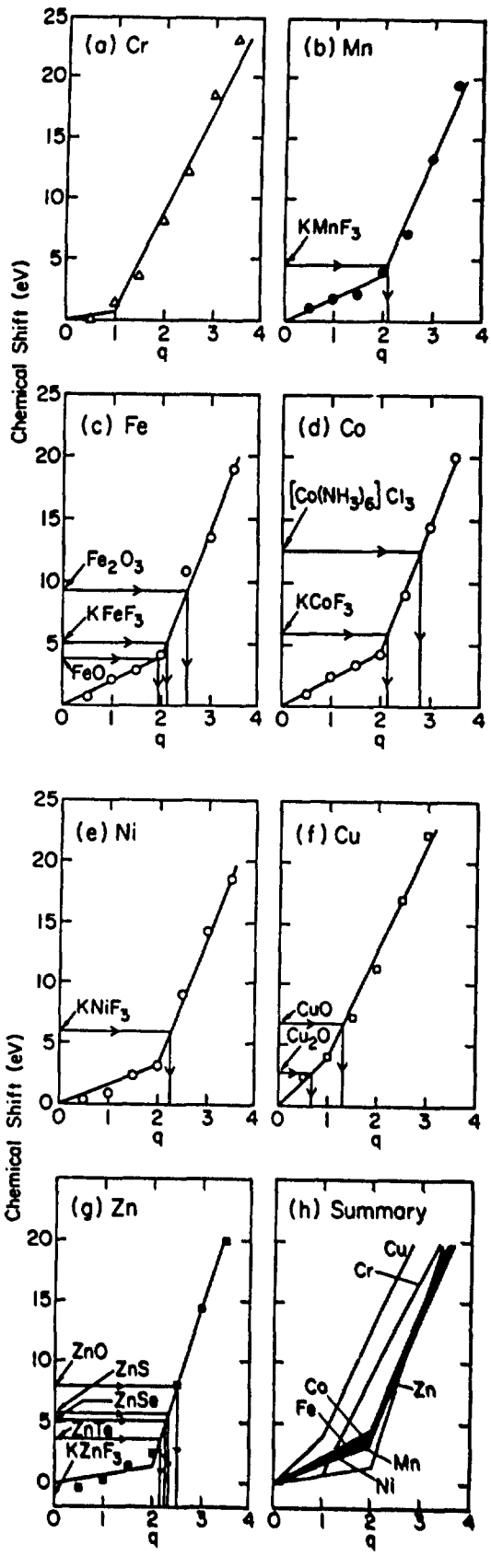

Fig. 1. Plot of K-absorption edge chemical shifts (eV) calculated as a function of the cation charge q for (a) Cr, (b) Mn, (c) Fe, (d) Co, (e) Ni, (f) Cu, and (g) Zn ions. The experimentally measured chemical shifts as tabulated in Table 3 are also indicated on the plot. Figure (h) is a summary of the predicted lines for the charge dependence of the chemical shifts for all elements considered.

Table 3. Experimental values (eV) of the metal K-absorption edge and the chemical shift for various compounds. The charges predicted from Fig. 1 are also indicated

Material	Energy of the edge	Chemical shift	Predicted charge
$KMnF_3$	6542.1 [14]	4.5	2.1
$KFeF_3$	7116.3 [14]	5.1	2.1
$Fe_{0.885}O$	7115 [1]	3.8	1.95
$Fe_{0.905}O$	7115 [1]	3.8	1.95
Fe_2O_3	7120.5 [1]	9.3	2.55
$KCoF_3$	7715.4 [14]	5.86	2.15
$[Co(NH_3)_6]Cl_3$	7722 [8]	12.5	2.8
$KNiF_3$	8337.5 [14]	5.85	2.25
Cu_2O	8983 [15]	2.7	0.7
CuO	8987 [15]	6.7	1.3
$KZnF_3$	9660.2 [14]	−0.5	?
ZnTe		3.64 ± 0.4 [16]	2.15
ZnSe		5.05 ± 0.4 [16]	2.25
ZnS		5.68 ± 0.4 [16]	2.3
ZnO		7.87 ± 0.4 [16]	2.5

that a reasonable explanation for the absorption edge chemical shift of these crystals is beyond the present interpretation which is based on the atomic nature. Finally, let us consider the cases of Cu ion. In the case of Cu_2O crystals, the predicted charge 0.7 for Cu is reasonable when compared with a calculated value of 0.56 by Levine [17] using a dielectric theory. However, in the case of CuO, the predicted charge 1.3 is far from the formal charge 2. This discrepancy may or may not be clarified even if the effect of the covalent bonding is considered. The charge of the Cu ion is an important issue in the field of high T_c superconductors. Therefore, we strongly hope that more careful measurements of the Cu K-absorption edge chemical shifts can be carried out so that a comparison could be made with our calculated results. We believe that our calculated results are useful in this regard.

SUMMARY

Self-consistent-field calculations have been systematically carried out for the first time for common metals Cr, Mn, Fe, Co, Ni, Cu and Zn atoms and ions by using a concept of the transition state introduced by Slater, in order to obtain the X-ray absorption edge energy and the chemical shift due to the change of cation charge. The calculated K-absorption edge energies are in good agreement with the established values of the considered metals. The results of the K-absorption edge chemical shifts calculated as a function of the cation charge lead us to the conclusion that: (1) there is a linear correlation between the chemical shift and the cation charge of a crystal, and (2) the present calculation based only on the atomic nature is adequate for the understanding of the absorption edge chemical shift of an ionic crystal, but is not very good for that of a covalent one.

In order to investigate the applicability of our calculations to the prediction the degree of ionicity (or the cation charge) for various ionic compounds, it is necessary that the K-absorption edge chemical shifts are carefully measured and systematically compared with the present calculations.

Acknowledgements—This research was supported in part by a URI program of the Air Force Office of Scientific Research, Contract No. AFOSR 90-0174. One of us (M.K.) would like to acknowledge the support of the Japanese Ministry of Education for making his stay in the U.S.A. possible.

REFERENCES

1. Chen H., *J. Phys. Chem. Solids* **41**, 641 (1980).
2. Batsanov S. S., *Elektrootritsatel 'Nost' Elementov i Khimicheskaya Svyaz' (Electronegativity of Elements and Chemical Bonds)*. Novosibirsk (1962).
3. Kitamura M., Muramatsu S. and Sugiura C., *Phys. Rev.* **B33**, 5294 (1986).
4. Kitamura M., Sugiura C. and Muramatsu S., *Solid State Commun.* **62**, 663 (1987).
5. Kitamura M., Muramatsu S. and Sugiura C., *Phys. Stat. Sol. (b)* **142**, 191 (1987).
6. Kitamura M., Muramatsu S. and Sugiura C., *Phys. Rev.* **B37**, 6486 (1988).
7. Kitamura M., Sugiura C. and Muramatsu S., *Solid State Commun.* **67**, 313 (1988).
8. Kitamura M., Sugiura C. and Muramatsu S., *Phys. Stat. Sol. (b)* **149**, 791 (1988).
9. Kitamura M. and Muramatsu S., *Phys Rev.* **B42**, 1417 (1990).
10. Schwartz K., *Phys. Rev.* **B5**, 2466 (1972).
11. Herman F. and Skillman S., *Atomic Structure Calculation*. Prentice-Hall, Englewood Cliffs, NJ (1963).
12. Slater J. C., *The Calculation of Molecular Orbitals*. John Wiley, New York (1979).
13. Weast R. C., *CRC Handbook of Chemistry and Physics*, 64th edition. CRC Press, Boca Raton, Florida (1983–1984).
14. Shulman R. G., Yafet Y., Eisenberger P. and Blumberg W. E., *Proc. Natl. Acad. Sci., U.S.A.* **73**, 1384 (1976).
15. Rao C. N. R., Bhat V., Nagarajan R., Ranga Rao G. and Sankar G., *Phys. Rev.* **B39**, 9621 (1989).
16. Adhyapak S. V. and Nigavekar A. S., *J. Phys. Chem. Solids* **37**, 1037 (1976).
17. Levine B. P., *Phys. Rev.* **B7**, 2591 (1973).

PHILOSOPHICAL MAGAZINE LETTERS, 1991, VOL. 63, NO. 6, 345–353

Phase stability of Al_3Nb as a function of nickel additions

By H. R. P. INOUE†, M. KITAMURA‡, C. M. WAYMAN and HAYDN CHEN

Department of Materials Science and Engineering, University of Illinois, Urbana, Illinois 61801, U.S.A.

[*Received 29 September 1990§ and accepted 8 March 1991*]

ABSTRACT

Phase stability of the intermetallic compound Al_3Nb is investigated as a function of nickel additions by band structure calculations based on an extended Hueckel tight-binding method. With this method, the electronic structure and total energies of the $Al_{6-n}Ni_nNb_2$ compounds (where n is an integer from 0 to 6) are calculated for both $D0_{22}$ and $L1_2$ structures under the assumption that nickel substitutes for aluminium. The electronic total energies obtained from integration of the energy states of all electrons considered have shown that the $D0_{22}$ structure is stable in the binary Al_3Nb compound as compared with the $L1_2$ structure; conversely, the $L1_2$ structure is stable for compounds with n values greater than 1. These calculations are in good agreement with X-ray diffraction results reported by Schubert and co-workers. Differences in the electronic total energy per atom between $D0_{22}$ and $L1_2$ are $-0{\cdot}79$ eV and $0{\cdot}56$ eV for n equal to 0 and 2, respectively.

§1. INTRODUCTION

There is considerable interest in trialuminide-based intermetallic compounds containing transition elements, such as Ti, Zr, Hf, Nb and Ta, as promising structural materials because of their relatively high melting point, low density and good oxidation resistance. However, partly because of the low symmetry, and ordered tetragonal $D0_{22}$ structure, they are mostly brittle at ambient temperature (Yamaguchi, Umakoshi and Yamane 1987). A legitimate approach to ductilize these trialuminides is to transform them to structures having higher symmetry such as an ordered cubic $L1_2$ structure. It is well known that Al_3Ti transforms from the $D0_{22}$ to the $L1_2$ structure (fig. 1) by the addition of transition elements in the third period of the periodic table (Raman and Schubert 1965, Seibold 1981, George, Porter, Henson, Oliver and Oliver 1989). Recent compression tests have shown appreciable improvement of room temperature ductility for $L1_2$ Al_3Ti containing iron that was produced through hot isostatic pressing by reducing cavities formed during casting (Inoue, Cooper, Favrow, Hamada and Wayman 1990).

In an attempt to determine the relationship between phase stability, bonding characteristics, and mechanical properties of Al_3Ti, theoretical investigations have recently been made by means of calculations of electronic total energies using three

§Received in final form 2 January 1991.

† Formerly: H. R. Pak.

‡ Permanent address: Department of Electrical and Electronic Engineering, Faculty of Engineering, Utsunomiya University, Utsunomiya, Tochigi 321, Japan.

Fig. 1

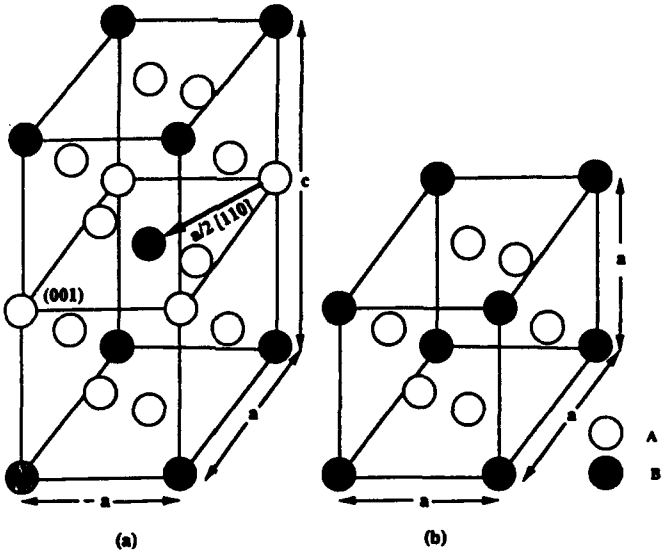

Unit cells of (*a*) a $D0_{22}$-type and (*b*) an $L1_2$-type structure for A_3B compounds.

methods: an augmented spherical-wave method, ASW (Carlsson and Meschter 1989), a full-potential linearized augmented plane-wave method, FLAPW (Fu 1990), and a linear muffin tin orbital method, LMTO, (Asta, Sluiter, de Fontaine, Hong, Freeman and Singh 1990). Calculations using the ASW and FLAPW methods have shown that the $D0_{22}$ structure is stable in Al_3Ti, as compared with the $L1_2$ structure, in agreement with X-ray experiments (Raman and Schubert 1965). Calculations with the LMTO method, conversely, disagree thereby indicating that this method needs to be modified. Despite the fact that most attractive trialuminides require the presence of the $L1_2$ structure stabilized by ternary additions, no theoretical studies based on first principle calculations have been conducted to determine the effect of ternary additions on phase stability of trialuminides. To determine such effects, we have performed a series of calculations using an extended Hueckel tight-binding method, XHTB (Grunes, Leapman, Wilker, Hoffmann and Kunz 1982).

The XHTB method has recently been applied to ionic perovskite-type compounds such as $KNiF_3$ (Kitamura and Muramatsu 1990a) and a K_2PdCl_6 crystal (Kitamura and Muramatsu 1990b). It has been widely believed that a calculation based on the tight binding method is applicable for evaluation of valence band structure, but not necessarily applicable for evaluation of conduction band structure. However, the band structure calculations for the above two compounds are in good agreement with experiments related not only with the valence band but also with the conduction band (Kitamura and Muramatsu 1990a, b). This is because in the calculation processes, atomic data from self-consistent-field calculations are used instead of empirical atomic data. This indicates that the XHTB method may be useful for evaluation of electronic structures for metallic compounds if self-consistently obtained atomic data are used. Another reason for adoption of this method is that it is more powerful when applied to compounds whose unit cells are either larger or more complicated, such as K_2PdCl_6 and $Al_{19}Ti_5$, which is composed of six f.c.c. lattices, in Fe-modified $L1_2$-type Al_3Ti

(Pak, Pak, Wayman and Cooper 1990). That is not always the case for the FLAPW and LMTO methods. The present paper deals with some results relating to phase stability of the intermetallic ompounds Al_3Nb as a function of nickel composition. This compound is believed to be more attractive than Al_3Ti because of its high melting point (1600°C) and relatively low density (4·91 g cm^{-3}) (the melting point and density of Al_3Ti are 1350°3 and 3·36 g cm^{-3}, respectively).

§2. Theoretical background

In this section we briefly describe the XHTB method, and a practical calculation procedure. Details of the theory is found in a paper by Kitamura and Muramatsu (1990a). We solve the Schroedinger equation

$$H\Psi_{\mathbf{k}}(\mathbf{r}) = E_{\mathbf{k}}\Psi_{\mathbf{k}}(\mathbf{r}), \tag{1}$$

where H is a one-electron Hamiltonian consisting of a kinetic-energy term and the crystal potential, which is periodic with the periodicity of the lattice. The one-electron wave function $\Psi_{\mathbf{k}}(\mathbf{r})$ is specified by a wave vector $\mathbf{k}$ within the first Brillouin zone (BZ). According to the Bloch theorem in the tight-binding scheme the wave function is written as

$$\Psi_{\mathbf{k}}(\mathbf{r}) = \sum_{\mu}\sum_{L} u_L^{(\mu)}(\mathbf{k})\chi_L^{(\mu)}(\mathbf{k},\mathbf{r}), \tag{2a}$$

$$\chi_L^{(\mu)}(\mathbf{k},\mathbf{r}) = \sum_{\mathbf{r}_\mu} \exp i\mathbf{k}\cdot\mathbf{r}_\mu\, \phi_L^{(\mu)}(\mathbf{r}-\mathbf{r}_\mu)N^{-1/2}, \tag{2b}$$

where summation over μ is taken for eight independent atoms, fig. 2; $\mathbf{r}_\mu$ denotes their positions throughout the crystal. In the present paper, the same crystal structure, fig. 2, is used for both the $D0_{22}$ and $L1_2$ structures in order to eliminate the possible program dependency of energy calculations; that is, using the structure in fig. 2 (with c/a being 2), we simply obtain energies that are twice as much as what an $L1_2$ structure would have.

Fig. 2

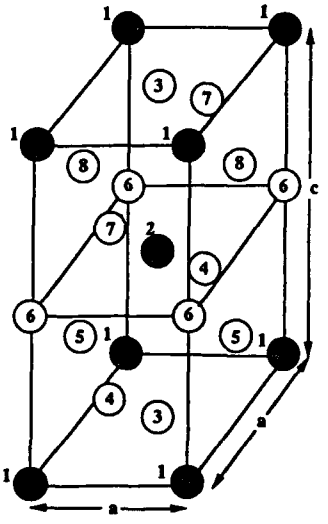

Eight independent sites in a $D0_{22}$ unit cell.

Here, $\phi_L^{(\mu)}(\mathbf{r}-\mathbf{r}_\mu)$ is the atomic orbital function with a quantum state denoted by the collective index $L=(l,m)$ for the μ atoms located at $\mathbf{r}_\mu$, where l is the quanum number containing a principal quantum number and the usual orbital angular-momentum quantum number, and m denoting its degenerate components for a real base. N_μ is the number of the μ atoms, being equal to $N/8$, where N is the total number of atoms forming the compounds. The coefficient $u_L^{(\mu)}(\mathbf{k})$ and energy $E_\mathbf{k}$ are obtained as a function of the wave vector $\mathbf{k}$ by solving the secular equation given in eqns. (3 *a*), (3 *b*) and (3 *c*) in the reference Kitamura and Muramatsu (1990a). In the evaluation of the matrix elements of $\mathbf{H}$ given in eqn. (3 *b*) in the reference, the Wolfsberg–Helmholtz approximation (Wolfsberg and Helmholtz 1962) is used:

$$\langle\phi_L^{(\mu)}(\mathbf{r})|\mathbf{H}|\phi_{L'}^{(\nu)}(\mathbf{r}-\mathbf{r}_\nu)\rangle=\frac{G}{2}(\varepsilon_L^{(\mu)}+\varepsilon_{L'}^{(\nu)})\langle\phi_L^{(\mu)}(\mathbf{r})|\phi_{L'}^{(\nu)}(\mathbf{r}-\mathbf{r}_\nu)\rangle. \tag{3}$$

Here, G is an adjustable parameter with value chosen to be 1·75 (Kitamura and Muramatsu 1990a), and $\varepsilon_L^{(\mu)}$ is the atomic energy for the L state of the μ atom. In the present calculation, no charge transfer is taken into account because all atoms in the Al_3Nb-based intermetallic compounds are treated to be neutral because of their metallic nature. The overlap integral, the third term in (3), is obtained in a similar way to those described by Kitamura and Muramatsu (1990a).

The primary objective of this study is to compare electronic total energies for the $D0_{22}$ and $L1_2$ structures of Al_2Nb-based compounds, which are calculated from the total density of states, $D(E)$, and to discuss the phase stability. The electronic total energy E_{total} is given by $E_F E\,D(E)\,dE$, where E_F is the Fermi level of the compounds.

Now we go into a practical calculation procedure. Input data for calculations are atomic data given by Herman and Skillman (1963), the value (1·75) of the adjustable parameter G, and the lattice parameters adopted for Al_3Nb: $a=7{\cdot}264$ au (i.e. 0·3844 nm) and $c/a=2{\cdot}239$ for the $D0_{22}$ structure (Lundin and Yamamoto 1966); and $a=7{\cdot}6158$ au (i.e. 0·403 nm) for the $L1_2$ structure (Schubert, Meissner, Raman and Rossteutscher 1964). Using a self-consistent-field calculation (Kitamura, Sugiura and Muramatsu 1989) based on the prescription of Herman and Skillman with the following exchange-correlation parameters given by Schwarz (1972), we obtain atomic orbitals. The Schwarz exchange parameters are: 0·72795 for aluminium; 0·70357 for niobium; and 0·70843 for nickel. Throughout the present band structure calculations, we use the two outer atomic orbitals for each atom, which are: 3s and 3p orbitals for Al ($1s^22s^22p^63s^23p^1$); 3d and 4s for Ni ($1s^22s^22p^63s^23p^63d^84s^2$); and 4d and 5s for Nb ($1s^22s^22p^63s^23p^63d^{10}4s^24p^64d^45s^1$).

§3. Results and discussion

Let us first apply the XHTB method to Al_3Ti to calculate its electronic total energy for comparison with the results obtained by means of the ASW method (Carlsson and Meschter 1989) and FLAPW method (Fu 1990). For this purpose, we use the Schwarz exchange parameter of 0·71648 and the 3d and 4s orbitals for Ti ($1s^22s^22p^63s^23p^63d^24s^2$), and adopt the following lattice parameters for Al_3Ti: $a=7{\cdot}2717$ au (i.e. 0·3848 nm) and $c/a=2{\cdot}231$ for the $D0_{22}$ structure; and $a=7{\cdot}3702$ au (i.e. 0·3968 nm) for the $L1_2$ structure (Porter, Hisatsune, Sparks, Oliver and Dhere 1989). Since no $L1_2$ phase exists in the binary Al_3Ti, the lattice parameter taken from $Al_{69}Fe_6Ti_{25}$ is used. According to the electronic total energy as a function of unit formula volume reported by Fu (1990), this lattice parameter is most likely because it

gives a minimum of the total energy. Our results for the electronic total energy show that the $D0_{22}$ structure is stable as opposed to the $L1_2$ structure, in agreement with experiments (Porter *et al.* 1989). The energy difference per atom between these two structures is 0·19 eV, whereas, in work by Carlsson and Meschter (1989) and by Fu (1990), the energy difference per atom is 0·06 eV and 0·025 eV, respectively. The values obtained by these two methods differ by a factor of 4 and 8, respectively, from that by the present XHTB method. We believe that this discrepancy is incurred by neglecting the contribution of the 3p orbital for Ti. Nevertheless, the XHTB method can predict the stability of the $D0_{22}$ phase over the $L1_2$ phase in Al_3Ti in a similar way to that using the ASW and FLAPW methods.

It should be pointed out, prior to going further into results from Al_3Nb-based compounds, that we compare the difference in electronic total energy between the $D0_{22}$ and $L1_2$ structures to evaluate the phase stability. The reason is that the difference of Gibbs' free energies corresponding to these two phases, $\Delta G = \Delta H - T\Delta S$, is essentially equal to the difference in enthalpy ΔH because of the negligible change in the configurational entropy ΔS. The enthalpy differences are internal energy changes, and are primiarly from electronic band energies.

Now we go into band structure calculations for $Al_{6-n}Ni_nNb_2$ compounds. For the binary Al_3Nb, calculations are made in a similar way to those for Al_3Ti, while for the case of the ternary compounds, calculations are made for specific atomic configurations, fig. 3, in order to maintain lattice periodicity. As seen in fig. 3, every site is occupied by an individual atom with an occupation probability of 1. That is, the value of n must be an integer between 0 and 6, provided that there is a quasi-binary phase between Al_3Nb and Ni_3Nb. As shown in the table, the value n can only be even for the $L1_2$ structure, while for the $D0_{22}$ structure, it can be either even or odd. For each n value, there is only one atom configuration in the case of the $L1_2$ structure, shown in parts (1)–(4) of fig. 3 (note niobium atoms occupying sites 1 and 6). In the case of the $D0_{22}$ structure, conversely, there are several configurations because of non-equivalency of sites: 1 configuration for n being 0 and 6; 3 for n being 1 and 5; 6 for n being 2 and 4; and 8 for n being 3. Figure 3 show all atomic configurations used for band structure calculations. For example, taking the case of n being 1, this aspect is explained. As seen in fig. 2, sites 4, 5, 7, 8 are equivalent from symmetrical considerations, while sites 3, 4 (5, 7 or 8), and 6 are not. As a result, there are three sites at which one nickel atom can be placed in the unit cell. They are either 3, 4 (5, 7 or 8) or 6, whose corresponding atomic configurations are shown in parts (6)–8) of fig. 3, respectively. In fig. 3, all atomic configurations used for band structure calculations are shown.

Using atom positions defined in fig. 3 and other input parameters mentioned above, band structure calculations can be performed. Figure 4 shows two examples of the total density of states (TDOS) obtained using the XHTB method. From these TDOSs, the values of the electronic total energy E_{total} are obtained, and are listed in the table along with differences in E_{total} between the $D0_{22}$ and $L1_2$ structures. From this table it is seen that the $D0_{22}$ structure is stable for the binary Al_3Nb compound as opposed to the $L1_2$ structure, in agreement with X-ray experiments (Lundin and Yamamoto 1966). Here it should be emphasized from the table that the $L1_2$ structure is found to be stable when nickel is added to Al_3Nb, provided that nickel substitutes for aluminium in the quasi-binary system Al_3NbNi_3Nb. This effect of nickel additions on phase stability is visualized by plotting the E_{total} values as a function of nickel composition (and the value of n). As seen in fig. 5, a stable phase with the $L1_2$ structure appears in the Al–Ni–Nb

Fig. 3

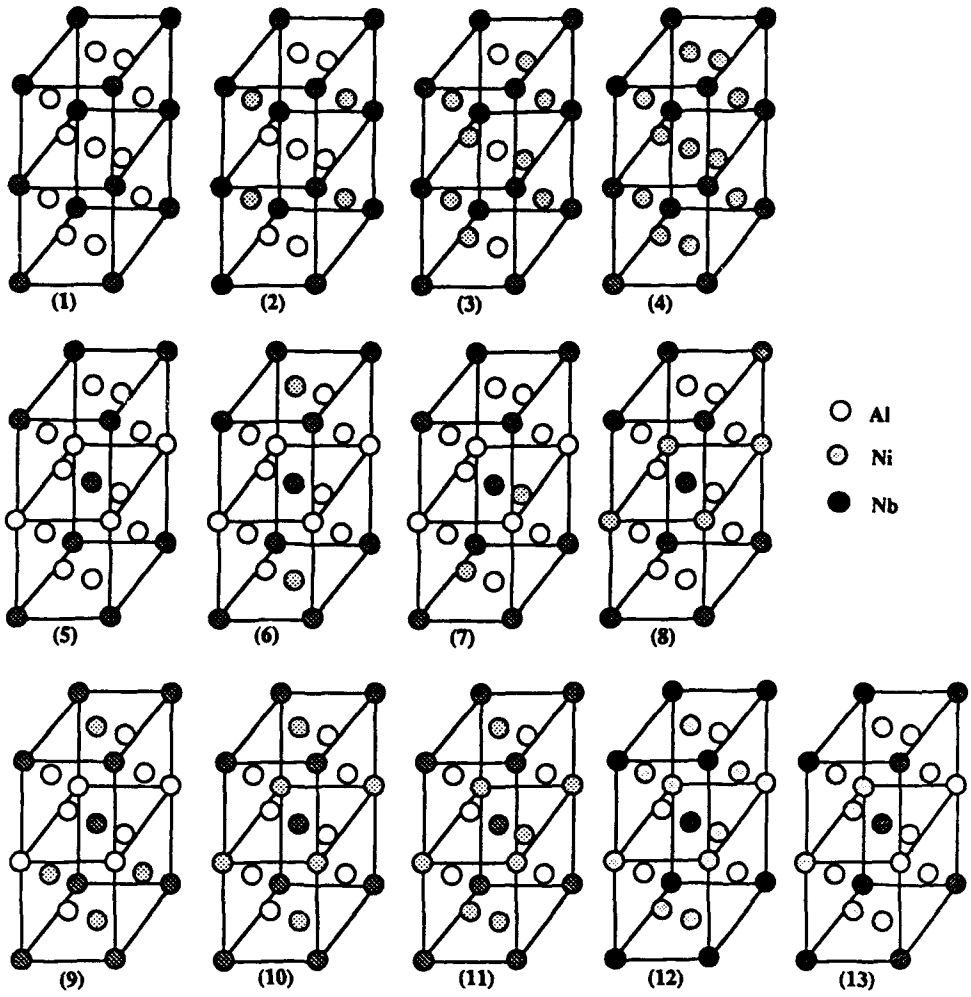

Atom positions in $D0_{22}$ and $L1_2$ unit cells of $Al_{6-n}Ni_nNb_2$ compounds, used for calculation of electronic total energies.

system at a nickel composition near 10 at.%. This is surprising when the results of X-ray experiments by Schubert *et al.* (1964) are compared; that is, they found an $L1_2Al_5Ni_1Nb_2$ phase with lattice parameter of 0·403 nm. In the present band structure calculations for the $L1_2$ structure, we have adopted this lattice parameter. Although electronic total energies are dependent on lattice parameters, this adoption is reasonable because changes in the lattice parameter by ternary additions are not critical (Porter *et al.* 1989), especially for compounds with low concentrations of ternary additions. A recent X-ray study (Subramanian, Simmons, Mendiratta, Dimiduk 1989), however, disagrees with the results by Schubert *et al.* (1964); no $L1_2$ phase has been detected in two Al_3Nb alloys containing nickel. In order to resolve this experimental discrepancy, we suggest that Al_3Nb alloys containing nickel should be heat treated at different temperatures followed by detail analysis of the X-ray data.

Fig. 4

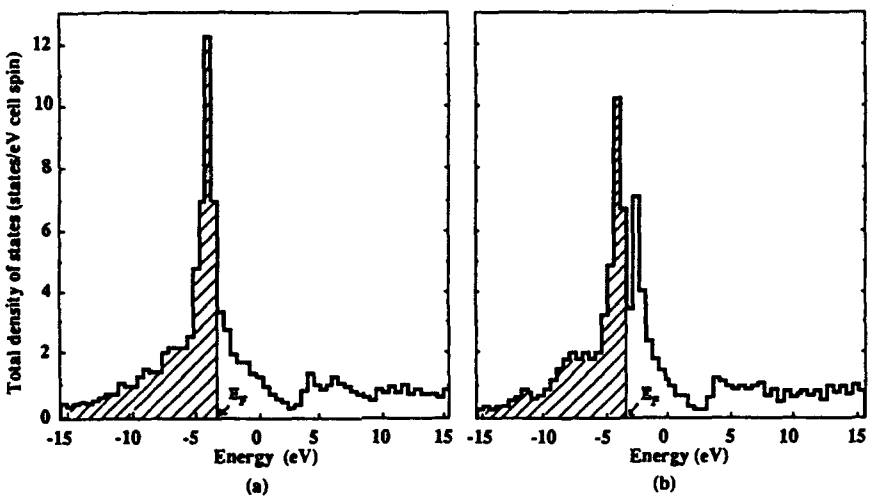

Total density of states of Al_3Nb in (*a*) the $D0_{22}$ and (*b*) the $L1_2$ structures, measured from vacuum level.

Fig. 5

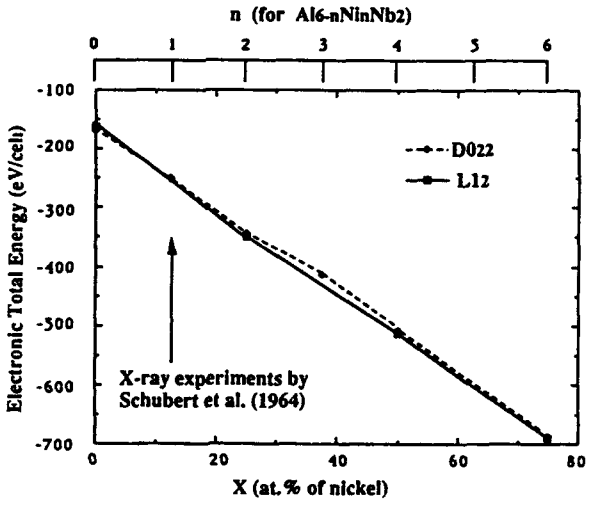

Electronic total energies for the $D0_{22}$ and $L1_2$ structures of Al_3Nb as a function of nickel composition. Arrow indicates Al_3Nb containing 12·5 at.% Ni (i.e. $n=1$) which was found to have an $L1_2$ structure by Schubert *et al.* (1964).

Electronic total energy for $Al_{6-n}Ni_nNb_2$ and Al_3Ti.

Crystal	n	E_{total} (eV/cell)	$\Delta E_{D0_{22}} - \Delta E_{L1_2}$ (eV/atom)	Remarks
$Al_{6-n}Ni_nNb_2$				
$L1_2$	0	−162·80		Fig. 3 (1)
$D0_{22}$	0	−169·14		Fig. 3 (5)
			−0·79	
			−0·08	(Carlsson and Meschter 1989)
$D0_{22}$	1	−250·41		Fig. 3 (6)
$D0_{22}$	1	−252·30		Fig. 3 (7)
$D0_{22}$	1	−250·41		Fig. 3 (8)
			—	
$L1_2$	2	−349·37		Fig. 3 (2)
$D0_{22}$	2	−344·91		Fig. 3 (9)
$D0_{22}$	2	−343·78		Fig. 3 (10)
			0·56	
$D0_{22}$	3	−413·51		Fig. 3 (11)
			—	
$L1_2$	4	−513·29		Fig. 3 (3)
$D0_{22}$	4	−509·25		Fig. 3 (12)
			0·51	
$L1_2$	6	−689·67		Fig. 3 (4)
$D0_{22}$	6	−688·59		Fig. 3 (13)
			0·14	
Al_3Ti				
$L1_2$	0	−170·50		
$D0_{22}$	0	−171·97		
			−0·19	
			−0·06	(Carlsson and Meschter 1989)
			0·025	(Fu 1990)

Of 28 atomic configurations for the n value in $Al_{6-n}Ni_nNb_2$, electronic total energy calculations have been performed for 13 configurations, fig. 3. As seen in the table (for n being 1 and 2), the results show that there are some differences in E_{total} among $D0_{22}$ configurations for the same value of n. However, these differences are not significant because of rather large energy differences present between the $D0_{22}$ and $L1_2$ structures for the same n value. We believe that all the possible atomic configurations for a given n value are mixed in a fashion to construct a compound with the $D0_{22}$ structure, if it is stable in comparison with the $L1_2$ structure. In the present XHTB calculations for the binary and ternary $Al_{6-n}Ni_nNb_2$ alloys, we have neglected the contribution of the third outer orbitals for Ni (i.e. 3p orbital) and Nb (i.e. 4p orbital). This may result in relatively large structural energy differences between $L1_2$ and $L1_2$ structures, compared with those reported for the binary Al_3Nb alloy (Carlsson and Meschter 1989). Although we do not think such a contribution reverts the present prediction of phase stability, XHTB calculations including those p orbitals are underway in order to obtain more accurate structure energies.

§4. Conclusion

Band structure calculations of binary intermetallic compounds Al_3Nb and Al_3Ti and ternary intermetallic compounds $Al_{6-n}Ni_nNb_2(n=1,2,3,4,6)$ in the $D0_{22}$ and $L1_2$ structures have been performed based on an extended Hueckel tight-binding method. The total density of states and electronic total energies are presented. In both binary compounds, the $D0_{22}$ structure is shown to be stable as compared with the $L1_2$ structure, in good agreement with X-ray diffraction experiments. The effect of nickel additions on phase stability of Al_3Nb has been investigated and it has been found that nickel additions stabilize the $L1_2$ structure. The present results have shown that there is a stable $L1_2Al_3Nb$ phase bearing nickel whose composition is greater than 10 at.%. This is in good agreement with X-ray experiments by Schubert *et al.* (1964) who found an $L1_2Al_3Nb$ phase containing 12·5 at.% Ni, although in a recent report by Subramanian *et al.* (1989) no such phase has been detected. Detailed X-ray experiments need to be carried out for clarification of this experimental disagreement.

Acknowledgments

Two of the authors (H.R.P.I. and C.M.W.) are grateful to Memory Storage Devices, Inc. for partial support. One author (M.K.) would like to thank the Japan Ministry of Education for supporting a visit to the University of Illinois. The computer calculations have been conducted by use of a VAX computer at the Materials Research Laboratory of the University of Illinois.

References

Asta, T., Sluiter, M., de Fontaine, D., Hong, T., Freeman, A. J., and Singh, P. P., 1990, *Mater. Res. Soc. Symp. I, Proc.* (in press).

Carlsson, A. E., and Meschter, P. J., 1989, *J. Mater. Res.*, **4**, 1060.

Fu, C. L., 1990, *J. Mater. Res.*, **5**, 971.

George, E. P., Porter, W. D., Henson, H. M., Oliver, W. C., and Oliver, B. F., 1989, *J. Mater. Res.*, **4**, 78.

Grunes, L. A., Leapman, R. D., Wilker, C. N., Hoffmann, R., and Kunz, A. B., 1982, *Phys. Rev.* B, **25**, 7157.

Herman, F., and Skillman, S., 1963, *Atomic Structure Calculations* (Englewood Cliffs, NJ: Prentice Hall).

Inoue, H. R. P., Cooper, C. V., Favrow, L. H., Hamada, Y., and Wayman, C. M., 1990 (to be published).

Kitamura, M., and Muramatsu, S., 1990a, *Phys. Rev.* B, **41**, 1158; 1990b, **42**, 1417.

Kitamura, M., Sugiura, C., and Muramatsu, S., 1989, *Phys. Rev.* B, **39**, 10288.

Lundin, C. E., and Yamamoto, A. S., 1966, *Trans. Met. Soc. AIME*, **669**, 863.

Pak, H. R., Pak, J. S. L., Wayman, C. M., and Cooper, C. V., 1990, *Morris E. Fine Symp. Proc.*, TMS (in press).

Porter, W. D., Hisatsune, K., Sparks, C. J., Oliver, W. C., and Dhere, A., 1989, *Mat. Res. Soc. Symp. Proc.*, **133**, 657.

Raman, A., and Schubert, K., 1965, *Z. Metallkund*, **56**, 44, 99.

Schubert, K., Meissner, H.-G., Raman, A., and Rossteutscher, W., 1964, *Naturwissenschaften*, **51**, 287.

Schwarz, K., 1972, *Phys. Rev.* B, **5**, 2466.

Seibold, A., 1981, *Z. Metallkund*, **72**, 712.

Subramanian, P. R., Simmons, J. P., Mendritta, M. G., and Dimiduk, D. M., 1989, *Mat. Res. Soc. Symp. Proc.*, **133**, 51.

Wolfsberg, M., and Helmholtz, L., 1962, *J. chem. Phys.*, **20**, 837.

Yamaguchi, M., Umakoshi, Y., and Yamane, T., 1987, *Phil. Mag.* A, **55**, 301.

Submitted to J. Am. Ceram. Soc.

Phase Stability of Chemically Derived Enstatite ($MgSiO_3$) Powders

C. M. Huang*, D. H. Kuo*, Y. J. Kim*#, and W. M. Kriven*

Department of Materials Science and Engineering,
University of Illinois at Urbana-Champaign,
Urbana, Illinois 61801

Supported by the US Air Force of Scientific Research through a grant, number AFOSR-URI-90-0174

* Member, The American Ceramic Society.
# Now at: Korea Basic Science Center, Yusung, Daejun, Korea.

Abstract

A modified Pechini chemical preparation technique was used to produce enstatite ($MgSiO_3$) powder. By this method, low temperature stable orthoenstatite (OE) was obtained at 850 °C after 2 h of calcination. The effects of annealing temperature/time, initial particle size, chemical dopants and shear stress on the conversion of protoenstatite (PE) to clinoenstatite (CE) on the powder have been studied. The results indicated that the transformation of orthorhombic PE to monoclinic CE was sensitive to the initial powder particle size as well as type and amount of chemical dopant used. Sodium ions (Na^+), which were found to cause the formation of glassy phase around the PE grains, destabilized the PE phase physically. In comparison, manganese ions (Mn^{2+}), were found to preferentially substitute for the smaller Mg^{2+} ions in solid solution, and stabilized the PE phase chemically. The powders with different chemical dopants annealed at different temperatures were carefully examined by TEM and EDS. Stacking disorder of PE and CE, which gave rise to streaking in TEM selected area diffraction patterns (SADP), was observed.

Key words: [enstatite, $MgSiO_3$, powder preparation, phase transformation, physical stabilization,chemical stabilization.]

I. Introduction

Enstatite exists in three distinct crystalline modifications: ortho-, proto- and clino-enstatite (designated OE, CE and PE, respectively). The structures of these polymorphs and the nature of the transformations between them have been studied extensively and reviewed by several investigators.[1-8] The transformation of PE to CE, nominally at 865 °C on cooling, is reported to be instantaneous, diffusionless, oriented, athermal, stress inducible and reversible, thereby showing features of a martensitic phase transformation. Several workers reported a critical size effect for the PE to CE transformation.[9-11] A minimum size of 7 μm was given.[10] However, Mielcarek[12] found that the transformation also occurred for grains as small as 40 nm at a temperature of 500 K.

The effect of chemical dopants on the stabilization of PE was studied by Sarver and Hummel and others.[9,7,13] Addition of 1~2 mole % of $MnSiO_3$ in solid solution with $MgSiO_3$ stabilized the PE under certain conditions. Bloor[10] found that a CaO dopant in $MgSiO_3$ enhanced PE crystallite growth, thereby destabilizing the PE form. The early efforts at applying the PE to CE transformation to toughening of glass-ceramics in poorly nucleated compositions indicated that toughening from the metastable presence of the PE did not occur by simple analogy with the tetragonal to monoclinic transformation in zirconia.[7] A similar result was also obtained by Beall[14] in his study of enstatite glass-ceramics. In contrast to the transformation in zirconia which has a positive volume increase on cooling (3 % at 950 °C), the PE to CE transformation is accompanied by a molar unit cell volume change of -5.5% and a unit cell shape change of 18.3°.[8] Bloor [10] associated this PE to CE transformation with the mechanical degradation of steatite ceramics whose major component was enstatite. Kriven [8] point out that the large negative volume change and unit cell shape change were responsible for this, and indicated that this behavior was a form of "transformation weakening".

The transformation between PE and OE is much more sluggish compared to PE to CE.[5] Slow cooling rates and prolonged annealing are required to produce the order-

disorder type of transformation between OE and PE phase.

The phase transformations in enstatite have been comprehensively studied. However, most of work was done on single crystals,[5,15,16] natural minerals [2,5] and synthesized polycrystalline materials.[7,9,14] Little work has been done on synthesized powders, and in particular, chemically synthesized powder. Enstatite powders have usually been fabricated by a high temperature solid state reaction between MgO and SiO_2. Several previous studies have shown the difficulties of obtaining pure enstatite by solid state reaction, and mineralizers such as MgF_2 or LiF have been commonly used to drive the reaction to completion.[1, 9] Even with the mineralizers, prolonged firing is still required to form enstatite.[9] More recently, pure, fine-grained, enstatite monoliths have been synthesized by a sol-gel method.[17] However, no detailed phase transformation study was made.

Among the chemical synthetic processes, a modified version of the Pechini process has been demonstrated to be a quick and relatively easy method for preparing oxide powders.[18,19,20] The advantages of this process are that it allows a low temperature synthesis of high purity, high surface area, homogeneous powders without the use of expensive and unstable alkoxides. The main purposes of the present work were to prepare enstatite powder by the modified Pechini method and to understand how to control the PE to CE transformation by physical and chemical methods, in the chemically derived powder. The effects of annealing temperature/time, initial powder particle size, shear stress, and chemical dopants (Mn^{2+}, Na^{+}) on the PE to CE conversion were studied in detail using XRD, SEM and TEM/EDS.

II. Experimental Procedure

Enstatite powder ($MgSiO_3$) was prepared by a modified "Pechini method". The details of the preparation method are described in Fig. 1. The precursor used for magnesium was magnesium nitrate hexahydrate (Aldrich Chemical Co., Milwaukee, WI), silica (SiO_2) sol (AS-40, Ludox SM, Dupont Chemical Co., Wilmington, DE) which contained

0.08 wt % of sodium oxide (Na_2O), citric acid monohydrate (EM Science, Gibbstown, NJ) and ethylene glycol (Fisher Chemicals, Pittsburgh, PA). The decomposition of the Pechini prepared, organic precursors was monitored by differential thermal analysis (DTA, Model 910, TA Instruments (formerly Dupont), Wilmington, DE) and thermogravimetric analysis (TGA, Model 951, TA Instruments (formerly Dupont), Wilmington, DE) in the temperature range room temperature to 1000 °C. A heating rate of 5 °C/min was used for both analyses. Powders calcined at temperatures from 600 °C to 1100 °C were examined for phase distribution using an X-ray powder diffractometer (XRG 3100 R-ray Generator, Philips Electronic Instruments, Mahwah, NJ). The surface area of calcined powders was measured by BET (Model ASAP 2400, Micromeritics, Norcross, GA) nitrogen gas adsorption analysis.

In this study, two powders with different particle sizes were prepared in order to observe the effect of initial powder particle size on phase stability. The first, designated as powder A, was calcined at 900 °C for 2 h with a heating rate of 5 °C/min and furnace cooling. The second, designated as powder B, was as-calcined powder, followed by 5 h of attrition milling. Powders A and B were annealed at temperatures ranging from 1000 °C to1400 °C respectively. The annealing time was 10 h for each temperature, with a heating rate of 10 °C/min and furnace cooling.

Two chemical dopants, $Mn(NO_3)_2$ and $Na(NO_3)$, were used in the precursor. The powder doped with $Mn(NO_3)_2$ remained as-calcined, while the powder doped with $Na(NO_3)$ was attritor milled for 5 h after calcination. The dopants of $Mn(NO_3)_2$ and $Na(NO_3)_2$ were added to the precursors at levels of 1, 2, 4, and 6 mol % and 1, 3, 5, and 10 mol %, respectively. After calcination at 900 °C for 2 h, the powders were annealed at 1400 °C for 10 h, respectively.

The stress induced PE to CE transformation was conducted by grinding the powders in a mortar and pestle or in an attritor mill using yttria stabilized zirconia (TZP) media (5 mm diameter, 3 mol % Y_2O_3 stabilized ZrO_2, Union Process, Akron, OH) and a

high density polyethylene (HDPE) container. X-ray analyses of phase distributions were conducted on both annealed and ground powders. Semi-quantitative analyses using integrated intensity measurements from single peaks were difficult because of the complexity of the diffraction patterns and extensive peak overlap for PE and CE. Hence direct comparison of X-ray traces was used to obtained a qualitative indication of the changes in the phase distribution. SEM (Model ISI-130, International Scientific Instruments, Santa Clara, CA) and TEM (Model Hitachi 650, 100 KV, Hitachi Instruments, Inc., Conroe, TX) was conducted on the as-annealed and ground powders.

III. Results and Discussion

(1) Phase Development on Calcination

The X-ray spectra for the powder without chemical dopant, but calcined at temperatures between 600 °C and 900 °C for 2 h is given in Fig. 2. At 700 °C or below, the XRD of the powder revealed MgO peaks. As the temperature was increased to 800 °C, the MgO peaks disappeared and an amorphous material was obtained. Enstatite (OE) started to form at 850 °C. The surface area of calcined powders decreased rapidly from ~ 85 m^2/g at 700 °C to ~15 m^2/g at 850 °C, as indicated in Fig. 3. The powders tended to aggregate and even to sinter at higher calcination temperatures, thereby causing a drop in surface area. The morphology of $MgSiO_3$ powder calcined at 900 °C for 2 h is shown in Fig. 4. The agglomerates were highly porous and consisted of crystallites in the range of 0.1~0.2 μm in size.

Figs. 5(a) and (b) show TGA and DTA results for the $MgSiO_3$ gel respectively. The first weight loss in the TGA correlating with the first exotherm in the DTA at about 300 °C, as seen in Fig. 5(a) and (b) respectively, was thought to be associated with the decomposition of the gel. Another major weight loss occurred at about ~480 °C (Fig. 5(a)), which corresponded to the large exothermic DTA peak in Fig. 5(b). The exotherm observed during the large abrupt weight loss at 480 °C indicated that rapid de-polymerization

and pyrolysis may have occurred. Further weight loss at higher temperatures was attributed to the removal of carbon formed during the pyrolysis. The DTA analysis also revealed a small second exothermic peak at 850 °C, which was exactly the temperature of $MgSiO_3$ formation as indicated by X-ray analysis. The TGA analysis did not show any weight change in this temperature stage.

(2) Effects of Annealing Temperature/Time

Fig. 6 shows the phase distribution for the as-calcined powder (powder A) after 10 h of annealing at temperatures from 1000 °C to 1400 °C. The starting powder was identified as OE by X-ray diffractometry. After annealing at a temperature of 1150 °C for 10 h, PE peaks were observed in XRD patterns. PE to CE conversion took place at 1200 °C. The intensity of CE peaks increased with increasing annealing temperature. The effect of annealing time on the PE to CE transformation was investigated at a temperature of 1150 °C. A CE peak was observed after annealing for 30 h at this temperature stage.

Fig. 7 is an SEM micrograph of the morphology of powder A annealed at 1400 °C for 10 h, in which the agglomerates were sintered to density. Cracks generated from the PE to CE transformation were observed in each individual large grain.

The temperature for the OE to PE transformation observed for powder A was consistent with previous reports. Lee and Heuer reported,[7] from the study of crystallization of $MgSiO_3$ glass, that PE formed at temperatures ≥ 1200 °C and OE formed at temperatures ≤ 1000 °C. Murakami et al.[21] found that the OE to PE inversion proceeded at 1000 °C in synthetic specimens. The Sarver and Hummel [9] work revealed that OE inverted to PE at 1035°C, as determined by high temperature X-ray methods on pellets prepared with 2% LiF mineralizer. The transformation of CE to PE was assumed to occurr on cooling. Early studies suggested that there was a grain size effect controlling the PE to CE transformation.[9-11] The results of the present study, indicating that powders fired at higher temperatures produced more CE phase, were consistent with such an effect.

(3) Effects of Initial Powder Particle Size

To investigate the initial particle size effect, as-calcined powder (powder A) was attritor milled for 5 h. The attritor-milled powder (powder B), in which the particle size was reduced to less than 1 μm, was also annealed at the same temperatures and with the same heating and cooling conditions as for as-calcined powder A. The phase distribution for annealed powder B is seen in Fig. 8. Only small traces of PE were found at a temperature of 1150 °C. The conversion of OE to PE was almost complete at 1300 °C, and PE started to invert to CE at 1400 °C. These temperatures were shifted upward by 150 ~ 200 °C when compared with as-calcined powders. The morphologies of as-calcined and attrition milled powders are shown in Fig. 9(a) and 9(b), respectively. As calcined powders consisted of agglomerates composed of tiny crystallites, as seen in Figs 9 (a) and 4. During attrition the agglomerates were milled into tiny crystallites (Fig. 9 (b)). At higher annealing temperatures sintering and grain growth would be favored in agglomerates, but would be difficult in individually separated crystallites. This could explain the higher annealing temperature for phase conversion in attritor milled powders. A particle size effect controlling the onset of transformation was observed in dicalcium silicate (Ca_2SiO_4).[22,23] The results of the present study were consistent with such an effect.

(4) Effects of Chemical Dopants

The effects of Mn^{2+} versus Na^+ dopants on the phase stability of enstatite were completely different from each other. As seen in Fig. 10, the stability of PE increased with increasing of Mn^{2+} dopant in as-calcined powder A, at the expense of CE. With 1 mol % Mn^{2+}, the amount of PE to CE conversion was significantly reduced, while with 2 mol % or more Mn^{2+}, the CE peaks almost disappeared.

Sarver and Hummel [9] found that 1~2 mole % Mn^{2+} in solid solution with $MgSiO_3$ stabilized PE in a dense bar specimen. However, the same amount of Mn^{2+} in $MgSiO_3$ did

not stabilize PE in loose powders prepared by solid state reaction. Our current results indicated that the 1 ~ 2 mole % Mn^{2+} in solid solution with chemically derived $MgSiO_3$ powder significantly inhibited the PE to CE transformation.

In comparison, as shown in Fig. 11, the stability of PE decreased with the increasing levels of Na^+dopant in attritor milled powder B. For the powder containing 1 mol % Na^+, the pure PE was obtained after the powder was annealed at 1400 °C for 10 h. When the powder was doped with 3 mol % or more Na^+, PE to CE conversion was obvious. The intensity of CE peaks increased with the amount of Na^+.

Thus the Mn^{2+} dopant increased the stability of PE against conversion to CE, while Na+ decreased its stability. The mechanism of Na^+ and Mn^{2+} effects on PE stability was further examined by TEM.

(5) Effects of Shear Stress

The transformation of PE to CE is markedly susceptible to the influence of stress. In fact, CE has been claimed as a "stress mineral", in the sense that its formation is greatly facilitated by the presence of shear stress and/or strain.[24] Shear stress induced PE to CE conversion for as-calcined powder without chemical dopants is demonstrated in Fig. 12. Both attritor-milling for 1 h, or grinding by hand in a mortar and pestle, produced the PE to CE transformation. The amount of stress induced CE increased with increasing annealing temperature. For the same annealing temperature and heating and cooling conditions, it was more difficult to shear stress induce the PE to CE conversion in the powder doped with Mn^{2+} than in the powder doped with Na^+. Thus, the dopant effects were also reflected in the shear stress induced transformation behavior.

(6) TEM Observations

(A) Powders without Dopant: The $MgSiO_3$ powder calcined at 1100 °C for 10 h contained agglomerates of submicon-size grains, typically 0.1~0.2 μm in diameter. Their shapes were mostly irregular to semi-regular. Even though XRD of this powder indicated a major phase of OE (Fig. 2), TEM examination of the individual grains frequently revealed the presence of a stacking disorder composed of OE and PE layers as seen in Fig.13 (a). The strong streaking in the corresponding selected area diffraction pattern (SADP) indicated that the stacking disorder was perpendicular to the {100} planes of OE and PE.

The $MgSiO_3$ powder calcined at 1150 °C for 10 h had a few large grains of wider size range, typically 0.2 ~ 0.5 μm. Their shapes were more regular than those calcined at 1100 °C. XRD of this powder indicated a major phase of PE (Fig.2), whereas TEM examination showed that some smaller grains had a stacking disorder similar to the one observed in the powder calcined at 1100 °C. The [010] SADP of a larger grain in Fig.13 (c) and (d) illustrated the presence of a single phase, PE. In addition, forsterite grains (Mg_2SiO_4) were occasionally observed in this powder.

The grains from the $MgSiO_3$ powder calcined at 1400 °C for 10 h were much larger, and mostly larger than 1 μm. Although some grains were CE, more grains had stacking disorders mainly composed of PE and CE. The CE portions were frequently twinned. Figs.14 (a) and (b) displayed a BF image and corresponding [010] SADP, indicating the coexistence of PE and twinned CE phases. The stepped microstructure, which seemed to be responsible for the discontinuous rings shown in the SADP, possibly originated from the displacive PE to CE transformation. Another large grain (Fig.14 (c)), had a severe stacking disorder composed of PE layers and twinned CE layers in slightly different orientation, which was more evidently reflected in the corresponding SADP (Fig.14 (d)).

(B) Powders with Dopant: As explained for the XRD results, enstatite powders

doped with Mn^{2+} tended to stabilize the PE phase against conversion to CE. The $MgSiO_3$ powders with 4 mol % Mn^{2+}, calcined at 1400 °C for 10 h, had primarily PE grains of a wide size range, mostly larger than 0.5 μm. Figs. 15(a) and (b) show such a grain of PE and its [100] SADP. EDS analysis of this grain indicated that Mn^{2+} was present in solid solution with Mg^{2+} (Fig. 15(c)).

In contrast to Mn^{2+}, Na^+ doping destabilized the PE phase. TEM examination of the enstatite powders with 10 mol % Na^+, calcined at 1400 °C for 10 h, revealed large grains (>1 μm) of CE as well as some glassy phase and forsterite grains. Some CE grains appeared as slightly disordered rectangles with linear features in them. An example is shown in Fig. 16 (a) and (b), with its SADP. EDS of these CE grains indicated that there was no Na^+ inside the grains (Fig. 16(c)). The glassy phase, however, contained more Na^+ and less Mg^{2+} than expected (Figs. 17 (a) and (b)). The very diffuse ring patterns of the amorphous phase turned into more distinct ring patterns under electron beam induction, possibly due to microcrystallization of the glassy phase (Fig. 17 (c) and (d)).

From TEM observation, the effects of Na^+ ions on the conversion of PE to CE may be examined in the light of Bloor and others' early work. Bloor[10] found that PE crystals needed a glassy phase before they could grow appreciably. He found that a glass composed of MgO-BaO-Al_2O_3-SiO_2 provided less crystal growth than did one of MgO-CaO-Al_2O_3-SiO_2, with or without BaO. According to phase diagrams, CaO produces a glassy phase at an earlier stage in firing than does BaO, thereby allowing more time for crystal growth. However, the studies in Ca_2SiO_4 are apparently contrary to this argument. From the work of Chan et al.,[23] it was found that doping of K_2O in Ca_2SiO_4 caused the formation of glassy phase which surrounded Ca_2SiO_4 grains, resulting in metastable retention of β-phase at room temperature. The increased stability of β-phase was explained as the glass exerting a hydrostatic constraining force on the particle. Crystallization of glassy phase by low temperature annealing released this constraining force and permitted the transformation to occur. Contrary to the shear stress induced by mechanical grinding,

hydrostatic pressure favored the stabilization of β-phase, as reviewed by Guinier and Regourd.[25]

The difference between the $\beta \rightarrow \gamma$ conversion in Ca_2SiO_4 when compared to the PE → CE transformation in $MgSiO_3$ is, that the former experienced a volume increase, while the later experienced a volume shrinkage. The hydrostatic force from the glassy phase constrained the phase transformation with a volume expansion, but, it assisted the phase transformation with a volume contraction. Thus, the glass may have a dual role in enhancing grain growth as well as to provide a hydrostatic constraining force around PE particles. Both effects work to destabilize PE. In comparison, the stabilization of PE by the dopant Mn^{2+} was assumed by Sarver and Hummel [9] to be due to preferential substitution of the larger Mn^{2+} ions (r = 0.91 Å) for Mg^{2+} ions (r = 0.78 Å), which retarded the PE to CE transformation.

IV. Conclusion

In contrast to $MgSiO_3$ produced from mixed oxide powders, pure enstatite has been prepared by a relatively simple chemical method. By this method, OE can be produced at a relatively low firing temperature of 850 °C. The effects of annealing temperature/time, initial particle size, chemical dopants and shear stress on the conversion of PE to CE have been studied in the chemically prepared powders.

The temperatures at which OE to PE and PE to CE conversions occur were discovered to be significantly influenced by the initial powder particle size. As-calcined powder showed that large agglomerate particles tended to sinter and undergo grain growth upon firing, and thus the phase conversion of OE to PE and PE to CE occurred at much lower temperatures. On the other hand, attritor-milled powder, in which agglomerates were separated into fine crystallites, required much higher temperatures for transformation. The fact that powders fired at higher temperatures produced more CE, indicated that a grain size dependence operated for the PE to CE transformation. Sodium

ions (Na^+) were discovered to destabilize the PE phase through the presence of a glassy phase which enhanced grain growth, and provided a hydrostatic force assisting the imminent volume contraction on transformation. Thus, the role of the glassy phase may be looked upon as a physical effect on the transformation, as was demonstrated for Ca_2SiO_4.

In comparison, manganese ions (Mn^{2+}) were found to stabilize the PE phase through the preferential substitution of larger Mn^{2+} ions for Mg^{2+} ions, which discouraged the PE to CE conversion. This effect may be viewed as chemical stabilization.

TEM observations revealed stacking disorder of PE and CE, and twinned CE grains due to the PE to CE conversion.

Acknowledgments

The authors wish to thank Mehmet Gülgün for his help in preparing the enstatite powder by the Pechini process and for the powder surface analysis. Use of the electron microscopy facilities at the Center for Microanalysis of Materials in the Materials Research Laboratory at UIUC are acknowledged.

References

1. L. Atlas, "The Polymorphism of $MgSiO_3$ and Solid-State Equilibria in the System $MgSiO_3$-$CaMgSi_2O_6$," *J. Geol.* **60** [2] 152-197 (1952).

2. W. L. Brown, N. Morimoto, and J. V. Smith ,"A Structural Explanation of the Polymorphism and Transitions of $MgSiO_3$," *J. Geol.* **69** 609-616 (1961).

3. W. L. Brown and J. V. Smith, "High Temperature X-ray Studies on the Polymorphism of $MgSiO_3$," *Z. Kristallogr.*, **118** 186-212 (1963).

4. J. V. Smith, "Crystal Structure and Stability of the $MgSiO_3$ Polymorphs: Physical Properties and Phase Relations of Mg, Fe Pyroxenes," *Miner. Soc. Amer. Spec. Pap.*, **2** 3-30 (1969).

5. J. R. Smyth, "Experimental Study on the Polymorphism of Enstatite," *Amer. Mineral.*, **59** 345-353 (1974).

6. S. Sueno and C. T. Prewitt, "Models for the Phase Transition between Orthoferrosilite and High Clinoferrosilite," *Fortschr Mineral.*, **61** 223-241 (1983).

7. W. Lee and A.H. Heuer, "On the Polymorphism of Enstatite," *J. Am. Ceram. Soc.*, **70** [5] 349-360 (1987).

8. W. M. Kriven, "Possible Alternative Transformation Toughners to Zirconia: Crystallographic Aspects," *J. Am. Ceram. Soc.* **71** [12] 1021-1029 (1988).

9. J. V. Sarver and F. A. Hummel,"Stability Relations of Magnesium Metasilicate Polymorphs," *J. Am. Ceram. Soc.*, **55** [4]152-157 (1962).

10. E. C. Bloor,"Conversion in Steatite Ceramics," *Proc. Br. Ceram. Soc.*, **1-2** 320-325 (1964).

11. H. Thurnauer and A. R. Rodriguez, "Notes on the Constitution of Steatite," *J. Am. Ceram. Soc.*, **25** [15] 443-50 (1942).

12. W. Mielcarek, "The Influence of Proto-Clinoenstatite Transition on Mechanical Strength of Barium Steatite," *XIIth European Cryst. Meeting Coll. Abs.*, **3** 219 (1989)

13. C. B. Raleigh, S. H. Kirby, N. L. Carter, and H. G. Ave Lallement," Slip and the

Clinoenstatite Transformation as Competing Rate Processes in Enstatite," *J. Geophys. Res.*, **76** [17] 4011-22 (1971).

14. G. H. Beall,"Chain Silicate Glass-Ceramics," *J. of Non-Crytal. Solid*, **129** 163-173 (1991).

15. J. V. Smith, "The Crystal Structure of Protoenstatite," *Acta Cryst.*, **12** 515-519 (1959).

16. H. Boysen, F. Frey, H. Schrader, and G. Eckold, "On the Proto to Ortho-/Clino Enstatite Phase Transformation: Single Crystal X-ray and Inelastic Neutron Scattering," *Phys. Chem. Minerals.*, **17** 629-635 (1991).

17. L. M. Echeverria, "Enstatite Ceramic: A Multicomponent System via Sol-Gel," *J. Non-Cryst. Solid*, **147 & 148** 559-564 (1992).

18. M. Pechini, U. S. Patent No. 3 330697, July 11, 1967.

19. I. Nettleship, K. G. Slavick, Y. J. Kim, and W. M. Kriven,"Phase Transformation in Dicalcium Silicate: I, Fabrication and Phase Stability of Fine-Grain β Phase," *J. Am. Ceram. Soc.*, **75** [9] 2400-406 (1992).

20. I. Nettleship, J. L. Shull, Jr. and W. M. Kriven," Chemical Preparation and Phase Stability of Ca_2SiO_4 and Sr_2SiO_4 Powders," *J. Europ. Ceram. Soc.*, 11 291-298 (1993)

21. J. Murakami, Y. Takeuchi, and T. Yamanaka, "The Transition of Orthoenstatite to Protoenstatite and the Structure at 1080 °C," *Z. Kristallogr.*, **160** 299-312 (1982).

22. W. M. Kriven, C. J. Chan and E. A. Barinek, "The Particle-Size Effect of Dicalcium Silicate in a Calcium Zirconate Matrix," pp. 145-55 in Advances in Ceramics, Vol. **24A**, *Science and Technology of Zirconia III*, Edited by S. Somiya, N. Yamamoto, and H. Yanagida. American Ceramic Society, Westerville, OH, 1988.

23. C. J. Chan, W. M. Kriven and J. F. Young,"Physical Stabilization of the $\beta \rightarrow \gamma$ Transformation in Dicalcium Silicate," *J. Am. Ceram. Soc.*, **75** [6] 1621-1627 (1992).

24. A. Harker, Metamorphism, pp. 362, Methuen & Co. Ltd., London, 1950.

25. A. Guinier and M. Regourd, "Structure of Portland Cement Minerals," *Proc. Int.*

Symp. Chem. Cem., 5th, 1 1-43 (1968).

Figure Captions:

Fig. 1. Flow diagram showing the processing route for $MgSiO_3$ powder.

Fig. 2. XRD phase distribution for the $MgSiO_3$ gel without chemical dopants after calcination at different temperatures for 2 h (O = OE).

Fig. 3. Surface areas of undoped $MgSiO_3$ powders calcined in the temperature range 700 °C to 1000 °C.

Fig. 4. SEM micrograph of $MgSiO_3$ powder derived from the modified Pechini method and calcined at 900 °C for 2 h.

Fig. 5. Thermal analysis of $MgSiO_3$ gel prepared by the Pechini method (a) TGA (b) DTA.

Fig. 6. XRD phase distribution in powder A, after annealing for 10 h at temperatures ranging from 1100 °C to 1400 °C (O = OE, P = PE, and C = CE).

Fig. 7. SEM micrograph of $MgSiO_3$ powder calcined at 900 °C for 2 h, followed by annealing at 1400 °C for 10 h.

Fig. 8. XRD phase distribution in attritor milled powder B after annealing at temperatures ranging from 1100 °C to 1400 °C for 10 h (O = OE, P = PE).

Fig. 9. (a) SEM micrograph of $MgSiO_3$ powder calcined at 900 °C for 2 h (powder A). (b) The same powder after 5 h of attrition milling (powder B).

Fig. 10. XRD phase distributions in as calcined powder A, with different Mn^{2+} contents, after calcination at 1400 °C for 10 h (C = CE, P = PE).

Fig. 11. XRD phase distributions in attritor milled powder B, with different Na^{+} contents after calcination at 1400 °C for 10 h (P = PE, C = CE).

Fig. 12. XRD phase distributions showing shear stress induced PE to CE conversion for powder A annealed at 1400 °C for 10 h after calcination (P = PE, C = CE).

Fig. 13. TEM of image as-calcined powder A which was annealed at low temperatures without dopant. (a) BF image indicating a stacking disorder composed of OE and PE layers for powder annealed at 1100 °C for 10 h. (b) SADP of (a). (c) BF image of PE in the powder annealed at 1150 °C for 10 h. (d) SADP of (c).

Fig. 14. TEM image of $MgSiO_3$ without chemical dopant, and annealed at 1400 °C for 10 h. (a) BF image. (b) SADP of (a) in the [010] orientation, indicating coexisting PE and twinned CE (arrowed). (c) Stacking disorder composed of PE and twinned CE. (d) SADP of (c).

Fig. 15. TEM image of $MgSiO_3$ powder doped with 4 mol % Mn^{2+} and annealed at 1400 °C for 10 h. (a) BF image showing a PE grain. (b) Corresponding SADP in [100] orientation. (c) EDS analysis indicating Mn^{2+} present as a solid solution with Mg^{2+}.

Fig. 16. TEM image of $MgSiO_3$ powder doped with 10 mol % Na^{+} and annealed at 1400 °C for 10 h. (a) BF image of CE grain showing slightly distorted rectangles with linear features in the grain. (b) Corresponding SADP in [100] orientation. (c) EDS analysis indicating that there was no Na^{+} inside the grain.

Fig 17. TEM image of glassy phase found in attritor milled powder B doped with 10 mol % Na^+. (a) BF image of glassy phase. (b) EDS analysis indicating Na^+ in the glassy phase. (c) Glassy phase diffuse ring SAD patterns. (d) Crystallization of the amorphous phase under electron beam irradiation.

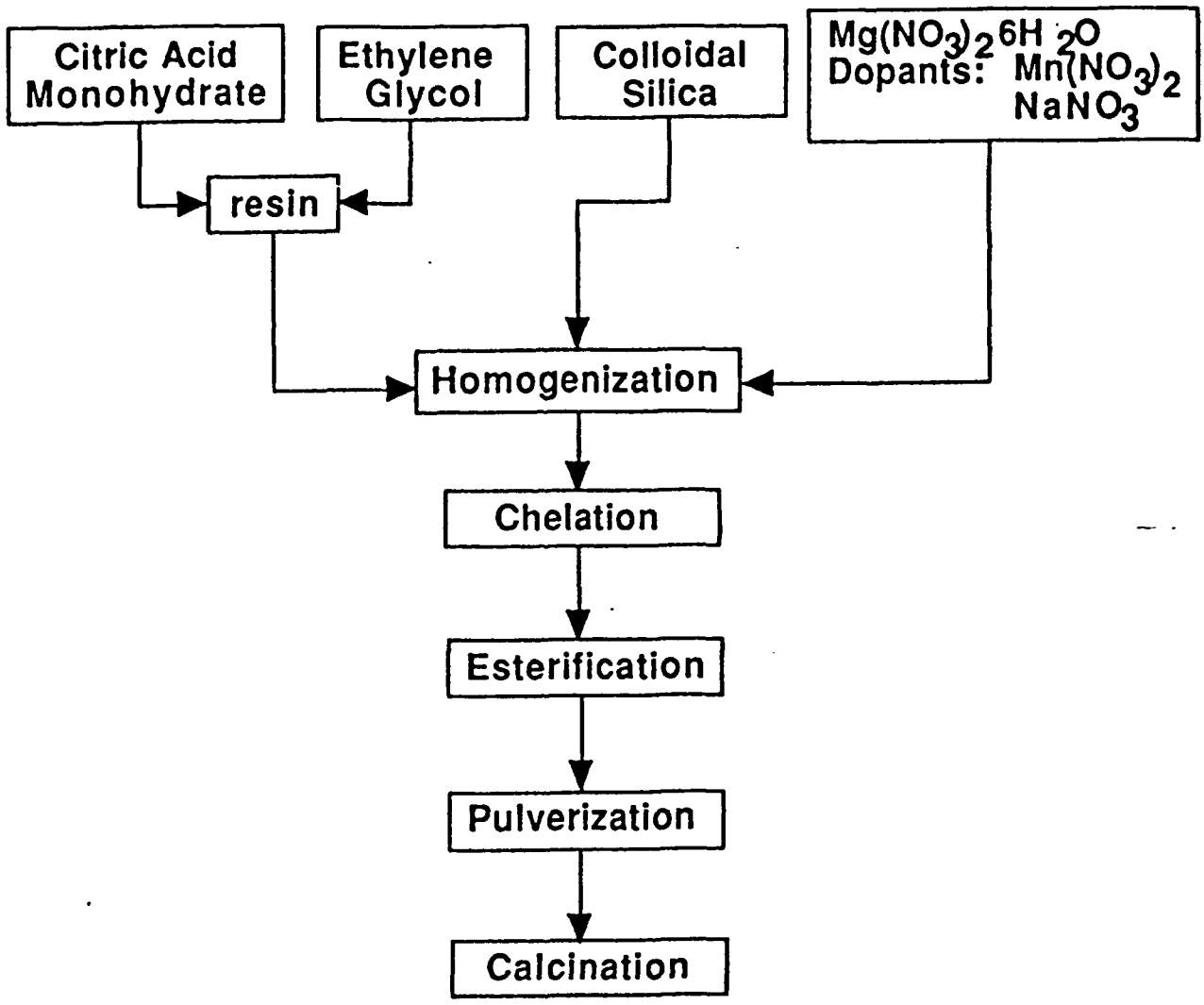

Fig. 1. Flow diagram showing the processing route for $MgSiO_3$ powder.

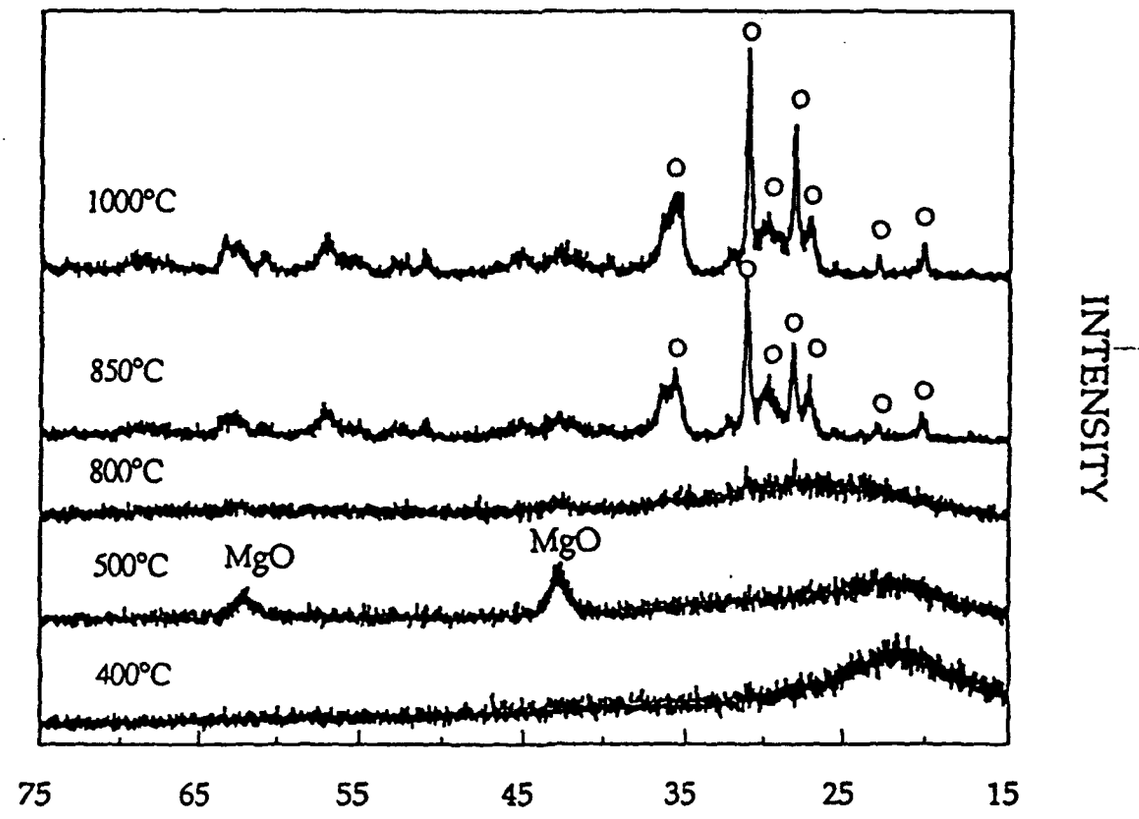

Fig. 2. XRD phase distribution for the $MgSiO_3$ gel without chemical dopants after calcination at different temperatures for 2 h (O = OE).

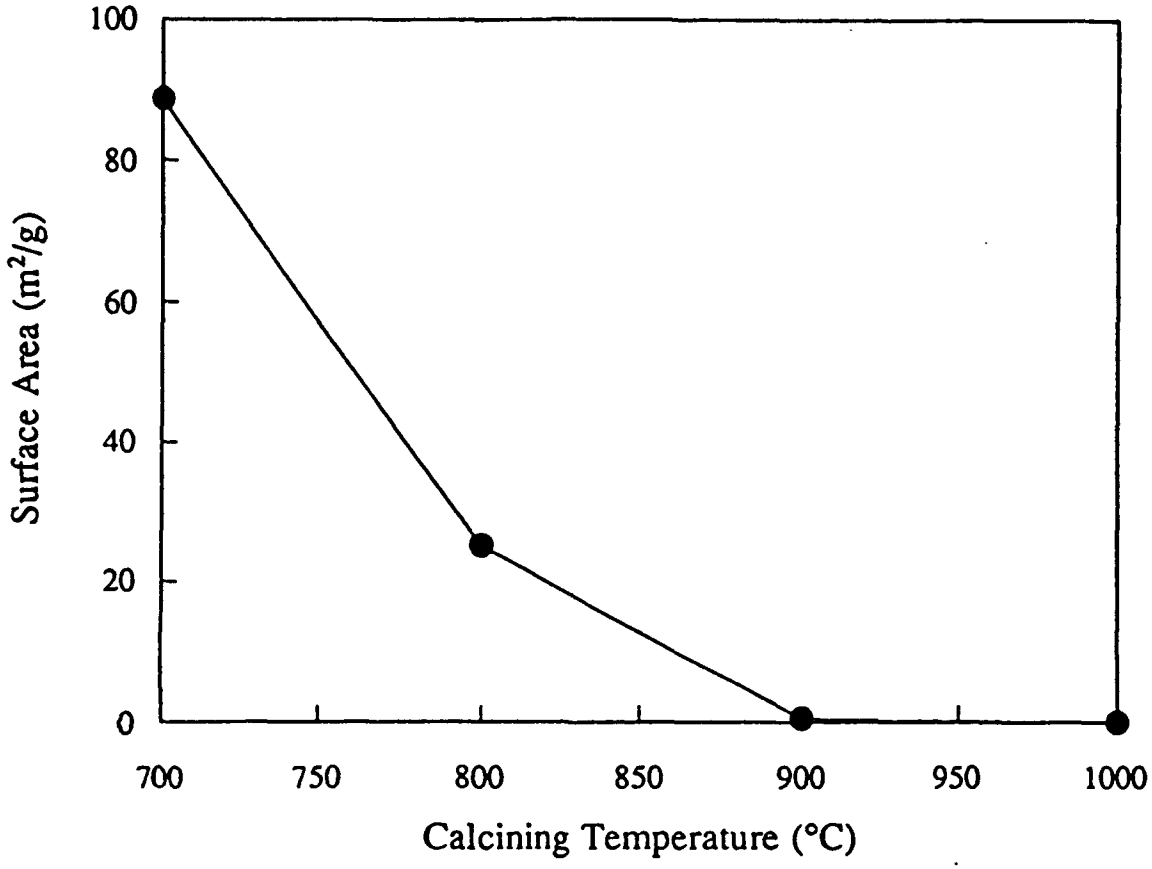

Fig. 3. Surface areas of undoped $MgSiO_3$ powders calcined in the temperature range 700 °C to 1000 °C.

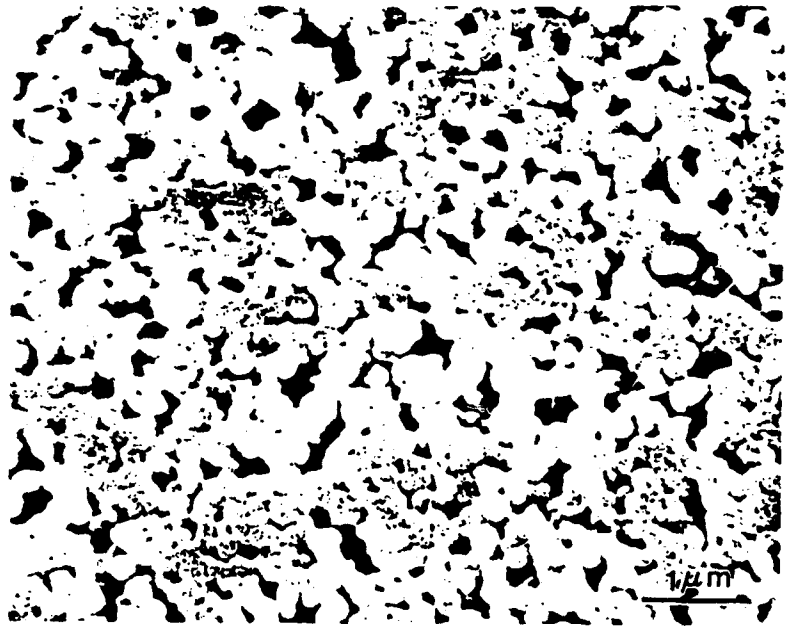

Fig. 4. SEM micrograph of $MgSiO_3$ powder derived from the modified Pechini method and calcined at 900 °C for 2 h.

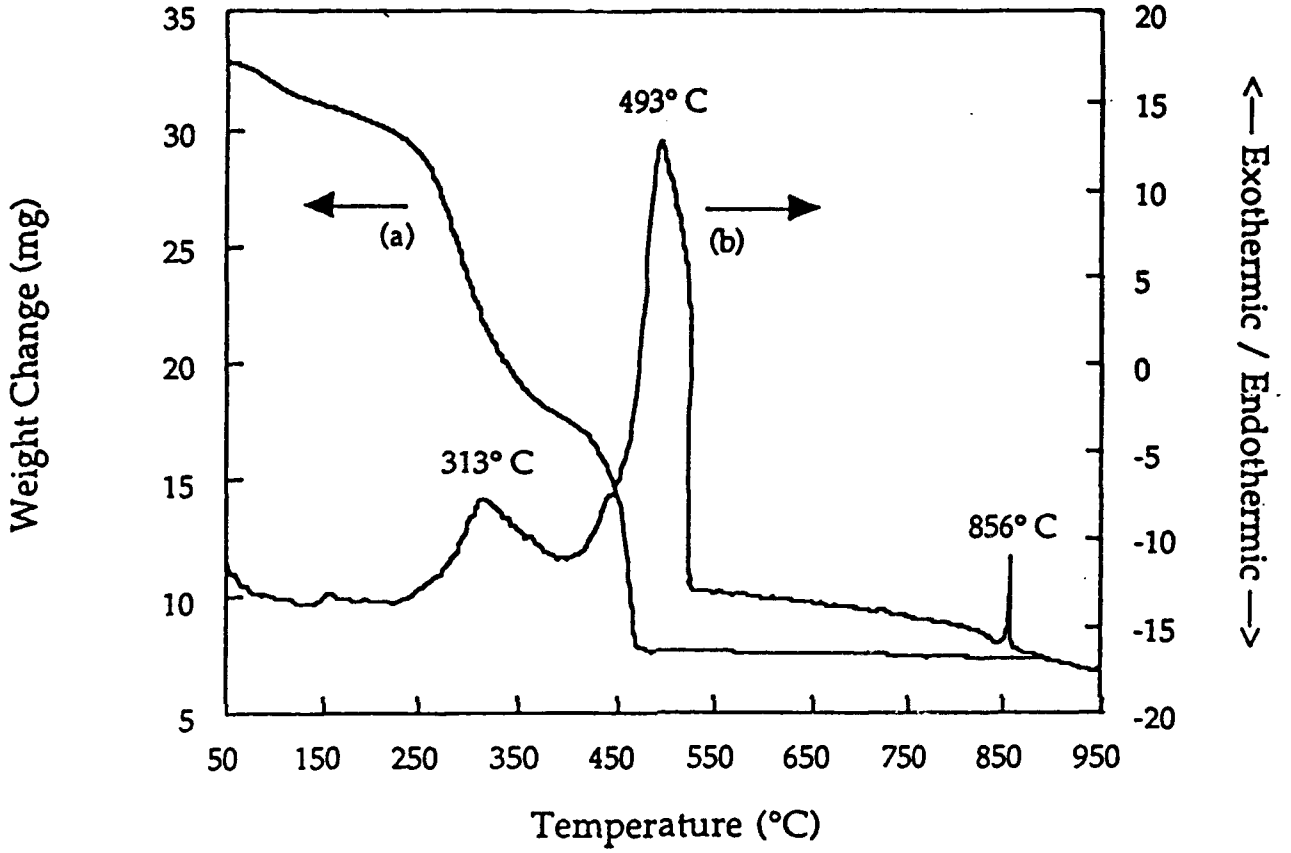

Fig. 5. Thermal analysis of $MgSiO_3$ gel prepared by the Pechini method (a) TGA (b) DTA.

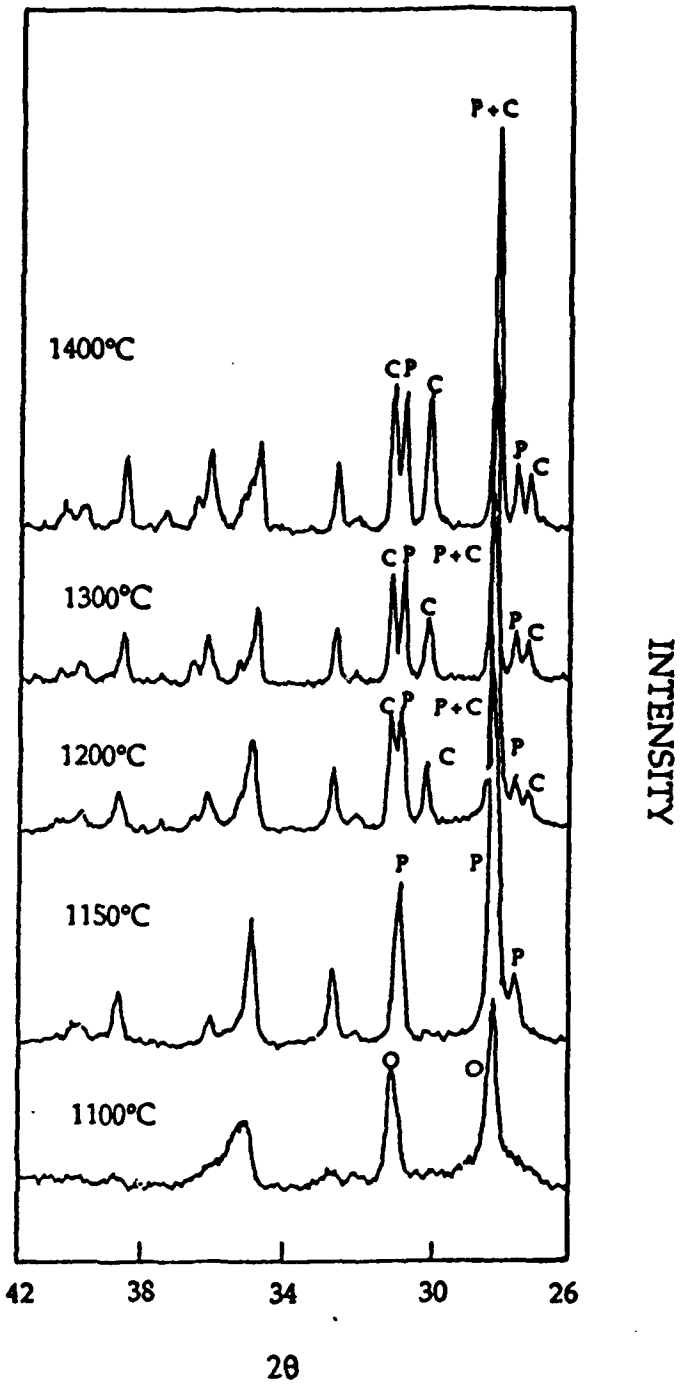

Fig. 6. XRD phase distribution in powder A, after annealing for 10 h at temperatures ranging from 1100 °C to 1400 °C (O = OE, P = PE, and C = CE).

Fig. 7. SEM micrograph of $MgSiO_3$ powder calcined at 900 °C for 2 h, followed by annealing at 1400 °C for 10 h.

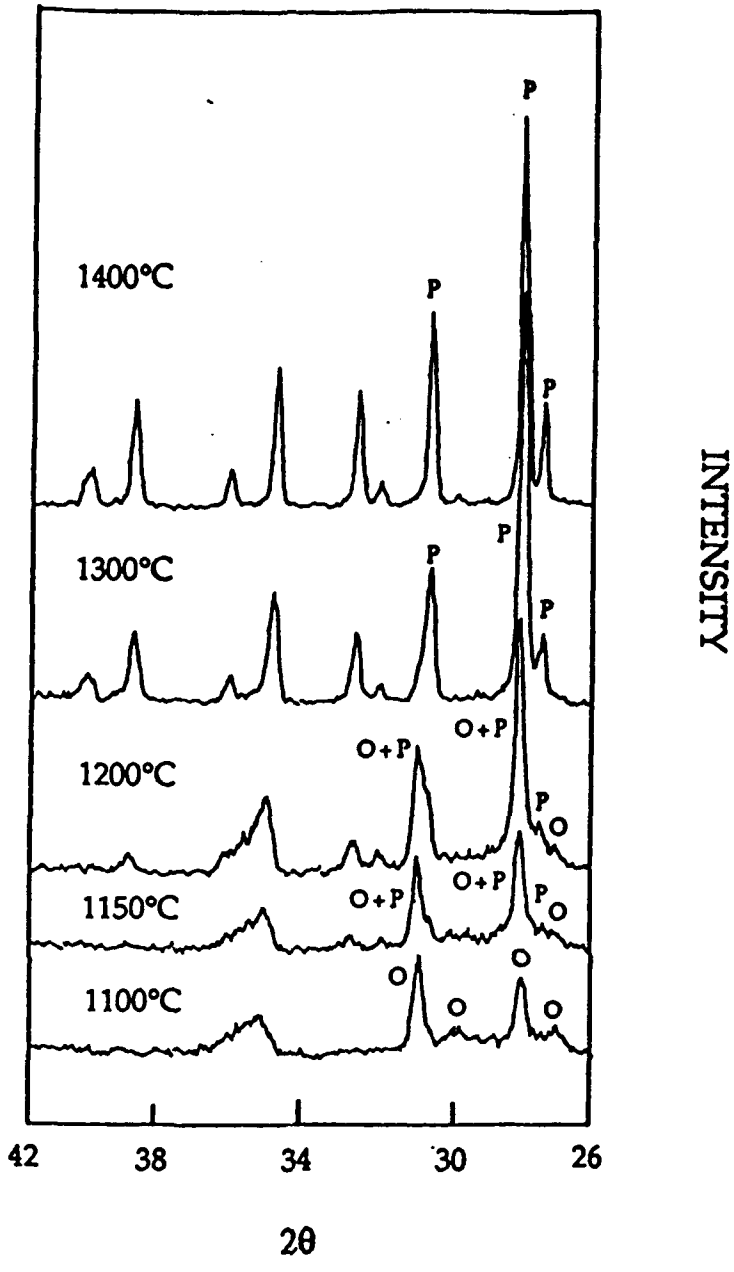

Fig. 8. XRD phase distribution in attritor milled powder B after annealing at temperatures ranging from 1100 °C to 1400 °C for 10 h (O = OE, P = PE).

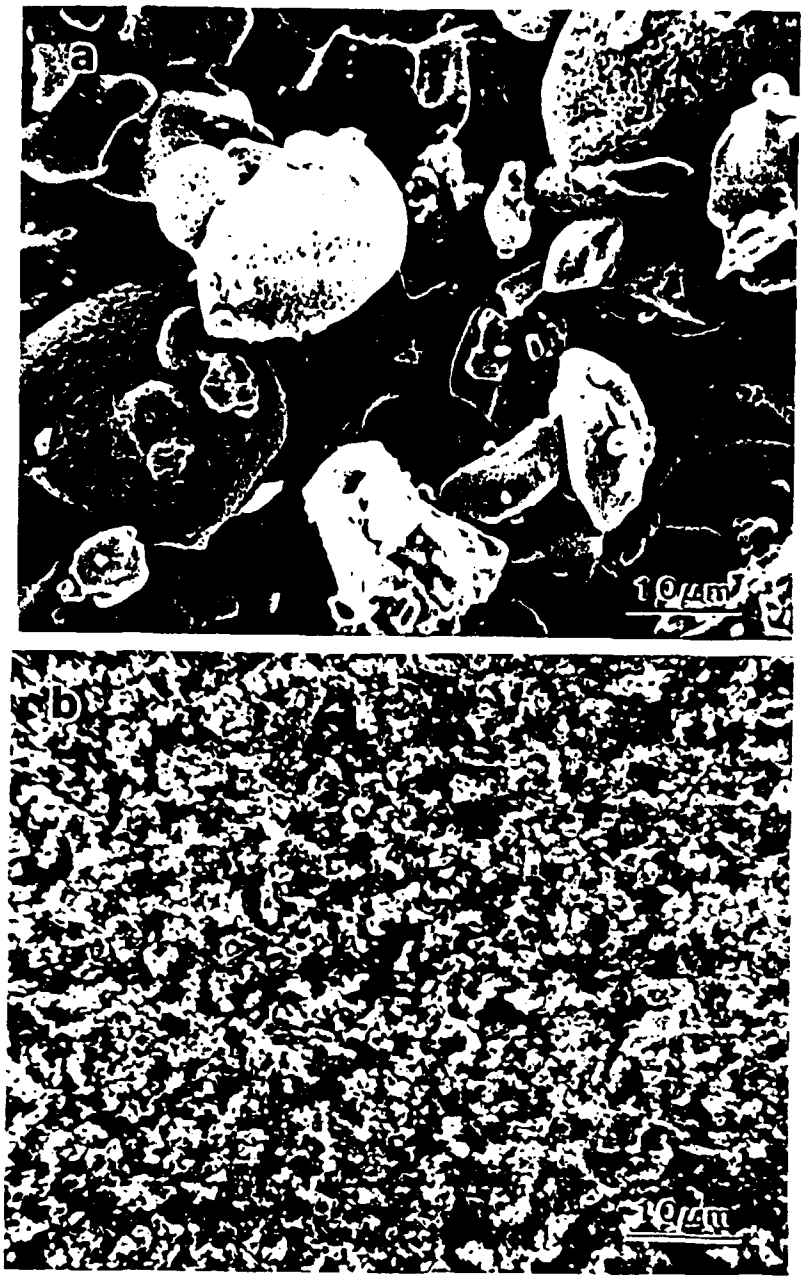

Fig. 9. (a) SEM micrograph of $MgSiO_3$ powder calcined at 900 °C for 2 h (powder A). (b) The same powder after 5 h of attrition milling (powder B).

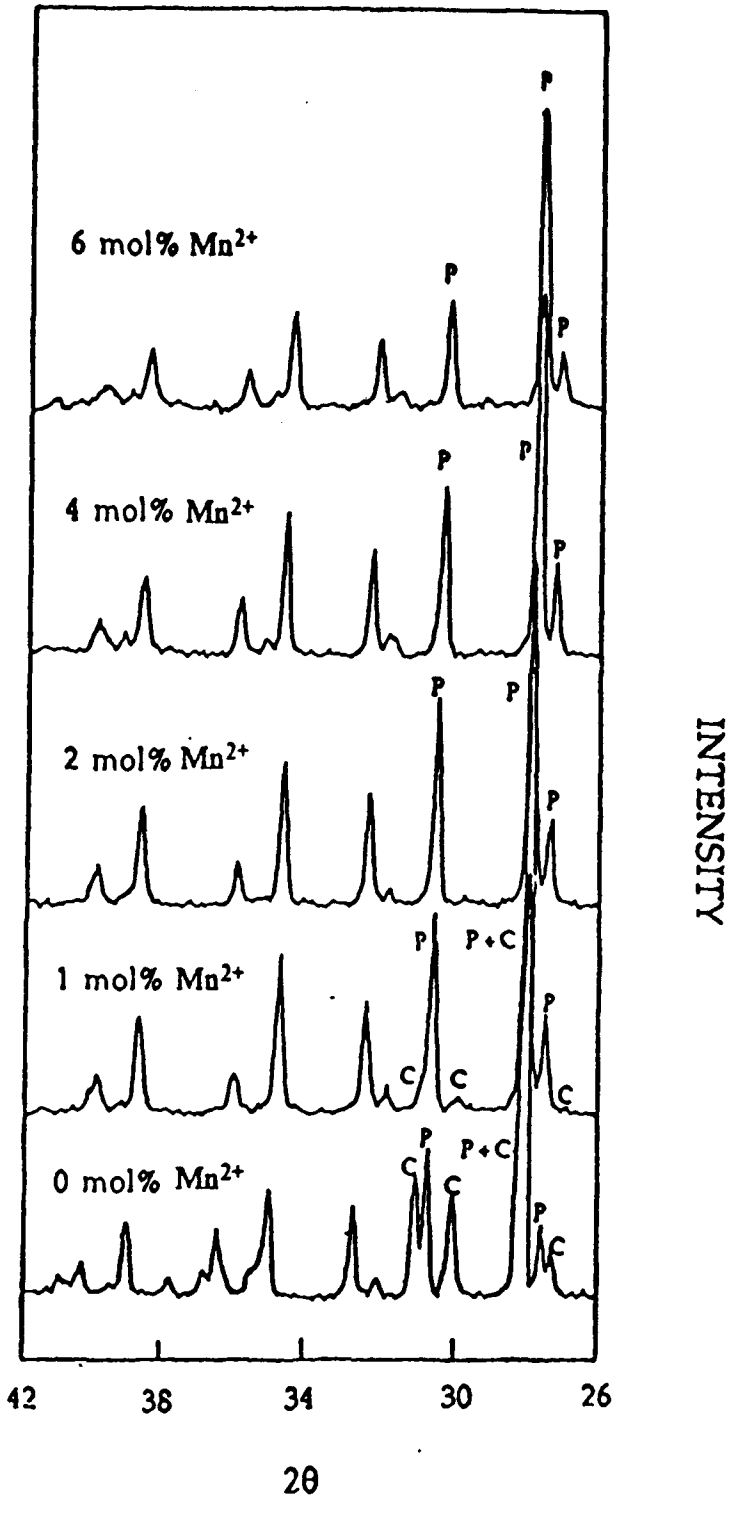

Fig. 10. XRD phase distributions in as calcined powder A, with different Mn^{2+} contents, after calcination at 1400 °C for 10 h (C = CE, P = PE).

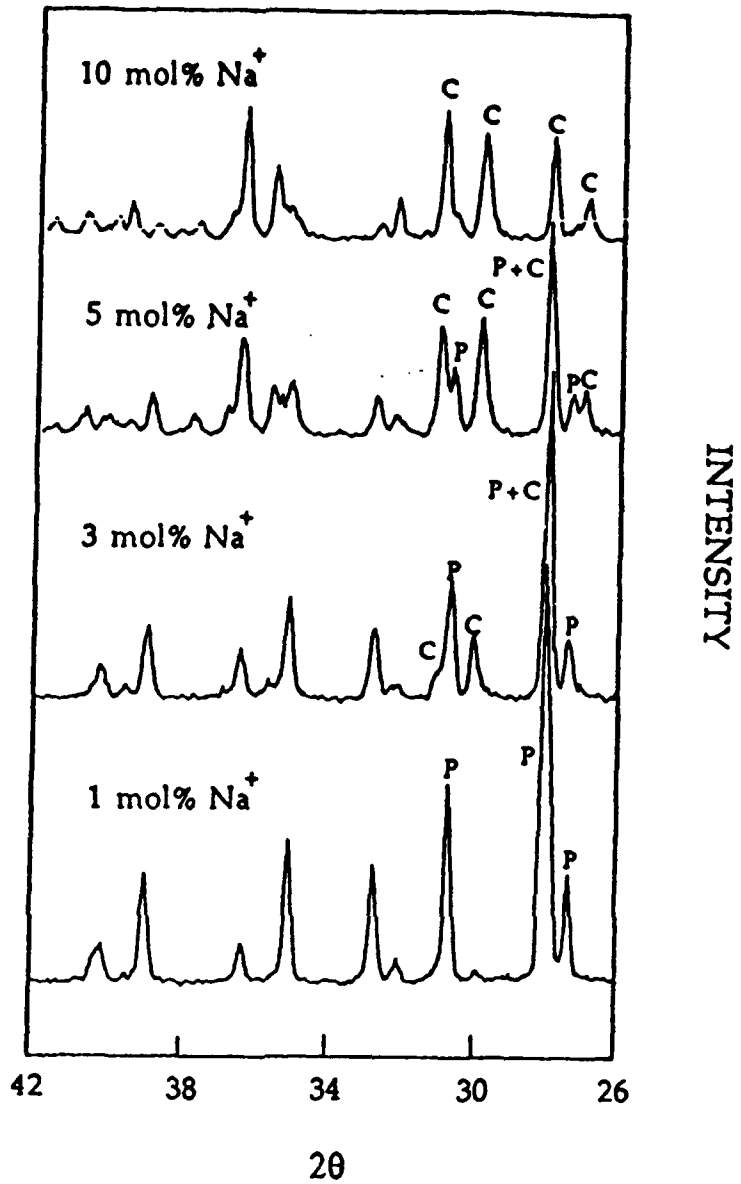

Fig. 11. XRD phase distributions in attritor milled powder B, with different Na^+ contents after calcination at 1400 °C for 10 h (P = PE, C = CE).

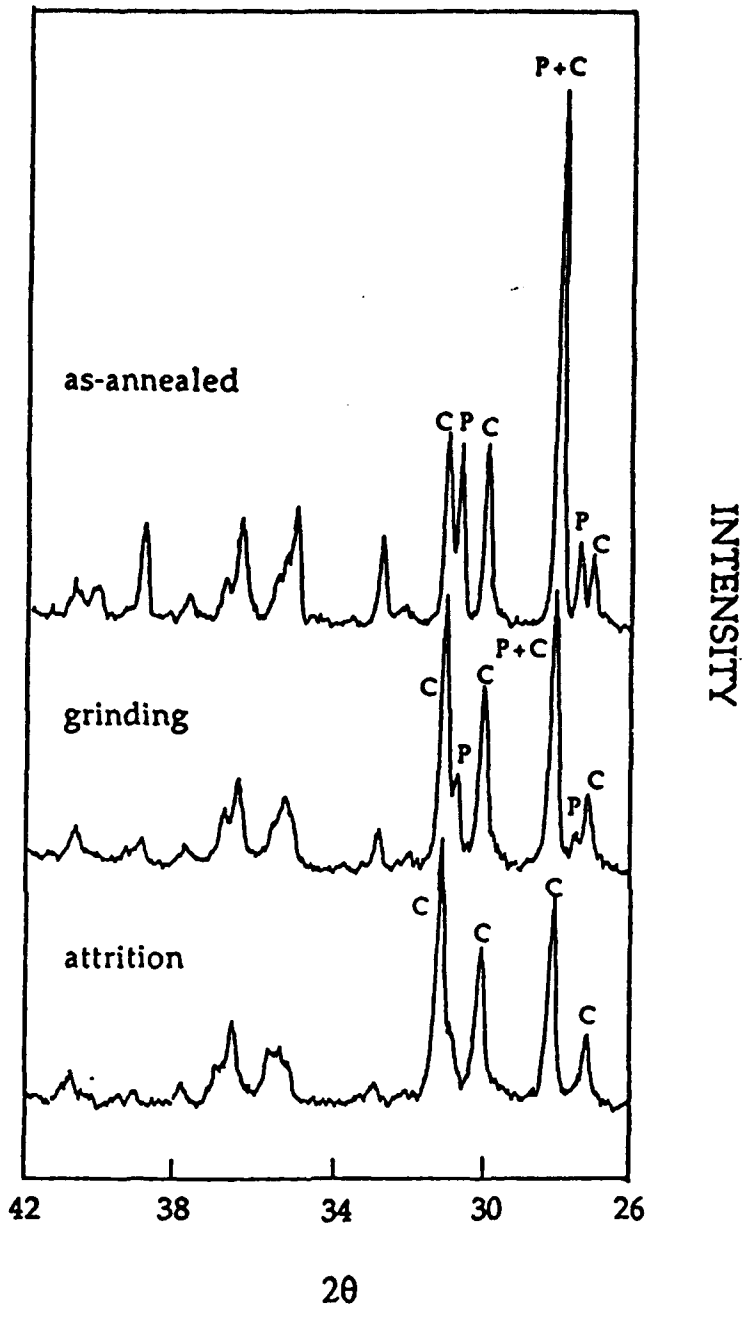

Fig. 12. XRD phase distributions showing shear stress induced PE to CE conversion for powder A annealed at 1400 °C for 10 h after calcination (P = PE, C = CE).

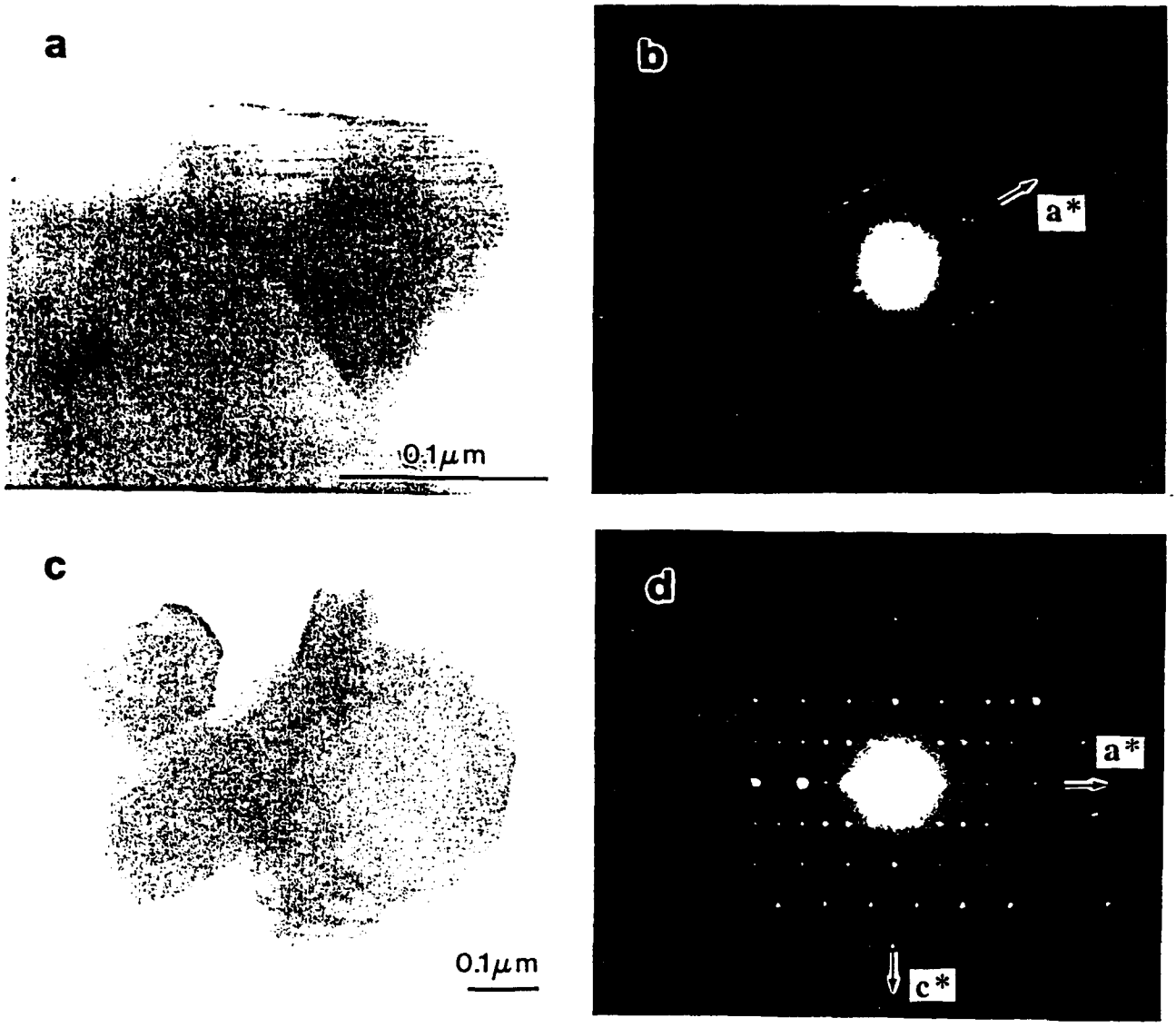

Fig. 13. TEM of image as-calcined powder A which was annealed at low temperatures without dopant. (a) BF image indicating a stacking disorder composed of OE and PE layers for powder annealed at 1100 °C for 10 h. (b) SADP of (a). (c) BF image of PE in the powder annealed at 1150 °C for 10 h. (d) SADP of (c).

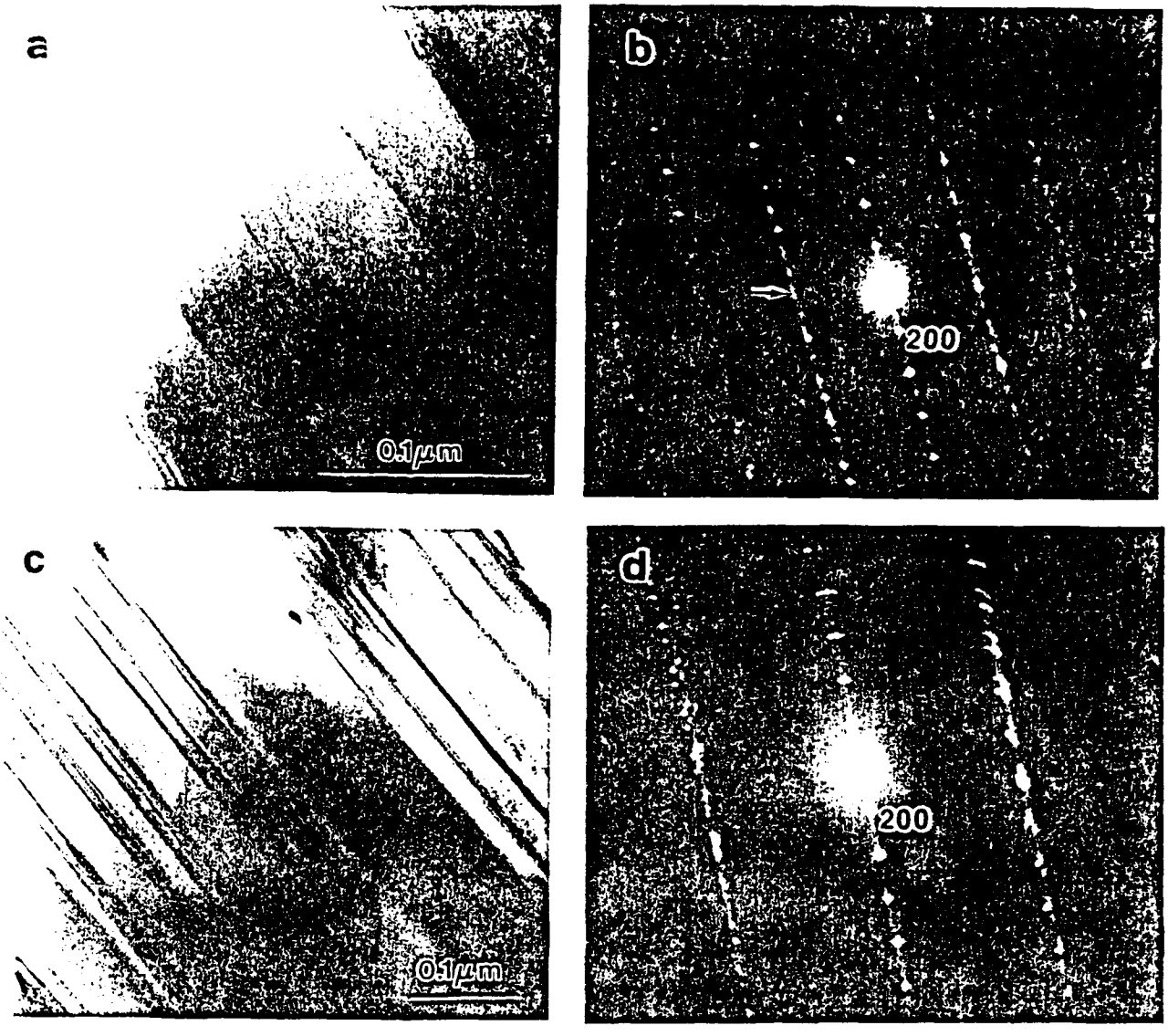

Fig. 14. TEM image of $MgSiO_3$ without chemical dopant, and annealed at 1400 °C for 10 h. (a) BF image. (b) SADP of (a) in the [010] orientation, indicating coexisting PE and twinned CE (arrowed). (c) Stacking disorder composed of PE and twinned CE. (d) SADP of (c).

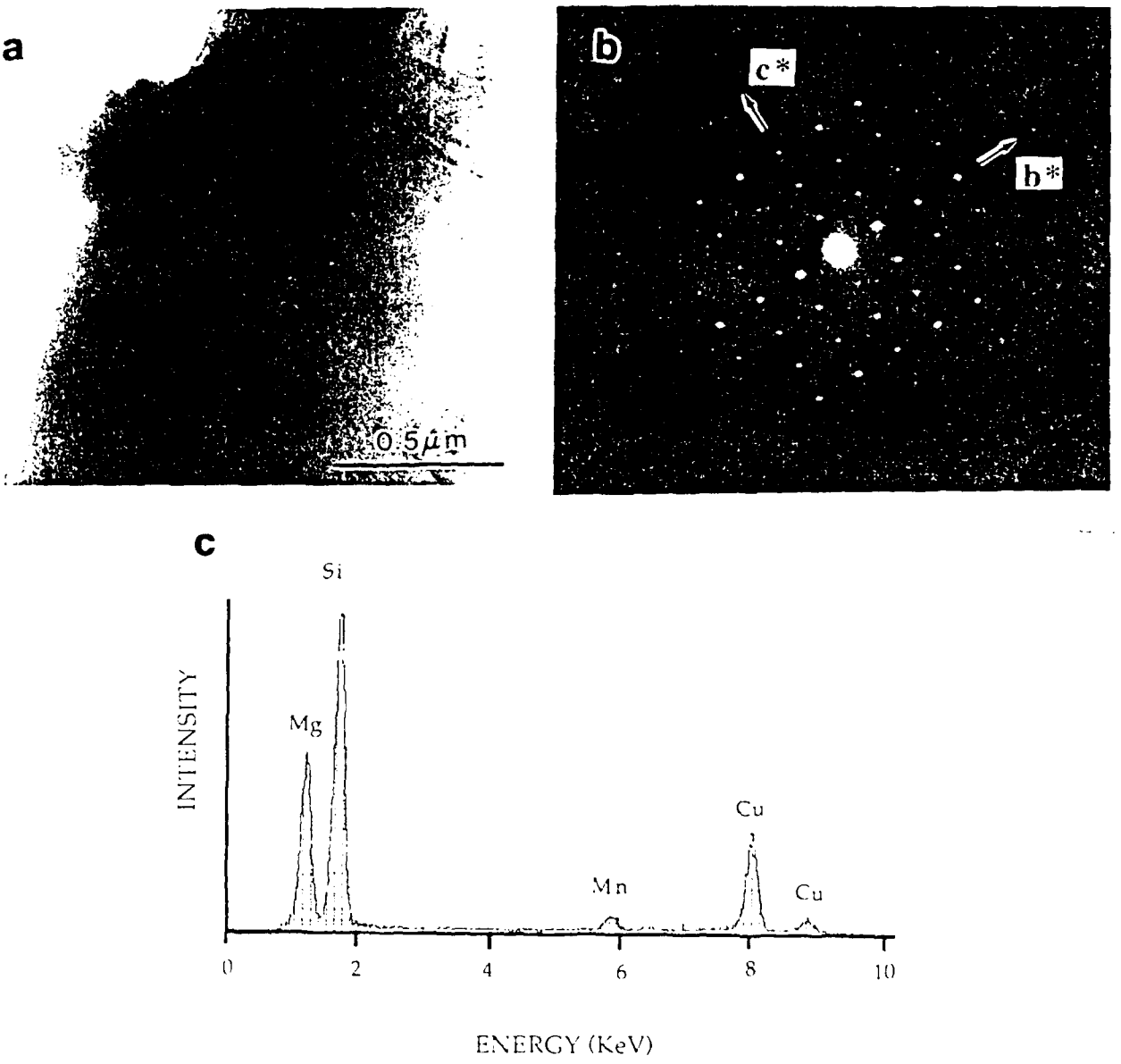

Fig. 15. TEM image of $MgSiO_3$ powder doped with 4 mol % Mn^{2+} and annealed at 1400 °C for 10 h. (a) BF image showing a PE grain. (b) Corresponding SADP in [100] orientation. (c) EDS analysis indicating Mn^{2+} present as a solid solution with Mg^{2+}.

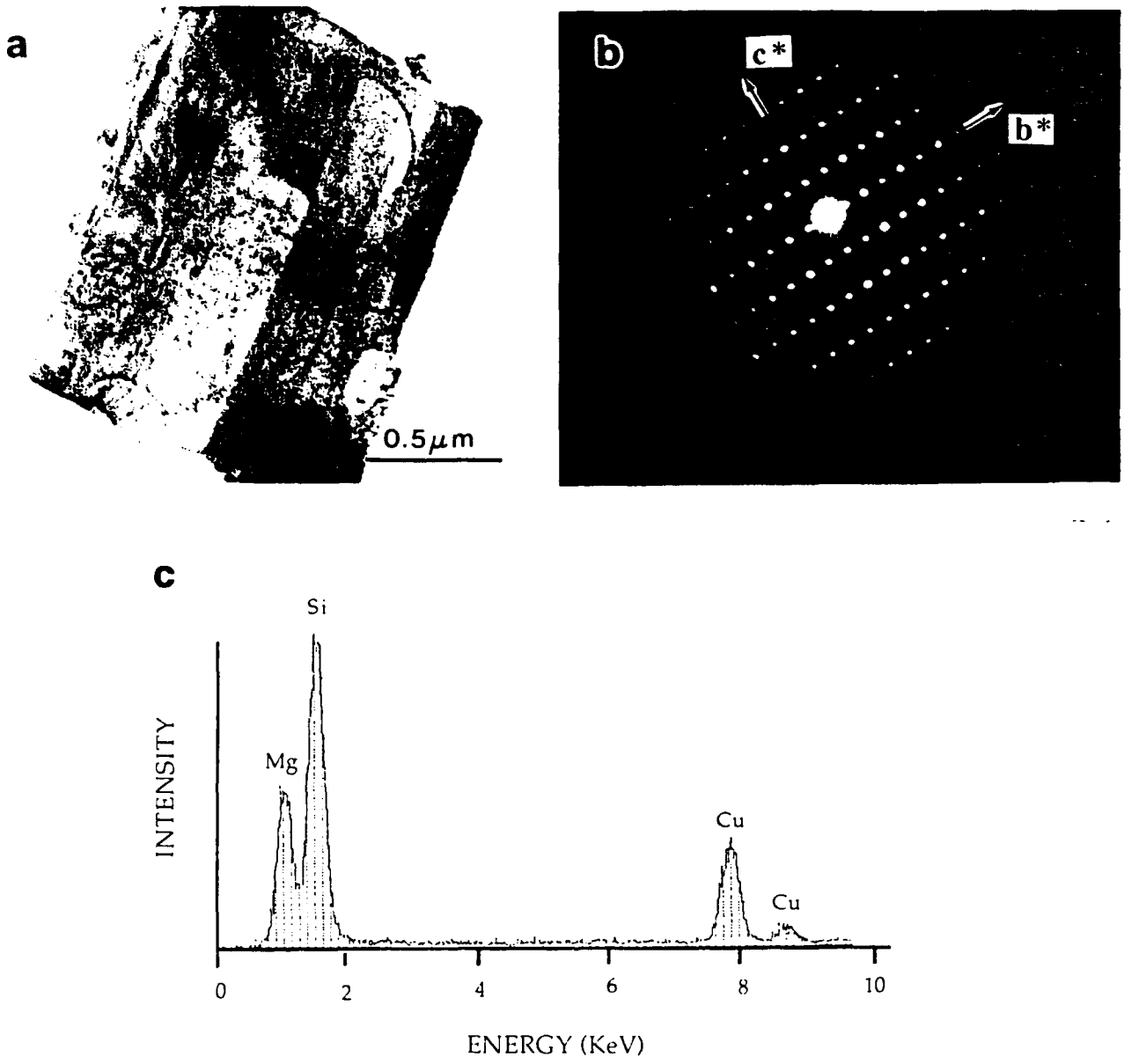

Fig. 16. TEM image of $MgSiO_3$ powder doped with 10 mol % Na^+ and annealed at 1400 °C for 10 h. (a) BF image of CE grain showing slightly distorted rectangles with linear features in the grain. (b) Corresponding SADP in [100] orientation. (c) EDS analysis indicating that there was no Na^+ inside the grain.

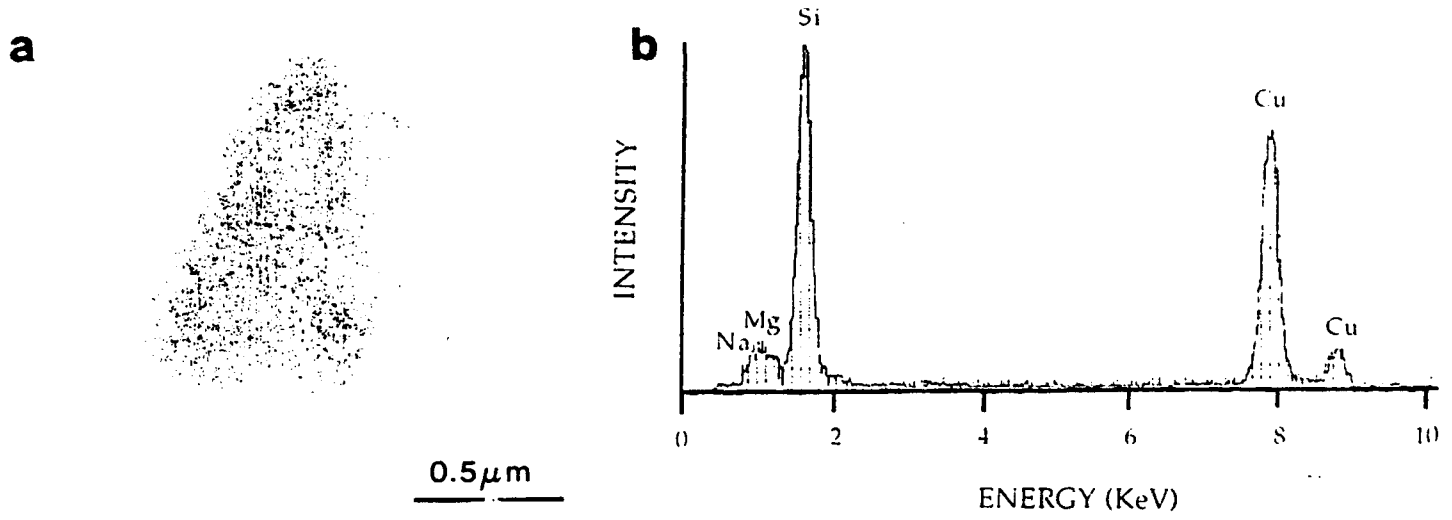

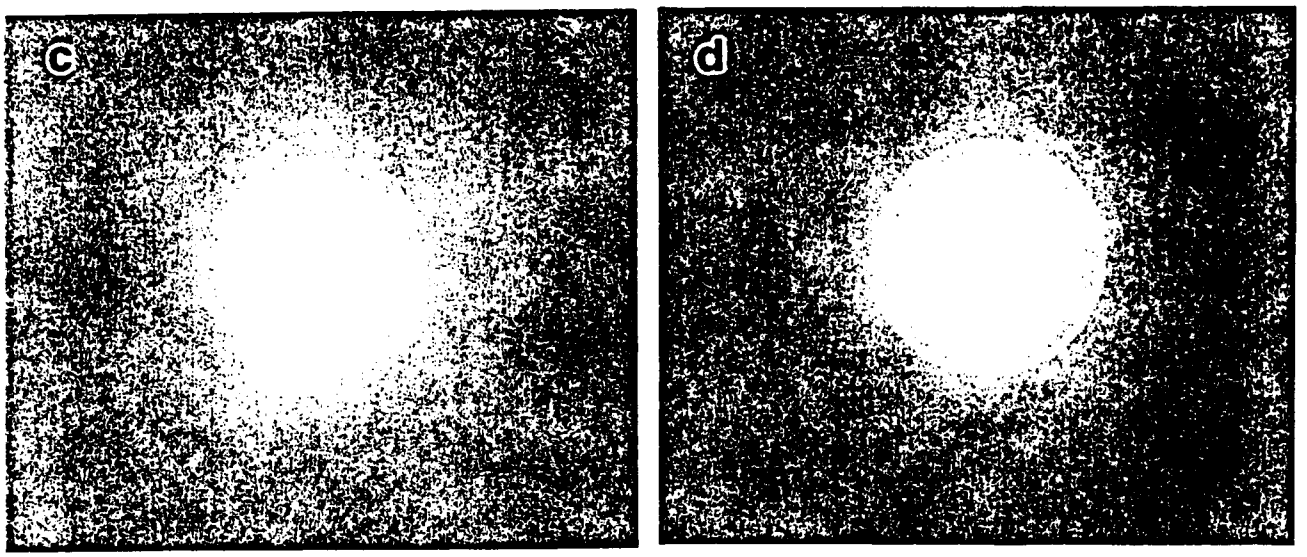

Fig 17. TEM image of glassy phase found in attritor milled powder B doped with 10 mol $^{o}_{o}$ Na^{+}. (a) BF image of glassy phase. (b) EDS analysis indicating Na^{+} in the glassy phase. (c) Glassy phase diffuse ring SAD patterns. (d) Crystallization of the amorphous phase under electron beam irradiation.

journal

J. Am. Ceram. Soc., 77 [2] 531–39 (1994)

Chemical Synthesis and Characterization of Calcium Aluminate Powders

Mehmet A. Gülgün,* Oludele O. Popoola,*,* and Waltraud M. Kriven*

Department of Materials Science and Engineering, University of Illinois at Urbana-Champaign, Urbana, Illinois 61801

The Pechini process was used to produce high-purity, monocalcium aluminate ($CaAl_2O_4$) powders at temperatures as low as 900°C. Absorption spectrometry and BET measurements revealed particles with sizes ranging from submicrometer to 100 μm, with specific surface areas as high as 10 m²/g. Auger electron spectrometry (AES) was used to study the progressive elimination of surface carbon from the organic burnout as a function of temperature. The growth kinetics of calcium aluminate crystallites from a polymeric precursor were studied during calcination as a function of temperature, using transmission electron microscopy (TEM). At the early stages of crystallization, the activation energy for crystallite growth was found to be 118 kJ/mol. This is substantially less than the 356 kJ/mol previously reported. A growth kinetic exponent of $n = 1.68$ was determined for the amorphous-to-crystalline transformation in the temperature range 700° to 850°C. These values were consistent with growth by short-range diffusion.

I. Introduction

CALCIUM ALUMINATES have long been known as a refractory mixed oxide in the steel industry and as a hydraulic material in the cement community. In recent years new applications for calcium aluminates have emerged in optical and structural ceramics. Some amorphous calcium aluminate compositions are photosensitive, and hence potential candidates for optical information storage devices.[1,2] They also have very desirable infrared (IR) transmission properties for optical fiber applications. Crystalline calcium aluminates are used in high-strength and high-toughness ceramic–polymer composite materials.[3,4]

Conventionally, monocalcium aluminate powders are produced by solid-state reactions between calcia (CaO), or calcium carbonate ($CaCO_3$) and alumina (Al_2O_3) powders at temperatures in excess of 1400°C. Powders produced by this method typically have very low specific surface areas (<1 m²/g).[5,6] The completion of such reactions depends on the particle size, specific surface area, and the mixing of the reactant powders. Even after repeated firing–grinding cycles to eliminate all of the unreacted material, the product batch frequently contains undesirable $CaAl_4O_7$, $Ca_{12}Al_{14}O_{33}$, and starting reactants. The kinetics of the pertinent high-temperature solid-state reactions in the CaO–Al_2O_3 system have been studied in some detail by Weisweiler *et al.*[7] and by Singh *et al.*[8] When a 1:1 mixture of CaO and Al_2O_3 was heated to the temperature range 1200–1400°C, all of the thermodynamically stable phases, i.e., $Ca_3Al_2O_6$, $Ca_{12}Al_{14}O_{33}$, $CaAl_2O_4$, $CaAl_4O_7$, and $CaAl_{12}O_{19}$, were initially formed.[8,9] A single-phase monocalcium aluminate was produced only after a prolonged reaction time at high temperatures in a batch that was proportioned for $CaAl_2O_4$. The formation sequence of phases in these mixtures was always from calcia-rich phases to the proportioned phase. For example, when the starting mix was prepared for $CaAl_4O_7$($CaO:Al_2O_3$ = 1:2), initially $CaAl_2O_4$ formed in large amounts which, with time and temperature, converted to $CaAl_4O_7$.[10]

Uberoi and Risbud,[11] and Goktas and Weinberg,[1] synthesized amorphous calcium aluminate powders using chemical processing techniques. The powder produced by the former was prepared with aluminum di-*sec*-butoxide acetoacetic ester chelate ($Al(OC_4H_9)_2(C_6H_9O_3)$) and calcium nitrate ($Ca(NO_3)_2$) precursors in a composition adjusted for $Ca_{12}Al_{14}O_{33}$ synthesis. When calcined below 900°C, these powders proved to be X-ray amorphous and had high surface areas. Goktas and Weinberg[1] used aluminum *sec*-butoxide as an aluminum ion source and calcium nitrate tetrahydrate as the calcium ion source. Roy *et al.*[12] prepared $CaAl_2O_4$ by evaporative decomposition of a solution made from calcium and aluminum nitrate precursors. After a heat treatment at 900°C for less than 1 h, crystalline $CaAl_2O_4$ was obtained. However, the powders thus produced were not fully characterized in terms of specific surface area, particle size distribution, morphology, purity, etc. To date, there have been no attempts made to understand the kinetics of crystallite formation from the amorphous precursors in chemically derived calcium aluminates.

Crystal growth has been studied extensively in some ceramic and metallic systems. The formal theory of growth kinetics can be found in the literature.[13–38] Briefly, the kinetics of isothermal growth are described by the phenomenological rate equation

$$G^n - G_0^n = K_0 t \exp(-E_a/RT) \quad (1)$$

where n is the growth kinetic exponent, G is the average crystallite size at time t, G_0 is the nucleus size, and K_0 is the temperature-independent rate constant and includes frequency and geometric factors as well as entropy terms. E_a is the activation energy for the growth process. R and T are the universal gas constant and the absolute temperature, respectively. Taking the time derivative of G for constant n gives the reaction rate, q. The activation energy E_a can be then determined from the plot of ln (q) vs $1/T$.

$$\ln(q) = \ln(K_0) - (E_a/R)(1/T) \quad (2)$$

The crystallite growth kinetic exponent, n, and the activation energy, E_a, are the most descriptive parameters of the growth process. Determining these two parameters is crucial in obtaining information about the type of boundary migration, and specific mass transport mechanism during isothermal annealing.

In a pure single-phase material having two grains in contact with each other, theoretical considerations assume the following: (1) that a pressure difference arises as a result of the curvature of the boundary; (2) one of the grains grows at the expense

M. Weinberg—contributing editor

Manuscript No. 194395. Received July 13, 1993; approved October 29, 1993.
Presented at the 93rd and 95th Annual Meetings of the American Ceramic Society, Cincinnati, OH, May 1, 1991 (2-JVII-91), and April 21, 1993 (SXIII-68-93).
Supported by the U.S. Air Force Office of Scientific Research under Grant No. AFOSR-URI-90-0242. The work of O. Popoola was funded under Grant No. AFOSR URI-90-0174.
*Member, American Ceramic Society.
*Now in the Materials Reliability Systems Division, Ford Research Laboratory, Dearborn, Michigan 48121.

of the other, due to transfer of atoms across the boundary; and (3) the driving force for atomic migration is the chemical potential difference caused by the pressure gradient across the boundary.[14] Under these conditions, the boundary will move toward its center, with a growth kinetic exponent of $n = 2$. The width of the boundary is taken to be constant during the growth process.[14,37]

In this paper, a chemical preparation route is outlined for single-phase, high-purity, and high-specific-surface-area monocalcium aluminate. The product powders are fully characterized (phase distribution, specific surface area, particle size distribution, and morphology). Equations (1) and (2) are used to analyze the growth kinetics of calcium aluminate crystallites from a chemically derived amorphous matrix. Comparison is made with the conventional solid-state reaction method.

II. Experimental Procedure

(1) Powder Preparation

The powders were synthesized from $Ca(NO_3)_2 \cdot 4H_2O$ (reagent grade, EM Science, Gibbstown, NJ) and $Al(NO_3)_3 \cdot 9H_2O$ (reagent grade, Aldrich Chemical Co., Milwaukee, WI). A Pechini-type process was employed to prepare the polymeric precursors.[39,40] For each precursor, nitrate salts corresponding to a 20-g yield of monocalcium aluminate were dissolved in 100 mL of deionized water. Citric acid monohydrate (60 wt%)–ethylene glycol (40 wt%) resin was added to the mixture. The resulting solution was heated and stirred until a crisp aerated gel formed. The gel was finely ground and calcined in air at various temperatures and times. For each mixture, the resin content, R_c, of the gel was defined as

$$R_c = \text{wt\% resin content} = 100 \times \left\{ \frac{W_{\text{resin}}}{W_{\text{resin}} + W_{\text{oxide}}} \right\} \qquad (3)$$

where W_{oxide} is the weight of the final product calculated from the known weight of precursors used. W_{resin} is the weight of the resin. This definition avoids the problems of determining both the moisture content of the gel prior to calcination and processing yield. Each calcination batch was heated to the specified temperature at a rate of 5°C/min, annealed at this temperature for the specified time, and furnace cooled to room temperature.

(2) Powder Characterization

(A) X-ray Diffraction Analysis: The phase distribution in the powders was analyzed as a function of calcination temperature, resin content, and calcination time, using a Rigaku spectrometer (DMax automated powder diffractometer, Rigaku/USA, Danvers, MA) and Cu$K\alpha$ radiation (40 kV, 40 mA).

(B) Thermal Analyses: Pyrolysis of the ground gel samples of 15 mg with different resin content was monitored by differential thermal analysis (DTA) (Model 910, TA Instruments, formerly Du Pont, Wilmington, DE) at a rate of 10°C/min. The decomposition of selected gels was studied by simultaneous differential thermal analysis and thermogravimetric analysis (DTA/TGA) (Model STA 409, Netzsch GmbH, Selb, Germany) at 5°C/min.

(C) Specific Surface Area Measurements: The effect of resin content, calcination time, and temperature on the specific surface area of powders was studied by nitrogen gas adsorption (Model ASAP 2400, Micromeritics, Norcross, GA). The surface area data were obtained by five-point BET analysis.

(D) Particle Size Distribution Analyses: The particle size distribution of powders was studied using a Laser absorption spectrometer (Sedigraph Model 5000E, Micromeritics). The powders were suspended in a calibrated dispersing liquid (Sedisperse A-12, Micromeritics). The suspension was sonically agitated with a quartz tip ultrasonic processor (Heat System Model W385, Farmingdale, NY) for 5 min before analysis.

(E) Auger Electron Spectroscopy: The residual carbon content of powders calcined at 800°, 900°, and 1000°C for 3 h was studied by auger electron spectroscopy (AES) (Model PHI660 SA Multiprobe, Perkin-Elmer, Eden Prairie, MN). AES is a surface-sensitive technique which can give semiquantitative analysis of the first few atomic layers on metals, ceramics, or thin films. When used in conjunction with sputtering it can perform semiquantitative depth profiling for major elemental species, including light elements such as carbon, which are present in amounts above 1 atom%. The AES analyses were made in the kinetic energy range 50 to 600 eV. $C_{(KLL)}$, $Al_{(LMM)}$, and $Ca_{(LMM)}$ auger peaks were monitored. The incident electron beam energy was 3 kV. The thickness of the impurity layer was determined by carbon depth profiling. Sputtering of the surface layers was achieved by argon ion bombardment at a current of 45 mA/cm^2 (3 kV). Between the sputter cleaning process steps, the amount of residual carbon was monitored by AES.

(F) Electron Microscopy: The morphology, internal microstructure, and microchemistry of powders were studied by scanning and transmission electron microscopy (SEM and TEM). SEM samples were prepared by sprinkling the powders onto aluminum stubs, followed by carbon coating. For TEM, holey formvar films were supported on copper grids. A drop of powder suspended in isopropyl alcohol was deposited on the film, dried, and carbon coated. The SEM (ISI DS-130, International Scientific Instruments, Santa Clara, CA) was operated at 10 kV and the TEM at 120 kV (Philips EM 420, Philips Instruments, Inc., Mahwah, NJ). Both were equipped with energy dispersive spectroscopy facilities (EDS) (Tracor Nothern TN2000, Middleton, WI (on SEM), EDAX PV 9900, EDAX International, Inc., Prairie View, IL (on TEM)). Crystallite sizes were measured from dark-field (DF) and bright-field (BF) TEM images. The reported values represent the average of about 20 of the largest crystallite diameters in each case.

III. Results

(1) Phase Distribution

Control over the phase distribution in the powders was achieved by optimizing the processing parameters such as resin content, time, temperature, and furnace atmosphere during calcination. In powders calcined at 900°C or higher for 3 h, the amount of resin in the starting solution had no significant effect on the phase distribution for resin contents of 50 to 92.5 wt%. Single-phase $CaAl_2O_4$ powders were always obtained. For precursors with less than 50 wt% resin, other phases, i.e., $Ca_3Al_2O_6$ and $CaAl_4O_7$, coexisted with the $CaAl_2O_4$ phase. The effects of temperature and time of calcination, and the furnace atmosphere, are shown in Figs. 1(a,b) and 2. Powders calcined at 800°C or below were X-ray amorphous, while above 800°C the powders were crystalline (Fig. 1(a)). However, TEM analysis showed that powders calcined below 800°C contained some microcrystalline particles. The effect of calcination time is seen in Fig. 1(b) for powders annealed at 900°C in a closed box furnace. Initially, only $CaAl_4O_7$ peaks were observed in the X-ray spectrum. With increased calcination time $CaAl_2O_4$ X-ray peaks appeared with simultaneous decrease in $CaAl_4O_7$ X-ray intensity. After 3 h of calcination at 900°C, the X-ray diffraction pattern consisted mainly of $CaAl_2O_4$ peaks. The initial formation of $CaAl_4O_7$ was mostly suppressed when a constant air flow (0.6 mL of air/(g of precursor)) was introduced into the furnace atmosphere during calcination, as shown in Fig. 2.

(2) Thermal Analysis of Gels

Apart from the gel with 92.5 wt% resin, the DTA traces showed exotherms at 400°, 500°, and 900°C (Fig. 3(a)). The first exotherm was associated with charring of the polymer, the second with pyrolysis of the organics, and the last exotherm resulted from char burnout. The third exotherm was absent in DTA traces for gels with 92.5 wt% resin content. This may have been due to the fact that only a small amount of char was

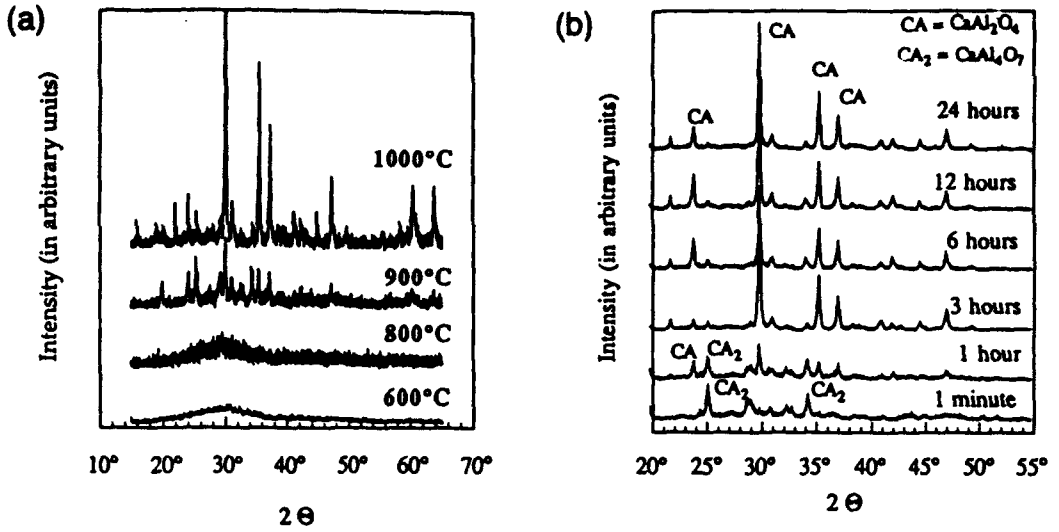

Fig. 1. X-ray diffraction spectra of powders calcined at (a) various temperatures and (b) various times at 900°C.

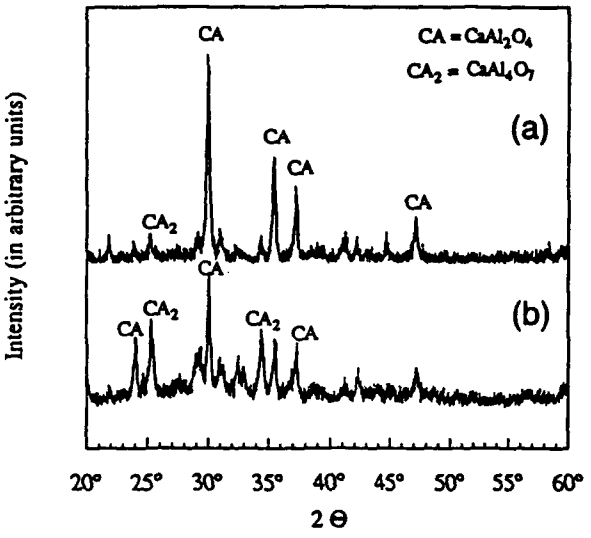

Fig. 2. X-ray diffraction spectra from precursors calcined at 900°C for 1 h (a) with air flow, (b) in a closed atmosphere box furnace.

formed, and that enough heat was generated during pyrolysis at 500°C to eliminate that char. Moreover, TGA analysis in Fig. 3(b) showed that most of the weight loss occurred at temperatures between 400° and 530°C. This corresponded to the range where polymer burnout occurred. The precursors with lower resin contents also revealed a slight weight loss at around 900°C which might have been due to the char burnout process.

(3) Particle Size Distribution

Powders in this study had a wide particle size distribution with agglomerates and particles in sizes ranging from submicrometer to 100 μm. Most of the particles were of irregular shape with sharp corners and edges. Increased calcination temperatures caused agglomeration and hence narrowed the particle size distribution. The particle size was independent of calcination time. Figure 4 shows the effect of resin content on particle size distribution. Powders prepared from the highest and lowest resin content precursors (i.e., 92.5% and 50%, respectively) gave a median size of 25 μm equivalent spherical diameter (ESD), whereas powders from 85% and 70% resin content precursors had a median particle size of 8 μm ESD.

(4) Specific Surface Area

(A) Effect of Temperature: The specific surface area of powders was sensitive to calcination temperature, time, and composition of the starting gel. The powder calcined from 70

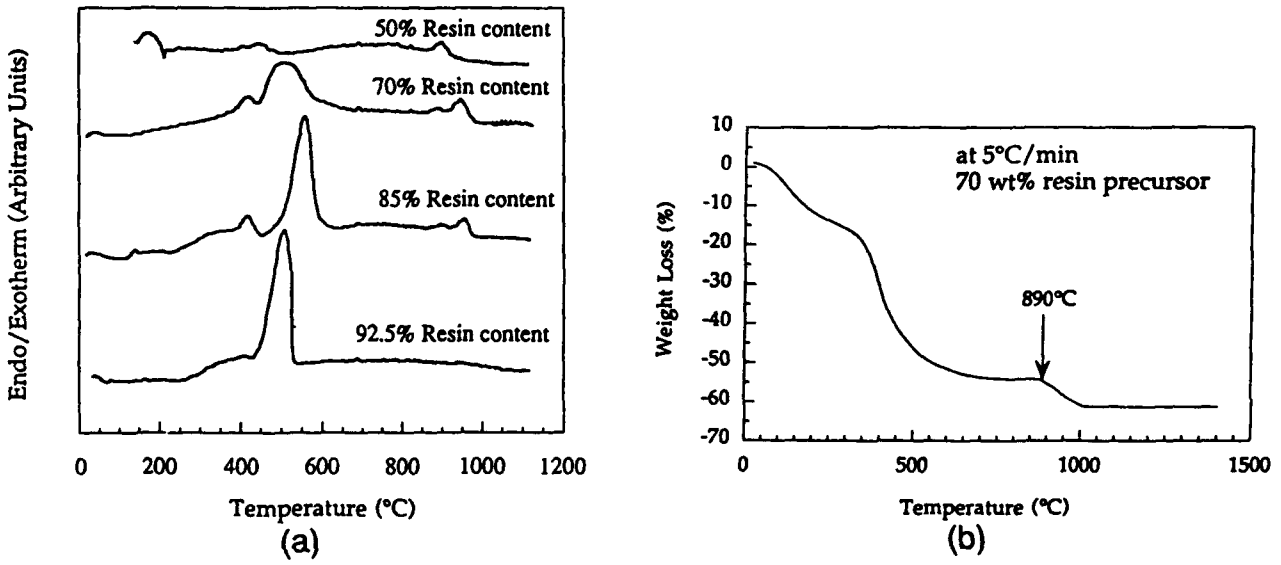

Fig. 3. (a) Differential thermal analysis (DTA) traces of the calcination behavior for precursors with different resin contents. (b) Thermogravimetric analysis (TGA) of 70 wt% precursor performed in the temperature range 20–1400°C with a heating rate of 5°C/min.

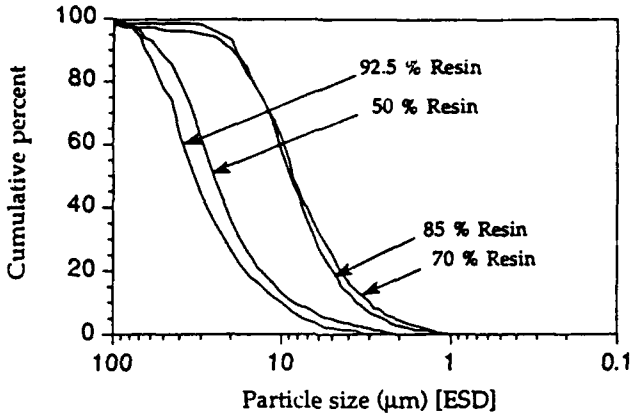

(a)

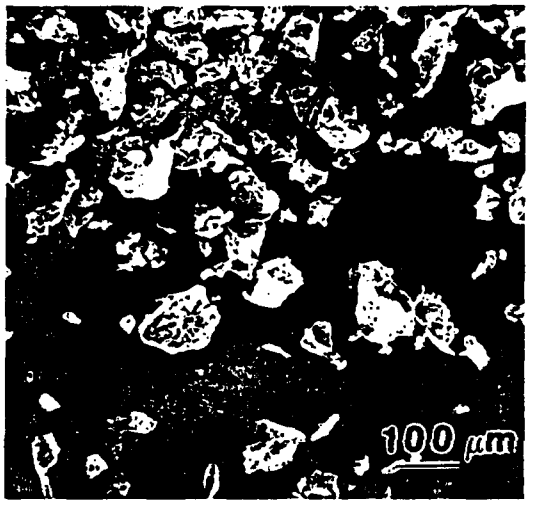

(b)

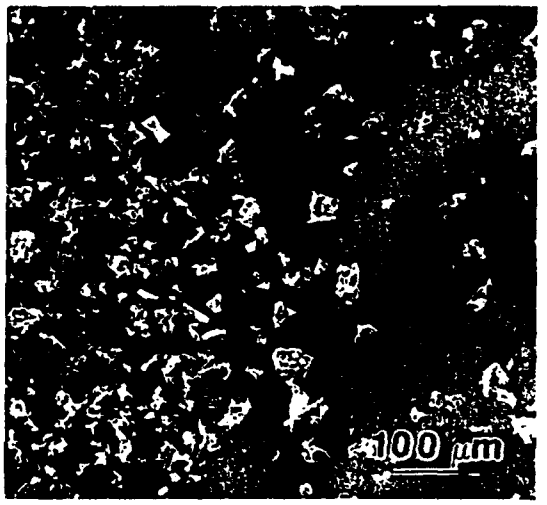

(c)

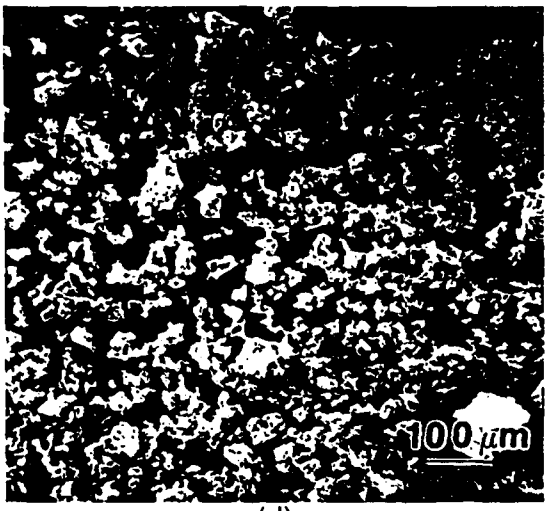

(d)

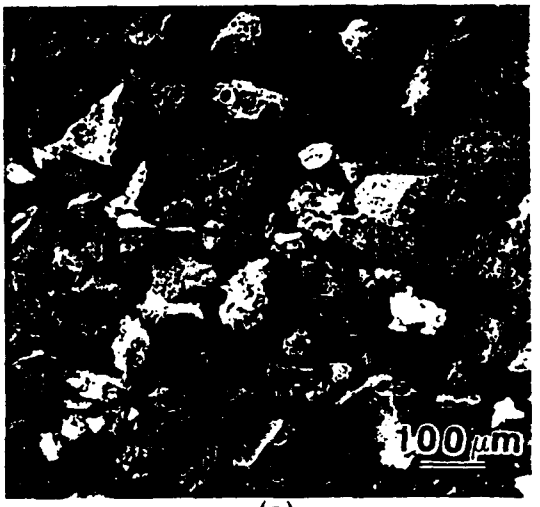

(e)

Fig. 4. (a) Effect of resin content on the particle size distribution of the powders. SEM micrographs showing the effect of the resin content in the precursors on the particle size distribution of the powders calcined from (b) 50, (c) 70, (d) 85, and (e) 92.5 wt% precursor gels.

wt% resin gels at 800°C for 1 h had a BET specific surface area of 1.7 m^2/g. This powder was visibly black in color, indicating the presence of residual carbon. At 900°C, the specific surface area as measured by BET peaked at a value of 10.0 m^2/g. Most of the residual carbon was burnt out and the powder was light gray in color. Further increase in temperature resulted in lower specific surface area (Fig. 5). Since the organics were burnt out by 530°C (Fig. 3), the low specific surface area observed in 800°C calcined powders was anomalous. Less coarsening and hence higher specific surface area would be expected at 800°C than at 900°C. TEM observations of the 800°C powders revealed an internal microstructure having interconnected porosity. The average pore diameter was 10–20 nm (Fig. 6).

Comparative AES analysis of powders calcined at 800°, 900°, and 1000°C (Fig. 7) showed a significant decrease in the amount of surface carbon with increasing temperature. AES

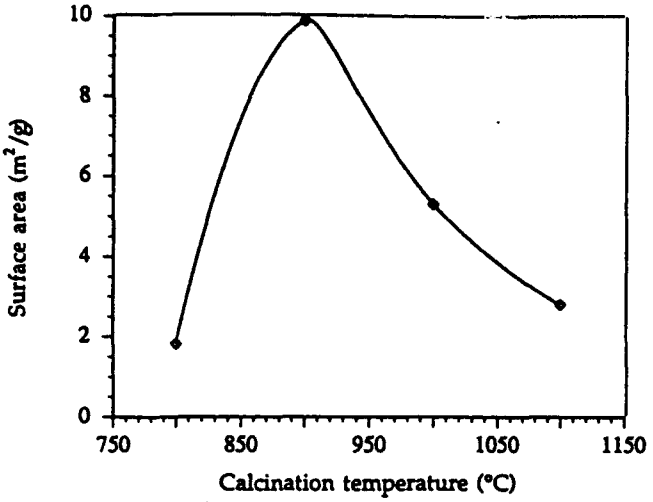

Fig. 5. Effect of calcination temperature on the specific surface area of $CaAl_2O_4$ powders.

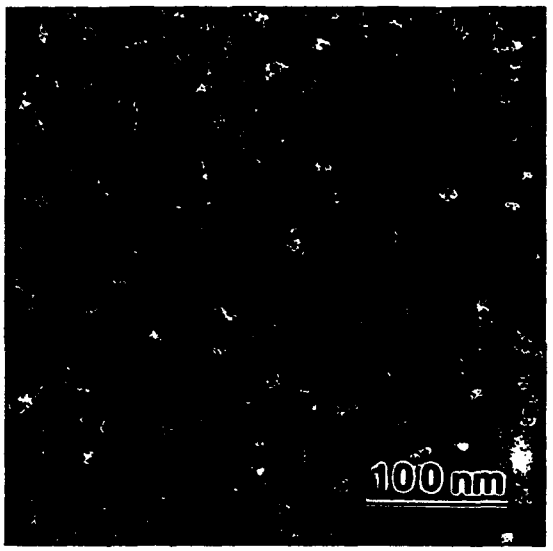

Fig. 6. TEM bright-field image of a typical powder calcined at 800°C for 6 h. The lighter areas are the internal porosity with approximately 10–20 nm pore diameter. The interconnected nature of the porosity is evident.

analysis between successive *in situ* Ar^+ sputtering of the 800°C calcined powder yielded a carbon depth profile. The significant decrease in the $C_{(KLL)}$ peak intensity from as calcined to sputtered 800°C powders indicates that most of the residual carbon was concentrated at the surface (Fig. 7).

(B) Effect of Resin Content: The specific surface area of powders calcined from gels containing between 70 and 92.7 wt% resin at 900°C for 3 h showed an unusual quasi-parabolic dependence on the resin content (Fig. 8). Figures 9(a–d) are SEM micrographs showing the morphology of powders as a function of resin content. The amount of porosity in the powders can be directly correlated to the specific surface area. Figure 9(c) confirms the low specific surface area observed in 85 wt% resin content powder (Fig. 8). It was noted that the specific surface area can be further increased to 24 m^2/g by ball milling the powders for 40 min with ZrO_2 media.

(5) *Crystallization*

TEM selected area diffraction patterns (SADP) obtained from powders calcined at various temperatures are shown in Fig. 10. Powders calcined at 600°C were completely amorphous, as evidenced by the diffuse hallow ring in Fig. 10(a).

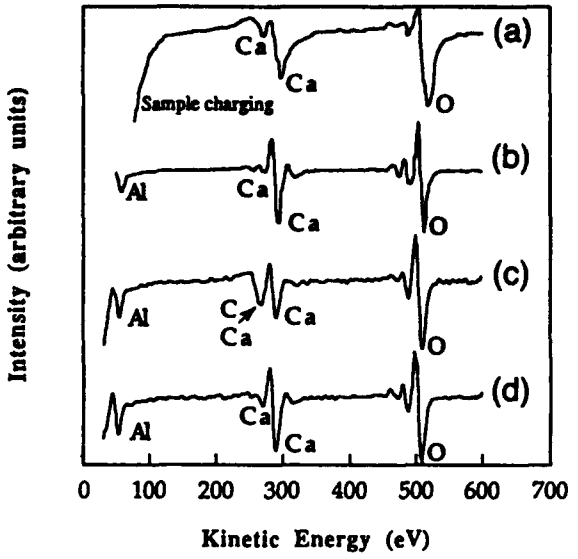

Fig. 7. Auger electron analysis (AES) spectra of powders derived from 30 wt% resin precursors. The powders were calcined at (a) 1000°, (b) 900°, (c) 800°C, before sputtering, and (d) 800°C after sputtering. $C_{(KLL)}$ and $Ca_{(MNN)}$ are at the same energy. However, the significant decrease in $C_{(KLL)}$ peak intensity with sputtering time can be seen in (c) and (d).

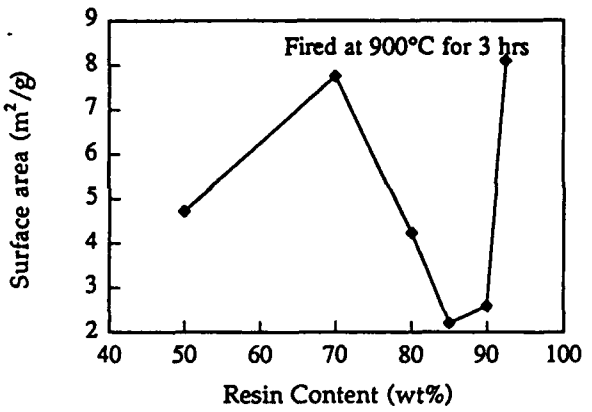

Fig. 8. Effect of composition of the gel on the specific surface area of the as-calcined powders.

The SADP from the powders calcined at 700°C contained four distinct Dirac peaks (arrowed in Fig. 10(b)). This indicated local (short-range) ordering in the amorphous phase. As the calcination temperature was further increased, dotted rings signifying microcrystalline formation were observed (Fig. 10(c)). Microcrystals appeared in the amorphous matrix at temperatures as low as 700°C. With time and/or temperature of heat treatment, bright- and dark-field imaging showed that the existing crystallites grew, and new ones formed in the highly porous matrix. After calcination at 1000°C, the crystallites were big enough to allow zone axis identification from the spot SADP's as illustrated in Fig. 10(d). The time dependence of crystallite size during isothermal heat treatment is plotted in Fig. 11(a). The parallelism between the curves indicated a constant growth kinetic exponent, n, over the temperature range considered. From the slope of these curves n was determined to be ~1.68. The initial crystallite size, G_0 (i.e., minimum size observed in DF and BF images of powders calcined at 700°C for 1 min) was 9.9 nm. The relative crystallite size ($G^n - G_0^n$) is plotted versus time for various calcination temperatures in Fig. 11(b). The slopes of these curves give the growth rate, q. Figure 11(c) represents ln (q) vs $1/T$ (Eq. (2)). From this plot, the activation energy, E_a, was found to be 118 kJ/mol.

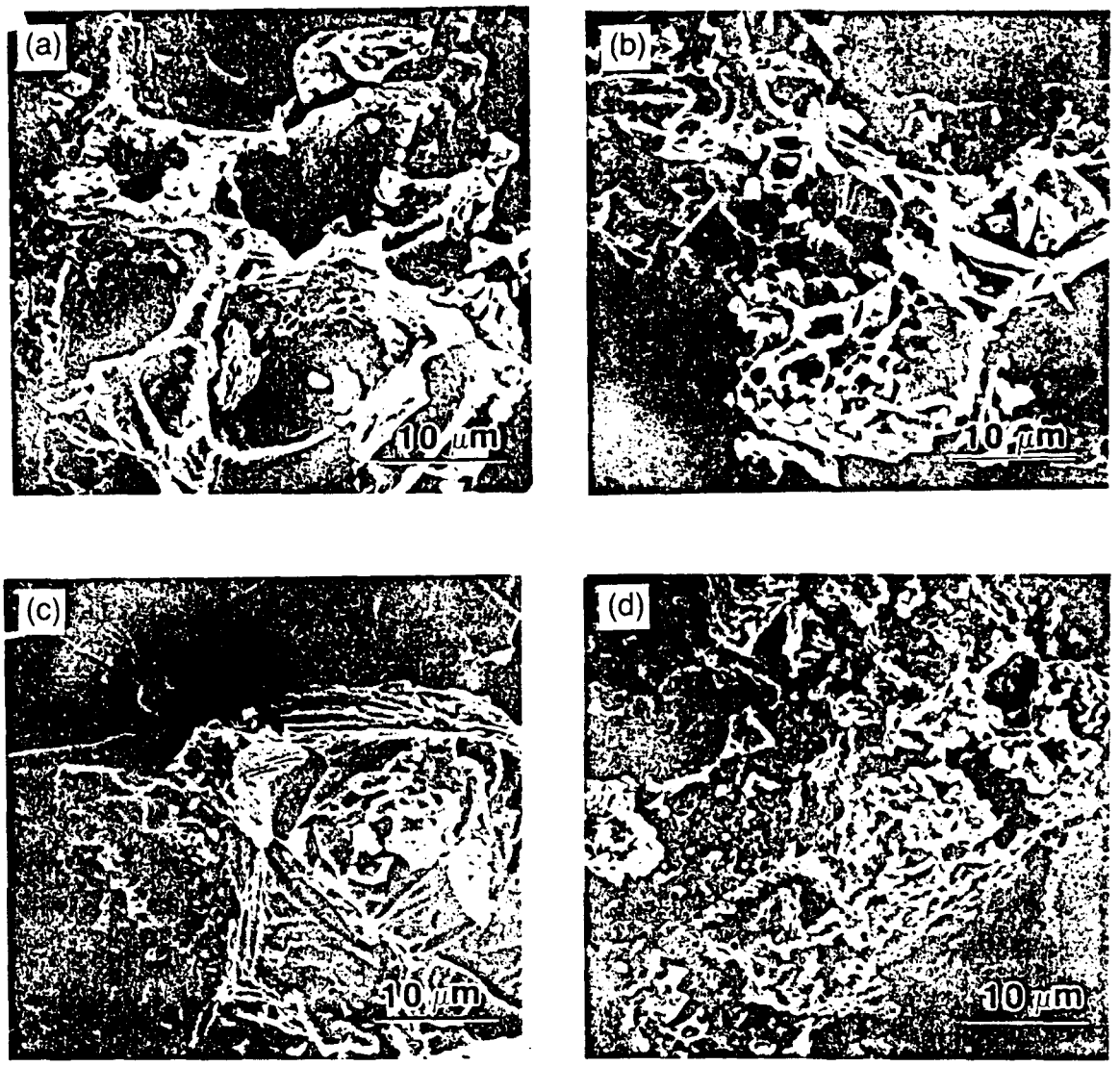

Fig. 9. Morphology of the powders calcined from precursors with different resin content at 900°C for 3 h: (a) 50, (b) 70, (c) 85, (d) 92.5 wt%.

The nonsimultaneous nucleation at pore surfaces observed by TEM indicated a heterogeneous nucleation process. A direct correlation between the amount of internal porosity and number of nucleated crystallites was observed. Although with increasing temperature crystallite size became larger, the microstructure retained most of its internal porosity up to 1000°C.

IV. Discussion

(1) Phase Formation

$Ca_3Al_2O_6$, $CaAl_2O_4$, $CaAl_4O_7$, and $CaAl_{12}O_{19}$ are the readily formed and thermodynamically stable compounds in the CaO–Al_2O_3 binary system with increasing refractoriness, respectively.[41,42] In the conventional preparation route by high-temperature solid-state synthesis, the batch usually contains CaO-rich phases and unreacted Al_2O_3 before the appearance of desired product phase. For example, $CaAl_2O_4$ formed at early stages of the process when CaO and Al_2O_3 were mixed in $Ca_3Al_2O_6$ (1:2) proportions. Singh *et al.*[5] explained this behavior by a higher reactivity of CaO with respect to Al_2O_3. Contrary to this observation, calcium dialuminate ($CaAl_4O_7$) and monocalcium aluminate ($CaAl_2O_4$) were both observed at early stages of crystallization in chemically prepared monocalcium aluminate powders. Even under oxygen atmosphere, small amounts of $CaAl_4O_7$ initially formed, indicating a disproportionation of cations in the precursor. Similar observations were made during the chemical synthesis of distrontium silicate.[43] The disproportionation in this case was due to $SrCO_3$ formation following pyrolysis of the organics at 500°C. In the present study, no carbonate was detected.

The heterogeneity in the calcined powder may be due to preferential complexing of one of the cations with the polymer leading to formation of a char during the burnout process. Calcium ions, due to their higher reactivity, might preferentially associate themselves with the polymer. Fourier transform infrared spectroscopy (FTIR) studies are under way to clarify this point. Preferential linkage of calcium cations to the polymer will cause them to remain trapped in the char until its decomposition at 900°C. Thus, excess aluminum ions would be available at the early stages of the reaction, resulting in the formation of aluminum-rich phases. When the char burnt out at 900°C, as manifested by the third exotherm in DTA and the weight loss at 900°C in TGA, calcium ions became available. The calcium ions thus liberated could then react with the previously formed calcium dialuminate and unreacted aluminum ions, also in the char, to give monocalcium aluminate as the final product. The following reaction sequence from the amorphous matrix is suggested:

Initial reaction

$$CaO + Ca^{2+}_{(aq)} + 2Al_2O_3 \xrightarrow{(pH>7)} CaAl_4O_7 + Ca^{2+}_{(aq)} \quad (6)$$

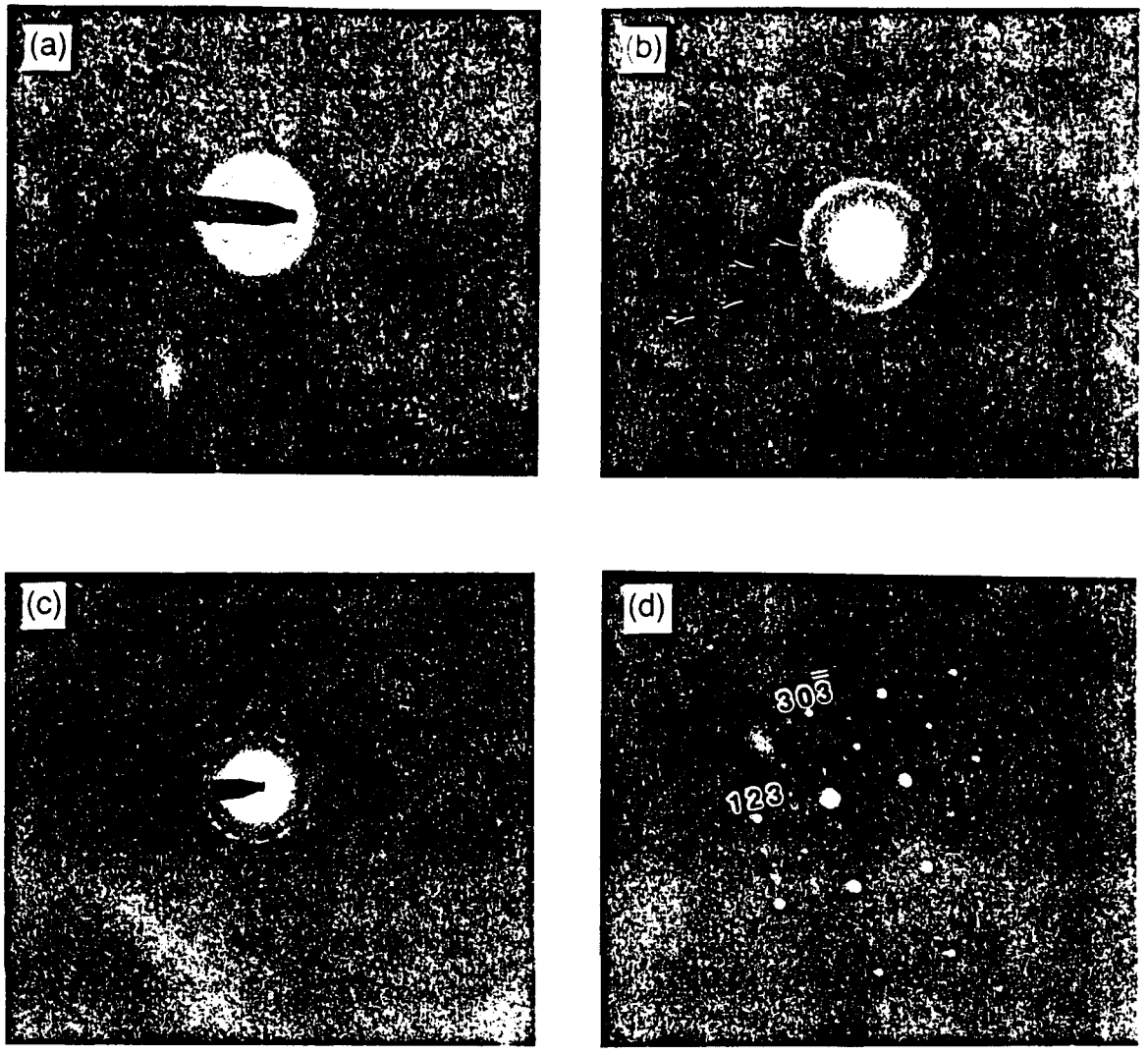

Fig. 10. SADP's from powder samples calcined from 70 wt% resin containing precursors at temperatures (a) 600°, (b) 700°, (c) 800°, and (d) 1000°C. The Dirac peaks are arrowed in (b).

Final reaction

$$CaAl_2O_4 + Ca^{2+}_{\text{in the char}} + O^{2-} \xrightarrow{\text{oxygen}} 2CaAl_2O_4 \qquad (5)$$

Supply of extra oxygen to the system will shift the equilibrium Eq. (5) toward the right, and hence more $CaAl_2O_4$ will be produced at early stages of detectable crystallization, in agreement with the present observations.

(2) *Effect of Resin Content*

The resin content in the gel precursor had a drastic impact on the porosity, specific surface area, and morphology of the powder. High resin content (92.5 wt%) yielded partially sintered large agglomerates of 25 μm ESD. In such high-resin-content precursors the cation species are widely separated by the organics. This leads to local formation of fine oxide particles in a three-dimensional network. The heat released during burnout of the large amount of polymer causes the particles to neck and to form large agglomerates with extremely fine internal porosity (Fig. 9(d)).

On the other hand, in a low-resin-content precursor of 50 wt%, the cation species are closer together. This leads to large oxide particles linked in a coarser framework to form agglomerates of approximately the same size, i.e., 25 μm ESD. This appears the coral-like morphology seen in Fig. 9(a). The open network permits an easy escape of gaseous pyrolysis products. Intermediate behavior was observed for 70 wt% resin powders which had a smaller agglomerate size of 8 μm ESD (Fig. 9(b)). The 85 wt% resin derived powder with the same 8 μm ESD agglomerate size (Fig. 4) has no internal porosity (Fig. 9(c)). This is consistent with the minimum observed in the BET measurements (Fig. 8).

(3) *Closure of Surface Pores by Residual Carbon*

At temperatures below the char burnout which occurs at 900°C, the residual carbon seals off surface pores, making the internal porosity inaccessible to N_2 molecules during BET analysis. Thus, for 800°C calcined powders, although TEM revealed high internal porosity in agglomerates (Fig. 6), the specific surface area was anomalously low at 1.7 m^2/g (Fig. 5). Carbon depth profiling by AES confirmed the carbon concentration at the surface (Fig. 7). For 900°C calcined powders, the char, including the surface carbon, was burnt out. The internal porosity was now accessible to N_2 adsorption, giving a surface area of 10 m^2/g. This value is 40 times larger than that of conventionally prepared $CaAl_2O_4$ powders.[5,6] The removal of surface carbon at 900°C and above was confirmed by AES (Fig. 7).

(4) *Mechanism and Kinetics of $CaAl_2O_4$ Formation*

Activation energies (E_a) for various growth and diffusion processes are compared in Table I. It is seen that a different mechanism operates for $CaAl_2O_4$ crystallite growth from an amorphous matrix (118 kJ/mol) than for solid-state reactions between crystalline CaO and Al_2O_3 (159–376 kJ/mol[34,35]). The high E_a for Al diffusion in Al_2O_3 (477 kJ/mol[36]) versus the lower (E_a) for Ca in CaO (142–268 kJ/mol[37]) indicates that Ca diffuses

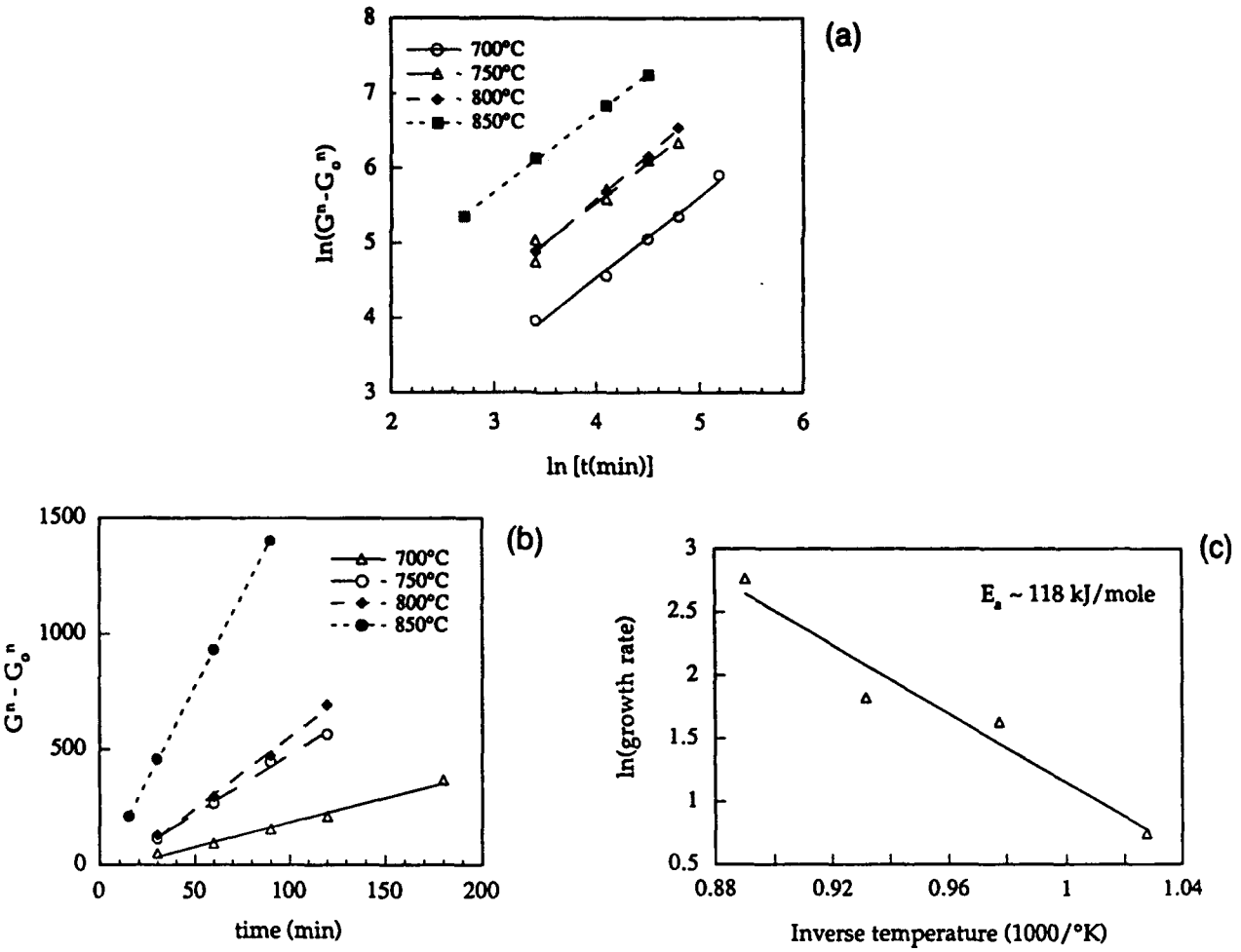

Fig. 11. Determination of various kinetic parameters: (a) ln $(G^n - G_0^n)$ vs ln (t), (b) $G^n - G_0^n$ vs t, (c) ln (q) vs $1/T$. From these curves, $n = 1.68$, $G_0 = 9.9$ nm, and $E_a = 118$ kJ/mol.

Table I. Comparison of Activation Energies for Various Processes

	Growth of chemically prepared $CaAl_2O_4$ (this study)	Growth of conventionally prepared $CaAl_2O_4$[9,43,44]	Diffusion of Al *in* Al_2O_3[9]	Diffusion of Ca *in* CaO[9]
Activation energy, E_a (kJ/mol)	~118	159–376	477	142–268

into Al_2O_3 to form $CaAl_2O_4$. This explains why the E_a for conventional $CaAl_2O_4$ formation is comparable with the E_a for Ca diffusion in CaO.

The mechanism for solid-state reaction between crystalline CaO and Al_2O_3 to form $CaAl_2O_4$ is schematically depicted in Fig. 12(a). Growth of $CaAl_2O_4$ occurs at the $CaAl_2O_4$–Al_2O_3 interface and necessitates the diffusion of Ca through the product phase toward Al_2O_3. Consequently the growth rate decreases as the product layer thickens. The growth kinetic exponent, n, for this type of reaction is considered to be 2.[14,37]

A model for $CaAl_2O_4$ crystal growth from an amorphous matrix of the same composition is proposed in Fig. 12(b). Growth occurs by viscoelastic relaxation of the amorphous phase involving only a few atomic jumps across the amorphous–crystalline interface. The growth rate is independent of crystal size and is constant. In this study the growth kinetic exponent, n, was found to be 1.68. This lower value of n (1.68 vs 2) indicates a faster growth rate for the mechanism involving crystal growth from an amorphous phase. Overall, the process is analogous to a polymorphic transformation in crystalline materials which involves atomic jumps across the transformation front, without any change in the composition, and does not necessitate any long-range diffusion.

Thus, this microstructural-kinetic study of the Pechini process gives an insight into the advantages of chemical synthesis over conventional solid-state reacted processes. Whereas the latter process involves repeated grinding and firing and may still yield unreacted and/or intermediate phases, the Pechini route produces a completely reacted, single-phase product, at comparatively lower temperatures.

V. Conclusions

High-purity, high-specific-surface-area, single-phase $CaAl_2O_4$ powders have been chemically synthesized at temperatures at or below 900°C using the Pechini process. Specific surface areas of 10 m^2/g were routinely obtained at 900°C after 3 h of calcination.

TEM studies of the early stages of crystallization from an amorphous matrix enabled a detailed kinetic analysis of crystallite growth. The activation energy of 118 kJ/mol and a

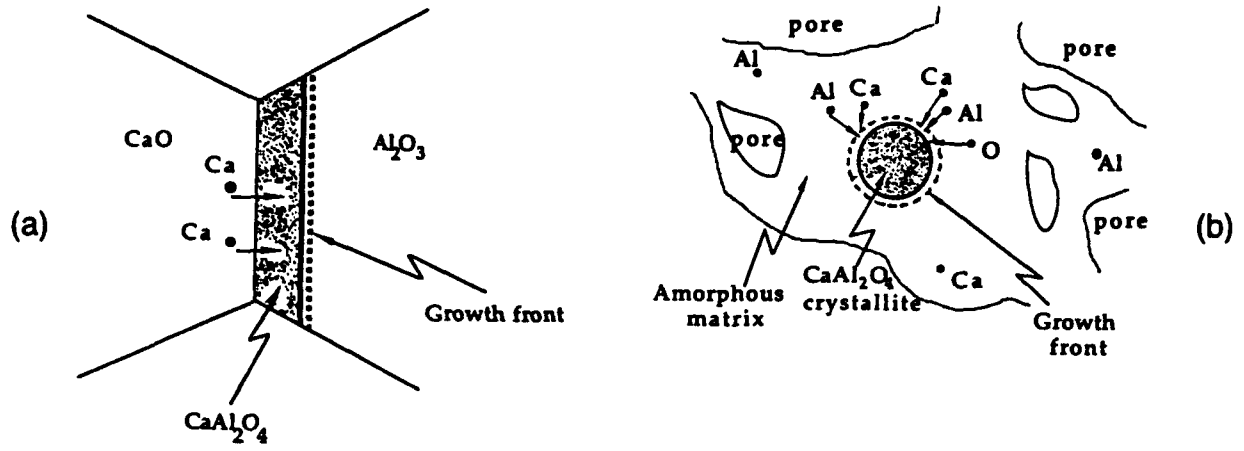

Fig. 12. Schematic representation of $CaAl_2O_4$ growth mechanism during (a) high-temperature solid-state reactions, (b) crystallization from chemically derived amorphous matrix.

growth kinetic exponent n of 1.68 were determined. These values were consistent with a short-range diffusion model.

Acknowledgments: We thank Dr. I. Nettleship, now at the University of Pittsburgh, for valuable discussions on the Pechini process. The use of facilities at the Center for Microanalysis of Materials in the Materials Research Laboratory, at the University of Illinois, is acknowledged. The authors are indebted to Dr. Nancy Finnegan of the MRL for the AES analyses.

References

[1]A. A. Goktas and M. C. Weinberg, "Preparation and Crystallization of Sol–Gel Calcia–Alumina Compositions," *J. Am. Ceram. Soc.*, **74** [5] 1066–70 (1991).

[2]F. T. Wallenberger, N. E. Weston, and S. D. Brown, "Melt Processed Calcium Aluminate Fibers: Structural and Optical Properties"; pp. 116–24 in Proceedings of the Society of Photo-Optical Instrumentation Engineers, Vol. 1484, *Growth and Characterization of Materials for Infrared Detectors*. SPIE–The International Society for Optical Engineering, Bellingham, WA, 1991.

[3]J. D. Birchall, A. J. Howard, and K. Kendall, "Flexural Strength and Porosity of Cements," *Nature (London)*, **289**, 388–89 (1981).

[4]K. Kendall, J. D. Birchall, and A. J. Howard, "The Relation between Porosity, Microstructure and Strength, and the Approach to Advanced Cement-Based Materials," *Philos. Trans. R. Soc.*, **A310**, 139–50 (1983).

[5]K. Fujii, W. Kondo, and H. Ueno, "Kinetics of Hydration of Monocalcium Aluminate," *J. Am. Ceram. Soc.*, **69** [4] 361–64 (1986).

[6]R. N. Edmonds and A. J. Majumdar, "The Hydration of Monocalcium Aluminate at Different Temperatures," *Cem. Concr. Res.*, **18**, 311–20 (1988).

[7]W. Weisweiler and S. J. Ahmed, "Kinetik der Festkörperreaktionen im System CaO–Al_2O_3," (in Ger.) *Zem.-Kalk-Gips*, **33** [2] 84–89 (1980).

[8]V. K. Singh, M. M. Ali, and U. K. Mandal, "Formation Kinetics of Calcium Aluminates," *J. Am. Ceram. Soc.*, **73** [4] 872–76 (1990).

[9]V. K. Singh and M. M. Ali, "Formation Kinetics of High Alumina Cement Phases," *Trans. J. Br. Ceram. Soc.*, **79**, 112–14 (1980).

[10]V. K. Singh and U. K. Mandal, "Kinetic Study of the Thermal Synthesis of Calcium Dialuminate above 1400°C, *Trans. J. Br. Ceram. Soc.*, **81** [4] 112–13 (1982).

[11]M. Uberoi and S. H. Risbud, "Processing of Amorphous Calcium Aluminate Powders at <900°C," *J. Am. Ceram. Soc.*, **73** [6] 1768–70 (1990).

[12]D. M. Roy, R. R. Neurgaonkar, T. P. O'Holleran, and R. Roy, "Preparation of Fine Oxide Powders by Evaporative Decomposition of Solutions," *Am. Ceram. Soc. Bull.*, **56** [11] 1023–24 (1977).

[13]J. B. Baldo and R. C. Bradt, "Grain Growth of the Lime and Periclase Phases in a Synthetic Doloma," *J. Am. Ceram. Soc.*, **71** [9] 720–25 (1988).

[14]R. J. Brook, "Controlled Grain Growth"; pp. 331–64 in Treatise on Materials Science and Technology, Vol. 9, *Ceramic Fabrication Processes*. Edited by F. F. Wang. Academic Press, New York, 1976.

[15]A. U. Daniels, Jr., R. C. Lowrie, Jr., R. L. Gibby, and I. B. Cutler, "Observations on Normal Grain Growth of Magnesia and Calcia," *J. Am. Ceram. Soc.*, **45** [6] 282–85 (1962).

[16]C. Greskovich and K. W. Lay, "Grain Growth in Very Porous Al_2O_3 Compacts," *J. Am. Ceram. Soc.*, **55** [3] 142–46 (1972).

[17]S. W. Freiman and L. L. Hench, "Kinetics of Crystallization in Li_2O–SiO_2 Glasses," *J. Am. Ceram. Soc.*, **51** [7] 382–87 (1968).

[18]S. W. Freiman and L. L. Hench, "Further Analysis of Glass Crystallization Kinetics," *J. Am. Ceram. Soc.*, **52** [2] 111–12 (1969).

[19]R. A. Ligero, J. Vazquez, P. Villares, and R. Jimenez-Garay, "A Study of the Crystallization Kinetics of Some Cu-As-Te Glasses," *J. Mater. Sci.*, **26**, 211–15 (1991).

[20]G. C. Nicholson, "Grain Growth in Magnesium Oxide Containing Iron Oxide or Titanium Dioxide," *J. Am. Ceram. Soc.*, **49** [1] 47–49 (1966).

[21]C. S. Ray, W. Huang, and D. E. Day, "Crystallization Kinetics of a Lithia–Silica Glass: Effect of Sample Characteristics and Thermal Analysis Measurement Techniques," *J. Am. Ceram. Soc.*, **74** [1] 60–66 (1991).

[22]T. J. Clark and J. S. Reed, "Kinetic Processes Involved in the Sintering and Crystallization of Glass Powders," *J. Am. Ceram. Soc.*, **69** [11] 837–46 (1986).

[23]R. M. Spriggs, L. A. Brissette, and T. Vasilos, "Grain Growth in Fully Dense Magnesia," *J. Am. Ceram. Soc.*, **47** [8] 417–18 (1964).

[24]T. Tsuchida, "Formation of $ZnAl_2O_4$ in the Presence of Cl_2," *J. Am. Ceram. Soc.*, **71** [9] C-404–C-405 (1988).

[25]S. C. Yang and R. M. German, "Grain Growth Kinetics in Liquid-Phase-Sintered Zinc Oxide–Barium Oxide Ceramics," *J. Am. Ceram. Soc.*, **74** [12] 3085–90 (1990).

[26]J. E. Burke, "Fundamentals of Recrystallization and Grain Growth"; pp. 1–73 in *Grain Control in Industrial Metallurgy*. Edited by J. E. Burke, R. L. Kenyon, H. Burghoff, and J. T. Hobbs. ASM, Cleveland, OH, 1949.

[27]F. Cebollada and J. M. Gonzales, "Microstructural Study of the Crystallization Product of the $Co_{100-x}P_x$ Amorphous System," *J. Mater. Res.*, **8** [1] 105–11 (1993).

[28]J. Y. Cheng and L. J. Chen, "Growth Kinetics of Amorphous Interlayers by Solid-State Diffusion in Polycrystalline Zr and Hf Films on (111) Si," *J. Appl. Phys.*, **68** [8] 4002–4007 (1990).

[29]R. Chiba and N. Funakoshi, "Crystallization of Vacuum Deposited Te-Se-Cu Alloy Films," *J. Non-Cryst. Solids*, **105**, 149–54 (1988).

[30]T. Ikari, M. Izaki, T. Fukumori, and K. Futagami, "The Activation Energies of the Crystallization of Amorphous Ni_xP_y Alloy Films," *J. Mater. Sci.*, **26**, 583–87 (1991).

[31]K. Maki and Y. Shigeta, "Formation of Some Hierarchy in hous Structure During the Crystallization of Vacuum-Deposited Amorp emiconductor Films," *J. Appl. Phys.*, **63** [12] 5747–50 (1988).

[32]F. Yan, J. M. Parker, and B. J. Ainslie, "Kinetic Study of Growth o Se) Microcrystals in a Glass Matrix," *J. Phys. D*, **21**, S82–S84 (1988).

[33]M. Avrami, "Kinetics of Phase Change. II," *J. Chem. Phys.*, **8**, 212–24 (1940).

[34]D. Turnbull, "Phase Changes"; pp. 252–56 in *Solid State Physics*, Vol. 3. Edited by F. Seitz and D. Turnbull. Academic Press, New York, 1956.

[35]J. E. Burke and D. Turnbull, "Recrystalization and Grain Growth"; pp. 220–92 in *Progress in Metal Physics*, Vol. 3. Edited by B. Chalmers. Interscience, New York, 1952.

[36]M. Hillert, "On the Theory of Normal and Abnormal Grain Growth," *Acta Metall.*, **13**, 227–38 (1965).

[37]A. M. Glaesar, "Microstructure Development in Ceramics: The Role of Grain Growth," *Yogyo Kyokaishi*, **92** [10] 537–46 (1984).

[38]J. W. Christian, *The Theory of Transformations in Metals and Alloys*, Part I, Equilibrium and General Kinetic Theory, 2nd ed.; pp. 534–48. Pergamon Press, Oxford, U.K., 1975.

[39]M. Pechini, "Method of Preparing Lead and Alkaline-Earth Titanates and Niobates and Coating Method Using the Same to Form a Capacitor," U.S. Pat. No. 3 330 697, July 11, 1967.

[40]P. A. Lessing, "Mixed-Cation Oxide Powders via Polymeric Precursors," *Am. Ceram. Soc. Bull.*, **68** [5] 1002–1007 (1989).

[41]R. W. Nurse, J. H. Welch, and A. J. Majumdar, "System CaO–Al_2O_3 in a Moist-Free Atmosphere"; Fig. 4308, p. 103 in *Phase Diagrams for Ceramists, 1975 Supplement*. Edited by M. K. Reser. American Ceramic Society, Columbus, OH, 1975.

[42]O. Kubaschewski, "The Thermodynamic Properties of Double Oxides (A Review)," *High Temp.–High Pressures*, **4** [1] 1–12 (1972).

[43]I. Nettleship, J. L. Shull, Jr., and W. M. Kriven, "Chemical Preparation and Phase Stability of Ca_2SiO_4 and Sr_2SiO_4 Powders," *J. Eur. Ceram. Soc.*, **11**, 291–98 (1993).

[44]K. S. Chou and G. Burnet, "Formation of Calcium Aluminates in the Lime-Sinter Process. Part I. Qualitative Studies," *Cem. Concr. Res.*, **11**, 57–64 (1981).

[45]K. S. Chou and G. Burnet, "Formation of Calcium Aluminates in the Lime-Sinter Process. Part II. Kinetic Study," *Cem. Concr. Res.*, **11**, 167–74 (1981). □

XPS Studies of Bond Structure Between Polyvinyl Alcohol and a Titanate Cross Coupling Agent

Mehmet A. Gülgün*, Oludele O. Popoola*†, and Waltraud M. Kriven*

Department of Materials Science and Engineering, University of Illinois at Urbana-Champaign, 105 S. Goodwin Avenue, Urbana, IL 61801, U.S.A.

Chemical interactions between polyvinyl alcohol (PVA) and triethanol amine titanate chelate were studied using X-ray photoelectron spectroscopy (XPS) and scanning electron microscopy (SEM). The titanate chelate cross coupled the PVA solution and produced a viscous gel. The gel had a three dimensional cage structure containing -C_{PVA}-O-Ti-O-C_{PVA}- organic complexes. The water of the PVA solution was physically retained in the cage structure and was readily available for chemical reactions. The removal of this entrapped water was irreversible and lead to a collapsed film of Ti-cross linked PVA.

I. INTRODUCTION

Polyvinyl alcohol (PVA) is one of the key components of the high alumina based (HAC), macro-defect-free (MDF) cement composite materials. These composites were introduced in the early 1980's and had superior mechanical properties compared to any cement paste known at that time [1, 2]. Microstructural and microchemical studies of HAC-MDF have shown that the polymer not only acted as a rheological aid that facilitated effective particle

---

* Member of the Materials Research Society.

Supported by the US Air Force Office of Scientific Research under grant number AFOSR-URI-90-0242. The work of O. Popoola was funded under grant number AFOSR URI-90-0174.

† Now at Material Systems Reliability Dept., Ford Research Laboratory, Dearborn, MI 48121.

packing during processing, but its chemical reaction with the ceramic grains also contributed to the improved properties of the composite [3]. The microstructure consisted of anhydrous cement grains, the polymer, and an interphase region composed of a mixture of amorphous and crystalline hydrates of calcium aluminate [3, 4]. Although the water soluble polymer was essential in obtaining the improved properties of the composite, it also proved itself to be the Achilles' heel of the system. HAC-MDF cement lost ~32% of its dry strength upon prolonged exposure to moisture [5]. Other properties such as electrical resistivity and dielectric loss constant followed the trend of strength after moisture exposure. In-situ environmental transmission electron microscopy (TEM) studies of the composite showed that the polymer and the interphase region absorbed moisture when exposed to humidity. Water swelled up the polymer and the interphase, leading to degradation of the properties [6]. It appeared thus that the polymer matrix and the interphase region needed to be rendered insensitive to moisture after the setting reactions in the composite.

Incorporation of an organic cross-coupling agent into the composition of the HAC-MDF during processing has been a promising solution to this problem [5]. The basic requirements for a cross coupling agent for the composite are (1) its addition should not impair the processability of the composite, and (2) It must be stable and active at the high pH values present during composite processing.

A titanate cross-coupling agent, triethanol amine titanate chelate (Tyzor TE®, DuPont de Nemours) have been incorporated into the composition of MDF cement. The composite thus modified, had a significant increase in moisture resistance when compared with the original one [5]. While the original composite retained only 68% of its strength after 28 days of moisture exposure, the modified one retained up to 84% after the same treatment. However, there was a practical limit to the amount of the titanate cross-coupling agent that could be added to the system. Higher than 0.21 parts by weight of triethanol amine titanate chelate interfered with the processing of the composite [5]. Studies on titanate modified HAC-MDF composites showed that the torque required during high shear mixing increased with the addition of cross coupling agent, and the window of processability decreased[7]. It is surprising that such a small quantity of triethanol amine titanate chelate could significantly modify both the processing window and the moisture resistance of this composite. It was therefore imperative to understand the nature of the chemical interactions between various components

of the modified composite. The interactions between the PVA and a calcium aluminate ceramic have been previously reported [8].

In this paper, X-ray photoelectron spectroscopy (XPS) was used to study the bond structure and the chemical reactions between triethanol amine titanate chelate and polyvinyl alcohol.

II. EXPERIMENTAL

A. Materials

1. Polyvinyl alcohol (PVA):

100% hydrolyzed polyvinyl alcohol (PVA) with an average molecular weight of 50,000 was used in all experiments. 2 wt% PVA was dissolved in de-ionized water, by simply stirring the solution at room temperature. Solutions with higher PVA contents were prepared at temperatures below 67°C. The pH of the solutions was measured as a function of PVA content using a microprocessor controlled pH meter.

2. Triethanol amine titanate chelate (Tyzor TE®):

This titanate cross coupling agent is compatible with high pH environments, and its cross linking reactions can be activated in aqueous solutions [9]. It is "a mixture of various chelates with at least one component in the solution having a cage structure" as depicted in Fig. 1 [9]. No further detail on possible other structures in the solution was available in the product literature. It was observed that the Tyzor solution aged with time and changed its color from pale yellow to amber. The material was also suspected to decompose on standing for extended time at room temperature. The Tyzor series of organic titanates cross linked polymers through the active hydrogen of hydroxyl, amino, amide, carbonyl, and thio functional groups [9]. They were not very susceptible to hydrolysis. The chelates were supposedly unreactive when mixed with cross linkable materials at room temperature. Raising the temperature between 100°C and 250°C activated the chelates by decomposing their structure. The cross linking reactions could also be initiated by increasing the pH of the system in the

range of 6 to 10. The chelates were known to cross link at room temperature in a few seconds in an aqueous guar gum solution at pH 7.0 [9].

B. Sample Preparation

1. XPS

Three sample configurations used are schematically shown in Fig. 2 (a-c). The films were prepared by spin coating the appropriate solutions on to a pre-cleaned glass slide under a rotation speed of 4,000 rpm. In the first configuration the Tyzor solution was spread on the glass substrate. A PVA solution was then spun coated on the Tyzor layer. The order of the layering was reversed in the second configuration. While the PVA layer uniformly spread over the Tyzor layer in the first configuration, in the second, the instantaneous reaction prevented a uniform spread of Tyzor over the PVA. The third was a reference configuration with an intermediate gold layer between the Tyzor and the PVA covering half of the specimen. The purpose was to assure that the depth probed during XPS was completely within the top PVA layer. The whole procedure was carried out in a Class-1000 clean room. The samples were stored in a dessicator for one day prior to XPS analysis.

2. SEM and XRD

In a vial, a droplet of triethanol amine titanate chelate solution (approximately 0.02 g of 1/50 by weight Tyzor TE/isopropyl alcohol solution) was added to 5 ml of 2 wt% PVA solution. The mixture gelled instantaneously. Highly reactive, fine monocalcium aluminate powders [10, 11] were sprinkled on to the PVA-Tyzor TE gel thus produced. After 48 h, the powders were separated from the gel. Microstructural characterization and microchemical analysis of the separated powders were performed using X-ray diffraction, scanning electron microscopy (SEM) and energy dispersive spectroscopy (EDS).

C. Characterization

1. XPS Analysis

A PHI 5400 X-ray photoelectron spectrometer equipped with a Perkin-Elmer hemispherical analyzer was used to collect the XPS data. The Mg anode (Mg Kα at 1253.6 eV) was operated at 400 W (15 kV) under a base pressure of 2×10^{-8} Pa. The X-ray source was approximately 15 mm directly above the sample surface. The hemispherical analyzer was operated in the constant energy mode with a pass energy at 17.9 eV giving a resolution of 1 eV. It was reported earlier that some degradation of the polymer occurred after 1 hr of continuous exposure to X-ray irradiation under the above conditions [8, 12]. Multiplex data acquisition was completed in 30 to 40 min. The C(1s), O(1s), and Ti($2p_{3/2}$) energy lines were analyzed. Mixed Gaussian and Lorentzian line shapes were used for spectral deconvolution. The full widths at half maximum (FWHM) were set at 1.33 ± 0.1 eV for C(1s), 1.70 ± 0.1 eV for O(1s) and 1.20 ± 0.1 eV for Ti($2p_{3/2}$) [8, 12-16]. Plasma deposited gold film was used to calibrate the binding energies in the spectra. The Au($4f_{7/2}$) peak was set to 84.0 eV [17-20] and all the other peak positions were referred to this binding energy level. Under these conditions the binding energy of the C(1s) peak associated with the CH_2 group in PVA was 285.0 eV [8, 12, 13, 21].

III. RESULTS

When an aqueous solution of 100% hydrolyzed polyvinyl alcohol (PVA) was mixed with triethanol amine titanate chelate in a weight ratio of 4/1000 : Tyzor TE/PVA, the whole solution formed a very viscous gel at room temperature within seconds. This gel did not flow when the vial containing it was turned upside down as shown in Fig. 3. No water rejection was observed after several months in a closed container. When the gelled solution was left in air on the other hand, the structure lost its water and shrunk. Thermogravimetric analysis (TGA) of the gel at a heating rate of 1°C/min. revealed that most of the water was lost below 80°C. Once the gel was dried and shrunk leaving a filmy residue, it did not dissolve or swell in cold or boiling water.

The XPS survey spectrum indicated that the sample was free of impurities. The survey spectrum from the sample with the configuration depicted in Figure

2 c. did not reveal any gold peaks. Thus, it was concluded that the spectra observed originated from the reacted PVA layer. Fig. 4 shows the experimental and synthesized O(1s) spectra from pure PVA (a), and from PVA coated on to Tyzor TE (b). After the correction for sample charging effects, the spectrum from pure PVA revealed a single O(1s) peak centered at 533.0 ± 0.1 eV having a FWHM of 1.70 ± 0.1 eV, in agreement with the values reported in the literature [13, 14]. Although there may be more than one type of oxygen-carbon bond in PVA, the various O(1s) peaks due to these could not be distinguished given the resolution limit of 1 eV. The possible bond structures contributing to the observed O(1s) spectrum were C-OH, C=O and C-O-C groups. The binding energy for the O(1s) photoelectron from the C-OH group was at 533.0 eV (Table I). A comparison of the two O(1s) spectra from pure PVA and from PVA on Tyzor TE, in Figs. 4 (a and b) indicates clearly that oxygen is taking part in an additional type of bonding in the later configuration. Fig. 4 b reveals a new O(1s) peak at 531.3 eV in addition to that from the C-OH group.

The C(1s) multiplex spectra from pure PVA and PVA coated on to Tyzor TE are shown in Fig. 5. In the pure PVA film, the C(1s) spectrum can be deconvolved into 3 peaks. The first, located at 285.0 eV is associated with the CH_2 group, while the second, at 286.5 eV is due to the C-OH group. The third peak at 288.3 eV resulted from C=O and C-O-C groups (Table II). These groups formed as a result of X-ray irradiation induced degradation of the -OH groups in the polymer [8, 12]. Consequently the C(1s) peak associated with the -OH group is slightly attenuated. The experimental C(1s) spectrum from PVA coated on Tyzor TE (Fig. 5 b) reveals another peak in addition to the three PVA peaks mentioned above. This new carbon 1s peak is at 285.7 eV. The peak from the C-OH group is further reduced in intensity. The intensities of this new peak and the peak which is due to C=O and/or C-O-C groups are such that their sum equals the reduction in intensity of the C-OH peak from the 50:50 ratio with CH_2 peak intensity.

The experimental multiplex and synthesized Ti(2p) duplets from a Tyzor film and from PVA reacted with Tyzor are shown in Figure 6. In Fig. 6 a the $Ti(2p_{3/2})$ and $Ti(2p_{1/2})$ peaks are separated by 5.75±0.05 eV, indicating that titanium in Tyzor was surrounded by oxygen atoms. Moreover the $Ti(2p_{3/2})$ can be deconvolved into two peaks located at 459.0 eV and 457.5 eV. These peaks can be attributed to Ti^{4+} and Ti^{3+} valence states, respectively (Table III). Fig. 6 b shows exactly the same features as does Fig. 6 a. This indicates that there was no

change in the chemical environment around the titanium atoms in Tyzor and in PVA reacted with Tyzor.

The X-ray diffraction studies of the calcium aluminate powders sprinkled on to the gel that formed during PVA/Tyzor TE interaction revealed that hydration had occurred. Fig. 7 shows that hydrates ($CaAl_2O_{14}H_{20}$) and carbohydrates ($Ca_4Al_2CO_{21}H_{22}$) formed. Fig. 8 is the SEM micrograph from the same powders. It clearly shows needle-shaped morphology typical of carbohydrates. The EDS analysis revealed Ca, Al and very small amounts of Ti in the hydrated powders. However, the Ti peak may have been due to the polymer which adhered to the powder surface.

IV. DISCUSSION

From a visual inspection of the PVA solution mixed with Tyzor TE in the vial it was apparent that the two had reacted at room temperature. This was evidenced by the instantaneous viscosity increase and immediate gelation of the mixture. The XPS analyses of the reacted polymer revealed new peaks in the O(1s) and C(1s) spectra. The new oxygen signature at 531.25 ± 0.1 eV and the carbon signature at 285.7 ± 0.1 eV were indicative of the formation of a new complex.

By analogy with the binding energies obtained for the O(1s) peak in other transition metal carboxylates (Table I), the new O(1s) peak could be assigned to a C-O-Ti-O-C organic complex. Consistent with this, the binding energy of the C(1s) peak would be expected to lie in the range 285.6-285.9 eV (Table II). A value of 285.7 eV was observed in the Tyzor-reacted PVA. Since titanium had the same chemical environment in Tyzor as in the C-O-Ti-O-C complex formed during the Tyzor-PVA reaction, no binding energy change was expected, as was observed. The formation of the C-O-Ti-O-C complex and corresponding decrease in the C-OH peak intensity indicated a mechanism involving cation exchange with the OH group of the PVA. Such a mechanism is schematically depicted in Fig. 9.

The exceedingly low concentration of titanium added indicated that the cross linking occurred at only a few sites between the PVA chains. One could envision that the joining of chains in the solution will increase the viscosity by limiting the molecular configurations. Consequently, the average molecular

weight per chain is increased. Random cross linking across chains would form a three dimensional cage structure which could entrap water molecules by Van der Waals' interactions and stearic hindrance (Fig. 10). Such a model could explain why there was no water rejected during instantaneous gelation, although water made up approximately 95 wt% of the solution. Furthermore, this non-chemically bonded water was easily extracted by the highly reactive calcium aluminate powders forming hydrates. Removal of this water left a collapsed residue film of Ti-cross linked PVA, and was irreversible.

Earlier in situ environmental TEM studies showed that water was absorbed by the polymer matrix phase in MDF-HAC, leading to a degradation in mechanical and electrical properties [8]. The present study suggests that the polymer could be rendered insensitive to water resulting in a water resistant film encapsulating the partially hydrated calcium aluminate grains. Such a mechanism could eliminate the water sensitivity problem of MDF cement.

V. CONCLUSION

A commercial titanate cross coupling agent, Tyzor TE, reacted with an aqueous solution of 100% hydrolyzed PVA and formed a viscous gel at room temperature. The XPS analysis indicated that cross linking of the PVA chains occurred through formation of C_{PVA}-O-Ti-O-C_{PVA} bonds. Some hydroxyl functional groups of the polymer reacted with the titanate agent to form a three dimensional cage structure. This cross linked structure retained the water of solution in the network of the gel. The water was only physically held in the structure and was available for reaction with calcium aluminate powder. The irreversible removal of the physically entrapped water left a collapsed residual film of Ti-cross linked PVA.

ACKNOWLEDGMENT

This work was supported by the U.S. Air Force Office of Scientific Research under grant number AFOSR-URI-90-0242 and AFOSR-URI-90-0174. We are grateful to Professor D. J. Van Harlingen for providing the clean room facilities, and to Mr. R. Haasch for useful discussions. The XPS analyses were

carried out in the Center for Microanalysis of Materials, University of Illinois, which is supported by the U.S. Department of Energy under contract DEFG02-91-ER45439.

REFERENCES

1. J. D. Birchall, A. J. Howard, and K. Kendall, Nature, **289**, 388 (1981).

2. K. Kendall, J. D. Birchall, and A. J. Howard, Phil. Trans. Royal Soc., **A310**, 139 (1983).

3. O. O. Popoola, W. M. Kriven and J. F. Young, Edited by L. D. Peachey and D. B. Williams (Proceedings of the XIIth International Congress for Electron Microscopy **4**, Seattle, WA, 1990), pp 1068-1069.

4. O. O. Popoola, W. M. Kriven and J. F. Young, Ultramicroscopy, **37**, 318 (1991).

5. R. A. Desai, M. S. Thesis, University of Illinois at Urbana-Champaign, Urbana, IL, 1990.

6. O. O. Popoola, W. M. Kriven and J. F. Young, J. Am. Ceram. Soc., **74**[8], 1928 (1991).

7. M. A. Boyer, M. S. Thesis, University of Illinois at Urbana-Champaign, Urbana, IL, 1993.

8. O. O. Popoola and W. M. Kriven, J. Mater. Res., 7[6], 1545 (1992).

9. "Tyzor, Organic Titanates", Product Literature by DuPont, E.I. du Pont de Nemours & Co., Wilmington, DE.

10. M. A. Gulgun, O. O. Popoola and W. M. Kriven, J. Am. Ceram. Soc., in press (1994).

11. M. A. Gulgun, O. O. Popoola, I. Nettleship, W. M. Kriven and J. F. Young, in Advanced Cementitious Systems: Mechanisms and Properties, edited by F. P. Glasser, P. L. Pratt, T. O. Mason, J. F. Young, and G. J. McCarthy. Mater. Res. Soc. Symp. Proc. **245**, , Pittsburgh, PA, 1992), pp. 199-204.

12. S. Akther, K. Allan, D. Buchanan, J. A. Cook, A. Campion and J. M. White, Appl. Surf. Sci., **35**, 241 (1988-89).

13. S. Akther, X.-L. Zhou and J. M. White, Appl. Surf. Sci., **37**, 201 (1989).

14. D. T. Clark and H. R. Thomas, J. Polymer Sci.: Polymer Chem. Ed., **14**, 1701 (1976).

15. H. Idriss, K. S. Kim and M. A. Barteau, Surface Science, **262**, 113 (1992).

16. M. Murata, K. Wakino and S. Ikeda, J. Electr. Spect and Rel. Phenom., **6**, 459 (1975).

17. J. P. S. Badyal, R. D. Chambers and Z. Chvatal, J. Fluorine Chem. **57**, 159 (1992).

18 D. T. Clark and H. R. Thomas, J. Polym. Sci.: Polymer Chemistry Edition, **14**, 1671 (1976).

19. D. T. Clark and A. Dilks, J. Polymer Sci.: Polymer Chem. Ed., **14**, 533 (1976).

20. D. T. Clark, A. Dilks and H. R. Thomas, J. Polym. Sci.: Polymer Chemistry Edition, **16**, 1461 (1978).

21. J. M. Burkstrand, J. Appl. Phys., **52**[7], 4795 (1981).

22. C. M. Greenlief and J. M. White, J. Phys Chem., **89**, 5025 (1985).

23. G. M. Porta, J. D. Rancourt and L. T. Taylor, Chem. Mater., **3**[3], 423 (1991).

24. N. C. Saha and H. G. Tompkins, J. Appl. Phys, **72**[7], 3072 (1992).

25. F. Werfel and O. Brummer, Phys. Scripta, **28**, 92 (1983).

26. R. Jerome, Ph. Teyssie, J. J. Pireaux and J. J. Verbist, Appl. Surf. Sci., **27**, 93 (1986).

27. C. A. Tolman, W. M. Riggs, W. J. Linn, C. M. King and R. C. Wendt, Inorg. Chem., **12**, 2770 (1973).

28. M. V. Zeller and R. G. Hayes, Chem. Phys. Lett., **10**[5], 610 (1971).

29. D. Briggs and C. R. Kendall, Int. J. Adhesion and Adhesives, **2**[1], 13 (1982).

30. M. C. Asensio, M. Kerkar. D. P. Woodruff, A. V. de Carvalho, A. Fernandez, A. R. Gonzales-Elipe, M. Fernandez-Garcia, and J. C. Conesa, Surface Science, **273**, 31 (1992).

31. C. N. R. Rao, D. D. Sarma, S. Vasudevan and M. S. Hegde, Proc. R. Soc. Lond., **A367**, 239 (1979).

32. L. Z. Zhao, S. H. Liu, D. H. Wang and C. H. Pan, J. Electr. Spec. Rel. Phenom., **52**, 571 (1990).

33. L. I. Johansson, A. L. Hagstrom, B. E. Jacbson, and S. B. M. Hagstrom, J. Electr. Spec. Rel. Phenom., **10**, 259 (1977).

34. A. L. Hagstrom, L. I. Johansson, B. E. Jacobsson and S. B. M. Hagstrom, Solid state Communications, **19**, 647 (1976).

35. O. O. Popoola, M. F. Denanot, P. Moine, M. Cahoreau and J. Caisso, Acta. Metall., **37**[3], 867 (1989).

36. L. Porte, M. Demonsthenous and T. M. Duc, (in French), J. Less-Comm. Met., **56**, 183 (1977).

37. L. Porte, M. Demonsthenous, G. Hollinger, Y. Jugnet, P. Pertosa and T. M. Duc, Proc. 7th Intern. Vac. Congr. & 3rd Intern. Conf. Solid Surfaces (Vienna 1977), p. 923.

FIG. 1. Schematic of one of the structures present in Tyzor TE solution.

FIG. 2. Schematic of the sample configurations used in XPS experiments.

FIG. 3. Triethanol amine titanate chelate cross coupled PVA solution shown in a vial that has been turned upside down. The 2 wt% PVA solution does not flow, and no water rejection from the reacted structure was observed.

FIG. 4. Experimental and synthesized O(1s) spectra from pure PVA (a), and from PVA coated on Tyzor TE (b)

FIG. 5. C(1s) spectra from pure PVA (a) and PVA coated on Tyzor TE (b).

FIG. 6. Experimental multiplex and synthesized Ti(2p) duplets from Tyzor TE film (a), and from PVA reacted with Tyzor TE (b). The experimental Ti(2p) spectrum from reacted PVA is much weaker compared to Tyzor TE spectrum.

FIG. 7. X-ray spectrum of calcium aluminate powder sprinkled on "gelled" PVA-Tyzor TE solution. Hydrates and carbohydrates of calcium aluminate formed as result of reactions with the water in the "gelled" structure.

FIG. 8. SEM micrograph showing typical rod-like morphology of carbohydrates of calcium aluminates.

FIG. 9. Schematics of cross linking reactions in PVA-titanate cross coupling agent mixture.

FIG. 10. Two dimensional schematic model of the three dimensional cage structure of titanate cross coupled PVA solution with the retained water of solution.

Table I. Binding energy levels of O(1s) photoelectrons in related compounds.

Compound/ environment	Binding Energy in (eV)	Reference
in TiO_2	530.2 - 530.3	22-24
in Ti_2O_3	529.8 - 531.4	22, 24, 25
in M-O-M-OOC*	529.9	26
$Ni(acac)_2$	532.0	27
$Cr(acac)_3$	531.4	28
metal carboxylate	531.6	25
C-OH	533.0 - 533.4	13, 21
C-OH	533.1 ± 0.05	this study
C-O-Ti	531.25 ± 0.1	this study

* carboxylato oxohydroxide type compound with transition metals (M)

Table II. Binding energies for the C(1s) photoelectrons in certain compounds.

Compound/ environment	Binding Energy in (eV)	Reference
C-OH	286.5	29
O-C-H (carbonyl)	288.0	29
O-C-OH (carboxyl)	289.5	29
CH_3O (methoxy)	286.3	15
$Ni(acac)_2$	286.4	27
$Cr(acac)_3$	285.3	28
C-O-Zr	285.6-285.9	25
$C-C/CH_2$	285.0	this study
C-OH	286.5 ± 0.2	this study
C-O	288.3 ± 0.2	this study
C-O-Ti	285.7 ± 0.1	this study

Table III. Binding energies of Ti ($2p_{3/2}$) XPS line in different compounds.

Ti($2p_{3/2}$) XPS Line/ Valence State	Binding enrgy in (eV)	Compound/ environment	Reference
Ti^{4+}	458.5 - 459.1	in TiO_2	15, 16, 21-23, 25, 30, 31-35
Ti^{4+}	458.4	in [TiO(acac)]	22
Ti^{4+}	459.1	in carboxylate environment	25
Ti^{3+}	456.2 - 458.2	in Ti_2O_3	15, 21, 24, 27, 31, 36-37
Ti^{2+}	454.7 - 457.3	in TiO	15, 25, 27, 31, 36-37
Ti^{1+}	454.9	in reduced titanium oxide	15
Ti^{o}	453.8 - 454.0	Ti-metal	15, 25, 30
Ti^{4+}	459.0 ± 0.2	Ti-O-C	this study
Ti^{3+}	457.5		this study

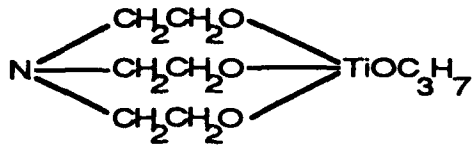

FIG. 1. Schematic of one of the structures present in Tyzor TE solution.

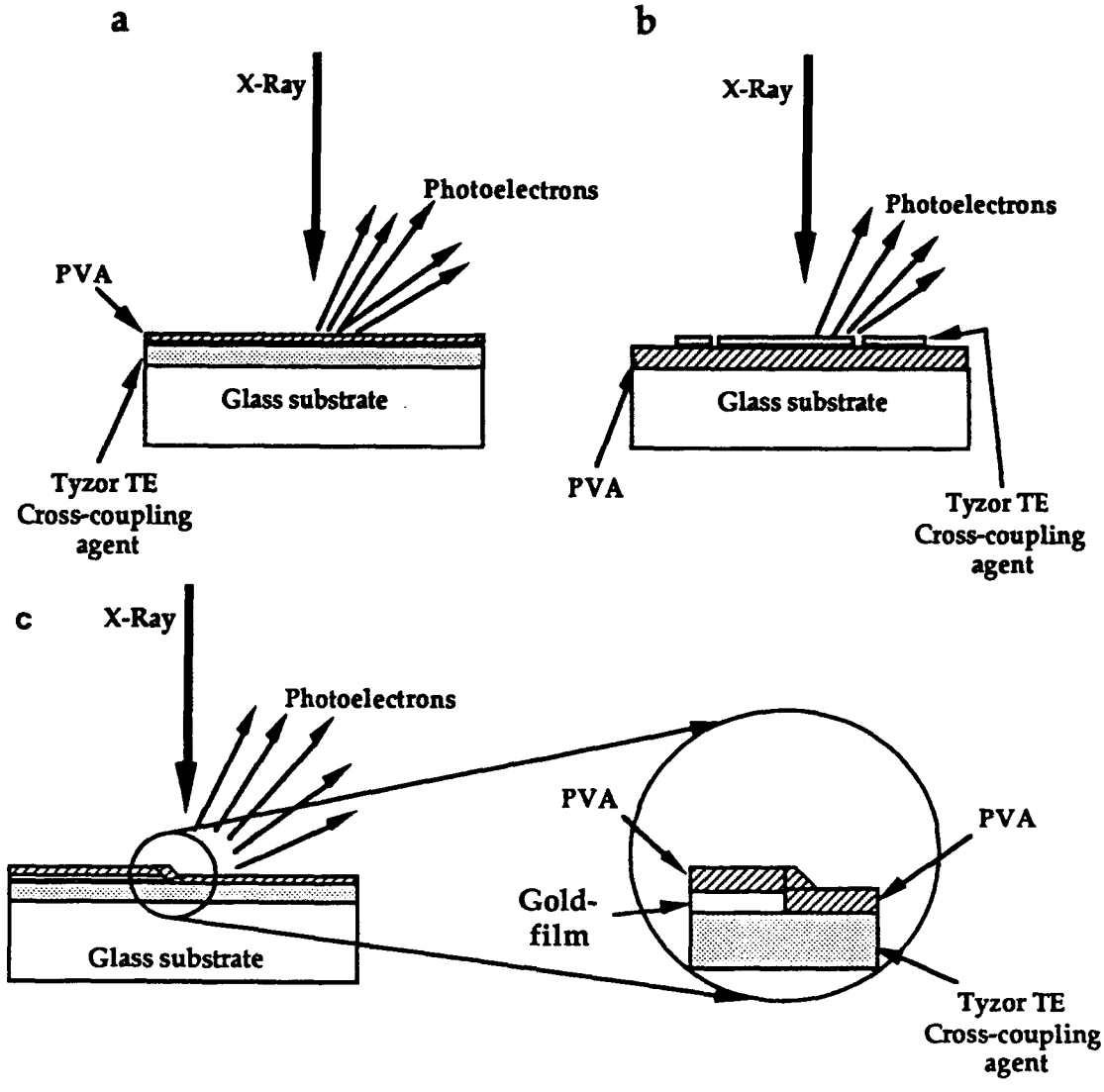

FIG. 2. Schematic of the sample configurations used in XPS experiments.

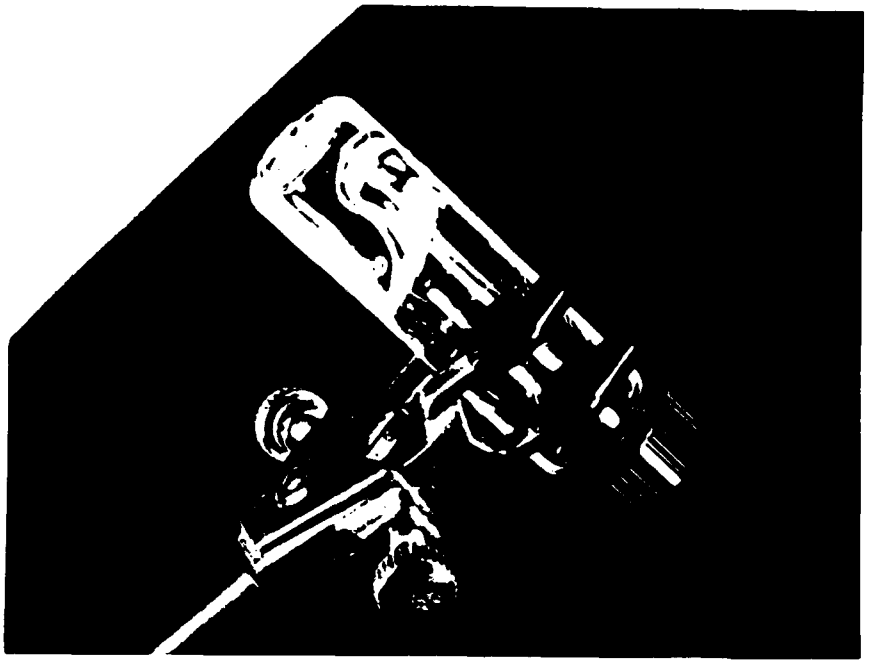

FIG. 3. Triethanol amine titanate chelate cross coupled PVA solution shown in a vial that has been turned upside down. The 2 wt% PVA solution does not flow, and no water rejection from the reacted structure was observed.

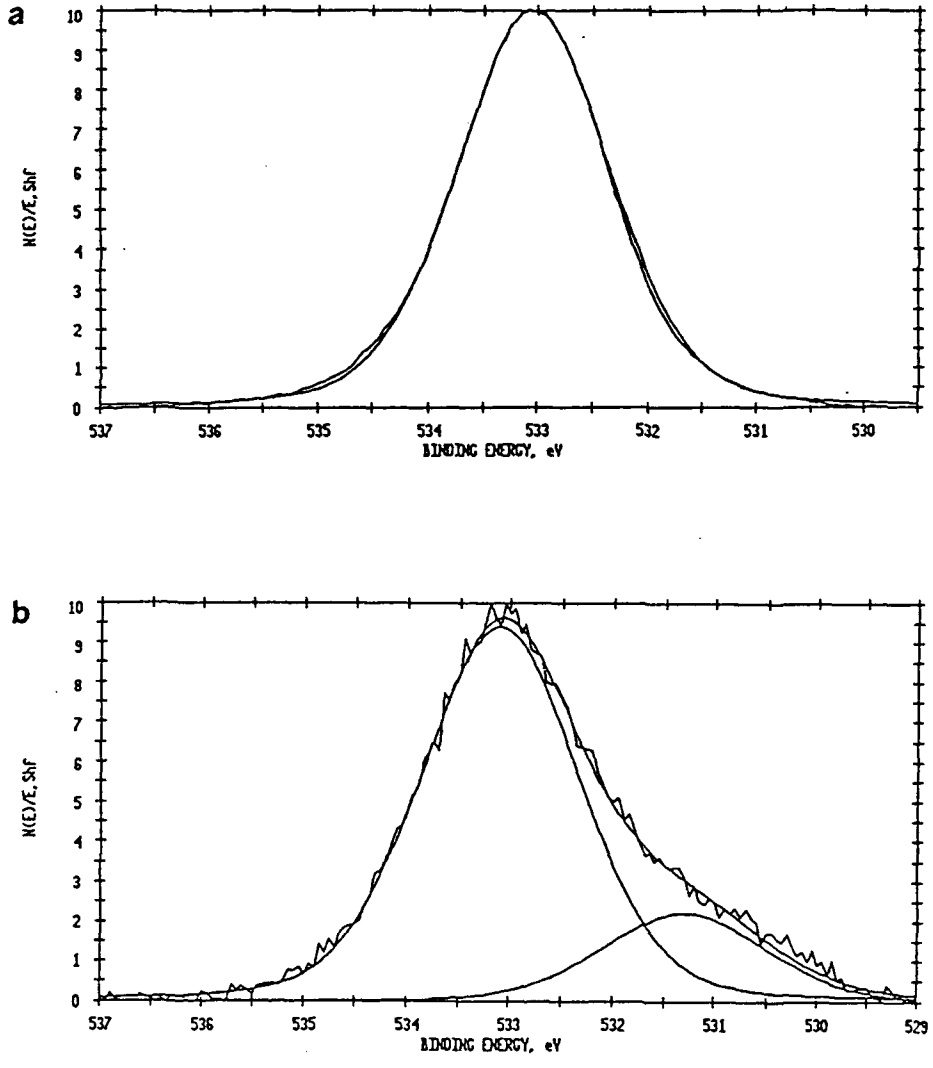

FIG. 4. Experimental and synthesized O(1s) spectra from pure PVA (a), and from PVA coated on Tyzor TE (b).

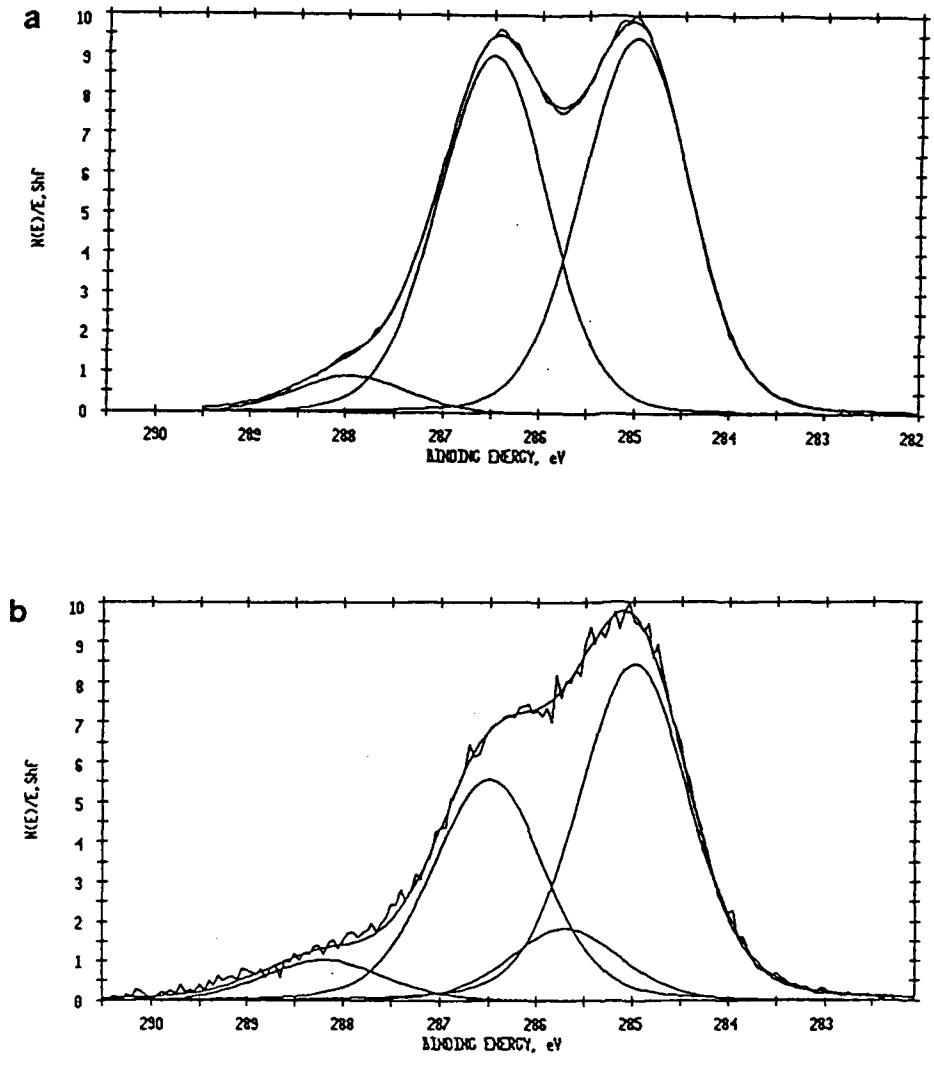

FIG. 5. C(1s) spectra from pure PVA (a) and PVA coated on Tyzor TE (b).

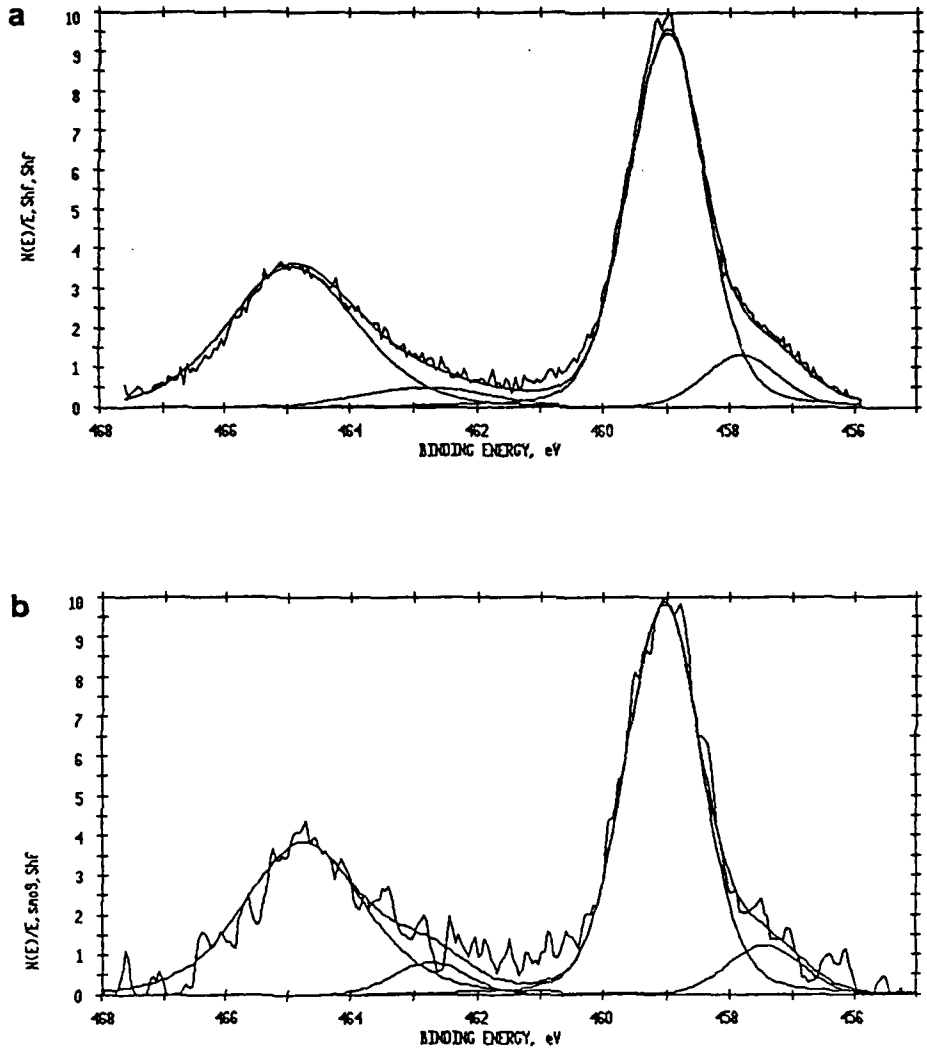

FIG. 6. Experimental multiplex and synthesized Ti(2p) duplets from Tyzor TE film (a), and from PVA reacted with Tyzor TE (b). The experimental Ti(2p) spectrum from reacted PVA is much weaker compared to Tyzor TE spectrum.

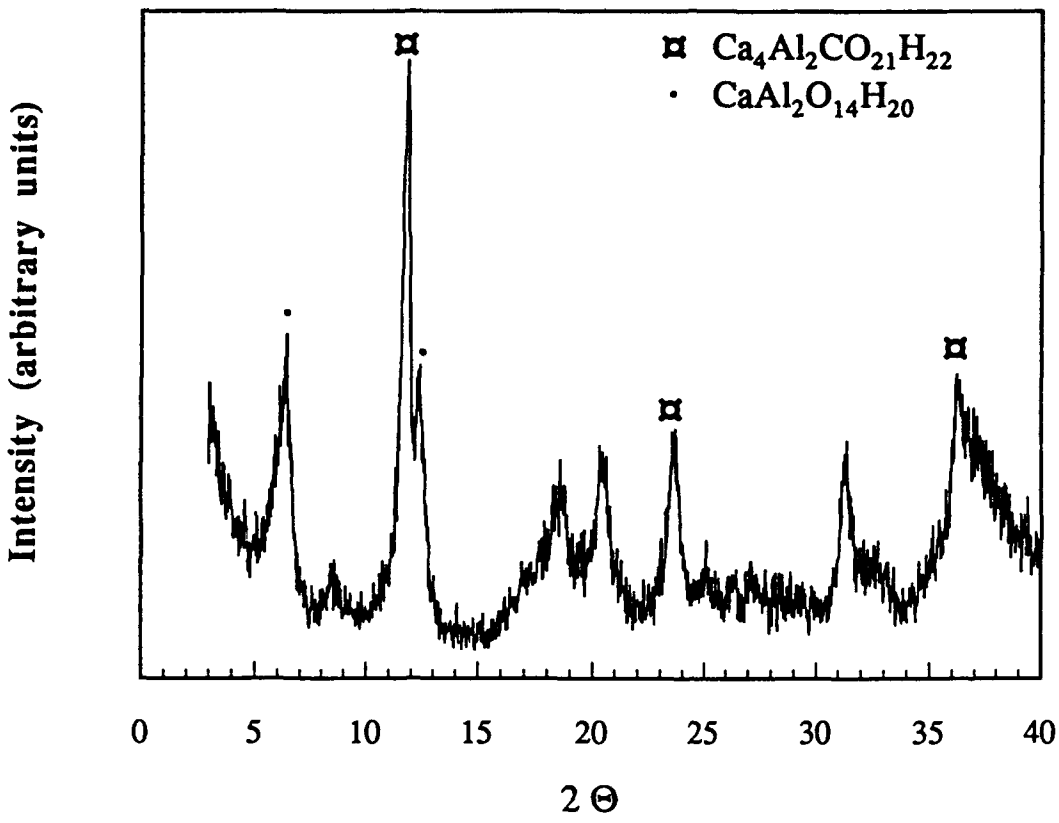

FIG. 7. X-ray spectrum of calcium aluminate powder sprinkled on "gelled" PVA-Tyzor TE solution. Hydrates and carbohydrates of calcium aluminate formed as result of reactions with the water in the "gelled" structure.

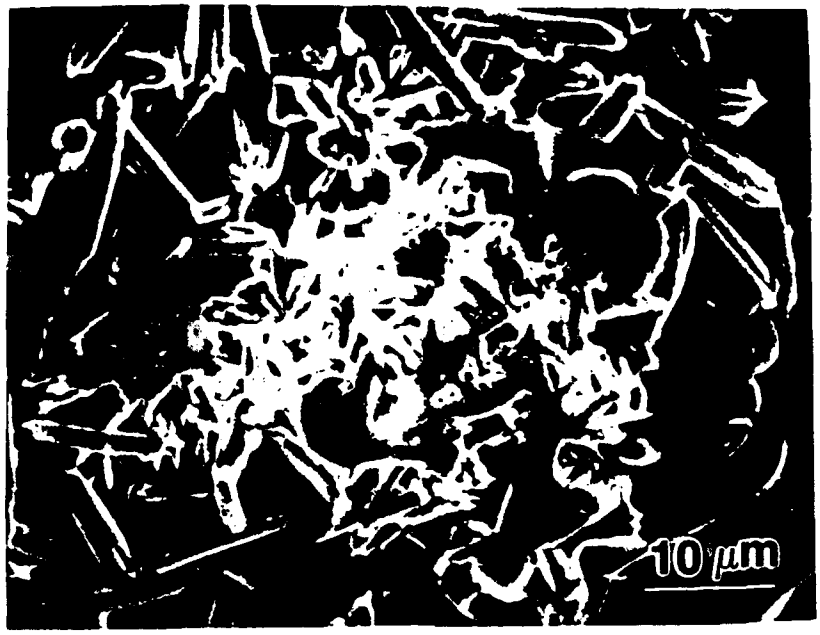

FIG. 8. SEM micrograph showing typical rod-like morphology of carbohydrates of calcium aluminates.

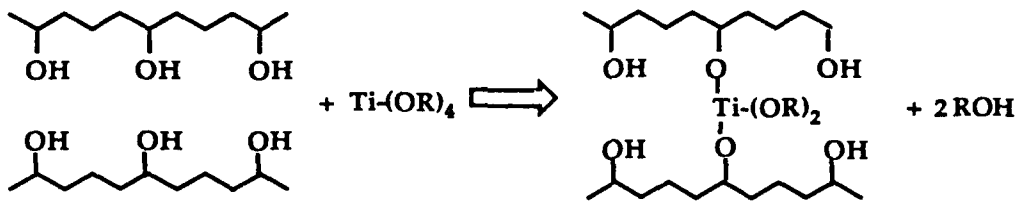

FIG. 9. Schematics of cross linking reactions in PVA-titanate cross coupling agent mixture.

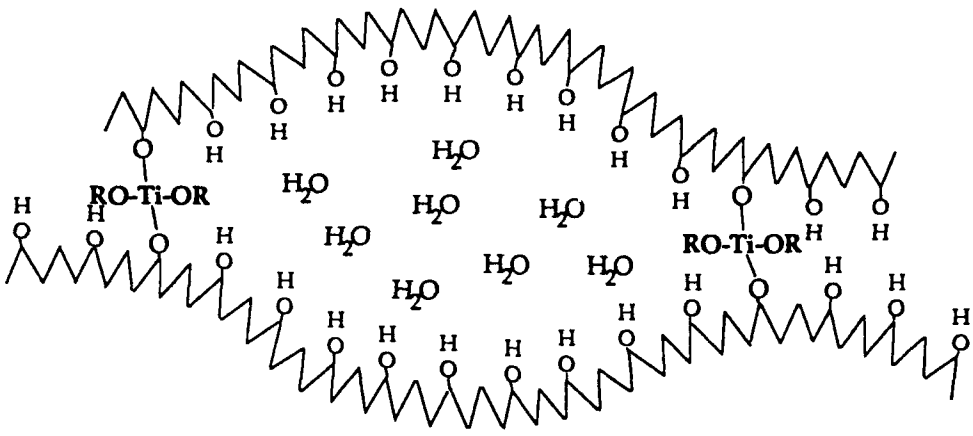

FIG. 10. Two dimensional schematic model of the three dimensional cage structure of titanate cross coupled PVA solution with the retained water of solution.

Materials Chemistry and Physics, 33 (1993) 214–220

Phase stability of Ni-based intermetallic compounds Ni_3X studied by the recursion method

Jinho Park*, Shinji Muramatsu and Michihide Kitamura
Department of Electrical and Electronic Engineering, Utsunomiya University, Utsunomiya 321 (Japan)

Han R. P. Inoue and Haydn Chen
Department of Materials Science and Engineering, University of Illinois at Urbana–Champaign, Urbana, IL 61801 (USA)

(Received May 27, 1992; accepted July 15, 1992)

Abstract

The phase stability of the Ni-based compounds Ni_3Al, Ni_3Si, Ni_3Ga and Ni_3Ge was studied by calculating the total electronic energy in the $L1_2$ and $D0_{22}$ phases on the basis of the recursion method within the tight-binding approximation. A close relationship was observed between the total electronic energy difference of the $L1_2$ and $D0_{22}$ phases and the number of valence electrons in the Ni-based compounds as well as in Al-based ones, Al_3X (X = Ti, Y, Zr and Nb). For the Ni-based compounds, a structural change from $L1_2$ to $D0_{22}$ by alloying, in which Ni atoms are replaced by substitutional solute elements, is predicted.

Introduction

Several attempts have been made to understand the structural stability of the Al_3X and Ni_3X (X is metalloid or metal) intermetallic compounds through calculations of electronic structures using various methods [1–8]. For example, Guo *et al.* [5] and Sluiter *et al.* [6] used a full potential linear augmented plane-wave (FLAPW) method to study the relationship between phase stability, bonding nature and mechanical properties for Al_3Li; Xu and Freeman [3] used a linear muffin-tin orbital method associated with the atomic-sphere approximation to study Al_3X (X = Y, Zr) and Ni_3V. Moreover, Freeman's group proposed a criterion for phase stability based upon their theoretical work using the linear muffin-tin orbital (LMTO) method [3, 4].

Recently, Inoue *et al.* [8] have studied the phase stability of Al_3Nb as a function of Ni addition and of Al_3Ti using the extended Hückel tight-binding (XHTB) method developed by Kitamura and Muramatsu [9]. Results obtained were in good agreement with experiment. This indicates that the XHTB band structure calculation is a useful tool for studying the phase stability of intermetallic compounds. Intermetallic compounds such as aluminides and silicides have attracted much attention lately; their relatively high melting points, together with other attributes such as low density, high strength and good corrosion resistance, make them highly promising as high-temperature structural materials. The biggest drawback of intermetallics is their brittle nature. Therefore, finding ways to improve their ductility is an important area of alloy development. One of the approaches to ductilize these intermetallics is to promote a structural transformation to a structure with higher symmetry, such as an ordered $L1_2$ structure. This gave us the impetus to investigate the phase stability in Ni-based intermetallic compounds.

We investigated the phase stability of intermetallic compounds Ni_3X (X = Al, Si, Ga and Ge) and Al_3X (X = Ti, Y, Zr and Nb) using a recursion tight-binding (RTB) method [11] focusing our attention on the tetragonal $D0_{22}$ and the cubic $L1_2$ phases. For the former compounds we also considered the possible structural change caused by alloying in which Ni atoms are replaced by substitutional solute elements. The advantage of the recursion tight-binding method based on a cluster calculation is that it does not use the Bloch theorem, so the method can be applied to disordered systems [11]. It has the further advantage that one can easily calculate the density of states, unlike the band structure calculations based on the Bloch

*Present address: Department of Physics, University of Yeongnam, Kyungsan 713-749, South Korea.

0254-0584/93/$6.00

theorem. In this paper, we wish to demonstrate that the recursion tight-binding method works well in treating the phase stability of intermetallic compounds.

Calculational procedure

We briefly describe the essence of the recursion method (see ref. 11 for details). In this method the local density of states $\rho(E, r_i)$ at site r_i is expressed as

$$\rho(E, r_i) = -(1/\pi) \lim_{\epsilon \to 0} \operatorname{Im} G(E + i\epsilon, r_i) \tag{1}$$

Here $G(z, r_i)$ is Green's function, which can be represented by a continued fraction involving the recursion coefficients a_n and b_n:

$$G(z, r_i) = \cfrac{1}{z - a_0 - \cfrac{b_1^2}{z - a_1 - \cfrac{b_2^2}{\ddots}}} \tag{2a}$$

where the recursion coefficients a_n and b_n satisfy the following recursion relation:

$$H|u_n\rangle = a_n|u_n\rangle + b_{n+1}|u_{n+1}\rangle + b_n|u_{n-1}\rangle \tag{2b}$$

Here H is a one-electron Hamiltonian, and $\{u_n\}$ denotes the orthonormal basis set, which tridiagonalizes the Hamiltonian matrix consisting of elements $\langle\phi_\mu|H|\phi_\nu\rangle$ between atomic orbitals ϕ_μ and ϕ_ν. Suffixes μ and ν indicate atom sites.

The total electronic energy E_{total} can be calculated as

$$E_{\text{total}} = \sum_{r_i} \int_{-\infty}^{E_F} E\rho(E, r_i)\, dE \tag{3}$$

where summation over r_i is taken for all inequivalent sites in the unit cell, and E_F denotes the Fermi energy.

TABLE 1. Lattice constants (Å) used in this work

Compound	$L1_2$	$D0_{22}$		Ref.
	a	a	c	
Al_3Ti	3.968	3.848	8.585	8
Al_3Y	4.275	4.123	9.194	4
Al_3Zr	4.073	3.928	8.759	4
Al_3Nb	3.991	3.845	8.601	4
Ni_3Al	3.570	3.570	7.140	15
Ni_3Si	3.507	3.507	7.014	15
Ni_3Ga	3.582	3.582	7.164	15
Ni_3Ge	3.567	3.567	7.134	15

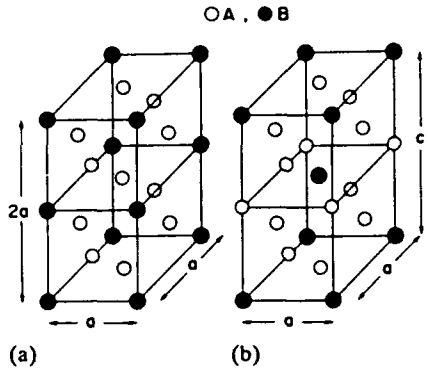

Fig. 1. Crystal structures for A_3B compounds: (a) cubic $L1_2$; (b) tetragonal $D0_{22}$.

We need to evaluate the Hamiltonian matrix elements such as $\langle\phi_\mu|H|\phi_\mu\rangle$ between orbitals on the same atom, and ones such as $\langle\phi_\mu|H|\phi_\nu\rangle$ between orbitals on nearest-neighbor atoms. The former corresponds to the on-site atomic energy (ϵ_{nl}), whereas the latter corresponds to the hopping energy (ϵ_{hop}) of an electron from atom to atom. We use the atomic energy values obtained from a self-consistent field calculation based on the prescription of Herman and Skillman [12] using Schwarz exchange-correlation parameters [13], and ϵ_{hop} values obtained from universal parameters proposed by Harrison [14]. We have treated clusters of 2046 atoms for all the compounds investigated here, taking a recurrence chain length as $L = 17$. Gaussian quadrature was used when integration was involved, such as in eqn. (3). We checked the convergence of E_{total}, varying L from 15 up to 25, and found that sufficient convergence is obtained at $L = 17$. The total energies of each compound in the $D0_{22}$ and $L1_2$ structures were calculated for a given lattice constant. Experimentally obtained lattice constants were used for stable phases, and for the other virtual phases theoretical values, determined by Xu and Freeman [3], were used. For Ni-based compounds, however, there are no theoretical data available. We therefore set the value of the c/a ratio of $D0_{22}$ to be 2, since this is close to the experimental values of 2.037 in Ni_3V and 2.055 in Ni_3Ta [15]. The lattice parameters used are listed in Table 1. Crystal structures for $L1_2$ and $D0_{22}$ are shown in Fig. 1.

Results and discussion

In order to verify the validity of our approach, based on the RTB method, we chose Al_3Nb and Al_3Ti as test cases. Results for E_{total} obtained using

TABLE 2. Total electronic energy E_{total} in eV per unit cell and the energy difference $\Delta E = E_{total}(L1_2) - E_{total}(D0_{22})$ in eV per atom for the Al-based compounds

Compound	$E_{total}(L1_2)$	$E_{total}(D0_{22})$	ΔE	Ref.
Al_3Ti	−270.085	−271.324	+0.155	this work
			+0.19	8
			+0.06	2
			+0.05	4
			+0.025	7
Al_3Y	−267.784	−266.797	−0.123	this work
			−0.115	2
			−0.115	3
Al_3Zr	−269.015	−269.662	+0.081	this work
			+0.03	2
			+0.01	3
Al_3Nb	−273.143	−274.662	+0.19	this work
			+0.79	8
			+0.20	2
			+0.265	3

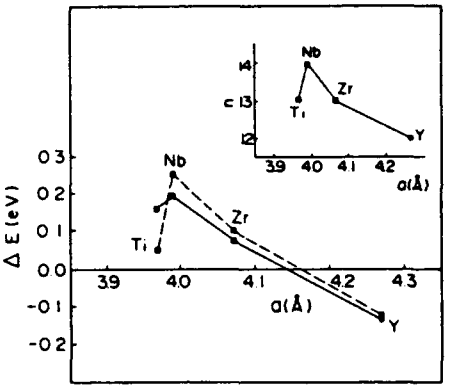

Fig. 2. Total energy difference ΔE between the $L1_2$ and $D0_{22}$ phases for Al-based compounds as a function of the lattice constant in the $L1_2$ phase. The solid line denotes the present results; the dashed line, the results of Freeman's group [3, 4]. The insert shows the number of valence electrons (n) for the compounds.

the same lattice constants and the same atomic orbitals as in ref. 8 are tabulated in Table 2 along with the results for other compounds investigated in this study and the results obtained by other researchers [2–4, 7, 8]. The atomic orbitals used were Al 3s and 3p, Ti 3d and 4s, and 4d and 5s of Y, Zr and Nb. Our results for the energy difference between the $D0_{22}$ and $L1_2$ phases show that the $D0_{22}$ phase is stable against the $L1_2$ phase in both compounds, in agreement with experiment [16]. Our value of the energy difference per atom for Al_3Ti is in good accord with that of Inoue *et al.* [8], who used the XHTB method, but differs by factors of 2.5 and 6, respectively, from those obtained by Carlsson and Meschter [2] using an augmented spherical-wave (ASW) method and by Fu [7] using the FLAPW method.

For Al_3Nb the energy difference per atom is about one half of the value obtained by Xu and Freeman [3] using the LMTO method; it is a factor of 4 smaller than the value of Inoue *et al.* [8] using the XHTB method. Nevertheless, the RTB method does correctly predict the stability of the $D0_{22}$ phase against the $L1_2$ phase in Al_3Ti and Al_3Nb.

Al-based compounds

In Fig. 2, the values of the energy difference ($\Delta E \equiv E_{total}(L1_2) - E_{total}(D0_{22})$) per atom between the $D0_{22}$ and $L1_2$ phases for various Al-based compounds are shown together with the values obtained by Freeman's group [3, 4]. The compounds are arranged on the abscissa in Fig. 2 in such a way that their lattice constants in the $L1_2$ phase increase from left to right. Although our results are not in complete agreement with those of Freeman's group [3, 4], we nevertheless are satisfied with our approach, because – within the framework of the tight-binding approximation – we can reproduce results derived from much more sophisticated calculations based on the LMTO method. The insert in Fig. 2 indicates the number of valence electrons (n) versus the lattice constant. It is seen that the change in n correlates with the change in ΔE, particularly for the results of Freeman's group. Xu and Freeman [3] have pointed out that the structural stability of these Al-based compounds can be adequately explained in terms of a simple rigid-band concept.

Ni-based compounds

Before presenting the results for phase stability, let us check the results for the density of states (DOS), which is an important quantity in determining whether or not a phase is stable. Tanaka *et al.* [17] studied valence electronic structures of Ni_3Si using soft-X-ray spectroscopy. They measured Si Kβ and Ni L_3 emission spectra, which reflect the partial densities of states (PDOS) of Si p and Ni d states, respectively, as well as the self-absorption spectrum corresponding to the Ni L_3 emission. The latter measurement allowed them to determine the Fermi energy.

In the Ni-based compounds, empty orbitals were used in addition to the occupied orbitals, namely the Ni 3d, 4s and 4p orbitals and the 3s (4s), 3p (4p) and 3d (4d) orbitals of Al (Ga) and Si (Ge). Otherwise we could not reproduce the experimentally determined energy separation [17] between the peak of the Ni L_3 emission spectrum and the Fermi energy in Ni_3Si. In order to take

the d states into account, it is necessary to know the values of the parameter r_d characterizing a length of the d state [14], which enter into the expression for the hopping energy of an electron between different sites. However, the r_d value for the empty d states is not known, so we estimated it by extrapolation from known values. The known values [14] of r_d for transition metals are plotted against the metallic bonding radius (r_B) proposed by Pauling [18] in Fig. 3, where the dashed curves denote the extrapolation. We inferred that Al and Si atoms, which have values of 1.375 and 1.429 Å for r_B, should be located on the extrapolated curve for the 3d transition metal series, and that Ga ($r_B = 1.404$ Å) and Ge ($r_B = 1.444$ Å) should be located on the curve for the 4d transition metal series. The adopted values of r_d are 0.59, 0.60, 0.91 and 0.89 for the empty d states of Al, Si, Ga and Ge, respectively. The PDOS calculated by the RTB method are compared with the experimental Ni L_3 and Si Kβ emission spectra of Tanaka *et al.* [17] in Fig. 4, where the results for Si p-PDOS obtained using another value of r_d are also shown. Both values of r_d gave almost the same results for the Ni d-PDOS, but different results for the Si p-PDOS with respect to its peak position, as seen from Fig. 4. This is the reason why we adopted a smaller r_d value. The peak positions of the Ni d- and Si p-PDOS calculated using $r_d = 0.60$ agree well with experiment [17]. The low-energy side of the PDOS for the Si p state deviates considerably from the experimental results. The reason for this deviation seems to lie in the tight-binding approximation. We should note that the Ni d-PDOS is dominant, being much larger than the Si p-PDOS by an order of magnitude. Therefore, the deviation in the low-energy side of the Si p-PDOS causes little problem in a discussion of the total energy, which will be made below.

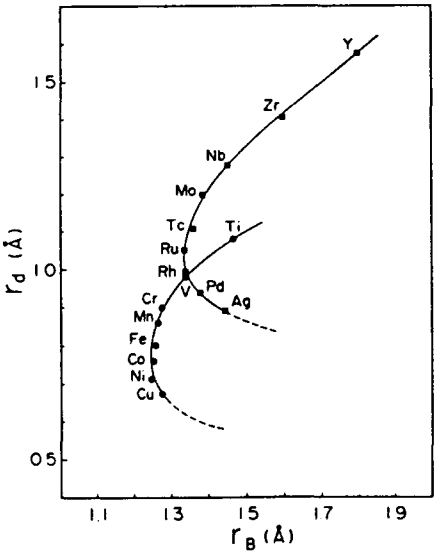

Fig. 3. The parameter r_d for transition metals vs. metallic bonding radius r_B: (●) 3d transition metals; (■) 4d transition metals. The dashed curves are extrapolated so as to form smooth lines. The r_d values are from ref. 14; r_B values from ref. 18.

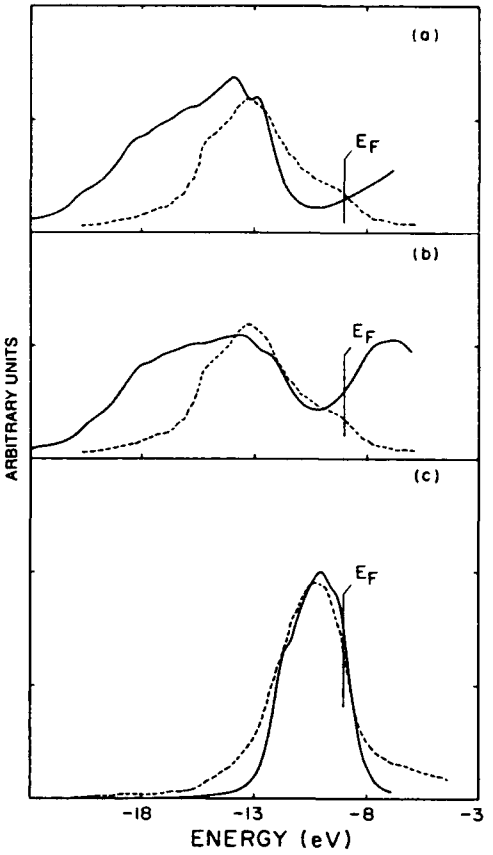

Fig. 4. Calculated Ni d-PDOS and Si p-PDOS (solid curves) for Ni_3Si compared with Ni L_3 and Si Kβ emission spectra (broken curves), respectively. (a) Si p-PDOS calculated using $r_d = 1.0$; (b) Si p-PDOS calculated using $r_d = 0.60$; (c) Ni d-PDOS calculated using $r_d = 0.60$. Emission spectra taken from ref. 17.

TABLE 3. Total electronic energy E_{total} in eV per unit cell and the energy difference $\Delta E = E_{total}(L1_2) - E_{total}(D0_{22})$ in eV per atom for the Ni-based compounds

Compound	$E_{total}(L1_2)$	$E_{total}(D0_{22})$	ΔE
Ni_3Al	−785.944	−785.857	−0.011
			−0.045[a]
Ni_3Ga	−791.825	−791.759	−0.008
Ni_3Si	−821.135	−821.054	−0.010
Ni_3Ge	−819.906	−819.835	−0.009

[a]Ref. 1.

The results for the total energy E_{total} for the Ni-based compounds are listed in Table 3, and a plot of the total energy difference ΔE (the same

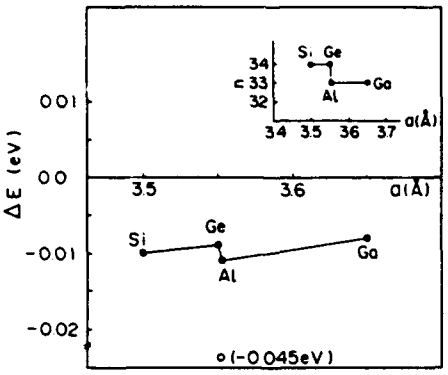

Fig. 5. Total energy difference ΔE between the $L1_2$ and $D0_{22}$ phases for Ni-based compounds as a function of the lattice constant. The result for Ni_3Al obtained by Xu *et al.* [1] is shown as an open circle for comparison. The insert is the same as in Fig. 2.

plot as that for the Al-based compounds) is shown in Fig. 5, where the result for Ni_3Al obtained by Xu *et al.* [1] is also illustrated for comparison. On the basis of our results the $L1_2$ phase is predicted to be stable in Ni_3Al, Ni_3Ga, Ni_3Si and Ni_3Ge. This is consistent with experiment [16]. The ΔE value for Ni_3Ga is the smallest of the four Ni-based compounds. The variation in the value of ΔE from compound to compound seems to be related to the number of valence electrons (n), illustrated in the insert in Fig. 5. We note that ΔE for the Ni-based compounds is smaller by an order of magnitude than that for the Al-based compounds. Therefore no marked difference in the total density of states (TDOS) between the $D0_{22}$ and $L1_2$ phases was observed. The TDOS of the Ni-based compounds are very similar to each other: they have a main peak located at -10.07 eV, corresponding to the atomic 3d level of the Ni atom, with a shoulder at the Fermi energy side, their separation being 0.75 eV. This indicates that the rigid-band concept holds for the Ni-based compounds studied here, as it does for the Al-based compounds, as pointed out by Xu and Freeman [3]. In the following, let us compare the various calculations. The Fermi energies are -9.066 (-9.068), -9.062 (-9.071), -8.812 (-8.806) and -8.852 (-8.859) eV for the $L1_2$ ($D0_{22}$) phases of Ni_3Al, Ni_3Ga, Ni_3Si and Ni_3Ge, respectively; and their densities of states at the Fermi energy are 1.67 (1.70), 1.56 (1.60), 1.29 (1.30) and 1.23 (1.25) (states eV^{-1} $atom^{-1}$). The TDOS of the Ni_3Si and Ni_3Ge group are to be compared with those of Ni_3Al and Ni_3Ga, since the former group has one more electron than the latter group per formula unit. The shift of E_F in Ni_3Si from E_F in Ni_3Al is about 0.25

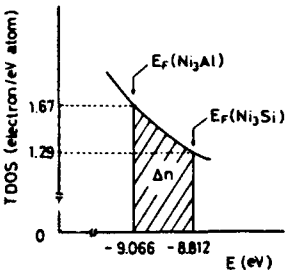

Fig. 6. Illustration of Δn for the case of Ni_3Si and Ni_3Al. The curve is the TDOS for the $L1_2$ phase. We note that the TDOS of Ni_3Si and Ni_3Al are hardly distinguishable from each other.

($=9.066-8.812$) eV in the $L1_2$ phase and about 0.21 ($=9.062-8.852$) eV for Ni_3Ge and Ni_3Ga. Therefore the number of electrons accommodated in this shifted energy range, Δn, is approximately $\Delta n = (1.67+1.29)\times 0.25/2 = 0.37$ (electron $atom^{-1}$) for Ni_3Si and $(1.56+1.23)\times 0.21/2 = 0.29$ (electron $atom^{-1}$) for Ni_3Ge. Figure 6 illustrates Δn for the case of Ni_3Si and Ni_3Al. These values are close to 1 electron per formula unit, which is equal to 1/4 (electron $atom^{-1}$). We note that in the Al-based compounds the number of electrons accommodated in the energy range shifted in going from Al_3Y to Al_3Zr is about 0.36 (electron $atom^{-1}$), and it is about 0.19 (electron $atom^{-1}$) between Al_3Zr and Al_3Nb. These values are interpreted from Fig. 3 in ref. 3.

Under the assumption that the rigid-band approximation holds, we made an attempt to examine how ΔE varies with the change in the number of valence electrons n and to investigate whether the structural change from $L1_2$ to $D0_{22}$ occurs by elemental addition of atoms such as Co and Cu into Ni-based compounds. We calculated $\Delta E(n)$, defined below, as a function of n, assuming the rigid-band approximation:

$$\Delta E(n) = \int_{-\infty}^{E_F^L(n)} E D_L(E)\,dE - \int_{-\infty}^{E_F^D(n)} E D_D(E)\,dE \qquad (4a)$$

where $D_L(E)$ and $D_D(E)$ are the total densities of states for the $L1_2$ and $D0_{22}$ phases; $E_F^L(n)$ and $E_F^D(n)$ denote the Fermi energy determined as a function of n in the $L1_2$ and $D0_{22}$ phases as follows:

$$n = \int_{-\infty}^{E_F^L(n)} D_L(E)\,dE = \int_{-\infty}^{E_F^D(n)} D_D(E)\,dE \qquad (4b)$$

The calculated values of $\Delta E(n)$ are shown in Fig. 7. The value of ΔE for Ni_3Al and Ni_3Ga, whose constituent atoms belong to the same group, increases and changes sign with increasing n, while that for Ni_3Si and Ni_3Ge, belonging to the same

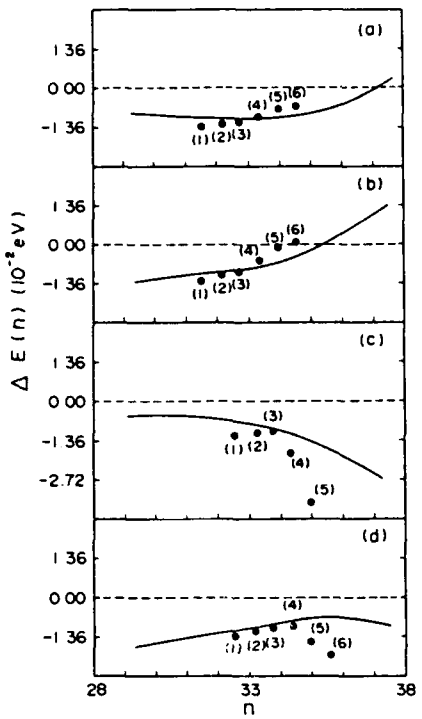

Fig. 7. The results for eqn. (4), which indicates the variation of the total energy difference $\Delta E(n)$ between the $L1_2$ and $D0_{22}$ phases with the number of valence electrons n in the rigid-band approximation: (a) Ni_3Al; (b) Ni_3Ga; (c) Ni_3Si; (d) Ni_3Ge. The results of model calculations (see text for details) are also shown using solid circles: (1) 50% Co; (2) 30% Co; (3) 10% Co; (4) 10% Cu; (5) 30% Cu; (6) 50% Cu.

group, does not change sign in the range of n investigated. It follows that in the former group there is a possibility of structural change by addition of Co and Cu, whereas in the latter group such a possibility is unlikely. We are interested in alloying in which Ni atoms are replaced by substitutional solute elements. However, we should note that the results obtained in the rigid-band approximation do not reflect the effect of site preference of solute elements, depending only on the change in the number of valence electrons. Therefore, in the following we will try to do a model calculation in which we can specify the sites at which the solute elements substitute.

It is not difficult to carry out actual calculations for the compounds with alloying. However, there are so many possible configurations to be taken into account that a large computational time is required. Instead of doing rigorous calculations for each configuration, we performed a model calculation in which the effect of alloying is assumed to be represented by a change in the nature of the atoms caused by the replacement of Ni atoms by substitutional solute elements. Let us remember here that in our present treatment atomic properties are completely characterized by atomic energies and Harrison's universal parameters [14]. For example, in the case of $[Ni_{1-x}Cu_x]_3Al$, where $x\%$ Cu atoms substitute for Ni sites, we thus assign a virtual atom in all Ni sites. This virtual atom is made in such a way that its atomic properties are defined by a virtual crystal approximation for describing disordered systems. For instance, the on-site atomic energy ϵ_{nl} for a virtual atom is given by $x\epsilon_{nl}(\mathrm{Cu}) + (1-x)\epsilon_{nl}(\mathrm{Ni})$. We assume that all other atomic values, such as hopping energies, are defined by Vegard's rule. We have performed the calculations for the total energy, choosing Co and Cu atoms as alloying elements substituting Ni atoms. The results are compared with the values predicted by the rigid-band approximation in Fig. 7. The addition of 50% Co shifts E_F to the low-energy side by about 0.2 eV, and the addition of 50% Cu causes a shift in E_F of about +2.0 eV for all Ni-based compounds investigated here. Model calculations show a variation in ΔE qualitatively similar to that in the rigid-band approximation. Our model is not exact, as it involves some assumptions, but we believe that it provides a qualitatively accurate picture concerning phase stability in the case when substitutional atoms are added to replace Ni atoms.

Conclusions

We studied the phase stability of Ni-based compounds Ni_3X (X = Al, Si, Ga and Ge) as well as Al-based ones Al_3X (X = Ti, Y, Zr and Nb) using the recursion method within the tight-binding approximation. When our results were compared with previous studies, it was found that the value of the total electronic energy difference ΔE $[= E_{\mathrm{total}}(L1_2) - E_{\mathrm{total}}(D0_{22})]$ between the $L1_2$ and $D0_{22}$ phases is correlated with the number of valence electrons in both the Al- and Ni-based compounds. We also investigated how ΔE varies when substitutional solutes are added to the Ni-based compounds in the rigid-band approximation and performed a model calculation in which the effect of solute addition was expressed by a change in the atomic nature of the host atoms. Qualitatively, the same results were obtained from both the rigid-band approximation and the model calculation. They predict that there is a possibility for the structural change from $L1_2$ to $D0_{22}$ in Ni_3Al and Ni_3Ga, when solute atoms are added so as to substitute Ni atoms and increase the number of valence electrons.

Acknowledgement

One of the authors (H.C.) would like to acknowledge the US Dept. of Energy (Contract No. DEFG02-91ER45439) for supporting his contributions to this investigation.

References

1 J.-H. Xu, T. Oguchi and A. J. Freeman, *Phys. Rev. B, 36* (1987) 4186.
2 A. E. Carlsson and P. J. Meschter, *J. Mater. Res., 4* (1989) 1060.
3 Jian-hua Xu and A. J. Freeman, *Phys. Rev. B, 40* (1989) 11927.
4 T. Hong, T. J. Watson-Yang, A. J. Freeman, T. Oguchi and Jian-hua Xu, *Phys. Rev. B, 41* (1990) 12462.
5 X.-Q. Guo, R. Podloucky, Jian-hua Xu and A. J. Freeman, *Phys. Rev. B, 41* (1990) 12432.
6 M. Sluiter, D. de Fontaine, X. Q. Guo, R. Podloucky and A. J. Freeman, *Phys. Rev. B, 42* (1990) 10460.
7 C. L. Fu, *J. Mater. Res., 5* (1990) 971.
8 H. R. P. Inoue, M. Kitamura, C. M. Wayman and H. Chen, *Philos. Mag. Lett., 63* (1991) 345.
9 M. Kitamura and S. Muramatsu, *Phys. Rev. B, 41* (1990) 1158.
10 J. A. Anderson, H. Chen and J. E. Epperson, *Metall. Trans. A, 23* (1992) 769.
11 V. Heine, in H. Ehenriech, F. Seitz and D. Turnbull (eds.), *Solid State Physics,* Vol. 35, Academic Press, New York, 1980.
12 F. Herman and S. Skillman, *Atomic Structure Calculations,* Prentice-Hall, Englewood Cliffs, NJ, 1963.
13 K. Schwarz, *Phys. Rev. B, 5* (1972) 2466.
14 W. A. Harrison, *Electronic Structure and the Properties of Solids,* Freeman, New York, 1980.
15 The Japan Institute of Metals (ed.), *Data Book for Metals* (in Japanese), Maruzen, Tokyo, 1974.
16 P. Villars, K. Mathis and F. Hullinger, in F. R. de Boer and D. G. Pettifor (eds.), *The Structure of Binary Compounds,* North-Holland, Amsterdam, 1989.
17 K. Tanaka, T. Saito, K. Suzuki and R. Hasegawa, *Phys. Rev. B, 32* (1985) 6853.
18 L. Pauling, *The Nature of the Chemical Bond,* Oxford Univ. Press and IBH, New Delhi, 1960.

Accepted abstract for the International Conference on Solid to Solid Phase Transformations, Pittsburgh, PA July,1994.

The Mechanism of the Tetragonal to Monoclinic Transformation in $YNbO_4$

J. L. SHULL, B. N. Sun, and W. M. Kriven, Department of Materials Science and Engineering, University of Illinois at Urbana-Champaign, Urbana, IL 61801.

The tetragonal (scheelite) and monoclinic (fergusonite) phases of yttrium niobate ($YNbO_4$) have been shown to be structurally analogous to the tetragonal and monoclinic phases of zirconia. In yttrium niobate, however, the tetragonal to monoclinic transformation occurs at approximately 810°C compared to 950°C for zirconia. The mechanism of the transformation in yttrium niobate also appears to be quite different from that of zirconia. Other investigators have observed that extensive cracking does not occur in yttrium and other rare earth niobates when they are cooled through the transformation. This suggests that there is no discontinuous volume change associated with the transformation in $YNbO_4$ as there is in zirconia. In this study the authors have attempted to verify the order of the transformation and determine the actual transformation mechanism.

Powders of $YNbO_4$ were prepared using a chemical synthesis method, and these were used to fabricate polycrystalline yttrium niobate disks. Single crystals of $YNbO_4$ were also grown using the Czocharlski technique. The tetragonal $\rightarrow$ monoclinic and monoclinic $\rightarrow$ tetragonal transformations were observed directly using hot stage optical microscopy of single crystal $YNbO_4$ and hot stage TEM studies of polycrystalline $YNbO_4$. The transformation was also studied using high temperature thermal analysis (dilatometry and differential scanning calorimetry) and high temperature x-ray diffraction.

High Temperature Phase Transformation in $Y_4Al_2O_9$, $Gd_4Al_2O_9$, and $Dy_4Al_2O_9$, J. L. SHULL and W. M. Kriven, Department of Materials Science and Engineering, University of Illinois at Urbana-Champaign, Urbana, IL 61801.

Some dilanthanide aluminates ($2Ln_2O_3 \cdot Al_2O_3$, where Ln = Y and Tb) have been observed to undergo first order displacive phase transformations at temperatures above 1000°C. These transformations are characterize by a thermal hysteresis of ~90°C and a volume increase on cooling of approximately 0.7%. The low temperature phase has a monoclinic structure, but the high temperature phase has yet to be determined. It is believed that similar phase transformations also exist in dysprosium and gadolinium aluminate. In this study the authors have attempted to determine the high temperature crystal structure and characterize the transformation mechanism.

Single phase homogeneous powders of $Y_4Al_2O_9$, $Gd_4Al_2O_9$, and $Dy_4Al_2O_9$, were synthesized using a chemical preparation method. These powders were studied as powders and were used to make polycrystalline material. High temperature thermal analysis (DSC and dilatometry) was used to determine the exact transformation temperatures, thermal hystereses, and volume changes. High temperature x-ray diffraction was used to determine the crystal structure of the high temperature phase. The phase transformation was observed by in-situ TEM studies and by hot stage polarized reflected light microscopy.

Accepted abstract for the International Conference on Solid to Solid Phase Transformations, Pittsburgh, PA July,1994.

STRUCTURAL RELAXATIONS IN THE GHz FREQUENCY RANGE IN GLASS FORMING SILICATE MELTS

JOHN E. MASNIK*, J. KIEFFER* AND J.D. BASS**
*Department of Materials Science & Engineering, University of Illinois, Urbana IL 61801
**Department of Geology, University of Illinois, Urbana IL 61801

ABSTRACT

The Brillouin light scattering technique is used for the investigation of structural relaxations in glass-forming liquids at high temperatures. From the analysis of the line shapes of Rayleigh and Brillouin peaks, the friction coefficients, which are associated with the atomic scale mechanisms of the structural relaxations in these systems, are determined. Results for a series of K_2O-SiO_2 compositions, which were chosen as model substances, are reported. As a function of temperature, maxima in the Brillouin line widths were observed, which reflect resonant conditions of molecular scale structural motions, where the relaxation time is of the order of the reciprocal Brillouin frequency shift. Due to thermal activation of the component mobilities, different relaxation mechanisms couple at different temperatures. Typically, at least one strongly absorbing regime is observed in between the glass transition and the equilibrium melting temperatures. The prominence of this regime decreases with increasing silica concentration. The friction coefficients approach the hydrodynamic viscosity in the high temperature limit, when the relaxation times become short in comparison with the time scale of the Brillouin shift.

INTRODUCTION

The predominant method for the production of glassy materials is the melt processing. There is much incentive for a better understanding of the visco-elastic behavior of glass forming substances at stages just before the structural constituents become trapped in their final structural state.

The formation of amorphous solids is the result of a kinetic arrest of structural relaxations. As the mobilities of molecular particles decrease, their motion becomes correlated with that of an increasing number of neighboring particles. The structural changes in the glass forming liquids and the dynamic response of their molecular constituents are closely coupled.

Relaxational spectroscopy has long been recognized as a powerful method for the investigation of complex structures.[1] The actuation of structural components into forced vibration can be done by direct mechanical coupling,[2-4] or through the intermediate of dielectric polarization.[5-7] In the latter case, one takes advantage of the polarized nature of atomic constituents of the structure and induces small scale deformation by applying an alternating electric field. This field can be established between electrically conducting electrodes or in the form of electromagnetic radiation. By changing the frequency of the applied force, one can create resonant conditions for various relaxation mechanisms and determine the characteristic relaxation times of these processes.

At temperatures above the glass transition, the size of structural features, that are likely to form by stochastic fluctuations and that act as nuclei for crystallization, varies between several and a few hundred nanometers. Since the density fluctuations can propagate with the velocity of sound, the lifetime of the clusters can be as short as picoseconds. The expected time and length scales suggests the Brillouin light scattering technique as the suitable tool of investigation, since it covers the frequency range between 10^9 and 10^{11} Hz.

RELAXATIONAL SPECTROSCOPY

When imposing constraints onto a visco-elastic substance that cause it to deviate from its current equilibrium, the system responds by flowing to a new equilibrium situation. If the imposed constraint oscillates with time, the relaxational behavior can be characterized by comparing the phase shift between the excitation and its response. In the limit of very small deformations, which may be localized within several interatomic distances, the reaction of the structure to the imposed

Mat. Res. Soc. Symp. Proc. Vol. 248. ©1992 Materials Research Society

constraint can be described by the response function, which is defined as the ratio between the magnitudes of a system variable, $X(\omega)$, and the exciting force, $F_0(\omega)$:

$$\frac{X(\omega)}{F_0(\omega)} = \mu^*(\omega) = \sum_j \frac{g_j}{\omega_{0,j}^2 - \omega^2 - i\omega\nu_j} = \sum_j g_j \cdot \frac{\omega_{0,j}^2 - \omega^2 + i\omega\nu_j}{\left(\omega_{0,j}^2 - \omega^2\right)^2 + \omega^2\nu_j^2} \tag{1}$$

The two coefficients that are used to describe the dynamic response of the material are the elastic constant, expressed as the resonant frequency, ω_0, and the kinematic friction coefficient, ν. Both these coefficients are normalized with respect to the mass of structural feature whose response they describe. The summation in eq. (1) is carried over all structural details whose behavior may influence the dynamic variable and the g_i are weighting factors.

Much of the speculation during the analysis of relaxational spectra concerns the nature of the mechanisms that contribute to the energy dissipation and their relative importance. In the least number of cases all mechanisms are known with precision, such that an enumeration as in eq. (1) is not possible. An alternative form of writing this equation is by replacing the individual weighting factors, g_i, with a continuous distribution, $g(\nu)$, and the sum with an integral:

$$\mu^*(\omega) = \int_\nu g(\nu) \cdot \frac{\omega_0^2 - \omega^2 + i\omega\nu}{\left(\omega_0^2 - \omega^2\right)^2 + \omega^2\nu^2} d\nu \tag{2}$$

The result of this integration is the complex modulus , $\mu^*(\omega) = M' + iM''$, which can be divided into a real and an imaginary part.

When resonant conditions are established between the exciting probe and a sufficiently mobile structural feature, the imaginary part of this complex modulus, which represents the amount of energy that is exchanged, is at a maximum. Hence, by measuring the amount of energy that is absorbed due to internal friction as a function of the frequency , one can determine the friction coefficient. On an atomic scale the friction in a liquid structure is due to the momentum exchange during collisions between atoms. The atomic displacements are thermally activated, such that in a first approximation, one can assume an Arrhenius dependence, $\nu = \nu_0 \cdot e^{E_A/T}$, where E_A is the activation energy. By substituting this expression in eq. (2), one recognizes that any activated processes involved in the relaxation introduce a temperature dependence in the complex modulus:

$$\mu^*(\omega) = \frac{1}{T}\int_\nu g(E_A) \cdot \nu_0 \cdot e^{E_A/T} \cdot \frac{\omega_0^2 - \omega^2 + i\omega \cdot \nu_0 \cdot e^{E_A/T}}{\left(\omega_0^2 - \omega^2\right)^2 + \omega^2 \cdot \nu_0^2 \cdot e^{2E_A/T}} dE_A \tag{3}$$

The additional difficulty arises from the need for information concerning the distribution function $g(E)$. In the simplest case of a single energy activation, $g(E)$, assumes the form of a Dirac function. For more complex structural relaxation processes, activation energies are distributed over a band of energies. It is customary to assume empirical functions that provide a best fit of the experimental data.[1,8] The examination of complex modulus according to eq. (3) reveals that for each mode of the distribution function, $g(E)$, the imaginary part of μ^* exhibits a maximum somewhere on the temperature scale.

INELASTIC LIGHT SCATTERING

In this research we used the electric field of light to excite the structure of liquid silicate systems. The Brillouin technique consists in examining the energy changes of electromagnetic waves that scatter inelastically when passing through a dielectric substance. For a substance to scatter light, there need to be inhomogeneities of the dielectric constant, which can be realized by density fluctuations or fluctuations in the chemical composition. In a chemically homogeneous liquid, density fluctuations can exist due to changes in pressure and temperature. The density fluctuations

due to temperature, $(\partial\rho/\partial T)_p$, cannot propagate but disappear due to a large thermal conductivity, λ. This leads to Rayleigh scattering at the frequency of the incident light, ω. The density fluctuations due to pressure, $(\partial\rho/\partial p)_T$, can propagate with the velocity of sound, c_0. This leads to Brillouin scattering at frequencies which are Doppler shifted with respect to that of the incident light by $\pm q \cdot c_0$, where q is the wavevector of the elastic wave.

The relationships between ρ, T and p in a fluid phase can be established through the balance equations for mass (continuity), momentum (linearized Navier-Stokes) and energy (Fourier's second law). The simultaneous solution of these balance equations yields an expression for the density fluctuations, $\langle \rho(-q,0) \cdot \rho(q,t) \rangle$, which after Fourier transform yields the dynamic structure factor, $S(q,\omega)$.[9,10] The normalized scattering intensity can be expressed as a function of the wavevector, q, and the frequency, ω, as

$$\frac{S(q,\omega)}{S(q,0)} = (1-\gamma) \cdot \frac{q^2 \cdot \kappa/\rho_0 c_p}{\omega^2 + \left(q^2 \cdot \kappa/\rho_0 c_p\right)^2} + \frac{1}{\gamma}\left[\frac{q^2 \cdot \Gamma}{(\omega + c_0 q)^2 + (q^2\Gamma)^2} + \frac{q^2 \cdot \Gamma}{(\omega - c_0 q)^2 + (q^2\Gamma)^2}\right], \qquad (4)$$

where $\gamma = \frac{c_p}{c_v}$, $\Gamma = \frac{\left(\frac{4}{3}\eta_s + \eta_v\right)}{2\rho_0} + \left(\frac{\kappa}{\rho_0 c_p}\right) \cdot (\gamma - 1)$, ρ_0 is the average density, c_p and c_v are the heat capacities at constant pressure and constant volume. Based on this formalism, the spectrum of the scattered light can be analyzed in terms of the transport coefficients in the liquid.

EXPERIMENTAL

The glass melts were prepared from powders of fumed silica and alkali carbonates, with less than 0.1% total impurities. The powders were intimately mixed before they were melted in a small platinum crucible. After several hours of equilibration in air the sample holders were filled with material by simply dipping them into the liquid silicates. The sample holders consisted of platinum-rhodium wire, that was bent in form of a double-loop spiral. This form allowed for an optimal containment of the liquid with a minimum of surrounding material, and resulted in a minimal scattering from the platinum surface. The liquid assumes the shape of a slightly bulged cylinder of about 3 mm height and 4 mm diameter. The menisci that form at the surfaces, and through which the incident and scattered light passed were sufficiently flat to conserve the 90° scattering geometry (the light beam entered through the bottom and the scattered light was collected off the center of the side). For the scattering experiments, the samples were suspended in a small furnace which was heated by a platinum coil.

For the collection of spectra, the samples were heated to the highest temperature and subsequently cooled in steps of approximately 20°C. The samples were held at each temperature for a few minutes to assure thermal adjustment before spectra were measured. The incident light was produced by a single-mode Argon laser at a wavelength of 0.5145 μm. The scattered light was analyzed using a six pass Fabry-Perot tandem interferometer.[11] Using standard non-linear least squares procedures, the data was fit with eq. (4). In this study we were mostly interested in the viscosity coefficients, which are reflected in the full width at half height of the Brillouin peaks, according to

$$\Delta\omega_B = q^2 \cdot \Gamma = q^2 \cdot \left[\frac{\left(\frac{4}{3}\eta_s + \eta_v\right)}{2\rho_0} + \left(\frac{\kappa}{\rho_0 c_p}\right) \cdot (\gamma - 1)\right] \qquad (5)$$

The magnitude q of the wavevector describing the elastic wave is related to the scattering angle, θ, of the light according to $q = \frac{2\omega_L \cdot n}{c_L} \cdot \sin\theta/2$, where n is the refractive index of the medium, ω_L is the frequency and c_L is the velocity in vacuum of the incident light. The room temperature values for n at the various compositions were taken from the literature.[12] Based on observations on crystalline oxides,[13] the temperature dependence of n was assumed to be negligible within the accuracy of the present data.

RESULTS AND DISCUSSION

The data reported in fig. 1 corresponds to the reduced linewidth Γ of eq. (5), which has the dimension of a kinematic viscosity, but contains a contribution due to thermal conductivity. In principle, it would be possible to eliminate the broadening of the Brillouin peak due to thermal conductivity by using the width of the Rayleigh peak according to

$$\nu = \frac{(4\eta_s/3 + \eta_v)}{\rho_0} = \frac{2}{q^2} \cdot [\Delta\omega_B - \Delta\omega_R \cdot (\gamma - 1)]. \qquad (6)$$

The direct measurement of the widths of the Rayleigh peaks is encumbered due to the strong background from black body radiation and the presence of macroscopic defects such as bubbles in some melts. The procedure for the elimination of the background described by Krol et al.,[14] was not reliable for all our samples. For the purpose of consistency, we prefer to base our discussion on the Brillouin line widths Γ, which are a direct measure of the kinematic viscosities ν and include an unspecified background.

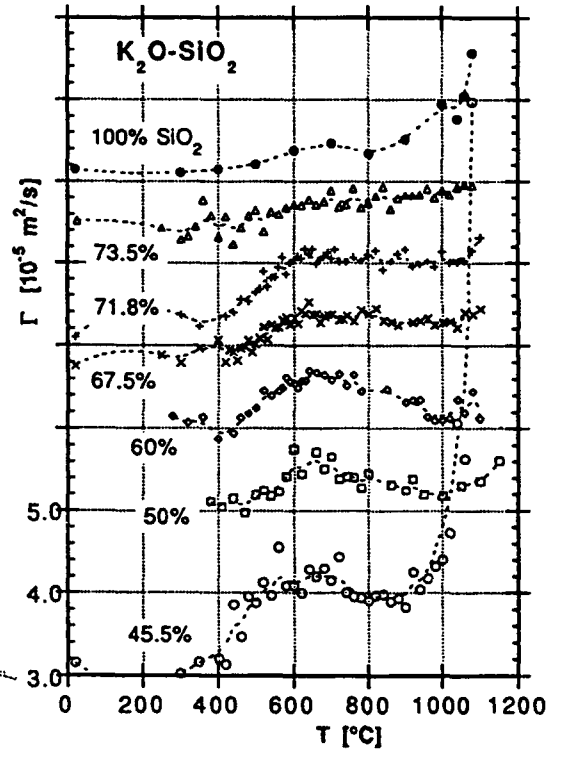

Fig. 1
Reduced Brillouin line widths Γ of amorphous K_2O-SiO_2 systems as a function of the temperature. The data for the different compositions, except for the lowest set, are offset to avoid overlaps, but they are all plotted on the same scale.

In fig. 1, we plotted the Γ values determined for a series of K_2O-SiO_2 compositions, including those for pure silica, as a function of the temperature. All measurements, except for those of pure silica, were taken in the sequence of decreasing temperatures. Γ increases with increasing temperature. This tendency reflects the increase of the mobility of structural components with increasing temperature, as it is expected for thermally activated transport mechanisms. With increasing temperatures, the relaxation times for the activated processes become smaller. When the relaxation times coincide with the reciprocal of the frequency of the light, the probe couples resonantly with the relaxation mechanism. In the limit of very high temperatures, where the relaxation time for hydrodynamic flow decreases below 10^{-10} sec, Γ reaches the value of the infinite frequency hydrodynamic viscosity. The friction coefficients determined for compositions with low silica concentrations show a tendency to rapidly increase at temperatures above 1100°C. This indicates that they approach the high temperature limit, where they coincide with the hydrodynamic viscosities of these liquids.

At temperatures around 650°C, the alkali-rich supercooled liquids show a small maximum in the friction coefficients. The prominence of this maximum is reduced with increasing silica concentration, and tends to disappear above 73% silica. This maximum indicates the activation of a dissipative process in the supercooled silicates. Its appearance is related to the abundance of the potassium cations, which suggests cation diffusion as the mechanism that is predominantly responsible for the energy dissipation at these temperatures. In fig. 2, we compare the friction coefficients for the K_2O-SiO_2 and the Na_2O-SiO_2 systems with comparable silica concentrations. It appears that the viscous dissipation in the sodium silicate is significantly stronger than in potassium silicate, which may reflect a higher cation mobility in the first system.

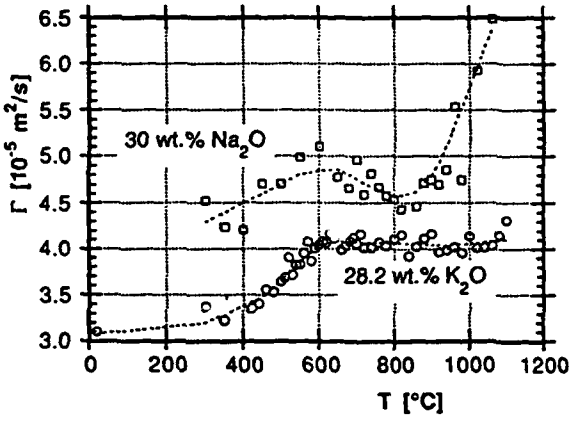

Fig. 2

Comparison between the reduced Brillouin line widths Γ for similar compositions of the systems K_2O-SiO_2 and Na_2O-SiO_2.

In fig. 3, we compare the Brillouin frequency shifts $q \cdot c_0$ for the series of K_2O-SiO_2 compositions as a function of temperature. This shift is proportional to the hypersonic velocity and is a measure for the isothermal compressibility of the substance. We notice that for pure silica the shifts, which were measured in sequence of increasing temperature, increase with increasing temperature. This behavior was also found by Krol et al.[14] In the supercooled melts, the opposite tendency is observed, at least until the glass transition temperature is reached. The kinks in the curves of fig. 3 indicate the glass transition temperature,[15,16] where the elastic properties change discontinuously. For binary systems we find the highest glass transition temperature at the composition with 67.5% SiO_2. However, the temperature dependence of the hypersonic velocity varies continuously with the increase of the silica concentration. The slope gradually decreases and the composition with 73.5% SiO_2 shows a negative temperature dependence below the glass transition, similar to pure SiO_2. Hence, with decreasing alkali cation concentration the formation of a silica network, which determines the elasto-mechanical properties of the glass, is carried to a higher degree of completion.The trends in the data on fig. 3 also provide room for the speculation

that with decreasing temperature, the cyclization of the silica network progresses until the glass transition temperature is reached.

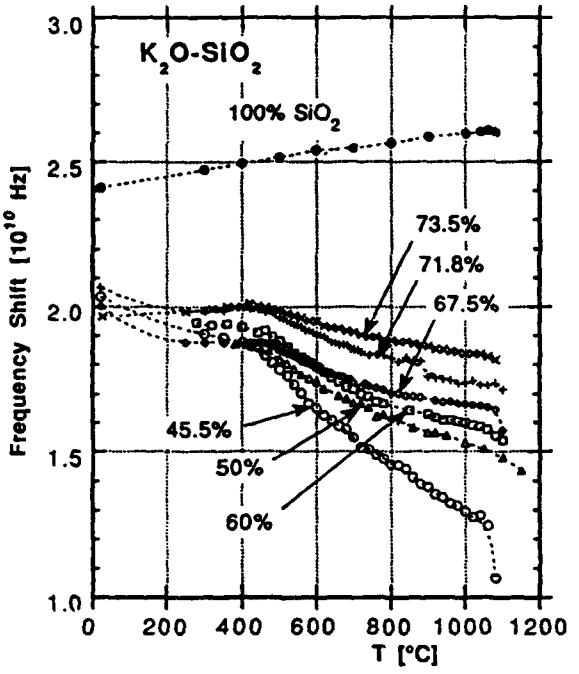

Fig. 3

Brillouin frequency shifts of amorphous K_2O-SiO_2 systems as a function of the temperature.

Acknowledgements

We appreciate the support of the National Science Foundation under the grants. DMR MSS-9008918 and EAR 90-18676, and of the Air Force Office of Scientific Research.

References:

[1] J. Wong and C.A. Angell in "Glass – Structure by Spectroscopy" (M. Decker 1976)
[2] D.E. Day in "Amorphous Materials" (J. Wiley & Sons 1972)
[3] J. DeBast and P. Gilard, Glastech. Ber. 37, 177 (1964)
[4] J.J. Mills, *J. Non-Cryst. Solids* 14, 255 (1974)
[5] C.P. Smyth, "Dielectric Behavior and Structure" (McGraw-Hill 1955)
[6] P.B. Macedo, C.T. Moynihan and R. Bose, *J. Phys. Chem. Glasses* 13, 171 (1972)
[7] V. Provenzano, L.P. Boesch, V. Volterra, C.T. Moynihan and P.B. Macedo, *J. Amer. Cer. Soc.* 55, 492 (1972)
[8] L. Börjesson, L.M. Torell and W.S. Howells, *Phil. Mag.* B59, 105 (1989)
[9] D.A. McQuarrie, "Statistical Mechanics", (Harper & Row 1976)
[10] J. Schroeder in "Treatise on Materials Science and Technology" vol. 12 (Academic Press 1977) p. 157
[11] J.R. Sandercock in "Light Scattering in Solids III", Topics in Applied Physics Vol 51, M. Cardona and G. Günherodt, eds., p 173 (Springer)
[12] A. Paul "Chemistry of Glass", Chapman & Hall 1990
[13] E.S. Zouboulis and M. Grimsditch, *J. Geophys. Research* 96, 4167 (1991)
[14] D.M. Krol, K.R. Lyons, S.A. Brawer and C.R. Kurkjian, Phys. Rev. B33 4196 (1986)
[15] J. Lordsch, M. Couzi, J. Pelous, R. Vacher and A. Levasseur, *J. Non-Cryst. Solids* 69, 1 (1984)
[16] P.J. Caroll and G.D. Patterson *J. Chem. Phys.* 81, 1666 (1984)